


2013

Using the Iowa K test and the gyratory compaction test to improve the Compaction Forecasting Expert Database

CHENG LI

Iowa State University

Follow this and additional works at: <https://lib.dr.iastate.edu/etd>

 Part of the [Civil Engineering Commons](#), and the [Geotechnical Engineering Commons](#)

Recommended Citation

LI, CHENG, "Using the Iowa K test and the gyratory compaction test to improve the Compaction Forecasting Expert Database" (2013). *Graduate Theses and Dissertations*. 13394.

<https://lib.dr.iastate.edu/etd/13394>

This Thesis is brought to you for free and open access by the Iowa State University Capstones, Theses and Dissertations at Iowa State University Digital Repository. It has been accepted for inclusion in Graduate Theses and Dissertations by an authorized administrator of Iowa State University Digital Repository. For more information, please contact digirep@iastate.edu.

**Using the Iowa K test and the gyratory compaction test to improve the
Compaction Forecasting Expert Database**

by

Cheng Li

A thesis submitted to the graduate faculty
In partial fulfillment of the requirements for the degree of
MASTER OF SCIENCE

Major: Civil Engineering (Geotechnical Engineering)

Program of Study Committee:
David J. White, Major Professor
Shauna Hallmark
Pavana Vennapusa

Iowa State University

Ames, Iowa

2013

Copyright © Cheng Li, 2013. All rights reserved.

This work is dedicated to
my parents, Li Yulin and Qiu Lanrong

In memory of my aunt, Li Guirong

TABLE OF CONTENTS

LIST OF TABLES	viii
LIST OF FIGURES	xi
LIST OF SYMBOLS	xix
ABSTRACT	xxi
CHAPTER 1. INTRODUCTION	1
Industry Problem	1
Technical Problem	1
Goal of the Research	2
Objectives	2
Significance of the Research	3
Organization of the Thesis	3
Key Terms	3
CHAPTER 2. BACKGROUND/LITERATURE REVEIW	4
Compaction of Geomaterials	4
The Engineering Properties of Compacted Geomaterials	5
The shear strength of compacted geomaterials	5
Mohr-Coulomb failure criterion	5
Stress path method	5
Factors that influence the shear strength of compacted geomaterials	8
The stiffness parameters of compacted geomaterials	13
Stiffness modulus	13
Poisson's ratio	14
Lateral earth pressure induced by compaction	17
Lab Testing Devices for Measuring Strength and Stiffness Parameters of Geomaterials	20
Direct shear and triaxial shear test	20
Hveem stabilometer test	22
UI-Fast Cell	24
K-mold test system	26
Pitt's K test device	28
Iowa K test	29
Cohesion (c) and internal friction angle (ϕ)	30
Elastic modulus (E) and Poisson's ratio (ν)	32
Lateral stress ratio (K value)	33
Soil to steel adhesion, friction angle, and pore water pressure of Iowa K test	33
Boundary stresses and correction method of Iowa K test	34
Gyratory compaction test	36
The mechanical parameters of gyratory compaction tests	37
Determining the compaction behavior of geomaterials	37
Measuring the shear resistance of compacted geomaterials	39
Estimating the compaction energy of gyratory compaction test	42
Correlating the shear resistance (τ_G) to standardized lab and field testing results	43

Compaction Forecasting Expert Database (CFED)	46
CHAPTER 3. METHODS	50
Research Design.....	50
Determine Soil Index Properties of Geomaterials	51
Particle size analysis	51
Liquid limit, plastic limit, and plasticity index of materials	52
Soil classification.....	52
Specific gravity	53
Evaluate the Compaction Behavior of Geomaterials.....	54
Proctor compaction test.....	54
Vibratory compaction test.....	55
Gyratory compaction test.....	57
Measure the Shear Strength and Stiffness Parameters of Compacted Geomaterials.....	59
Unconfined compression test.....	59
Direct shear test.....	60
Pressure distribution analyzer (PDA) in gyratory compaction test	61
Iowa K test.....	64
Building the Iowa K test device.....	64
Calibrating the Iowa K test device.....	67
Measuring shear strength and stiffness parameters of compacted geomaterials with the Iowa K test	70
Statistically Analyze the Results of Iowa K Test and Gyratory Compaction Test.....	72
Linear or multiple linear regression analysis	72
Repeatability and reproducibility analysis for of the gyratory compaction test	72
Repeatability analysis for the gyratory compaction test devices	73
Reproducibility analysis for the gyratory compaction test devices	74
CHAPTER 4. MATERIALS	77
Western Iowa Loess (CFED 1634).....	81
Texas Fat Clay (CFED 2043)	83
2011 Manatt's RAP (CFED 2051).....	85
CA-6-G (CFED 2052).....	87
WCF Fly Ash (CFED 2053)	89
WCF Gypsum (CFED 2054)	91
Temple Gypsum (CFED 2055).....	93
Reject Gypsum (CFED 2056).....	95
Loess Stabilized With 15% Fly Ash (CFED 2057)	97
Loess Stabilized With 9% Type I Cement (CFED 2058).....	99
Florida Highway 9B Embankment Fill (CFED 2059).....	101
Summary of Proctor Compaction Tests Results	103
2012 Manatt's RAP (CFED 2061).....	105
RPCC and RAP Mixture (CFED 2062).....	108
Crushed Limestone (CFED 2063)	111
Ottawa sand (ASTM 20-30 sand).....	114

CHAPTER 5. RESULTS AND DISCUSSION.....	117
Expanding CFED with Laboratory Test Data of 13 Geomaterials	117
Proctor test results.....	117
Vibratory compaction test results	140
Improving CFED Using Iowa K Test to Evaluate Shear Strength and Stiffness Properties of Geomaterials.....	142
Western Iowa loess (CFED 1634)	143
Undrained cohesion and internal friction angle	143
Vertical elastic modulus.....	146
Poisson's ratio and lateral stress ratio	148
Soil-to-steel friction	151
Summary of the Iowa K test results of western Iowa loess	153
Texas fat clay (CFED 2043)	155
Undrained cohesion and internal friction angle	155
Vertical elastic modulus.....	157
Poisson's ratio and lateral stress ratio	159
Soil to steel friction.....	162
Summary of the Iowa K test results of Texas fat clay	163
WCF fly ash (CFED 2053)	165
Undrained cohesion and internal friction angle	165
Vertical elastic modulus.....	167
Poisson's ratio and lateral stress ratio	168
Soil to steel friction.....	170
Summary of the Iowa K test results of WCF fly ash	170
WCF gypsum (CFED 2054)	173
Undrained cohesion and internal friction angle	173
Vertical elastic modulus.....	175
Poisson's ratio and lateral stress ratio	176
Soil to steel friction.....	178
Summary of the Iowa K test results of WCF gypsum	179
Ottawa sand (ASTM 20-30 sand)	181
Undrained cohesion and internal friction angle	181
Vertical elastic modulus.....	182
Poisson's ratio and lateral stress ratio	183
Soil to steel friction.....	183
Summary of the Iowa K test results of Ottawa sand.....	183
Improving CFED Using Gyrotory Compaction Test to Determine Compaction Behavior and Shear Resistance.....	185
Repeatability and reproducibility (R&R) analysis for the gyrotory compaction test devices.....	185
Feasibility of linking the shear resistance with moisture-density-compaction energy relationships	196
WCF fly ash and gypsum (CFED 2053 and 2054).....	196
2012 Manatt's RAP, RPCC and RAP mixture, and crushed limestone (CFED 2061, 2062 and 2063).....	207

CHAPTER 6. CONCLUSIONS	218
Laboratory Compaction Test Results.....	218
Proctor compaction test.....	218
Vibratory compaction test.....	219
Iowa K Test Results	219
Western Iowa loess (CFED 1634)	219
Texas fat clay (CFED 2043)	220
WCF fly ash (CFED 2053)	220
WCF gypsum (CFED 2054)	221
Ottawa sand (ASTM 20-30).....	221
Gyratory Compaction Test Results.....	222
Summary of Conclusions	223
CHAPTER 7. RECOMMENDATIONS.....	225
Recommendations for Future Research.....	225
Recommendations for Future Practice.....	227
WORKS CITED	228
APPENDIX A. PROCTOR AND VIBRATORY COMPACTION TEST RAW DATA	233
APPENDIX B. PROCTOR AND UNCONFINED COMPRESSION TEST RESULTS OF STABILIZED WESTERN IOWA LOESS	237
APPENDIX C. IOWA K TEST RESULTS OF THE FIVE COMPACTED GEOMATERIALS	239
Western Iowa loess (CFED 1634)	239
Texas fat clay (CFED 2043)	253
WCF fly ash (CFED 2053)	266
WCF gypsum (CFED 2054)	279
Ottawa sand (ASTM 20-30).....	291
APPENDIX D. DIRECT SHEAR TEST RESULTS OF THE FIVE COMPACTED GEOMATERIALS	295
Western Iowa loess (CFED 1634)	295
Texas fat clay (CFED 2043)	301
WCF fly ash (CFED 2053)	305
WCF gypsum (CFED 2054)	318
Ottawa Sand (ASTM 20-30).....	329
APPENDIX E. STATISTICAL MODELS FOR THE IOWA K TEST RESULTS	333
Western Iowa loess (CFED 1634)	333
Texas fat clay (CFED 2043)	349
WCF fly ash (CFED 2053)	365
WCF gypsum (CFED 2054)	373
Ottawa sand (ASTM 20-30).....	387
APPENDIX F. JMP OUTPUTS AND SPREADSHEETS FOR R&R ANALYSIS	389

APPENDIX G. UNCONFINED COMPRESSION TEST RESULTS FOR WCF FLY ASH AND GYPSUM	403
APPENDIX H. SIEVE ANALYSIS RESULTS FOR 2012 RAP, RPCC+RAP, AND CRUSHED LIMESTONE BEFORE AND AFTER GYRATORY TESTS.....	405
APPENDIX I. IN SITU LWD TEST DATA FOR TEXAS FAT CLAY (CFED 2043).....	407
ACKNOWLEDGEMENTS.....	408

LIST OF TABLES

Table 1. Representative values of the elastic modulus of soil (from Das 2009)	14
Table 2. Representative values of Poisson's ratio (from Das 2009)	15
Table 3. The proposed empirical equations for calculation of K_0	17
Table 4. Hysteretic K_0 loading/unloading model parameters (from Duncan and Seed 1986)	18
Table 6. ASTM standard triaxial shear tests	21
Table 7. Test procedures and stress states applied on aggregate samples (from Tutumluer and Seyhan 1999)	25
Table 8. K-Test results of loess (from Lutenegeger 1977)	31
Table 9. Trial corrections for the friction angle and cohesion of Iowa K test (from Lutenegeger 1977)	35
Table 10. Summary of compaction energies used for the Proctor compaction tests	55
Table 11. Parameters of the gyratory compaction test	58
Table 12. Typical Two-Way ANOVA table for the R&R analysis	75
Table 13. CFED soil ID, description, and geomaterial source	77
Table 14. Soil index properties of the 15 geomaterials	78
Table 15. Proctor compaction test parameters	80
Table 16. Material index properties of western Iowa loess	81
Table 17. Material index properties of Texas fat clay	83
Table 18. Material index properties of 2011 Manatt's RAP	85
Table 19. Material index properties of CA-6-G	87
Table 20. Material index properties of WCF fly ash	89
Table 21. Material index properties of WCF gypsum	91
Table 22. Material index properties of Temple gypsum	93
Table 23. Material index properties of Reject gypsum	95
Table 24. Material index properties of Loess with 15% fly ash	97
Table 25. Material index properties of Loess with 9% type I cement	99
Table 26. Material index properties of Florida highway 9B embankment fill	101
Table 27. Summary of Proctor compaction test results of CFED 1634 to 2059	104
Table 28. Material index properties of 2012 Manatt's RAP	105
Table 29. Minimum and maximum index densities and void ratios of oven dried 2012 Manatt's RAP	106
Table 30. Material index properties of RPCC and RAP mixture	108
Table 31. Minimum and maximum index densities and void ratios of oven dried RPCC and RAP mixture	109
Table 32. Material index properties of crushed limestone	111
Table 33. Minimum and maximum index densities and void ratios of oven dried crushed limestone	112
Table 34. Material index properties of Ottawa sand	114
Table 35. Minimum and maximum index densities and void ratios of the Ottawa sand	115
Table 36. Summary of Proctor compaction test results of CFED 1634 to 2059	120
Table 37. Proctor and vibratory compaction test results of the four coarse grained geomaterials	140
Table 38. Five types of geomaterials used for the Iowa K tests	142

Table 39. Iowa K test and direct shear test results of Western Iowa loess	144
Table 40. Iowa K test vertical elastic modulus of the loess samples for loading 1 and 2	147
Table 41. Iowa K test Poisson's ratio and lateral stress ratio of the loess samples for loadings 1 and 2	149
Table 42. Soil to soil and soil to steel shear strength parameters of the loess samples	152
Table 43. Summary of the Iowa K test results for western Iowa loess (CFED 1634).....	154
Table 44. Iowa K test and direct shear test results of Texas fat clay	155
Table 45. Iowa K test vertical elastic modulus of the Texas fat clay samples for loadings 1 and 2 of the Iowa K test.....	157
Table 46. Iowa K test Poisson's ratio and lateral stress ratio of the Texas fat clay samples for loadings 1 and 2.....	160
Table 47. Soil to soil and soil to steel shear strength parameters of the Texas fat clay samples.....	162
Table 48. Summary of the Iowa K test results for Texas fat clay (CFED 2043).....	164
Table 49. Iowa K test and direct shear test results of WCF fly ash.....	165
Table 50. Iowa K test vertical elastic modulus of the WCF fly ash samples for loadings 1 and 2.....	168
Table 51. Iowa K test Poisson's ratio and lateral stress ratio of the WCF fly ash samples for loadings 1 and 2.....	169
Table 52. Soil to soil and soil to steel shear strength parameters of the WCF fly ash samples.....	170
Table 53. Summary of the Iowa K test results for WCF fly ash (CFED 2053).....	172
Table 54. Iowa K test and direct shear test results of WCF gypsum	174
Table 55. Iowa K test vertical elastic modulus of the WCF gypsum samples for loadings 1 and 2	175
Table 56. Iowa K test Poisson's ratio and lateral stress ratio of the WCF gypsum samples for loadings 1 and 2.....	177
Table 57. Soil to soil and soil to steel shear strength parameters of the WCF gypsum.....	179
Table 58. Summary of the Iowa K test results for WCF gypsum (CFED 2054).....	180
Table 59. The Iowa K test and direct shear test results of Ottawa sand samples	181
Table 60. Iowa K test vertical elastic modulus of Ottawa sand samples for loading 1 and 2.....	182
Table 61. Iowa K test Poisson's ratio and lateral stress ratio of the Ottawa sand samples for loadings 1 and 2.....	183
Table 62. Soil to soil and soil to steel shear strength parameters of the Ottawa sand samples.....	183
Table 63. Summary of the Iowa K test results for the Ottawa sand	184
Table 64. The geomaterials used for gyratory compaction tests	185
Table 65. Results of R&R analysis for the gyratory compactor and two PDAs.....	187
Table 66. Proctor, vibratory, and gyratory compaction test results of the geomaterials	217
Table 67. Proctor test raw data of the 11 geomaterials.....	233
Table 68. Vibratory compaction test raw data of the four oven-dried geomaterials	236
Table 69. Proctor and unconfined compression test results for western Iowa loess with 15% fly ash	237

Table 70. Proctor and unconfined compression test results for western Iowa loess with 9% type I cement	238
Table 71. R&R analysis spreadsheet for 300kPa total load, eccentricity, and shear resistance.....	401
Table 72. R&R analysis spreadsheet for 600kPa total load, eccentricity, and shear resistance.....	402
Table 73. Unconfined compression test results of 1 and 48-hr cured WCF fly ash samples.....	403
Table 74. Unconfined compression test results of 1 and 48-hr cured WCF gypsum samples.....	404
Table 75. In situ LWD test data for Texas fat clay (CFED 2043).....	407

LIST OF FIGURES

Figure 1. The maximum shear stress points in Mohr circle system (A) and the stress path method (B)	6
Figure 2. Stress paths for triaxial tests (redrawn from Lambe 1967)	7
Figure 3. Failure condition (redrawn from Lambe and Marr 1979)	8
Figure 4. Relationships between dry density, water content and strength as compacted for samples of Silty Clay (redrawn from Seed et al. 1960)	9
Figure 5. Effect of compaction on structure of clay soils (redrawn from Lambe 1958)	10
Figure 6. Influence of method of compaction on strength of silty clay (redrawn from Seed et al. 1960).....	11
Figure 7. Tangent and secant stiffness modulus of soils	13
Figure 8. Poisson's ratio versus of volumetric strain to shear strain (from Brown and Hyde 1975)	16
Figure 9. Basic components of hysteretic K_0 -loading/unloading model (redrawn from Duncan and Seed 1986)	19
Figure 10. Schematic of the Hveem stabilometer (from Chua and Tenison 2003)	22
Figure 11. University of Illinois FastCell (UI-FastCell) triaxial testing device: (A) UI-FastCell; (B) representation of cylindrical specimen (from Seyhan and Tutumluer 2002)	24
Figure 12. Schematic layout of K-mold set-up (from Semmelink and de Beer 1995)	26
Figure 13. Typical K-mold system testing results of a weathered granite material (from Semmelink and de Beer 1995).....	27
Figure 14. Proposed adjustable deformation restraint apparatus (from Pitt 1981)	28
Figure 15. The constant-E Iowa K test mold (redrawn from Handy et al. 1978)	29
Figure 16. K-test ϕ , c , and γ_d versus moisture content for a glacial till (from Handy et al. 1978)	31
Figure 17. Proposed principal stresses directions in the K-Test (from Lutenegeger 1977)	35
Figure 18. The gyratory compactor and GLPA (from Faheem and Bahia 2004).....	36
Figure 19. Energy indices of gyratory compaction test for HMA (from Bahia 2002)	39
Figure 20. Gyratory load-cell and plate assembly (GLPA) (from Guler et al. 2000).....	40
Figure 21. Eccentricity of the resultant force calculated on basis of the three load cells (from Guler et al. 2000)	41
Figure 22. Three dimensional eccentricity plots for coarse (HV5) and fine (HV2) mixture HMA samples (from Guler et al. 2000)	42
Figure 23 Relationship between s_u and τ_G for Western Iowa loess (from Zhang 2010)	43
Figure 24 Relationships between τ_G and M_r for TH-60 soil 306 (from Zhang 2010)	44
Figure 25. Correlations between τ_G and LWD/DPI measurements with different boundary conditions of TH60 soil 306 material (USCS: CL) (from White et al. 2009)	45
Figure 26. CFED outputs of soil 1633 based on the Proctor test data (from Puls 2008).....	47
Figure 27. CFED outputs of soil 1633 based on field compaction data (from CFED).....	49
Figure 28. (A) Sieve analysis and (B) hydrometer test devices.....	51
Figure 29. Liquid limit test devices	52
Figure 30. Specific gravity test devices for (A) coarse (B) and fine materials.....	53
Figure 31. (A) Hobart mixer and (B) automated mechanical rammer.....	54

Figure 32. A 6-in. diameter mold on an electromagnetic vibratory table.....	56
Figure 33. (A) A schematic (from Faheem and Bahia 2004) and (B) photo of the Brovold Gyratory Compactor	57
Figure 34. Unconfined compression test for 2.8 in. gypsum sample.....	59
Figure 35. Direct shear test device.....	60
Figure 36. Pressure distribution analyzer (PDA).....	62
Figure 37. Eccentricity of the resultant force calculated on basis of the three load cells (adapted from Guler et al. 2000 by moving the x-axis).....	63
Figure 38. A schematic of the Iowa K test device	64
Figure 39. Iowa K test setup	65
Figure 40. The (A) top view and (B) front view of the Iowa K test mold	66
Figure 41. The bottom base and the bottom load cell.....	67
Figure 42. A gelatin cylinder for calibration of the Iowa K test mold.....	68
Figure 43. The horizontal stress and displacement relationship of the Iowa K test mold	69
Figure 44. The hyperbolic model from the calibration tests for the Iowa K test mold.....	69
Figure 45. An example JMP output for the Two-Way ANOVA table	75
Figure 46. Western Iowa loess at 17.2% moisture content.....	81
Figure 47. Particle size distribution curve of western Iowa loess.....	82
Figure 48. Moisture density relationships of western Iowa loess	82
Figure 49. 2011 Texas fat clay at 15.5% moisture content.....	83
Figure 50. Particle size distribution curve of Texas fat clay.....	84
Figure 51. Moisture density relationships of Texas fat clay.....	84
Figure 52. 2011 Manatt's RAP at 6.5% moisture content	85
Figure 53. Particle size distribution curve of 2011 Manatt's RAP	86
Figure 54. Moisture density relationships of 2011 Manatt's RAP	86
Figure 55. CA-6-G (110°C oven-dried)	87
Figure 56. Particle size distribution curve of CA-6-G.....	88
Figure 57. Moisture density relationships of CA-6-G	88
Figure 58. WCF fly ash at 23.0% moisture content.....	89
Figure 59. Particle size distribution curve of WCF fly ash.....	90
Figure 60. Moisture density relationships of WCF fly ash.....	90
Figure 61. WCF gypsum at 16.0% moisture content.....	91
Figure 62. Particle size distribution curve of WCF gypsum.....	92
Figure 63. Moisture density relationships of WCF gypsum (moisture contents were measured at 60°C).....	92
Figure 64. Temple gypsum at 9.4% moisture content	93
Figure 65. Particle size distribution curve of Temple gypsum	94
Figure 66. Moisture density relationships of Temple Gypsum (moisture contents were measured at 60°C).....	94
Figure 67. Reject gypsum at 19.4% moisture content	95
Figure 68. Particle size distribution curve of Reject gypsum	96
Figure 69. Moisture density relationships of Reject gypsum (moisture contents were measured at 60°C).....	96
Figure 70. Loess with 15% fly ash at 17.0% moisture content.....	97
Figure 71. Particle size distribution curve of Loess with 15% fly ash	98

Figure 72. Moisture density relationships of Loess with 15% fly ash	98
Figure 73. Loess with 9% type I cement at 12.6% moisture content.....	99
Figure 74. Particle size distribution curve of Loess with 9% type I cement	100
Figure 75. Moisture density relationships of Loess with 9% type I cement	100
Figure 76. Florida highway 9B embankment fill at 7.1% moisture content.....	101
Figure 77. Particle size distribution curve of Florida highway 9B embankment fill.....	102
Figure 78. Moisture density relationships of Florida 9B embankment fill.....	102
Figure 79. 2012 RAP at 4.8% moisture content	105
Figure 80. Particle size distribution curve of 2012 Manatt's RAP	106
Figure 81. Dry unit weight versus compaction time of 2012 Manatt's RAP	107
Figure 82. Dry unit weight versus compaction energy of 2012 Manatt's RAP.....	107
Figure 83. RPCC and RAP mixture (110°C oven-dried).....	108
Figure 84. Particle size distribution curve of RPCC and RAP mixture.....	109
Figure 85. Dry unit weight versus compaction time of RPCC and RAP mixture	110
Figure 86. Dry unit weight versus compaction energy of RPCC and RAP mixture	110
Figure 87. Crushed limestone (110°C oven-dried)	111
Figure 88. Particle size distribution curve of crushed limestone	112
Figure 89. Dry unit weight versus compaction time of crushed limestone	113
Figure 90. Dry unit weight versus compaction energy of crushed limestone.....	113
Figure 91. Ottawa sand	114
Figure 92. Particle size distribution curve of Ottawa sand	115
Figure 93. Dry unit weight versus compaction time of Ottawa sand.....	116
Figure 94. Dry unit weight versus compaction energy of Ottawa sand.....	116
Figure 95. Proctor compaction test results of the additional 9 geomaterials for CFED	118
Figure 96. CFED output graphs for 2011 Manatt's RAP (CFED 2051)	121
Figure 97. CFED output graphs for CA-6-G (CFED 2052)	123
Figure 98. CFED output graphs for WCF fly ash (CFED 2053)	125
Figure 99. CFED output graphs for WCF gypsum (CFED 2054)	127
Figure 100. CFED output graphs for Cumberland Temple gypsum (CFED 2055).....	129
Figure 101. CFED output graphs for Cumberland Reject gypsum (CFED 2056).....	131
Figure 102. CFED output graphs for western Iowa loess with 15% fly ash (CFED 2057)..	133
Figure 103. CFED output graphs for western Iowa loess with 9% Type I cement (CFED 2058)	135
Figure 104. CFED output graphs for Florida 9B fill (CFED 2059).....	137
Figure 105. Proctor and UC test results for the loess stabilized with (A and B) 15% fly ash and (C and D) 9% Type I cement	139
Figure 106. Dry unit weight versus vibratory compaction time for the four geomaterials ..	141
Figure 107. Dry unit weight versus vibratory compaction energy and Proctor test results of the four geomaterials	141
Figure 108. The Iowa K test stress path of a Western Iowa loess sample ($w\% = 12.2\%$, $\gamma_d = 96.9$ pcf).....	143
Figure 109. Statistical relationships between the moisture contents, dry unit weights, and (A) undrained cohesions and (B) internal friction angles of the loess samples.....	145
Figure 110. The (A) vertical stress-strain relationships and (B) elastic modulus under 50 to 100 vertical stress of a Western Iowa loess sample ($w\% = 12.2\%$, $\gamma_d = 96.9$ pcf).....	146

Figure 111. Statistical analysis results for (A) loading 1 and (B) loading vertical elastic modulus.....	147
Figure 112. The (A) Poisson's ratio and (B) lateral stress ratio versus average vertical stress of a Western Iowa loess sample ($w\% = 12.2\%$, $\gamma_d = 96.9$ pcf).....	148
Figure 113. Statistical relationships between Poisson's ratio, moisture content, and dry unit weight	150
Figure 114. Statistical analysis results for the lateral stress ratio under (A) 100 psi vertical stress of loading 1 and (B) 25 psi vertical stress of loading 2	150
Figure 115. The soil to steel friction of a Western Iowa loess sample ($w\% = 12.2\%$, $\gamma_d = 96.9$ pcf).....	151
Figure 116. Statistical analysis results for the soil-to-steel friction angles of the western Iowa loess.....	152
Figure 117. The statistical relationships between the moisture-density and (A) undrained cohesion and (B) internal friction angle of Texas fat clay.....	156
Figure 118. Statistical relationships between moisture content, dry unit weight, and vertical elastic modulus for (A) loading 1 and (B) loading 2	158
Figure 119. (A) Dry unit weight and moisture content of in-situ LWD test points and (B) A simple linear regression model for the LWD tests.....	159
Figure 120. Statistical relationships between moisture content, dry unit weight, and Poisson's ratio for first loading.....	161
Figure 121. Statistical analysis results for the lateral stress ratio under 100psi vertical pressure of loading 1 (A) and 25psi vertical pressure of loading 2 (B).....	161
Figure 122. Statistical analysis results for the soil-to-steel friction angles of Texas fat clay.....	163
Figure 123. Direct shear test results for determining the cohesion of a WCF fly ash sample ($w\% = 18.9\%$ and $\gamma_d = 84.4$ pcf)	166
Figure 124. Statistical analysis results for the (A) Iowa K test undrained and (B) drained friction angle of the WCF fly ash	167
Figure 125. Statistical analysis results for the (A) Poisson's ratio and (B) lateral stress ratio of WCF fly ash under 100psi vertical pressure of loading 1	169
Figure 126. The statistical relationships between the dry unit weight and undrained friction angle of WCF gypsum	174
Figure 127. Statistical relationships between moisture content and vertical elastic modulus for WCF gypsum under (A) loading 1 and (B) loading 2	176
Figure 128. Statistical analysis results for the Poisson's ratio of WCF gypsum under (A) loading 1 and (B) loading 2	177
Figure 129. Statistical analysis results for the lateral stress ratio of WCF gypsum under (A) loading 1 and (B) loading 2.....	178
Figure 130. The statistical relationships between the dry unit weight and undrained friction angle of Ottawa sand samples.....	182
Figure 131. The (A) dry unit weight and (B) total load versus number of gyrations of Ottawa sand under 300 kPa vertical pressure with PDA 1	188
Figure 132. The (A) eccentricity and (B) shear resistance versus number of gyrations of Ottawa sand under 300 kPa vertical pressure with PDA 1	189

Figure 133. The (A) dry unit weight and (B) total load versus number of gyrations of Ottawa sand under 600 kPa vertical pressure with PDA 1	190
Figure 134. The (A) eccentricity and (B) shear resistance versus number of gyrations of Ottawa sand under 600 kPa vertical pressure with PDA 1	191
Figure 135. The (A) dry unit weight and (B) total load versus number of gyrations of Ottawa sand under 300 kPa vertical pressure with PDA 2	192
Figure 136. The (A) eccentricity and (B) shear resistance versus number of gyrations of Ottawa sand under 300 kPa vertical pressure with PDA 2	193
Figure 137. The (A) dry unit weight and (B) total load versus number of gyrations of Ottawa sand under 600 kPa vertical pressure with PDA 2	194
Figure 138. The (A) eccentricity and (B) shear resistance versus number of gyrations of Ottawa sand under 600 kPa vertical pressure with PDA 2	195
Figure 139. The (A) dry unit weight and (B) shear resistance versus number of gyrations for WCF fly ash	198
Figure 140. (A) The dry unit weight-compaction energy and (B) dry unit weight-moisture content relationships of Proctor and gyratory compaction tests for WCF fly ash	199
Figure 141. The (A) dry unit weight and (B) shear resistance versus number of gyrations for WCF gypsum.....	200
Figure 142. (A) The dry unit weight-compaction energy and (B) dry unit weight-moisture content relationships of Proctor and gyratory compaction tests for WCF gypsum	201
Figure 143. An example of determining undrained shear strength and secant modulus from the applied stress versus axial strain curve	202
Figure 144. Statistical analysis results of gyratory compaction and 1-hr curing UC test of WCF fly ash	203
Figure 145. Statistical analysis results of gyratory compaction and 48-hr curing UC test of WCF fly ash.....	204
Figure 146. Statistical analysis results of gyratory compaction and UC test of 1-hr curing WCF fly ash	205
Figure 147. Statistical analysis results of gyratory compaction and UC test of 48-hr curing WCF fly ash.....	206
Figure 148. Gyratory, Proctor, and vibratory compaction test results for 2012 Manatt's RAP	207
Figure 149. Gyratory, Proctor, and vibratory compaction test results for RPCC+RAP	208
Figure 150. Gyratory, Proctor, and vibratory compaction test results for the crushed limestone.....	208
Figure 151. Effect of the maximum grain size on the (A) dry unit weight and (B) shear resistance of 2012 Manatt's RAP	210
Figure 152. Effect of the maximum grain size on the (A) dry unit weight and (B) shear resistance of RPCC+RAP	211
Figure 153. Effect of the maximum grain size on the (A) dry unit weight and (B) shear resistance of the crushed limestone.....	212
Figure 154. Dry unit weight versus compaction energy of gyratory, Proctor, and vibratory compaction test for 2012 Manatt's RAP	214
Figure 155. Dry unit weight versus compaction energy of gyratory, Proctor, and vibratory compaction test for RPCC and RAP mixture.....	215

Figure 156. Dry unit weight versus compaction energy of gyratory, Proctor, and vibratory compaction test for the crushed limestone	216
Figure 157. The proposed Iowa K test mold.....	226
Figure 158. Iowa K test results for western Iowa loess ($w\% = 12.2\%$ and $\gamma_d = 96.9\text{pcf}$)	239
Figure 159. Iowa K test results for western Iowa loess ($w\% = 12.3\%$ and $\gamma_d = 103.5\text{pcf}$) ..	240
Figure 160. Iowa K test results for western Iowa loess ($w\% = 12.3\%$ and $\gamma_d = 112.7\text{pcf}$) ..	241
Figure 161. Iowa K test results for western Iowa loess ($w\% = 14.1\%$ and $\gamma_d = 98.5\text{pcf}$)	242
Figure 162. Iowa K test results for western Iowa loess ($w\% = 14.1\%$ and $\gamma_d = 105.8\text{pcf}$) ..	243
Figure 163. Iowa K test results for western Iowa loess ($w\% = 14.2\%$ and $\gamma_d = 115.2\text{pcf}$) ..	244
Figure 164. Iowa K test results for western Iowa loess ($w\% = 15.9\%$ and $\gamma_d = 95.6\text{pcf}$)	245
Figure 165. Iowa K test results for western Iowa loess ($w\% = 15.9\%$ and $\gamma_d = 108.2\text{pcf}$) ..	246
Figure 166. Iowa K test results for western Iowa loess ($w\% = 15.9\%$ and $\gamma_d = 114.9\text{pcf}$) ..	247
Figure 167. Iowa K test results for western Iowa loess ($w\% = 18.3\%$ and $\gamma_d = 103.5\text{pcf}$) ..	248
Figure 168. Iowa K test results for western Iowa loess ($w\% = 18.5\%$ and $\gamma_d = 108.3\text{pcf}$) ..	249
Figure 169. Iowa K test results for western Iowa loess ($w\% = 20.6\%$ and $\gamma_d = 103.2\text{pcf}$) ..	250
Figure 170. Iowa K test results for western Iowa loess ($w\% = 21.6\%$ and $\gamma_d = 102.4\text{pcf}$) ..	251
Figure 171. Iowa K test results for western Iowa loess ($w\% = 21.9\%$ and $\gamma_d = 101.6\text{pcf}$) ..	252
Figure 172. Iowa K test results for Texas fat clay ($w\% = 15.7\%$ and $\gamma_d = 83.0\text{pcf}$)	253
Figure 173. Iowa K test results for Texas fat clay ($w\% = 15.7\%$ and $\gamma_d = 92.7\text{pcf}$)	254
Figure 174. Iowa K test results for Texas fat clay ($w\% = 16.6\%$ and $\gamma_d = 100.4\text{pcf}$)	255
Figure 175. Iowa K test results for Texas fat clay ($w\% = 18.2\%$ and $\gamma_d = 80.5\text{pcf}$)	256
Figure 176. Iowa K test results for Texas fat clay ($w\% = 18.6\%$ and $\gamma_d = 91.9\text{pcf}$)	257
Figure 177. Iowa K test results for Texas fat clay ($w\% = 19.8\%$ and $\gamma_d = 104.9\text{pcf}$)	258
Figure 178. Iowa K test results for Texas fat clay ($w\% = 22.5\%$ and $\gamma_d = 85.1\text{pcf}$)	259
Figure 179. Iowa K test results for Texas fat clay ($w\% = 21.6\%$ and $\gamma_d = 92.7\text{pcf}$)	260
Figure 180. Iowa K test results for Texas fat clay ($w\% = 22.9\%$ and $\gamma_d = 103.6\text{pcf}$)	261
Figure 181. Iowa K test results for Texas fat clay ($w\% = 24.5\%$ and $\gamma_d = 81.6\text{pcf}$)	262
Figure 182. Iowa K test results for Texas fat clay ($w\% = 25.6\%$ and $\gamma_d = 91.6\text{pcf}$)	263
Figure 183. Iowa K test results for Texas fat clay ($w\% = 28.2\%$ and $\gamma_d = 83.6\text{pcf}$)	264
Figure 184. Iowa K test results for Texas fat clay ($w\% = 27.8\%$ and $\gamma_d = 93.7\text{pcf}$)	265
Figure 185. Iowa K test results for WCF fly ash ($w\% = 15.9\%$ and $\gamma_d = 84.4\text{pcf}$)	266
Figure 186. Iowa K test results for WCF fly ash ($w\% = 15.6\%$ and $\gamma_d = 85.8\text{pcf}$)	267
Figure 187. Iowa K test results for WCF fly ash ($w\% = 17.4\%$ and $\gamma_d = 81.2\text{pcf}$)	268
Figure 188. Iowa K test results for WCF fly ash ($w\% = 17.7\%$ and $\gamma_d = 84.2\text{pcf}$)	269
Figure 189. Iowa K test results for WCF fly ash ($w\% = 18.0\%$ and $\gamma_d = 86.6\text{pcf}$)	270
Figure 190. Iowa K test results for WCF fly ash ($w\% = 18.9\%$ and $\gamma_d = 82.7\text{pcf}$)	271
Figure 191. Iowa K test results for WCF fly ash ($w\% = 18.9\%$ and $\gamma_d = 85.2\text{pcf}$)	272
Figure 192. Iowa K test results for WCF fly ash ($w\% = 21.2\%$ and $\gamma_d = 79.6\text{pcf}$)	273
Figure 193. Iowa K test results for WCF fly ash ($w\% = 22.4\%$ and $\gamma_d = 84.4\text{pcf}$)	274
Figure 194. Iowa K test results for WCF fly ash ($w\% = 24.3\%$ and $\gamma_d = 82.3\text{pcf}$)	275
Figure 195. Iowa K test results for WCF fly ash ($w\% = 24.4\%$ and $\gamma_d = 81.5\text{pcf}$)	276
Figure 196. Iowa K test results for WCF fly ash ($w\% = 25.6\%$ and $\gamma_d = 78.7\text{pcf}$)	277
Figure 197. Iowa K test results for WCF fly ash ($w\% = 27.5\%$ and $\gamma_d = 79.5\text{pcf}$)	278
Figure 198. Iowa K test results for WCF gypsum ($w\% = 9.5\%$ and $\gamma_d = 97.7\text{pcf}$)	279
Figure 199. Iowa K test results for WCF gypsum ($w\% = 9.7\%$ and $\gamma_d = 101.3\text{pcf}$)	280

Figure 200. Iowa K test results for WCF gypsum ($w\% = 9.9\%$ and $\gamma_d = 106.1\text{pcf}$)	281
Figure 201. Iowa K test results for WCF gypsum ($w\% = 10.9\%$ and $\gamma_d = 100.9\text{pcf}$)	282
Figure 202. Iowa K test results for WCF gypsum ($w\% = 11.6\%$ and $\gamma_d = 103.5\text{pcf}$)	283
Figure 203. Iowa K test results for WCF gypsum ($w\% = 15.5\%$ and $\gamma_d = 100.4\text{pcf}$)	284
Figure 204. Iowa K test results for WCF gypsum ($w\% = 15.4\%$ and $\gamma_d = 100.5\text{pcf}$)	285
Figure 205. Iowa K test results for WCF gypsum ($w\% = 17.8\%$ and $\gamma_d = 101.9\text{pcf}$)	286
Figure 206. Iowa K test results for WCF gypsum ($w\% = 17.9\%$ and $\gamma_d = 101.0\text{pcf}$)	287
Figure 207. Iowa K test results for WCF gypsum ($w\% = 18.0\%$ and $\gamma_d = 100.5\text{pcf}$)	288
Figure 208. Iowa K test results for WCF gypsum ($w\% = 17.1\%$ and $\gamma_d = 100.0\text{pcf}$)	289
Figure 209. Iowa K test results for WCF gypsum ($w\% = 20.8\%$ and $\gamma_d = 95.9\text{pcf}$)	290
Figure 210. Iowa K test results for Ottawa sand ($\gamma_d = 97.6\text{pcf}$ and $e_0 = 0.69$)	291
Figure 211. Iowa K test results for Ottawa sand ($\gamma_d = 101.8\text{pcf}$ and $e_0 = 0.62$)	292
Figure 212. Iowa K test results for Ottawa sand ($\gamma_d = 105.9\text{pcf}$ and $e_0 = 0.56$)	293
Figure 213. Iowa K test results for Ottawa sand ($\gamma_d = 107.7\text{pcf}$ and $e_0 = 0.54$)	294
Figure 214. Direct shear test results of western Iowa loess ($w\% = 11.8\%$ and $\gamma_d = 114.9\text{pcf}$).....	295
Figure 215. Direct shear test results of western Iowa loess ($w\% = 13.6\%$ and $\gamma_d = 107.2\text{pcf}$).....	296
Figure 216. Direct shear test results of western Iowa loess ($w\% = 15.4\%$ and $\gamma_d = 106.9\text{pcf}$).....	297
Figure 217. Direct shear test results of western Iowa loess ($w\% = 17.5\%$ and $\gamma_d = 105.0\text{pcf}$).....	298
Figure 218. Direct shear test results of western Iowa loess ($w\% = 19.5\%$ and $\gamma_d = 103.2\text{pcf}$).....	299
Figure 219. Direct shear test results of western Iowa loess ($w\% = 20.7\%$ and $\gamma_d = 102.2\text{pcf}$).....	300
Figure 220. Direct shear test results of Texas fat clay ($w\% = 18.6\%$ and $\gamma_d = 98.2\text{pcf}$)	301
Figure 221. Direct shear test results of Texas fat clay ($w\% = 22.8\%$ and $\gamma_d = 96.2\text{pcf}$)	302
Figure 222. Direct shear test results of Texas fat clay ($w\% = 25.7\%$ and $\gamma_d = 102.4\text{pcf}$)	303
Figure 223. Direct shear test results of Texas fat clay ($w\% = 27.5\%$ and $\gamma_d = 100.9\text{pcf}$)	304
Figure 224. Direct shear test results of WCF fly ash ($w\% = 15.6\%$ and $\gamma_d = 81.5\text{pcf}$)	305
Figure 225. Direct shear test results of WCF fly ash ($w\% = 15.4\%$ and $\gamma_d = 85.1\text{pcf}$)	306
Figure 226. Direct shear test results of WCF fly ash ($w\% = 17.2\%$ and $\gamma_d = 78.1\text{pcf}$)	307
Figure 227. Direct shear test results of WCF fly ash ($w\% = 17.5\%$ and $\gamma_d = 81.8\text{pcf}$)	308
Figure 228. Direct shear test results of WCF fly ash ($w\% = 18.0\%$ and $\gamma_d = 86.0\text{pcf}$)	309
Figure 229. Direct shear test results of WCF fly ash ($w\% = 19.5\%$ and $\gamma_d = 82.6\text{pcf}$)	310
Figure 230. Direct shear test results of WCF fly ash ($w\% = 19.7\%$ and $\gamma_d = 83.8\text{pcf}$)	311
Figure 231. Direct shear test results of WCF fly ash ($w\% = 21.7\%$ and $\gamma_d = 82.3\text{pcf}$)	312
Figure 232. Direct shear test results of WCF fly ash ($w\% = 22.4\%$ and $\gamma_d = 84.1\text{pcf}$)	313
Figure 233. Direct shear test results of WCF fly ash ($w\% = 23.9\%$ and $\gamma_d = 84.1\text{pcf}$)	314
Figure 234. Direct shear test results of WCF fly ash ($w\% = 23.6\%$ and $\gamma_d = 85.1\text{pcf}$)	315
Figure 235. Direct shear test results of WCF fly ash ($w\% = 25.3\%$ and $\gamma_d = 83.3\text{pcf}$)	316
Figure 236. Direct shear test results of WCF fly ash ($w\% = 25.0\%$, $\gamma_d = 84.9\text{pcf}$).....	317
Figure 237. Direct shear test results of WCF gypsum ($w\% = 9.9\%$ and $\gamma_d = 94.2\text{pcf}$)	318
Figure 238. Direct shear test results of WCF gypsum ($w\% = 9.9\%$ and $\gamma_d = 102.3\text{pcf}$)	319

Figure 239. Direct shear test results of WCF gypsum ($w\% = 11.6\%$ and $\gamma_d = 97.9\text{pcf}$)	320
Figure 240. Direct shear test results of WCF gypsum ($w\% = 11.6\%$ and $\gamma_d = 100.3\text{pcf}$)	321
Figure 241. Direct shear test results of WCF gypsum ($w\% = 15.6\%$ and $\gamma_d = 101.1\text{pcf}$)	322
Figure 242. Direct shear test results of WCF gypsum ($w\% = 15.5\%$ and $\gamma_d = 102.2\text{pcf}$)	323
Figure 243. Direct shear test results of WCF gypsum ($w\% = 15.9\%$ and $\gamma_d = 101.8\text{pcf}$)	324
Figure 244. Direct shear test results of WCF gypsum ($w\% = 16.7\%$ and $\gamma_d = 104.7\text{pcf}$)	325
Figure 245. Direct shear test results of WCF gypsum ($w\% = 17.3\%$ and $\gamma_d = 103.3\text{pcf}$)	326
Figure 246. Direct shear test results of WCF gypsum ($w\% = 17.8\%$ and $\gamma_d = 102.6\text{pcf}$)	327
Figure 247. Direct shear test results of WCF gypsum ($w\% = 18.0\%$ and $\gamma_d = 101.3\text{pcf}$)	328
Figure 248. Direct shear test results of Ottawa sand ($\gamma_d = 97.1\text{pcf}$ and $e_0 = 0.70$)	329
Figure 249. Direct shear test results of Ottawa sand ($\gamma_d = 101.2\text{pcf}$ and $e_0 = 0.63$)	330
Figure 250. Direct shear test results of Ottawa sand ($\gamma_d = 105.2\text{pcf}$ and $e_0 = 0.57$)	331
Figure 251. Direct shear test results of Ottawa sand ($\gamma_d = 106.9\text{pcf}$ and $e_0 = 0.55$)	332
Figure 252. Sieve analysis results of 2012 Manatt's RAP (CFED 2061) before and after three gyratory compaction tests	405
Figure 253. Sieve analysis results of RPCC + RAP (CFED 2062) before and after three gyratory compaction tests	405
Figure 254. Sieve analysis results of crushed limestone (CFED 2063) before and after three gyratory compaction tests	406

LIST OF SYMBOLS

Symbol	Description	Unit
a	Cohesion intercept of the stress path method	—
b_0	Intercept in a linear regression equation	—
b_1, b_2, b_3	Regression coefficients	—
c	Undrained cohesion	psi
c'	Drained cohesion	psi
c_c	Coefficient of curvature	—
c_s	Soil to steel adhesion	psi
c_u	Coefficient of uniformity	—
CV	Coefficient of variation	—
D_{10}	Diameter corresponding to 10% finer	mm
D_{30}	Diameter corresponding to 30% finer	mm
D_{60}	Diameter corresponding to 60% finer	mm
E	Eccentricity of the gyratory compaction test	in.
e_0	Initial void ratio	—
e_{max}	Maximum index void ratio	—
e_{min}	Minimum index void ratio	—
E_{LWD-Z2}	Zorn 200mm light weight deflectometer (LWD) elastic modulus	ksi
E_v	Undrained vertical elastic modulus	ksi
F	Compactibility	—
G _s	Specific gravity	—
K	Lateral stress ratio	—
LL	Liquid limit	%
n	Number of test measurements	—
P	Total vertical load of the gyratory compaction test	lb
PI	Plasticity index	—
PL	Plastic limit	—
S_p	Pooled estimator of the standard deviations	—
R^2	Coefficient of determination	—
RMSE	Root mean square standard error	—
w	Moisture content	%
w_{opt}	Optimum moisture content	%
α	Slope of the Kf line of the stress path method	—
γ_d	Dry unit weight	lb/ft ³
γ_{dmax}	Maximum dry unit weight	lb/ft ³
ϵ_v	Vertical strain	%
ϵ_h	Horizontal strain	%
ν	Poisson's ratio	—
ρ_{dmax}	Maximum index density	lb/ft ³
ρ_{dmin}	Minimum index density	lb/ft ³
σ	Statistical standard deviation	—
$\sigma_{repeatability}$	Statistical standard deviation for repeatability analysis	—

$\sigma_{\text{reproducibility}}$	Statistical standard deviation for reproducibility analysis	—
$\sigma_{\text{R\&R}}$	Combined standard deviations of $\sigma_{\text{repeatability}}$ and $\sigma_{\text{reproducibility}}$	—
σ_h	Iowa K test horizontal stress	psi
σ_v	Iowa K test average vertical stress	psi
τ_G	Shear resistance determined using gyratory compaction test	psi
ϕ	Undrained friction angle	—
ϕ'	Drained friction angle	—
ϕ_s	Soil to steel friction angle	—

ABSTRACT

Contractors and engineers in the earthwork engineering industry desire a more effective pre-bid and QA/QC tool that links moisture-density-compaction energy relationships with shear strength and stiffness properties for compacted geomaterials. The Compaction Forecasting Expert Database (CFED) is being developed by Caterpillar Inc. and the Center for Earthworks Engineering Research (CEER) to predict the compaction behavior of geomaterials and provide recommendations for earthwork construction. However, in the current version of CFED, the Proctor test is the only laboratory method used to evaluate compaction behavior of geomaterials, and it does not provide shear strength and stiffness properties of compacted geomaterials. The goal of this research was to improve the CFED by linking moisture-density-compaction energy relationships with shear strength and stiffness properties to predict and evaluate the compaction performance of geomaterials. The objectives of this study were to expand the CFED with more lab testing data; evaluate two laboratory tests, the Iowa K and gyration compaction tests, to quickly determine compaction behavior; and evaluate relationships between moisture content, density, compaction energy, shear strength, and stiffness parameters of geomaterials. A range of non-granular and granular geomaterials were tested to evaluate the performance of the Iowa K test and a gyratory compaction test equipped with a pressure distribution analyzer (PDA). The important outcomes of this research are that (1) the Iowa K test and gyratory compaction test with a PDA can simply, quickly, and inexpensively simulate field conditions, determine compaction behaviors, and test the shear strength and stiffness of compacted geomaterials; (2) moisture content and dry unit weight can significantly influence shear strength and stiffness properties of non-granular compacted geomaterials; and (3) gyratory compaction tests with a PDA results showed that the maximum aggregate size can significantly influence the shear resistance of granular geomaterials. Owners, contractors, and taxpayers will benefit from this research because the improved CFED will be a more cost-effective tool for predicting and monitoring the compaction performance of geomaterials.

CHAPTER 1. INTRODUCTION

This chapter discusses the industry and technical problems addressed in this project. The research goal, specific objectives, and a discussion of the significance of this research are presented in the following discussion. The final section of this chapter forecasts the organization of the thesis.

Industry Problem

Ensuring stable soil support conditions is essential for successful performance of many civil infrastructure systems. Compaction is the most commonly used soil improvement method to increase the bearing capacity, shear strength, and stability for engineering projects. In most geotechnical projects, compaction performance is usually evaluated by measuring the dry unit weight and moisture content of compacted geomaterials. Field specifications typically require that the moisture content of the material be within certain limits (e.g., ± 2 to 4% of optimum) and the material be compacted to a certain minimum percent relative compaction (e.g., 95% of maximum dry unit weight), based on standard or modified Proctor tests. However, the safety and stability of sustained structures are governed by shear strength and stiffness of foundation materials that are difficult to determine and control during the compaction process. Conventional lab tests for shear strength and stiffness parameters are time consuming and expensive, and as a result, those parameters of compacted geomaterials are not usually specified for projects.

Contractors and engineers in the geotechnical engineering industry can benefit with having an effective pre-bid and quality control tool that links moisture content, density, shear strength, and stiffness for pre- and post-saturated conditions for compacted geomaterials.

Technical Problem

The Proctor compaction test is the standard test for determining relationships between moisture content, density, and compaction energy relationships. According to some studies (e.g., Coyle and West 1956), Proctor compaction test cannot simulate field conditions well for some types of geomaterials. Because of advances in compaction equipment, some researchers (e.g., Ping et al. 2003; White et al. 2007; White et al. 2009) have identified challenges relating laboratory moisture-density relationships with field moisture-density

relationships. Further, Proctor tests are time consuming and do not provide shear strength and stiffness information of testing samples.

The Compaction Forecasting Expert Database (CFED) uses Proctor results to predict relationships between moisture content, density, and compaction energy of compacted geomaterials (Puls 2008). However, the current version of CFED does not yet provide shear strength and stiffness parameters of geomaterials.

Three technical problems with CFED guide this study. First, the research sponsor wants CFED to provide strength and stiffness measurements for pre- and post-saturated conditions be added to the database. Second, CFED does not currently include lab testing data for chemically stabilized geomaterial (e.g., soil index properties, moisture content and density, and undrained shear strength parameters), and recycled material (e.g., fly ash and gypsum). Finally, an alternative to standard laboratory compaction tests (Proctor and vibratory compaction test) for compacted geomaterials is needed for CFED.

Goal of the Research

The main goal of this research is to improve the CFED by linking moisture content, density, compaction energy, shear strength, and stiffness parameters to predict and monitor the compaction performance of geomaterials.

Objectives

The objectives of this research are to:

- Expand the Compaction Forecasting Expert Database (CFED) with more lab testing data for recycled, by-product, and chemically stabilized geomaterials,
- Evaluate the gyratory compaction test that uses a pressure distribution analyzer (PDA) to determine relationships between moisture content, density, compaction energy and shear resistance of geomaterials and then correlate the gyratory compaction test data with conventional test results,
- Build and calibrate the Iowa K test equipment with more accurate measurement devices, and
- Evaluate shear strength and stiffness parameters by using the Iowa K test of CFED geomaterials and then compare with conventional test results.

Significance of the Research

Owners, contractors, tax payers, and researchers will benefit from this research because a new version of CFED can provide an efficient method for estimating and monitoring compaction performance of their projects. The new CFED can also provide shear strength and stiffness for compacted geomaterials that will help owners or contractors to better select target value for field moisture content ranges and choose the most suitable compaction method. The Iowa K test will provide a relatively quick and accurate test method to evaluate strength and stiffness parameters of geomaterials for both engineers and researchers. In addition, this research demonstrated that the gyratory compaction test potentially be an alternative to standard laboratory compaction tests for compacted geomaterials.

Organization of the Thesis

Following this introduction chapter, chapter 2 reviews previous literature and provides background information about the engineering properties of compacted geomaterials; conventional and innovative lab testing devices for measuring strength and stiffness parameters; the Caterpillar, Inc. CFED. Chapter 3 presents the lab test methods, equipment set up, calibration, and statistical analysis method used in this study.

Chapter 4 provides the soil index properties and compaction behaviors of the 15 geomaterials used in this study. Chapter 5 presents the lab testing and statistical analysis results of the geomaterials, and chapter 6 summarizes the conclusions and outcomes derived from this study, discusses the impacts and benefits of this study to both industry and technical area, and offers some suggestions for future research.

Supporting materials are included as appendices that follow the list of works cited.

Key Terms

Iowa K test, gyratory compaction test, undrained cohesion, undrained friction angle, K value, Poisson's ratio, Proctor and vibratory compaction, direct shear test, and moisture-density-compaction energy relationships.

CHAPTER 2. BACKGROUND/LITERATURE REVIEW

This chapter consists of four parts that address compaction in general, the performance related parameters of compacted geomaterials, conventional and innovative lab testing methods to determine the parameters, and the current Compaction Forecasting Expert Database (CFED). The purpose of this chapter is to provide background information about some engineering parameters of compacted geomaterials, the relationships within the parameters, and to discuss and compare the lab testing methods to evaluate these parameters.

Compaction of Geomaterials

Compaction of soils to improve engineering properties can be traced back hundreds years when people threw heavy stones repeatedly to increase the density of the soil. Today soil is still the most abundant and commonly used construction material, but it must meet engineering design requirements (e.g., shear strength, compressibility, and permeability). In most conditions, soil is a three-phase system that consists of solid soil particles, water, and air. Proper compaction will improve the compressibility, shear strength, and stiffness of soils by compressing the voids filled with air and water. Hilf (1991) observed that a properly compacted well-graded gravel may be 15 times as resistant to deformation under a load as the same material in the loose state. For cohesive soils, Pitt (1981) found that the shear strength parameters with different levels of compaction are more variable than the granular geomaterials.

In the field, dry unit weight and moisture content of compacted geomaterials are the most commonly used engineering parameters to evaluate the compaction performance. Most specifications require the contractor to achieve a compacted field dry unit weight of 90% to 95% of the maximum dry unit weight and plus or minus 2% of optimum moisture content determined by either standard or modified Proctor test. In some cases, soil can be compacted above the minimum compaction requirement in terms of dry unit weight and moisture content, but can still be unstable due to low shear strength, stiffness, and high compressibility. Therefore, it is desirable but very difficult and time consuming to determine the relationships between dry unit weight, moisture content, and other significant engineering properties (i.e., shear strength, stiffness, and compressibility) of compacted geomaterials.

The Engineering Properties of Compacted Geomaterials

As the increased number and size of construction projects being designed and constructed, the importance of the strength and stiffness characteristics of compacted geomaterials has long been recognized by researchers and engineers. A basic knowledge of these engineering properties and behaviors of compacted geomaterials is very essential and will be discussed below.

The shear strength of compacted geomaterials

Das defined “the shear strength of a soil mass is the internal resistance per unit area that the soil mass can offer to resist failure and sliding along any plane inside it” (2009, 365). The safety and stability of sustained structures (e.g., embankments, buildings, dams, and retaining walls) depends on the shear strength of soils underneath the structures.

Mohr-Coulomb failure criterion

The Mohr-Coulomb failure criterion is most commonly used to estimate the failure of materials under different drainage and strain conditions based on the critical combination of normal (σ) and shear stress (τ) instead of the extreme value of normal or shear stress alone. The shear stress on a failure plane is a function of normal stress and the failure envelope is a curved line. However, for most soil mechanics problems, the shear stress on the failure plane (τ_f) can be considered as a linear function of the normal stress (Equation 1). Shear strength parameter values are defined as the cohesion (c) and internal friction angle (ϕ) of soils which can be determined by lab tests; these tests are discussed below. The values of cohesion and internal friction angle are not constant for different loading conditions, stress history, testing conditions, or soil structures and can vary over a considerable range (Seed et al. 1960).

$$\tau_f = c + \sigma (\tan\phi) \quad (1)$$

Equation 1 is an expression of the shear strength criterion based on total stress. In saturated soils, the effective stress (total stress minus pore water pressure) is the stress carried by soil solids, and the cohesion and internal friction angle in Equation 1 will be based on effective stress.

Stress path method

The states of stress of Mohr-Coulomb failure criterion are represented in a Mohr circle coordinate system. Sometimes it is more convenient to represent that state of stress using a

stress path method. Lambe (1967) proposed a stress path method that uses lines to connect the points of a Mohr circles to analyze the history and variation of soil stresses and strains. A series of points that the maximum shear stress point of each Mohr circle (Figure 1A) can be represented on a p-q coordinate system (Figure 1B).

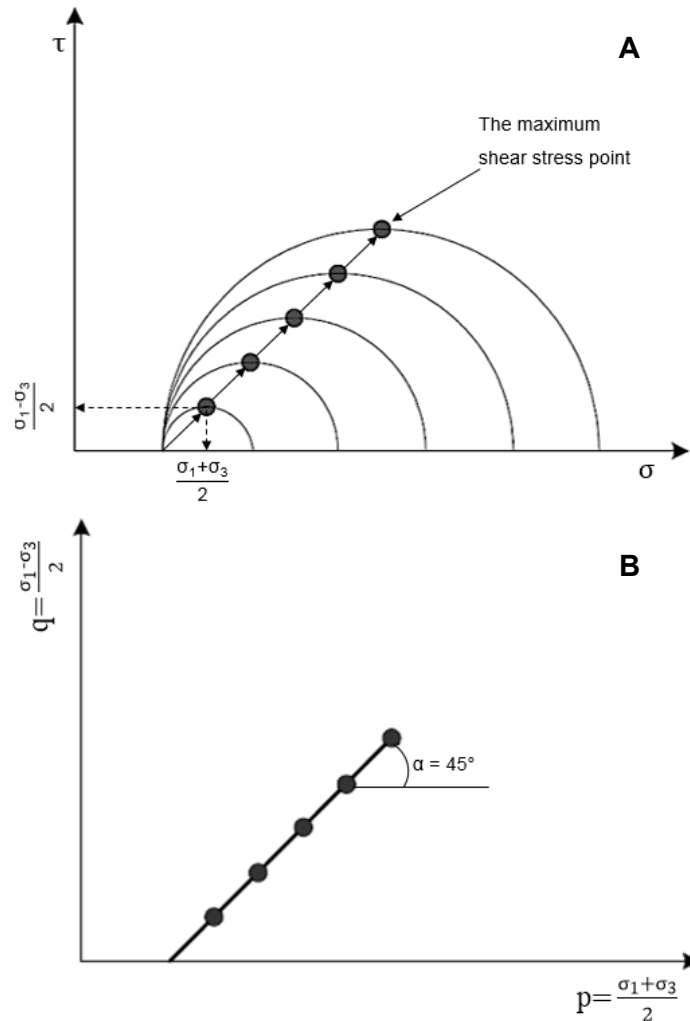


Figure 1. The maximum shear stress points in Mohr circle system (A) and the stress path method (B)

Figure 2 shows a theoretical diagram of the stress paths for four types of triaxial tests simulating all the possible field stress and deformation changes due to active and passive retaining walls, foundation loading, and excavation. For convenience, the vertical and horizontal stresses that acted on the samples were assumed as major and minor principal stresses.

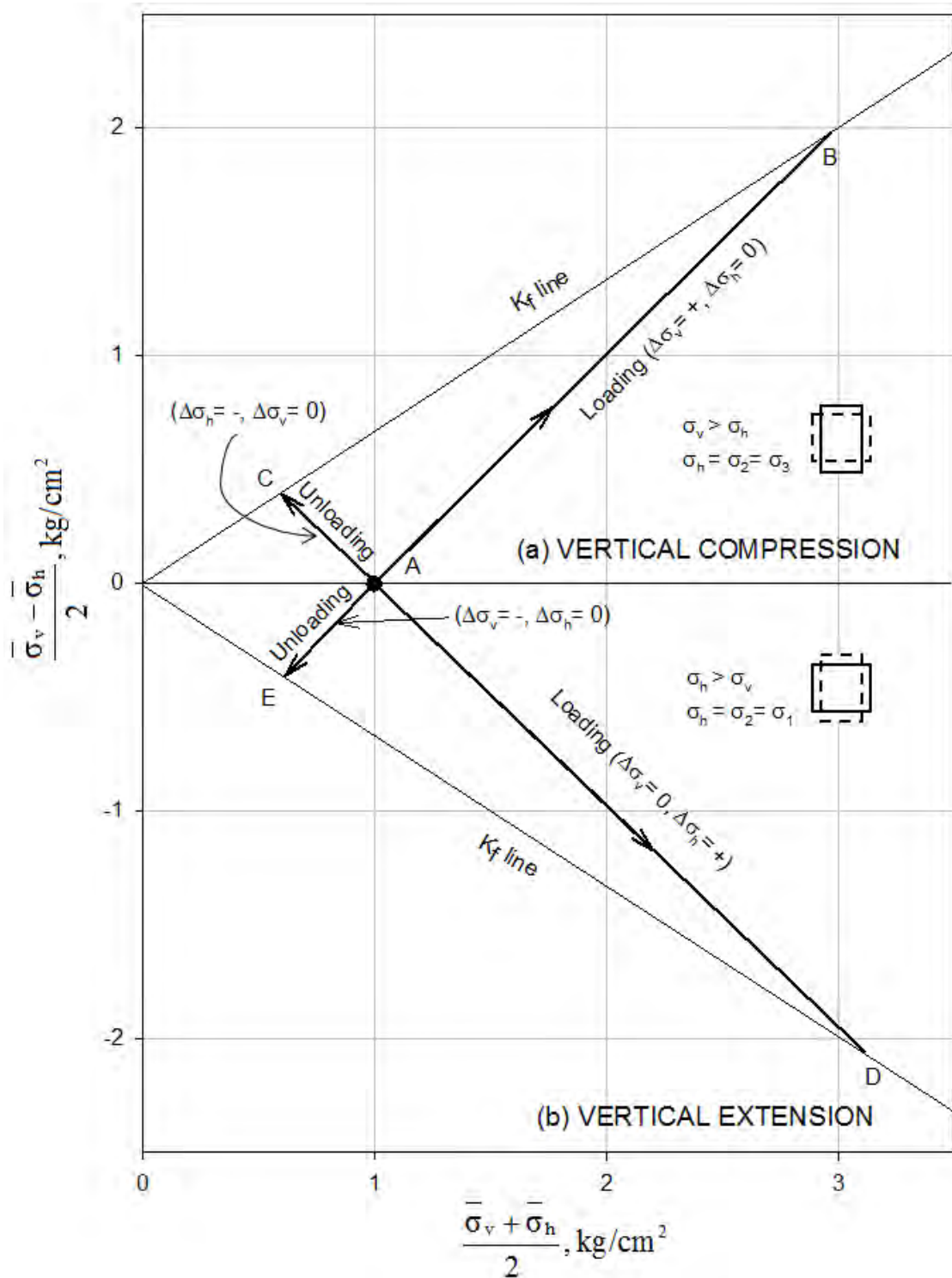


Figure 2. Stress paths for triaxial tests (redrawn from Lambe 1967)

Lambe and Marr (1979) later demonstrated that the stress path method can also determine soil cohesion and internal friction angles based on the strength envelope in the Mohr circle coordinate system (Figure 3).

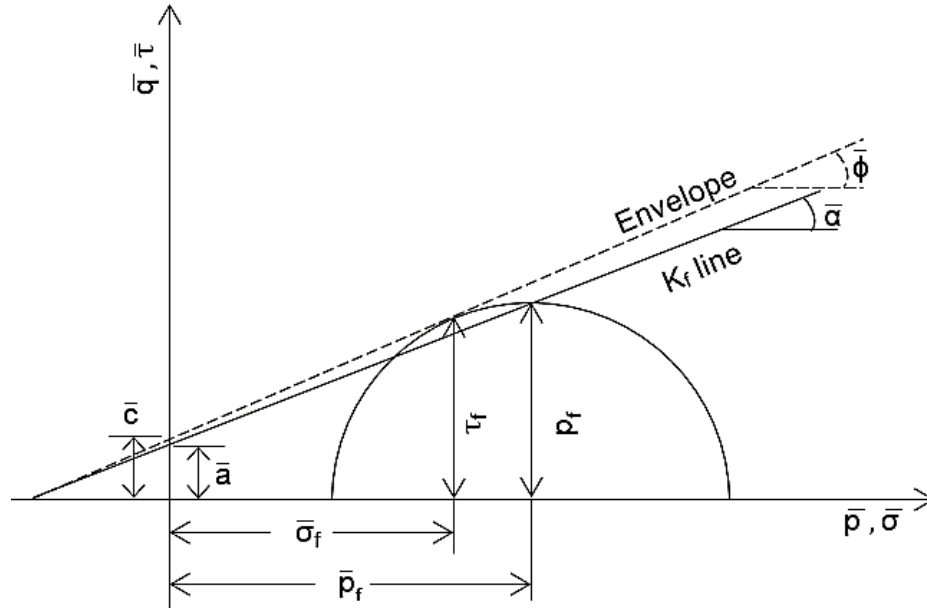


Figure 3. Failure condition (redrawn from Lambe and Marr 1979)

The geometric relationships between the “cohesion intercept (\bar{a})” (Lambe and Marr 1979), slope of K_f line ($\bar{\alpha}$), cohesion of soil (\bar{c}), and internal friction angle ($\bar{\phi}$) are shown in Equation 2 and Equation 3.

$$\bar{\phi} = \sin^{-1}(\tan \bar{\alpha}) \quad (2)$$

$$\bar{c} = \frac{\bar{a}}{\cos \bar{\phi}} \quad (3)$$

Factors that influence the shear strength of compacted geomaterials

In the field, the relationships between dry density, water content at compaction, and the resulting shear strength are important considerations for compacting cohesive soils. For example, the shear strength of soils having the same dry density but different moisture contents could be very different even when the moisture contents are close to the optimum moisture content, because of the influences of soil structure, method of compaction, pore pressure, and aging of the compacted geomaterials (Hilf 1991). In most cases, when higher compaction energy is applied to geomaterials with the same moisture contents, higher dry densities and higher shear strengths will result. However, Figure 4 shows that with the same

compaction energy, as molding water content increases the shear strength decreases, and the highest dry density sample does not produce the highest shear strength. Also, at a given molding water content, higher compaction energy does not always result in higher shear strength. Seed et al. (1960) explained that increasing the dry density does not always result in increased shear strength because in some soils with high moisture contents, higher pore water pressure will cause more dispersed soil particle structures, and the structures are of primary importance in determining the strength. Although compaction generally increases the shear strength of soils, when interparticle forces are not strongly attractive or repulsive, the amount and nature of applied compaction energy can have the greatest effects on shear strength. Hilf (1991) also indicated that capillary pressures in voids play an important role on shear strength when the moisture content of compacted cohesive soils is below the optimum moisture content.

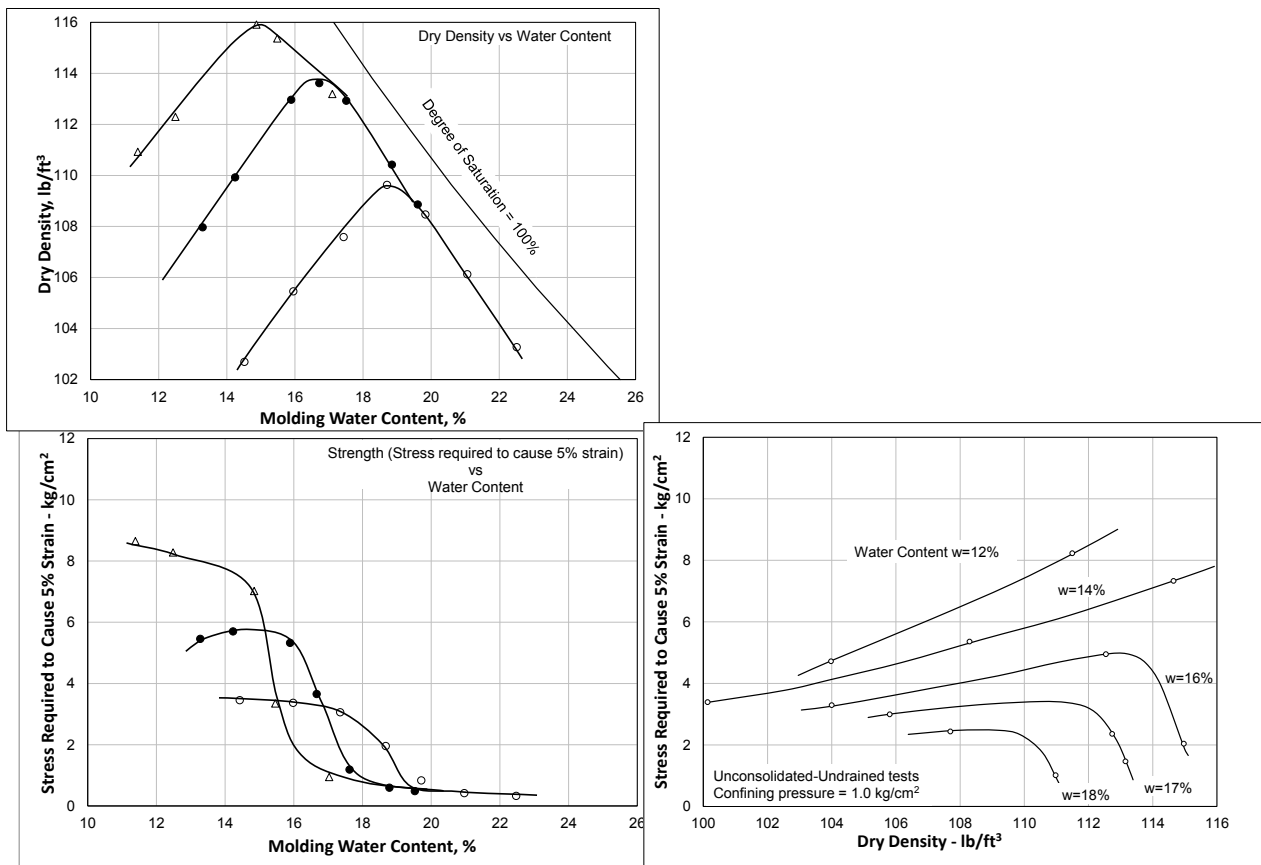


Figure 4. Relationships between dry density, water content and strength as compacted for samples of Silty Clay (redrawn from Seed et al. 1960)

Lambe (1958) also indicated that higher compaction energy may yield more dispersed structure of clays at a given moisture content (Figure 5). Since high moisture content tends to reduce the shear strength of uncompactd clay and higher compaction energy increases the interparticle repulsive force that permits more shifting of clay particles. As a result, clay particles with higher compaction energy are more parallel and thus yield higher compacted density, but the shear strength may be decreased.

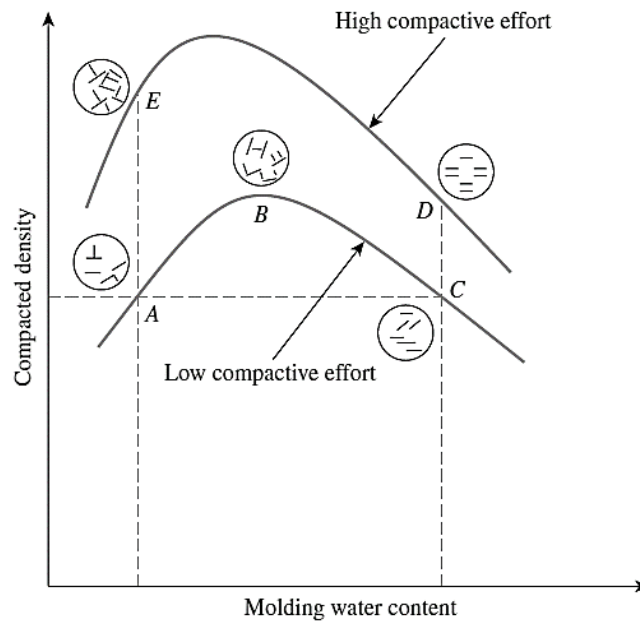


Figure 5. Effect of compaction on structure of clay soils (redrawn from Lambe 1958)

Seed et al. (1960) also illustrated that the compaction method may be the most important factor that affects the shear strength of some compacted cohesive soils at low strains. Figure 6 shows the shear strength of compacted silty clay samples prepared by static, vibratory, and kneading compaction. The compaction method has little effect on the shear strength of samples at dry of optimum which indicates the different compaction methods produce similar soil structures. However, during compaction on wet of optimum, the compaction methods have great effect on the resulting shear strength. The author explained that the fact is because none of the compaction methods induce big shear strains at water contents below optimum, but at wet of optimum, the kneading compaction induces the most shear strains and thus the highest degree of dispersion in soil structure that yielded least shear strength than the other two methods.

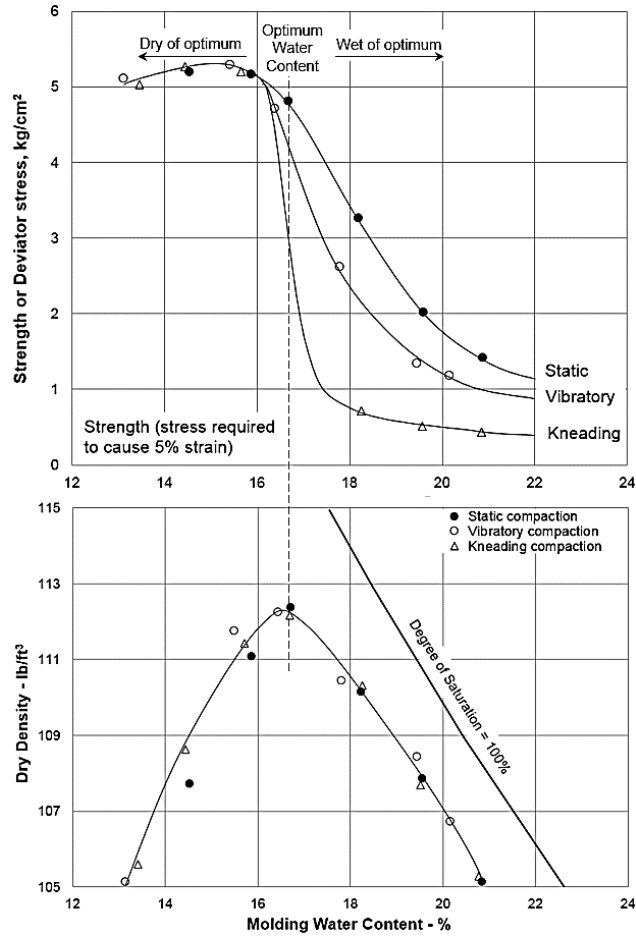


Figure 6. Influence of method of compaction on strength of silty clay (redrawn from Seed et al. 1960)

Seed et al. (1960) used three functions (Equation 4 through Equation 6) to describe total strength of the soil and the strength contribution of the granular particles and clay particles,

$$S_g = \bar{\sigma} \tan \phi_g \quad (4)$$

$$S_c = f(\bar{\sigma}, e_f, d, t) \quad (5)$$

$$S = S_g + S_c = \bar{\sigma} \tan \phi_g + f(\bar{\sigma}, e_f, d, t) \quad (6)$$

where:

$\bar{\sigma}$ = Effective normal stress,

ϕ_g = Internal friction angle of granular particles,

e_f = Void ratio at failure,

d = spacing of the clay particles at points of closest proximity, and

t = time.

Compared to compacted cohesive soils, Hilf (1991) discussed that the shear strength of cohesionless soils depends more on the relative density (Equation 7) and the internal friction angles of coarse grained materials are affected by the gradations and particle shapes.

$$D_d = \frac{e_{max} - e}{e_{max} - e_{min}} \quad (7)$$

where:

D_d = Relative density,

e = void ratio of the soil being tested,

e_{max} = maximum index void ratio (ASTM-4253), and

e_{min} = minimum index void ratio (ASTM-4254).

Hilf (1991) also observed that the compaction behaviors of cohesionless soils are not significantly affected by water content during compaction process. However, the bulking phenomenon of some granular soils should be determined and avoided during compaction because somewhat low densities occurring when the soils are partially saturated due to capillary stress within particles.

The stiffness parameters of compacted geomaterials

Duncan and Chang (1970) stated that to fully represent stress-strain behaviors of anisotropic materials under a general system of changing stresses, stiffness modulus and Poisson's ratio are the basic coefficients need to be determined. In the following sections, the stiffness modulus, Poisson's ratio, and the lateral earth pressure induced by compaction will be introduced and discussed.

Stiffness modulus

Atkinson defined stiffness as “the gradient of the stress-strain line of a material and largely determines the strains and displacements in structure, or in the ground, as they are loaded or unloaded” (2007, 24). For soils, the stress-strain relationship is curved (Figure 7) and affected by density, moisture content, structure, drainage conditions, strain conditions (i.e., plain strain, triaxial), duration of loading, stress history, confining pressure, and shear stress (Duncan and Chang, 1970). Therefore, selecting samples and determining test conditions which can simulate corresponding field conditions is very important to evaluate stress-strain behaviors of geomaterials.

Elastic modulus (E) of geomaterials is a stress to strain ratio within the elastic and recoverable portion of the stress-strain curve. Das (2009) showed some representative values of the elastic modulus of soils (Table 1). There is a marked change in the gradient of the curve at yield point. When the stress-strain relationship passed the yield point, the secant (E_s) and tangent (E_t) modulus are most commonly used engineering terms.

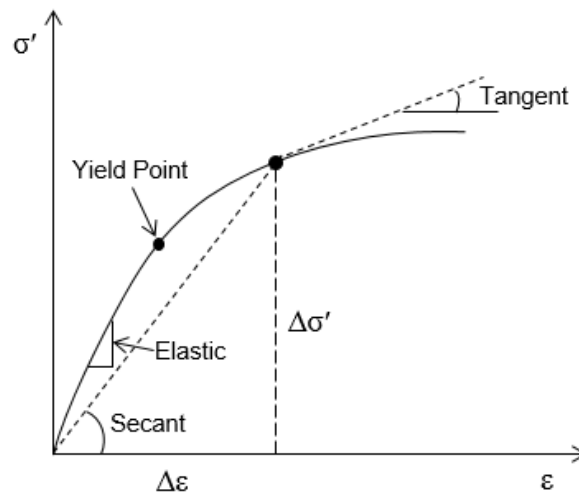


Figure 7. Tangent and secant stiffness modulus of soils

Table 1. Representative values of the elastic modulus of soil (from Das 2009)

Soil type	E (kN/m ²)	E (lb/in ²)
Soft clay	1,800 – 3,500	250 – 500
Hard clay	6,000 – 14,000	850 – 2,000
Loose sand	10,000 – 28,000	1,500 – 4,000
Dense sand	35,000 – 70,000	5,000 – 10,000

Resilient modulus (M_r) is a stiffness modulus that is widely used to evaluate the resilient response of pavement foundation materials under cyclic loading and unloading conditions.

The resilient modulus can be calculated by Equation 8,

$$M_r = \frac{\sigma_d}{\varepsilon_r} \quad (8)$$

where: M_r = resilient modulus,

σ_d = deviator stress, and

ε_r = resilient (recoverable) strain.

Brown and Hyde (1975) conducted cyclic triaxial tests on a type of crushed stone with cyclic and constant confining (i.e., constant stress was equal to the mean of the cyclic value) pressures. The results of the two confining pressure tests showed similar results of the resilient modulus and permanent strain for this type material. Wolfe (2011) also conducted cyclic triaxial test on granular and cohesive soil samples with variable density and moisture content to evaluate relationships between resilient modulus, moisture content, dry unit weight, and degree of saturation. Wolfe showed that increasing moisture content and degree of saturation tend to reduce the resilient modulus values but the relationship between M_r values and dry unit weight did not show a clearly trend.

Poisson's ratio

Terzaghi defined that “the positive vertical strain produced by a vertical pressure is associated with a negative horizontal strain and the absolute value of the ratio between the horizontal and vertical strain is called Poisson's ratio” (1943, 368). Poisson's ratio (ν) can be determined by measuring lateral (ε_r) and axial strain (ε_a) of a material under uniaxial compression or extension tests with zero confining stress (Equation 9).

$$\nu = -\frac{d\varepsilon_r}{d\varepsilon_a} \quad (9)$$

Poisson's ratio for perfect elastic materials is constant. Duncan and Chang, (1970) discussed that Poisson's ratio is one of the required coefficients to fully represent stress-strain behaviors under a general system of changing stresses. The authors calculated the Poisson's ratio for silica sand with increments of applied axial stress by Equation 10,

$$\nu = \frac{\Delta\epsilon_1 - \Delta\epsilon_v}{2\Delta\epsilon_1} \quad (10)$$

where:

ϵ_1 = axial strains (compression positive),

ϵ_v = volumetric strains (compression positive), and

Δ = *an incremental change*.

However, for soil samples, Poisson's ratio is commonly measured under a triaxial state of stress. Bowers (1978) discussed that it is not easy to accurately determine the Poisson's ratio of soils due to difficulties in measuring the horizontal deformation of soil samples under either uniaxial or triaxial compression conditions. The sophisticated instruments for these measurements are generally not available in most laboratories. Hence, in most cases, Poisson's ratio was simply assumed as a constant value even though many researchers had noted that the Poisson's ratio varies with some controlling parameters such as stress and strain level (Bowers 1978). Some representative values of Poisson's ratio for soils are shown in Table 2.

Table 2. Representative values of Poisson's ratio (from Das 2009)

Type of soil	Poisson's ratio
Loose sand	0.20 – 0.40
Medium sand	0.25 – 0.40
Dense sand	0.30 – 0.45
Silty sand	0.20 – 0.40
Soft clay	0.15 – 0.25
Medium clay	0.20 – 0.50

Different nonlinear stress dependent Poisson's ratio relationships were observed from some lab testing data. The initial and tangent Poisson's ratio have been defined for finite element analysis. The introductions and detailed discussions of these parameters and relationships are presented in Bowers (1978).

Bowers (1978) also conducted consolidated-drained triaxial tests to define Poisson's ratio for a remolded loess from near St. Louis, MO. A total of nine tests were conducted on the

samples with same water content (16%) and different dry densities (94, 97, and 100 pcf). The confining pressure of 10, 30 and 50 psi was used for each density and three samples with same density (94 pcf) and different water contents (10%, 13%, and 16%) were tested to evaluate the effect of changes in water content to Poisson's. For this soil type and testing conditions, Bowers (1978) concluded that the Poisson's ratio is predominately influenced by stress level, but the dry density, molding water content, and confining pressure appear to have little influence. For this type loess, a finite element analysis model with a constant value of 0.32 for Poisson's ratio showed close results to other models with varying Poisson's ratios.

Resilient Poisson's ratio (ν_r) is used to represent the stress-strain behavior of pavement foundation materials under cyclic loading and unloading condition. The fact that constant confining pressure (CCP) cannot simulate field condition well has long been recognized. Brown and Hyde (1975) showed an apparent difference between resilient Poisson's ratios of a well-graded crushed stone that were determined under both constant and variable confining pressure. Figure 8 shows the Poisson's ratios varied from 0.1 to more than 0.5 (when dilation occurring) under constant confining pressure but the Poisson's ratios under cyclic confining pressure were relatively constant.

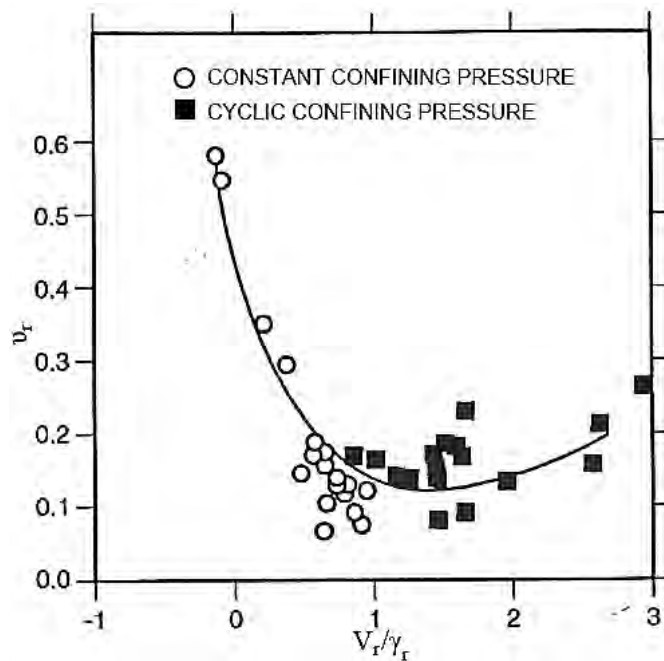


**Figure 8. Poisson's ratio versus of volumetric strain to shear strain
(from Brown and Hyde 1975)**

Lateral earth pressure induced by compaction

The lateral stress ratio, K , is the ratio of lateral to vertical stress of soil that acts as a fundamental engineering value for foundation and retaining structure design. A bearing capacity failure of adjacent soil and failure may be caused by insufficiently mobilized lateral stress called rutting, so, it is important to monitor K values and evaluate whether soil can withstand the stress from structures or loads upon the soil. Three possible cases of K value (K_a , K_p and K_o) need to be considered for design of retaining structures.

Das (2009) illustrated that the active and passive earth pressure coefficient (K_a and K_p) of soils at failure can be calculated based on Equation 11 and Equation 12. The value of K_a and K_p depends on the cohesion, friction angle and applied vertical stress (σ_1) for each case. For cohesionless materials, the second portion of the equations will be zero.

$$K_a = \frac{\sigma_3}{\sigma_1} = \tan^2 \left(45^\circ - \frac{\phi}{2} \right) - \left(\frac{2c}{\sigma_1} \right) \tan \left(45^\circ - \frac{\phi}{2} \right) \quad (11)$$

$$K_p = \frac{\sigma_3}{\sigma_1} = \tan^2 \left(45^\circ + \frac{\phi}{2} \right) + \left(\frac{2c}{\sigma_1} \right) \tan \left(45^\circ + \frac{\phi}{2} \right) \quad (12)$$

The at-rest pressure coefficient (K_o) is a special lateral stress ratio that happens when the lateral deformation of a soil mass is zero under a vertical stress. Brooker (1965) indicated that the value of K_o is nearly constant for a given soil during the first loading (primary compression) and can be correlated to effective internal friction angle. Some empirical relationships between the K_o and the shear strength properties of soils have been established due to the difficulties of directly measurement in both lab and field (Table 3).

Table 3. The proposed empirical equations for calculation of K_o

Proposed Equation:	Proposer	Suitability
$K_o = 1 - \sin \phi'$	Jaky	For loose coarse-grained soils
$K_o = (1 - \sin \phi')(OCR)^{\sin \phi'}$	Maybe and Kulhawy	All range
$K_o = 0.44 - 0.42 \left[\frac{PI}{100} \right]$	Massarsch	Normally consolidated fine-grained soils
$K_o = 0.9(1 - \sin \phi')$	Frazer	—
$K_o = \left(1 + \frac{2}{3} \sin \phi' \right) \frac{1 - \sin \phi'}{1 + \sin \phi'}$	Kezdi	—
$K_o = 0.95 - \sin \phi'$	Brooker and Ireland	For cohesive soils
$K_o = 0.19 + 0.233 \log PI$	Kenney	For clays

Note: PI is the plastic index in %.

The effects of compaction induced earth pressure and the resulting structural deflections have long been a serious concern in geotechnical design and construction but not yet accurately determined or analyzed. Compaction is a process of transient, moving, surficial, and cyclic loading and unloading to a soil mass that can result in significant increases in peak and residual lateral earth pressures. Duncan and Seed (1986) proposed an incremental numerical analysis method and a hysteretic model to evaluate the peak and residual compaction-induced lateral stresses under K_0 conditions. The model predictions provided very good agreement with some field measurements. In this model, the peak and residual lateral earth pressure resulting from placement and each compaction lift can be calculated based on five parameters related to the post-compaction shear strength parameters (Table 4).

Table 4. Hysteretic K_0 loading/unloading model parameters (from Duncan and Seed 1986)

Parameter	Name	Recommended limits
α	Unloading coefficient	$0 < \alpha < 1$
β	Reloading coefficient	$0 < \beta < 1$
K_0	Coefficient of at-rest lateral earth pressure for virgin loading	$0 < K_0 < 1$
$K_{1, \phi'}$	Frictional component of limiting coefficient of lateral earth pressure	$K_a \leq K_{1, \phi'} \leq K_p$
c'	Effective stress envelope cohesion intercept	

Figure 9 shows the vertical and horizontal stresses path and some basic components of the hysteretic model. The definitions of the symbols and acronyms are show in Table 5.

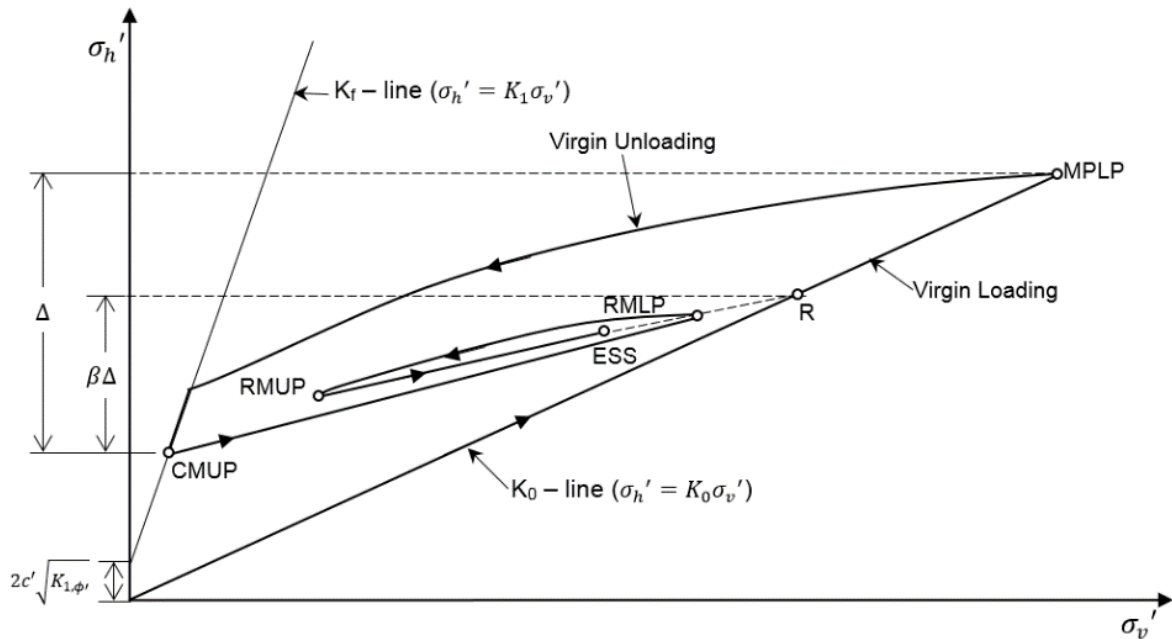


Figure 9. Basic components of hysteretic K_0 -loading/unloading model (redrawn from Duncan and Seed 1986)

Table 5. Hysteretic K_0 -loading/unloading model definitions

Hysteretic model terms	Definitions
Existing stress state (ESS)	Existing lateral and vertical effective stresses
Maximum past loading point (MPLP)	Maximum past lateral and vertical effective stresses
Current minimum unloading point (CMUP)	Lateral and vertical effective stresses at stress state corresponding to minimum σ'_h achieved since last MPLP
Recent maximum loading point (RMLP)	Lateral and vertical effective stresses at stress state corresponding to maximum σ'_h achieved during most recent loading cycle
Recent minimum unloading point (RMUP)	Lateral and vertical effective stresses at stress state corresponding to minimum σ'_h achieved during most recent unloading cycle
Reloading point (R)	Point of intersection between reloading stress path and virgin K_0 -line
Δ	Difference in horizontal effective stresses between MPLP and CMUP
β	Fraction of Δ regained in fully reloading from CMUP to R
α	Modified unloading coefficient

Lab Testing Devices for Measuring Strength and Stiffness Parameters of Geomaterials

Many different lab testing methods have been developed and widely used to measure shear strength and stiffness parameters of geomaterials. However, all of them have some advantages and shortcomings. Some conventional (direct shear and triaxial test) and innovative lab tests will be introduced and discussed below:

Direct shear and triaxial shear test

Direct shear test is an ASTM standardized (ASTM D3080) lab testing method to determine the consolidated drained shear strength of fine grained soils. The detailed testing procedures are described in ASTM D3080 and the chapter 3 of this thesis. To determine the Mohr strength envelopes, at least three tests need to be performed on samples under different normal pressure. The test procedures consists of three main stages: sample preparation, consolidation, and shearing. The consolidation stage proceeds as standard one dimensional consolidation test (ASTM D2435). Samples have to reach to equilibrium prior to shearing stage and the shearing rate should be determined based on the coefficient of consolidation for the last loading increment of consolidation stage. Olson (1989) also pointed out, for highly overconsolidated clays that have undrained strength exceeding the drained strength, the time-settlement curve cannot yield useful coefficient of consolidation, so a time to failure ranging from one to four days should be used based on experience. Direct shear test is very economical and simple to perform, but it also has some shortcomings such as soil samples fail on a designated plane which may not be the weakest one, rotation of principal stresses cannot be determined, and the sample size of the test is small. ASTM D3080 also stated that the shear stress and strain relationship cannot be determined based on direct shear test results due to an appropriate height cannot be defined for calculation of shear strains.

Three types triaxial shear tests (Table 6) were developed and standardized to simulate different field conditions and evaluate the drained and undrained shear strength properties of soils. According to Das (2009) the triaxial shear test is one of the most reliable methods available for determining shear strength parameters.

Table 6. ASTM standard triaxial shear tests

Test Type	ASTM Standard
Unconsolidated-undrained test (UU test)	ASTM D2850
Consolidated-undrained test (CU test)	ASTM D4767
Consolidated-drained test (CD test)	ASTM D7181

The CU and CD test can be conducted on different types of soils, but UU test usually is only conducted on clay samples and depends on a concept that internal friction angles are equal to zero of saturated cohesive soils. The total stress failure envelopes of UU test are horizontal lines due to the drainage is prevented in all stages of the test.

Compared to direct shear test, the triaxial shear test is more versatile and pore water pressures can be measured during the tests. Also, the principal stresses are well defined and the weakest failure plane can occur anywhere in the soil samples. However, it is time-consuming and expensive to conduct the triaxial tests due to the complicated test set-up and procedures. Some innovative triaxial testing devices such as cyclic triaxial test device and UI-FastCell have been developed to evaluate the shearing behaviors of soils under different field conditions.

Hveem stabilometer test

F.N. Hveem designed the Hveem stabilometer in the 1920s at the California Department of Transportation to evaluate the performance of base, subbase, and subgrade layers under traffic loads (Chua and Tenison 2003). The stabilometer test measures structural adequacy, and resistance value, R-value, and then correlate R-value to the elastic modulus of the materials. A schematic of Hveem stabilometer is shown in Figure 10.

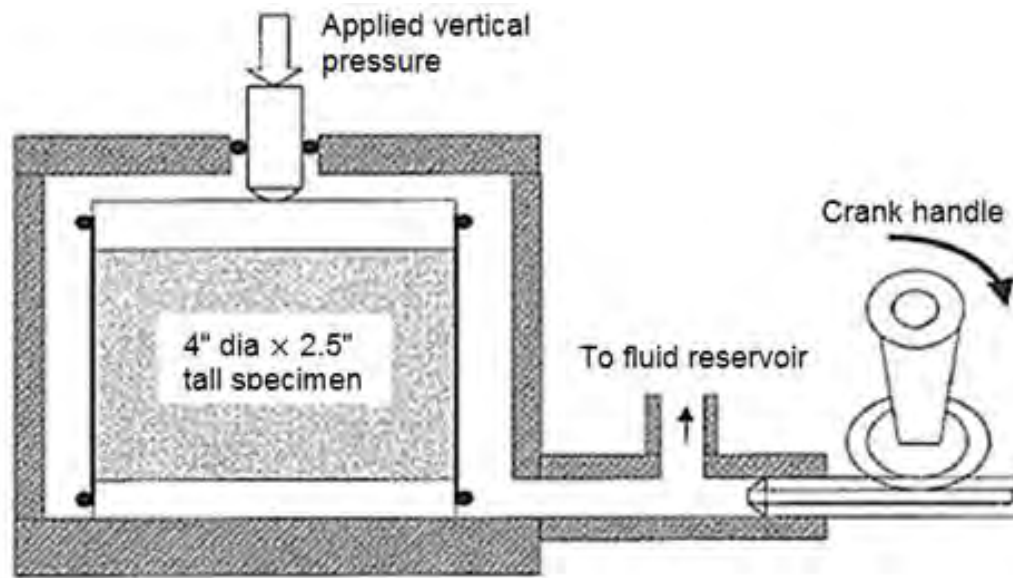


Figure 10. Schematic of the Hveem stabilometer (from Chua and Tenison 2003)

According to ASTM D2844, to perform the test, at least four soil samples with different moisture contents need to be prepared by kneading compactor. To simulate the field condition, Garber and Hoel (2009) recommended the moisture content of soil samples for stabilometer test should be set at the moisture content that can exude water at 300 psi vertical pressure. Since, several tests performed in California were observed that the soil supporting highway pavement will exude moisture under pressure of 300 psi. Exudation pressure needs to be determined for preparing fully saturated soil samples by using an exudation pressure sensor. The second stage is to determine the horizontal pressure, P_h , for calculating R-value. At beginning of stage two, a horizontal pressure of 5 psi is applied on soil specimen and then increase vertical pressure until 160 psi. At the same time, a horizontal pressure, P_h , is measured without allowing any horizontal strain. After stage two, the top pressure will be decreased to 80 psi and the horizontal pressure will be adjusted to 5 psi.

Then, the horizontal pressure will be increased to 100 psi by turning the handle to inject hydraulic fluid into the chamber. The number of turns needs to be recorded as D_2 value.

The resistance value, R-value, can be calculate by Equation 13 (ASTM D2844) and the correlation between R-value and elastic modulus (E) is shown in Equation 14 (Chua and Tenison, 2003)

$$R = 100 - \frac{100}{\frac{2.5(160 - 1)}{D_2(P_h - 1)} + 1} \quad (13)$$

$$E = \frac{\pi D^2}{4C} (1 - \nu) \frac{R}{100 - R} P_h \quad (14)$$

where:

P_h = horizontal pressure from stage two of the test,

D_2 = number of turns of the horizontal pressure handle in stage three of the test,

D = diameter of soil specimen,

C = 0.2 (conversion for volume of fluid inject to chamber), and

ν = Poisson's ratio

According to Chua and Tenison (2003), the elastic modulus correlated from Hveem stabilometer is also dependent on the exudation pressure, overconsolidation pressure (OCR), Poisson's ration (ν), and internal friction angle (ϕ) of soils.

The stabilometer test also has some limitation. The sample preparation and test procedure of stabilometer test are slow and complicated that usually need two persons to perform the test. The exudation pressure for saturating soil sample and the boundary stress between soil sample and the flexible confinement have big influence on testing results of cohesive soils (Chua and Tenison, 2003). The stress-strain behavior of samples under different vertical and horizontal pressures cannot be continuously monitored.

UI-Fast Cell

University of Illinois FastCell (UI-FC) is an innovative laboratory triaxial test machine invented at the University of Illinois to study behaviors of cross-anisotropic stress-path-dependent aggregates and determine anisotropic resilient properties (Figure 11). Compared to conventional triaxial test, UI-FC permits stresses to be cycled and pulsed independently in the vertical and horizontal directions. According to Seyhan and Tutumluer (2002), this feature allows the device to better simulate field conditions of pavement systems where the materials are subjected to the continuous rotated principal stresses caused by the rolling nature of wheel loads. The vertical and radial linear variable differential transformers (LVDTs) are used to monitor the vertical and horizontal displacement. The sample size used in UI-FC is 6 in. in diameter by 6 in. in height ($H/D=1$).

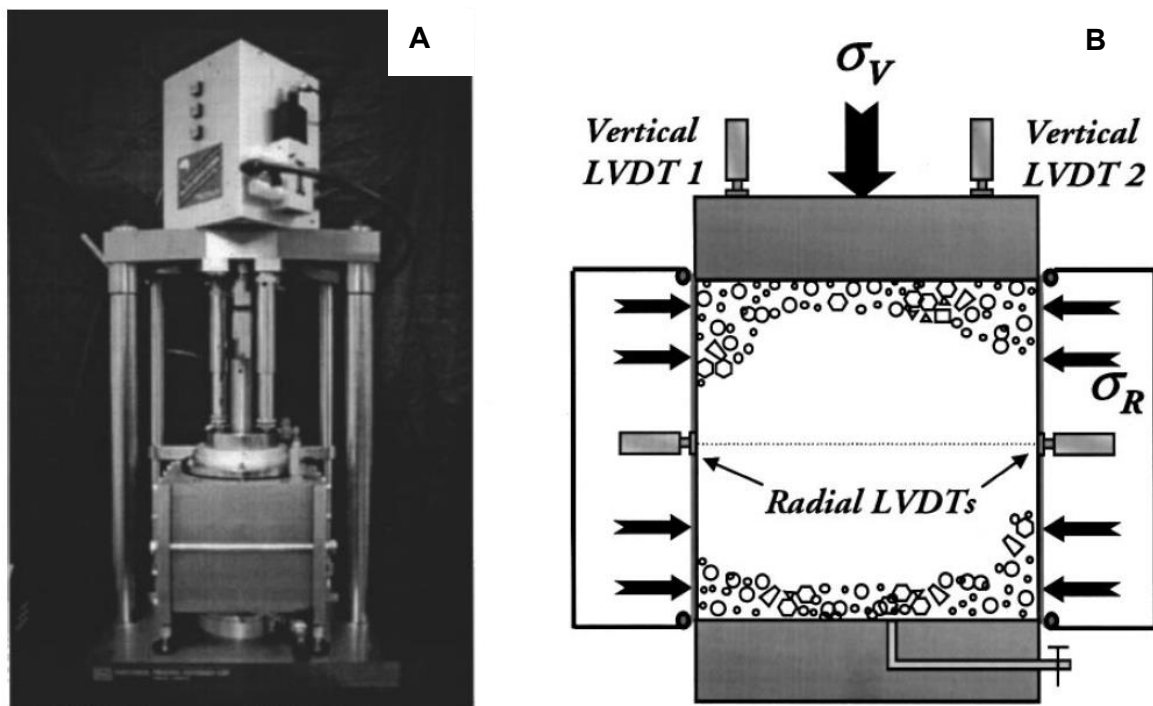


Figure 11. University of Illinois FastCell (UI-FastCell) triaxial testing device: (A) UI-FastCell; (B) representation of cylindrical specimen (from Seyhan and Tutumluer 2002)

Sample preparation and testing procedures of the UI-FC test basically follow the standard cyclic triaxial test (AASHTO T294-94) that the samples are subjected to 15 triaxial stress states with 100 load repetitions. Two proposed UI-FC test procedures and the schedule of

applied deviator stresses are shown in Table 7. According to Tutumluer and Seyhan (1999), to study the directional dependency of the granular material stiffness, both of the two procedures need to be conducted on each type material.

Table 7. Test procedures and stress states applied on aggregate samples (from Tutumluer and Seyhan 1999)

			Hydrostatic Stress, $\sigma_{\text{hydrostatic}}$ (kPa/psi)															
			21/3			35/5			69/10			103/15			138/20			
			1	2	3	4	5	6	7	8	9	10	11	12	13	14	15	
Test Procedure A	1	Vertical Pulsing	σ_{1d} (kPa/psi)	21/ 3	42/ 6	62/ 9	35/ 5	69/ 10	103/ 15	69/ 10	138/ 20	207/ 30	69/ 10	103/ 15	207/ 30	103/ 15	138/ 20	276/ 40
			σ_{3d} (kPa/psi)	0/0	0/0	0/0	0/0	0/0	0/0	0/0	0/0	0/0	0/0	0/0	0/0	0/0	0/0	0/0
	2	Radial Pulsing	σ_{1d} (kPa/psi)	0/0	0/0	0/0	0/0	0/0	0/0	0/0	0/0	0/0	0/0	0/0	0/0	0/0	0/0	0/0
			σ_{3d} (kPa/psi)	21/ 3	42/ 6	62/ 9	35/ 5	69/ 10	103/ 15	69/ 10	138/ 20	207/ 30	69/ 10	103/ 15	207/ 30	103/ 15	138/ 20	276/ 40
Test Procedure B	1	Radial Pulsing	σ_{1d} (kPa/psi)	0/0	0/0	0/0	0/0	0/0	0/0	0/0	0/0	0/0	0/0	0/0	0/0	0/0	0/0	0/0
			σ_{3d} (kPa/psi)	21/ 3	42/ 6	62/ 9	35/ 5	69/ 10	103/ 15	69/ 10	138/ 20	207/ 30	69/ 10	103/ 15	207/ 30	103/ 15	138/ 20	276/ 40
	2	Vertical Pulsing	σ_{1d} (kPa/psi)	21/ 3	42/ 6	62/ 9	35/ 5	69/ 10	103/ 15	69/ 10	138/ 20	207/ 30	69/ 10	103/ 15	207/ 30	103/ 15	138/ 20	276/ 40
			σ_{3d} (kPa/psi)	0/0	0/0	0/0	0/0	0/0	0/0	0/0	0/0	0/0	0/0	0/0	0/0	0/0	0/0	0/0

The vertical and horizontal resilient modulus can be determined based on the dynamic stress and recoverable strain. The preliminary testing results of four different granular materials were reported and shown in Tutumluer and Seyhan (1999). The horizontal resilient modulus are smaller than vertical resilient modulus for three of the four coarse grained granular materials except for a sand gravel material with high fines content (13.9%). All the test results showed good agreement with conventional cyclic triaxial tests.

K-mold test system

A K-mold test system was designed to evaluate the stress dependent elastic modulus, Poisson's ratio, cohesions and friction angles of soils in South Africa (Simmelink and de Beer 1995). The setup of the K-mold system is shown in Figure 12. The stiffness of the mold ranging from totally constrained and unconfined can be controlled. During the test, the variation of horizontal confining pressure is induced by the applied vertical stress. The loading frame of this system is controlled by computer system to apply haversine wave loads on testing samples to simulate the different field conditions for pavement geomaterials. A data acquisition system is used to continuously collect data from load cells and LVDTs.

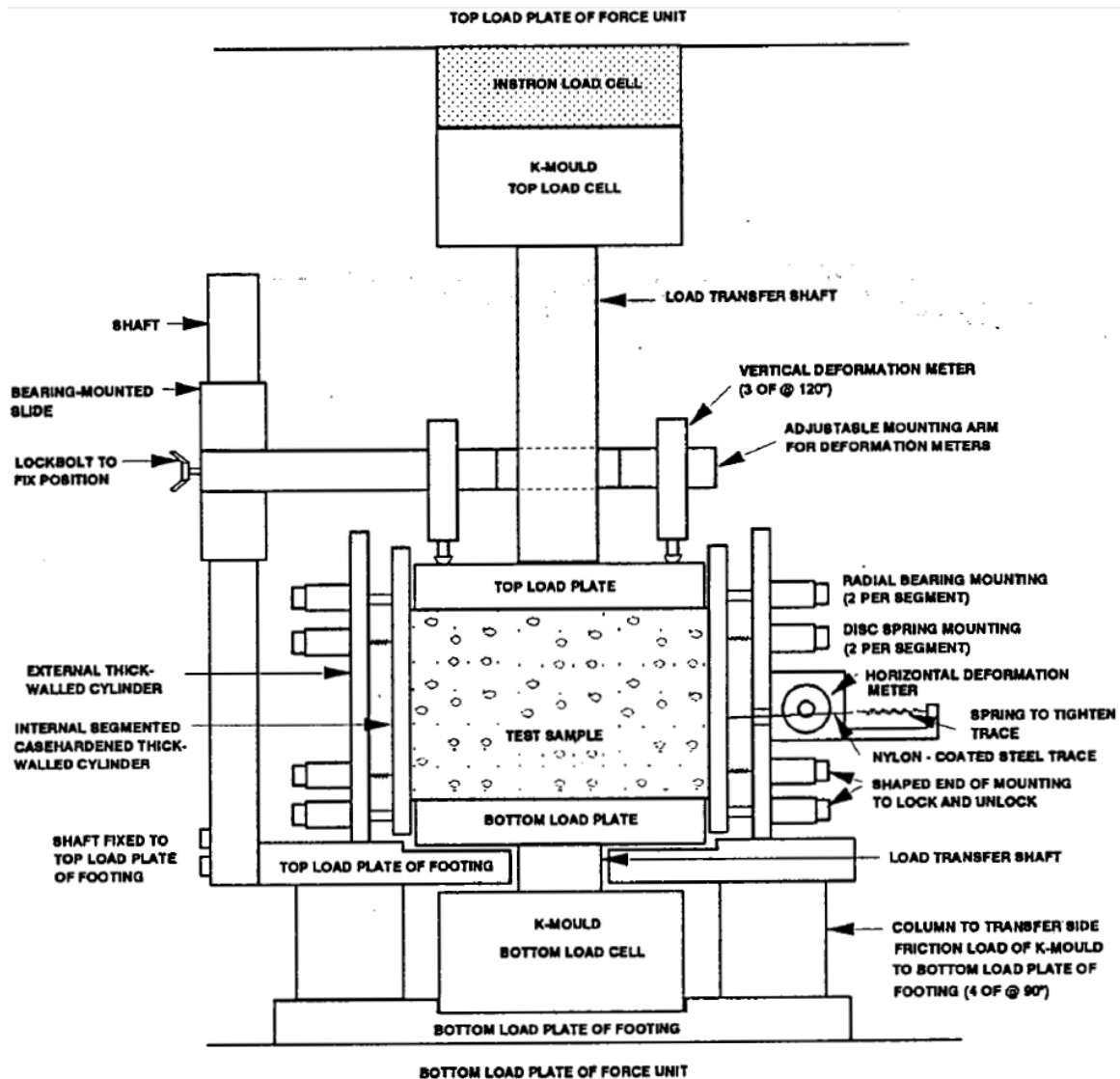


Figure 12. Schematic layout of K-mold set-up (from Semmelink and de Beer 1995)

The methods for calculating cohesion, friction angle, elastic modulus, and Poisson's ratio are exactly same with the methods used in the Iowa K test that will be discussed below. The K-mold test results showed four distinct sub-phases in the stress-strain relationship, stress path, and the elastic modulus of one loading and unloading cycle. Some typical testing results of a weathered granite material is shown in Figure 13. Semmelink and de Beer (1995) defined the steeper slopes of both loading and unloading curves as "rigid" sub-phases and the flatter slopes as "dynamic" sub-phases. The elastic behaviors and shear properties of samples are different in the four sub-phases. The authors also discussed that the stiffness of the mold (ranging from 15 to 45 MPa) has very little effect on the values of cohesion, friction angle, and Poisson's ratio from this test system.

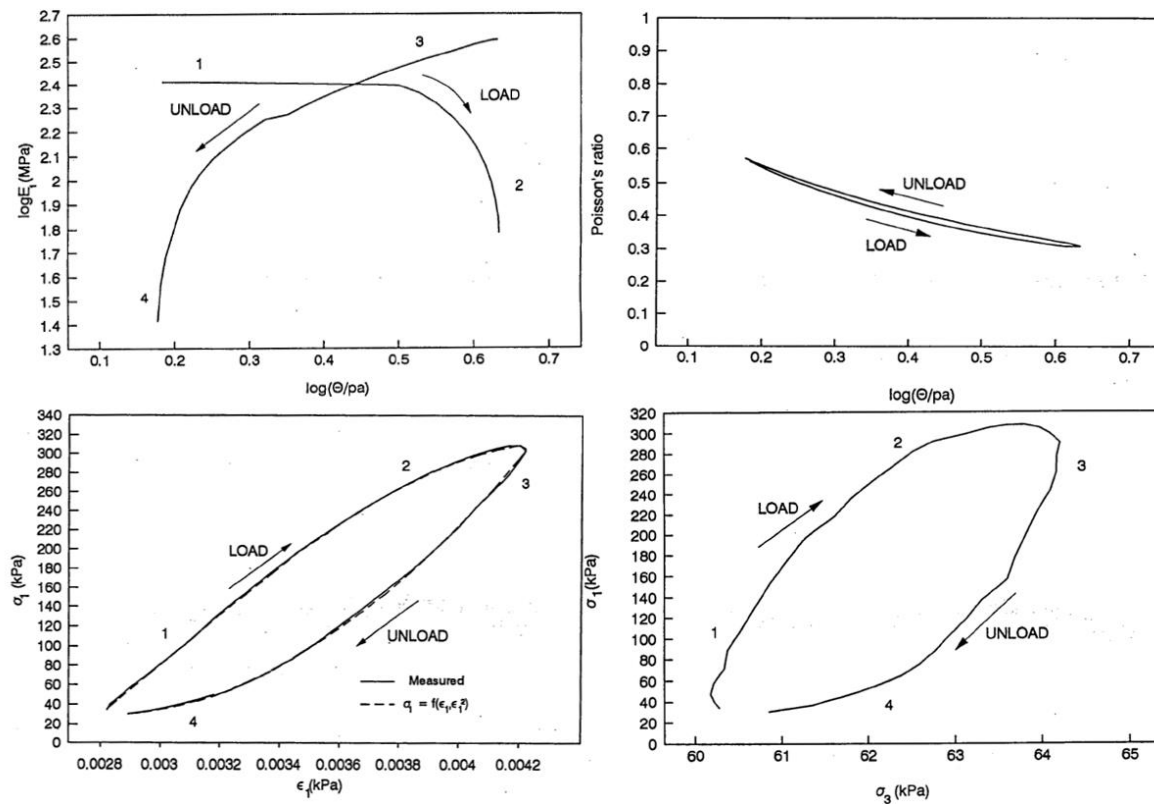


Figure 13. Typical K-mold system testing results of a weathered granite material (from Semmelink and de Beer 1995)

Pitt's K test device

Pitt (1981) proposed an apparatus to measure the stress ratio (K-value) of soil samples. A schematic of the proposed apparatus is shown in Figure 14. The mold consists of eight segments and constrained by a hinged band that can allow the mold achieve a better approximation of axisymmetric conditions. A U-shaped restraint spring installed in the spring housing to provide reactive restraint. The spring housing can be moved along the U-shaped spring with a screw that allows the spring to protrude different amounts, thus providing adjustable spring constants. The stress control device used to force the hinged restraint spring inward has not been decided yet and Pitt recommended the threaded stress adjustment can be replaced with an air cylinder. According to Pitt (1981), the calibration for the mold should provide a relationship between spring housing position, restraint constant, radial strain, and radial stress based on the strain gage readings. The author also recommended the interior friction of the mold may be reduced using overlapped Teflon segments and the plastic films (Parafilm M) to warp the samples, since it not only can prevent moisture content loss, also the friction between the films and lubricate Teflon is near frictionless.

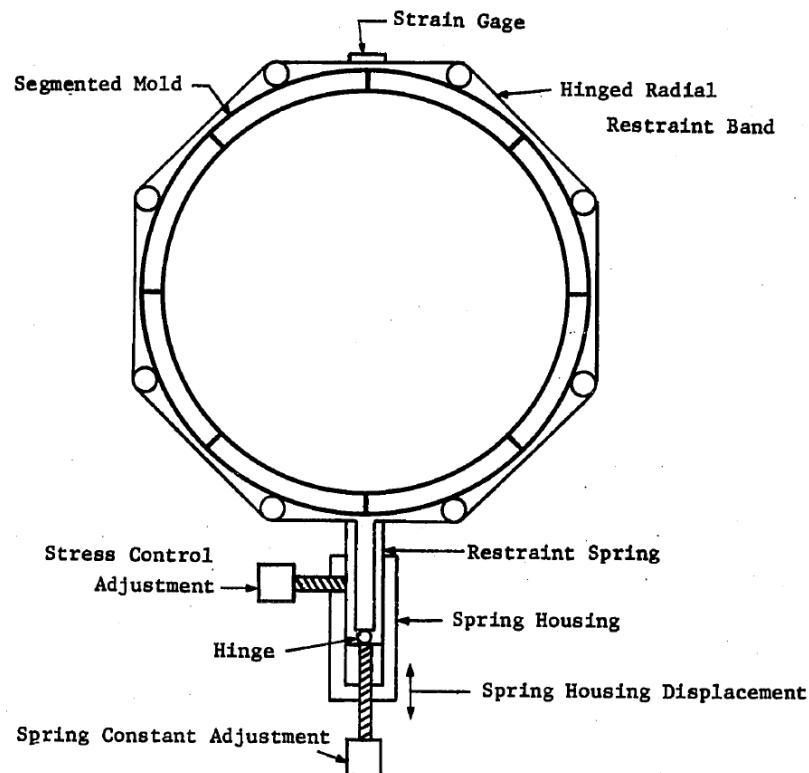


Figure 14. Proposed adjustable deformation restraint apparatus (from Pitt 1981)

Iowa K test

The Iowa K test was first conducted by Handy and Hoover in 1974 (Handy et al. 1978) who designed a portable split steel mold to evaluate undrained cohesion, internal friction angle, and other strength and stiffness parameters of soils for highway projects. Lutenege stated that the purpose of the Iowa K test is to “provide a simple, fast, and inexpensive method of testing soil shear strength, easily operated, simulating field conditions, and at the same time generating a multitude of unique soil data” (1977, 128). Iowa K tests are conducted on Proctor compaction samples (ASTM D698) or undisturbed soil samples that are the same size as Proctor samples. The original design of a constant elasticity Iowa K test mold is shown in Figure 15. A thin-walled Iowa K test mold with variable elasticity was also tested and compared in Lutenege (1977).

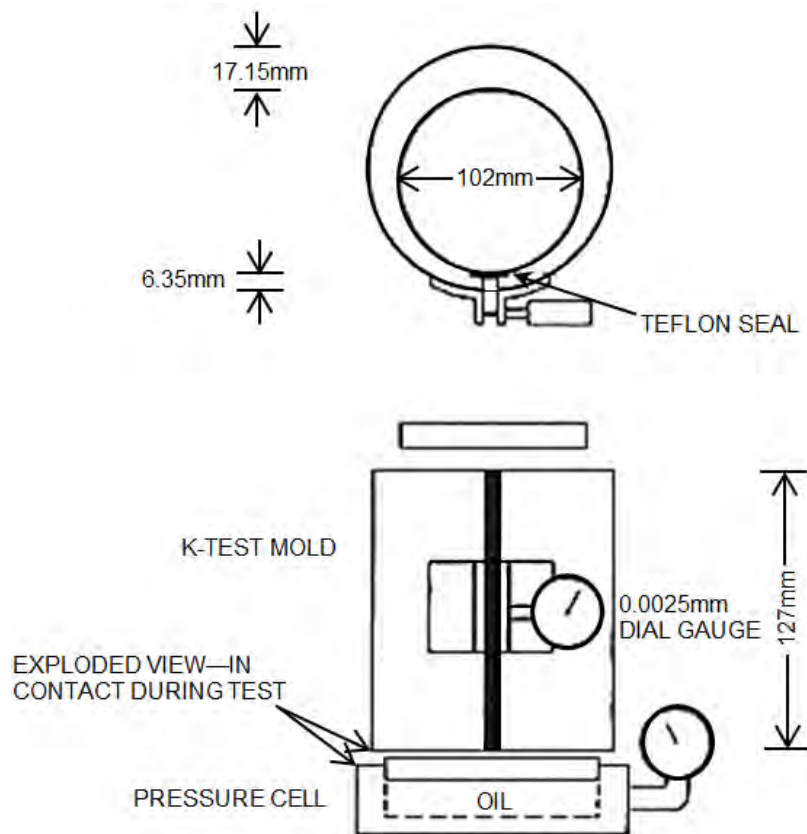


Figure 15. The constant-E Iowa K test mold (redrawn from Handy et al. 1978)

Cohesion (c) and internal friction angle (ϕ)

The cohesion (c) and internal friction angle (ϕ) of soil samples can be determined using the stress path method based on the Iowa K test data. The vertical and horizontal stress acted on soil samples were assumed as the major and minor principal stress (σ_1 and σ_3) and can be continually recorded during the tests. The stress path method to calculate the cohesion and internal friction angle of soil has been discussed in previous section of this chapter.

Lutenegger (1977) conducted 20 Iowa K tests with a constant elasticity K mold on standard Ottawa sand with different initial void ratios. The average cohesion and internal friction angle were determined. However, the average internal friction angle was overestimated by 5° as compared to data in Taylor and Leps (1938) that may be due to the friction between sand particles and the mold. Also, the results showed a value of 3.1 ± 1.8 psi of cohesion. The author conjectured that the cohesions from Iowa K test may be caused by the overestimation of vertical stress and underestimation of horizontal stress due to the high elasticity of the constant elasticity K mold that increased the radius of Mohr circle and then produced cohesions. Another 25 Iowa K tests were conducted on Ottawa sand using a variable elasticity K mold. The variable elasticity K mold produced even higher value of internal friction angles than the constant elasticity K mold. A median cohesion was -3.1 ± 1.8 psi were observed that may be caused by the non-uniform boundary stresses induced by the friction developing along the side of the mold during loading. Base on the comparison, the author concluded that variable elasticity K mold is more reliable for Ottawa sand in terms of the repeatability of internal friction angle and cohesion results.

Lutenegger (1977) also conducted the Iowa K test in field on some undisturbed loess samples using a variable elasticity mold. Table 8 summarized the Iowa K test data of nine loess samples. The negative cohesions of loess were observed and the author gave the same conjecture with the negative cohesions of Ottawa sand tests. In this study, two Bore-Hole Shear tests were also conducted in the same holes and elevations from which the K test samples were obtained. The average internal friction angle was 36.7° and cohesion was 0.7psi.

Table 8. K-Test results of loess (from Lutenecker 1977)

Specimen	Moisture Content (%)	Bulk Density (g/cm ³)	ϕ (deg)	c (psi)
Ha-1	12.7	--a	39.4	-2.1
Ha-2	13.5	--a	38.6	2.8
Ha-3	11.1	1.52	39.6	-0.1
Ha-4	17.3	--a	38.3	-5.9
Ha-5	15.3	--a	38.8	-3.5
Ha-6	14.5	--a	38.3	-1.3
Ha-7	13.8	1.39	35.7	-1.1
Ha-8	15.9	1.47	40.0	-2.9
Ha-9	14.4	1.58	39.7	1.8
Median	14.3 \pm 1.8		38.7 \pm 1.3	-2.4 \pm 1.9

Note: --a means no measurement available.

Handy et al. (1978) conducted some Iowa K tests on a type of glacial till with plastic limit of 32% and reported that the trends of both the c and ϕ , as expected, decreased with increasing of moisture content. The testing results are shown in Figure 16:

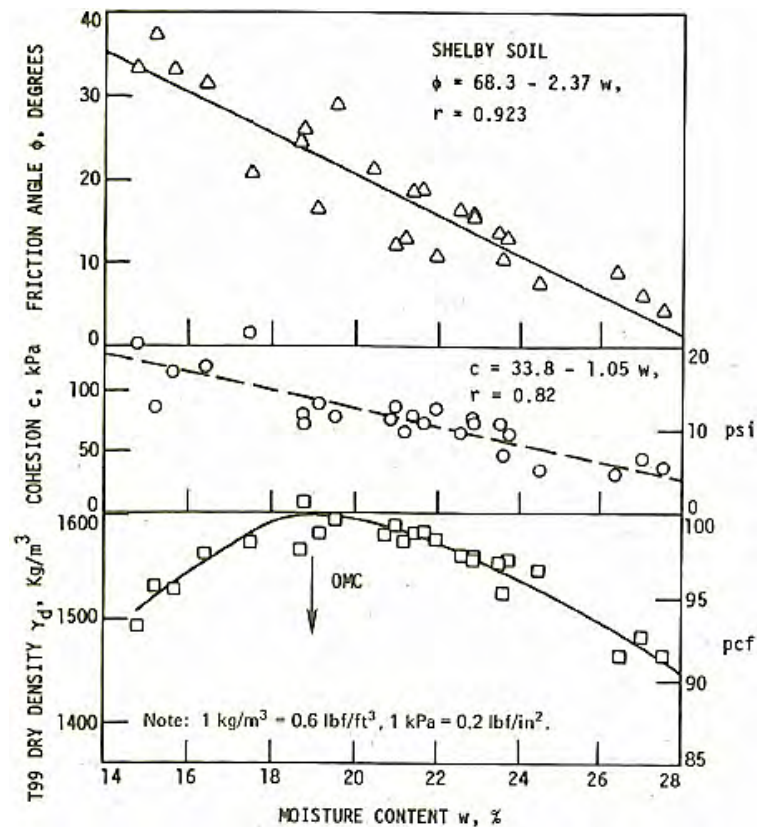


Figure 16. K-test ϕ , c, and γ_d versus moisture content for a glacial till (from Handy et al. 1978)

According to Hoover et al. (1982), the cohesion and internal friction angle determined by the Iowa K test can be theoretically used to calculate the undrained ultimate bearing capacity (q_{ult}) of soil under a circular footing in accordance with Terzaghi's equation (Equation 15),

$$q_{ult} = cN_c + \gamma D_f N_q + \frac{1}{2} \gamma B N_r \quad (15)$$

where: c = cohesion,

D_f = depth of footing; 0 inches can be used for subgrade and subbase cases,

γ = soil unit weight, and

N_c , N_q , and N_r = Terzaghi empirical bearing capacity factors dependent on ϕ .

Hoover et al. (1982) used the Iowa K test to evaluate the bearing capacity and freeze-thaw performance of some fibrous reinforced granular soils. The relationships between moisture content, fiber content, and some engineering parameters (i.e., elastic modulus, internal friction angle, cohesion, and stress ratio) of the treated soils were statistically evaluated. The Iowa K test results showed that addition of the fiber content can decrease the cohesion, internal friction angle, and, the elastic modulus and stress ratio slightly increased with increasing fiber content. However, Hoover et al. (1982) concluded that, due to the lack of predictability of the statistical model based on the Iowa K test data, the constant elasticity mold is inapplicable to the evaluation of the fiber reinforced soil samples, because the limitation of radial strain may affect the ability to transfer the induced stresses to the fibers.

Elastic modulus (E) and Poisson's ratio (ν)

Elastic modulus and Poisson ratio are important parameters for finite element analysis and geotechnical design. Both of the parameters can be measured from the stress and strain plots of the Iowa K test. According to Handy et al. (1978), the deformation modulus measured by the Iowa K test is not a true elastic modulus because the soil sample is in the process of failure. However, it is applicable to field conditions such as the compaction practice and design of retaining structures.

Hoover et al. (1982) used the cyclic triaxial test device equipped with a variable elasticity Iowa K test mold to determine volumetric strains, vertical strain modulus and permanent strains of some untreated and fiber reinforced soils. The variable confining pressure induced by the cyclic applied vertical pressure allow the test condition to better simulate the loading condition of pavement systems.

Also, according to Handy et al. (1978), the Poisson's ratio (ν) may be calculated by using the Equation 16 for homogeneous, isotropic, and elastic material,

$$\nu = \frac{\epsilon_r \sigma_z - \epsilon_z \sigma_r}{2\epsilon_r \sigma_r - \epsilon_z (\sigma_r + \sigma_z)} \quad (16)$$

where: ϵ_r, ϵ_z = radial and vertical unit strain;

σ_r, σ_z = radial stress and vertical stress.

Lateral stress ratio (K value)

The lateral stress ratio, K, is the ratio of lateral to vertical stress of soil. According to Handy et al. (1978), during the Iowa K test, vertical compression stress is applied to the top surface of a soil sample to induce lateral stress that can be continuously monitored by a dial gauge mounted on the K test mold, so, the nominal uncorrected stress ratio of soil samples under variable vertical and lateral pressure condition can be calculated and correlated to the lateral stress ratio (K). Also, the cohesion and internal friction angle that is determined by the Iowa K test could be used to estimate the at-rest pressure coefficient based on some empirical relationships.

Soil to steel adhesion, friction angle, and pore water pressure of Iowa K test

According to Handy et al. (1978), soil to steel frictions, between soil samples and the mold and loading plates, are main influence factor that can affect Iowa K test results. However, the boundary stress can be measured by recording the stress difference between the top and bottom of the soil sample under vertical load. The relationship between the frictions and horizontal stresses can also be determined and plotted. The slope of each plot is the soil to steel friction angle and the intercept is the soil to steel adhesion. In most cases, the soil to steel friction angle should be lower than internal friction angle of the same sample due to less friction between soil particles to steel.

Lutenegger (1977) also illustrated that the buildup pore water pressure due to rapid loading condition during the Iowa K test and may be determined by the reduction of soil sample to steel frictions. Since, the total soil to steel adhesion, c_s , is small and probably not appreciably affected by the pore water pressure, so the effective soil to steel adhesion, c_s' , equals to c_s was assumed. The effective soil to steel friction angle, ϕ_s' , is the slope in the initial stages of the plot, because, at the initial stage of test, the pore water pressure does not

build up. Therefore, the soil to steel friction angle, adhesion, and the pore water pressure can be determined by Equation 17 through Equation 20,

$$F_t = F_B + F_S \quad (17)$$

$$\tau_s = \frac{A_e(\sigma_t - \sigma_b)}{A_s} \quad (18)$$

$$\tau_s = c_s + \sigma_h(\tan\phi_s) \quad (19)$$

$$\mu = \sigma_h \left\{ 1 - \left[\frac{\tan\phi_s}{\tan\phi_s'} + \frac{c_s' - c_s}{\tan\phi_s} \right] \right\} \quad (20)$$

where: F_t, F_B, F_S = the top, bottom, and side friction load, respectively,

τ_s = the average side frictional stress,

A_e, A_s = end and side area of the soil specimen, respectively,

$\sigma_t, \sigma_b, \sigma_h$ = the vertical stress on the top and bottom of specimen and horizontal stress, respectively,

μ = pore water pressure,

c_s, c_s' = total and effective soil to steel adhesion, and

ϕ_s, ϕ_s' = total and effective soil to steel friction angle.

Boundary stresses and correction method of Iowa K test

The boundary stresses and correction method of the Iowa K test had been discussed by in Lutenege (1977). Figure 17 shows the proposed the principal stresses direction without friction (A), with side friction alone (B), and with both side and end friction (C). Based on the geometrical relationships that shown in Figure 17 C, the average major principal stress and minor principal stress can be estimated by Equation 21 and Equation 22,

$$\sigma_{1av} = \frac{1}{2} (\sigma_t + \sigma_b) \cos\phi_s \quad (21)$$

$$\sigma_3 = \sigma_h \sec\phi_s \quad (22)$$

where: σ_{1av} = average major principal stress,

σ_t = top vertical stress,

σ_b = bottom vertical stress,

ϕ_s = soil to steel friction angle,

σ_3 = minor principal stress, and

σ_h = horizontal stress.

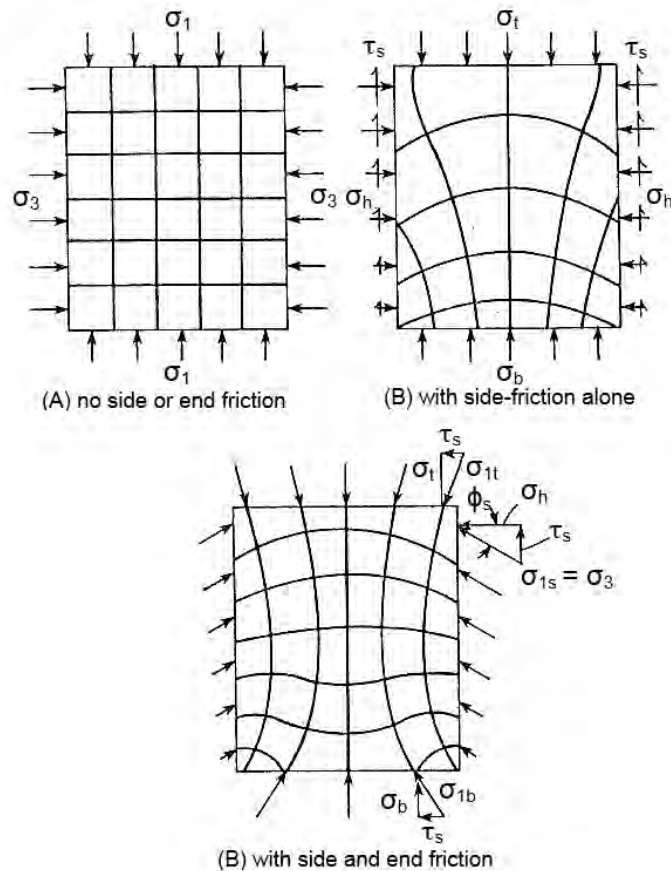


Figure 17. Proposed principal stresses directions in the K-Test (from Lutenege 1977)

The correction method may be used to determine the true major and minor principal stress, friction angle and cohesion results of Iowa K test. Lutenege (1977) performed some trial corrections on Ottawa sand and a Kansas Till Shelby soils. Table 9 shows that the internal friction angle is greatly reduced and cohesion is not changed too much by using the correction method.

Table 9. Trial corrections for the friction angle and cohesion of Iowa K test (from Lutenege 1977)

Specimen	Moisture content (%) or Initial void ratio	Uncorrected ϕ (deg)	Corrected ϕ (deg)	Uncorrected c (psi)	Corrected c (psi)
Shelby soil S-449	12.4	39.1	23.4	19.2	23.1
Shelby soil S-459	22.6	16.1	9.7	9.5	10.0
Ottawa sand	Initial void ratio $e_o = 0.549$	32.5	25.9	1.0	1.3

Gyratory compaction test

The gyratory compaction method has been widely used for preparing and testing specimens of bituminous mixtures and standardized in ASTM D3387 and AASHTO T312-09. The objective of this test was described as “to determine the ultimate in place density under the anticipated vertical stress while monitoring the process in terms of unit mass and shearing resistance including the plastic properties for asphalt materials” (ASTM D3387). However, the gyratory compaction method for evaluating the compaction characteristics of geomaterials has not been fully studied.

According to DelRio-Prat et al. (2011), the gyratory compactor operates on a “shear-compaction” principle. Compaction occurs due to two mechanisms that enable the distortion and reorientation of the particles: a constant vertical pressure at the top of the specimen and shear stress induced by the gyratory movement. A schematic of the gyratory compactor and a gyratory load-cell and plate assembly (GLPA) device is shown in Figure 18. The gyration angle of the mold that showed in Figure 18 is 1.25° . The function of the GLPA will be discussed below.

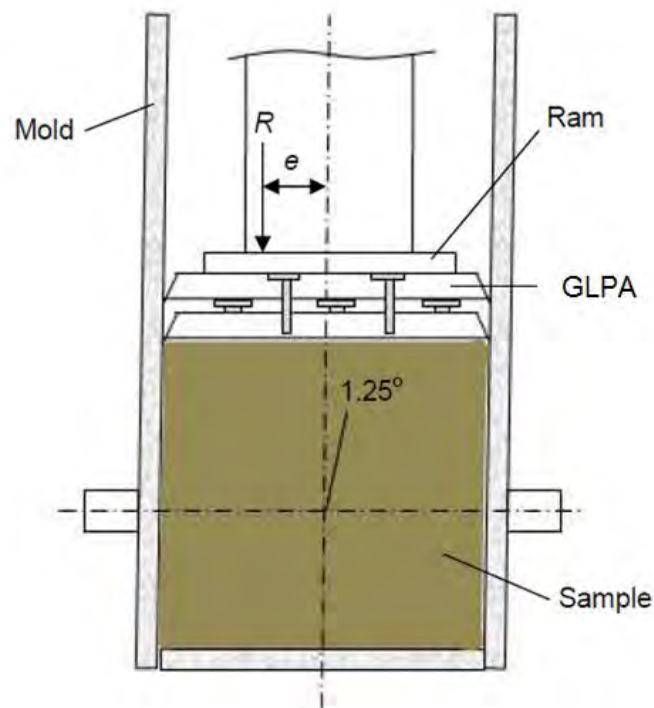


Figure 18. The gyratory compactor and GLPA (from Faheem and Bahia 2004)

The mechanical parameters of gyratory compaction tests

Four mechanical parameters (i.e., vertical confinement pressure, gyratory angle, gyratory rate, and number of gyrations) involved in this test method can affect the gyratory compaction test results. Huber (1996) conducted a series of tests to evaluate the effects of the gyratory angle, vertical confinement pressure, and gyratory rate of the test for hot-mix asphalt (HMA) materials. The author showed that 5° gyratory angle yields the compaction curves difficult to interpret due to the rapid compaction of materials and 1° angle does not allow a significant compaction. However, 1.25° gyratory angle can produce more reliable and easy to interpret compaction curves. This study also revealed that the vertical confinement pressure and gyratory rate have little effect on the testing results. A vertical confinement pressure of 600 kPa is commonly used and has been standardized in AASHTO T312 for asphalt materials to simulate the contact pressure between typical tractor-trailers tires and pavement surface. Ping et al. (2003) also concluded the gyratory compaction method with (vertical pressure = 200 kPa, gyration angle = 1.25°, number of gyrations = 90, gyration rate = 20 gyrations/minute) was the most suitable testing condition for soils to simulate the field test results.

According to the procedure described in U.S. Army Corps of Engineers (USACE) testing standards, the gyratory tests should be terminated until 1 lb/ft³ dry unit weight increase requires more than 100 gyrations for HMA materials. Browne (2006) recommended that 200-350 gyrations should be used for fine grained soils and more than 500 gyrations for coarse grained to monitor the entire compaction process.

Determining the compaction behavior of geomaterials

According to Ping et al. (2003), for some types of soils, gyratory compaction tests results are the closest lab compaction method to simulate field conditions. Browne (2006) conducted gyratory compaction test on four types of geomaterials (A-1-a, A-3, A-4, and A-7-6) to determine the relationships between the compaction characteristics and different vertical confinement pressures. Both dry and wet geomaterials were tested with variable vertical pressure ranging from 200 kPa to 600 kPa in this study. The author observed that the granular material (A-1-a and A-3) obtained most of their compaction in the first 100 gyrations and then the dry unit weight continued to increase with a slower rate until the compaction is terminated at 500 gyrations. The cohesive fine grained materials (A-4 and A-

7-6) also achieved the majority of their compaction initially but then reach to a relatively constant state during the rest of the tests. The author concluded that increasing the confining pressure is the most effective method of increasing the dry density for fine-grained soils, while increasing the number of gyrations is the most effective way to increase the dry density of granular soils. The gyratory compaction test results were also compared with standard and modified Proctor test results in Browne (2006). Gyratory compaction curves were created using the dry unit weight values at 0, 75, 90, and 500 gyrations for each vertical pressure. The results showed that the gyratory compaction test of fine grained soils can produce similar compaction curves with the Proctor compaction results which allow the optimum moisture content and maximum dry unit weight to be readily estimated. However, gyratory compaction curves of coarse grained and free draining soils did not show the similar pattern due to moisture loss during the tests.

The gyratory compaction test method has been used to evaluate of the compaction characteristics of different materials include HMA, geomaterials, and pervious concrete. However, the curves of density versus number of gyrations of different materials showed similar pattern that consists of two phases (Figure 19). Some indices based on the compaction curve were used to define the areas under the compaction curves and optimize the densification characteristics of different materials. Bahia (2002) defined the Compaction Energy Index (CEI) as the area from 8th gyration to 92% of the maximum theoretical specific gravity (G_{mm}) of HMA and the Traffic Energy Index (TEI) for the area from 92% of G_{mm} to 98% of G_{mm} . The CEI can be used to represent the work applied by the compactor to required density and the TEI represents the amount of energy induced by traffic loads. Kevern et al. (2009) also defined two similar indices for gyratory compaction curves (Workability Energy Index and Compaction Densification Index) to evaluate the workability and compatibility of the pervious concrete.

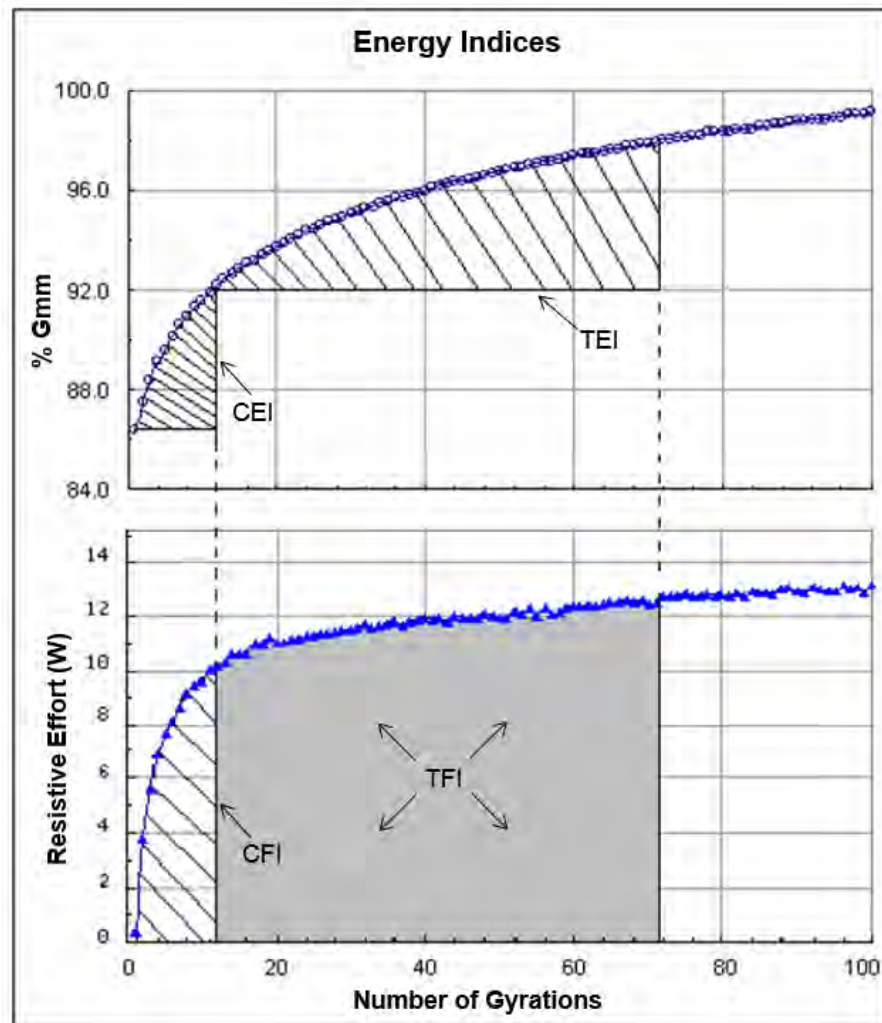


Figure 19. Energy indices of gyratory compaction test for HMA (from Bahia 2002)

Measuring the shear resistance of compacted geomaterials

A gyratory load-cell and plate assembly (GLPA) was developed for gyratory compactor to measure the resultant gyratory force and eccentricity, and then correlate to shear resistance of HMA samples during compaction (Guler et al. 2000). The GLPA is placed on the top surface of compaction specimen during the test. The eccentricity and resultant load from GLPA can be used to calculate required moments to overcome the shear resistance of compaction specimen and tilt the mold to maintain a certain angle.

The design of GLPA is shown in Figure 20. Three load cells were installed to measure and track the resultant force and its eccentricity.

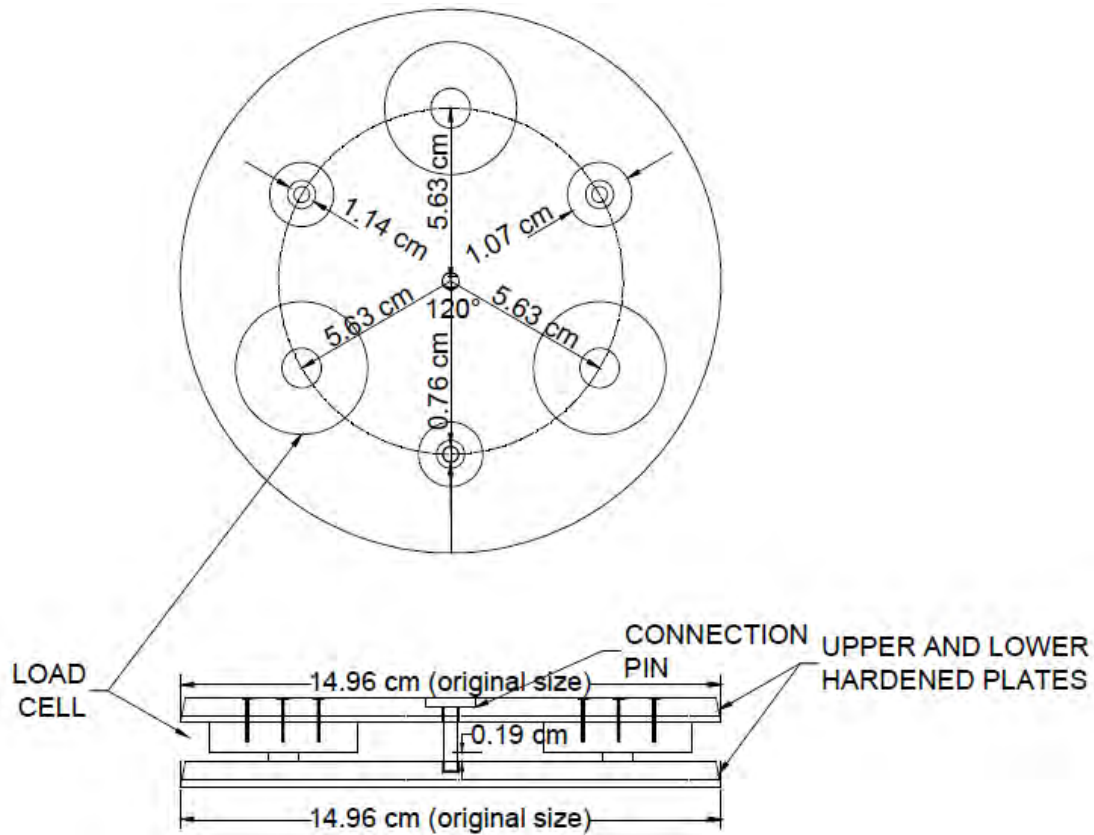


Figure 20. Gyratory load-cell and plate assembly (GLPA) (from Guler et al. 2000)

Guler et al. (2000) discussed that bulk shear resistance of HMA samples can be determined by using the GLPA. Since the effective moment is a direct measure of shear resistance and the GLPA measured moment can be used to separate the energy spent in densification from the energy spent in distortion. The resultant force (R) is the summation of the three load cells forces (P_1 , P_2 , and P_3) at the each moment of the gyrations. The eccentricity (e) of the resultant force relative to the center (O) of the GLPA can be calculated based on the general moment equilibrium equations (Equation 23 through Equation 25) along two perpendicular axes which is shown in Figure 21.

$$\Sigma M_y = 0 \Rightarrow e_x \quad (23)$$

$$\Sigma M_x = 0 \Rightarrow e_y \quad (24)$$

$$e = \sqrt{e_x^2 + (r_y - e_y)^2} \quad (25)$$

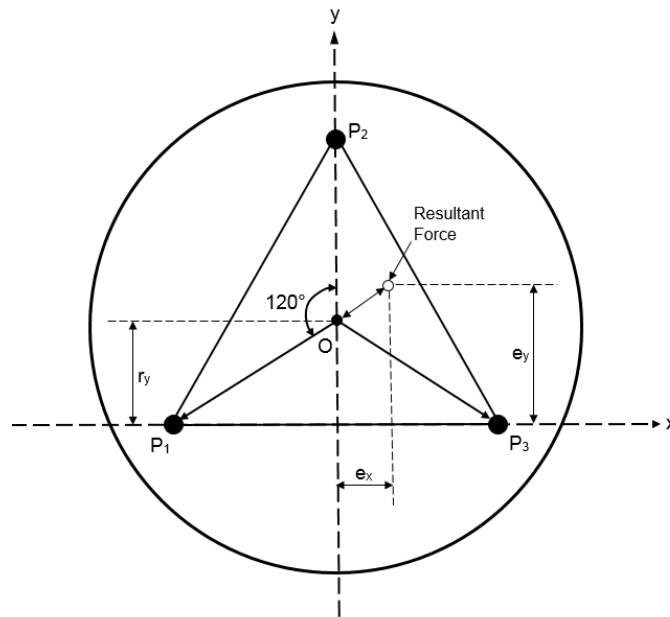


**Figure 21. Eccentricity of the resultant force calculated on basis of the three load cells
(from Guler et al. 2000)**

Guler et al. (2000) suggested that the shear resistance of each gyration can be calculated using Equation 26,

$$\tau_G = \frac{Re}{Ah} \quad (26)$$

where:

τ_G = bulk frictional shear resistance,

R = resultant ram force,

e = eccentricity,

A = the sample cross-section area, and

h = the sample height.

According to Guler et al. (2000), the eccentricity based on the GLPA data is also a good indication of shear resistance, because, at the beginning of test, the eccentricity is low due to the excess air voids that dramatically reduced frictional resistance, and then it increased with compaction process and reach to a peak value that indicate the frictional resistance also reach the maximum value. Figure 22 shows that the eccentricity value for fine mixture HMA continues maintaining at high values which indicates high frictional resistance to distortion. However, for coarse mixture sample, it starts showing a progressive decrease in the

eccentricity values, which indicates a reduction in frictional resistance due to rearrangement of solid particles of granular material.

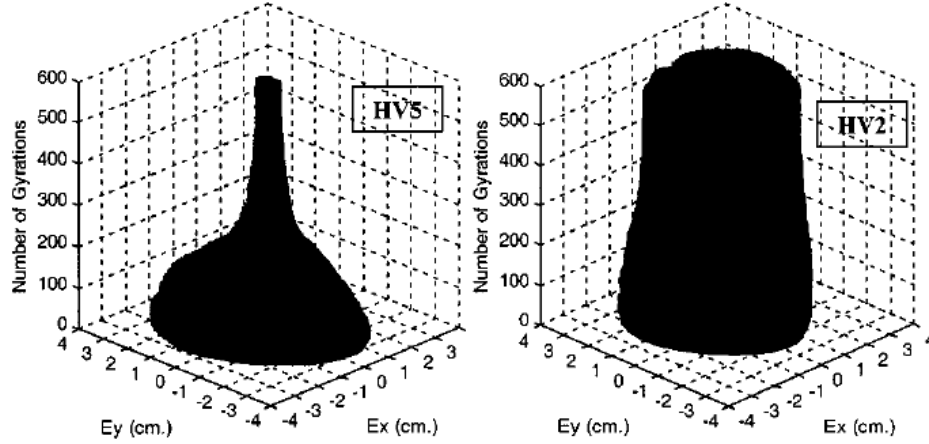


Figure 22. Three dimensional eccentricity plots for coarse (HV5) and fine (HV2) mixture HMA samples (from Guler et al. 2000)

Estimating the compaction energy of gyratory compaction test

The compaction energy can be separated from the vertical compression and distortion by the GLPA. The total compaction energy consumed during the gyratory compaction test consists two parts and can be calculated based on Equation 27

$$Energy_{gyratory} = \frac{PA(H_0 - H_i)}{V_i} + 4\theta \sum_0^N \tau_G V_i \quad (27)$$

where:

P = vertical confinement pressure (kN/m² or psf),

A = area of sample (m² or ft²),

H_0 = initial height of sample before compaction (m or ft),

H_i = height of sample of each gyration (m or ft),

τ_G = applied shear stress (kN/m² or psf) will be discussed below,

θ = gyration angle (radians), and

V_i = volume of sample of each gyration (m³ or ft³).

The first part of this equation is the energy due to the vertical compression of resultant force. According to (DelRio-Prat, 2011), the first part of the equation can be considered negligible compared to the second part which is the compaction energy caused by the moment of the resultant force.

DelRio-Prat et al. (2011) also defined the area under the curve of shear resistance versus number of gyrations as “A” (Equation 28) that can be correlated to the compaction energy. The author indicated the area will give an idea of the energy consumed during the compaction process. Lower area of A implies less energy consumption and higher compactibility of the testing sample.

$$A = \sum_1^m \frac{S_{ci} + S_{ci+1}}{2} \times (C_{i+1} - C_i) \quad (28)$$

where:

A = area under the curve of shear resistance versus gyrations (cycle * kN/m²),

S_{ci} = the shear stress for the applied gyration (kN/m²), and

C_i = the number of gyrations corresponding to the registered step.

Correlating the shear resistance (τ_G) to standardized lab and field testing results

Zhang (2010) conducted gyratory compaction, unconfined compression, and resilient modulus test on Western Iowa Loess (USCS: ML) and a type of subgrades called TH-60 soil 306 (USCS: CL) and tried to correlate the shear resistance (τ_G) with undrained shear strength (S_u) and resilient modulus (M_r). The samples with variable moisture content and dry unit weight were prepared using the gyratory compactor with three vertical confinement pressures (100, 300, and 600 kPa). Shear resistance changes were monitored and determined by a GLPA during the sample preparation process. Figure 23 shows a strong relationship between shear resistance and undrained shear strength of the Western Iowa Loess.

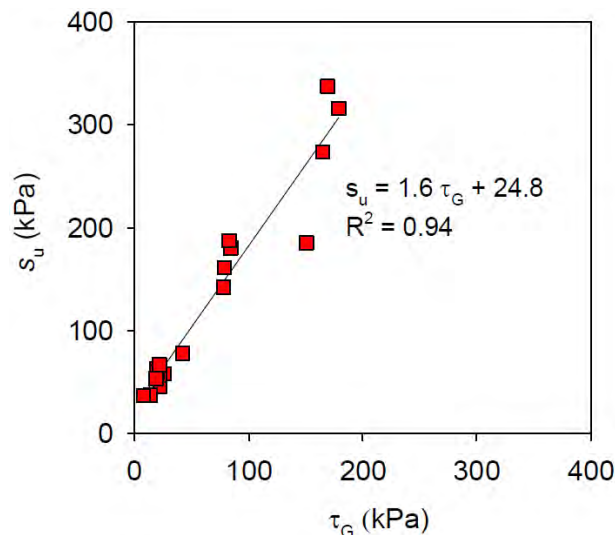


Figure 23 Relationship between s_u and τ_G for Western Iowa loess (from Zhang 2010)

In this study, two height to diameter ratio ($H/D = 1:1$ and $2:1$) sizes of TH-60 samples were also prepared to evaluate the slenderness effect. The statistical correlations between τ_G and M_r of two sizes samples are shown in Figure 24.

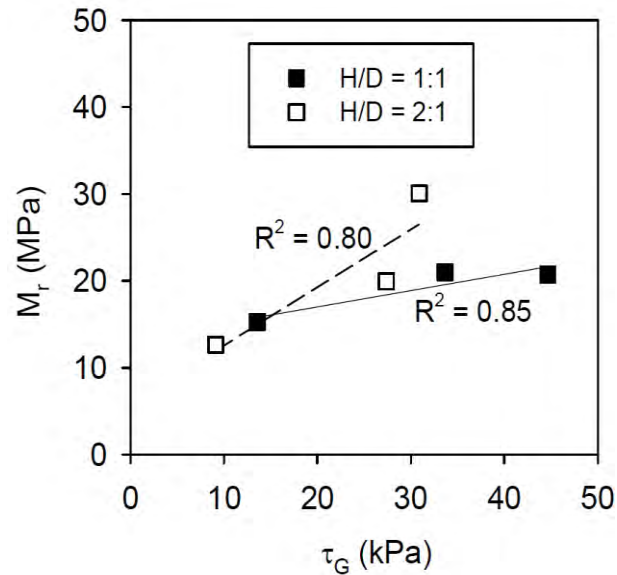


Figure 24 Relationships between τ_G and M_r for TH-60 soil 306 (from Zhang 2010)

White et al. (2009) conducted two field tests, Light Weight Deflectometer (LWD) and Dynamic Cone Penetrometer (DCP) test, on gyratory compacted geomaterials to correlate τ_G to the in situ elastic modulus (E_{LWD}) and DCP Index (DPI). Four different boundary conditions (no, soft, stiff, and rigid confinement) were prepared using different stiffness polyurethane molds and a steel mold. Figure 25 shows a sample of the statistical relationships between τ_G , E_{LWD} , DPI and S_u under different boundary conditions.

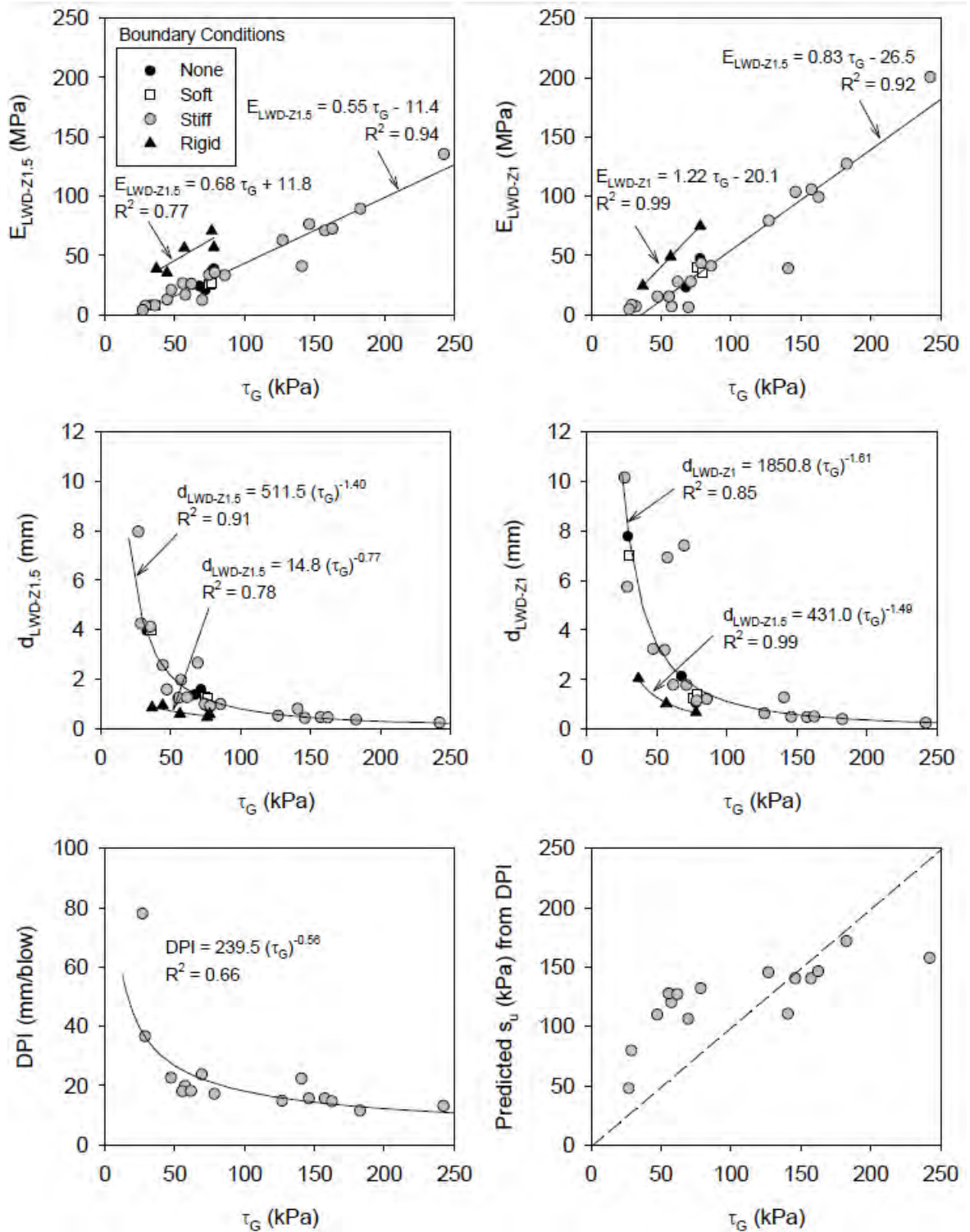


Figure 25. Correlations between τ_G and LWD/DPI measurements with different boundary conditions of TH60 soil 306 material (USCS: CL) (from White et al. 2009)

Compaction Forecasting Expert Database (CFED)

The Compaction Forecasting Expert Database (CFED) is a compaction analysis tool and database developed by Caterpillar, Inc. and Dr. David White's research group since 2005.

The original specific goals of CFED were to:

- predict the capability of compaction machines to meet compaction specifications,
- estimate productivity for specific machine,
- determine sensitivity of compaction and productivity to soil moisture, and
- recommend soil lift thickness with number of machine passes to meet compaction specifications (Puls 2008).

Lab testing data include soil index properties and compaction behavior of 45 geomaterials from 14 states, Canada, and China have been tested and input into CFED to evaluate its compaction performance. Some field testing data in CFED such as the dynamic cone penetration index (DCPI), Clegg impact value (CIV), light-weight deflectometer (LWD), and plate load testing (PLT) data after each pass of compaction machine enable CFED to provide some recommendations for field compaction such as the suitable compaction machine and machine passes for different geomaterials (White et al. 2010). According to Puls (2008), compared to other compaction prediction models, CFED is able to link soil compaction performance with compaction energy. This advantage allows CFED to predict more than one compaction curve for each geomaterial, and the difference between CFED predictions and lab testing data is within 1.2 lb/ft³ for maximum dry density and 1.0% for optimum moisture content which are determined by Proctor compaction test.

An example of CFED outputs based on the Proctor test data of a glacial till obtained from Edwards, Illinois is shown in Figure 26 (Puls 2008). Figure 27 shows some CFED outputs of the geomaterial based on the field testing data.

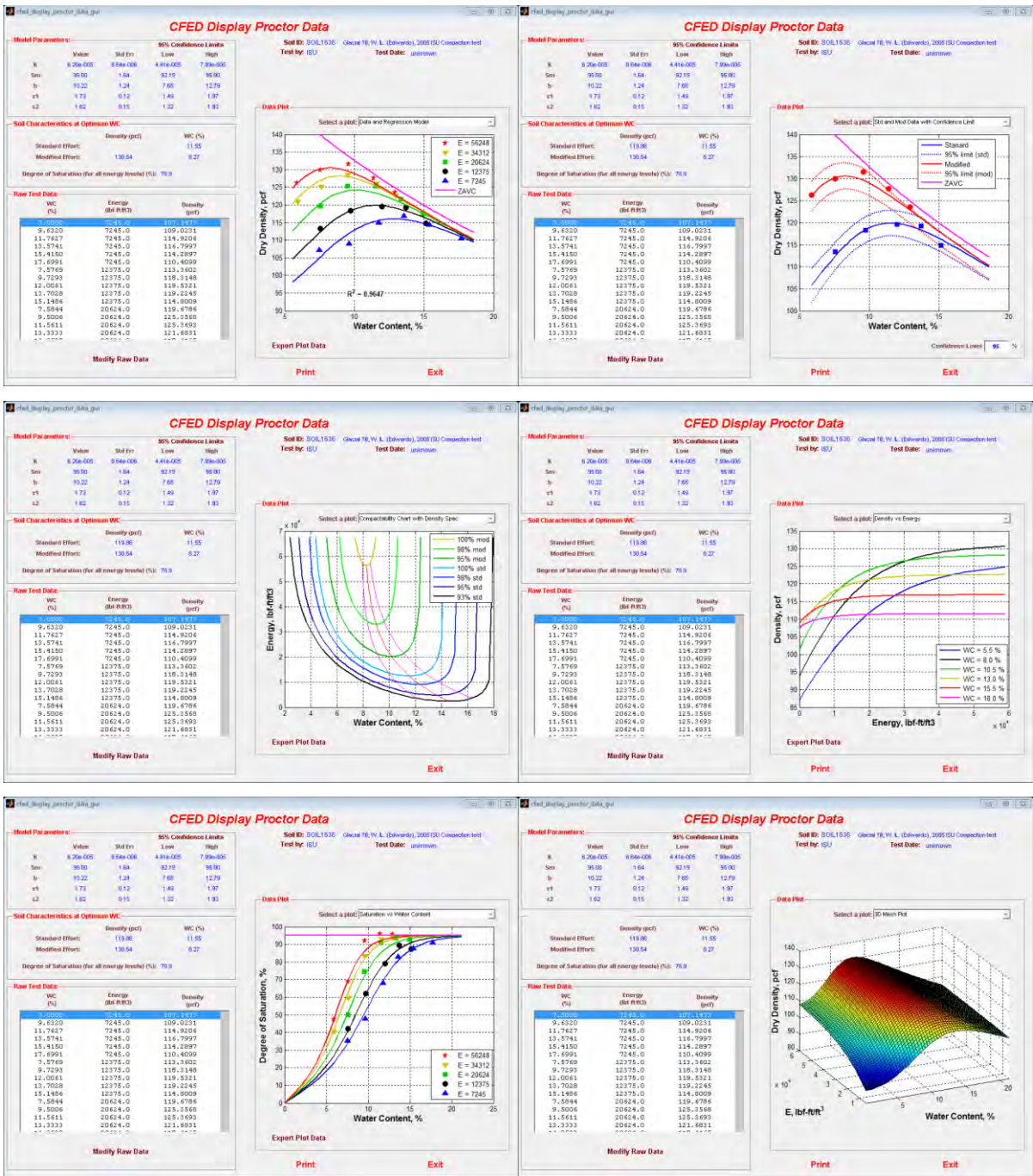


Figure 26. CFED outputs of soil 1633 based on the Proctor test data (from Puls 2008)

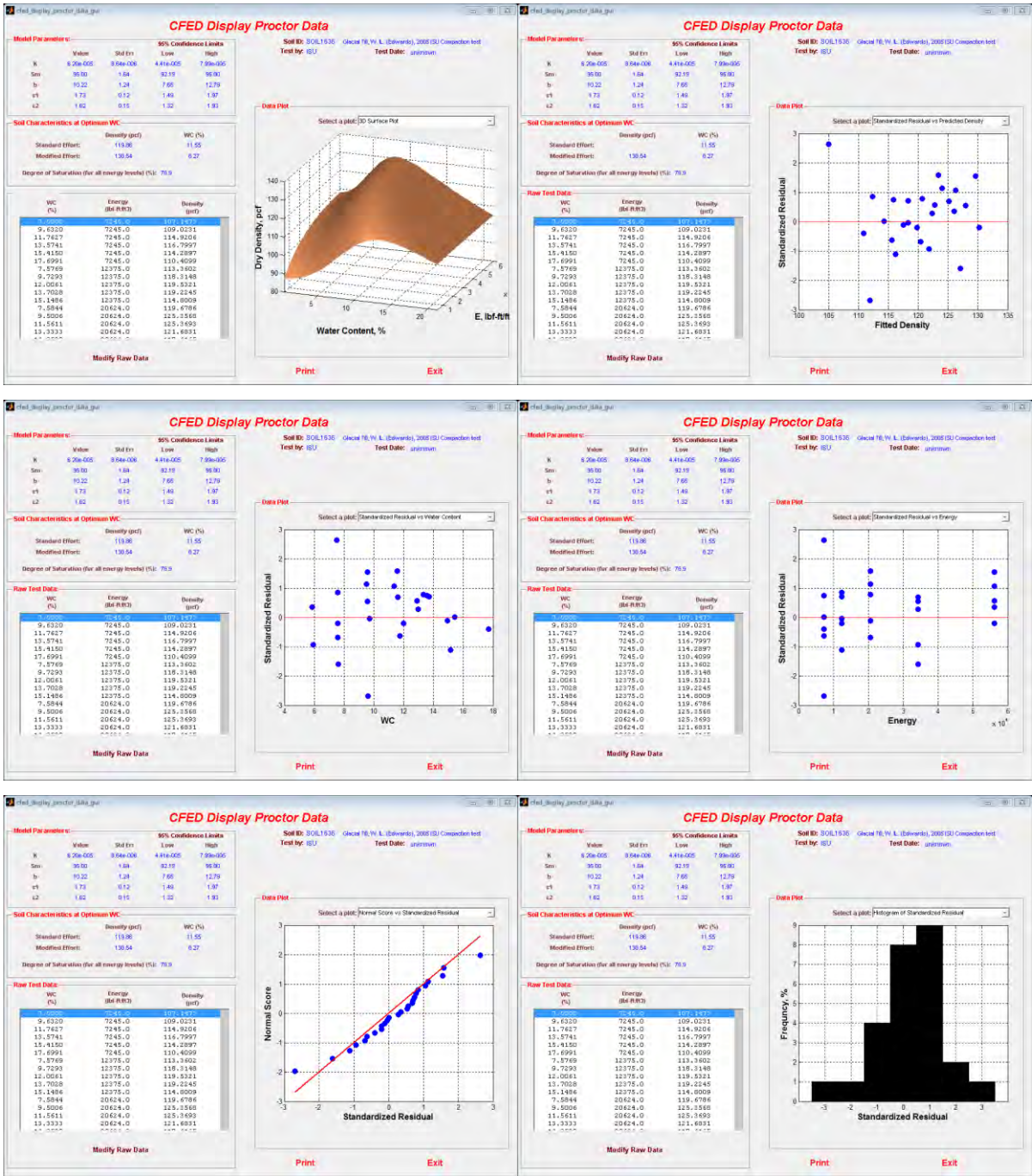


Figure 26 (continued). CFED outputs of soil 1633 based on the Proctor test data (from Puls 2008)



Figure 27. CFED outputs of soil 1633 based on field compaction data (from CFED)

CHAPTER 3. METHODS

This chapter has two parts. The research design and objectives of the study are presented first, followed by three sections about the lab testing methods, and a section that describes how the results of the lab testing methods were compared and the statistical methods used to correlate the results.

Research Design

The methods selected for this research address the four objectives of the study.

- Expand the Compaction Forecasting Expert Database (CFED) with more lab testing data for recycled, by-product, and chemically stabilized geomaterials.
- Build and calibrate the Iowa K test equipment with more accurate measurement devices,
- Evaluate shear strength and stiffness parameters by using the Iowa K test of CFED geomaterials and then compare with conventional test results, and
- Evaluate the gyratory compaction test that uses a pressure distribution analyzer (PDA) to determine relationships between moisture content, density, compaction energy and shear resistance of geomaterials and then correlate the gyratory compaction test data with conventional test results.

To expand the CFED database and characterize different geomaterials, the index properties of each material were determined by sieve analysis, Atterberg limits, and specific gravity test. The soil classification of each geomaterial determined which compaction tests (i.e., the Proctor compaction, vibratory compaction, and gyratory compaction test) would be used to evaluate the compaction behavior of materials.

The shear strength and stiffness of compacted geomaterials were tested using a gyratory compaction device that was assembled with a PDA and an Iowa K test device. Unconfined compression tests were conducted and the results were compared with results from gyratory compaction and Iowa K tests.

Determine Soil Index Properties of Geomaterials

Particle size analysis, liquid limits, plastic limits, and specific gravity were conducted in accordance with American Society for Testing and Materials (ASTM) standards to classify and determine index properties of geomaterials of this study.

Particle size analysis

Two methods were involved in particle-size analysis for the geomaterials in this study, ASTM D422-63 “Standard test method for particle-size analysis of soils” and ASTM D421-85 “Standard Practice for Dry Preparation of Soil Samples for Particle-Size Analysis and Determination of Soil Constants.” Representative samples of air-dried, coarse grained materials were obtained by using a riffle sample splitter.

Particle size analysis consists of two main parts, sieve analysis and hydrometer test. Sieve analysis was used for material retained on the No. 200 sieve (75 μm) and hydrometer tests were used for determining proportions of silt and clay particles size smaller than No. 200 sieve. After completing the hydrometer test, the suspended material was washed through the No. 200 sieve. The material retained on the No. 200 sieve was then oven dried to complete the rest sieve analysis test for particles between No. 10 (2.00 mm) and No. 200. The equipment of sieve analysis and hydrometer test is shown in Figure 28.

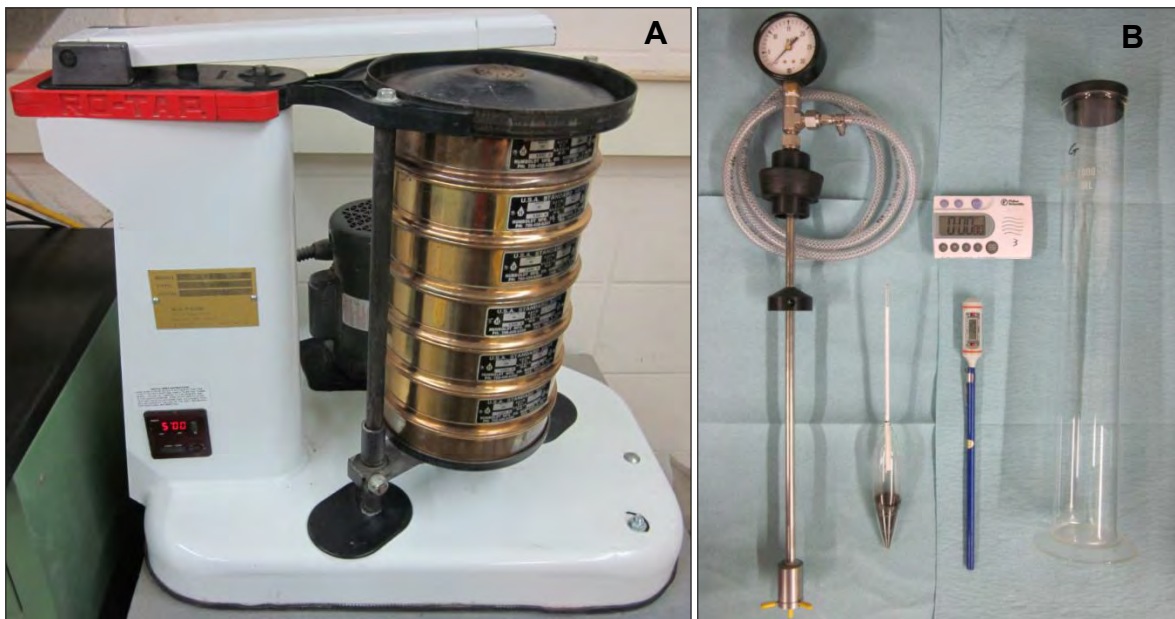


Figure 28. (A) Sieve analysis and (B) hydrometer test devices

Liquid limit, plastic limit, and plasticity index of materials

Liquid limit (LL), plastic limit (PL), and plasticity index (PI) of materials were determined in accordance with ASTM D4318-10 “Standard Test Methods for Liquid Limit, Plastic Limit, and Plasticity Index of Soils.” The wet preparation method was followed for preparing representative samples for the tests. Distilled water was used for preparing samples to prevent cations exchange from altering the results. Liquid limit tests were performed according to the multi-point liquid limit method, and at least three points were measured for each material. Plastic limit tests were conducted in accordance with the hand method. Both LL and PL were rounded to whole numbers for calculating PI. According to ASTM D4318-10, if either the LL or PL could not be determined, or if the PL is equal to or greater than the LL, the material was reported as nonplastic (NP). The liquid limit devices are shown in Figure 29. A ground glass plate was used for plastic limit test.



Figure 29. Liquid limit test devices

Soil classification

The particle-size analysis test results and Atterberg limits test results were used to classify materials in accordance with ASTM D2487-10 “Standard Practice for Classification of Soils for Engineering Purposes (Unified Soil Classification System (USCS))” and ASTM D3282-09 “Standard Practice for Classification of Soils and Soil-Aggregate Mixtures for Highway Construction Purposes (AASHTO classification system).”

Specific gravity

Specific gravity of coarse particles that retained on No. 4 sieve (4.75 mm) was determined in accordance with ASTM C127 “Standard Test Method for Density, Relative Density (Specific Gravity), and Absorption of Coarse Aggregate,” and ASTM D854 “Standard Test Methods for Specific Gravity of Soil Solids by Water Pycnometer” was the method used for determining specific gravity of fine materials that pass the No. 4 sieve (4.75 mm). The average specific gravity was computed based on the percentage of coarse and fine materials as retained and passing the No. 4 sieve. The de-aired water was prepared using a water de-airing system. The specific gravity test apparatus for both coarse and fine materials are shown in Figure 30.

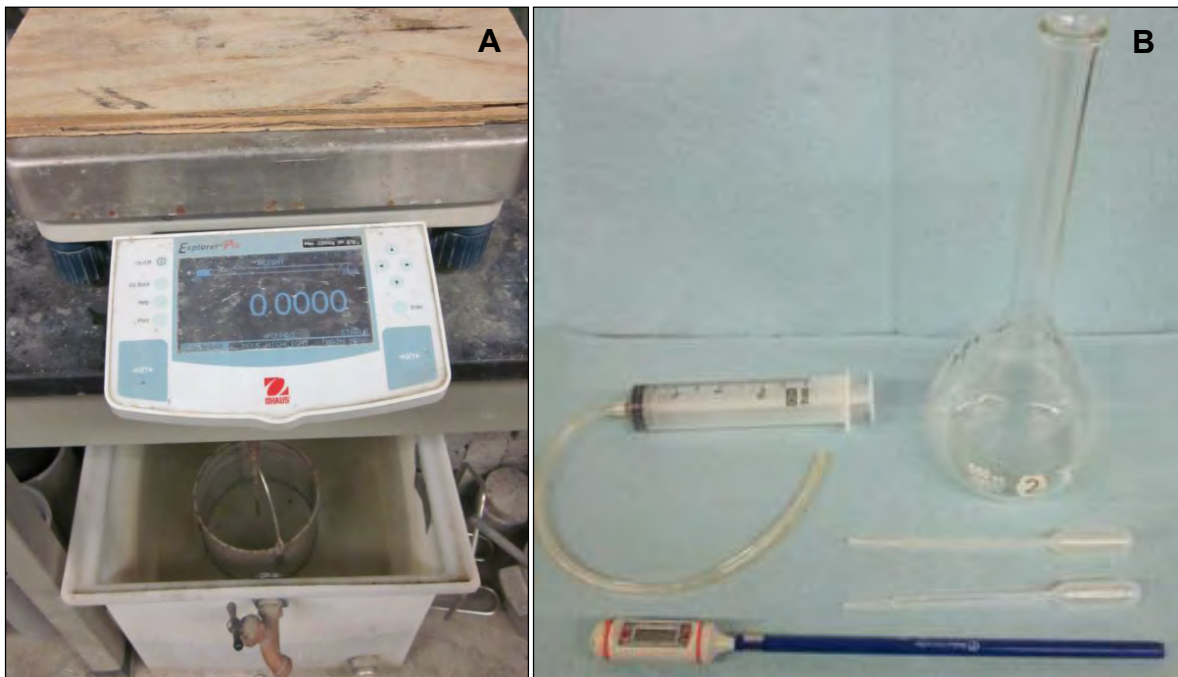


Figure 30. Specific gravity test devices for (A) coarse (B) and fine materials

Evaluate the Compaction Behavior of Geomaterials

Proctor and vibratory compaction tests were conducted to determine the compaction behavior of geomaterials in this study. Gyrotory compaction tests were conducted to evaluate its feasibility of determining compaction behavior of geomaterials. The results from different compaction tests of same geomaterial were compared.

Proctor compaction test

Proctor compaction tests determine the relationships between water content, dry unit weight, and compaction energy of geomaterials according to ASTM D698 “Standard test methods for laboratory compaction characteristics of soil using standard effort (12 400 ft-lbf/ft³ (600 kN-m/m³))” and ASTM D1557 “Standard test methods for laboratory compaction characteristics of soil using Modified Effort (56,000 ft-lbf/ft³ (2,700 kN-m/m³)).” A Hobart mixer was used to prepare fine grained geomaterials to predetermined moisture content. An automated mechanical rammer was used to conduct Proctor tests. The Hobart mixer and automated mechanical rammer used for Proctor compaction test are shown in Figure 31.

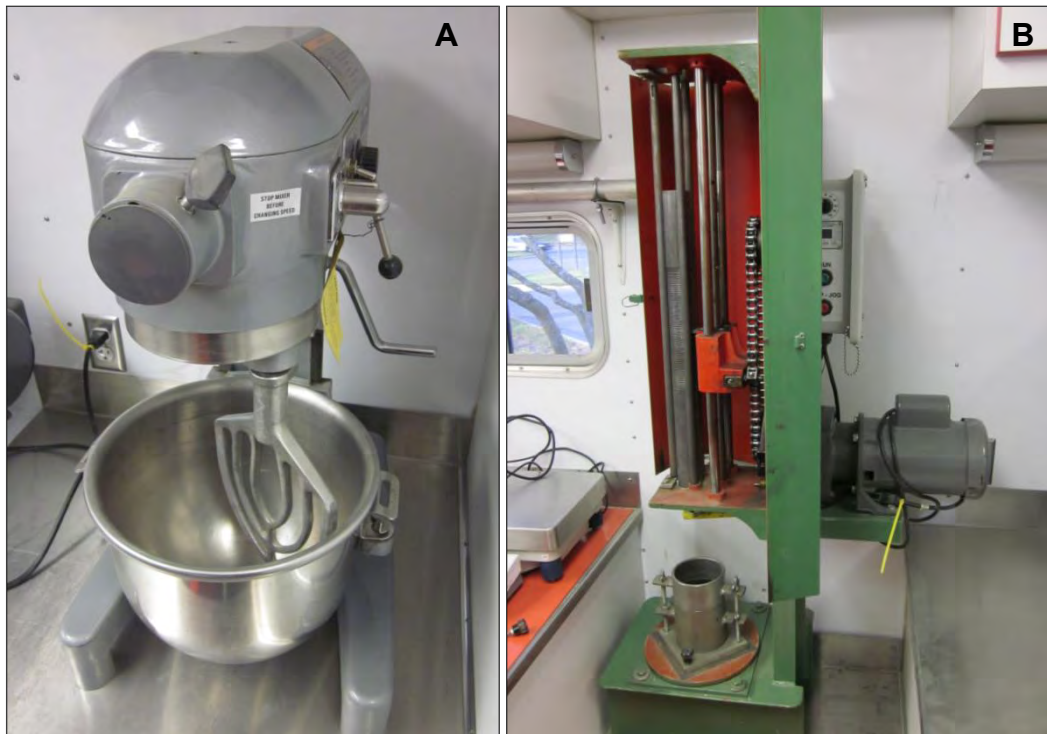


Figure 31. (A) Hobart mixer and (B) automated mechanical rammer

In this study, three additional energy levels were used, one below the standard Proctor energy level and two between the standard and modified Proctor energy levels (Table 10).

Table 10. Summary of compaction energies used for the Proctor compaction tests

Energy Level	Layers	Blows per Layer by mold		Weight of Hammer (lb)	Drop Height (ft)	Energy (lb-ft/ft ³)
		4 in.	6 in.			
Sub-Standard (SS)	3	15	35	5.5	1.0	7425
Standard (S)	3	25	56	5.5	1.0	12375
Super-Sub-Modified (SSM)	5	25	56	5.5	1.0	20790
Sub-Modified (SM)	5	25	56	5.5	1.5	34650
Modified (M)	5	25	56	10.0	1.5	56250

A total of five energy levels were used to more accurately establish the relationships between compaction behavior and compaction energy. The compaction energy was calculated using Equation 29.

$$\text{Energy}_{\text{impact}} = \frac{\left(\text{Number of blows per layer} \right) \times \left(\text{Number of layers} \right) \times \left(\text{Weight of hammer} \right) \times \left(\text{Height of drop hammer} \right)}{\text{Volume of mold}} \quad (29)$$

ASTM D698 and ASTM D1557 specified the mold size and the methods for preparing the samples based on the gradation of the geomaterial. Corrections were made to the unit weight and molding water content in accordance with ASTM D4718 “Standard Practice for Correction of Unit Weight and Water Content for Soils Containing Oversize Particles” for geomaterials that contained 5% by mass of oversize fraction.

Vibratory compaction test

Vibratory compaction tests determine the minimum and maximum index densities and compaction behavior of cohesionless, free-draining geomaterials according to ASTM D4254 “Standard Test Methods for Minimum Index Density and Unit Weight of Soils and Calculation of Relative Density” and ASTM D4253 “Standard Test Methods for Maximum Index Density and Unit Weight of Soils Using a Vibratory Table.” ASTM D4253 provides for two kinds of vibrating tables, an electromagnetic vertically vibrating table and a cam-driven table. The maximum index density of geomaterials decided by the electromagnetic table is slightly higher than using cam-driven table. In this study, an electromagnetic table

was used for all tests and shown in Figure 33. The standards specified the mold size (6 in. or 11 in. inside diameter) based on the maximum particle size of the samples. Representative samples were selected using a riffle sample splitter.



Figure 32. A 6-in. diameter mold on an electromagnetic vibratory table

ASTM D4253 specifies eight minutes (480 seconds) as the time for determining maximum index densities of test samples. In this study, the sample height was measured before and after placing the dead weight and after 10, 20, 30, 60, 120, 240, 480, and 960 seconds of vibratory compaction to determine the relationship between compaction behavior and compaction energy. The vibratory compaction energy can be estimated using Equation 30.

$$\text{Energy}_{\text{vibratory}} = \frac{\left(\text{Weight of surcharge} \right) \times \left(\text{Frequency of vibration} \right) \times \left(\text{Amplitude of vibration} \right) \times (\text{Time})}{(\text{Volume of mold})} \quad (30)$$

Gyratory compaction test

Gyratory compaction tests to determine the relationships between moisture content, dry unit weight, and compaction energy of geomaterials were conducted using Brovold Gyratory compactor (Figure 33). A pressure distribution analyzer (PDA) shown in Figure 33A was used to measure shear resistance of compacted geomaterials and will be introduced later of this chapter.

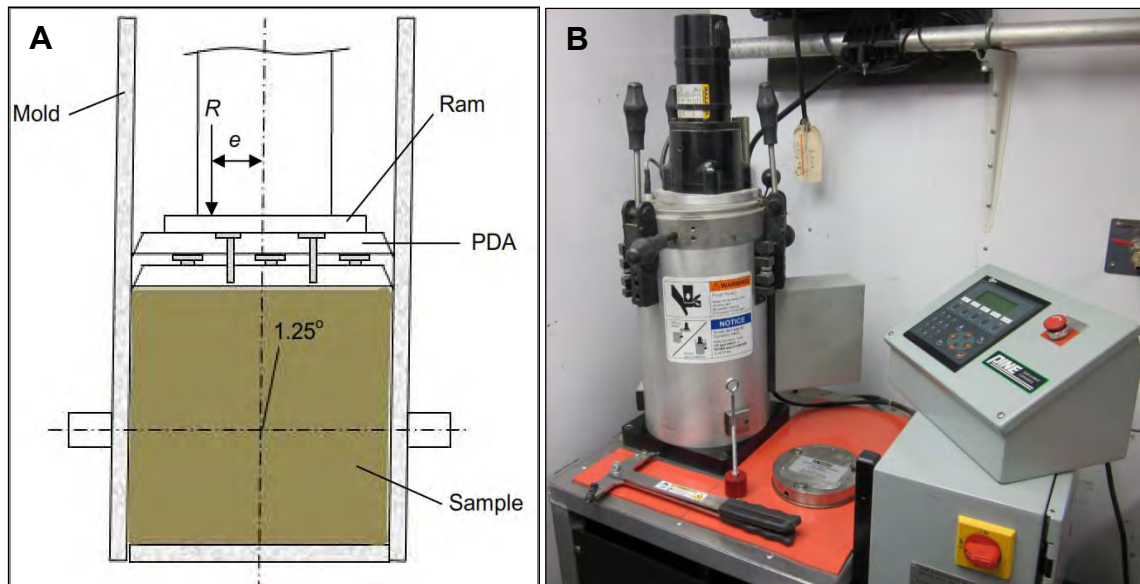


Figure 33. (A) A schematic (from Faheem and Bahia 2004) and (B) photo of the Brovold Gyratory Compactor

The testing procedure basically followed AASHTO T 312 “Standard Method of Test for Preparing and Determining the Density of Hot-Mix Asphalt (HMA) Specimens by Means of the Superpave Gyratory Compactor,” but the compactor does not need to warm up and temperature change was not recorded for the geomaterials tests. The pressure applied vertically and number of gyrations was not all ways same for all the geomaterials. Loose material was placed in the rigid steel mold with 150 mm in diameter and 200 mm internal height available. Two steel loading plates and filter papers were placed on the top and bottom surfaces of each specimen. The PDA was placed above the top loading plate. The compaction process occurs due to two mechanisms that distort and reorient soil particles: constant vertical pressure at the top of the specimen and shear stress induced by gyratory movement. The gyratory will automatically start until the specified vertical pressure

(300kPa or 600kPa) achieved and stop when the specified number of gyrations completed. Two dwell gyrations with no pressure applied vertically were set to “square” the each specimen, because, after the last gyration of compaction, the mold still remains tilted at the angle of gyration. The operation parameters used in the gyratory compaction tests are shown in Table 11.

Table 11. Parameters of the gyratory compaction test

Parameters	Value
Vertical Pressure	300 or 600 \pm 10 kPa
Gyration Angle	1.25 \pm 0.02°
Number of Gyrations	100 or 200
Gyration Rate	30 \pm 0.5 RPM
Number of Dwell Gyrations	2

The specimen height was recorded by the compactor once per gyration (reported to nearest 0.1 mm). Changes in the specimen height can be used to calculate the change of dry unit weight of samples. The moisture content was measured before and after each test.

The total compaction energy during the compaction with the gyratory compactor is the sum of the work per volume due to the resulting force (P) and the work per volume due to the moment caused by the eccentricity of the applied force. It can be calculated by Equation 31

$$\text{Energy}_{\text{gyratory}} = \frac{[P_{\text{vertical}} A_{\text{sample}} (H_0 - H_i)]}{V_i} + 4\theta \sum_0^N \tau_G V_i \quad (31)$$

Where,

P_{vertical} = vertical applied pressure (kN/m² or psf),

A_{sample} = area of sample (m² or ft²),

H_0 = initial height of sample before compaction (m or ft),

H_i = height of sample of each gyration (m or ft),

τ_G = applied shear stress (kN/m² or psf) will be discussed below,

θ = gyration angle (radians) and

V_i = volume of sample of each gyration (m³ or ft³).

Measure the Shear Strength and Stiffness Parameters of Compacted Geomaterials

The unconfined compression test, direct shear test, Iowa K test, and gyratory compaction with assembled PDA sensor test were conducted to evaluate and compare the undrained shear strength and stiffness parameters of compacted geomaterials.

Unconfined compression test

Unconfined compression (UC) test determines unconfined compressive strength of geomaterials in accordance with ASTM D2166 “Standard Test Method for Unconfined Compressive Strength of Cohesive Soil.” The compression device is shown in Figure 34.

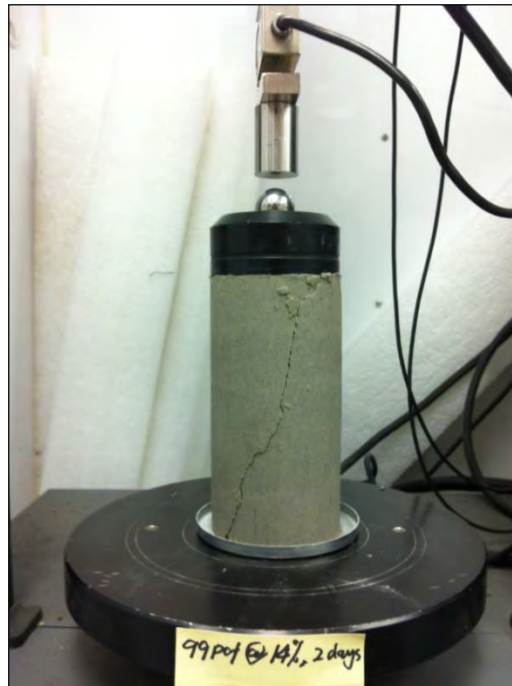


Figure 34. Unconfined compression test for 2.8 in. gypsum sample

All the samples in this study were reconstituted samples those were compacted to predetermined moisture content and density. The sample size was 2.8 in. in diameter and 5.6 in. in height (H/D ratio is 2). Load, deformation, and time data were continuously recorded by the compaction device. The compressive strength, σ_c , for a given applied load can be calculated using Equation 32.

$$\sigma_c = \frac{P \text{ (Given applied load)}}{A \text{ (corresponding average cross-sectional area)}} \quad (32)$$

The compression tests determine compressive strength of molded soil-cement cylinders and other chemically stabilized geomaterials in accordance with ASTM D1633 “Standard Test Methods for Compressive Strength of Molded Soil-Cement Cylinders.” ASTM D1633 Method A specifies the sample diameter = 101.6 mm (4 in.) and height = 116.8 mm (4.6 in.). The samples were extruded from the four inches Proctor mold and wrapped with plastic film and aluminum foil to retain moisture during curing. The samples were cured in a 38°C (100°F) controlled temperature environment.

Direct shear test

Direct shear test determines the consolidated drained shear strength parameter and Mohr strength envelopes of the compacted geomaterials in accordance with ASTM D3080 “Standard Test Method for Direct Shear Test of Soils Under Consolidated Drained Conditions.” A direct shear apparatus is shown in Figure 35.

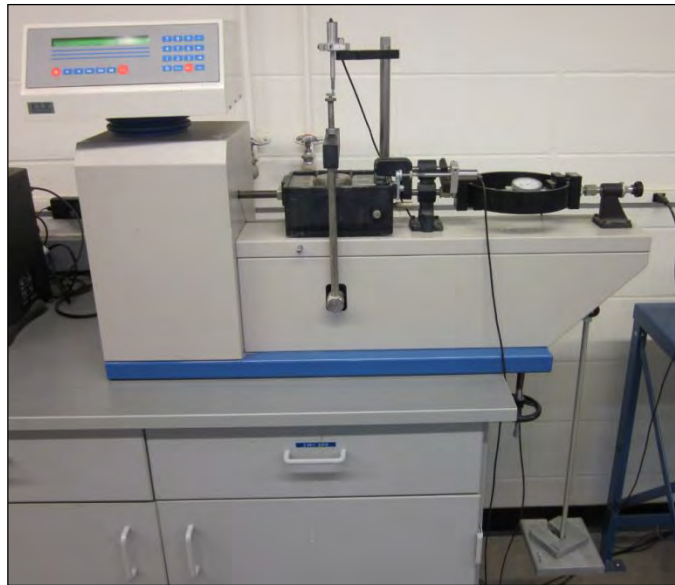


Figure 35. Direct shear test device

The specimens were trimmed from Proctor samples (ASTM D698 or D1557) compacted to predetermined moisture content and density. Consolidation normal load were applied in one increment for stiff materials or several intermediate increments for soft geomaterials. To simulate fast loading condition, the shearing rate was set at 0.05 in/min (1.27 mm/min). For drained shearing tests, the shear box bowl was filled with portable

water at the beginning of consolidation stage. The shearing rate was determined based on the normal deformation versus root time curve and Equation 33 and Equation 34 for low clay content or granular materials. For highly overconsolidated clay, time-settlement curve for the consolidation stage typically cannot be interpreted to yield useful coefficients of consolidation due to the swelling issue at low normal pressure, so to select a time to failure based on experience. For samples with a thickness of the order of 0.25 to 0.5 inch, typically use times to failure ranging from 1 to four days.

$$R_d = \frac{d_f}{t_f} \quad (33)$$

$$t_f = 11.6 t_{90} \quad (34)$$

Where:

R_d = displacement rate, in/min [mm/min],

d_f = estimated relative lateral displacement at failure, in. [mm],

t_f = total estimated elapsed time to failure, min, and

t_{90} = time required for the specimen to achieve 90 % consolidation under the maximum normal stress (increment), min.

The data of time, normal and relative lateral displacement, and shear force were continuously recorded by a data acquisition system during shearing stage of each test. The moisture contents were measured before and after the test for each specimen. Three or more tests were performed on each type geomaterial (approximately same initial moisture content and dry unit weight), under a different normal load to determine shear strength properties such as Mohr strength envelopes.

Pressure distribution analyzer (PDA) in gyratory compaction test

A pressure distribution analyzer (Test Quip LLC.) used in Gyratory compactor (Brovoid Inc).to measure the resultant gyratory force and eccentricity, and then correlate to shear resistance of geomaterials (Figure 36). The procedure of the gyratory compaction test had been described in Gyratory compaction test section of this chapter. The PDA was placed on the top surface of compaction specimens and the data of resultant force and eccentricity was continuously recorded during the tests.



Figure 36. Pressure distribution analyzer (PDA)

An Excel analysis program (PDA Analysis v1.4) is developed by the manufacture for the PDA sensors to calculate the resultant force and eccentricity. The program recognizes the gyrations of tests based on the trends of the data from load cells, and calculates the average resultant force and eccentricity of each gyration.

The resultant force (R) was the summation of the three load cells forces (P_1 , P_2 , and P_3) at the each moment of the gyrations. The eccentricity (e) of the resultant force relative to the center (O) of the PDA can be calculated based on the general moment equilibrium equations along two perpendicular axes which is shown in Figure 21. The distance between each two load cells of the PDA used in this study is 3.943 in. The calculation are shown from Equation 35 through Equation 37

$$\Sigma M_y = 0 \Rightarrow e_x(R) = P_3 \left(\frac{3.943}{2} \right) - P_1 \left(\frac{3.943}{2} \right) \quad (35)$$

$$\Sigma M_x = 0 \Rightarrow e_y(R) = P_2(3.943 \cdot \cos 30^\circ) \quad (36)$$

$$e = \sqrt{e_x^2 + (r_y - e_y)^2} \quad (37)$$

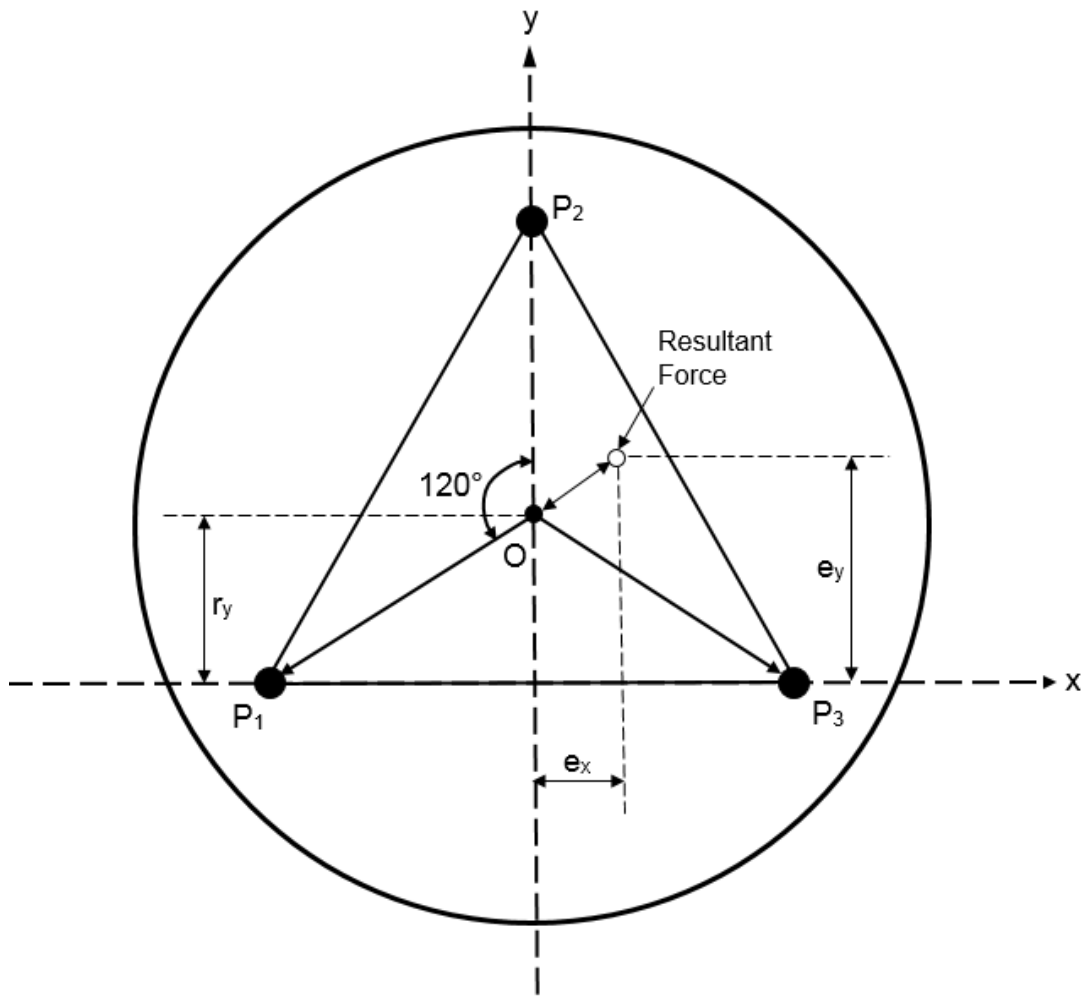


**Figure 37. Eccentricity of the resultant force calculated on basis of the three load cells
(adapted from Guler et al. 2000 by moving the x-axis)**

Guler et al. 2000 suggested that the shear resistance of each gyration can be calculated using Equation 38 that has been discussed in background chapter of this thesis.

$$\tau_G = \frac{Re}{Ah} \quad (38)$$

Where:

τ_G = bulk frictional shear resistance

R = resultant ram force

e = eccentricity

A = the sample cross-section area

h = the sample height

Iowa K test

The Iowa K test was first conducted by Handy and Hoover in 1974 (Handy et al. 1978) who designed a portable split steel mold to evaluate undrained cohesion, friction angle, and other strength and stiffness parameters of soils for highway projects. Iowa K tests are conducted on 4 in. diameter Proctor compaction samples (ASTM D698 or D1557) or intact samples.

Building the Iowa K test device

The Iowa K test device used in this study was modified with more accurate measurement devices and a real-time data acquisition system. Two 10,000 lb donut load cells were used to simultaneously monitor the loads at the top and bottom surfaces of the samples. One linear variable differential transformer (LVDT) was mounted on the mold to measure the horizontal expansion of the mold, and another LVDT measured the vertical displacement of the samples. Two acrylic disks were placed on the top and the bottom surfaces of the samples to minimize friction. A stainless steel bottom base was used to support the Iowa K test mold and the bottom load cell. A schematic and photo of the Iowa K test device is shown in Figure 38 and Figure 39.

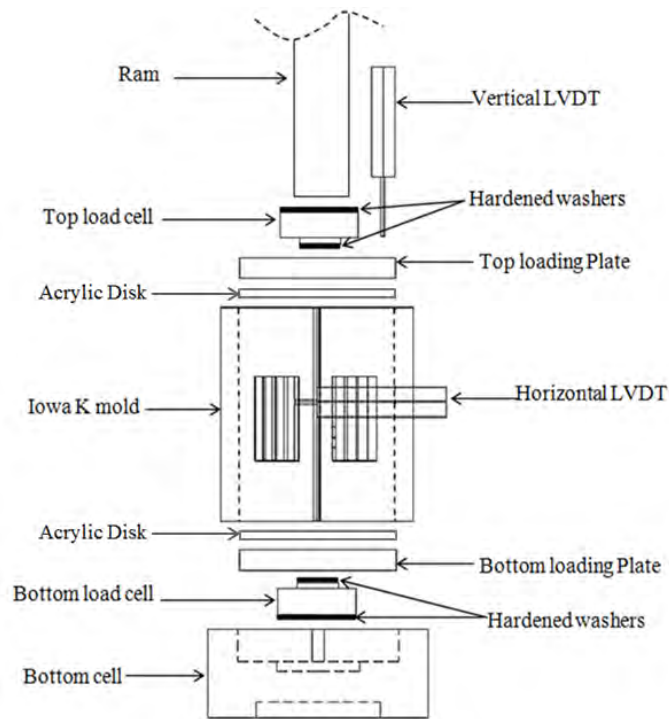


Figure 38. A schematic of the Iowa K test device

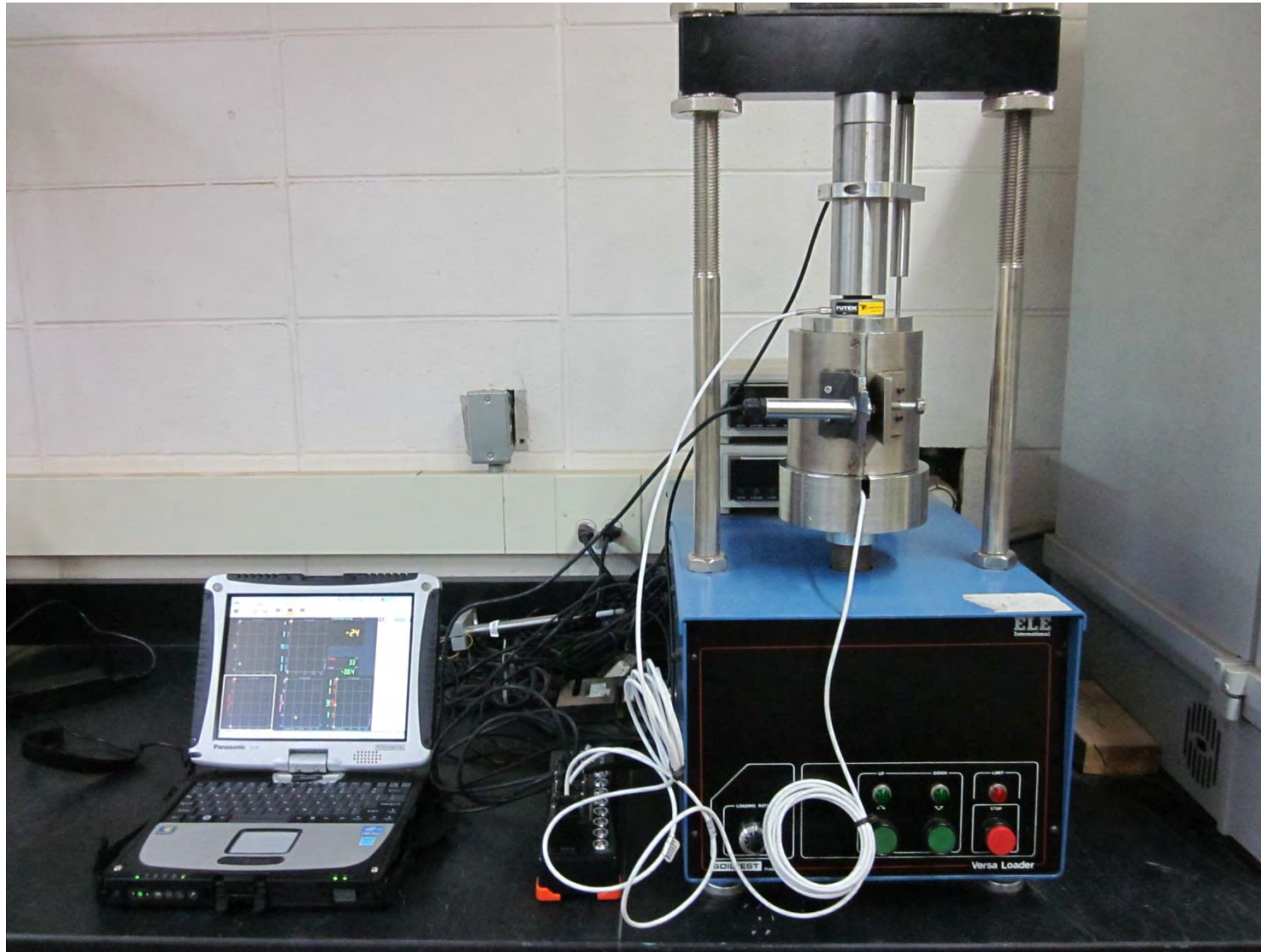


Figure 39. Iowa K test setup

The Iowa K test mold, a donut load cell, and the bottom base are shown in Figure 40 through Figure 41.

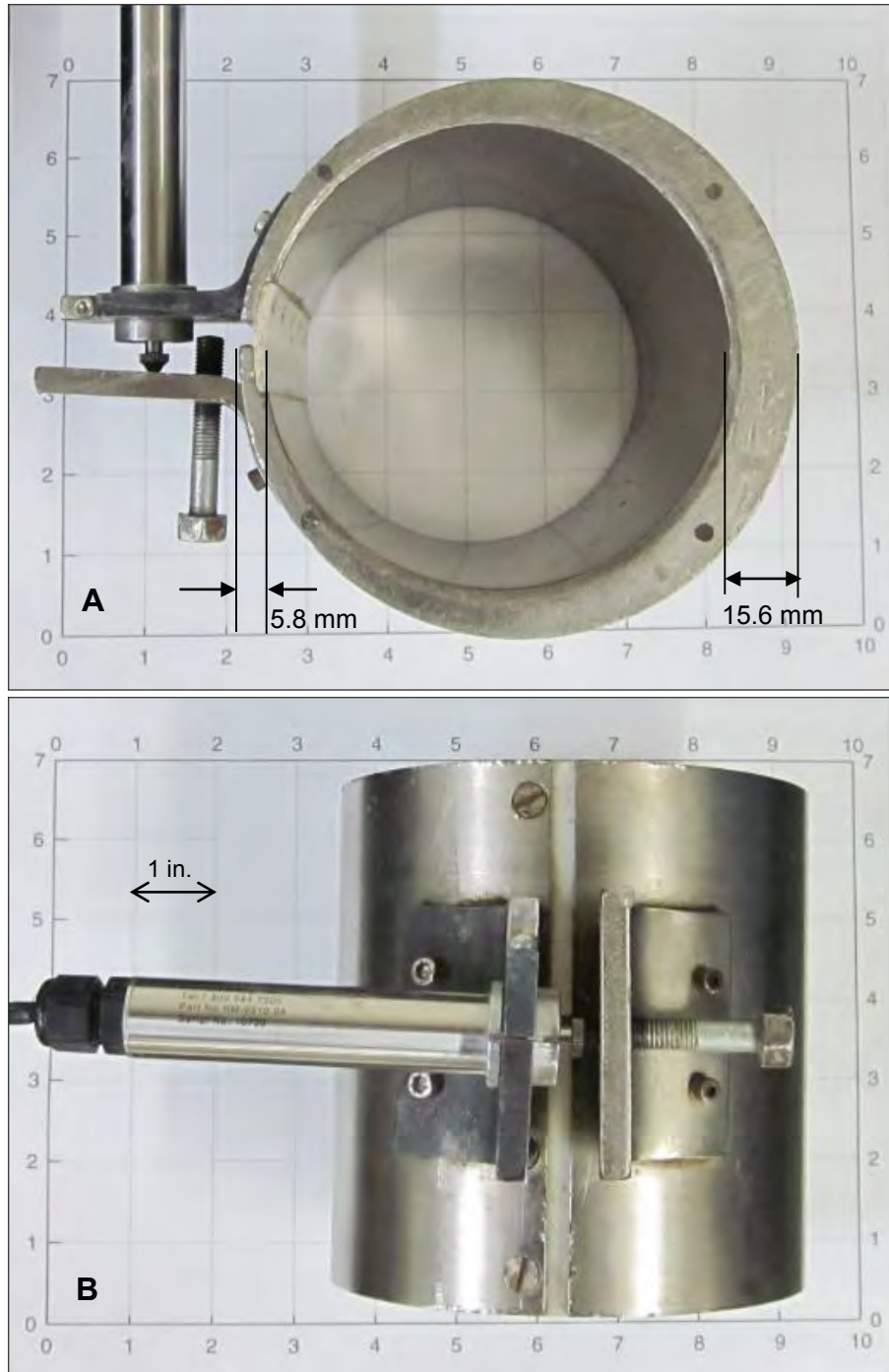


Figure 40. The (A) top view and (B) front view of the Iowa K test mold

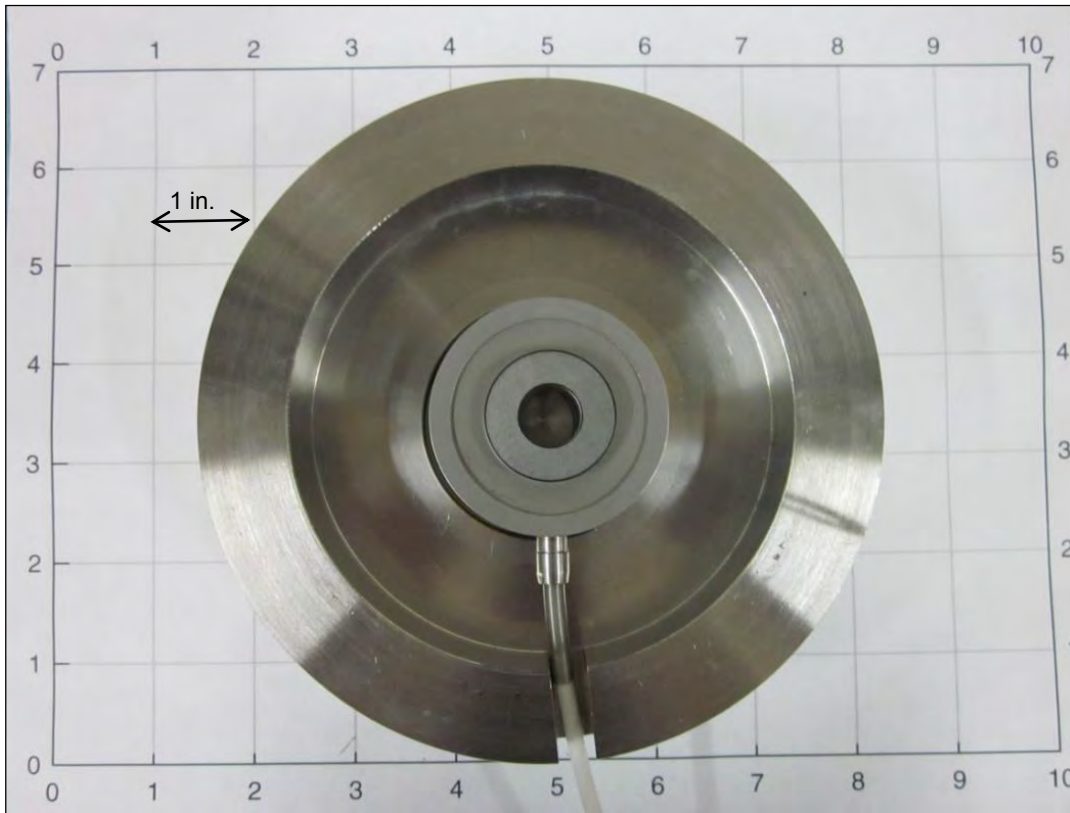


Figure 41. The bottom base and the bottom load cell

Calibrating the Iowa K test device

The K test mold was calibrated with a gelatin cylinder from Polytek Company (Poly 74-20). The gelatin cylinder consists of two part liquids. Part A is polyurethane prepolymer and part B is polyol. Two parts liquids were mixed (1A:2B by weight) and cured under room temperature to form cylinder with the same size as Proctor sample. The Rankine stress ratio, K , of the cylinder equals to one and Poisson ratio is 0.5. Therefore, when the gelatin cylinder subjected to known vertical stresses, the caused horizontal stresses would be same with the vertical stresses. The gelatin cylinder is shown in Figure 42.

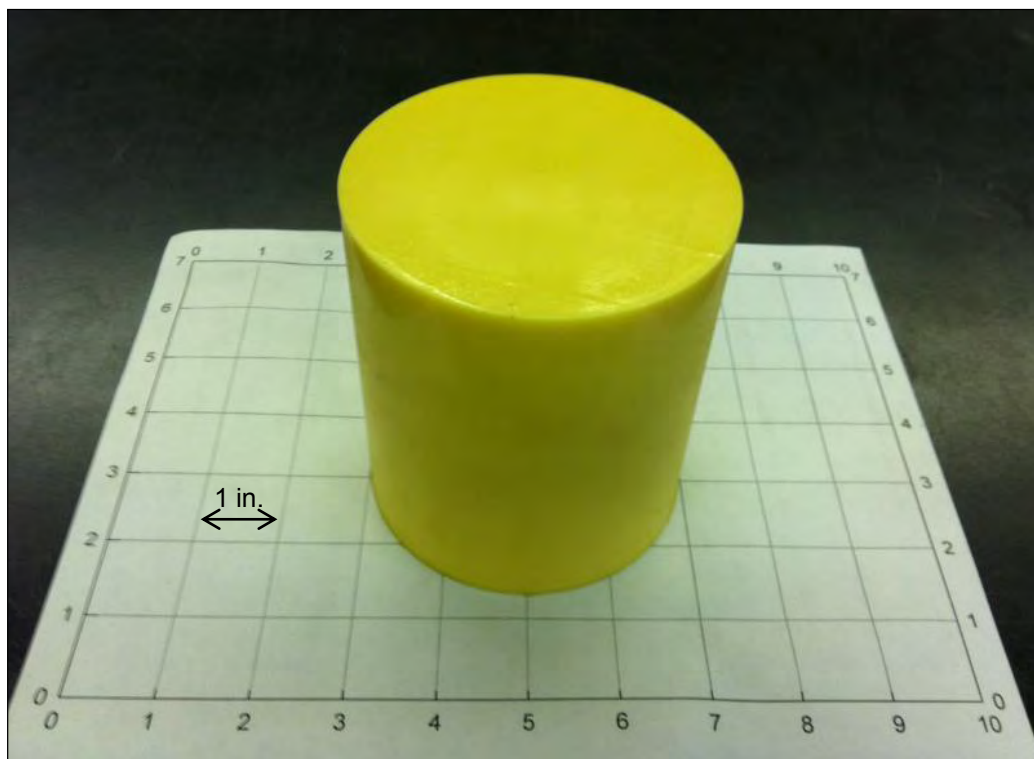


Figure 42. A gelatin cylinder for calibration of the Iowa K test mold

Totally, three calibration tests were conducted for the Iowa K test mold. The rubber cylinder was lubricated for the calibration tests to reduce the friction. The purpose of the calibration was to determine the relationship between horizontal displacement and the how much force to create the displacement for the Iowa K test mold. The horizontal stress versus horizontal displacement of all three calibration tests is shown in Figure 43. The horizontal force to create the displacement was calculated using the horizontal stress multiplied the circumferential area of the rubber cylinder. A hyperbolic model ($R^2 = 0.9999$) was determined based on all the calibration tests (Figure 44). The regular Iowa K tests will determine the diametric force applied on the mold based on the horizontal displacement by using a data analyzing software (Dewesoft v7.0.4).

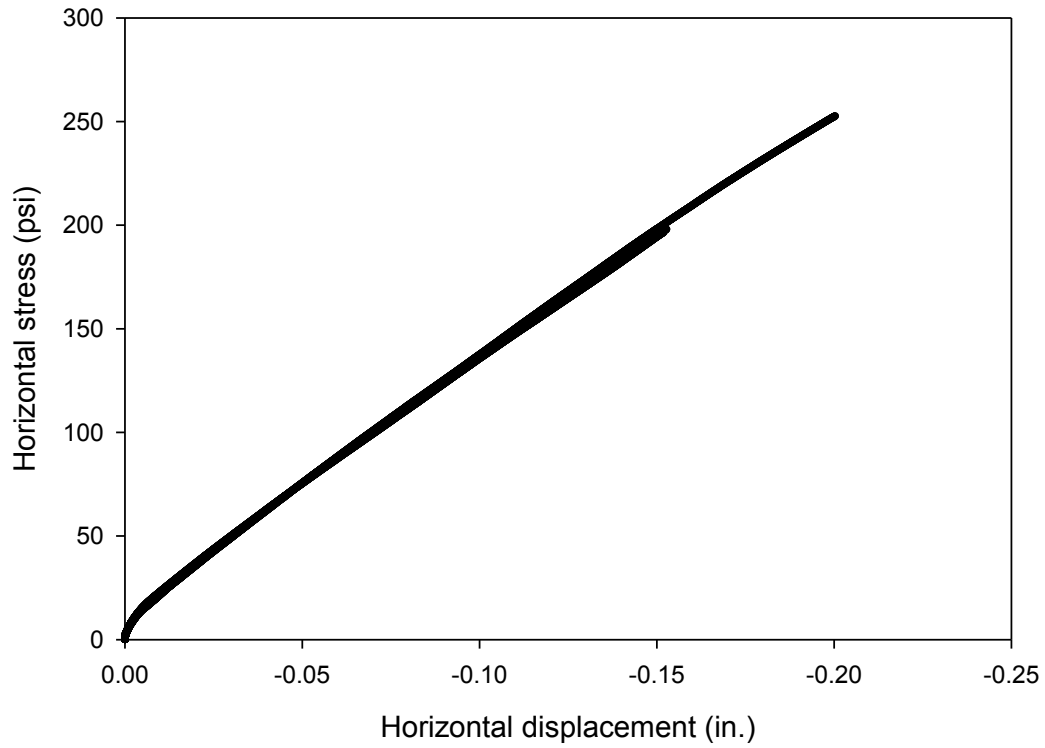


Figure 43. The horizontal stress and displacement relationship of the Iowa K test mold

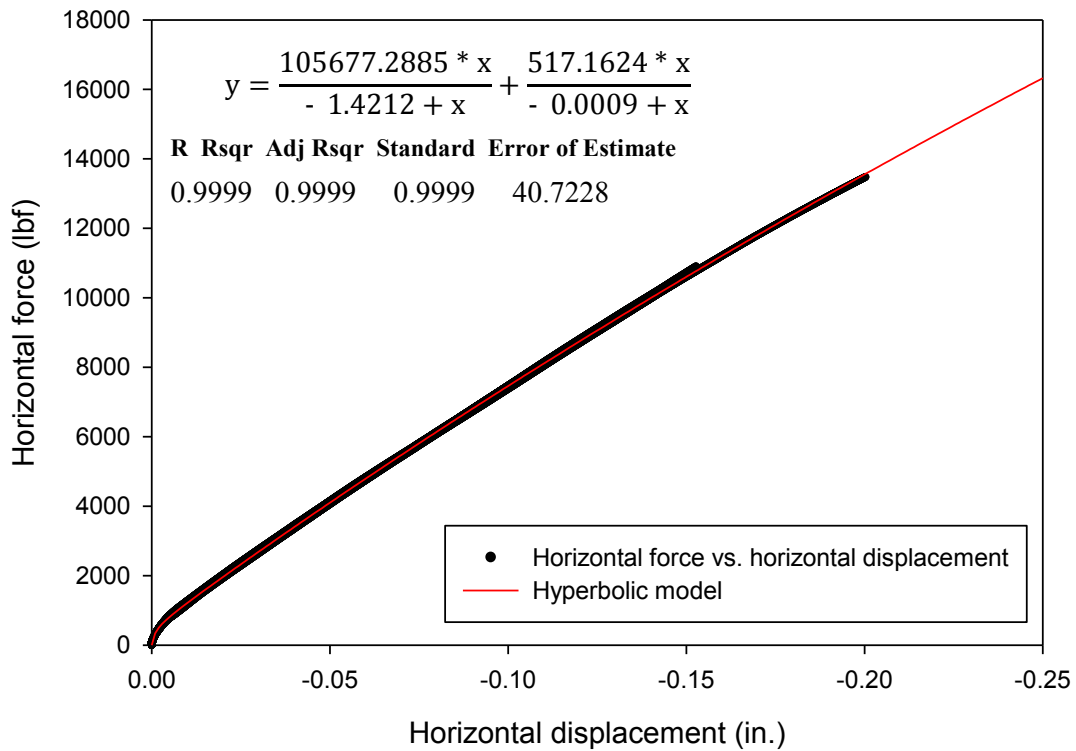


Figure 44. The hyperbolic model from the calibration tests for the Iowa K test mold

Measuring shear strength and stiffness parameters of compacted geomaterials with the Iowa K test

Iowa K tests were conducted on 4 in. Proctor compaction samples to measure shear strength and stiffness parameters. The samples were prepared according to the standard or modified Proctor test standards (ASTM D698 or D1557), and different compaction energies were used to compact the samples to predetermined dry unit weights. The dry unit weight and moisture content of samples were measured after compaction and used for the Iowa K test first loading data. After the compacted samples were extruded from the mold, all the samples were wrapped with plastic film and placed in a sealed container with a water source for curing. The curing times for the different USCS classified materials were recommended in ASTM D3080.

The heights of the samples were measured before the tests, and the 4 in. sample diameter was assumed unchanged. Two loading and unloading cycles (loading rate = 0.05 in/min) were performed on each sample. The vertical pressure applied to the samples ranged from 0 to 250 psi depending on the type of geomaterial. For high moisture content samples, the tests were terminated when the material began to squeeze out from the mold. Moisture contents of samples were also measured after Iowa K tests, but during the tests, the moisture content was assumed unchanged. The real-time data from the load cells and LVDTs was plotted and stored in the data analysis software (Dewesoft v 7.0.4).

The undrained shear strength parameters (i.e., undrained cohesion and friction angle) were calculated based on the Iowa K test first loading data. The stress path method that fits a linear regression line for the linear portion of the p-q curve of the first loading was used to calculate the two parameters. The undrained cohesion (c) was determined based on the intercept (a) using Equation 11.

$$c = \frac{\alpha}{\cos\phi} \quad (39)$$

The undrained friction angle (ϕ) was calculated based on the slope (α) of the linear regression line using Equation 12.

$$\phi = \sin^{-1}(\tan\alpha) \quad (40)$$

However, when the p-q curve showed a straight line with a 45° angle at the beginning of tests, that means the horizontal stress (σ_h) was still zero because there was still space

between the sample and the Iowa K test mold, so these data was deleted for fitting the linear regression line.

Three undrained stiffness parameters (Poisson's ratio, vertical elastic modulus, and lateral stress ratio) for the two loadings of the Iowa K test were determined based on the vertical and horizontal stress and strain data. The Poisson's ratio (ν) and lateral stress ratio (K) were calculated using Equation 41 and Equation 42

$$\nu = \frac{\epsilon_h \sigma_v - \epsilon_v \sigma_h}{2\epsilon_h \sigma_h - \epsilon_v (\sigma_h + \sigma_v)} \quad (41)$$

$$K = \frac{\sigma_h}{\sigma_v} \quad (42)$$

Where,

ϵ_h, ϵ_v = horizontal and vertical unit strain, and

σ_h, σ_v = horizontal stress and vertical stress.

The vertical elastic modulus (E_v) of samples was calculated from the slope of a linear regression line that fits the linear portion of vertical stress-strain curves of Iowa K test samples.

To calculate the three parameters under the second loading of the Iowa K test, both the vertical and horizontal displacement of samples before the second loading were zeroed. The heights and diameters and the dry unit weights of the samples at the beginning of the second loading were determined based on the initial height and diameter of the samples and the vertical and horizontal displacements that were recorded at the end of the first unloading of the tests.

Soil-to-steel frictions were estimated based on the differences between the top and bottom vertical stresses. The soil-to-steel adhesions (c_s) and friction angles (ϕ_s) were calculated based on the first loading data of the Iowa K tests. According to Handy et al. (1978), the slopes of the linear portion of the soil-to-steel friction versus normal stress curve from the mold expansion is the soil-to-steel friction angle, and the intercept with the ordinate of the linear regression line that fits the linear portion of the curve is soil-to-steel adhesion.

Statistically Analyze the Results of Iowa K Test and Gyrotory Compaction Test

Linear or multiple linear regression analysis

Simple and multiple linear regression analyses were performed to evaluate that how changes in moisture content and dry unit weight influence the undrained shear strength and stiffness parameters of the compacted geomaterials. Regression analyses were performed by incorporating moisture content and dry unit weight as independent variables into a general multiple linear regression model as shown in Equation 43

$$\text{Shear strength or stiffness parameters} = b_0 + b_1 \cdot w + b_2 \cdot \gamma_d \quad (43)$$

where

b_0 = intercept,

b_1, b_2 = regression coefficients,

w = moisture content in percentage, and

γ_d = dry unit weight.

Statistical significance of each variable was assessed based on p and t value. A statistical analysis software, JMP 10 was used to generate the statistical models based on testing data. The criteria for identifying the significance of a parameter was: p value < 0.05 = significant, < 0.10 = possibly significant, > 0.10 = not significant, and t- value < -2 or $> +2$ = significant. The p- value indicated the significance of a parameter and the t- ratio value indicates the relative importance. The multiple linear regression models were presented as contour lines in moisture content versus dry unit weight plots of the test samples. An advantage of presenting the results in contour format is that the shear strength and stiffness parameters with respect to interested moisture content and dry unit weight combinations of geomaterials can be graphically determined. The best fit model was determined based on the strength of the regression relationships assessed by the coefficient of determination (R^2) values.

Repeatability and reproducibility analysis for of the gyrotory compaction test

A gyrotory compactor (Brovold Inc. SN: AFGB1A) and two PDAs (PDA 1 and PDA 2) were used to measure variations in dry unit weight and shear resistance during compaction of geomaterials. Four sets of five tests with two vertical pressures of 6266 and 12531 psf

(300 and 600kPa) and two PDAs (PDA 1 and PDA 2) combinations were conducted on Ottawa sands for the repeatability and reproducibility analysis of the testing devices.

Repeatability analysis for the gyratory compaction test devices

The repeatability of using the gyratory compactor and each of the two PDA to measure the variations of dry unit weight, total load, eccentricity, and shear resistance for compacting geomaterials were statistically evaluated using a One-Way normal model and “a pooled estimator of variance” method that is introduced in Vardeman and Jobe (1999).

The standard deviations (S) of the dry unit weight, total load, eccentricity, and shear resistance at each gyration of the fixed set of process conditions were determined. A pooled estimator of the standard deviations (S_p) that combined the standard deviations of the 200 gyrations was calculated for each of the parameters based on the Equation 44

$$S_p = \sqrt{\frac{(n_1-1)s_1^2 + (n_2-1)s_2^2 + \dots + (n_r-1)s_r^2}{n-r}} \quad (44)$$

where,

r = the number of gyrations for each test,

n_i = the number of repeated tests, and

$n = n_1 + n_2 + \dots + n_r$.

For example, if 5 repeated gyratory compaction tests with the same vertical pressure and 200 gyrations are conducted on same material using the same PDA, n_r will be equal to 5. r is 200, and n is $5 \times 200 = 1000$.

Vardeman and Jobe (1999) indicated the terminology “pooled estimator of variance” is same meaning with the error mean square (MSE) where people emphasize the Analysis of Variance (ANOVA). The 95% confidence intervals also was calculated for each of the parameters based on the Equation 45

$$\bar{y}_i \pm t_{s_p} \sqrt{\frac{1}{n_i}} \quad (45)$$

Where,

t_{s_p} = t-distribution quantiles, and

n_i = number of repeated tests.

Reproducibility analysis for the gyratory compaction test devices

The reproducibility of using the two PDAs to measure the total load, eccentricity, and shear resistance for compacting geomaterials were statistically evaluated using the Two-Way ANOVA method provided in White et al. (2009). The data were obtained from the four sets tests for repeatability analysis. However, the dry unit weight of the samples were measured by only one gyratory compactor in this study, so the reproducibility analysis for the gyratory compactor was not performed.

Three variables (m, I, and J) needed be defined for the repeatability and reproducibility (R&R) analysis:

1. m: number of the repeated tests using each PDA,
2. I: number of the gyrations for each test, and
3. J: number of the PDAs used in the analysis.

The two-way random effects model and the three quantities are provided below:

$$y_{ijk} = \mu + \alpha_i + \gamma_j + \alpha\gamma_{ij} + \varepsilon_{ijk} \quad (46)$$

$$\sigma_{repeatability} = \sigma \quad (47)$$

$$\sigma_{reproducibility} = \sqrt{\sigma^2_{\gamma} + \sigma^2_{\alpha\gamma}} \quad (48)$$

$$\sigma_{R\&R} = \sqrt{\sigma^2_{reproducibility} + \sigma^2_{repeatability}} \quad (49)$$

For the PDA measurements (i.e., total load, eccentricity, and shear resistance), $\sigma_{repeatability}$ was simply the standard deviation of repeated measurements obtained under each vertical pressure which was discussed above. For the reproducibility analysis, the number of gyrations and number of PDAs were considered as nominal variables in the Two-Way ANOVA. Estimates of these Two-Way ANOVA results and the parameters of the equations are shown in Equation 50 through Equation 52 and Table 12.

$$\sigma_{repeatability} = \sigma = \sqrt{MSE} \quad (50)$$

$$\sigma_{reproducibility} = \sqrt{\max\left(0, \frac{MSC}{mI} + \frac{(I-1)MSAC}{mI} - \frac{MSE}{m}\right)} \quad (51)$$

$$\sigma_{R\&R} = \sqrt{\frac{MSC}{mI} + \frac{(I-1)MSAC}{mI} + \frac{(m-1)MSE}{m}} \quad (52)$$

Table 12. Typical Two-Way ANOVA table for the R&R analysis

Source	SS (sum of square)	DOF (degree of freedom)	MS (mean square)
Number of gyrations (I)	SSA	I-1	MSA = SSA/(I-1)
Number of PDAs (J)	SSC	J-1	MSC = SSC/(J-1)
I x J (interaction term)	SSAC	(I-1) (J-1)	MSAC = SSAC/(I-1) (J-1)
Error	SSE	IJ (m-1)	MSE = SSE/IJ(m-1)
Total	SSTot	IJm - 1	—

The two-way ANOVA tables such as indicated above were generated using the JMP 10. An example of the JMP output is presented in Figure 45.

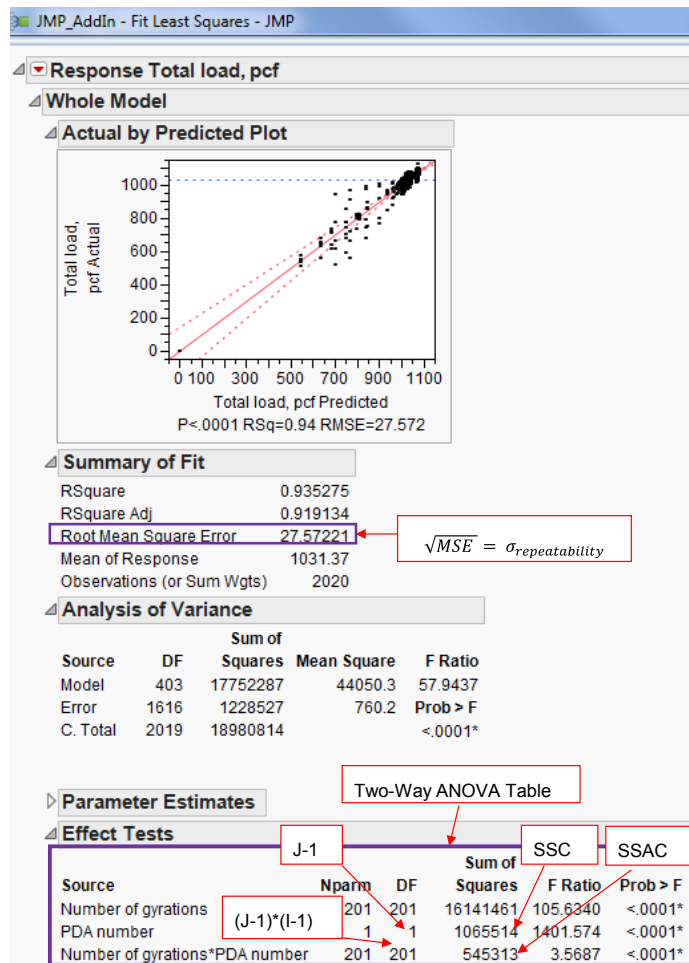


Figure 45. An example JMP output for the Two-Way ANOVA table

The Satterthwaite approximate confidence limits (e.g., 95% confidence interval) for $\sigma_{\text{reproducibility}}$ and $\sigma_{R\&R}$ can be calculated using the Equation 53 through Equation 56

$$v_{\text{reproducibility}} = \frac{\sigma_{\text{reproducibility}}^4}{\frac{1}{m^2} \left(\frac{MSC^2}{I^2(J-1)} + \frac{(I-1)MSAC^2}{(J-1)} + \frac{MSE^2}{IJ(m-1)} \right)} \quad (53)$$

$$v_{R\&R} = \frac{\sigma_{R\&R}^4}{\frac{1}{m^2} \left(\frac{MSC^2}{I^2(J-1)} + \frac{(I-1)MSAC^2}{I^2(J-1)} + \frac{(m-1)MSE^2}{IJ(m-1)} \right)} \quad (54)$$

$$\sigma_{\text{reproducibility}} \sqrt{\frac{v_{\text{reproducibility}}}{\chi_{v_{\text{reproducibility}}, \text{upper}}^2}} \text{ and } \sigma_{\text{reproducibility}} \sqrt{\frac{v_{\text{reproducibility}}}{\chi_{v_{\text{reproducibility}}, \text{lower}}^2}} \quad (55)$$

$$\sigma_{R\&R} \sqrt{\frac{v_{R\&R}}{\chi_{v_{R\&R}, \text{upper}}^2}} \text{ and } \sigma_{R\&R} \sqrt{\frac{v_{R\&R}}{\chi_{v_{R\&R}, \text{lower}}^2}} \quad (56)$$

where

$v_{\text{reproducibility}}$ and $v_{R\&R}$ = degree of freedom, and

χ_v^2 = percentage points of the chi-square distribution.

CHAPTER 4. MATERIALS

This chapter will present the soil index properties of the 15 geomaterials used in this study. These materials were obtained from Alabama, Florida, Illinois, Iowa, Tennessee and Texas ranged from coarse aggregate to clay. The materials were tested for gradation, liquid limit, plastic limit, specific gravity, and compaction behavior and the results were incorporated into the Compaction Forecasting Expert Database (CFED) (Puls 2008). Table 13 shows the CFED soil ID, material description, and material source of each material. Table 14 provides the particle size analysis, liquid limit, plastic limit, and specific gravity data of the 15 geomaterials.

Table 13. CFED soil ID, description, and geomaterial source

CFED Soil ID	Description	Geomaterial Source
1634	Western Iowa loess	West Iowa
2043	Texas fat clay	Fort Worth, Texas
2051	2011 Manatt's RAP	Manatt's Company, Ames, Iowa
2052	CA-6-G	Edwards, Illinois
2053	WCF fly ash	Widows Creek Fossil Plant, Stevenson, Alabama
2054	WCF gypsum	Widows Creek Fossil Plant, Stevenson, Alabama
2055	Temple gypsum	Cumberland Fossil Plant, Cumberland City, Tennessee
2056	Reject gypsum	Cumberland Fossil Plant, Cumberland City, Tennessee
2057	Loess stabilized with 15% fly ash	Western Iowa
2058	Loess stabilized with 9% Type I cement	Western Iowa
2059	Hwy 9B embankment fill	Highway 9B, Jacksonville, Florida
2061	2012 Manatt's RAP	Manatt's Company, Ames, Iowa
2062	RPCC and RAP mixture	Manatt's Company, Ames, Iowa
2063	Crushed limestone granular subbase	Martin Marietta, Ames, Iowa
N/A	Ottawa sand (ASTM 20-30 sand)	Ottawa, Illinois

Table 14. Soil index properties of the 15 geomaterials

Parameter	Western Iowa loess	Texas fat clay	2011 RAP	CA-6-G	WCF fly ash	WCF gypsum	Temple gypsum	Reject Gypsum
CFED soil ID	1634	2043	2051	2052	2053	2054	2055	2056
Particle-size analysis results (ASTM D 422)								
Gravel content (%) (> 4.75 mm)	0.0	0.3	47.0	32.2	2.0	0.0	0.0	0.0
Sand content (%) (4.75 mm – 75 μ m)	2.9	4.0	48.0	50.6	32.0	6.0	1.0	4.0
Silt content (%) (75 μ m – 2 μ m)	97.1	21.1	5.0	7.0	63.0	93.0	99.0	95.0
Clay content (%) (< 2 μ m)	6.5	74.6		3.7	3.0	1.0	0.0	1.0
D ₁₀ (mm)	—	< 0.001	0.330	0.051	0.006	0.008	0.027	0.019
D ₃₀ (mm)	0.013	< 0.001	1.350	0.783	0.021	0.017	0.037	0.032
D ₆₀ (mm)	0.028	< 0.001	6.040	4.500	0.059	0.039	0.050	0.047
Coefficient of uniformity, c_u	—	—	18.18	87.97	9.36	4.76	1.81	2.47
Coefficient of curvature, c_c	—	—	0.90	2.67	1.16	0.84	1.03	1.14
Atterberg limits test results (ASTM D4318)								
Liquid limit, LL (%)	29	68	NP	18	NP	NP	NP	NP
Plastic limit, PL (%)	23	23		NP				
AASHTO and USCS soil classification (ASTM D2487 & D3282)								
AASHTO classification	A-4(0)	A-7-6(49)	A-1-a	A-1-a	A-4(0)	A-4(0)	A-4(0)	A-4(0)
USCS classification	ML	CH	SP-SM	SW-SM	ML	ML	ML	ML
Specific gravity (ASTM C127 & D854)								
Specific gravity, G_s	2.72	2.70	2.50	2.80	2.23	2.48	2.36	2.40

Table 14 (continued). Soil index properties of the 15 geomaterials

Parameter	Loess + 15% FA	Loess + 9% Cement	Florida 9B Fill	2012 RAP	RPCC + RAP	Crushed Limestone	Ottawa sand
CFED soil ID	2057	2058	2059	2061	2062	2063	—
Particle-size analysis results (ASTM D 422)							
Gravel content (%) (> 4.75 mm)	0.0	0.0	0.0	52.0	79.0	69.0	0.0
Sand content (%) (4.75 mm – 75 µm)	3.0	15.0	96.6	45.0	19.0	23.0	100.0
Silt content (%) (75 µm – 2 µm)	82.0	75.0	3.4	2.0	2.0	7.0	0.0
Clay content (%) (< 2 µm)	15.0	10.0		1.0	0.0	1.0	0.0
D ₁₀ (mm)	< 0.001	0.002	0.095	0.507	1.387	0.171	—
D ₃₀ (mm)	0.011	0.017	0.159	2.172	7.362	4.536	—
D ₆₀ (mm)	0.030	0.034	0.1914	6.727	14.842	10.565	—
Coefficient of uniformity, c _u	—	15.01	2.01	13.27	10.70	61.98	—
Coefficient of curvature, c _c	—	3.86	1.38	1.38	2.63	11.42	—
Atterberg limits test results (ASTM D4318)							
Liquid limit, LL (%)	33	NP	NP	NP	NP	NP	NP
Plastic limit, PL (%)	NP						
AASHTO and USCS soil classification (ASTM D2487 & D3282)							
AASHTO classification	A-4(2)	A-4(0)	A-3	A-1-a	A-1-a	A-1-a	A-1-b
USCS classification	ML	ML	SP	GW	GW	GP-GM	SP
Specific gravity (ASTM C127 & D854)							
Specific gravity, G _s	2.68	2.74	2.63	2.47	2.1	2.71	2.65

This chapter is organized by the CFED soil IDs. The section for each geomaterial consists of a scaled photograph, a summary table of soil index properties, a gradation curve, and Proctor or vibratory compaction test results.

Proctor compaction tests with different compaction energy levels (ASTM D698 and D1557) were conducted for soils 2051 through 2059 to determine moisture-density-compaction energy relationships. The Proctor test parameters are shown in Table 15.

Table 15. Proctor compaction test parameters

Energy Level	Layers	Blows per Layer by mold		Weight of Hammer (lb)	Drop Height (ft)	Energy (lb-ft/ft ³)
		4 in.	6 in.			
Sub-Standard (SS)	3	15	35	5.5	1.0	7425
Standard (S)	3	25	56	5.5	1.0	12375
Super-Sub-Modified (SSM)	5	25	56	5.5	1.0	20790
Sub-Modified (SM)	5	25	56	5.5	1.5	34650
Modified (M)	5	25	56	10.0	1.5	56250

Corrections were made to the dry unit weights moisture contents for the geomaterials that contained 5% by mass of oversize fraction (ASTM D4718). The bulking phenomenon, lowest dry unit weight at its “bulking” moisture content (White et al 2012), of granular geomaterials are identified with line of bulking moisture content for CA-6-G (CFED 2052) and Florida highway 9B embankment fill (CFED 2059).

Vibratory compaction tests (ASTM D4253 and D4254) were conducted for CFED 2061 to 2063 and the Ottawa sand to determine moisture-density-compaction energy relationships. The materials retained on 0.75 in. sieve were scalped off before testing, and the 6 in. mold (0.1 ft³) was used for all the vibratory compaction tests. The minimum index density was determined at 0% moisture content (oven-dried sample). The sample height was measured before and after placing the dead weight, and after 10, 20, 30, 60, 120, 240, 480, and 960 seconds of vibratory compaction time.

Western Iowa Loess (CFED 1634)

Western Iowa loess was obtained from Western Iowa (Figure 46).



Figure 46. Western Iowa loess at 17.2% moisture content

Particle size analysis, specific gravity, and Atterberg limits test were conducted on western Iowa loess to determine material index properties. A summary table of the material index properties is shown in Table 16. The particle size distribution curve is shown in Figure 47.

Table 16. Material index properties of western Iowa loess

Material Index Property	Result	Testing Method
AASHTO classification	A-4(0)	ASTM D3282
USCS classification	ML	ASTM D2487
Liquid limit, LL (%)	29	ASTM D4318
Plastic limit, PL (%)	23	
Specific gravity, G_s	2.72	ASTM D854

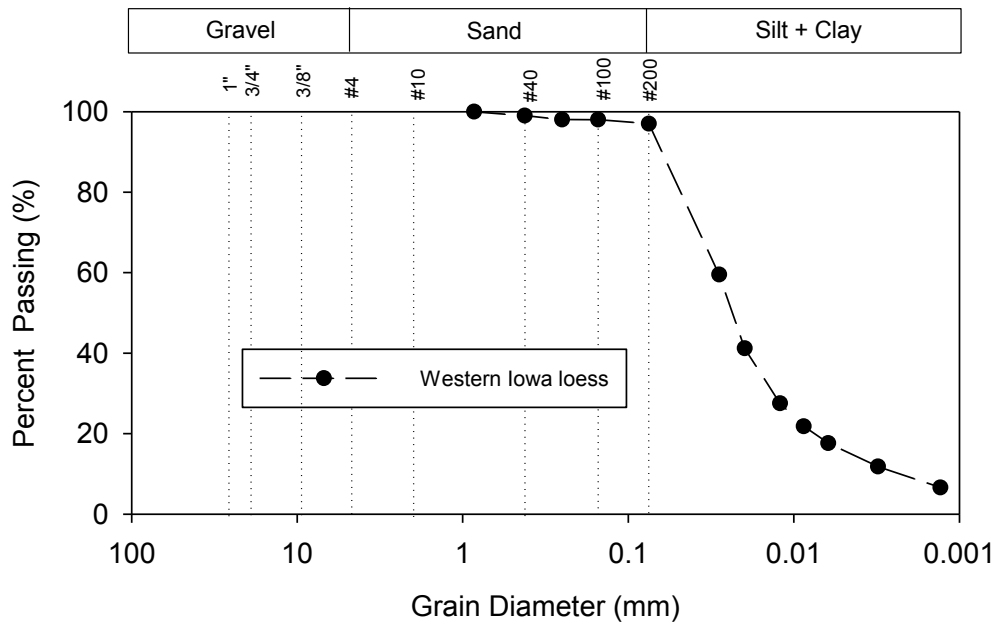


Figure 47. Particle size distribution curve of western Iowa loess

The moisture density relationships, optimum moisture contents, and maximum dry unit weights of western Iowa loess were determined by Proctor compaction tests at five energy levels (Figure 48).

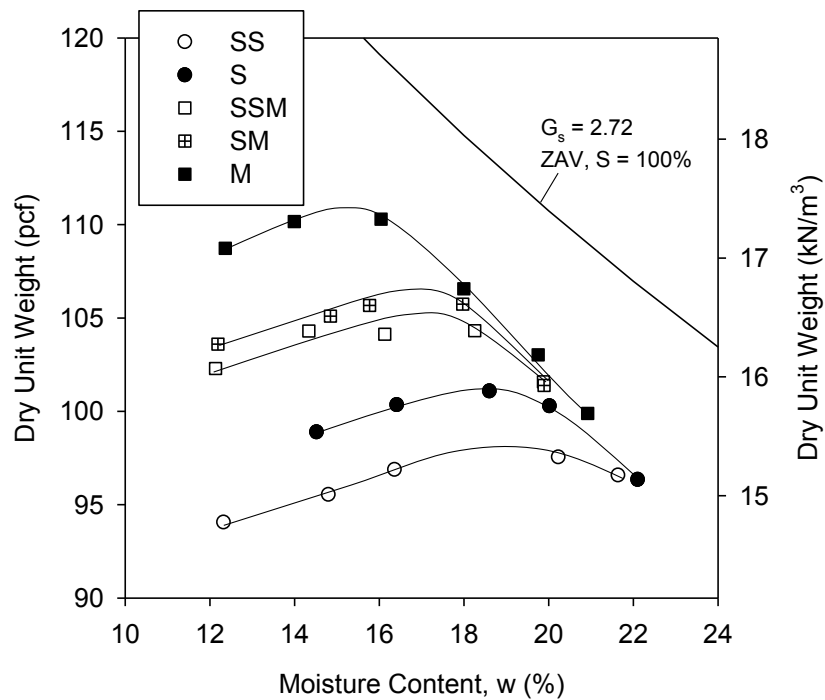


Figure 48. Moisture density relationships of western Iowa loess

Texas Fat Clay (CFED 2043)

Texas fat clay was obtained from Fort Worth, Texas in 2010 (Figure 49).



Figure 49. 2011 Texas fat clay at 15.5% moisture content

Particle size analysis, specific gravity, and Atterberg limits test were conducted on Texas fat clay to determine material index properties. A summary table of the material index properties is shown in Table 17. The particle size distribution curve is shown in Figure 50.

Table 17. Material index properties of Texas fat clay

Material Index Property	Result	Testing Method
AASHTO classification	A-7-6(49)	ASTM D3282
USCS classification	CH	ASTM D2487
Liquid limit, LL (%)	68	ASTM D4318
Plastic limit, PL (%)	23	
Specific gravity, G_s	2.70	ASTM D854

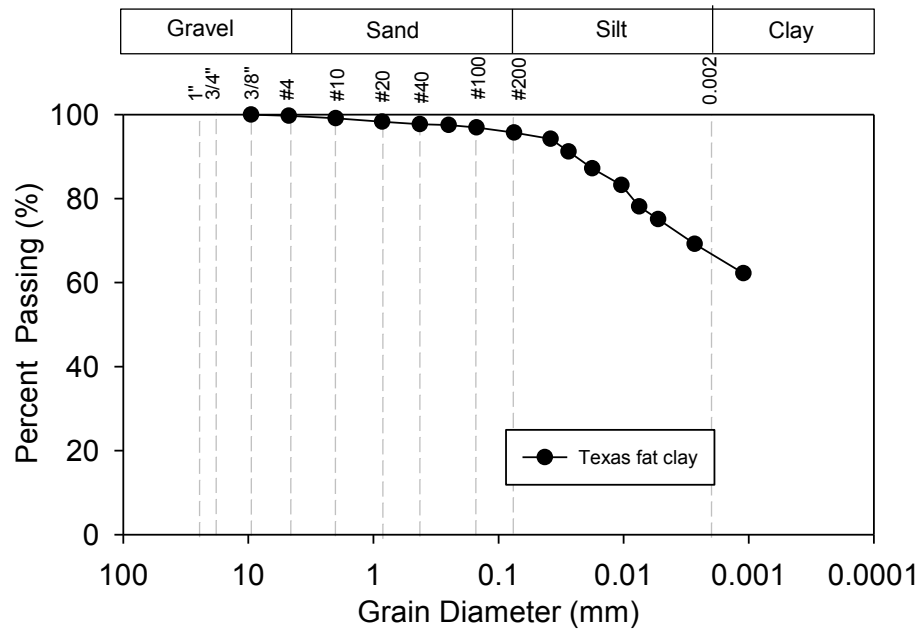


Figure 50. Particle size distribution curve of Texas fat clay

The moisture density relationships, optimum moisture contents, and maximum dry unit weights of Texas fat clay were determined by Proctor compaction tests at five energy levels (Figure 54).

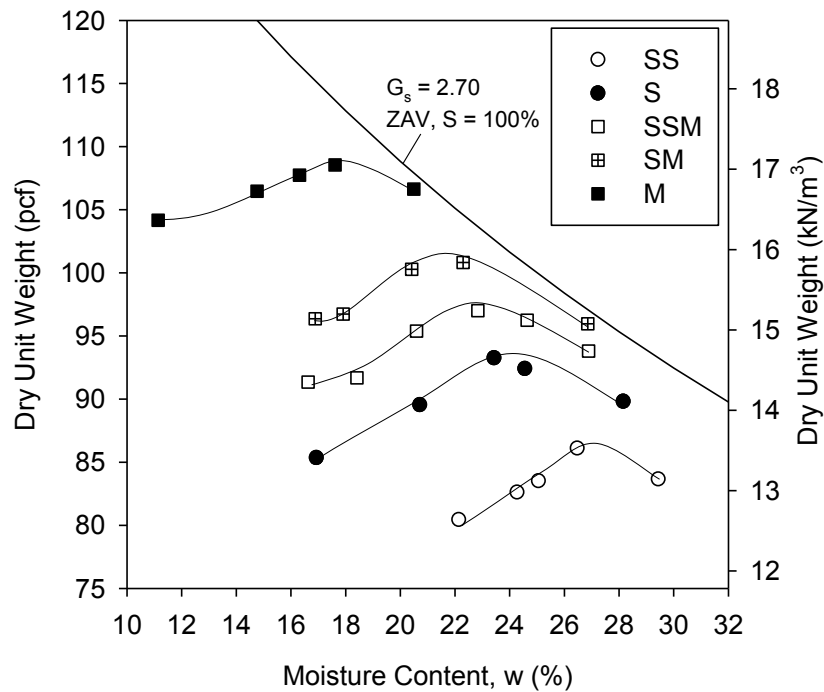


Figure 51. Moisture density relationships of Texas fat clay

2011 Manatt's RAP (CFED 2051)

2011 Manatt's recycled asphalt pavement (RAP) was obtained from Manatt's Company Ames, Iowa in 2011 (Figure 52).



Figure 52. 2011 Manatt's RAP at 6.5% moisture content

Particle size analysis, specific gravity, and Atterberg limits test were conducted on 2011 Manatt's RAP to determine material index properties. A summary table of the material index properties is shown in Table 18. The particle size distribution curve is shown in Figure 53.

Table 18. Material index properties of 2011 Manatt's RAP

Material Index Property	Result	Testing Method
AASHTO classification	A-1-a	ASTM D3282
USCS classification	SP-SM	ASTM D2487
Liquid limit, LL (%)	NP	ASTM D4318
Plastic limit, PL (%)		
Specific gravity, G_s	2.50	ASTM C127 and ASTM D854

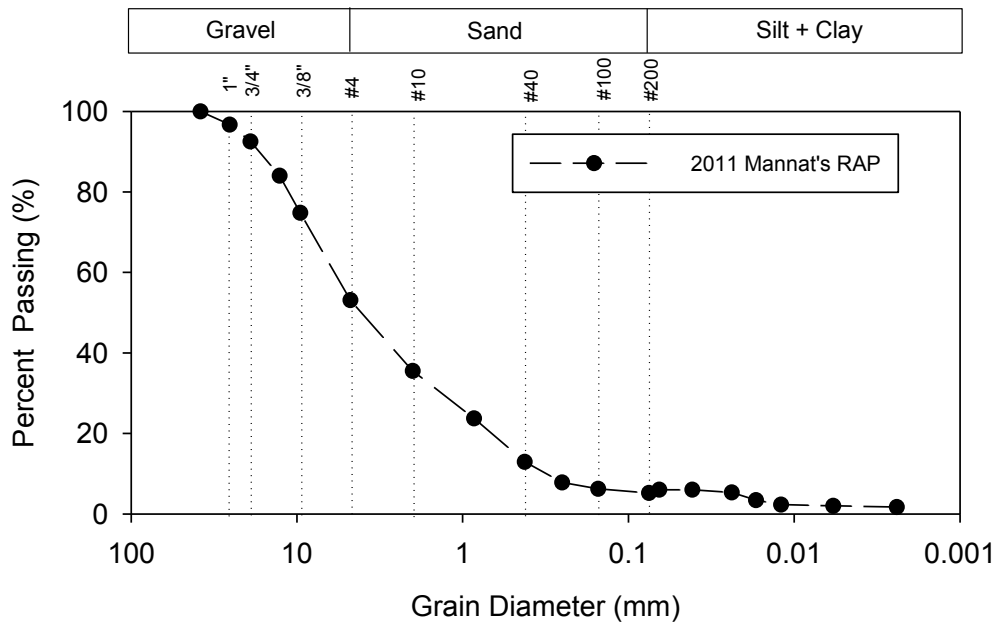


Figure 53. Particle size distribution curve of 2011 Manatt's RAP

The moisture density relationships, optimum moisture contents, and maximum dry unit weights of 2011 Manatt's RAP were determined by Proctor compaction tests at five energy levels (Figure 54). Bulking phenomenon was not observed for this type granular geomaterial.

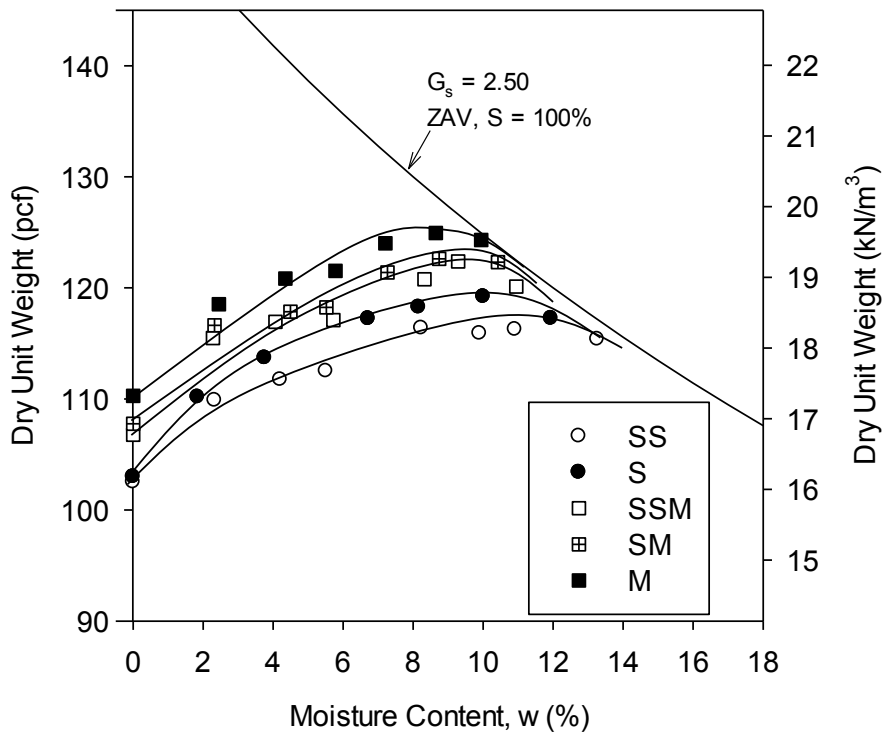


Figure 54. Moisture density relationships of 2011 Manatt's RAP

CA-6-G (CFED 2052)

Coarse aggregate CA-6-G was obtained from Edwards, Illinois (Figure 55).



Figure 55. CA-6-G (110°C oven-dried)

Particle size analysis, specific gravity, and Atterberg limits test were conducted on CA-6-G to determine material index properties. A summary table of the material index properties is shown in Table 19. The particle size distribution curve is shown in Figure 56.

Table 19. Material index properties of CA-6-G

Material Index Property	Result	Testing Method
AASHTO classification	A-1-a	ASTM D3282
USCS classification	SW-SM	ASTM D2487
Liquid limit, LL (%)	18	ASTM D4318
Plastic limit, PL (%)	NP	
Specific gravity, G_s	2.80	ASTM C127 & D854

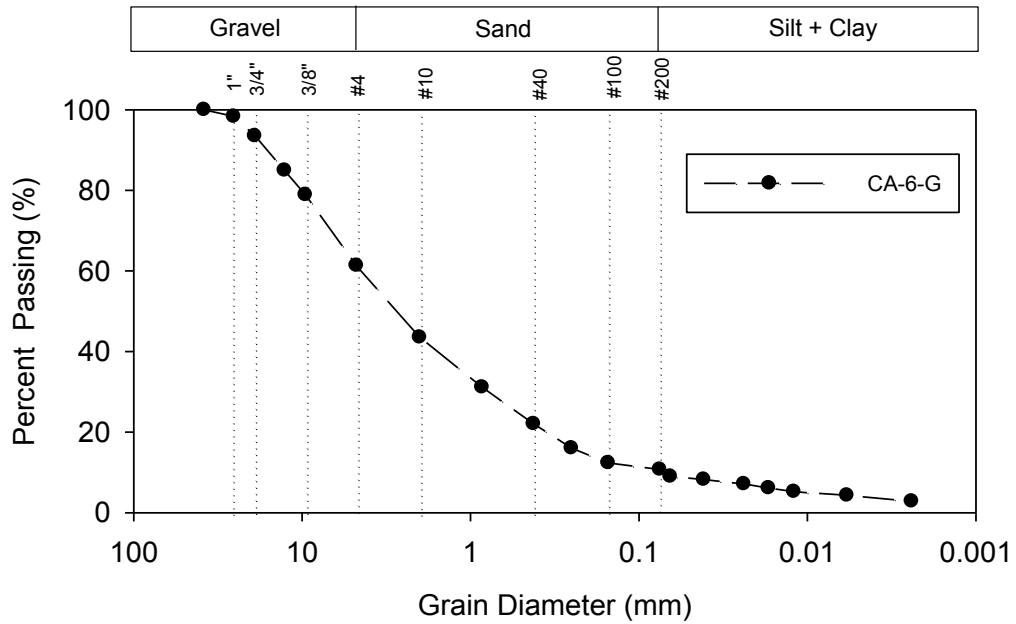


Figure 56. Particle size distribution curve of CA-6-G

The moisture density relationships, optimum moisture content, and maximum dry unit weight of CA-6-G were determined by Proctor compaction tests at five energy levels (Figure 57). The bulking phenomenon was observed and a line of bulking moisture content is shown in Figure 57.

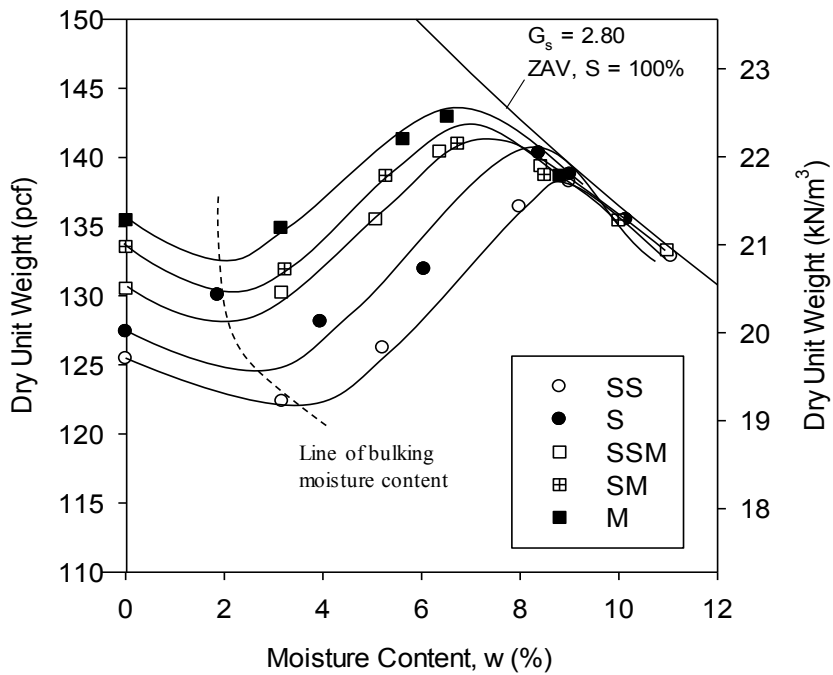


Figure 57. Moisture density relationships of CA-6-G

WCF Fly Ash (CFED 2053)

WCF fly ash was obtained from Widows Creek Fossil Plant, Stevenson, Alabama in 2012 (Figure 58).



Figure 58. WCF fly ash at 23.0% moisture content

Particle size analysis, specific gravity, and Atterberg limits test were conducted on WCF fly ash to determine material index properties. A summary table of the material index properties is shown in Table 20. The particle size distribution curve is shown in Figure 59.

Table 20. Material index properties of WCF fly ash

Material Index Property	Result	Testing Method
AASHTO classification	A-4(0)	ASTM D3282
USCS classification	ML	ASTM D2487
Liquid limit, LL (%)	NP	ASTM D4318
Plastic limit, PL (%)		
Specific gravity, G_s	2.23	ASTM D854

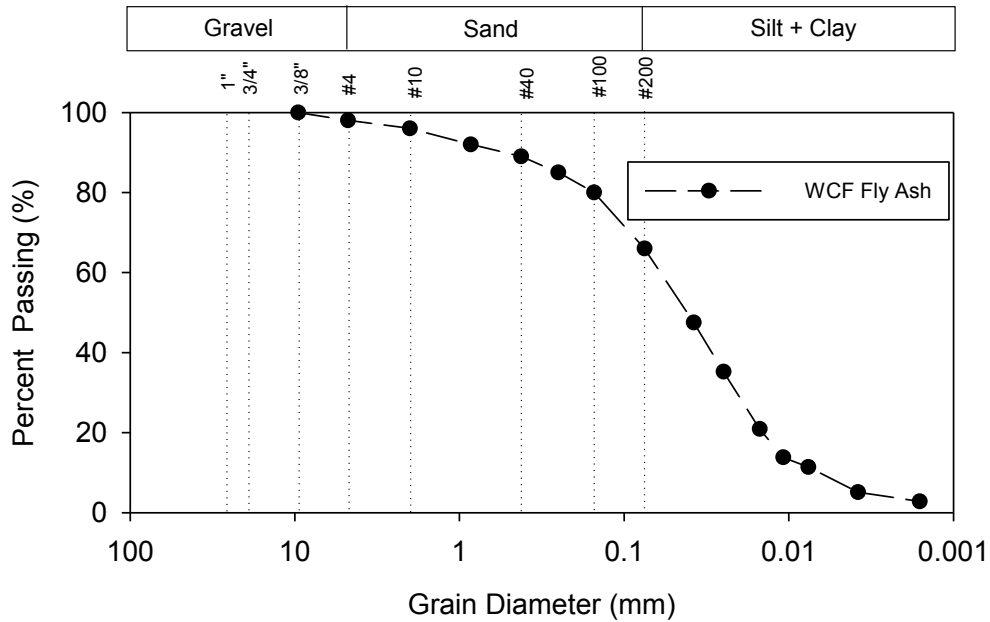


Figure 59. Particle size distribution curve of WCF fly ash

The moisture density relationships, optimum moisture contents, and maximum dry unit weights of WCF fly ash were determined by Proctor compaction tests at five energy levels (Figure 60).

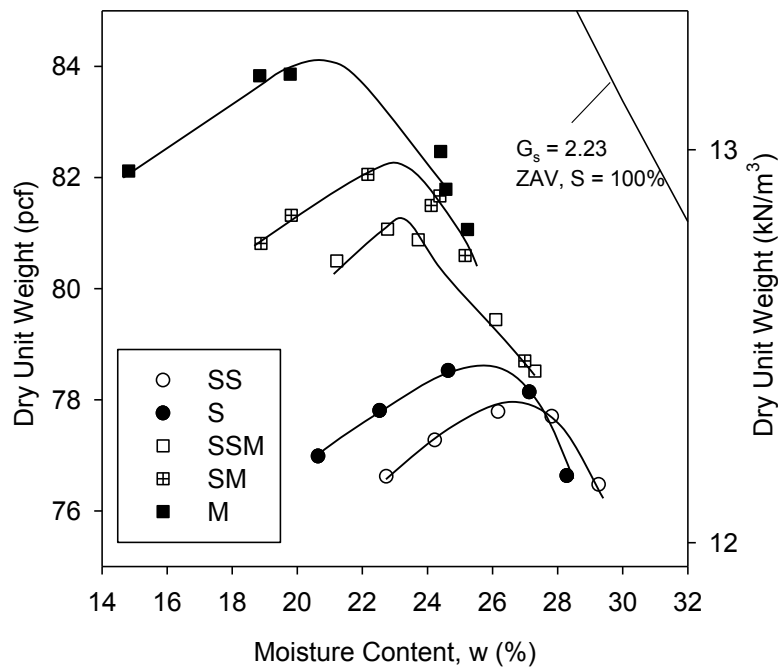


Figure 60. Moisture density relationships of WCF fly ash

WCF Gypsum (CFED 2054)

WCF gypsum was obtained from Widows Creek Fossil Plant, Stevenson, Alabama in 2012 (Figure 61).



Figure 61. WCF gypsum at 16.0% moisture content

Particle size analysis, specific gravity, and Atterberg limits test were conducted on WCF gypsum to determine material index properties. A summary table of the material index properties is shown in Table 21. The particle size distribution curve is shown in Figure 62.

Table 21. Material index properties of WCF gypsum

Material Index Property	Result	Testing Method
AASHTO classification	A-4(0)	ASTM D3282
USCS classification	ML	ASTM D2487
Liquid limit, LL (%)	NP	ASTM D4318
Plastic limit, PL (%)		
Specific gravity, G_s	2.48	ASTM D854

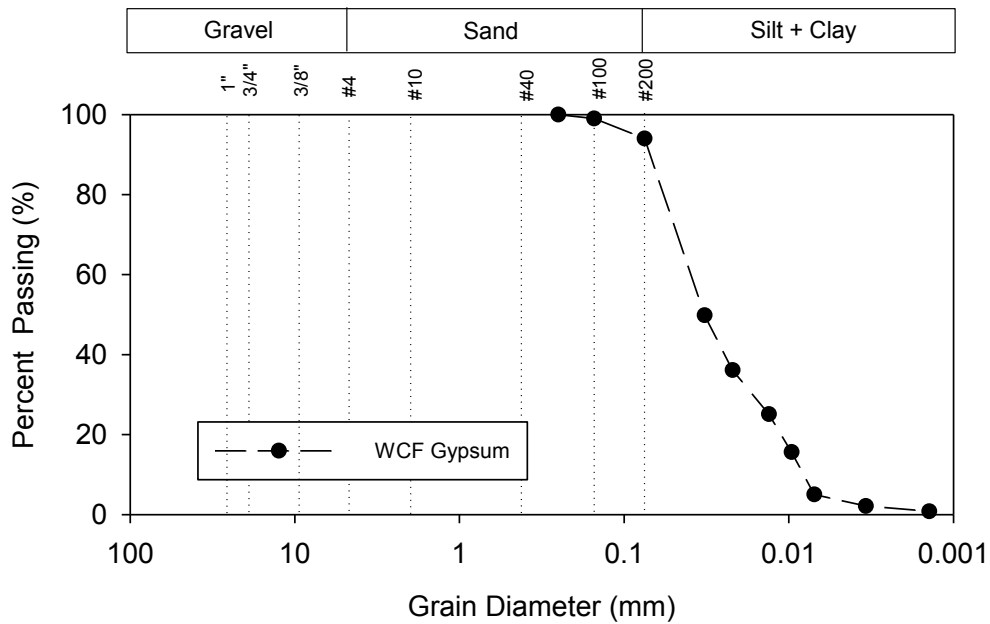


Figure 62. Particle size distribution curve of WCF gypsum

The moisture density relationships, optimum moisture contents, and maximum dry unit weights of WCF Fly Ash were determined by Proctor compaction tests at five energy levels (Figure 63).

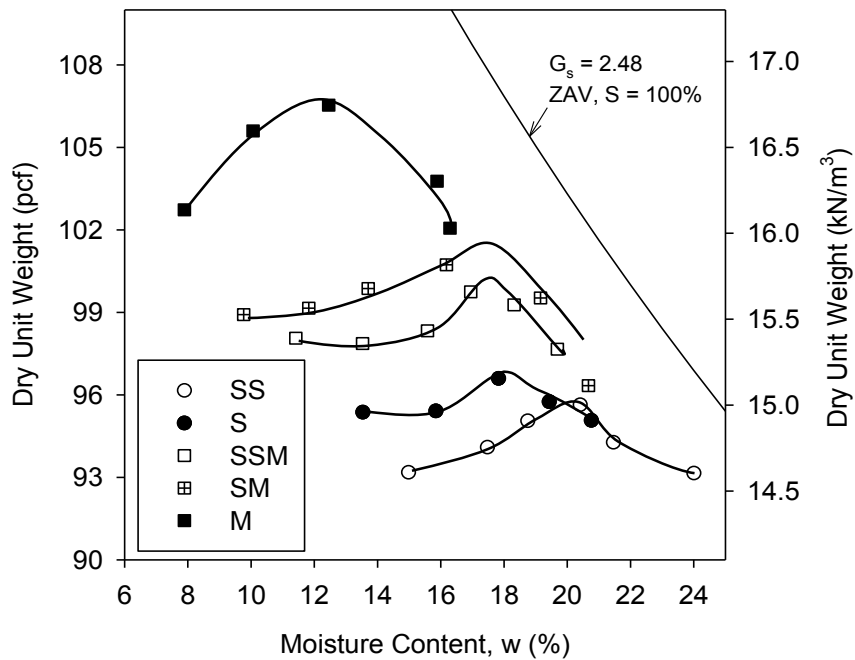


Figure 63. Moisture density relationships of WCF gypsum (moisture contents were measured at 60°C)

Temple Gypsum (CFED 2055)

Temple gypsum was obtained from Cumberland Fossil Plant, Cumberland City, Tennessee in 2012 (Figure 64).



Figure 64. Temple gypsum at 9.4% moisture content

Particle size analysis, specific gravity, and Atterberg limits test were conducted on Temple gypsum to determine material index properties. A summary table of the material index properties is shown in Table 22. The particle size distribution curve is shown in Figure 65.

Table 22. Material index properties of Temple gypsum

Material Index Property	Result	Testing Method
AASHTO classification	A-4(0)	ASTM D3282
USCS classification	ML	ASTM D2487
Liquid limit, LL (%)	NP	ASTM D4318
Plastic limit, PL (%)		
Specific gravity, G_s	2.36	ASTM D854

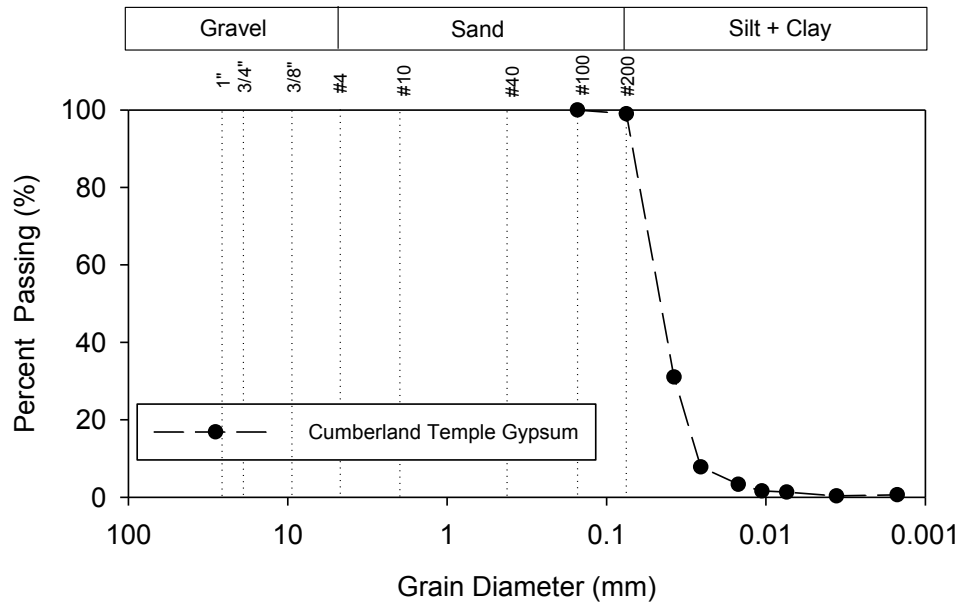


Figure 65. Particle size distribution curve of Temple gypsum

The moisture density relationships, optimum moisture contents, and maximum dry unit weights of Temple gypsum were determined by Proctor compaction tests at two energy levels (Figure 66).

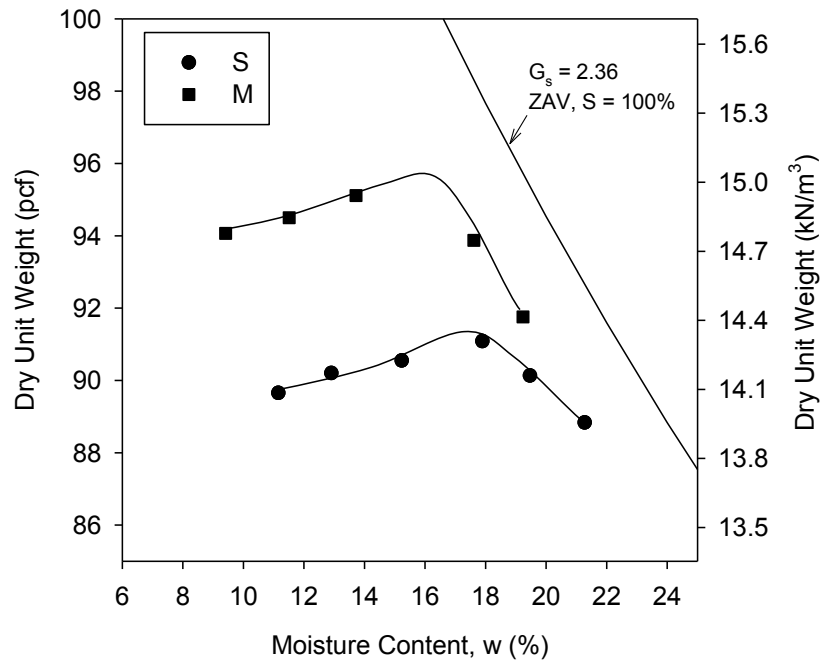


Figure 66. Moisture density relationships of Temple Gypsum (moisture contents were measured at 60°C)

Reject Gypsum (CFED 2056)

Reject gypsum was obtained from Cumberland Fossil Plant, Cumberland City, Tennessee in 2012 (Figure 67).



Figure 67. Reject gypsum at 19.4% moisture content

Particle size analysis, specific gravity, and Atterberg limits test were conducted on Reject gypsum to determine material index properties. A summary table of the material index properties is shown in Table 23. The particle size distribution curve is shown in Figure 68.

Table 23. Material index properties of Reject gypsum

Material Index Property	Result	Testing Method
AASHTO classification	A-4(0)	ASTM D3282
USCS classification	ML	ASTM D2487
Liquid limit, LL (%)	NP	ASTM D4318
Plastic limit, PL (%)		
Specific gravity, G_s	2.40	ASTM D854

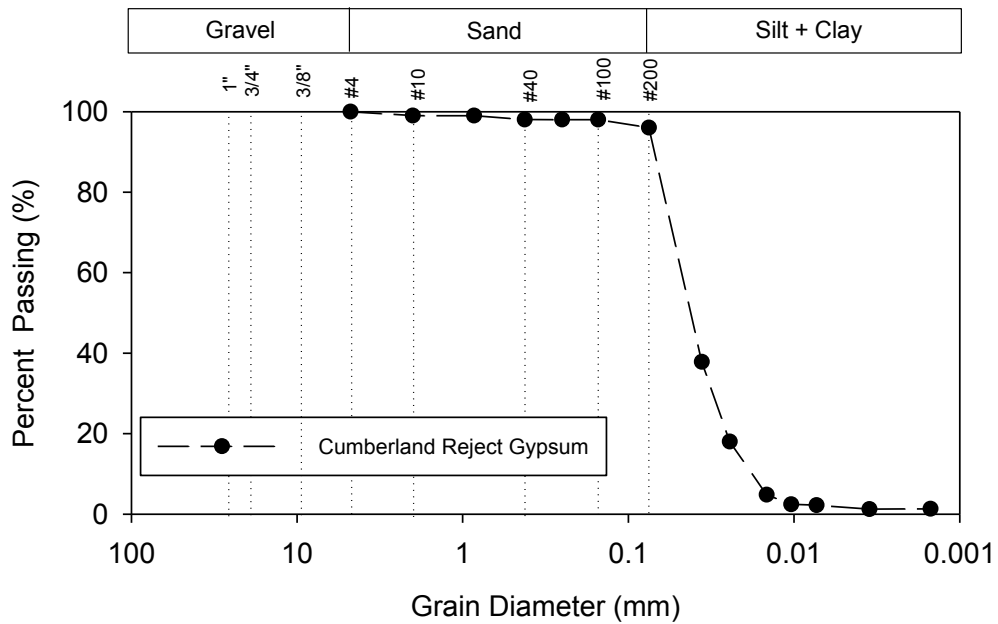


Figure 68. Particle size distribution curve of Reject gypsum

The moisture density relationships, optimum moisture contents, and maximum dry unit weights of Reject gypsum were determined by Proctor compaction tests at two energy levels (Figure 69).

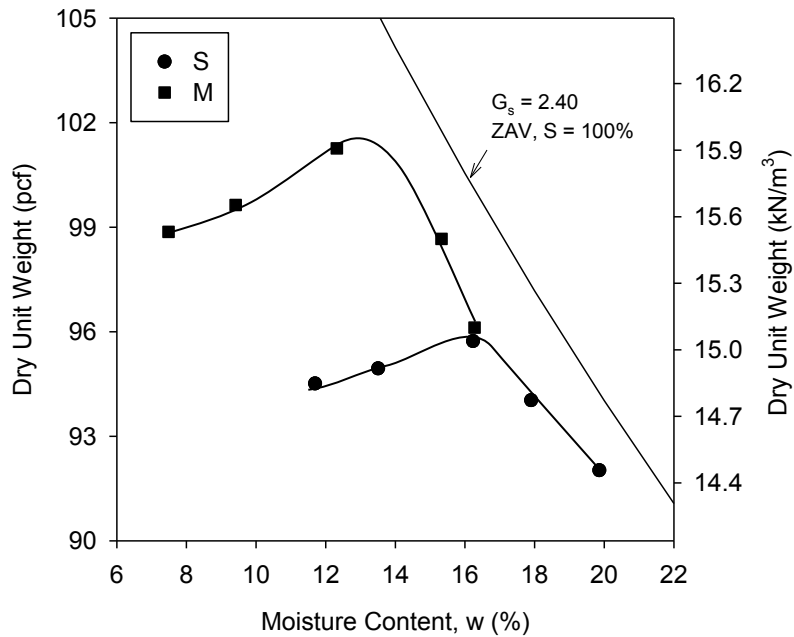


Figure 69. Moisture density relationships of Reject gypsum (moisture contents were measured at 60°C)

Loess Stabilized With 15% Fly Ash (CFED 2057)

Loess was obtained from Western Iowa. The fly ash was classified as class C (ASTM C618) and obtained from Municipal power plant, Ames, Iowa (Figure 70).



Figure 70. Loess with 15% fly ash at 17.0% moisture content

Particle size analysis, specific gravity, and Atterberg limits test were conducted on Loess with 15% fly ash to determine material index properties. A summary table of the material index properties is shown in Table 24. The particle size distribution curve is shown in Figure 71.

Table 24. Material index properties of Loess with 15% fly ash

Material Index Property	Result	Testing Method
AASHTO classification	A-4(2)	ASTM D3282
USCS classification	ML	ASTM D2487
Liquid limit, LL (%)	33	ASTM D4318
Plastic limit, PL (%)	NP	
Specific gravity, G_s	2.68	ASTM D854

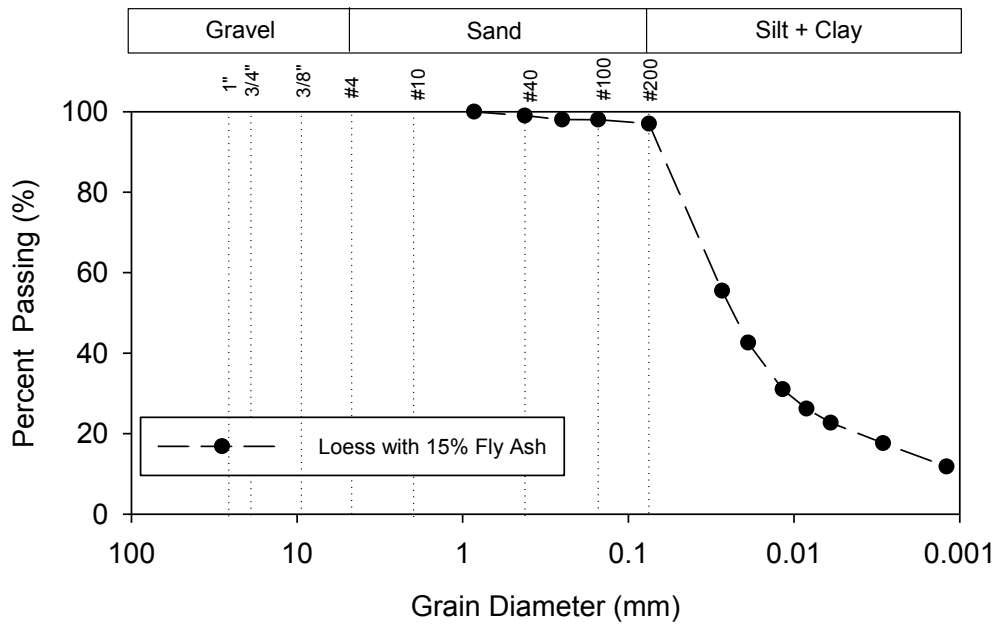


Figure 71. Particle size distribution curve of Loess with 15% fly ash

The moisture density relationships, optimum moisture contents, and maximum dry unit weights of Loess with 15% fly ash were determined by Proctor compaction tests at five energy levels (Figure 72). The delay time between mixing and compaction was about five minutes.

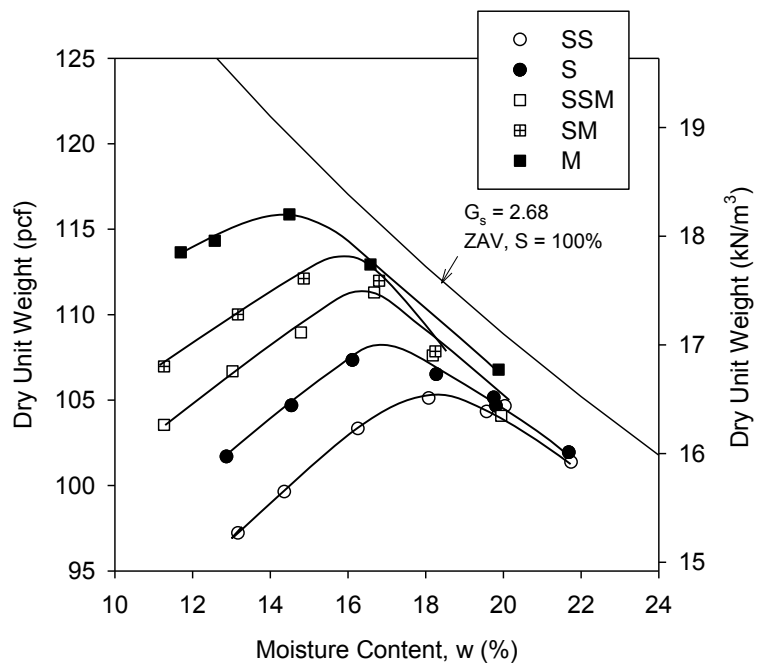


Figure 72. Moisture density relationships of Loess with 15% fly ash

Loess Stabilized With 9% Type I Cement (CFED 2058)

Loess was obtained from Western Iowa and the cement is type I cement specified in ASTM C150 for standard use (Figure 73).



Figure 73. Loess with 9% type I cement at 12.6% moisture content

Particle size analysis, specific gravity, and Atterberg limits test were conducted on Loess with 9% type I cement to determine material index properties. A summary table of the material index properties is shown in Table 25. The particle size distribution curve is shown in Figure 74.

Table 25. Material index properties of Loess with 9% type I cement

Material Index Property	Result	Testing Method
AASHTO classification	A-4(0)	ASTM D3282
USCS classification	ML	ASTM D2487
Liquid limit, LL (%)	NP	ASTM D4318
Plastic limit, PL (%)		
Specific gravity, G_s	2.74	ASTM D854

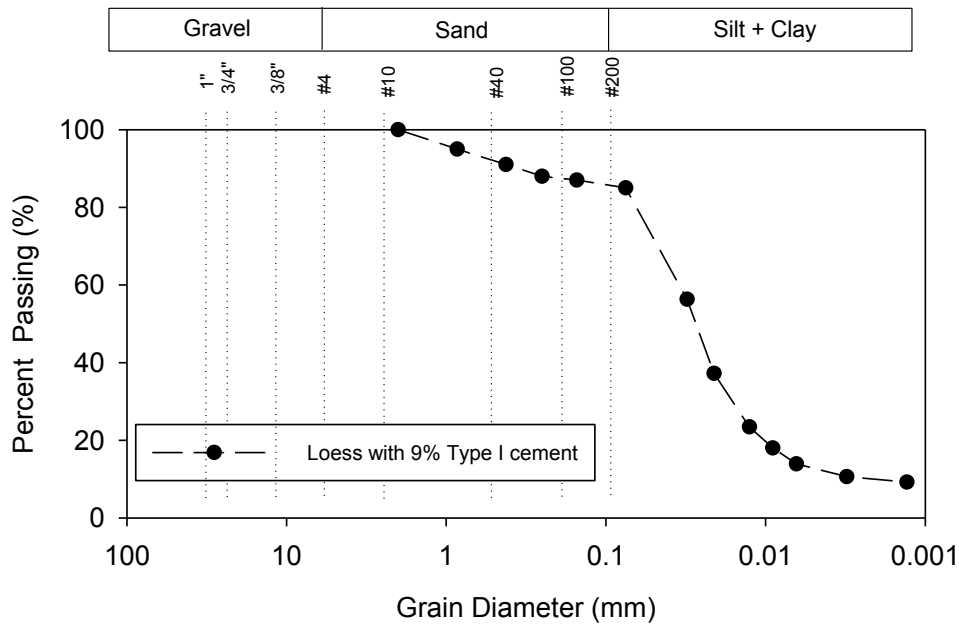


Figure 74. Particle size distribution curve of Loess with 9% type I cement

The moisture density relationships, optimum moisture contents, and maximum dry unit weights of Loess with 9% type I cement were determined by Proctor compaction tests at five energy levels (Figure 75). The delay time between mixing and compaction was five minutes to prevent reduction of durability and compressive strength (Winterkorn and Pamukcu 1991).

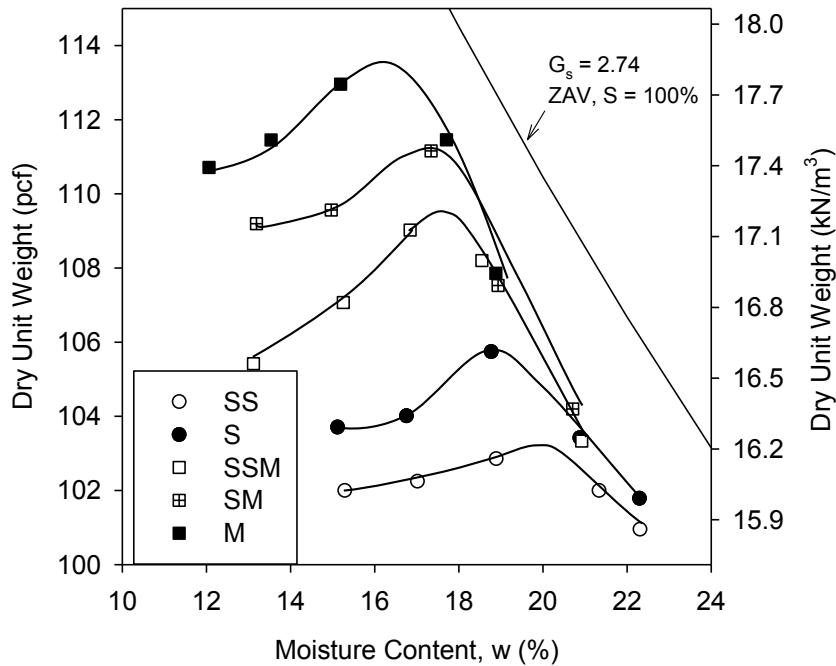


Figure 75. Moisture density relationships of Loess with 9% type I cement

Florida Highway 9B Embankment Fill (CFED 2059)

Florida highway 9B fill was obtained from, Jacksonville, Florida in 2011 (Figure 76).



Figure 76. Florida highway 9B embankment fill at 7.1% moisture content

Particle size analysis, specific gravity, and Atterberg limits test were conducted on Florida highway 9B embankment fill to determine material index properties. A summary table of the material index properties is shown in Table 26. The particle size distribution curve is shown in Figure 77.

Table 26. Material index properties of Florida highway 9B embankment fill

Material Index Property	Result	Testing Method
AASHTO classification	A-3	ASTM D3282
USCS classification	SP	ASTM D2487
Liquid limit, LL (%)	NP	ASTM D4318
Plastic limit, PL (%)		
Specific gravity, G_s	2.63	ASTM D854

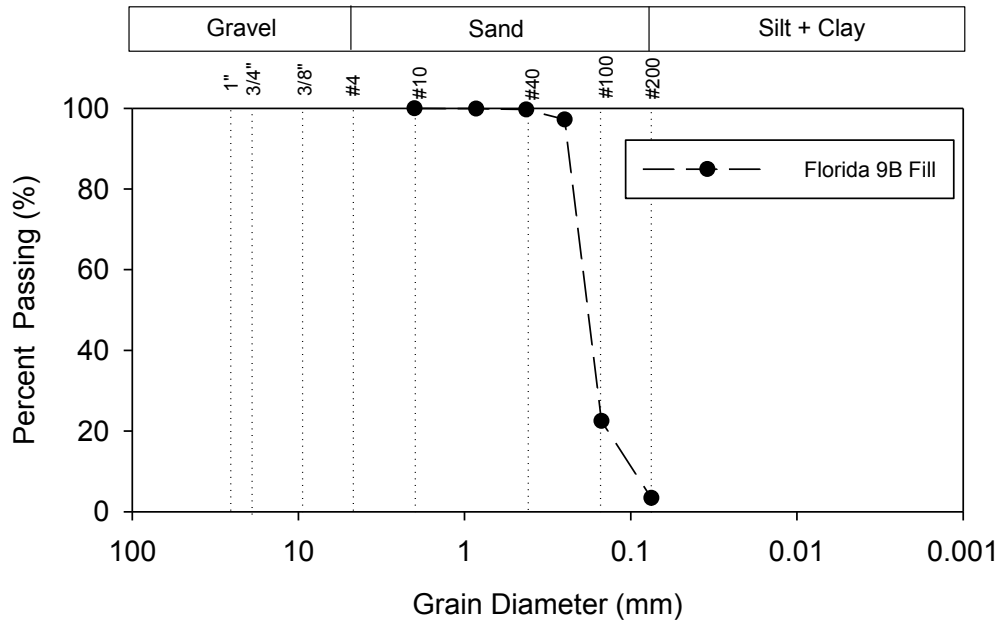


Figure 77. Particle size distribution curve of Florida highway 9B embankment fill

The moisture density relationships, optimum moisture contents, and maximum dry unit weights of Florida highway 9B embankment fill were determined by Proctor compaction tests at five energy levels (Figure 78). The bulking phenomenon was observed for this geomaterial and a line of bulking moisture content is shown in Figure 78.

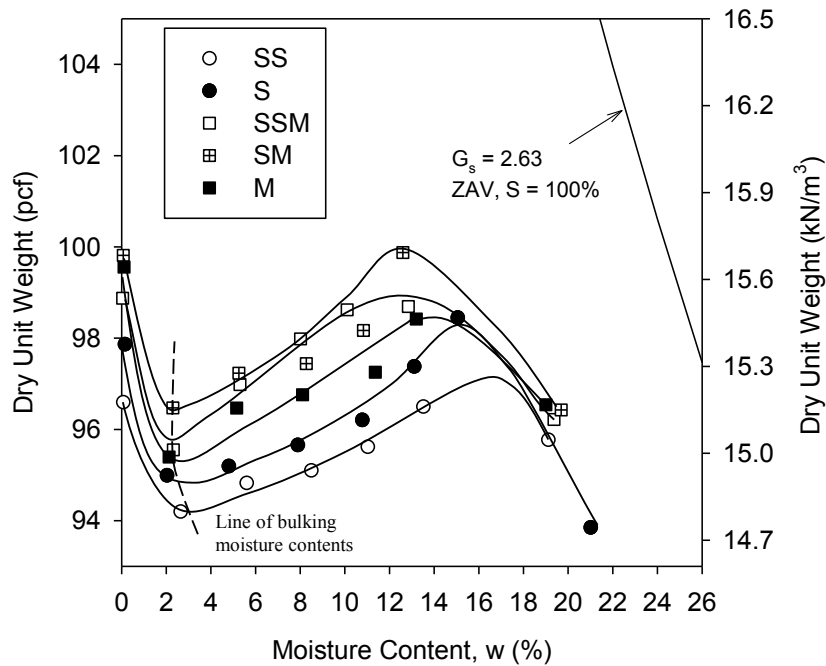


Figure 78. Moisture density relationships of Florida 9B embankment fill

Summary of Proctor Compaction Tests Results

Table 27 summarizes the maximum dry unit weight and optimum moisture content at each compaction energy level of the 11 geomaterials that were determined by Proctor test. Raw Proctor data for all geomaterials are provided in Appendix A.

The results from Proctor compaction at different energy levels for CFED 1634 to 2058 showed that with higher Proctor compaction energy the soils achieve higher maximum dry unit weight and lower optimum moisture content. For CFED 2059, there was a reduction in the maximum dry unit weight with increase in Proctor compaction energy from sub-modified (SM) to modified (M) energy level. It may be caused by the disturbance (or de-compaction) in the four inches Proctor mold due to over compaction. The curves on the wet side of optimum moisture content of the nine geomaterials tend to parallel the zero air void (ZAV) line (or 100% saturation line). The points of optimum moisture content of each energy level also tend to parallel the ZAV line. These relationships are common for non-granular geomaterials and some granular geomaterials from Proctor compaction tests.

Table 27. Summary of Proctor compaction test results of CFED 1634 to 2059

Material	CFED Soil ID	Energy Level	Compaction Energy (lb-ft/ft ³)	Maximum dry unit weight (lb/ft ³)	Optimum moisture content (%)
Western Iowa Loess	1634	SS	7425	94.5	19.0
		S	12375	101.1	18.6
		SSM	20790	104.7	17.5
		SM	34650	106.3	17.2
		M	56250	111.3	15.7
Texas Fat Clay	2043	SS	7425	86.0	27.0
		S	12375	93.4	23.8
		SSM	20790	97.0	22.8
		SM	34650	101.0	21.4
		M	56250	108.5	17.6
2011 Manatt's RAP	2051	SS	7425	116.9	10.7
		S	12375	119.5	9.8
		SSM	20790	121.8	9.5
		SM	34650	122.9	9.1
		M	56250	124.9	8.5
CA-6-G	2052	SS	7425	138.2	8.9
		S	12375	140.5	8.4
		SSM	20790	141.2	7.4
		SM	34650	142.3	7.0
		M	56250	143.6	6.7
WCF fly ash	2053	SS	7425	78.3	26.7
		S	12375	78.9	25.8
		SSM	20790	81.6	23.2
		SM	34650	82.6	23.0
		M	56250	84.4	20.8
WCF gypsum	2054	SS	7425	95.8	20.2
		S	12375	96.9	18.0
		SSM	20790	100.3	17.6
		SM	34650	101.6	17.4
		M	56250	106.8	12.2
Temple gypsum	2055	S	12375	91.3	17.4
		M	56250	95.8	15.9
Reject gypsum	2056	S	12375	95.9	16.3
		M	56250	101.6	13.0
Loess with 15% fly ash	2057	SS	7425	105.4	18.3
		S	12375	108.3	16.9
		SSM	20790	111.4	16.3
		SM	34650	113.4	15.9
		M	56250	115.7	14.4
Loess with 9% type I cement	2058	SS	7425	103.3	20.0
		S	12375	105.8	18.9
		SSM	20790	109.5	17.6
		SM	34650	111.2	17.3
		M	56250	113.6	16.2
Florida 9B embankment fill	2059	SS	7425	97.2	16.7
		S	12375	98.3	15.2
		SSM	20790	98.6	13.8
		SM	34650	98.9	12.7
		M	56250	100.0	12.4

2012 Manatt's RAP (CFED 2061)

2012 Manatt's recycled asphalt pavement (RAP) was obtained from Manatt's Company Ames, Iowa in 2012 (Figure 79).



Figure 79. 2012 RAP at 4.8% moisture content

Particle size analysis, specific gravity, and Atterberg limits test were conducted on 2012 Manatt's RAP to determine material index properties. A summary table of the material index properties is shown in Table 28. The particle size distribution curve is shown in Figure 80.

Table 28. Material index properties of 2012 Manatt's RAP

Material Index Property	Result	Testing Method
AASHTO classification	A-1-a	ASTM D3282
USCS classification	GW	ASTM D2487
Liquid limit, LL (%)	NP	ASTM D4318
Plastic limit, PL (%)		
Specific gravity, G_s	2.47	ASTM C127 & D854

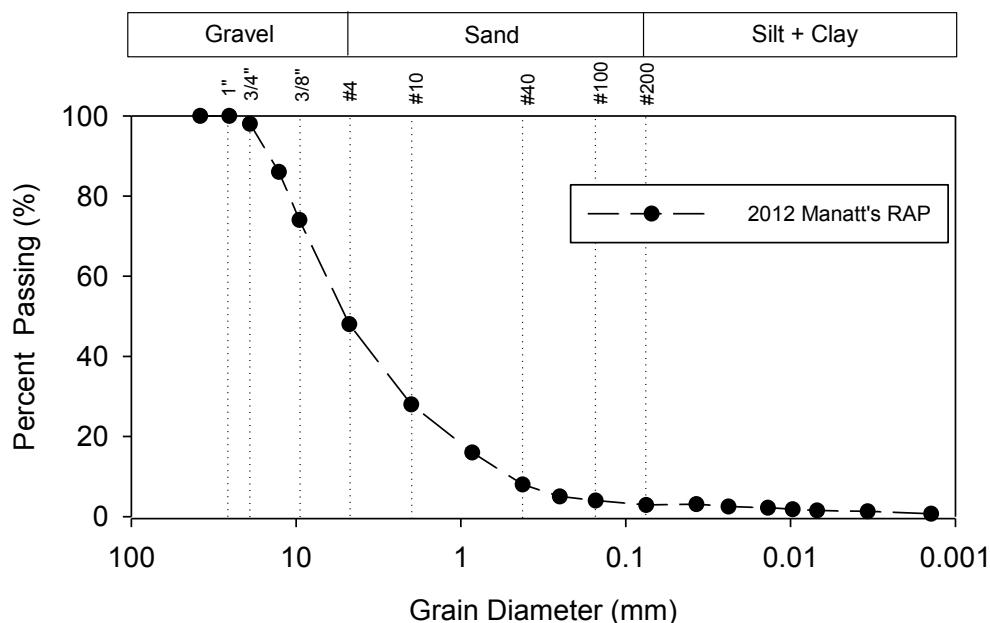


Figure 80. Particle size distribution curve of 2012 Manatt's RAP

The minimum and maximum index density and void ratio of the oven dried 2012 Manatt's RAP were determined by vibratory compaction tests (Table 29). The dry unit weights versus vibration compaction time and compaction energy for 2012 Manatt's RAP are shown in Figure 81 and Figure 82.

Table 29. Minimum and maximum index densities and void ratios of oven dried 2012 Manatt's RAP

Compaction Parameters	Results	Methods
Dry unit weight by standard Proctor, STD γ_d	100.0 pcf	ASTM D698
Dry unit weight by modified Proctor, MOD γ_d	108.8 pcf	ASTM D1557
Minimum index density, ρ_{dmin}	82.7 pcf	ASTM D4254
Maximum index density, ρ_{dmax}	95.4 pcf	ASTM D4253
Minimum index void ratio, e_{min}	0.62	ASTM D4253
Maximum index void ratio, e_{max}	0.86	ASTM D4254

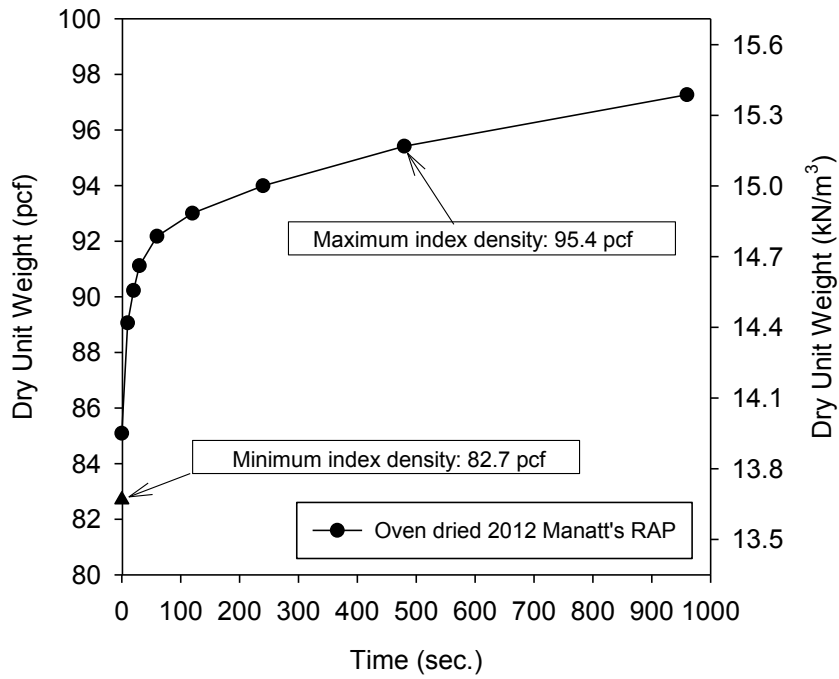


Figure 81. Dry unit weight versus compaction time of 2012 Manatt's RAP

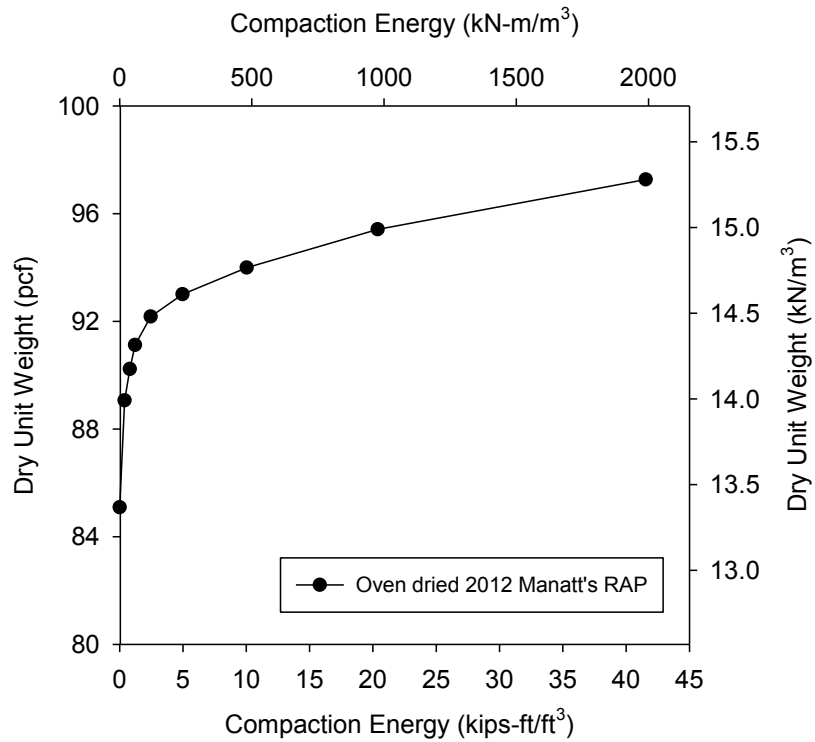


Figure 82. Dry unit weight versus compaction energy of 2012 Manatt's RAP

RPCC and RAP Mixture (CFED 2062)

Recycled Portland cement concrete (RPCC) and recycle asphalt pavement (RAP) mixture was obtained from Manatt's Company Ames, Iowa in 2012 (Figure 83).



Figure 83. RPCC and RAP mixture (110°C oven-dried)

Particle size analysis, specific gravity, and Atterberg limits test were conducted on RPCC and RAP mixture to determine material index properties. A summary table of the material index properties is shown in Table 30. The particle size distribution curve is shown in Figure 84.

Table 30. Material index properties of RPCC and RAP mixture

Material Index Property	Result	Testing Method
AASHTO classification	A-1-a	ASTM D3282
USCS classification	GW	ASTM D2487
Liquid limit, LL (%)	NP	ASTM D4318
Plastic limit, PL (%)		
Specific gravity, G_s	2.1	ASTM C127 & D854

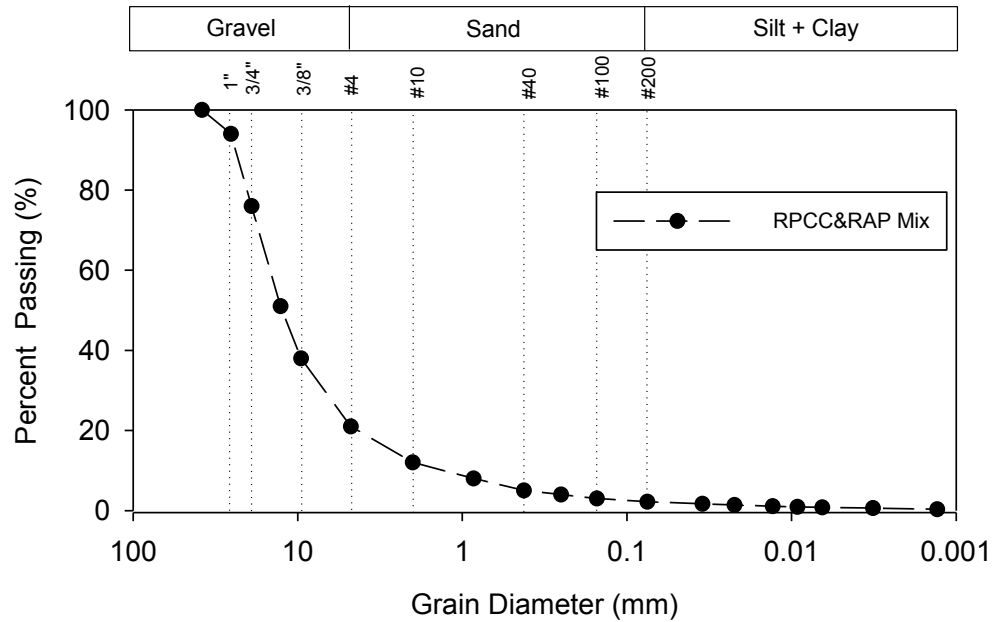


Figure 84. Particle size distribution curve of RPCC and RAP mixture

The minimum and maximum index density and void ratio of the oven dried RPCC and RAP mixture were determined by vibratory compaction tests (Table 31). The dry unit weights versus vibration compaction time and compaction energy for RPCC and RAP mixture are shown in Figure 85 and Figure 86.

Table 31. Minimum and maximum index densities and void ratios of oven dried RPCC and RAP mixture

Compaction Parameters	Results	Methods
Dry unit weight by standard Proctor, STD γ_d	99.2 pcf	ASTM D698
Dry unit weight by modified Proctor, MOD γ_d	111.6 pcf	ASTM D1557
Minimum index density, ρ_{dmin}	87.3 pcf	ASTM D4254
Maximum index density, ρ_{dmax}	102.1 pcf	ASTM D4253
Minimum index void ratio, e_{min}	0.28	ASTM D4253
Maximum index void ratio, e_{max}	0.50	ASTM D4254

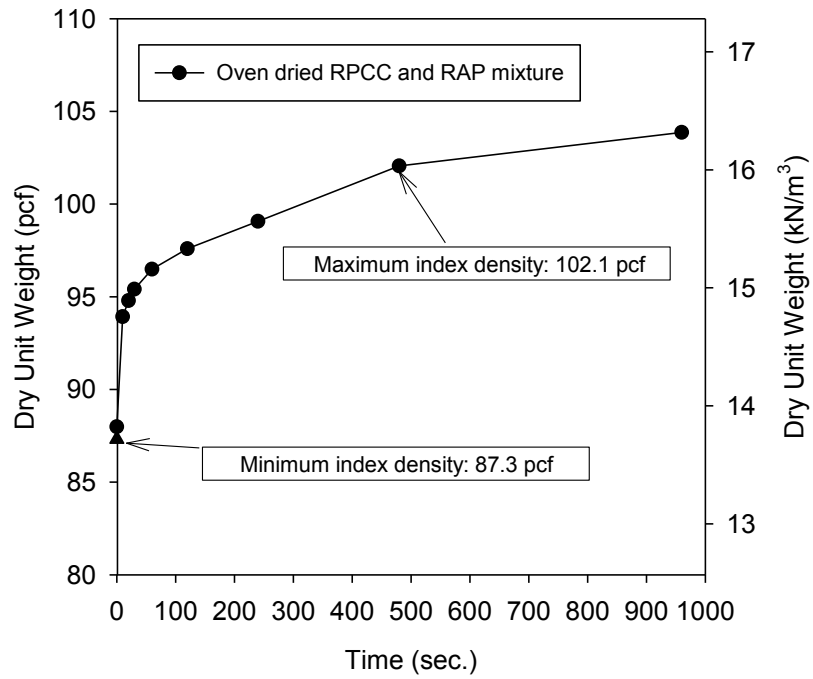


Figure 85. Dry unit weight versus compaction time of RPCC and RAP mixture

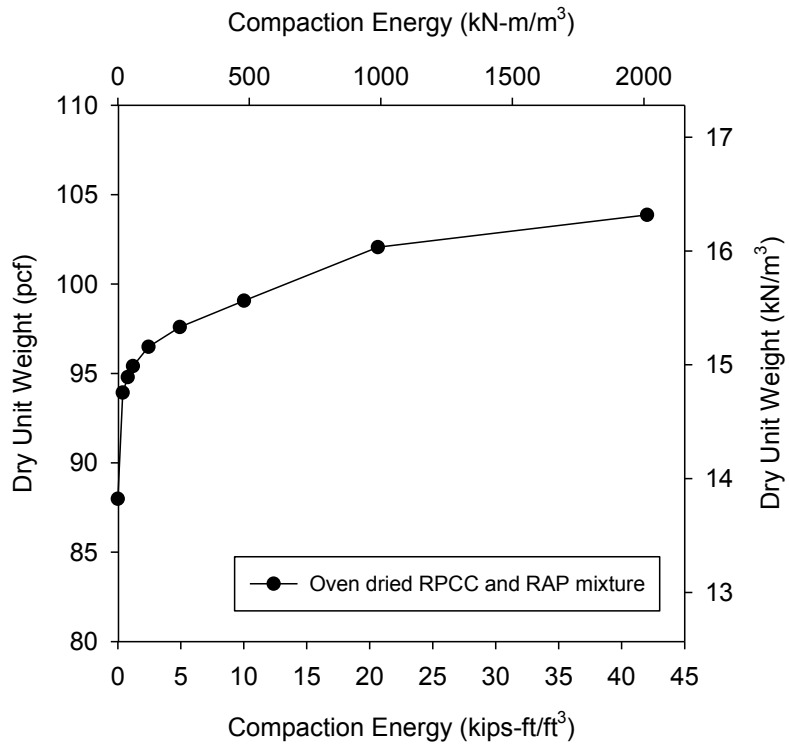


Figure 86. Dry unit weight versus compaction energy of RPCC and RAP mixture

Crushed Limestone (CFED 2063)

Crushed limestone was obtained from Martin Marietta, Ames, Iowa in 2012 (Figure 87).

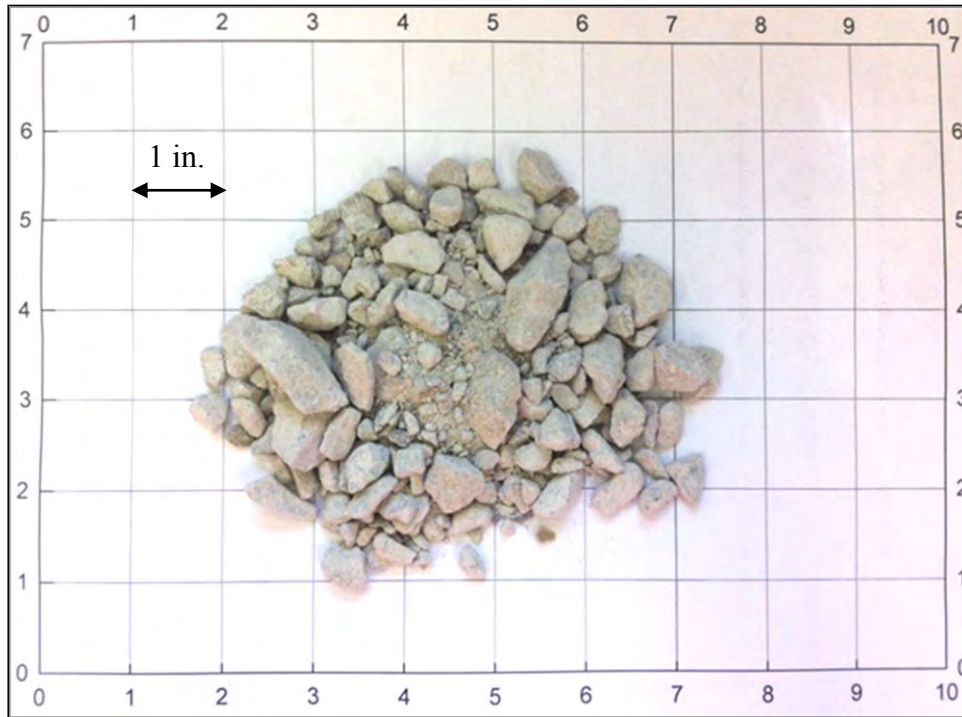


Figure 87. Crushed limestone (110°C oven-dried)

Particle size analysis and specific gravity, and Atterberg limits test were conducted on crushed limestone to determine material index properties. A summary table of the material index properties is shown in Table 32. The particle size distribution curve is shown in Figure 88.

Table 32. Material index properties of crushed limestone

Material Index Property	Result	Testing Method
AASHTO classification	A-1-a	ASTM D3282
USCS classification	GP-GM	ASTM D2487
Liquid limit, LL (%)	NP	ASTM D4318
Plastic limit, PL (%)		
Specific gravity, G_s	2.71	ASTM C127 & D854

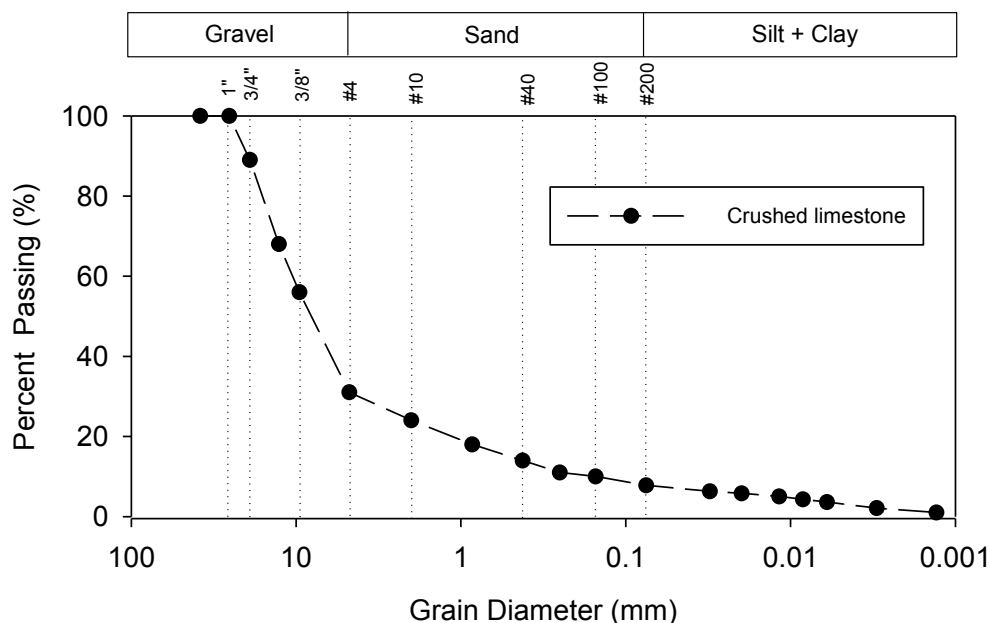


Figure 88. Particle size distribution curve of crushed limestone

The minimum and maximum index density and void ratio of the oven dried crushed limestone were determined by vibratory compaction test (Table 33). The dry unit weights versus vibration compaction time and compaction energy for crushed limestone are shown in Figure 85 and Figure 86.

Table 33. Minimum and maximum index densities and void ratios of oven dried crushed limestone

Compaction Parameters	Results	Methods
Dry unit weight by standard Proctor, STD γ_d	133.2 pcf	ASTM D698
Dry unit weight by modified Proctor, MOD γ_d	140.5 pcf	ASTM D1557
Minimum index density, ρ_{dmin}	99.8 pcf	ASTM D4254
Maximum index density, ρ_{dmax}	116.4 pcf	ASTM D4253
Minimum index void ratio, e_{min}	0.28	ASTM D4253
Maximum index void ratio, e_{max}	0.45	ASTM D4254

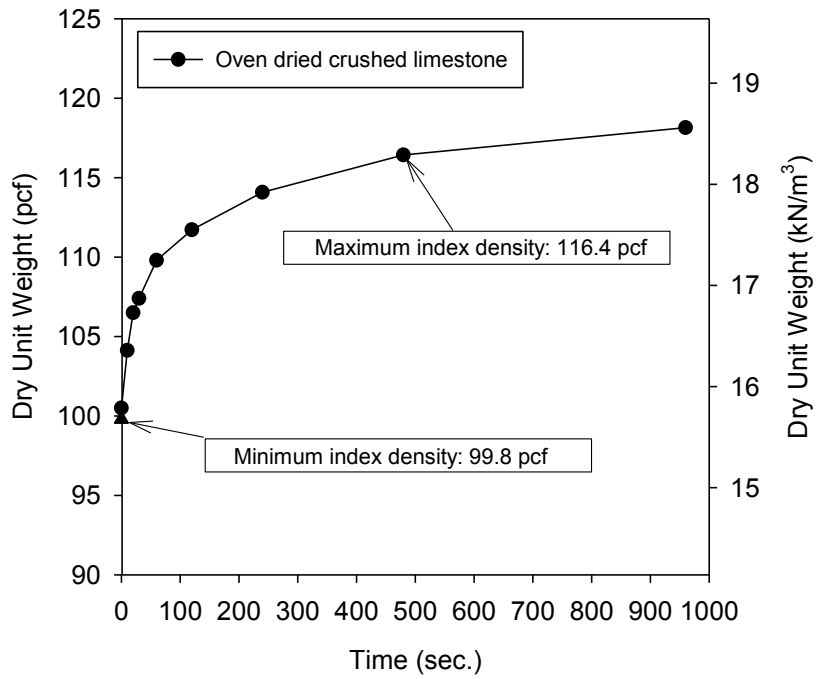


Figure 89. Dry unit weight versus compaction time of crushed limestone

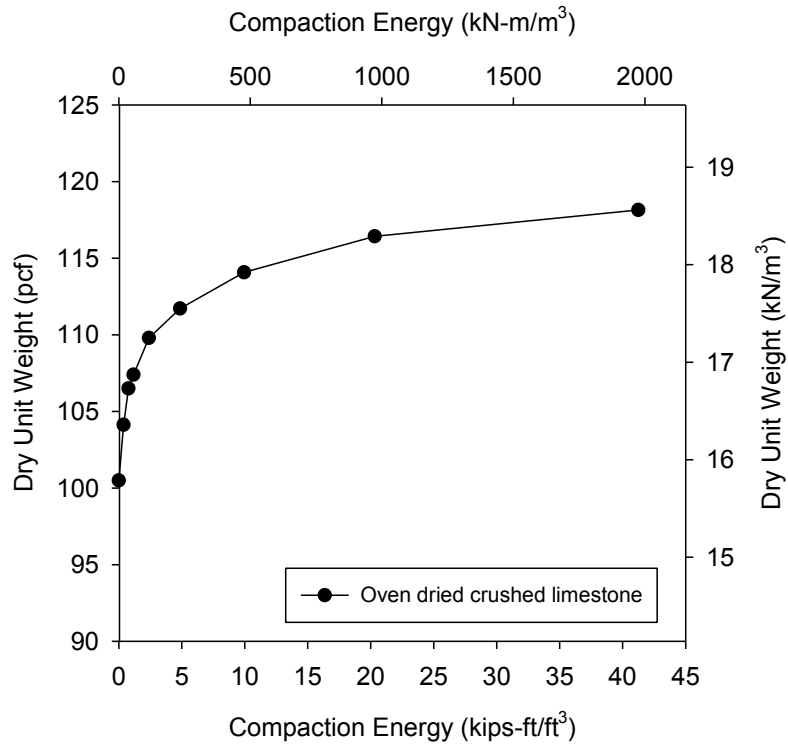


Figure 90. Dry unit weight versus compaction energy of crushed limestone

Ottawa sand (ASTM 20-30 sand)

Ottawa sand (ASTM 20-30 sand) was obtained from Ottawa, Illinois (Figure 87).



Figure 91. Ottawa sand

Particle size analysis and specific gravity test were conducted on Ottawa sand to determine material index properties. A summary table of the material index properties is shown in Table 34. The particle size distribution curve is shown in Figure 92.

Table 34. Material index properties of Ottawa sand

Material Index Property	Result	Testing Method
AASHTO classification	A-1-b	ASTM D3282
USCS classification	SP	ASTM D2487
Liquid limit, LL (%)	NP	ASTM D4318
Plastic limit, PL (%)		
Specific gravity, G_s	2.65	ASTM C127 & D854

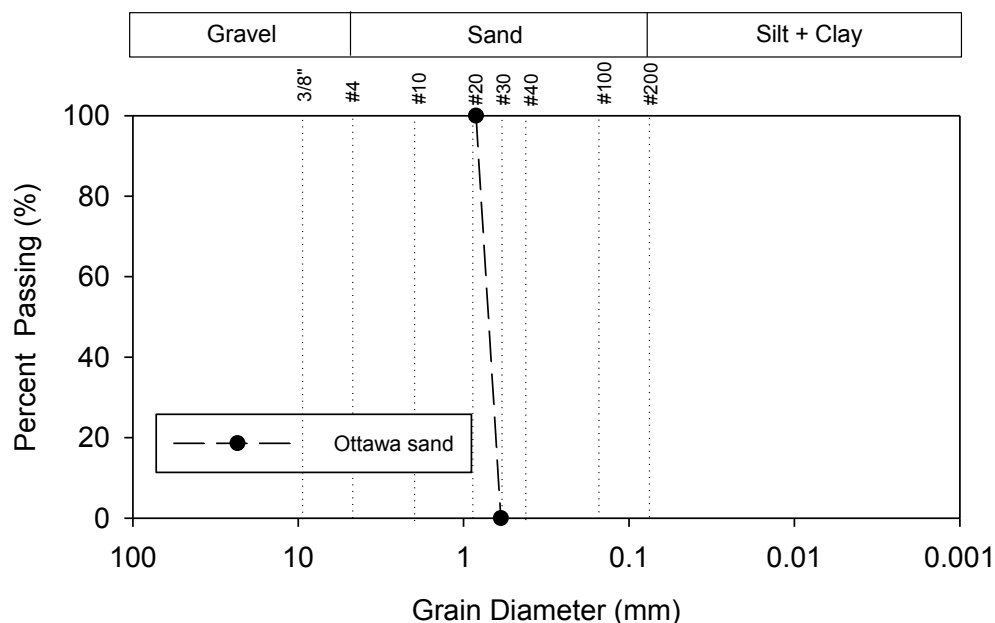


Figure 92. Particle size distribution curve of Ottawa sand

The minimum and maximum index density and void ratio of the oven dried Ottawa sand were determined by vibratory compaction test (Table 35). The dry unit weights versus vibration compaction time and compaction energy for crushed limestone are shown in Figure 93 and Figure 94.

Table 35. Minimum and maximum index densities and void ratios of the Ottawa sand

Compaction Parameters	Results	Methods
Minimum index density, ρ_{dmin}	97.5 pcf	ASTM D4254
Maximum index density, ρ_{dmax}	110.3 pcf	ASTM D4253
Minimum index void ratio, e_{min}	0.50	ASTM D4253
Maximum index void ratio, e_{max}	0.70	ASTM D4254

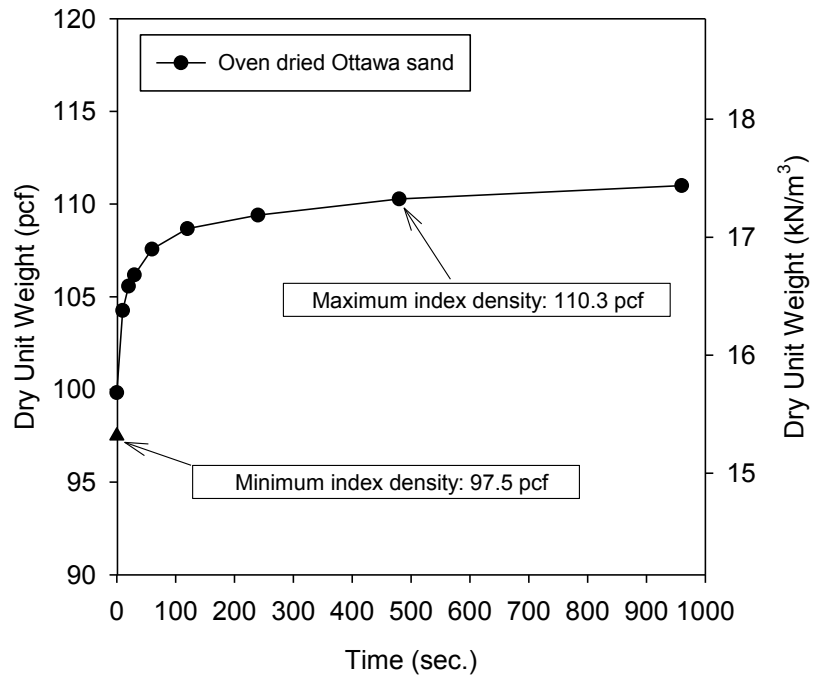


Figure 93. Dry unit weight versus compaction time of Ottawa sand

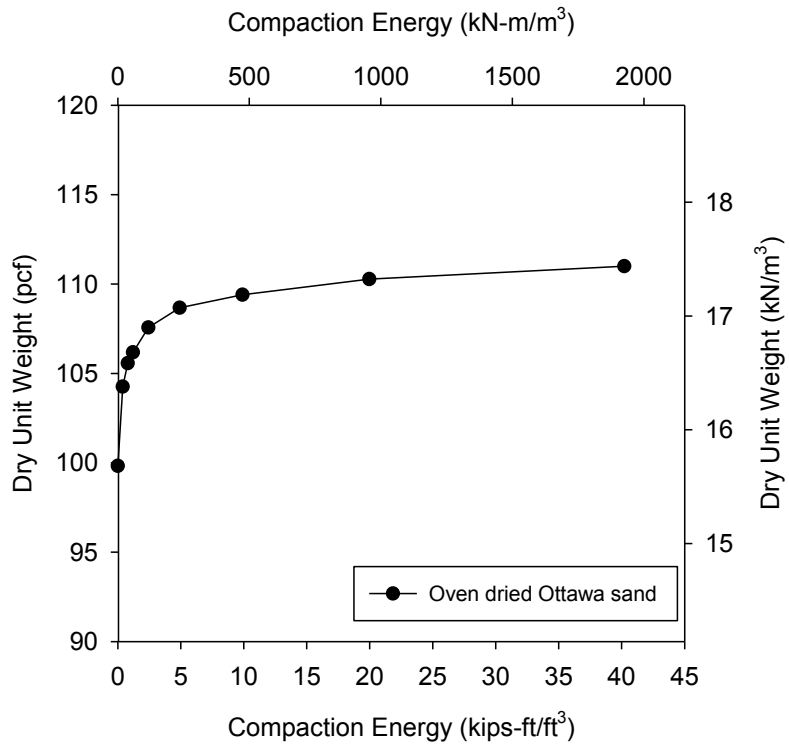


Figure 94. Dry unit weight versus compaction energy of Ottawa sand

CHAPTER 5. RESULTS AND DISCUSSION

Laboratory test data for soil index properties and compaction behaviors of 13 geomaterials were incorporated into the Caterpillar Inc. Compaction Forecasting Expert Database (CFED) to expand the database in this study. To improve the usefulness of CFED, two innovative laboratory test devices, Iowa K test and gyratory compaction test assembled with a pressure distribution analyzer (PDA), were evaluated. These devices can link shear strength and stiffness parameters with moisture-density-compaction energy relationships of compacted geomaterials.

This chapter consists of three parts: expanding CFED with lab testing data of 13 additional geomaterials, improving CFED using the Iowa K test to evaluate strength and stiffness parameters of compacted geomaterials, and improving CFED using the gyratory compaction test to determine the compaction behavior and shear strength of geomaterials.

Expanding CFED with Laboratory Test Data of 13 Geomaterials

Soil index properties data including particle-size analysis results, USCS and AASHTO soil classifications, Atterberg limits, and specific gravity values of the 13 geomaterials were tested and incorporated into CFED. Table 14 in Chapter 4 of this thesis summarizes the data. Proctor and vibratory compaction tests were conducted to determine the compaction behavior of the geomaterials. The laboratory test results are presented here in two sections, Proctor and vibratory compaction test results.

Proctor test results

Proctor tests with different compaction energy levels and moisture contents were conducted on nine geomaterials. The Cumberland Temple and reject gypsum (soils 2055 and 2056) materials only have standard and modified Proctor data, while the other seven geomaterials have Proctor compaction data for five energy levels. The Proctor compaction curves that show moisture-density relationships, optimum moisture content, and maximum dry unit weight of each compaction energy level of the nine geomaterials were determined and are shown in Figure 95. The results from Proctor compaction at different energy levels for CFED 2051 to 2058 showed that with higher Proctor compaction energy the soils achieve higher maximum dry unit weight and lower optimum moisture content. For CFED 2059,

there was a reduction in the maximum dry unit weight with increase in Proctor compaction energy from SM to M energy level. The reason for this decrease is disturbance (or de-compaction) caused to the material in the Proctor mold due to over compaction.

For CFED 2051 to 2059, the curves on the wet side of optimum moisture content tend to parallel the zero air void (ZAV) line (i.e., 100% saturation line). The points of optimum moisture content of each energy level also tend to parallel the ZAV line. These relationships are common for non-granular soils and some granular soils from Proctor tests. For granular soils CFED 2052 and 2059, the Proctor curves showed the lowest dry unit weight at its bulking moisture content and are identified with lines of bulking moisture content. All the Proctor test raw data is provided in Appendix A.

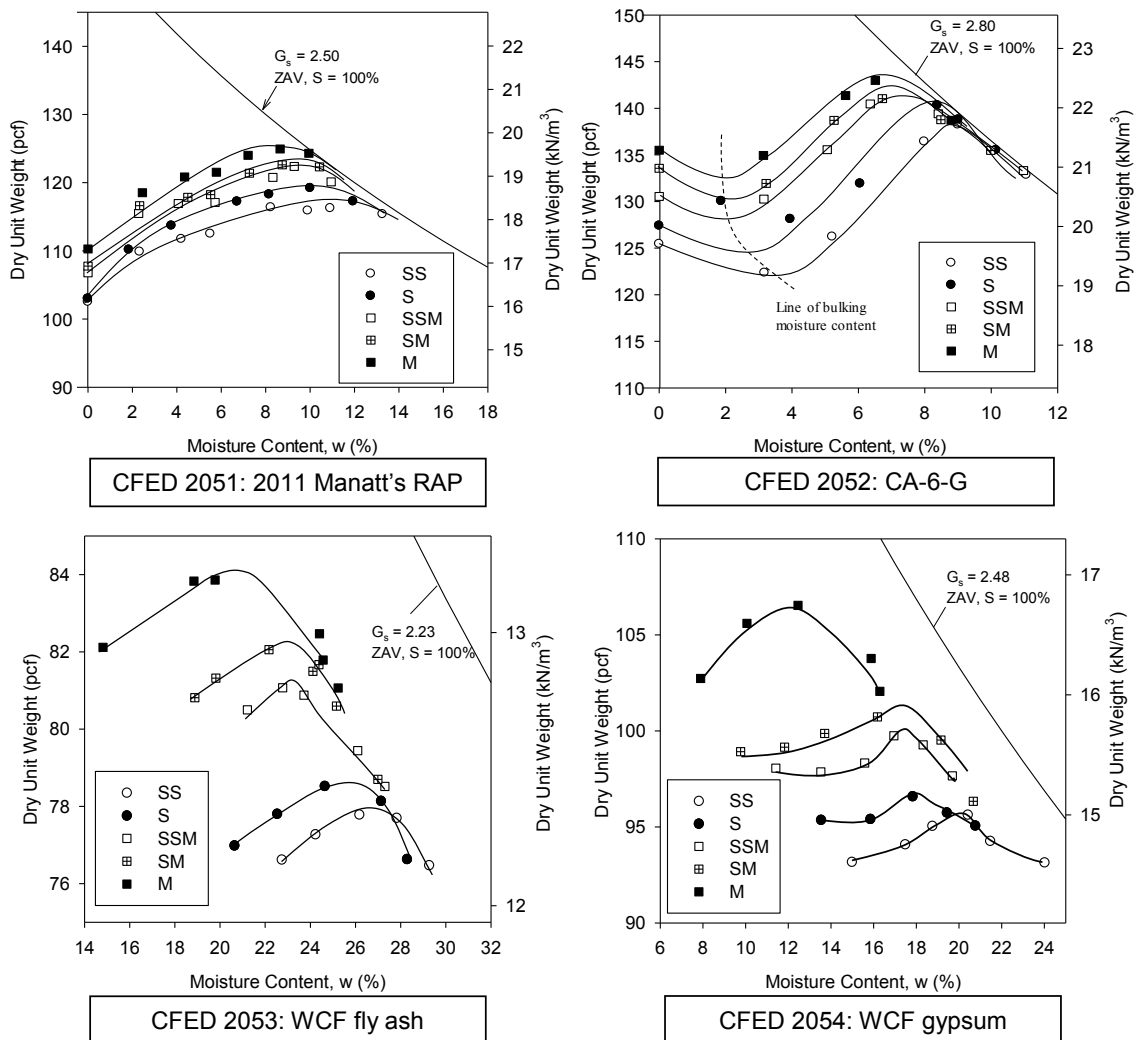


Figure 95. Proctor compaction test results of the additional 9 geomaterials for CFED

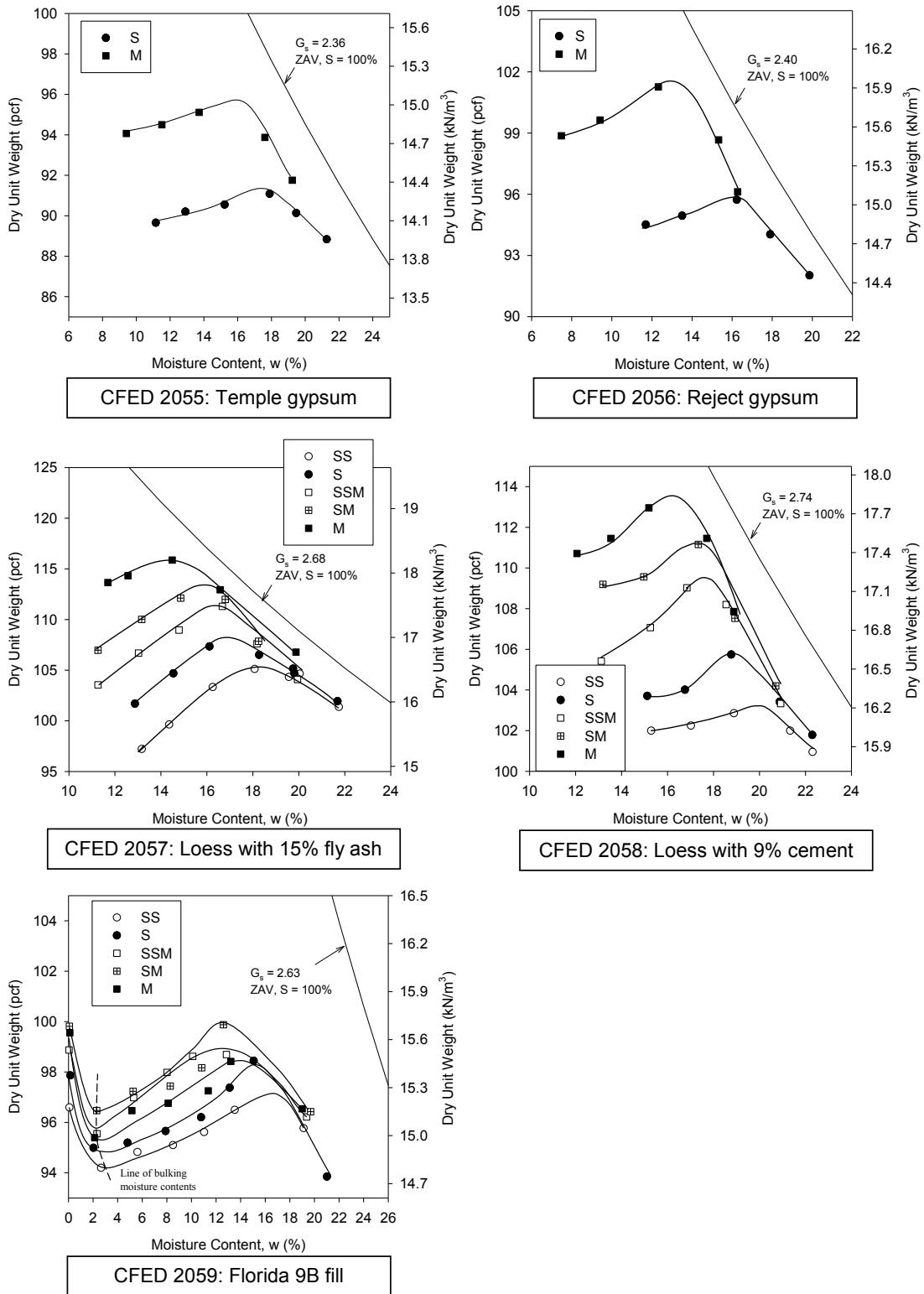


Figure 95 (continued). Proctor compaction test results of the additional 9 geomaterials for CFED

Table 36 summarizes the maximum dry unit weights and optimum moisture contents at each compaction energy level of the nine geomaterials. The CFED outputs for the nine geomaterials are shown in Figure 96 through Figure 104.

Table 36. Summary of Proctor compaction test results of CFED 1634 to 2059

Material	CFED Soil ID	Energy Level	Compaction Energy (lb-ft/ft ³)	Maximum dry unit weight (lb/ft ³)	Optimum moisture content (%)
2011 Manatt's RAP	2051	SS	7425	116.9	10.7
		S	12375	119.5	9.8
		SSM	20790	121.8	9.5
		SM	34650	122.9	9.1
		M	56250	124.9	8.5
CA-6-G	2052	SS	7425	138.2	8.9
		S	12375	140.5	8.4
		SSM	20790	141.2	7.4
		SM	34650	142.3	7.0
		M	56250	143.6	6.7
WCF fly ash	2053	SS	7425	78.3	26.7
		S	12375	78.9	25.8
		SSM	20790	81.6	23.2
		SM	34650	82.6	23.0
		M	56250	84.4	20.8
WCF gypsum	2054	SS	7425	95.8	20.2
		S	12375	96.9	18.0
		SSM	20790	100.3	17.6
		SM	34650	101.6	17.4
		M	56250	106.8	12.2
Temple gypsum	2055	S	12375	91.3	17.4
		M	56250	95.8	15.9
Reject gypsum	2056	S	12375	95.9	16.3
		M	56250	101.6	13.0
Loess with 15% fly ash	2057	SS	7425	105.4	18.3
		S	12375	108.3	16.9
		SSM	20790	111.4	16.3
		SM	34650	113.4	15.9
		M	56250	115.7	14.4
Loess with 9% type I cement	2058	SS	7425	103.3	20.0
		S	12375	105.8	18.9
		SSM	20790	109.5	17.6
		SM	34650	111.2	17.3
		M	56250	113.6	16.2
Florida 9B embankment fill	2059	SS	7425	97.2	16.7
		S	12375	98.3	15.2
		SSM	20790	98.6	13.8
		SM	34650	98.9	12.7
		M	56250	100.0	12.4

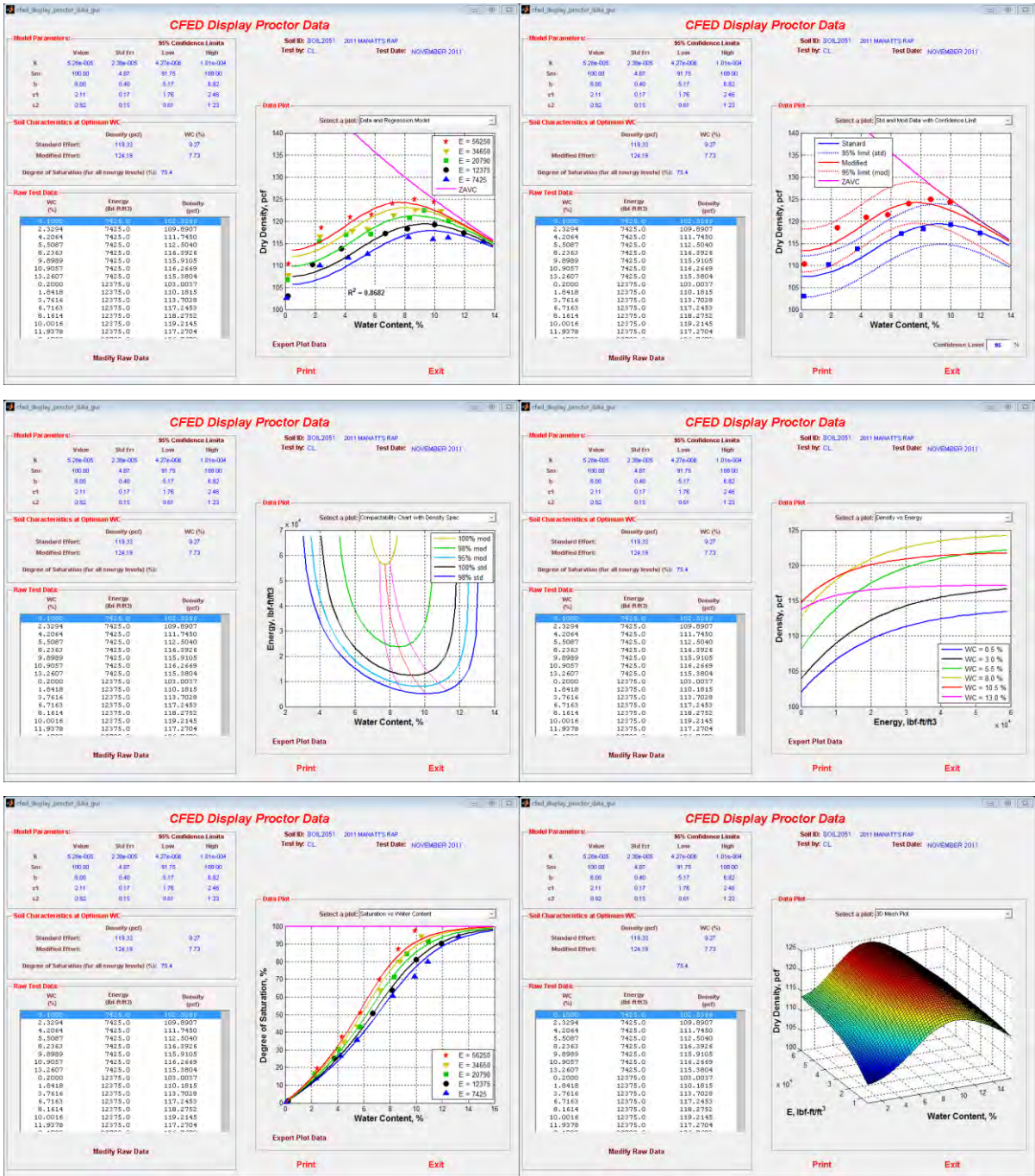


Figure 96. CFED output graphs for 2011 Manatt's RAP (CFED 2051)

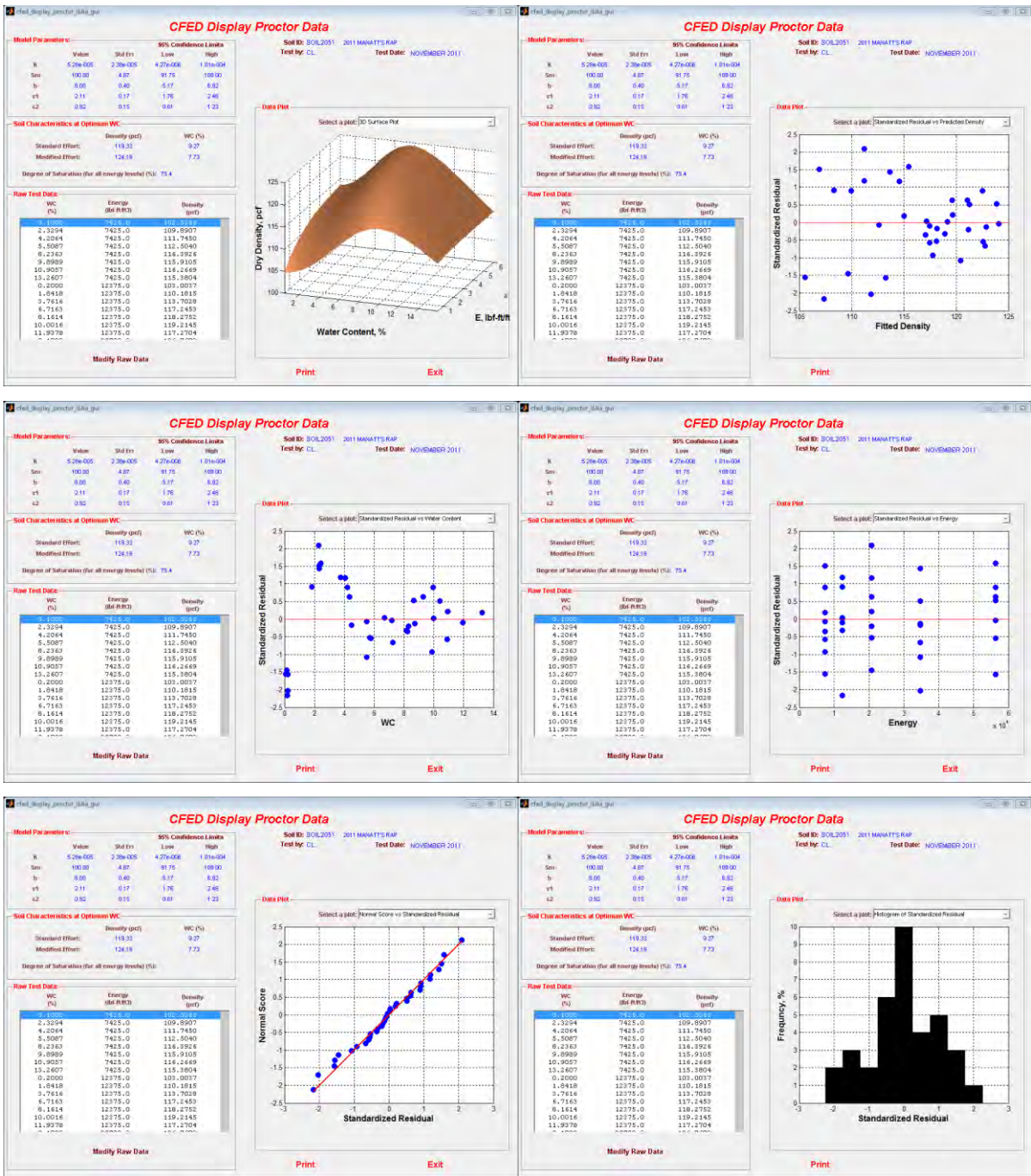


Figure 96 (continued). CFED output graphs for 2011 Manatt's RAP (CFED 2051)

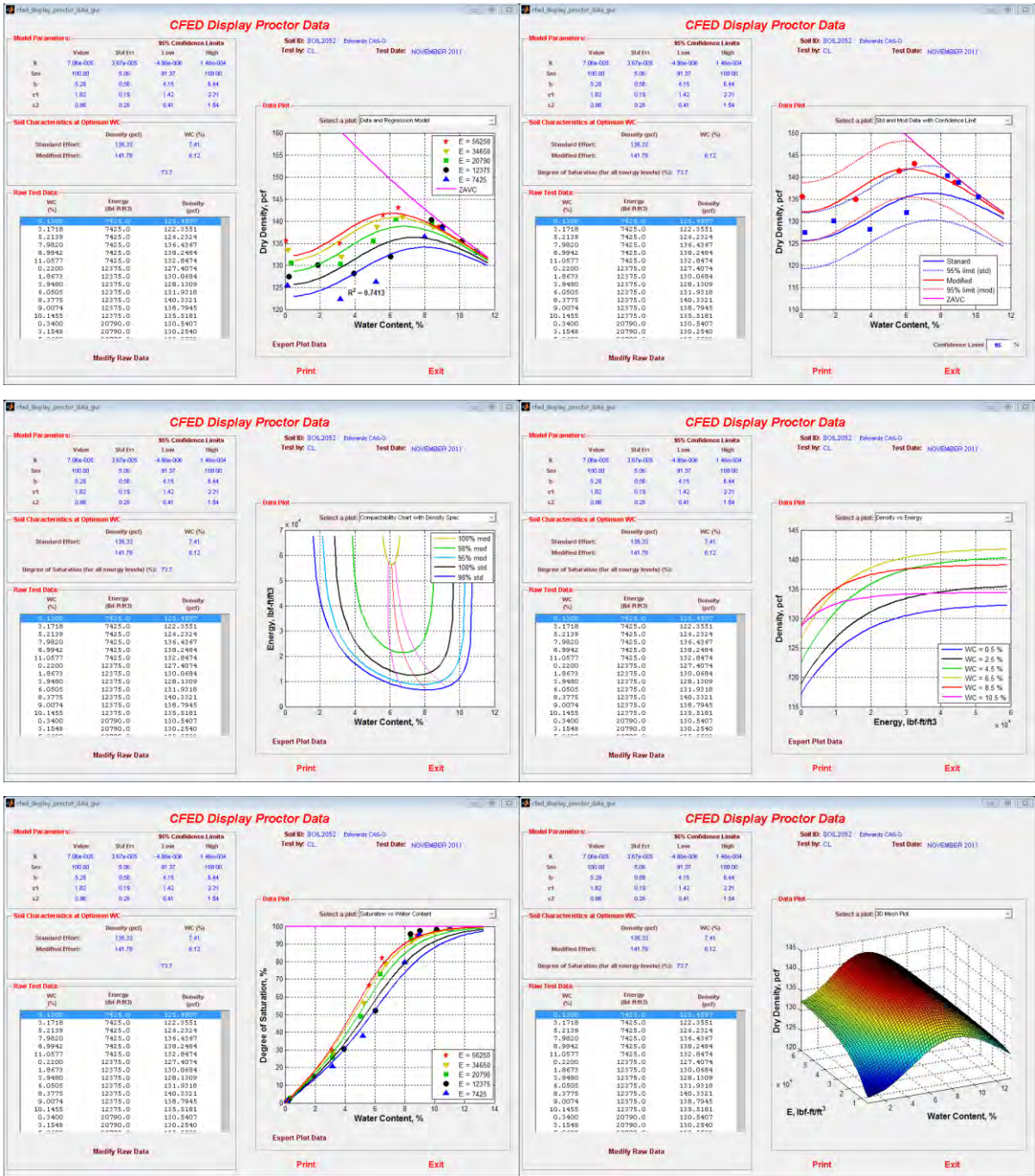


Figure 97. CFED output graphs for CA-6-G (CFED 2052)

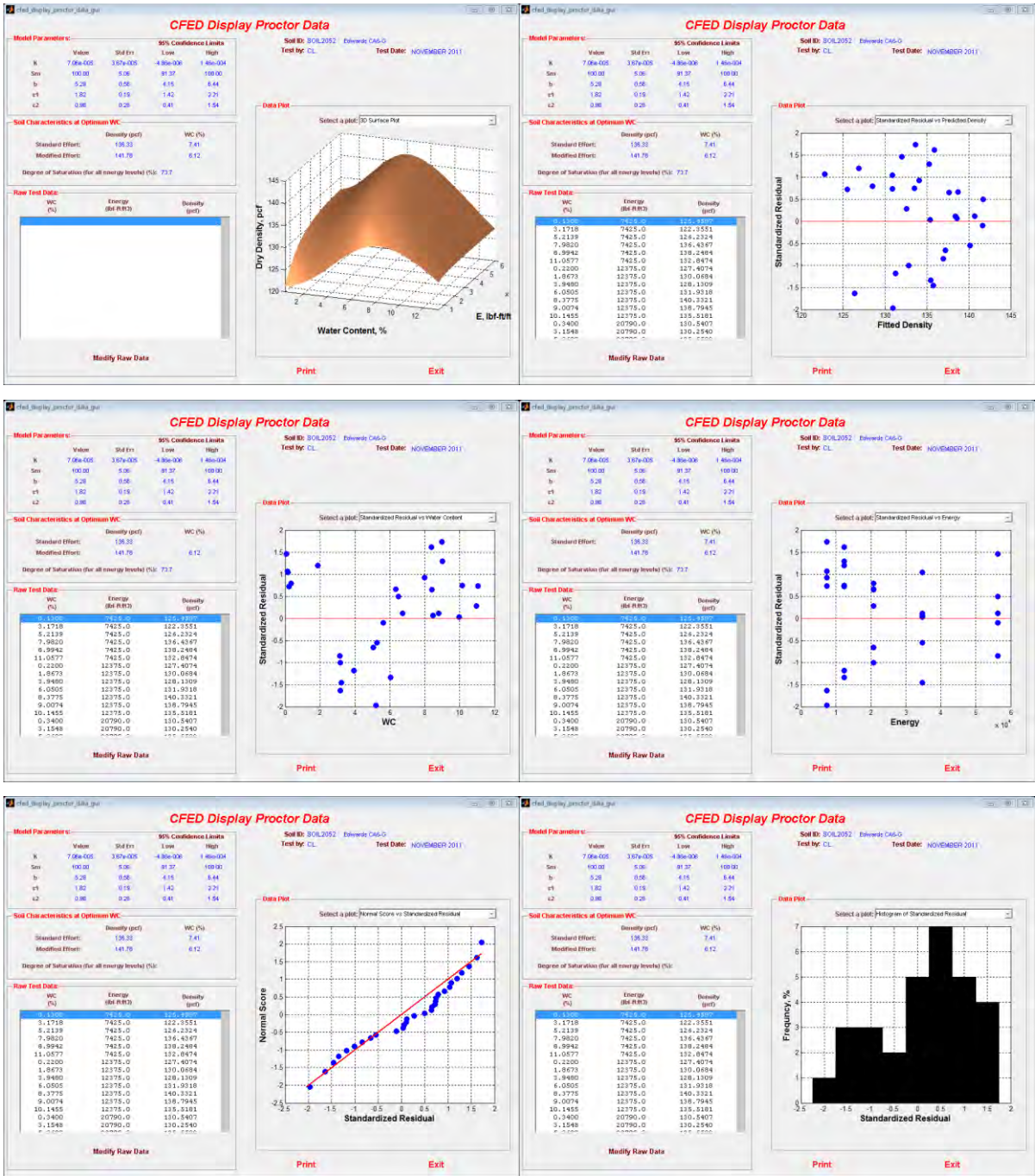


Figure 97 (continued). CFED output graphs for CA-6-G (CFED 2052)

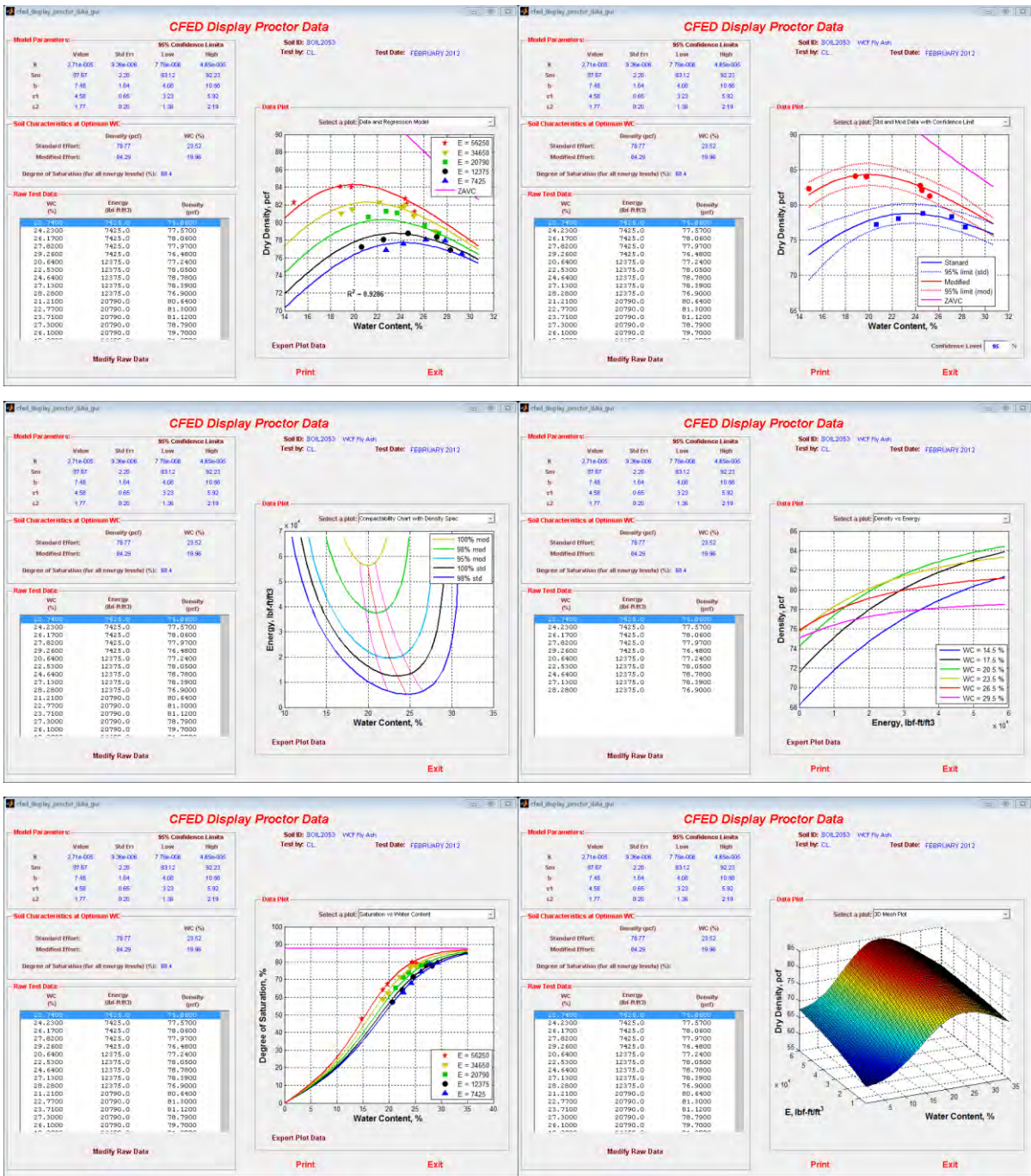


Figure 98. CFED output graphs for WCF fly ash (CFED 2053)

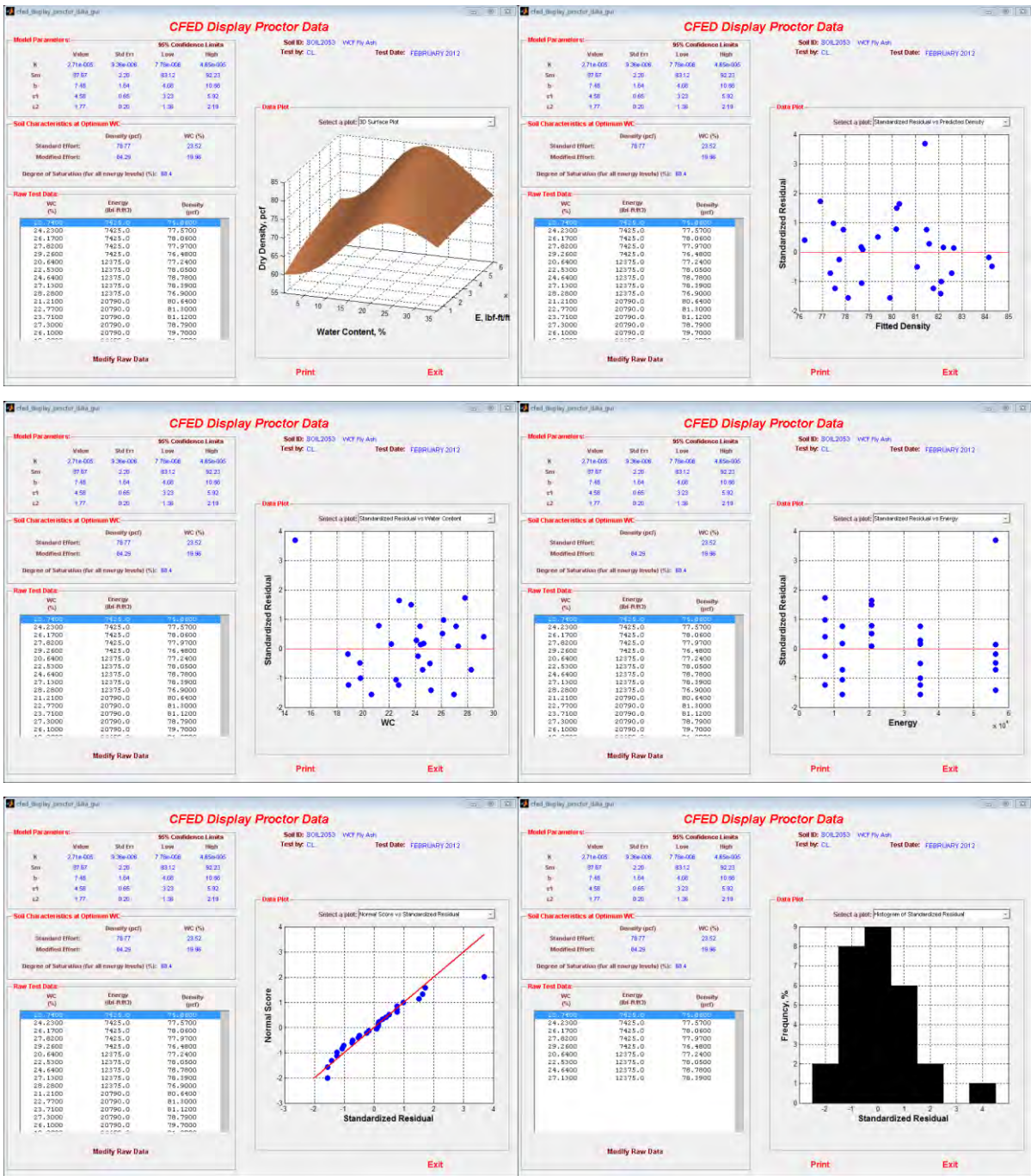


Figure 98 (continued). CFED output graphs for WCF fly ash (CFED 2053)

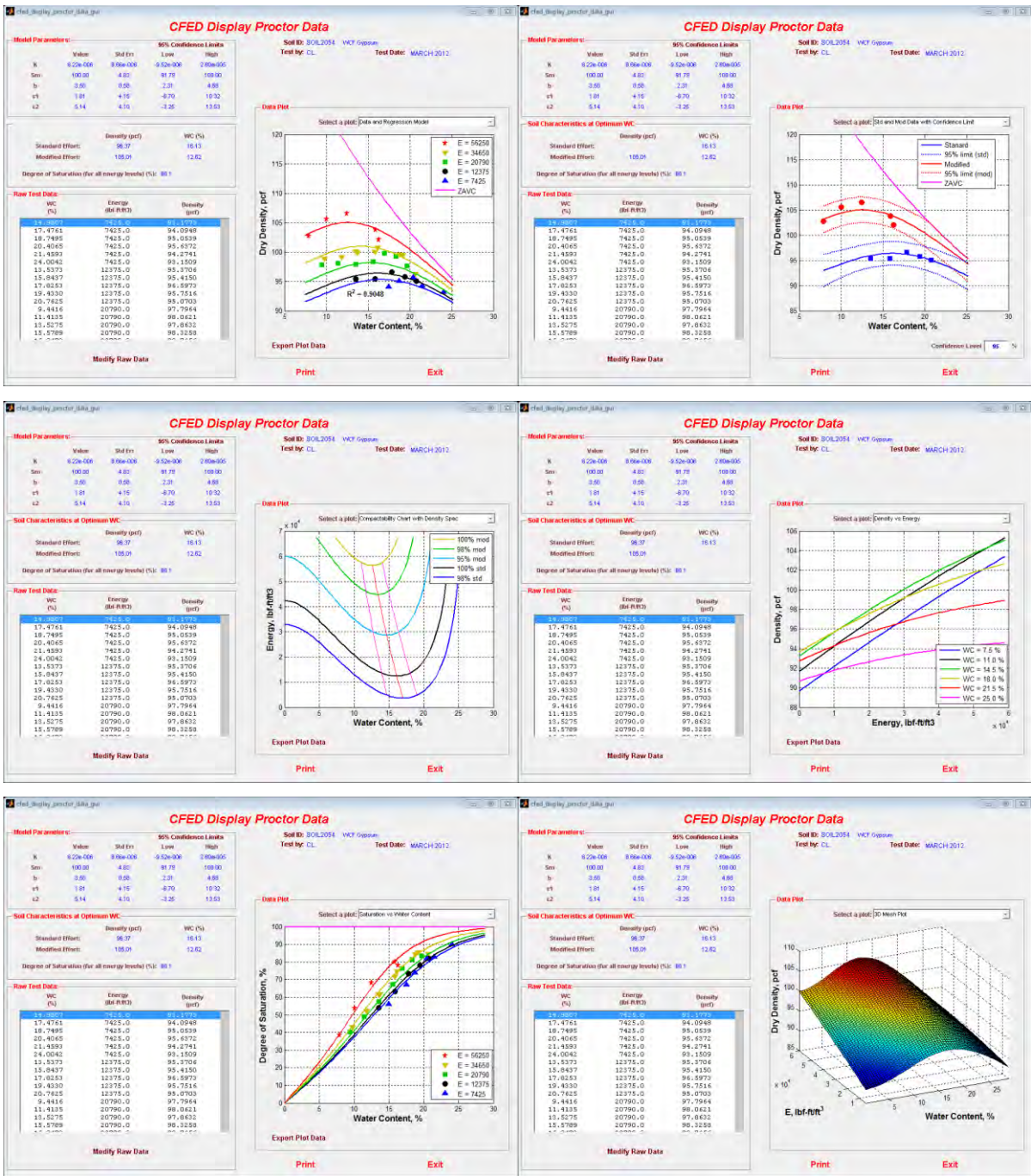


Figure 99. CFED output graphs for WCF gypsum (CFED 2054)

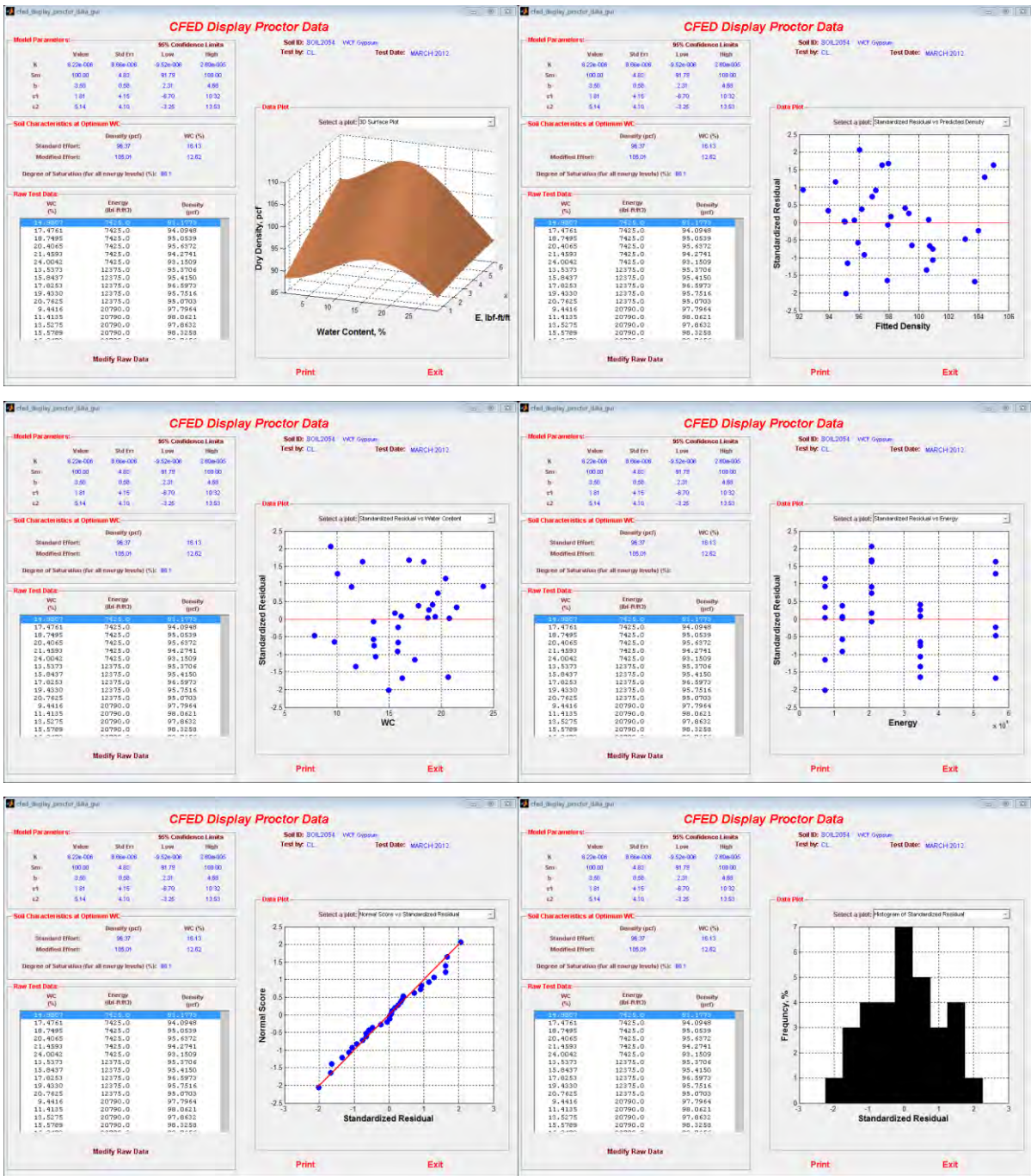


Figure 99 (continued). CFED output graphs for WCF gypsum (CFED 2054)

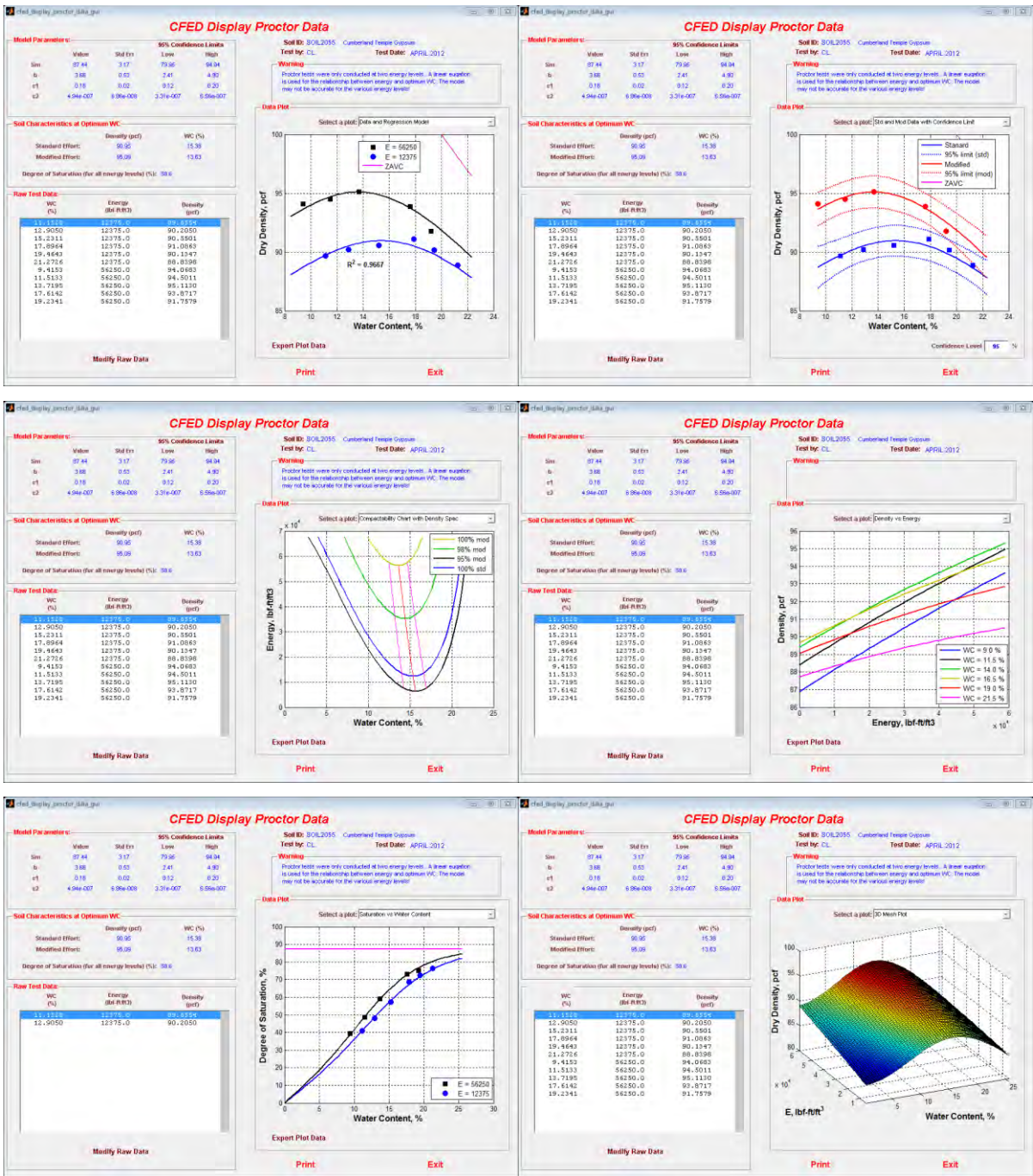


Figure 100. CFED output graphs for Cumberland Temple gypsum (CFED 2055)

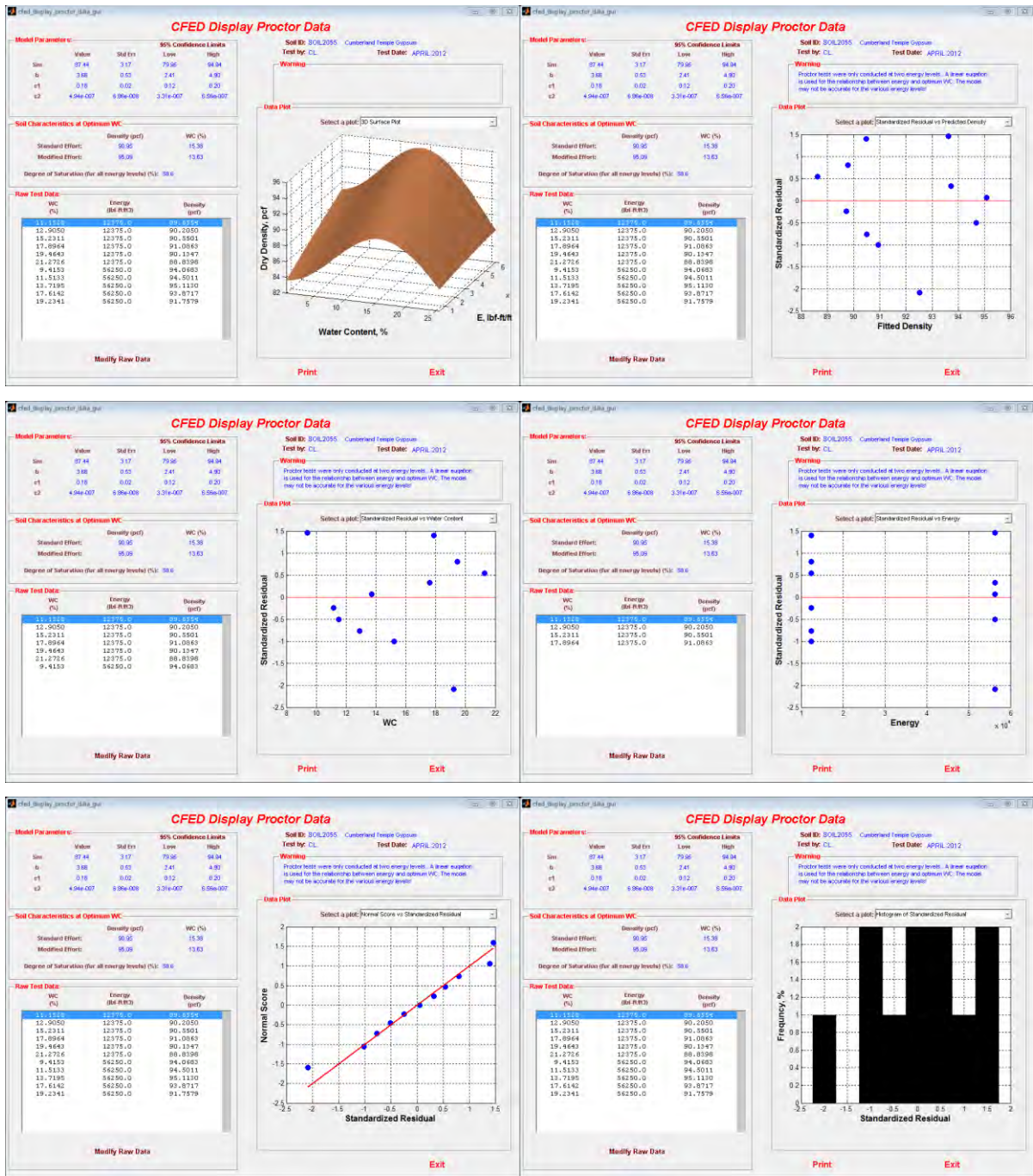


Figure 100 (continued). CFED output graphs for Cumberland Temple gypsum (CFED 2055)

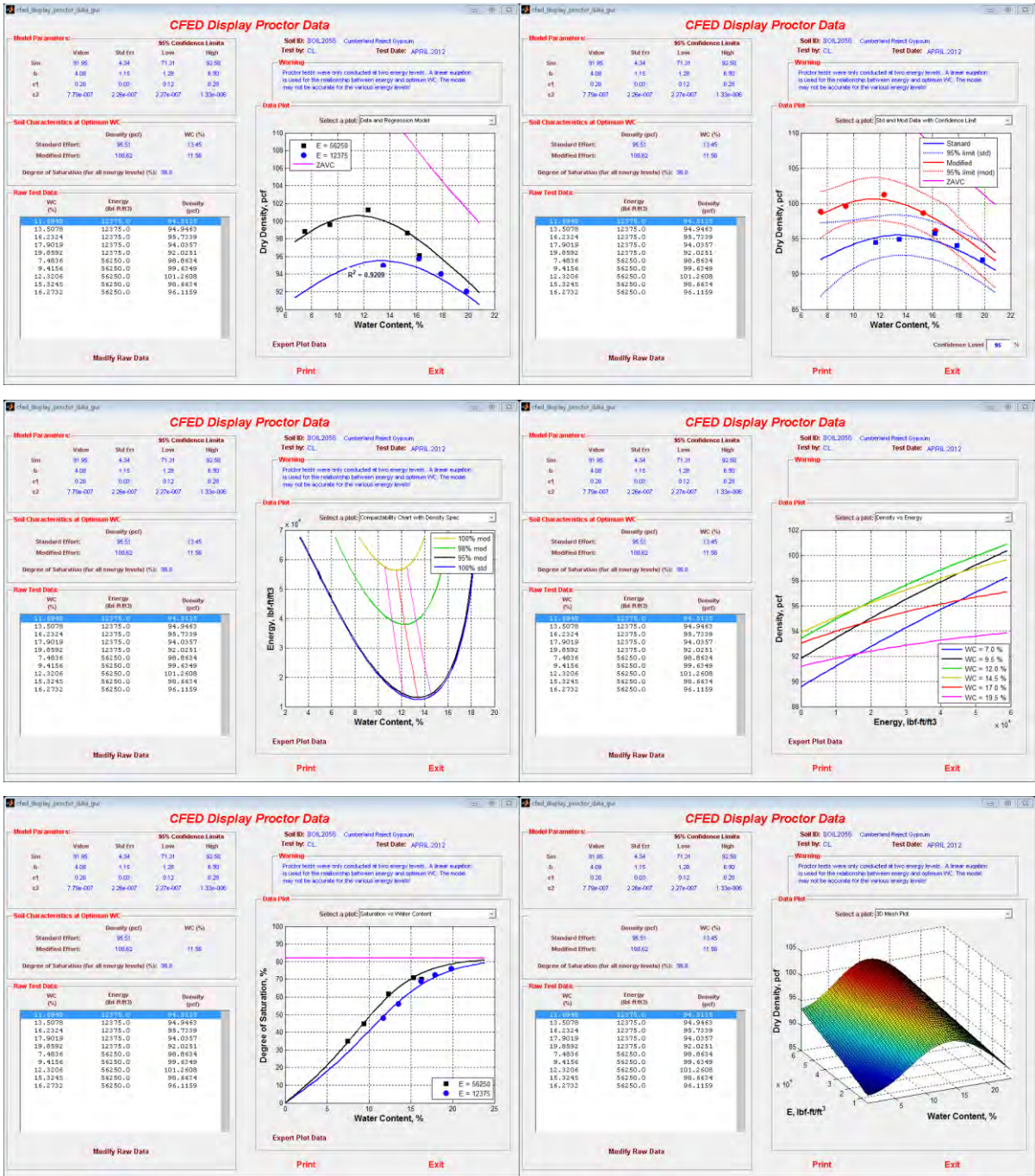


Figure 101. CFED output graphs for Cumberland Reject gypsum (CFED 2056)

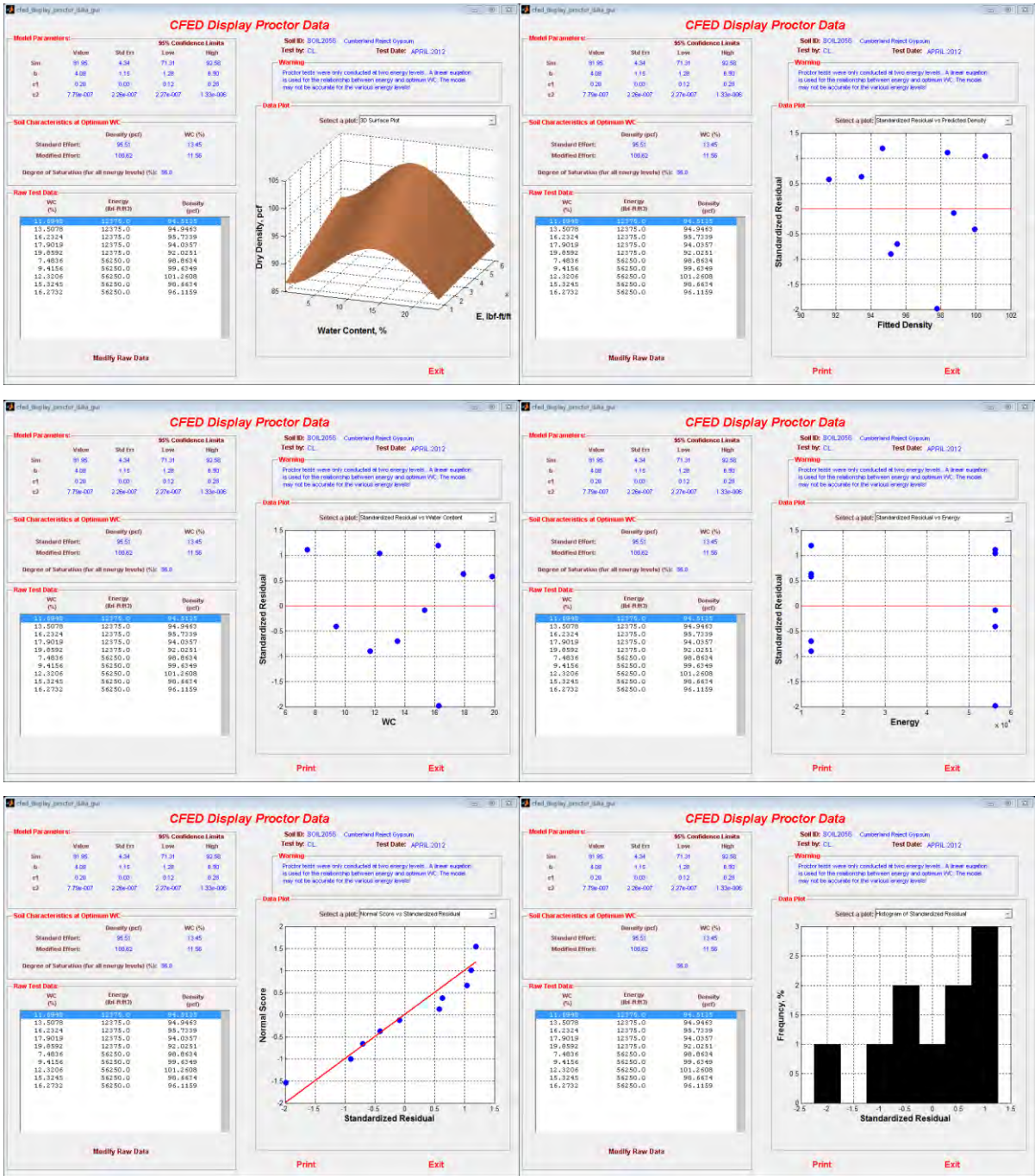


Figure 101 (continued). CFED output graphs for Cumberland Reject gypsum (CFED 2056)

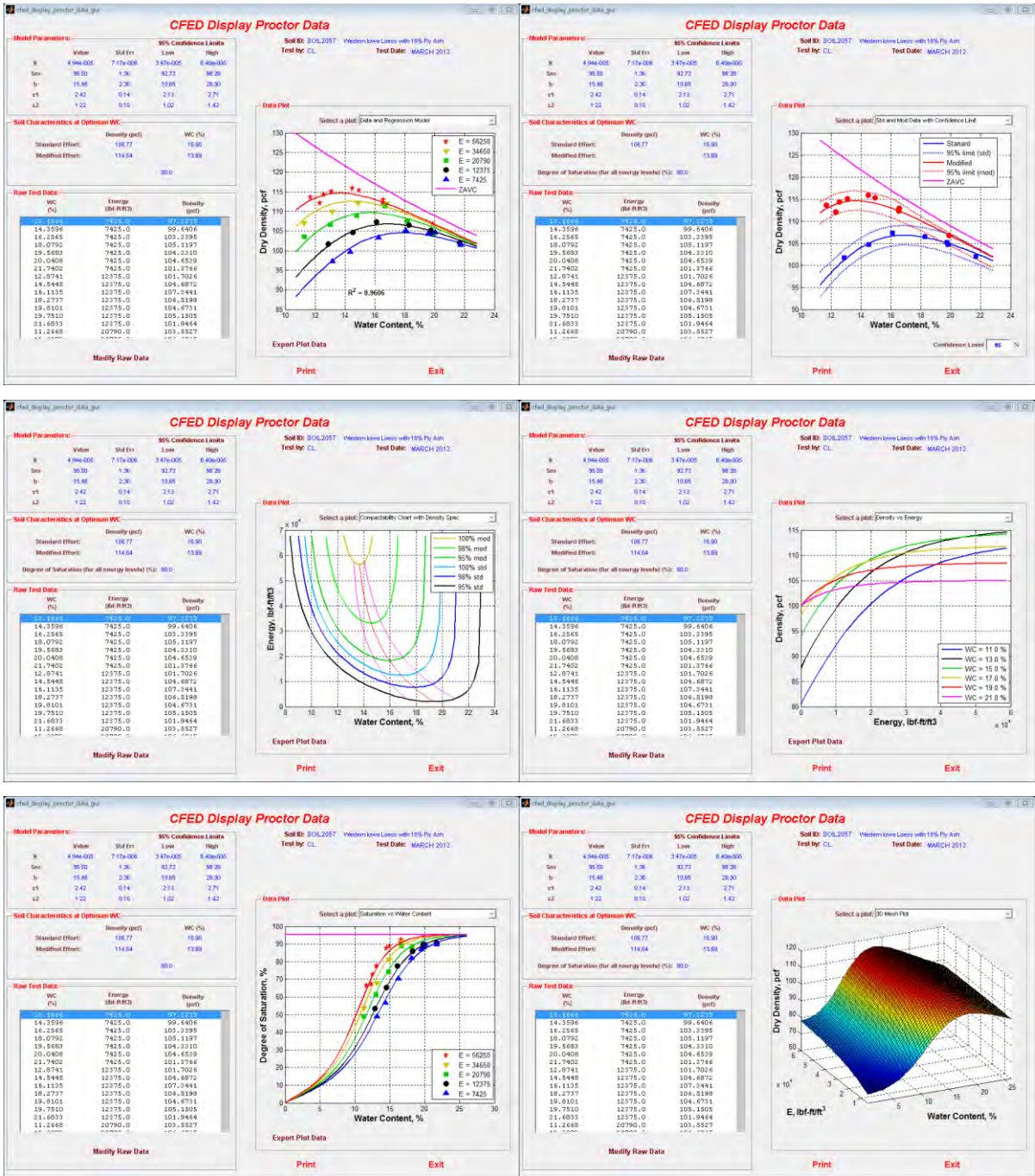


Figure 102. CFED output graphs for western Iowa loess with 15% fly ash (CFED 2057)

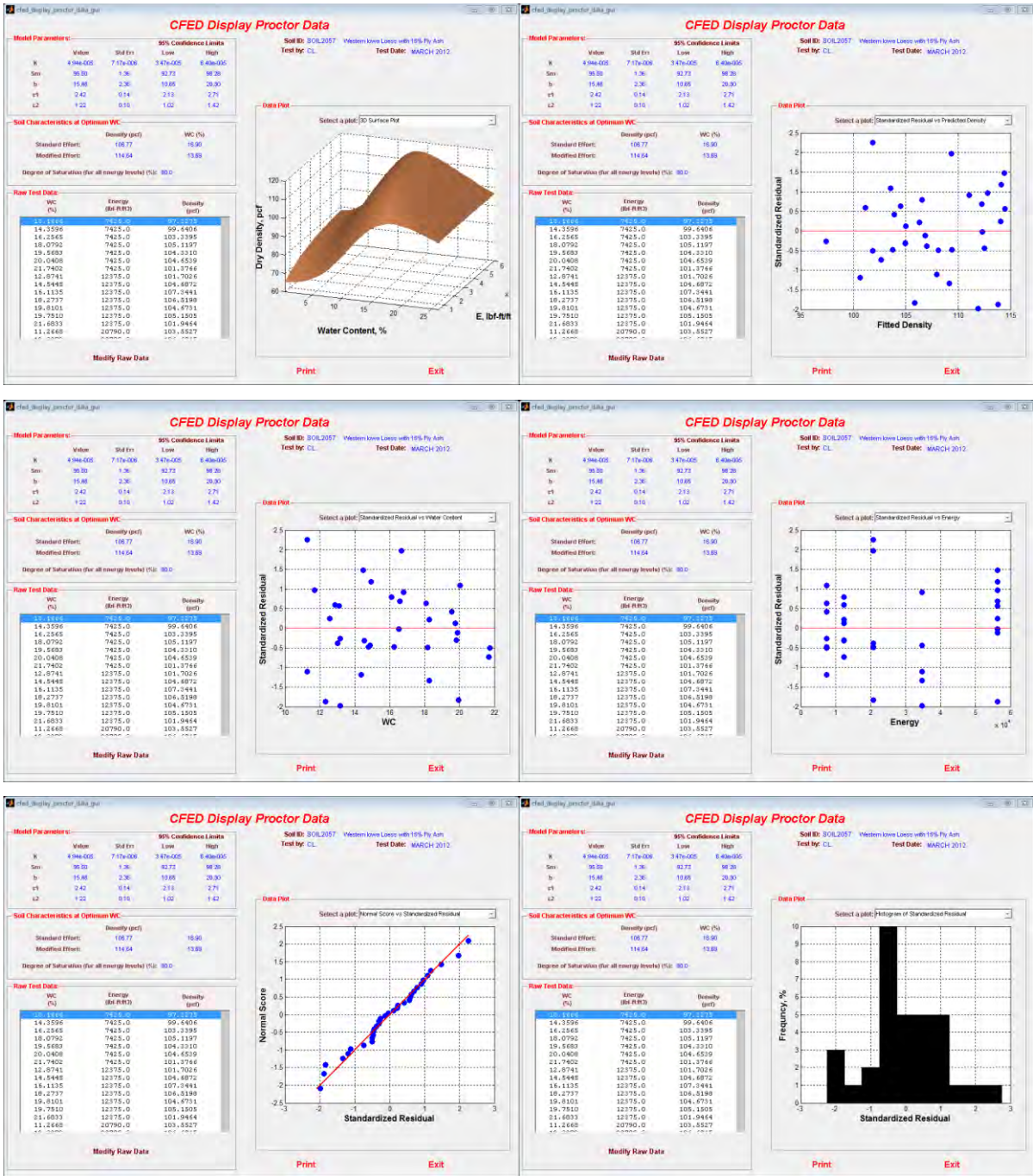


Figure 102 (continued). CFED output graphs for western Iowa loess with 15% fly ash (CFED 2057)

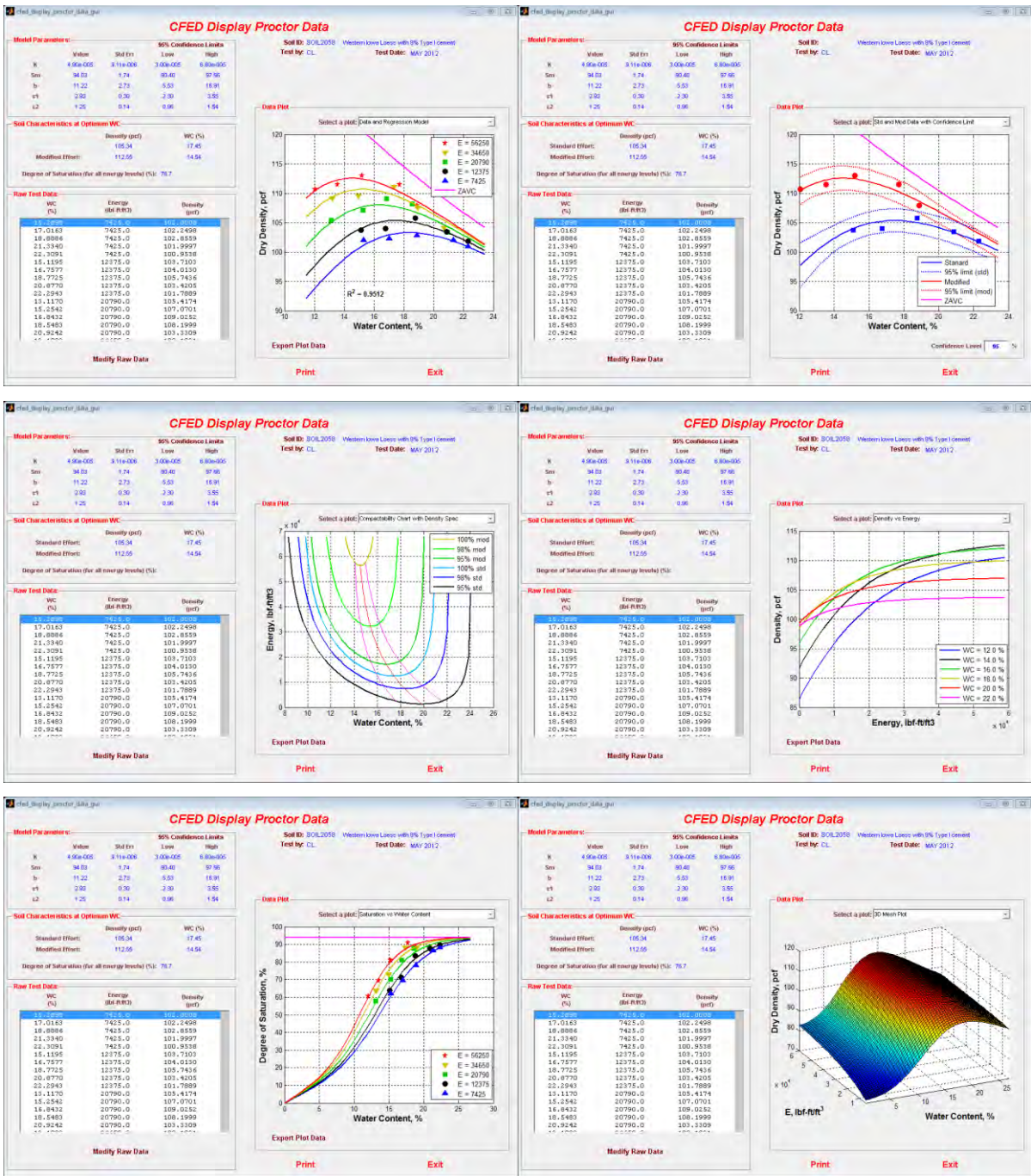


Figure 103. CFED output graphs for western Iowa loess with 9% Type I cement (CFED 2058)

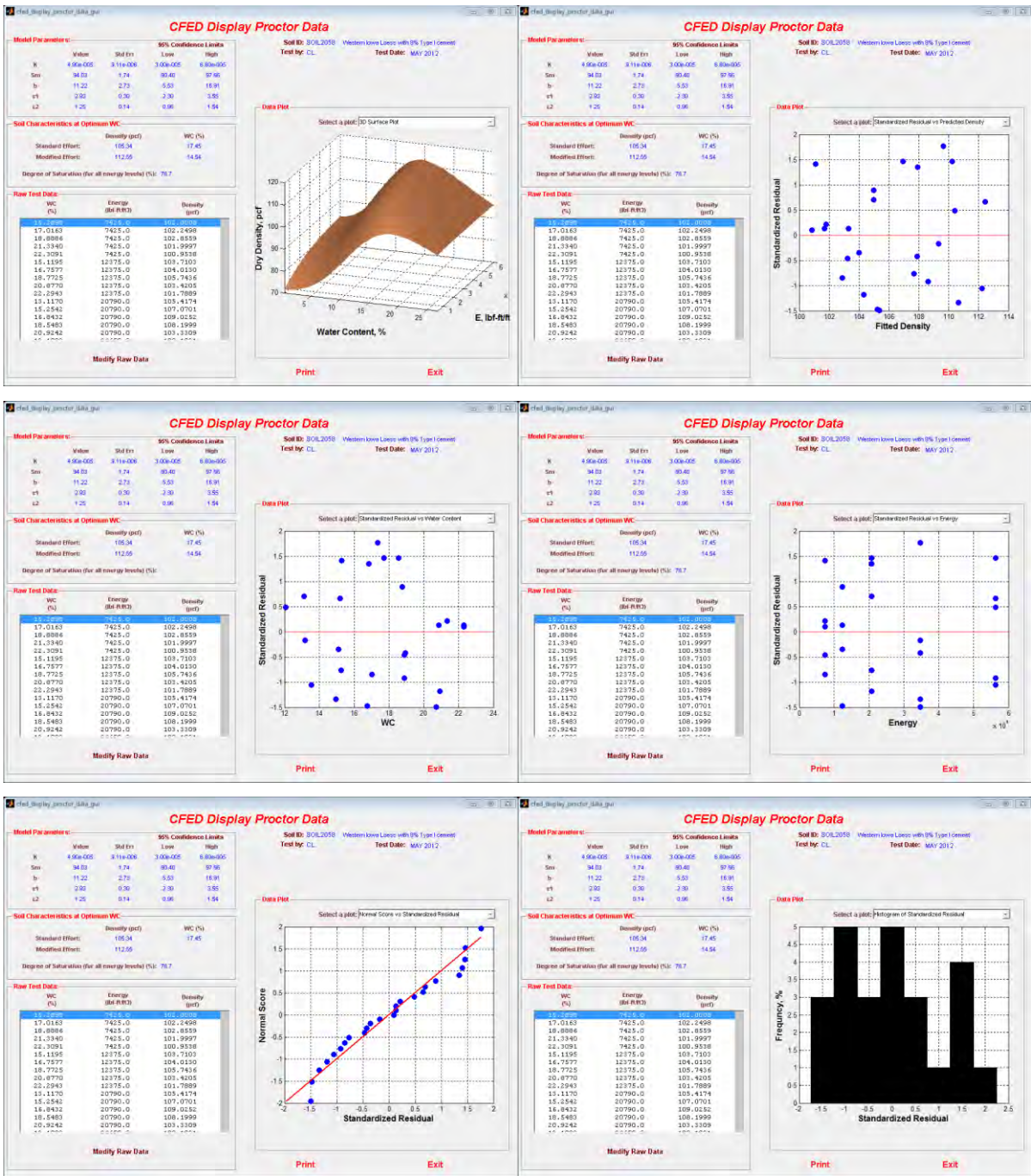


Figure 103 (continued). CFED output graphs for western Iowa loess with 9% Type I cement (CFED 2058)

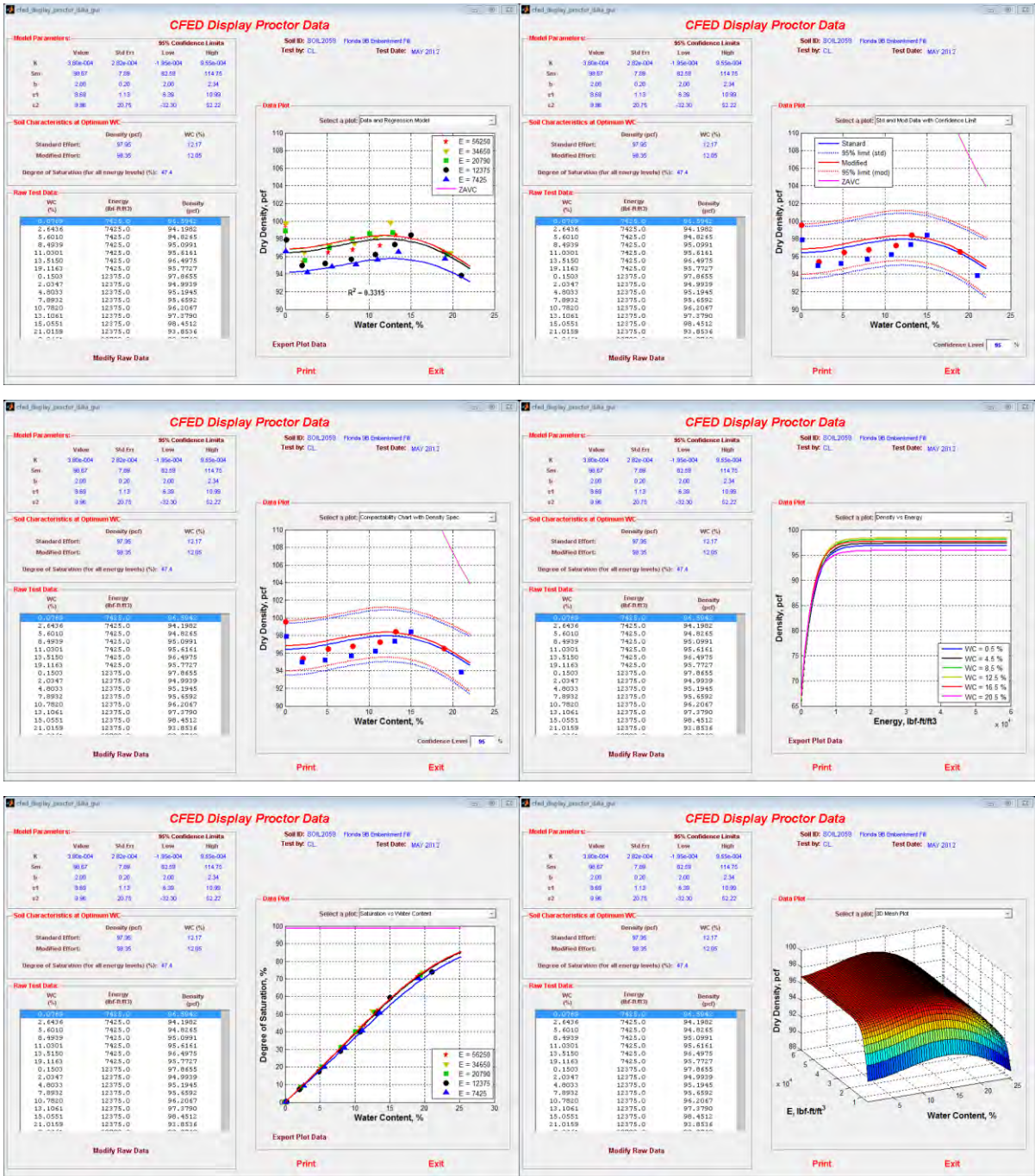


Figure 104. CFED output graphs for Florida 9B fill (CFED 2059)

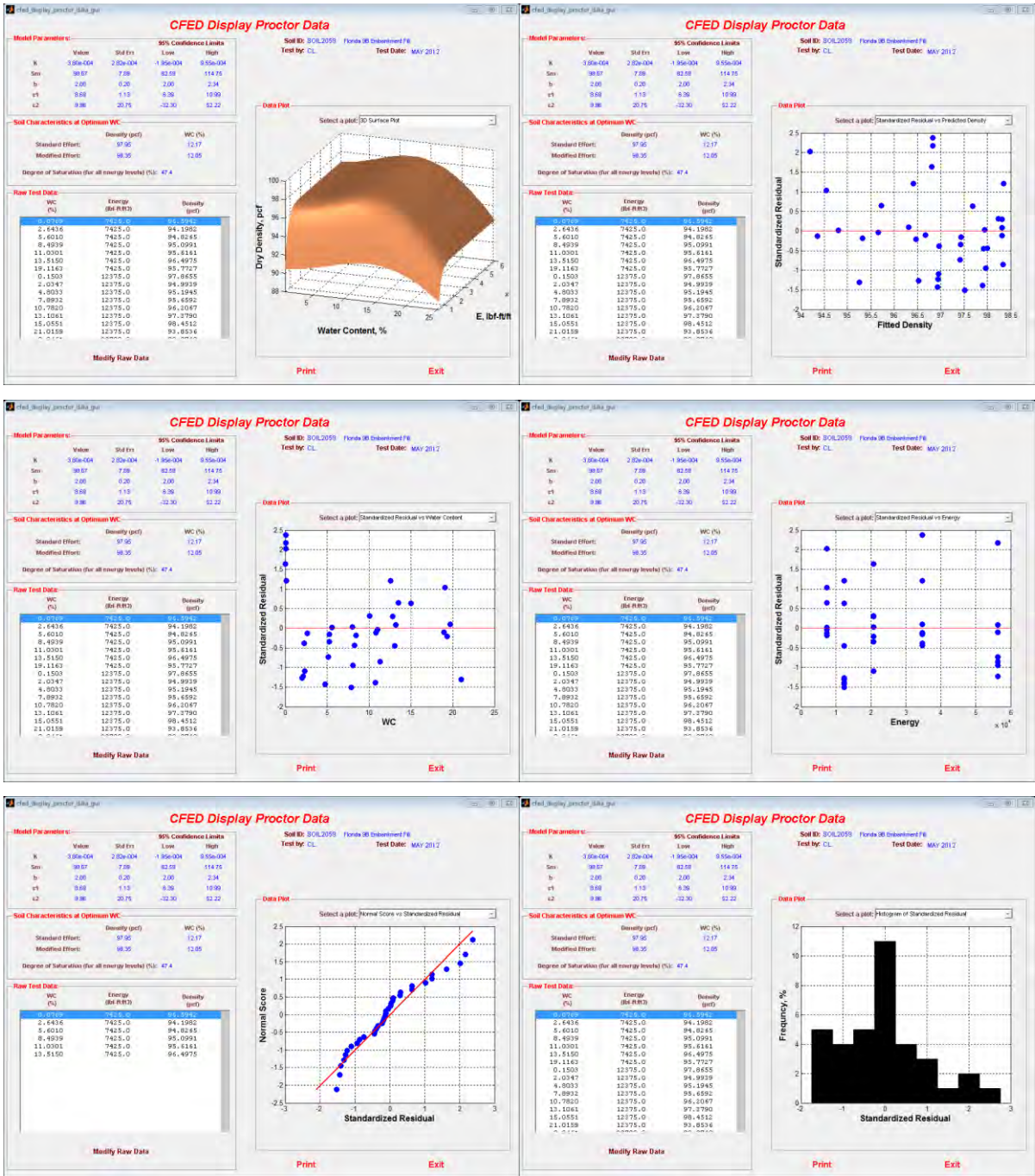


Figure 104 (continued). CFED output graphs for Florida 9B fill (CFED 2059)

Unconfined compression (UC) tests were conducted on the Proctor samples of western Iowa loess stabilized with 15% fly ash and 9% type I cement (CFED 2057 and 2058). The Proctor samples were wrapped and cured under constant temperature (32°C) environment for seven days before the UC tests. The maximum dry unit weight, optimum moisture content, and maximum unconfined compressive strength at each compaction energy level are shown in Figure 105. The moisture contents were measured after Proctor and UC testing for each sample. The results show that increasing compaction energy increases the compressive strength on the dry side of optimum moisture content, while there is little change in compressive strength with increasing compaction energy on the wet of optimum. Also, the unconfined compressive strength of the samples wet of optimum moisture content were significant lower than the samples dry of optimum. The compaction energy and moisture content were considered as the dominant influence factors to the compressive strength of the chemically stabilized loess. All the UC tests data is provided in Appendix B.

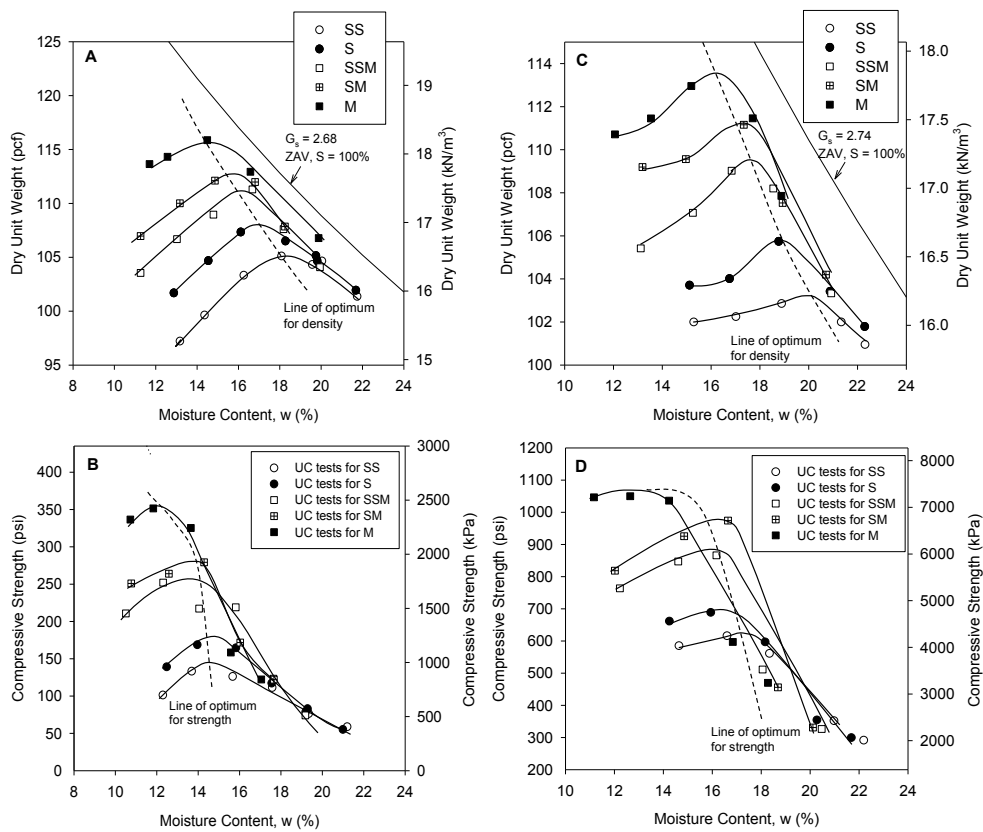


Figure 105. Proctor and UC test results for the loess stabilized with (A and B) 15% fly ash and (C and D) 9% Type I cement

Vibratory compaction test results

Vibratory compaction tests were conducted on 2012 Manatt's RAP (CFED 2061), RPCC and RAP mixture (CFED 2062), crushed limestone (CFED 2063), and Ottawa sand (ASTM 20-30 sand) to determine the compaction behaviors. All the samples were oven dried and the particles retained on $\frac{3}{4}$ in. sieve were scalped off before tests. A 6 in. mold (0.1 ft³) was used in accordance with ASTM D4253. The standard specifies that maximum dry unit weights are determined at 8 minutes (480 sec.), but in this study the test ran for 16 minutes (960 sec.) to see whether over-compaction occurred. All of the tests raw data are provided in Appendix A.

Standard and modified Proctor test were also conducted on 2012 Manatt's RAP, RPCC and RAP mixture, and crushed limestone to compare with vibratory compaction test results. The minimum and maximum index densities and void ratios and the Proctor tests results of the geomaterials are shown in Table 37. The vibratory compaction test yielded lower dry unit weights for the three geomaterials compared with the standard and modified Proctor test. The compactibility (F) was calculated based on the vibratory compaction test results.

Table 37. Proctor and vibratory compaction test results of the four coarse grained geomaterials

Parameters	2012 Manatt's RAP	RPCC + RAP	Crushed lime stone	Ottawa sand	Methods
Standard Proctor dry unit weight, STD γ_d , (pcf)	100.0	99.2	133.2	—	ASTM D698
Modified Proctor dry unit weight, MOD γ_d , (pcf)	108.8	111.6	140.5	—	ASTM D1557
Minimum index density, ρ_{dmin} , (pcf)	82.7	87.3	99.8	97.5	ASTM D4254
Maximum index density, ρ_{dmax} , (pcf)	95.4	102.1	116.4	110.3	ASTM D4253
Minimum index void ratio, e_{min}	0.62	0.28	0.28	0.50	ASTM D4253
Maximum index void ratio, e_{max}	0.86	0.50	0.45	0.70	ASTM D4254
Vibratory Compactibility, F	0.403	0.768	0.534	0.394	$F = \frac{e_{max} - e_{min}}{e_{min}}$

Note: — test not performed

The dry unit weight versus vibration compaction time that is in log scale for the four geomaterials are shown in Figure 106. The results show that dry unit weights increase with compaction time. The regression lines were used to fit the data points of each material and the slope of each line can be considered as an indication of the compactibility of the material.

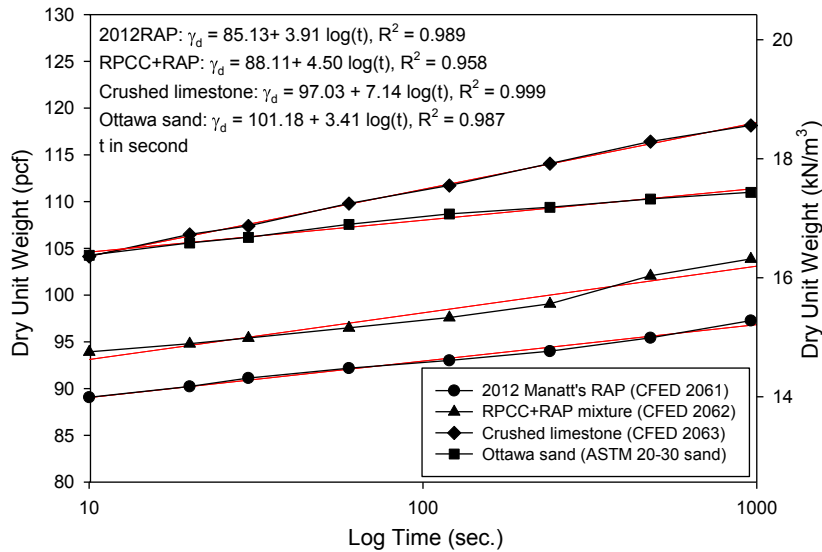


Figure 106. Dry unit weight versus vibratory compaction time for the four geomaterials

The dry unit weight versus compaction energy for the vibratory and Proctor tests are shown in Figure 107. Most of the maximum dry unit weights of each curve was achieved in the first 10 kips-ft/ft³ energy of the vibratory compaction tests. Modified Proctor tests produced most compaction energy and yielded the highest dry unit weight compared with the standard Proctor and vibratory compaction tests.

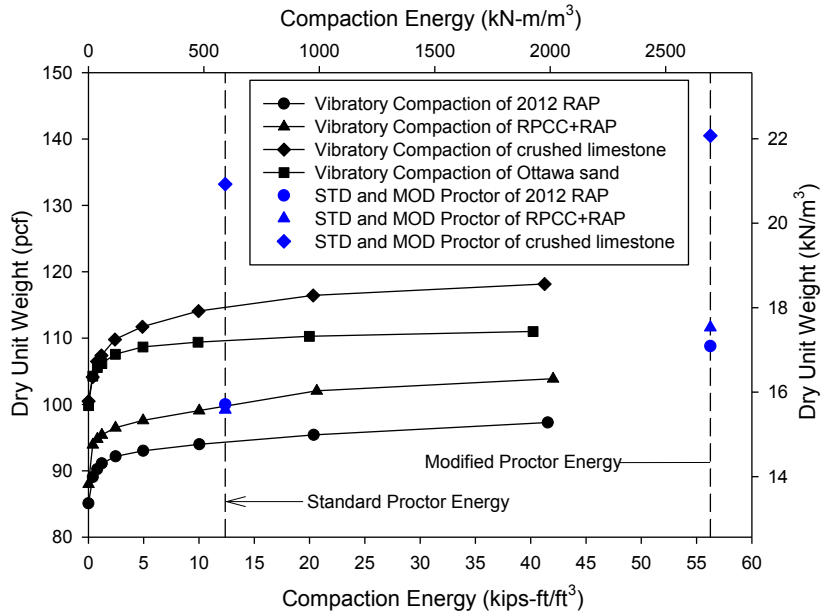


Figure 107. Dry unit weight versus vibratory compaction energy and Proctor test results of the four geomaterials

Improving CFED Using Iowa K Test to Evaluate Shear Strength and Stiffness Properties of Geomaterials

The Iowa K test was conducted on five geomaterials to evaluate its performance for measuring undrained shear strength and stiffness properties of compacted geomaterials. Table 38 shows the CFED soil IDs, descriptions, and USCS classifications of the materials used in this study. The variations in undrained shear strength parameters (i.e., cohesion and internal friction angle) and stiffness parameters (i.e., elastic modulus, Poisson's ratio, and lateral stress ratio) of the five compacted geomaterials were evaluated by the Iowa K test.

Table 38. Five types of geomaterials used for the Iowa K tests

CFED Soil ID	Description	USCS Classification
1634	Western Iowa loess	ML
2043	Texas fat clay	CH
2053	WCF fly ash	ML
2054	WCF gypsum	ML
N/A	Ottawa sand	SP

The Iowa K test samples were compacted in a 4 in. Proctor mold and extruded out from the mold then placed in a sealed container with a water source to maintain the moisture content. The curing time for the samples was 24-hr for WCF fly ash and gypsum, 48-hr for Western Iowa loess, and 72-hr for Texas fat clay. Dry Ottawa sands were compacted in the Iowa K test mold to four varying densities. The moisture contents and dry unit weights of the Iowa K test samples were measured after compaction. The height of each sample was measured before the Iowa K test and the diameter of the samples was assumed unchanged which is four inches. Two loading and unloading cycles (loading rate = 0.05 in/min) were performed on each sample. After the first loading cycle, the dry unit weights of the samples were calculated for the data analysis of the second loading based on the sample deformations. The moisture contents of the samples were assumed unchanged during the Iowa K tests. The vertical applied pressure ranged from 0 to 250 psi for different type of the geomaterials. For high moisture content samples, the tests were terminated when the materials squeezed out from the mold. All of the test results are included in Appendix C. In the following sections, the Iowa K test results are presented in four parts for each of the five materials: the undrained cohesion and friction angle, elastic modulus, Poisson's ratio and lateral stress ratio, and soil to steel friction.

Western Iowa loess (CFED 1634)

Fourteen western Iowa loess samples with varying moisture content and dry unit weight combinations were prepared to evaluate how changes in the moisture content and dry unit weight influenced the shear strength and stiffness of the compacted samples. The Iowa K test data and statistical analysis results are discussed below for each parameter.

Undrained cohesion and internal friction angle

The undrained cohesions and internal friction angles were determined using stress path method based on the Iowa K test first loading data. Figure 108 shows a typical example of using the stress path method to determine the undrained cohesion (c) and internal friction angle (ϕ) of the samples. The friction angle and cohesion were calculated based on the slope and intercept of a linear regression line that best fits the first loading data. When the p-q plot showed a straight line with 45° angle at the beginning of the first loading, the horizontal stress (σ_h) was still zero because there was still space between the sample and the Iowa K test mold, so these data were deleted for fitting the linear regression line.

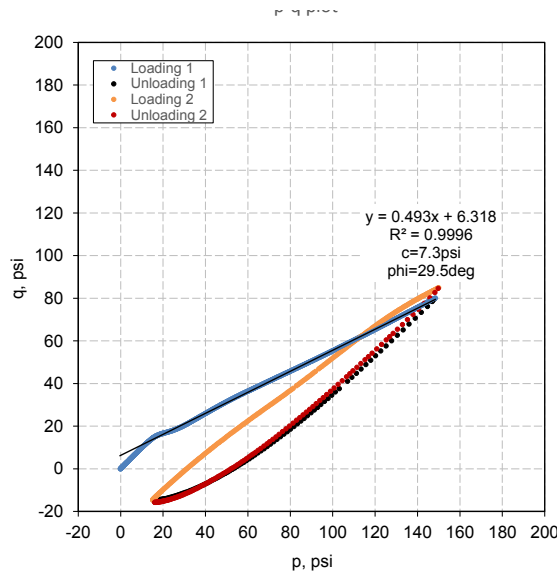


Figure 108. The Iowa K test stress path of a Western Iowa loess sample ($w\% = 12.2\%$, $\gamma_d = 96.9$ pcf)

Table 39 summarizes the Iowa K test undrained cohesions and friction angles of the 14 samples. Direct shear tests were conducted on six selected Iowa K test samples to determine drained cohesions and friction angles. Three 2.5 in. circular samples from each of the Iowa K test sample were trimmed for 29, 56, and 83 psi normal stress direct shear tests. The dry unit

weights and moisture contents of the direct shear test samples were measured before and after each test. Table 39 shows the initial moisture content of the direct shear test samples

The Iowa K test results show that both of the undrained cohesions and friction angles tend to increase as dry unit weight increases at a given moisture content, excluding a negative value of -0.3 for the sample with 18.5% moisture content. The undrained cohesion of the samples ranged from 0.2 psi for the samples with 20.6% moisture content to 16.9 psi for the sample with 12.3% moisture content. The undrained friction angles of the samples are all over 28°, but a significant reduction can be observed for the samples with above 21% moisture content.

The direct shear test results show that the drained friction angles increase as the moisture contents increase, but the trend of change in the drained cohesions is not determined. All of the direct shear test data are included in Appendix D. The drained friction angles of the samples with low moisture content are much lower compared to the undrained friction angles. That may be due to the direct shear test samples collapsed during the consolidation stage. For samples with high moisture content, the Iowa K test results show lower values than the direct shear test results as would be expected.

Table 39. Iowa K test and direct shear test results of Western Iowa loess

K test w (%)	K test γ_d (pcf)	K test c (psi)	K test ϕ (deg.)	DS test w (%)	DS test γ_d^* (pcf)	DS test c' (psi)	DS test ϕ' (deg.)
12.2	96.9	7.3	29.5	—			
12.3	103.5	9.8	40.0	—			
12.3	112.7	16.9	48.0	11.8	114.9	8.9	28.1
14.1	98.5	5.5	31.9	—			
14.1	105.8	13.5	36.5	13.6	107.2	2.1	34.1
14.2	115.2	14.4	43.6	—			
15.9	95.6	0.5	32.3	—			
15.9	108.2	10.3	40.1	15.4	106.9	1.5	42.3
15.9	114.9	3.9	32.8	—			
18.3	103.5	1.6	34.6	17.5	105.0	10.5	30.1
18.5	108.3	-0.3	28.5	—			
20.6	103.2	0.2	28.5	19.5	103.2	0.2	43.2
21.6	102.4	3.5	8.6	—			
21.9	101.6	2.3	9.7	20.7	102.2	2.0	42.1

Notes:

— Test not performed

* Average initial dry unit weight of the three samples

Statistical analyses were performed on the Iowa K test results to evaluate how changes in moisture content and dry unit weight influence the undrained cohesions and friction angles of the material. Multiple linear regression models with two variables (i.e., moisture content and dry unit weight) for the undrained cohesions and friction angles are generated (Figure 109). The coefficient of determination (R^2) of the two models are over 0.7 that means there are significant statistical relationships between moisture content, dry unit weight, and the shear strength parameters.

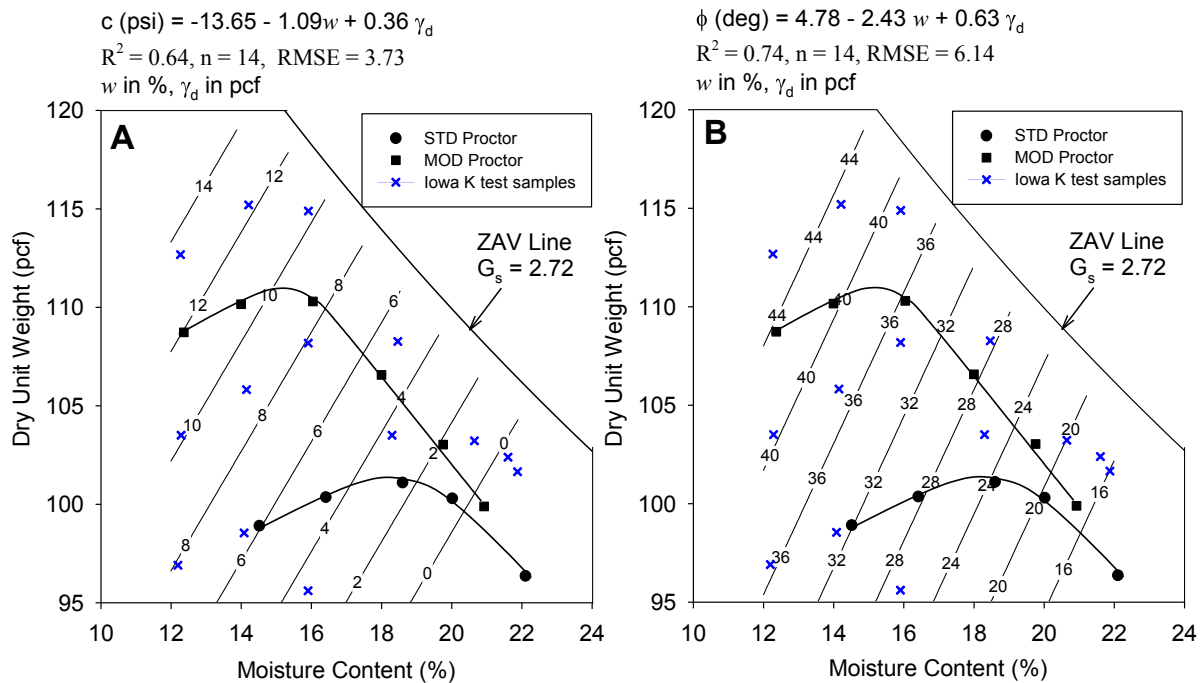


Figure 109. Statistical relationships between the moisture contents, dry unit weights, and (A) undrained cohesions and (B) internal friction angles of the loess samples

Lohnes and Handy (1968) conducted in situ borehole shear tests on friable loess of 14 sites in western Iowa. The drained cohesions ranged from 0.4 to 3.0 psi. Compared with this range, the Iowa K test results showed higher values for the samples with low moisture contents. These high values may be caused by the initial portion of stress path curve where the horizontal stresses cannot be measured. Handy (1995) also mentioned that Lutenegeer summarized that 120 borehole shear tests at 10 sites in the U.S., the average friction angle of friable loess is 35.5° with a coefficient of variation (CV) of 14.4%. The Iowa K test results for 12 of the 14 tests are within $\pm 7^\circ$ of Lutenegeer's average value, but the 2 samples with

high moisture contents were not in this range (e.g., 21.6% sample showed an undrained friction angle of 8.6°).

Vertical elastic modulus

The vertical stress-strain relationships of the 14 loess samples were determined for both of the two loading cycles of the Iowa K test, and the vertical elastic modulus (E_v) of each sample under 50 to 100 psi vertical pressure was calculated based on the slopes of the best fit linear regression lines for the stress-strain curves. Figure 110 shows an example of the stress-strain relationships and the method for determining the undrained vertical elastic modulus.

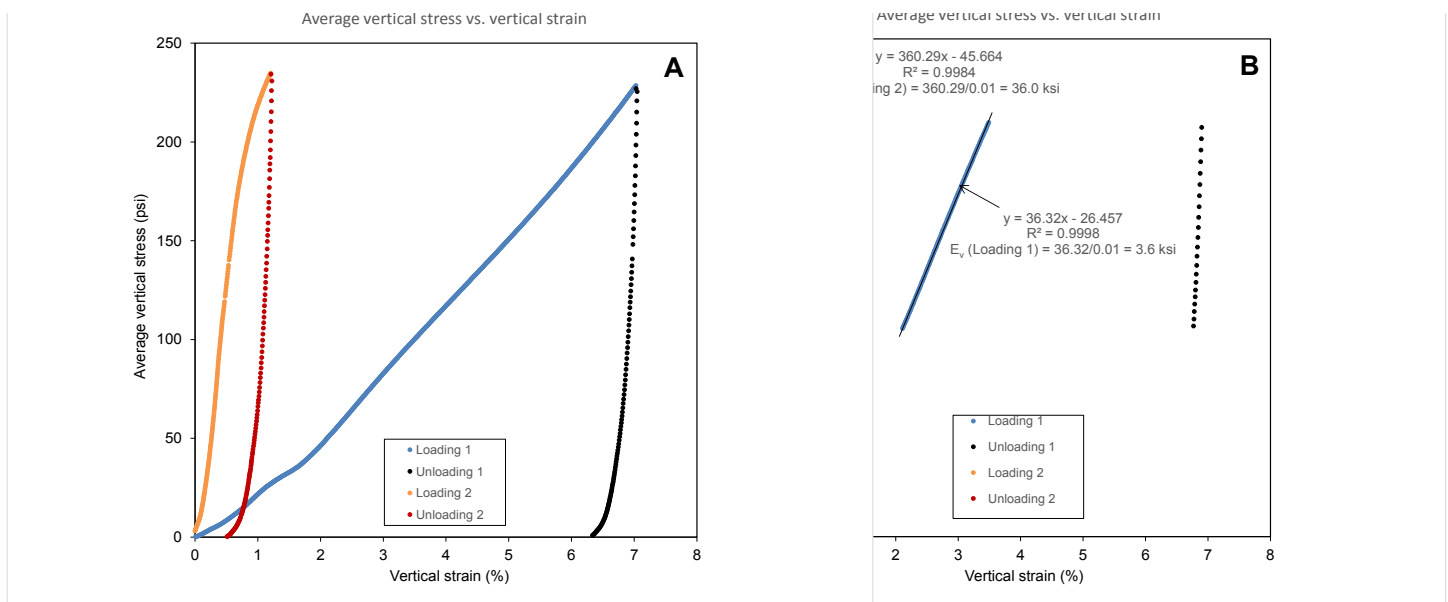


Figure 110. The (A) vertical stress-strain relationships and (B) elastic modulus under 50 to 100 vertical stress of a Western Iowa loess sample ($w\% = 12.2\%$, $\gamma_d = 96.9$ pcf)

Typical Iowa K test plots of the average vertical stress versus vertical strain give nearly linear relationships when vertical stress increased from 50 to 100 psi. Table 40 summarizes the vertical elastic modulus of the 14 samples for the two loadings of the tests. The second loading vertical elastic modulus of the sample with 12.2% moisture content is 10 times higher than the first loading. However, the difference between the two vertical elastic modulus of high moisture content samples (e.g., $w\% = 21.9\%$) is very close.

Figure 111 shows a multiple linear regression model for the first loading vertical elastic modulus and a linear regression model for the second loading. Figure 111A shows that the undrained vertical elastic modulus decreases as the moisture content increases and dry unit

weight decreases. However, for the second loading, Figure 111B shows that the vertical elastic modulus decreases as the moisture content increases, but the dry unit weight is not a significant influence factor.

Table 40. Iowa K test vertical elastic modulus of the loess samples for loading 1 and 2

w%	Loading 1 γ_d (pcf)	Loading 1 E_v (ksi) ($\sigma_v = 50-100$ psi)	Loading 2 γ_d (pcf)	Loading 2 E_v (ksi) ($\sigma_v = 50-100$ psi)
12.2	96.9	3.6	105.2	36.0
12.3	103.5	7.2	105.4	62.0
12.3	112.7	9.1	114.6	42.7
14.1	98.5	4.2	100.7	27.7
14.1	105.8	8.5	107.9	46.4
14.2	115.2	7.7	117.4	58.3
15.9	95.6	2.0	98.1	19.2
15.9	108.2	8.5	110.5	53.2
15.9	114.9	7.2	116.8	24.5
18.3	103.5	4.7	106.1	19.5
18.5	108.3	5.1	110.5	10.6
20.6	103.2	4.2	105.5	8.1
21.6	102.4	4.3	104.8	7.5
21.9	101.6	4.2	104.7	5.7

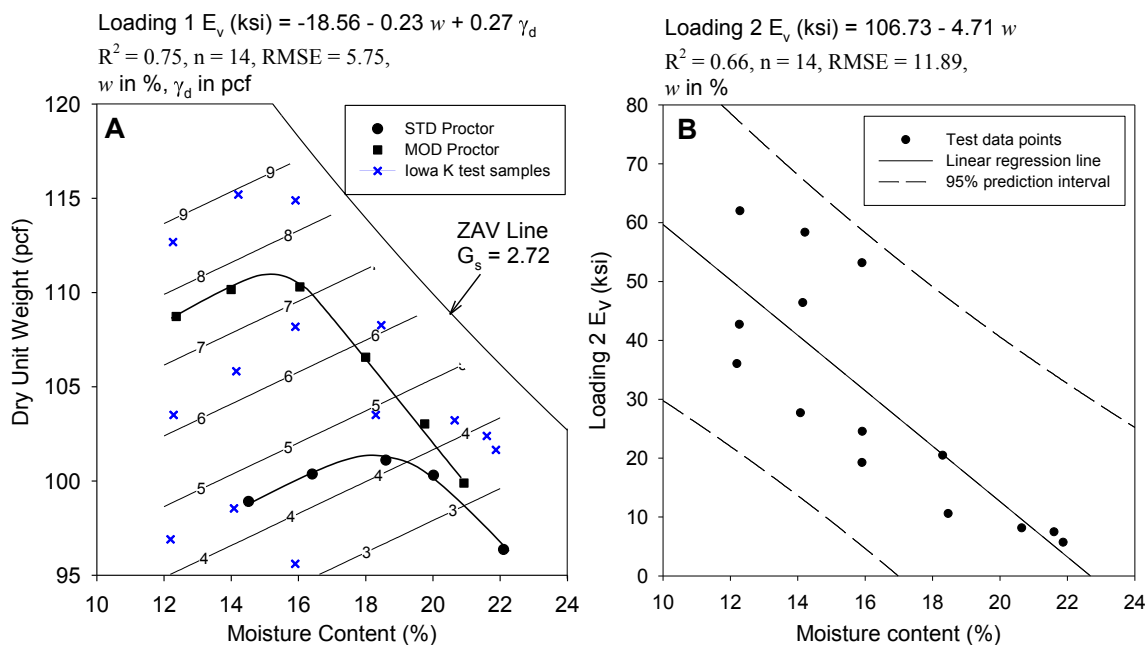


Figure 111. Statistical analysis results for (A) loading 1 and (B) loading vertical elastic modulus

Poisson's ratio and lateral stress ratio

The Poisson's ratio (ν) and lateral stress ratio (K) of the 14 loess samples were calculated based on the vertical and horizontal stress and strain data of the Iowa K test. Figure 112 shows a typical example of the Poisson's ratio and lateral stress ratio change versus the average vertical stress. All of the test results showed that both of the Poisson's ratio and lateral stress ratio increased rapidly and then maintain at a constant level as the vertical stresses increased in the first loading. However, during the second loading, both of the parameters decreased as the vertical stress increased and then reached to a relatively constant level.

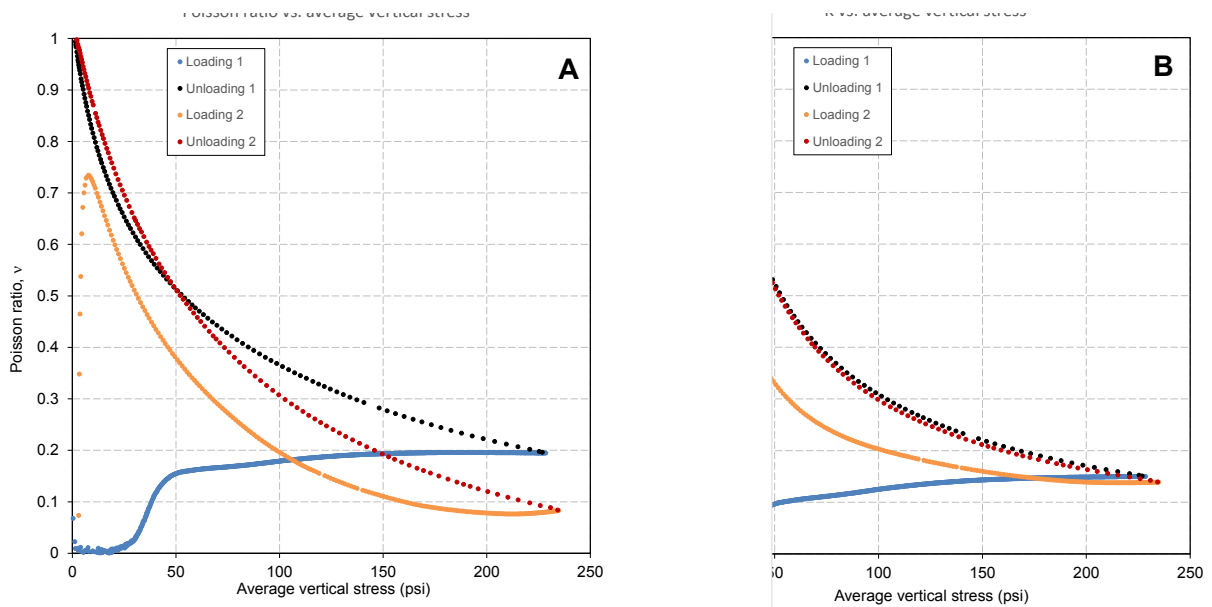


Figure 112. The (A) Poisson's ratio and (B) lateral stress ratio versus average vertical stress of a Western Iowa loess sample ($w\% = 12.2\%$, $\gamma_d = 96.9$ pcf)

The Poisson's ratio and lateral stress ratio of the samples under 100 psi vertical stress of the first loading and 25 psi of the second loading were selected for statistical analyses (Table 41). When the moisture content of the samples was below the standard Proctor optimum moisture content ($w_{opt} = 18.6\%$), the first loading data shows that both the Poisson's and lateral stress ratios increase as the moisture content increases, and within tests of samples with similar moisture contents both parameters decrease as the dry unit weight increases. When the moisture content higher than the optimum, both of the parameters has little change

as the dry unit weight increases. However, the second loading data shows opposite trends that the two parameters decreases as the moisture content increases.

Table 41. Iowa K test Poisson's ratio and lateral stress ratio of the loess samples for loadings 1 and 2

w (%)	Loading 1 γ_d (pcf)	Loading 1 ν ($\sigma_v = 100$ psi)	Loading 1 K ($\sigma_v = 100$ psi)	Loading 2 γ_d (pcf)	Loading 2 ν ($\sigma_v = 25$ psi)	Loading 2 K ($\sigma_v = 25$ psi)
12.2	96.9	0.18	0.25	105.2	0.56	1.27
12.3	103.5	0.10	0.13	105.4	0.43	0.78
12.3	112.7	0.01	0.01	114.6	0.19	0.23
14.1	98.5	0.18	0.25	100.7	0.52	1.09
14.1	105.8	0.10	0.12	107.9	0.49	0.95
14.2	115.2	0.06	0.06	117.4	0.30	0.44
15.9	95.6	0.22	0.31	98.1	0.53	1.12
15.9	108.2	0.10	0.12	110.5	0.39	0.66
15.9	114.9	0.18	0.25	116.8	0.41	0.72
18.3	103.5	0.19	0.26	106.1	0.45	0.84
18.5	108.3	0.24	0.35	110.5	0.49	0.98
20.6	103.2	0.24	0.35	105.5	0.54	1.17
21.6	102.4	0.39	0.67	104.8	0.47	0.87
21.9	101.6	0.39	0.67	104.7	0.46	0.85

A statistical model was generated for the Poisson's ratio under 100 psi vertical stress of the first loading (Figure 113). The model shows that Poisson's ratios ranges between 0.05 and 0.35 when the moisture contents of the material varied from 12% to 22%, and dry unit weight ranged from 95 to 115 pcf.

Figure 114 shows the statistical analyses results for the lateral stress ratio under 100 psi vertical stress of the first loading and 25 psi vertical stress of the second loading. The lateral stress ratios under the two loadings were selected to simulate the vertical stresses generated by compaction machines and stresses produced by sustained structures after compaction. Under the second loading, the lateral stress ratios of some samples were greater than unity, which may be caused by the rotation of the major and minor principal stresses on the samples at the beginning of the second loading. The first unloading and second loading of the Iowa K test can simulates field conditions after compaction and placement of sustained structures.

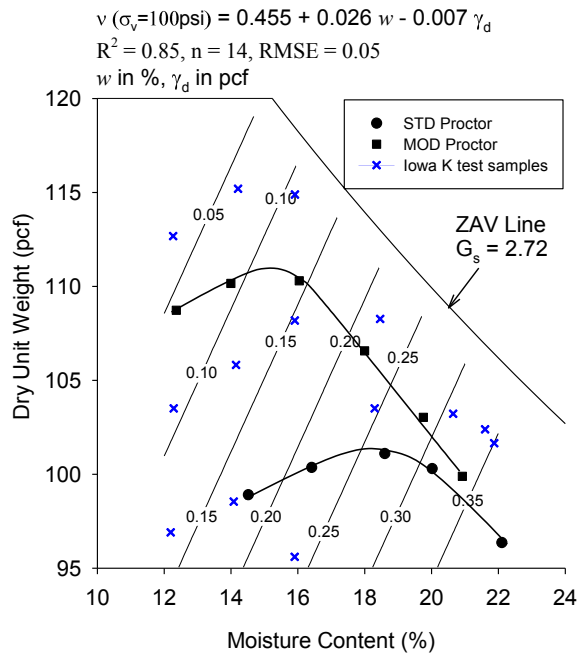


Figure 113. Statistical relationships between Poisson’s ratio, moisture content, and dry unit weight

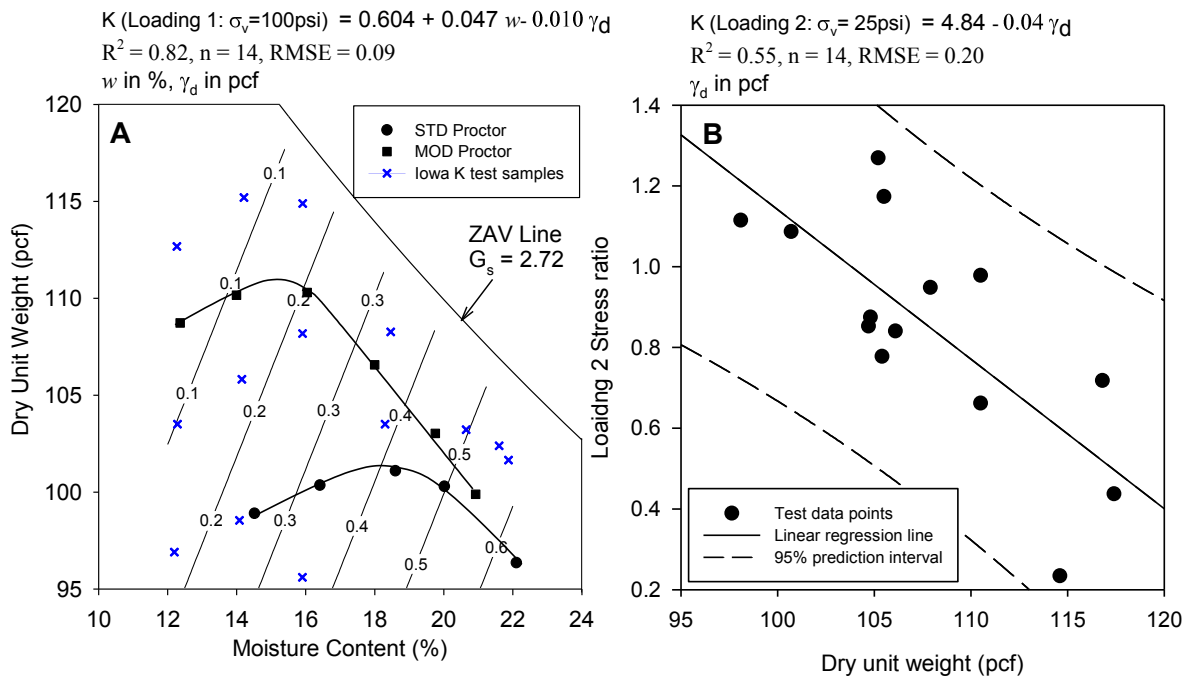


Figure 114. Statistical analysis results for the lateral stress ratio under (A) 100 psi vertical stress of loading 1 and (B) 25 psi vertical stress of loading 2

Soil-to-steel friction

Soil-to-steel frictions were determined based on the differences of the vertical stresses that were measured by the top and bottom load cell during the tests. According to Handy et al. (1978), the slopes of the soil-to-steel friction versus horizontal stress from the mold expansion can be used to calculate soil-to-steel friction angle (ϕ_s) and the intercept with the ordinate is soil-to-steel adhesion (c_s). Figure 115 shows an example of using the method of Handy et al. (1978) to estimate the soil-to-steel adhesions and friction angles based on the first loading data of the Iowa K test. The initial portion of the first loading data were deleted for fitting the linear regression line, because the samples were still in seating stage.

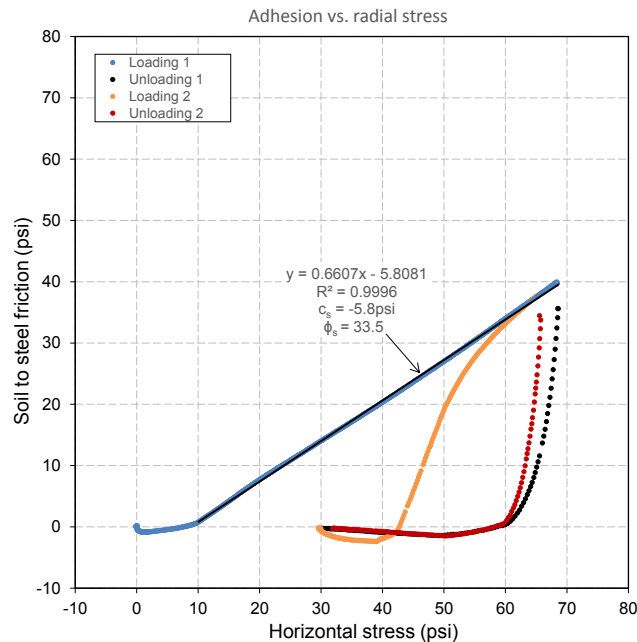


Figure 115. The soil to steel friction of a Western Iowa loess sample ($w\% = 12.2\%$, $\gamma_d = 96.9$ pcf)

Table 42 shows the soil-to-soil and soil-to-steel shear strength parameters of the 14 loess samples. The ϕ_s/ϕ ratios ranged from 0.5 to 1.2, and no specified ratio was determined as often assumed for pile design. The ϕ_s/ϕ ratio decreases as the moisture contents increases, and at a given moisture content, the samples with different dry unit weights show very similar values. All of the soil to steel adhesions determined using the method are negative that may be due to the high elasticity of the Iowa K test mold or the seating issue at the beginning of the tests.

Table 42. Soil to soil and soil to steel shear strength parameters of the loess samples

w (%)	γ_d (pcf)	ϕ (deg.)	ϕ_s (deg.)	ϕ_s/ϕ	c (psi)	c_s (psi)
12.2	96.9	29.5	33.5	1.1	7.3	-5.8
12.3	103.5	40.0	45.0	1.1	9.8	-8.3
12.3	112.7	48.0	46.2	1.0	16.9	-8.2
14.1	98.5	31.9	37.9	1.2	5.5	-5.3
14.1	105.8	36.5	38.5	1.1	13.5	-3.5
14.2	115.2	43.6	38.0	0.9	14.4	-3.2
15.9	95.6	32.3	38.3	1.2	0.5	-5.4
15.9	108.2	40.1	38.9	1.0	10.3	-1.5
15.9	114.9	32.8	30.1	0.9	3.9	-1.1
18.3	103.5	34.6	39.4	1.1	1.6	-5.2
18.5	108.3	28.5	18.2	0.6	-0.3	0.2
20.6	103.2	28.5	23.7	0.8	0.2	-1.9
21.6	102.4	8.6	4.3	0.5	3.5	1.5
21.9	101.6	9.7	5.3	0.5	2.3	0.7

Figure 116 shows two second order polynomial regression model for the ϕ_s and ϕ_s/ϕ of the material. The results shows that both the ϕ_s and ϕ_s/ϕ remain at a relative constant level when the moisture content on the dry of standard Proctor optimum moisture content (i.e., $w_{opt} = 18.6\%$). However, for the samples wet of optimum, the ϕ_s and ϕ_s/ϕ show obvious reductions as the moisture content increases.

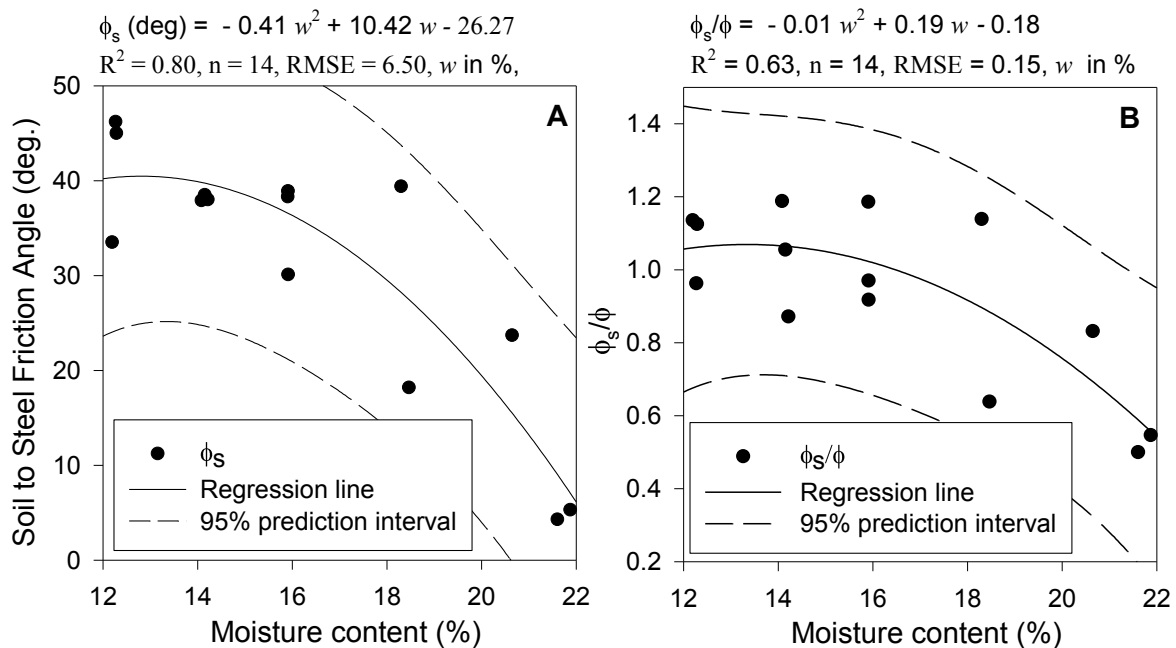


Figure 116. Statistical analysis results for the soil-to-steel friction angles of the western Iowa loess

Summary of the Iowa K test results of western Iowa loess

Table 43 summarizes the Iowa K test results of the 14 western Iowa loess samples. The initial moisture contents and dry unit weights of the samples ranged from 12.2% to 21.9% and 95.6 to 115.2 pcf (STD $w_{opt} = 18.6\%$ and STD $\gamma_{dmax} = 101.1$ pcf).

The undrained soil to soil and soil to steel cohesions and friction angles of the samples were determined based on the first loading data of the Iowa K test. The statistical analysis results showed that both the moisture content and dry unit weight were statistically significant to the undrained soil to soil cohesion and friction angles of the material. Both of the parameters decreased as the moisture content increased and dry unit weight decreased. Significant reduction in the friction angle can be observed when the moisture content was above 21.6%. For the soil to steel friction angles of the material, moisture content is the dominant influence factor. For samples where the moisture content was lower than the standard Proctor optimum moisture content ($w_{opt} = 18.6\%$), the soil to steel friction angles had little change compared to a significant reduction that occurred for samples wet of optimum. The ϕ_s/ϕ ratios ranged from 0.5 to 1.2, and no specified ratio can be determined as often assumed for pile design. Most of the soil to steel cohesions showed negative values that may be the result of the seating issue at the beginning of the tests.

The undrained vertical elastic modulus, Poisson's ratio, and lateral stress ratio under the two loadings of the Iowa K test were measured for each of the samples. The vertical elastic modulus of the samples under the first loading ranged between 2.0 and 9.1 ksi. The multiple regression model showed that the vertical elastic modulus decreased as moisture content increased and dry unit weight increased. The samples under the second loading show higher vertical elastic modulus that ranged between 5.7 and 62.0 ksi. Also, when the moisture content of the samples was below the standard Proctor optimum moisture content, both the Poisson's ratio and lateral stress ratios under the first loading increase as the moisture content increases, and within tests of samples with similar moisture contents both parameters decrease as the dry unit weight increases. However, for the samples wet of optimum, the dry unit weight did not influence the two parameters too much.

Table 43. Summary of the Iowa K test results for western Iowa loess (CFED 1634)

w (%)	Loading 1 Data								Loading 2 Data			
	γ_d (pcf)	c (psi)	ϕ	c_s (psi)	ϕ_s/ϕ	E_v^* (ksi)	ν^{**}	K^{**}	γ_d (pcf)	E_v^* (ksi)	ν^{***}	K^{***}
12.2	96.9	7.3	29.5	-5.8	1.1	3.6	0.18	0.25	105.2	36.0	0.56	1.27
12.3	103.5	9.8	40.0	-8.3	1.1	7.2	0.10	0.13	105.4	62.0	0.43	0.78
12.3	112.7	16.9	48.0	-8.2	1.0	9.1	0.01	0.01	114.6	42.7	0.19	0.23
14.1	98.5	5.5	31.9	-5.3	1.2	4.2	0.18	0.25	100.7	27.7	0.52	1.09
14.1	105.8	13.5	36.5	-3.5	1.1	8.5	0.10	0.12	107.9	46.4	0.49	0.95
14.2	115.2	14.4	43.6	-3.2	0.9	7.7	0.06	0.06	117.4	58.3	0.30	0.44
15.9	95.6	0.5	32.3	-5.4	1.2	2.0	0.22	0.31	98.1	19.2	0.53	1.12
15.9	108.2	10.3	40.1	-1.5	1.0	8.5	0.10	0.12	110.5	53.2	0.39	0.66
15.9	114.9	3.9	32.8	-1.1	0.9	7.2	0.18	0.25	116.8	24.5	0.41	0.72
18.3	103.5	1.6	34.6	-5.2	1.1	4.7	0.19	0.26	106.1	20.5	0.45	0.84
18.5	108.3	-0.3	28.5	0.2	0.6	5.1	0.24	0.35	110.5	10.6	0.49	0.98
20.6	103.2	0.2	28.5	-1.9	0.8	4.2	0.24	0.35	105.5	8.1	0.54	1.17
21.6	102.4	3.5	8.6	1.5	0.5	4.3	0.39	0.67	104.8	7.5	0.47	0.87
21.9	101.6	2.3	9.7	0.7	0.5	4.2	0.39	0.67	104.7	5.7	0.46	0.85

Notes:

* Parameters determined between 50 to 100 psi vertical stress

** Parameters determined under 100 psi vertical stress

*** Parameters determined under 25 psi vertical stress

Texas fat clay (CFED 2043)

Thirteen Texas fat clay samples with varying moisture content and dry unit weight combinations were prepared to evaluate how changes in the moisture content and dry unit weight influenced the shear strength and stiffness properties of this material.

Undrained cohesion and internal friction angle

The undrained cohesion and friction angle of the samples were determined based on the Iowa K test first loading data. Direct shear tests were conducted on four selected Iowa K test samples to determine drained cohesions and friction angles of the material. The shear stage lasted from one to four days for different samples. Olson (1989) indicated, for highly overconsolidated clays, the time-settlement curve cannot yield useful coefficient of consolidation, so a time to failure ranging from one to four days should be used based on experience. Three samples from each of the Iowa K test sample were prepared for 36, 74, and 146 psi normal stress direct shear tests. Table 39 summarizes the Iowa K test undrained cohesion and friction angle of the 13 samples and the direct shear test results.

The undrained cohesions determined by the Iowa K test ranged from 9.1 psi to 46.9 psi and at a given moisture content. The undrained friction angles decrease as the moisture content increases. Compared to Iowa K test results, the drained cohesion and friction angle measured using direct shear test show much lower values.

Table 44. Iowa K test and direct shear test results of Texas fat clay

K test w (%)	K test γ_d (pcf)	K test c (psi)	K test ϕ (deg.)	DS test w (%)	DS test γ_d^* (pcf)	DS test c' (psi)	DS test ϕ' (deg.)
15.7	83.0	10.4	28.6				
15.7	92.7	21.5	32.1				
16.6	100.4	39.6	34.1			—	
18.2	80.5	9.3	26.6				
18.6	91.9	29.7	19.7	18.6	98.2	8.3	11.4
19.8	104.9	47.9	20.2			—	
22.5	85.1	15.3	16.9	22.8	96.2	7.9	12.3
21.6	92.7	29.2	10.1				
22.9	103.6	47.1	5.6			—	
24.5	81.6	10.9	14.7	25.7	102.4	19.0	5.4
25.6	91.6	16.3	9.0			—	
28.2	83.6	6.9	6.4	27.5	100.9	12.5	6.8
27.8	93.7	13.0	4.7			—	

Notes: — Test not performed, and * Average initial dry unit weight of the three samples

Statistical analyses were performed on the Iowa K test results to determine the relationships between moisture content, dry unit weight, and the shear strength parameters of the material. Two simple linear regression models for the undrained cohesion and friction angle are shown in Figure 117. Figure 117A shows the undrained cohesion increases as the dry unit weight increases, but the moisture content variations of the material is not statistically significant to the undrained cohesion. Figure 117B shows that the undrained friction angle decreases as the moisture content increases. Both of the two parameters varied in a big range as the of the influence variables change.

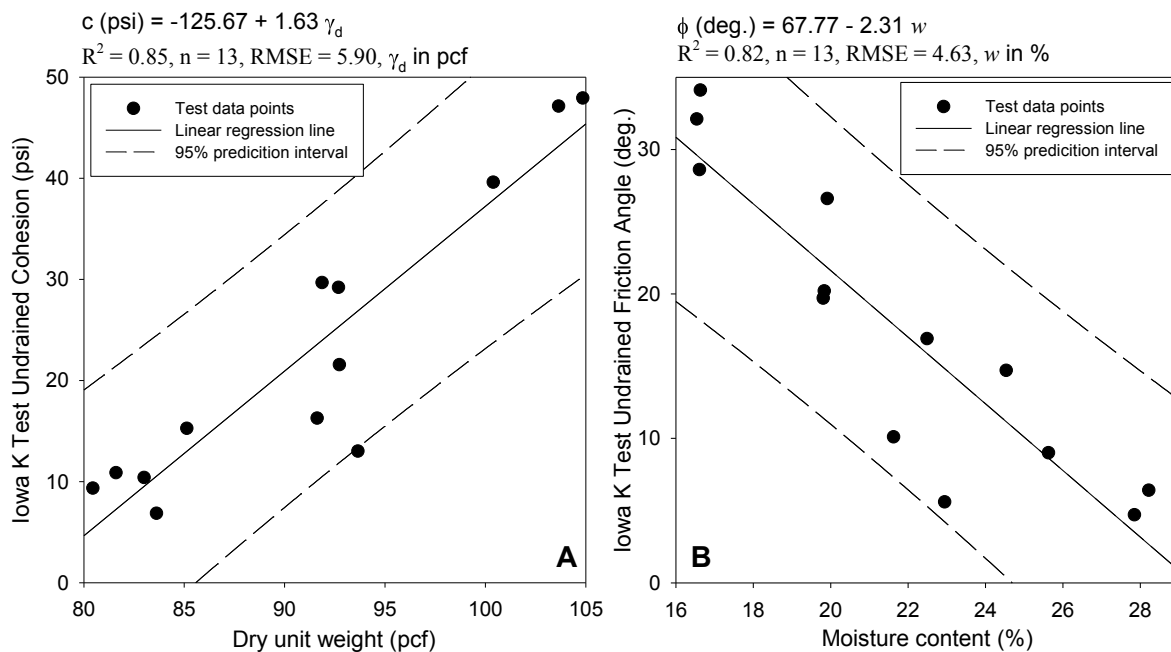


Figure 117. The statistical relationships between the moisture-density and (A) undrained cohesion and (B) internal friction angle of Texas fat clay

According to Seed et al. (1960), when compacted cohesive soils with low moisture content, it behaves more likely a granular materials, and the shear strength of the soils primarily provided by the interlocking of the granular particles. The high friction angles were observed for the samples with low moisture contents which can support this statement. Compared to the direct shear test results, the undrained cohesion determined by the Iowa K test shows much higher values for the samples with low moisture content. The high undrained cohesions may be due to the actual stress path cannot be determined when the

sample under low vertical stress, because at the beginning of the test, there is still space between the sample and the Iowa K test mold.

Vertical elastic modulus

The vertical stress-strain relationships of the 13 samples were determined for both of the two loadings during the Iowa K test. Vertical elastic modulus (E_v) of each sample under 50 to 100 psi vertical pressure were calculated.

Table 45 summarizes the vertical elastic modulus of the 13 samples under the two loadings of the tests. The second loading vertical elastic modulus of the samples are much higher than the first loading.

Table 45. Iowa K test vertical elastic modulus of the Texas fat clay samples for loadings 1 and 2 of the Iowa K test

w (%)	Loading 1 γ_d (pcf)	Loading 1 E_v (ksi) ($\sigma_v = 50-100$ psi)	Loading 2 γ_d (pcf)	Loading 2 E_v (ksi) ($\sigma_v = 50-100$ psi)
15.7	83.0	2.0	88.7	44.3
15.7	92.7	8.6	95.8	37.0
16.6	100.4	16.5	102.5	32.9
18.2	80.5	0.7	91.0	18.5
18.6	91.9	3.3	99.2	66.5
19.8	104.9	13.6	107.6	51.0
22.5	85.1	0.8	96.7	18.6
21.6	92.7	1.8	103.1	37.9
22.9	103.6	4.5	105.8	52.8
24.5	81.6	0.7	99.3	16.1
25.6	91.6	2.1	101.1	32.1
28.2	83.6	0.6	92.4	3.5
27.8	93.7	2.4	98.1	27.8

Figure 118 shows two multiple linear regression models for the undrained vertical elastic modulus of the samples under first and second loading. The statistical analysis results show that both of the moisture content and dry unit weight are statistically significant to the undrained vertical elastic modulus of the material, and the undrained vertical elastic modulus decreases as the moisture content increases and dry unit weight decreases. The two statistical

models give similar trends of variations under the two loadings. The values of the second loading are about five times higher than first loading.

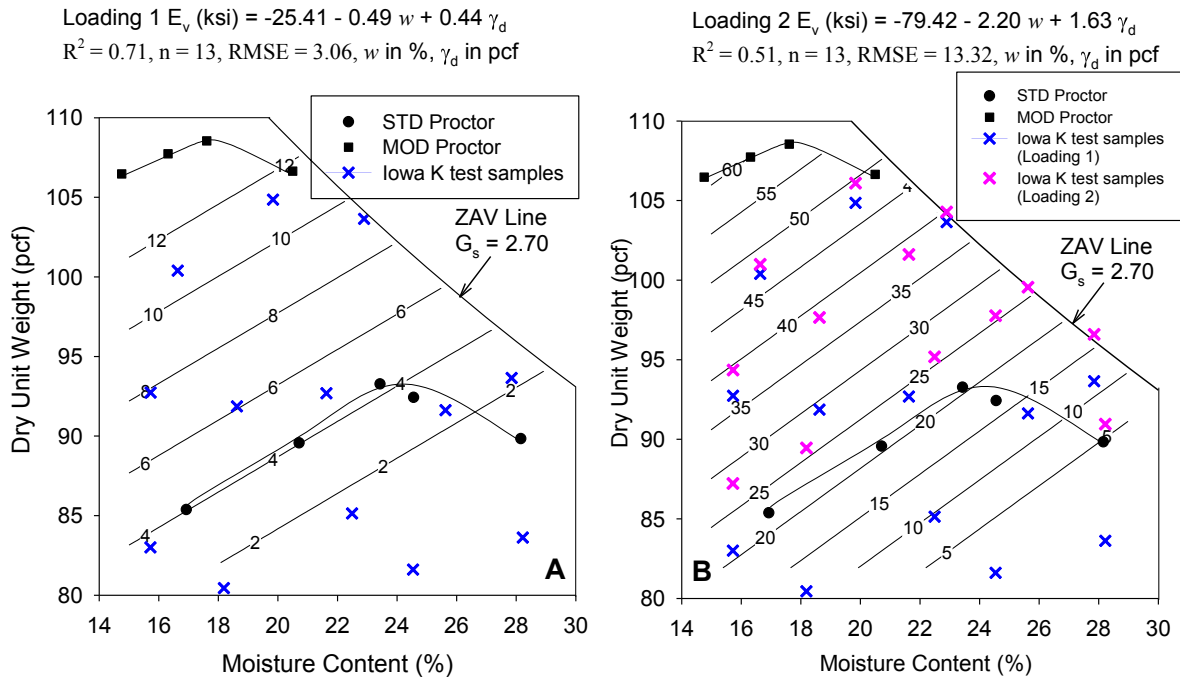


Figure 118. Statistical relationships between moisture content, dry unit weight, and vertical elastic modulus for (A) loading 1 and (B) loading 2

Fifty in situ light weight deflectometer (LWD) tests using Zorn 200 mm plate were conducted on the Texas fat clay to determine the elastic modulus (E_{LWD-Z2}) of the material with varying moisture content and dry unit weight combinations (White, 2010). All the raw data are provided in Appendix I. Figure 119A shows dry unit weight and moisture content of the 50 LWD test points with respect to contour plot that generated using the Iowa K test results. According to the statistical model, the elastic modulus of the LWD test points are between 1 to 9 ksi and increased as dry unit weight increased. Figure 119B shows a simple linear regression model generated based on the in-situ LWD test results. The statistical analysis results show that the moisture content is not statistically significant to E_{LWD-Z2} . The E_{LWD-Z2} increases as the dry unit weight increases and most of the data points fall in a range from 2 to 7 ksi. Compare to the Iowa K test statistical model, the in-situ LWD test results show great agreement.

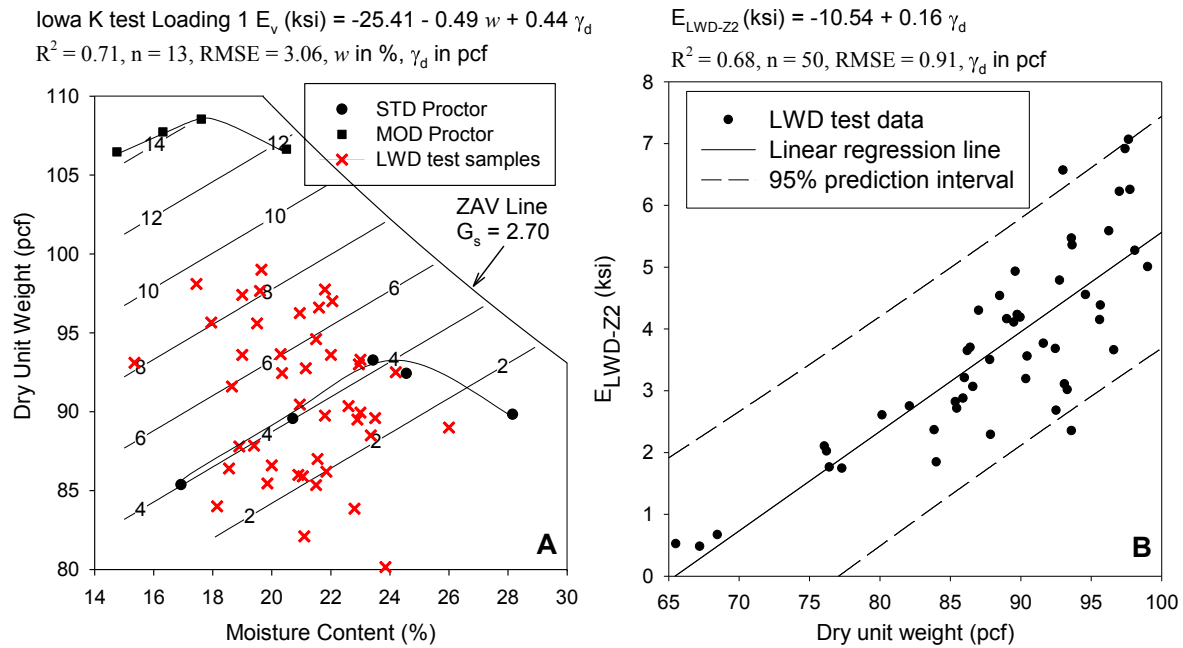


Figure 119. (A) Dry unit weight and moisture content of in-situ LWD test points and (B) A simple linear regression model for the LWD tests

Poisson’s ratio and lateral stress ratio

The Poisson’s ratio and lateral stress ratio of the 13 samples were calculated based on the vertical and horizontal stress and strain data of the Iowa K test. The variations of the Poisson’s ratio and lateral stress ratio of all the samples show similar trends with the western Iowa loess samples. Both of the two parameters increased rapidly at the beginning of the tests and then maintained at a constant level as the vertical stresses increased in the first loading. However, during the second loading, the two parameters decreased as the vertical and horizontal stress increased and then reached to a relatively constant level.

The Poisson’s ratio and lateral stress ratio of the samples under 100 psi vertical stress of the first loading and 30 psi of the second loading are selected for statistical analyses (Table 46). The first loading Poisson’s ratio and lateral stress of the samples show that both of the parameters increase as the moisture content increases, and within tests of samples with similar moisture contents both parameters decrease as the dry unit weight increases.

Table 46. Iowa K test Poisson's ratio and lateral stress ratio of the Texas fat clay samples for loadings 1 and 2

w (%)	Loading 1 γ_d (pcf)	Loading 1 ν ($\sigma_v = 100$ psi)	Loading 1 K ($\sigma_v = 100$ psi)	Loading 2 γ_d (pcf)	Loading 2 ν ($\sigma_v = 30$ psi)	Loading 2 K ($\sigma_v = 30$ psi)
15.7	83.0	0.16	0.22	88.7	0.42	0.76
15.7	92.7	0.06	0.08	95.8	0.40	0.68
16.6	100.4	0.05	0.06	102.5	0.36	0.58
18.2	80.5	0.20	0.27	91.0	0.34	0.58
18.6	91.9	0.08	0.09	99.2	0.37	0.67
19.8	104.9	0.04	0.05	107.6	0.32	0.49
22.5	85.1	0.24	0.33	96.7	0.37	0.64
21.6	92.7	0.15	0.19	103.1	0.51	1.02
22.9	103.6	0.11	0.15	105.8	0.54	1.35
24.5	81.6	0.29	0.43	99.3	0.44	0.82
25.6	91.6	0.29	0.44	101.1	-0.05	1.27
28.2	83.6	0.35	0.61	92.4	0.40	0.80
27.8	93.7	0.16	0.22	98.1	0.54	1.62

A statistical model was generated for the Poisson's ratio under 100 psi vertical stress of the first loading (Figure 120). The model shows the Poisson's ratio ranges from 0.05 to 0.35 and increases as the moisture content increases and dry unit weight decreases.

Figure 121 shows two statistical models for the lateral stress ratios under the two loadings of the tests. The lateral stress ratios under 100 psi vertical stress of the first loading and 30 psi of the second loading were selected for the statistical analyses. The K values of the different samples under first loading varies between 0.1 and 0.6, and both the dry unit weight and moisture content are statistically significant. However, the K values of the samples under second loading show higher values that ranged from 0.5 to 1.5.

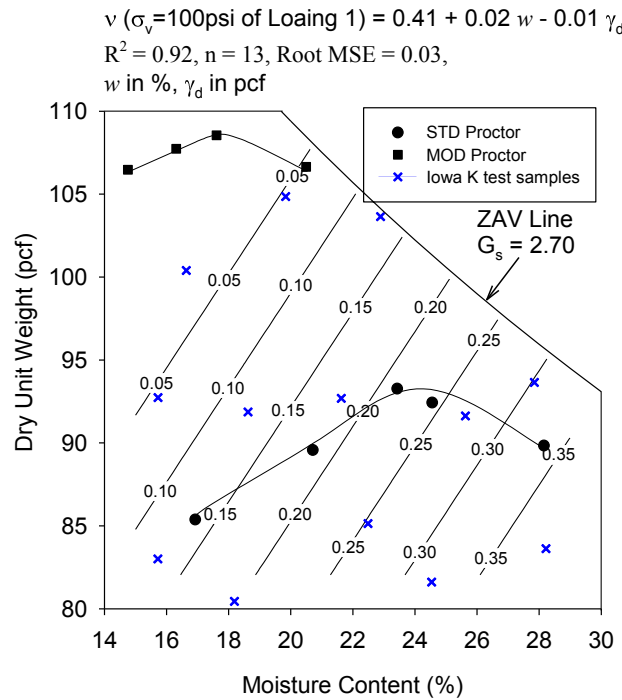


Figure 120. Statistical relationships between moisture content, dry unit weight, and Poisson's ratio for first loading

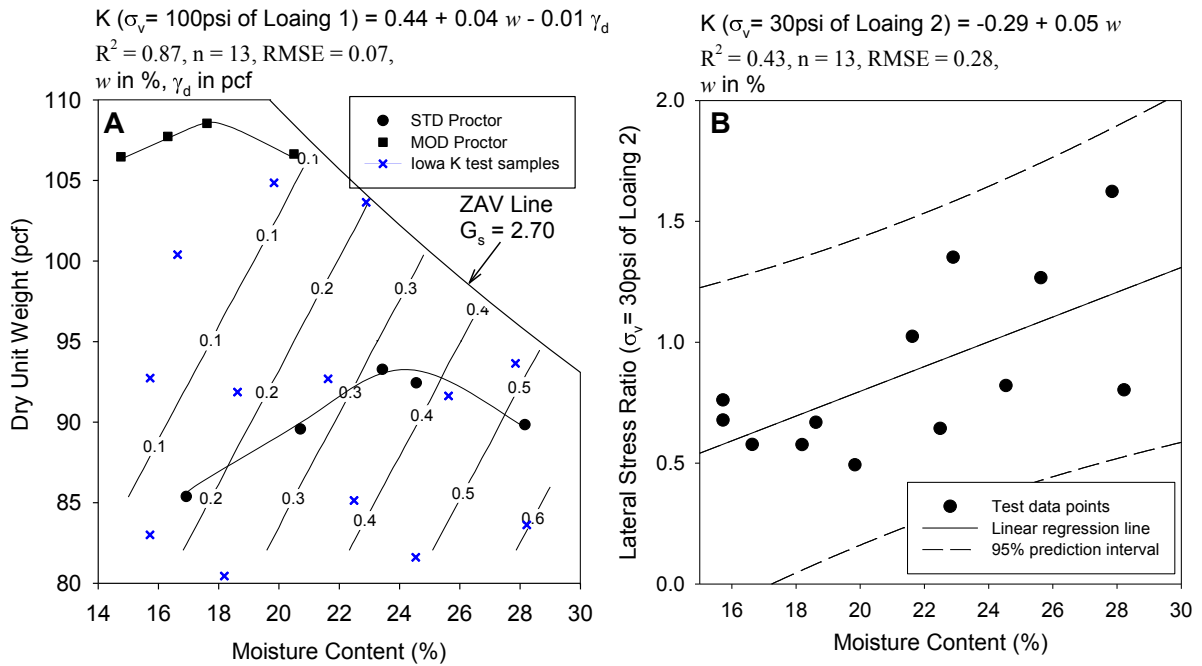


Figure 121. Statistical analysis results for the lateral stress ratio under 100psi vertical pressure of loading 1 (A) and 25psi vertical pressure of loading 2 (B)

Soil to steel friction

The soil-to-steel friction parameters were evaluated for the 13 Texas fat clay samples by the Iowa K test. Table 47 shows the soil-to-soil and soil-to-steel shear strength parameters of the 13 samples. The soil to steel friction angle of some samples is higher than the soil to soil friction angle. The ϕ_s/ϕ ratios increases as the moisture content increases on the dry side of standard Proctor optimum moisture content ($w_{opt} = 23.8\%$), and then an obvious reduction occurred for the samples wet of optimum. At a given moisture content, the samples with different dry unit weights show similar ϕ_s/ϕ . Some negative soil to steel adhesions were observed for the samples with low moisture content that may be caused by the same issue which has been discussed above.

Table 47. Soil to soil and soil to steel shear strength parameters of the Texas fat clay samples

w (%)	γ_d (pcf)	ϕ (deg.)	ϕ_s (deg.)	ϕ_s/ϕ	c (psi)	c_s (psi)
15.7	83.0	28.6	27.2	1.0	9.1	-2.1
15.7	92.7	32.1	30.8	1.0	18.2	-8.9
16.6	100.4	34.1	33.0	1.0	32.8	-10.4
18.2	80.5	26.6	26.9	1.0	17.8	-1.1
18.6	91.9	19.7	28.5	1.4	27.9	-2.0
19.8	104.9	20.2	24.9	1.2	45.0	-2.3
22.5	85.1	16.9	21.1	1.2	14.6	0.6
21.6	92.7	10.1	14.9	1.5	28.7	3.1
22.9	103.6	5.6	8.0	1.4	46.9	12.0
24.5	81.6	14.7	10.4	0.7	10.5	4.3
25.6	91.6	9.0	1.7	0.2	25.6	14.1
28.2	83.6	6.4	11.2	1.8	9.6	0.3
27.8	93.7	4.7	1.3	0.3	13.0	10.3

Figure 122 shows a simple linear regression model for the soil-to-steel friction angles of the material. The results shows that the ϕ_s decreases as the moisture content increases. The dry unit weight does not significantly influence the soil to steel friction angle of the material.

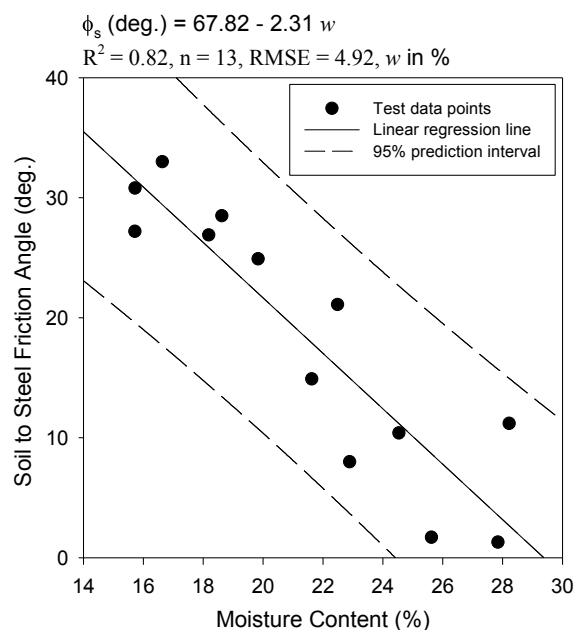


Figure 122. Statistical analysis results for the soil-to-steel friction angles of Texas fat clay

Summary of the Iowa K test results of Texas fat clay

Table 48 summarizes the Iowa K test results of the 13 Texas fat clay samples. The initial moisture contents and dry unit weights of the samples ranged from 15.7% to 28.2% and 80.5 to 104.9 pcf (STD $w_{opt} = 23.8\%$ and STD $\gamma_{dmax} = 93.4$ pcf).

The undrained soil to soil cohesions ranged from 6.9 to 47.9 psi and increased as the dry unit weight increased. The undrained friction angles decreased from 34.1° to 4.7° as the moisture content of the samples increased. For the soil to steel friction angles of the material, moisture content is the dominant influence factor. The ϕ_s/ϕ ranged from 0.2 to 1.8 and increased as the moisture content increased. Some negative soil to steel cohesions were observed for samples with low moisture content.

The statistical analyses results showed that the vertical elastic modulus of the samples decreases as moisture content increases and dry unit weight decreases. The vertical elastic modulus of the second loading is about five times higher than the first loading.

Table 48. Summary of the Iowa K test results for Texas fat clay (CFED 2043)

w (%)	Loading 1 Data								Loading 2 Data			
	γ_d (pcf)	c (psi)	ϕ	c_s (psi)	ϕ_s/ϕ	E_v * (ksi)	ν **	K **	γ_d (pcf)	E_v * (ksi)	ν ***	K ***
15.7	83.0	10.4	28.6	-2.1	1.0	2.0	0.16	0.22	88.7	44.3	0.42	0.76
15.7	92.7	21.5	32.1	-8.9	1.0	8.6	0.06	0.08	95.8	37.0	0.40	0.68
16.6	100.4	39.6	34.1	-10.4	1.0	16.5	0.05	0.06	102.5	32.9	0.36	0.58
18.2	80.5	9.3	26.6	-1.1	1.0	0.7	0.20	0.27	91.0	18.5	0.34	0.58
18.6	91.9	29.7	19.7	-2.0	1.4	3.3	0.08	0.09	99.2	66.5	0.37	0.67
19.8	104.9	47.9	20.2	-2.3	1.2	13.6	0.04	0.05	107.6	51.0	0.32	0.49
22.5	85.1	15.3	16.9	0.6	1.2	0.8	0.24	0.33	96.7	18.6	0.37	0.64
21.6	92.7	29.2	10.1	3.1	1.5	1.8	0.15	0.19	103.1	37.9	0.51	1.02
22.9	103.6	47.1	5.6	12.0	1.4	4.5	0.11	0.15	105.8	52.8	0.54	1.35
24.5	81.6	10.9	14.7	4.3	0.7	0.7	0.29	0.43	99.3	16.1	0.44	0.82
25.6	91.6	16.3	9.0	14.1	0.2	2.1	0.29	0.44	101.1	32.1	-0.05	1.27
28.2	83.6	6.9	6.4	0.3	1.8	0.6	0.35	0.61	92.4	3.5	0.40	0.80
27.8	93.7	13.0	4.7	10.3	0.3	2.4	0.16	0.22	98.1	27.8	0.54	1.62

Notes:

* Parameters determined between 50 to 100 psi vertical stress

** Parameters determined under 100 psi vertical stress

*** Parameters determined under 30 psi vertical stress

WCF fly ash (CFED 2053)

The Iowa K test was conducted on WCF fly ash to evaluate how changes in the moisture content and dry unit weight influenced the shear strength and stiffness of the compacted samples. Thirteen samples with varying moisture content and dry unit weight combinations were prepared. The Iowa K test data and statistical analysis results are discussed below.

Undrained cohesion and internal friction angle

Table 49 summarizes the undrained cohesion and friction angle of the 13 samples determined by the Iowa K test. Direct shear tests were conducted on each Iowa K test sample to determine drained cohesions and friction angles of the material. Three samples from each Iowa K test sample were prepared for 23, 45, 90 psi normal stress direct shear tests. The undrained friction angle determined by the Iowa K test of all the 13 samples show higher values than the drained friction angle. This may be due to the samples were compacted by the variable confining pressure provided by the high elasticity mold. The undrained cohesion of the samples show negative values that are not theoretically possible. The direct shear test results show that the drained cohesions ranged between 7.0 and 18.5 psi that are also too high for this cohesionless material.

Table 49. Iowa K test and direct shear test results of WCF fly ash

K test w (%)	K test γ_d (pcf)	K test c (psi)	K test ϕ (deg.)	DS test w (%)	DS test γ_d^* (pcf)	DS test c' (psi)	DS test ϕ' (deg.)
15.9	84.4	-3.4	32.6	15.6	81.5	18.5	31.2
15.6	85.8	-0.1	40.5	15.4	85.1	8.8	34.2
17.4	81.2	-0.5	36.0	17.2	78.1	7.0	29.9
17.7	84.2	-1.9	42.6	17.5	81.8	13.6	29.3
18.0	86.6	-1.7	43.4	18.0	86.0	10.8	33.8
18.9	82.7	-3.9	40.5	19.5	82.6	12.1	30.2
18.9	85.2	-2.4	41.3	19.7	83.8	10.0	34.3
21.2	79.6	-2.1	32.7	21.7	82.3	11.7	29.4
22.4	84.4	-3.2	42.2	22.4	84.1	14.4	31.2
24.3	82.3	-3.3	40.0	23.9	84.1	11.7	33.5
24.4	81.5	2.3	34.2	23.6	85.1	10.0	32.8
25.6	78.7	-3.4	32.6	25.3	83.3	12.3	31.4
27.5	79.5	-6.8	33.9	25.0	84.9	12.8	31.0

Notes:

— Test not performed

* Average initial dry unit weight of the three samples

To determine the true drained cohesion of the material, six direct shear test samples were trimmed from a 6 in. Proctor sample ($w\% = 18.9\%$ and $\gamma_d = 84.4$ pcf). Figure 123 shows the failure envelopes determined based on the six tests results. Based on the six data points, the Mohr-Coulomb failure envelop is a curved line and the drained cohesion is very close to zero. In Figure 123, the linear regression line used only to fit the three high normal stress tests (24, 47, and 70 psi) give 8.2 psi for the drained cohesion. Therefore, the direct shear tests with high normal stresses cannot be used to determine the drained cohesion of the material.

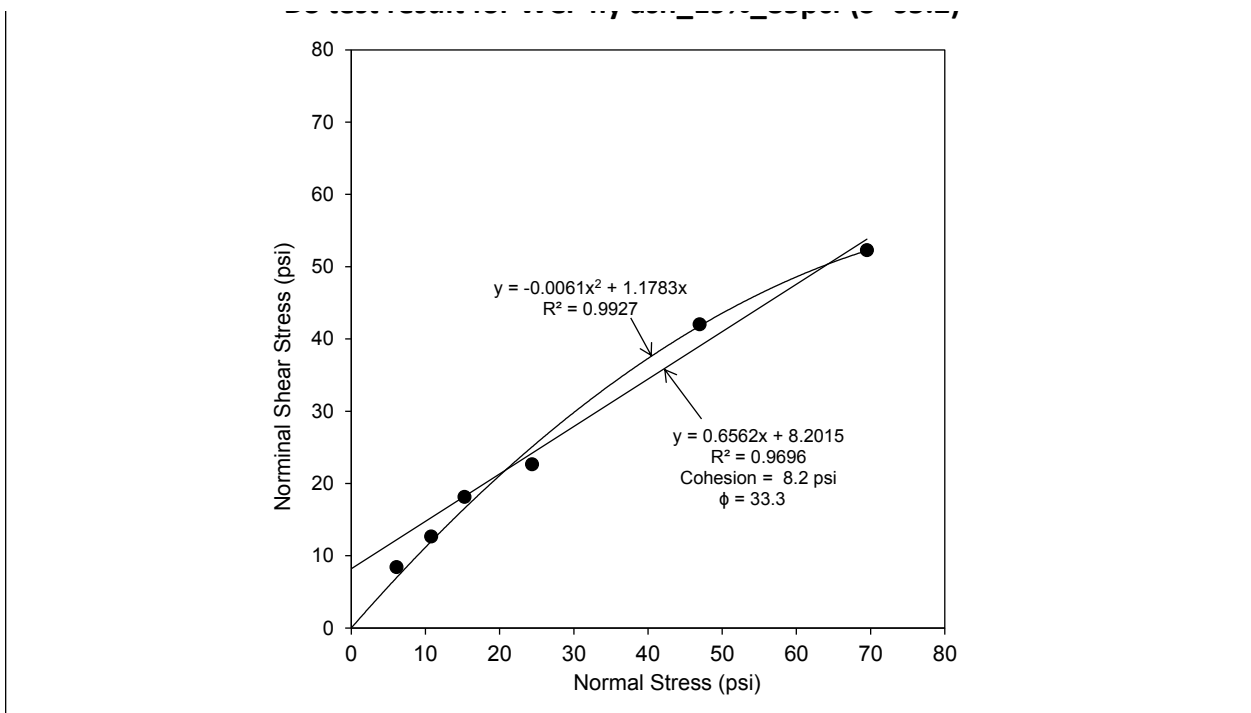


Figure 123. Direct shear test results for determining the cohesion of a WCF fly ash sample ($w\% = 18.9\%$ and $\gamma_d = 84.4$ pcf)

Statistical analyses were performed on the Iowa K test and direct shear test results. Figure 124A shows that the undrained friction angle increases as the dry unit weight increases. The moisture content is not statistically significant to the undrained friction angle of the material. For high moisture content samples, some moisture was squeezed out during the tests, because WCF fly ash is a free-draining material, so it may be a reason why the relationship between the moisture content and undrained friction angle is not statistically determined based on the tests data. Figure 124B shows the drained friction angle determined using direct shear tests.

From the two statistical models, the Iowa K test results show higher values than the direct shear test results for the samples with high dry unit weight.

White, D.J. et al. 2012 (unpublished final report submitted to the Tennessee Valley Authority) reported that 35.2° as the average drained friction angle and 0 psi for the cohesion of this material based on some in situ borehole shear test (BST) results. The average Iowa K test undrained friction angles is 37.9° which is very close but slightly higher.

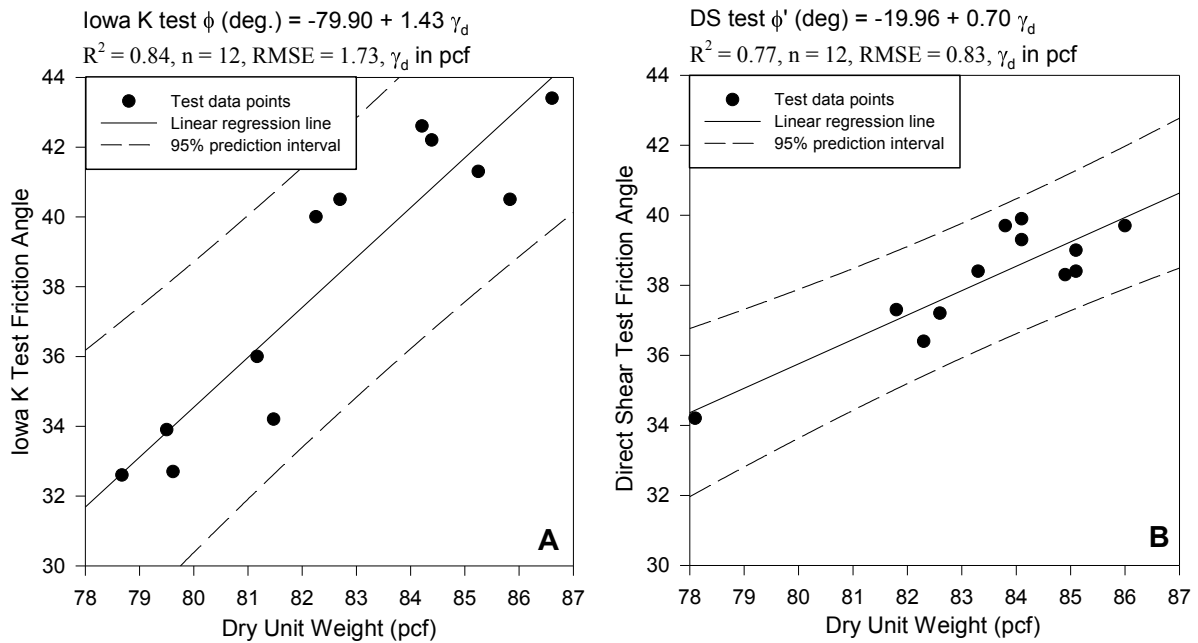


Figure 124. Statistical analysis results for the (A) Iowa K test undrained and (B) drained friction angle of the WCF fly ash

Vertical elastic modulus

Table 50 summarizes the vertical elastic modulus (E_v) of the 13 samples under 50 to 100 psi vertical pressure of the two loadings. The second loading vertical elastic modulus of the same samples are about four times higher than the first loading elastic modulus. For the first loading, the elastic modulus ranged between 5.5 and 12.4 ksi for samples with different moisture-density combinations, and 18.3 to 45.2 ksi for the second loading.

Table 50. Iowa K test vertical elastic modulus of the WCF fly ash samples for loadings 1 and 2

w (%)	Loading 1 γ_d (pcf)	Loading 1 E_v (ksi) ($\sigma_v = 50-100$ psi)	Loading 2 γ_d (pcf)	Loading 2 E_v (ksi) ($\sigma_v = 50-100$ psi)
15.9	84.4	11.0	85.9	44.2
15.6	85.8	7.2	88.0	30.7
17.4	81.2	8.8	82.8	33.9
17.7	84.2	11.7	85.1	40.7
18.0	86.6	12.4	88.1	45.2
18.9	82.7	9.6	84.3	36.5
18.9	85.2	8.1	88.4	33.1
21.2	79.6	6.5	83.3	22.3
22.4	84.4	10.8	88.7	34.3
24.3	82.3	9.5	84.1	30.5
24.4	81.5	6.8	18.9	18.9
25.6	78.7	10.7	34.4	34.4
27.5	79.5	5.5	18.3	18.3

Poisson's ratio and lateral stress ratio

The Poisson's ratio (ν) and lateral stress ratio (K) of the 13 WCF samples were calculated based on the Iowa K test results. The two parameters under 100 psi vertical stress of the first loading and 30 psi of the second loading were selected for statistical analyses (Table 51). The data shows that the average Poisson's ratio is 0.18 and the lateral stress ratio is 0.27 of the 13 samples under 100 psi of the first loading. Under 30 psi of the second loading, the average Poisson's ratio is 0.38 and the average lateral stress ratio is 0.66.

Two multiple linear regression models were generated for the Poisson's ratio and lateral stress ratio under 100 psi vertical stress of the first loading (Figure 121). The models show that both of the parameters increases as the moisture content increases and dry unit weight decreases. For the second loading data, the statistical relationships between the Poisson's ratio and lateral stress ratio were not determined.

Table 51. Iowa K test Poisson’s ratio and lateral stress ratio of the WCF fly ash samples for loadings 1 and 2

w%	Loading 1 γ_d (pcf)	Loading 1 ν ($\sigma_v = 100$ psi)	Loading 1 K ($\sigma_v = 100$ psi)	Loading 2 γ_d (pcf)	Loading 2 ν ($\sigma_v = 30$ psi)	Loading 2 K ($\sigma_v = 30$ psi)
15.9	84.4	0.14	0.20	85.9	0.35	0.58
15.6	85.8	0.15	0.21	88.0	0.32	0.51
17.4	81.2	0.18	0.27	82.8	0.38	0.67
17.7	84.2	0.13	0.21	85.1	0.32	0.52
18.0	86.6	0.14	0.20	88.1	0.40	0.73
18.9	82.7	0.17	0.26	84.3	0.38	0.64
18.9	85.2	0.17	0.24	88.4	0.35	0.57
21.2	79.6	0.22	0.34	83.3	0.41	0.71
22.4	84.4	0.16	0.24	88.7	0.35	0.56
24.3	82.3	0.17	0.26	84.1	0.37	0.62
24.4	81.5	0.22	0.33	86.5	0.48	0.95
25.6	78.7	0.20	0.35	84.5	0.42	0.71
27.5	79.5	0.25	0.38	86.3	0.41	0.74

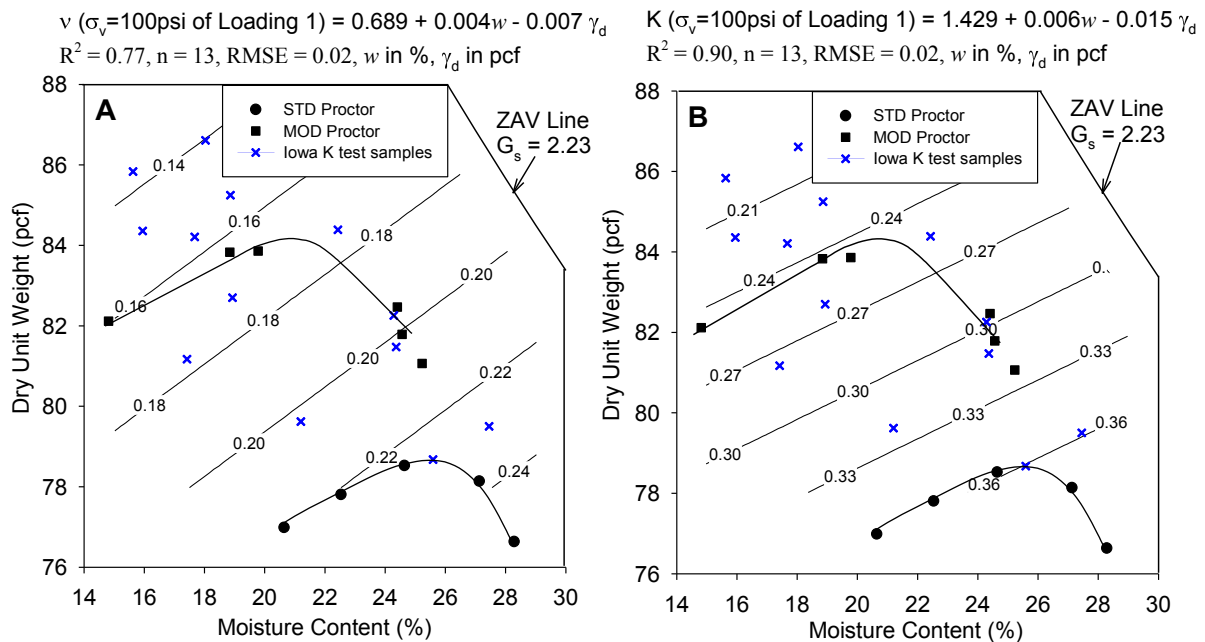


Figure 125. Statistical analysis results for the (A) Poisson’s ratio and (B) lateral stress ratio of WCF fly ash under 100psi vertical pressure of loading 1

Soil to steel friction

The soil-to-steel friction parameters were evaluated for the WCF fly ash samples by the Iowa K test. Table 52 summarizes the soil-to-soil and soil-to-steel shear strength parameters of the 13 samples. The data shows that the ϕ_s/ϕ of the samples are relatively independent of moisture content and dry unit weight changes of the samples. Most ϕ_s/ϕ of the samples show a value of 0.6 or 0.7. Therefore, based on the Iowa K test results, a ϕ_s/ϕ ratio of 0.6 or 0.7 may be used as often assumed in the conventional method for pile design. The negative soil to steel adhesions were calculated for the all of the samples. However, based on the observation, there is no any adhesion between the samples and the steel mold.

Table 52. Soil to soil and soil to steel shear strength parameters of the WCF fly ash samples

w (%)	γ_d (pcf)	ϕ (deg.)	ϕ_s (deg.)	ϕ_s/ϕ	c (psi)	c_s (psi)
15.9	84.4	32.6	18.0	0.6	-3.4	-2.1
15.6	85.8	40.5	26.9	0.7	-0.1	-1.3
17.4	81.2	36.0	22.9	0.6	-0.5	-4.5
17.7	84.2	42.6	26.0	0.6	-1.9	-3.0
18.0	86.6	43.4	25.3	0.6	-1.7	-2.3
18.9	82.7	40.5	25.9	0.6	-3.9	-4.4
18.9	85.2	41.3	29.5	0.7	-2.4	-6.8
21.2	79.6	32.7	23.9	0.7	-2.1	-4.7
22.4	84.4	42.2	25.8	0.6	-3.2	-5.0
24.3	82.3	40.0	26.0	0.7	-3.3	-4.5
24.4	81.5	34.2	26.5	0.8	2.3	-7.1
25.6	78.7	32.6	26.7	0.8	-3.4	-4.8
27.5	79.5	33.9	25.7	0.8	-6.8	-5.7

Summary of the Iowa K test results of WCF fly ash

Table 53 summarizes the Iowa K test results of the 13 WCF fly ash samples. The initial moisture contents and dry unit weights of the samples ranged from 15.6% to 27.9% and 78.7 to 86.6 pcf (STD $w_{opt} = 25.8\%$ and STD $\gamma_{dmax} = 78.9$ pcf).

The undrained soil to soil friction angles of the samples ranged between 32.6° to 43.4°. The average value is 37.9°. The statistical analysis result showed that the undrained friction angles increase as the dry unit weight increases, and the moisture content is not statistically significant to the undrained friction angles of the material. The undrained cohesions

determined using the Iowa K test showed negative values for this cohesionless material. Also, all of the soil to steel cohesions gave negative values. The ϕ_s/ϕ of the samples with varying moisture content and dry unit weight combinations was very constant that ranged between 0.6 and 0.8.

The vertical elastic modulus of the samples under the first loading ranged from 5.5 to 12.4 ksi and the second loading vertical elastic modulus ranged between 18.3 to 45.2 ksi. However, the relationships between moisture content, dry unit weight, and vertical elastic modulus were not statistically determined for this material. The statistical models for the Poisson's and lateral stress ratios under the first loading showed that the two parameters increase as the moisture content increases and dry unit weight decreases. Under 30 psi vertical stress of the second loading, the Poisson's ratio ranged from 0.32 to 0.48 and lateral stress ratio ranged from 0.51 to 0.95.

Table 53. Summary of the Iowa K test results for WCF fly ash (CFED 2053)

w (%)	Loading 1 Data								Loading 2 Data			
	γ_d (pcf)	c (psi)	ϕ	c_s (psi)	ϕ_s/ϕ	E_v^* (ksi)	ν^{**}	K ^{**}	γ_d (pcf)	E_v^* (ksi)	ν^{***}	K ^{***}
15.9	84.4	-3.4	32.6	-2.1	0.6	11.0	0.14	0.20	85.9	44.2	0.35	0.58
15.6	85.8	-0.1	40.5	-1.3	0.7	7.2	0.15	0.21	88.0	30.7	0.32	0.51
17.4	81.2	-0.5	36.0	-4.5	0.6	8.8	0.18	0.27	82.8	33.9	0.38	0.67
17.7	84.2	-1.9	42.6	-3.0	0.6	11.7	0.13	0.21	85.1	40.7	0.32	0.52
18.0	86.6	-1.7	43.4	-2.3	0.6	12.4	0.14	0.20	88.1	45.2	0.40	0.73
18.9	82.7	-3.9	40.5	-4.4	0.6	9.6	0.17	0.26	84.3	36.5	0.38	0.64
18.9	85.2	-2.4	41.3	-6.8	0.7	8.1	0.17	0.24	88.4	33.1	0.35	0.57
21.2	79.6	-2.1	32.7	-4.7	0.7	6.5	0.22	0.34	83.3	22.3	0.41	0.71
22.4	84.4	-3.2	42.2	-5.0	0.6	10.8	0.16	0.24	88.7	34.3	0.35	0.56
24.3	82.3	-3.3	40.0	-4.5	0.7	9.5	0.17	0.26	84.1	30.5	0.37	0.62
24.4	81.5	2.3	34.2	-7.1	0.8	6.8	0.22	0.33	86.5	18.9	0.48	0.95
25.6	78.7	-3.4	32.6	-4.8	0.8	10.7	0.20	0.35	84.5	34.4	0.42	0.71
27.5	79.5	-6.8	33.9	-5.7	0.8	5.5	0.25	0.38	86.3	18.3	0.41	0.74

Notes:

* Parameters determined between 50 to 100 psi vertical stress

** Parameters determined under 100 psi vertical stress

*** Parameters determined under 30 psi vertical stress

WCF gypsum (CFED 2054)

The Iowa K test was conducted on WCF gypsum to evaluate how changes in the moisture content and dry unit weight influenced the shear strength and stiffness of the compacted samples. Twelve samples with varying moisture content and dry unit weight combinations were prepared. The Iowa K test data and statistical analysis results are discussed below for each parameter.

Undrained cohesion and internal friction angle

Table 54 summarizes the undrained cohesion and friction angle of the 12 samples determined by the Iowa K test. Direct shear tests were conducted on each Iowa K test sample to determine drained cohesions and friction angles of the material. Three samples from each Iowa K test sample were prepared for 23, 45, 90 psi normal stress direct shear tests. The moisture content of the WCF gypsum samples was measured under 60°C to reduce the degree of dehydration of gypsum as specified in ASTM D2216.

The undrained friction angle of all the most of the 12 samples show higher values than the drained friction angles. When the moisture content of the samples below the standard Proctor optimum moisture content ($w_{opt} = 18.0\%$), the undrained friction angle varied in a small range as the moisture content and dry unit weight changes. However, when the samples wet of the optimum moisture content, obvious reductions can be observed. The undrained cohesion of all the samples show negative values as the results of WCF fly ash.

The direct shear test results show that the drained friction angles ranged from 29.5° to 42.7° with an average of 37.7°. However, the relationships between the drained friction angles, moisture content, and dry unit weight were not determined based on the data shown in Table 54. White, D.J. et al. 2012 (unpublished final report submitted to the Tennessee Valley Authority) determined the drained friction angle is 37.1° and cohesion is 0 psi for this material. The direct shear test show great agreement with the borehole shear test results for the drained friction angle, but the drained cohesions determined by the direct shear tests varied from 2.0 to 18.0 psi of samples with different moisture content and dry unit weight combinations. Compared to the drained friction angle (37.1° or 37.7°) of the material, the Iowa K test results show that the undrained friction angle of the dry optimum samples is 41.4° that is about 4° higher than the drained friction angle.

Table 54. Iowa K test and direct shear test results of WCF gypsum

K test w* (%)	K test γ_d (pcf)	K test c (psi)	K test ϕ (deg.)	DS test w* (%)	DS test γ_d^{**} (pcf)	DS test c' (psi)	DS test ϕ' (deg.)
9.5	97.7	-0.1	41.6	9.9	94.2	5.6	36.6
9.7	101.3	0.3	44.7	—			
9.9	106.1	-0.7	44.6	9.9	102.3	4.5	38.1
10.9	100.9	0.2	43.1	11.4	97.9	7.0	38.3
11.6	103.5	-0.9	44.8	11.6	100.3	9.9	34.5
15.5	100.4	-0.9	41.4	15.6	101.1	18.0	29.5
15.4	100.5	-2.4	43.0	15.5	102.2	7.5	39.0
17.8	101.9	-1.1	43.9	15.9	101.8	5.4	42.7
17.9	101.0	-4.2	40.1	16.7	104.7	7.9	39.1
18.0	100.5	-3.0	43.0	17.3	103.3	2.0	42.5
17.1	100.0	-4.6	36.5	17.8	102.6	14.9	34.2
20.8	95.9	-2.0	30.2	18.0	101.3	8.9	39.5

Notes:

— Test not performed

* Moisture contents measured under 60°C

** Average initial dry unit weight of the three samples

The relationship between the undrained friction angle and dry unit weight of the 12 samples were statistically evaluated and shown in Figure 126.

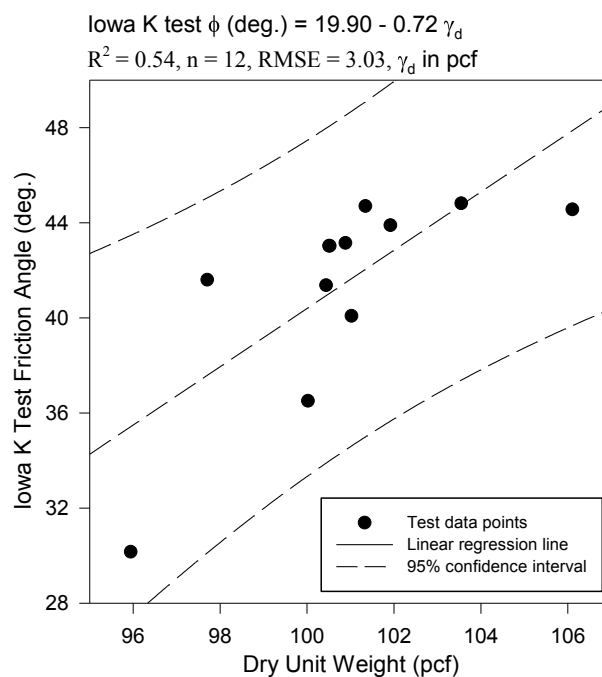


Figure 126. The statistical relationships between the dry unit weight and undrained friction angle of WCF gypsum

Vertical elastic modulus

Table 55 summarizes the vertical elastic modulus (E_v) of the 12 samples under 50 to 100 psi vertical pressure of the two loadings. The vertical elastic modulus of the samples under the second loading are about six times higher than the first loading, and for the samples with similar moisture contents, the vertical elastic modulus increase as the dry unit weight increase. Obvious reductions can be observed for samples wet of optimum moisture content ($w_{opt} = 18.0\%$).

Table 55. Iowa K test vertical elastic modulus of the WCF gypsum samples for loadings 1 and 2

w (%)	Loading 1 γ_d (pcf)	Loading 1 E_v (ksi) ($\sigma_v = 50-100$ psi)	Loading 2 γ_d (pcf)	Loading 2 E_v (ksi) ($\sigma_v = 50-100$ psi)
9.5	97.7	9.0	100.2	59.2
9.7	101.3	10.2	103.8	60.2
9.9	106.1	11.2	108.1	73.8
10.9	100.9	10.5	102.9	59.1
11.6	103.5	11.0	106.0	61.6
15.5	100.4	9.4	102.7	43.2
15.4	100.5	9.0	103.0	55.6
17.8	101.9	8.4	105.2	32.5
17.9	101.0	7.5	105.7	75.1
18.0	100.5	7.1	104.1	26.3
17.1	100.0	5.5	105.1	24.3
20.8	95.9	4.6	104.6	8.8

Figure 127A shows a multiple linear regression models for the undrained vertical elastic modulus of the samples under first loading. The undrained vertical elastic modulus decreases as the moisture content increases and dry unit weight decreases. Figure 127B shows a simple linear regression models for the undrained vertical elastic modulus of the samples under the second loading. The undrained vertical elastic modulus decreases as the moisture content increases which is same as the first loading. However, the dry unit weight of the samples is not statistically significant for the second loading samples.

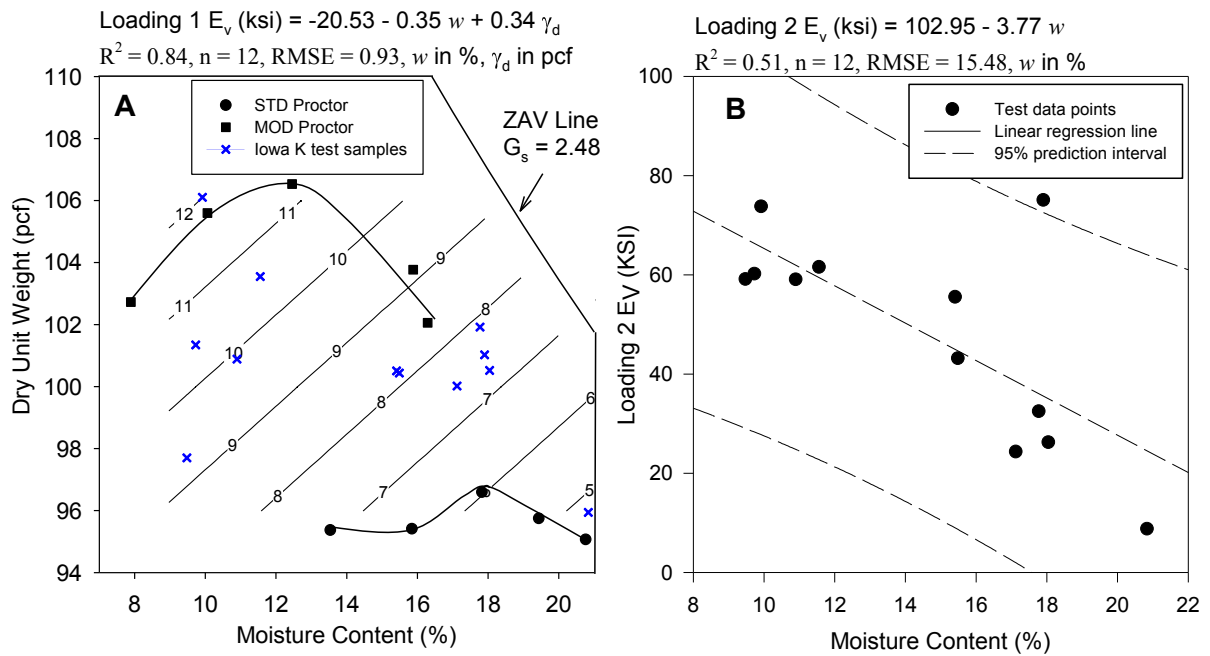


Figure 127. Statistical relationships between moisture content and vertical elastic modulus for WCF gypsum under (A) loading 1 and (B) loading 2

Poisson’s ratio and lateral stress ratio

The Poisson’s ratio and lateral stress ratio of the 12 WCF gypsum samples under 100 psi vertical stress of the first loading and 30 psi of the second loading are selected for statistical analyses (Table 56). During the first loading, both of the parameters tend to increase as the moisture content increases. However, at a given moisture content, the samples with different dry unit weights show nearly same values for both of the parameters.

Figure 128 and Figure 129 show the statistical analysis results for the Poisson’s ratio and lateral stress ratio of the WCF gypsum samples under the two loadings of Iowa K test. The results show that the Poisson’s ratio and lateral stress ratio increase as the moisture content increases, and the dry unit weight of the samples are statistical insignificant to the both of the parameters.

Table 56. Iowa K test Poisson's ratio and lateral stress ratio of the WCF gypsum samples for loadings 1 and 2

w%	Loading 1 γ_d (pcf)	Loading 1 ν ($\sigma_v = 100$ psi)	Loading 1 K ($\sigma_v = 100$ psi)	Loading 2 γ_d (pcf)	Loading 2 ν ($\sigma_v = 30$ psi)	Loading 2 K ($\sigma_v = 30$ psi)
9.5	97.7	0.14	0.20	100.2	0.27	0.46
9.7	101.3	0.13	0.17	103.8	0.26	0.41
9.9	106.1	0.13	0.18	108.1	0.28	0.42
10.9	100.9	0.13	0.18	102.9	0.28	0.48
11.6	103.5	0.13	0.18	106.0	0.26	0.46
15.5	100.4	0.15	0.22	102.7	0.29	0.52
15.4	100.5	0.15	0.22	103.0	0.33	0.57
17.8	101.9	0.14	0.20	105.2	0.30	0.46
17.9	101.0	0.19	0.27	105.7	0.34	0.56
18.0	100.5	0.19	0.27	104.1	0.38	0.55
17.1	100.0	0.21	0.31	105.1	0.34	0.58
20.8	95.9	0.25	0.35	104.6	0.28	0.46

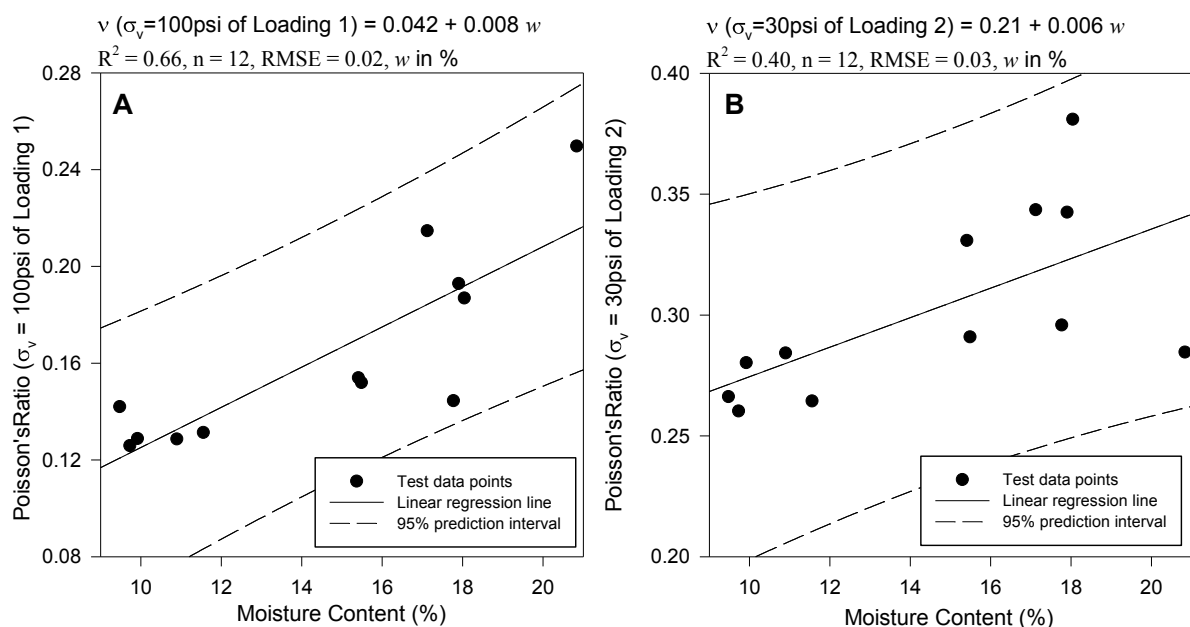


Figure 128. Statistical analysis results for the Poisson's ratio of WCF gypsum under (A) loading 1 and (B) loading 2

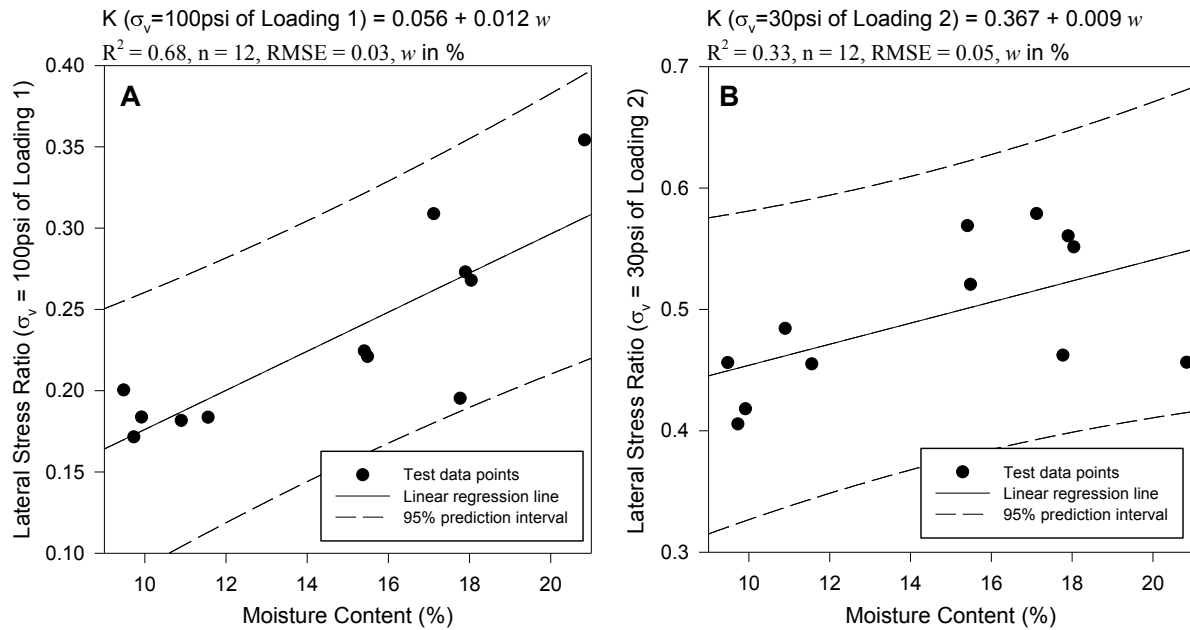


Figure 129. Statistical analysis results for the lateral stress ratio of WCF gypsum under (A) loading 1 and (B) loading 2

Soil to steel friction

Table 52 summarizes the soil-to-soil and soil-to-steel shear strength parameters of the 12 WCF gypsum samples. The results show that the ϕ_s/ϕ of the samples are relatively independent of moisture content and dry unit weight changes of the samples. Similar behavior were observed for the WCF fly ash samples. Based on the Iowa K test results, a ϕ_s/ϕ ratio of 0.7 or 0.8 may be used as often assumed in the conventional method for pile design. The negative soil to steel adhesions were calculated for the all the samples based on the Iowa K test results. However, WCF is also a cohesionless material, so there should be no any adhesion between the samples and the steel mold.

Table 57. Soil to soil and soil to steel shear strength parameters of the WCF gypsum

w (%)	γ_d (pcf)	ϕ (deg.)	ϕ_s (deg.)	ϕ_s/ϕ	c (psi)	c_s (psi)
9.5	97.7	41.6	30.2	0.7	-0.1	-2.5
9.7	101.3	44.7	36.3	0.8	0.3	-2.9
9.9	106.1	44.6	29.0	0.7	-0.7	-2.6
10.9	100.9	34.4	32.4	0.9	0.2	-2.5
11.6	103.5	44.8	33.4	0.7	-0.9	-3.6
15.5	100.4	41.4	36.3	0.9	-0.9	-5.4
15.4	100.5	43.0	36.4	0.8	-2.4	-6.0
17.8	101.9	43.9	30.6	0.7	-1.1	-2.4
17.9	101.0	40.1	32.2	0.8	-4.2	-3.9
18.0	100.5	43.0	31.9	0.7	-3.0	-3.9
17.1	100.0	36.5	31.0	0.8	-4.6	-5.0
20.8	95.9	30.2	28.3	0.9	-2.0	-2.0

Summary of the Iowa K test results of WCF gypsum

Table 58 summarizes the Iowa K test results of the 12 WCF gypsum samples. The initial moisture contents and dry unit weights of the samples ranged from 9.5% to 20.8% and 95.9 to 106.9 pcf (STD w_{opt} = 18.0% and STD γ_{dmax} = 96.9 pcf).

The undrained soil to soil friction angles of the samples ranged between 30.2° and 44.8°. The ϕ_s/ϕ of the samples with varying moisture content and dry unit weight combinations was very constant that ranged between 0.7 and 0.9.

The vertical elastic modulus of the samples under the first loading ranged from 4.6 to 11.2 ksi and the second loading vertical elastic modulus ranged from 8.8 to 75.1 ksi. The statistical analysis results showed that the vertical elastic modulus of the samples under the first loading increased as the dry unit weight increased and moisture content decreased, but under the second loading, the dry unit weight was not statistically significant to the vertical elastic modulus of the samples. Both of the Poisson's ratio and lateral stress ratio decreased as the moisture content increased. The Poisson's ratio of the samples ranged from 0.13 to 0.25 under first loading and 0.26 to 0.38 under the second loading. The lateral stress ratio of the samples ranged from 0.17 to 0.35 under the first loading and 0.41 to 0.58 under the second loading.

Table 58. Summary of the Iowa K test results for WCF gypsum (CFED 2054)

w (%)	Loading 1 Data								Loading 2 Data			
	γ_d (pcf)	c (psi)	ϕ	c_s (psi)	ϕ_s/ϕ	E_v^* (ksi)	ν^{**}	K ^{**}	γ_d (pcf)	E_v^* (ksi)	ν^{***}	K ^{***}
9.5	97.7	-0.1	41.6	-2.5	0.7	9.0	0.14	0.20	100.2	59.2	0.27	0.46
9.7	101.3	0.3	44.7	-2.9	0.8	10.2	0.13	0.17	103.8	60.2	0.26	0.41
9.9	106.1	-0.7	44.6	-2.6	0.7	11.2	0.13	0.18	108.1	73.8	0.28	0.42
10.9	100.9	0.2	43.1	-2.5	0.9	10.5	0.13	0.18	102.9	59.1	0.28	0.48
11.6	103.5	-0.9	44.8	-3.6	0.7	11.0	0.13	0.18	106.0	61.6	0.26	0.46
15.5	100.4	-0.9	41.4	-5.4	0.9	9.4	0.15	0.22	102.7	43.2	0.29	0.52
15.4	100.5	-2.4	43.0	-6.0	0.8	9.0	0.15	0.22	103.0	55.6	0.33	0.57
17.8	101.9	-1.1	43.9	-2.4	0.7	8.4	0.14	0.20	105.2	32.5	0.30	0.46
17.9	101.0	-4.2	40.1	-3.9	0.8	7.5	0.19	0.27	105.7	75.1	0.34	0.56
18.0	100.5	-3.0	43.0	-3.9	0.7	7.1	0.19	0.27	104.1	26.3	0.38	0.55
17.1	100.0	-4.6	36.5	-5.0	0.8	5.5	0.21	0.31	105.1	24.3	0.34	0.58
20.8	95.9	-2.0	30.2	-2.0	0.9	4.6	0.25	0.35	104.6	8.8	0.28	0.46

Notes:

* Parameters determined between 50 to 100 psi vertical stress

** Parameters determined under 100 psi vertical stress

*** Parameters determined under 30 psi vertical stress

Ottawa sand (ASTM 20-30 sand)

The Iowa K test was conducted on four dry Ottawa sand samples with different initial void ratios to evaluate how changes in the void ratios influenced the shear strength and stiffness of the compacted material. The Iowa K test results are discussed below for each parameter.

Undrained cohesion and internal friction angle

To compare the friction angle and cohesion results, three direct shear tests with 45, 90, and 180 psi normal stress were also conducted on the Ottawa sand samples with nearly same initial void ratio with Iowa K test samples. The test results are summarized in Table 59. The friction angle determined using the Iowa K test ranges from 31.3° to 35.6° and increases as the initial void ratio decreases. The Ottawa sand used for the tests is clean and dry granular material, so the cohesion should be zero. A linear regression line passing through the original point was used to fit the three test points and determine the friction angle of the samples. The friction angle determined using the direct shear test increases from 29.7° to 34.5° that are about one or two degrees lower than the friction angles from the Iowa K tests. However, the Iowa K tests gave all negative cohesions for the four samples.

Table 59. The Iowa K test and direct shear test results of Ottawa sand samples

K test initial γ_d (pcf)	K test initial e_0	K test c (psi)	K test ϕ (deg.)	DS test initial γ_d (pcf)	DS test initial e_0	DS test c (psi)	DS test ϕ (deg.)
97.6	0.69	-5.4	31.3	97.1	0.70	0.0	29.7
101.8	0.62	-6.0	32.8	101.2	0.63	0.0	30.8
105.9	0.56	-6.0	34.1	105.2	0.57	0.0	33.2
107.7	0.54	-7.6	35.6	106.9	0.55	0.0	34.5

Linear regression models were generated based on the Iowa K test and direct shear test results. The two models show that the friction angle of the Ottawa sand decreases as the initial void ratio increases and ranges between 29° and 36°.

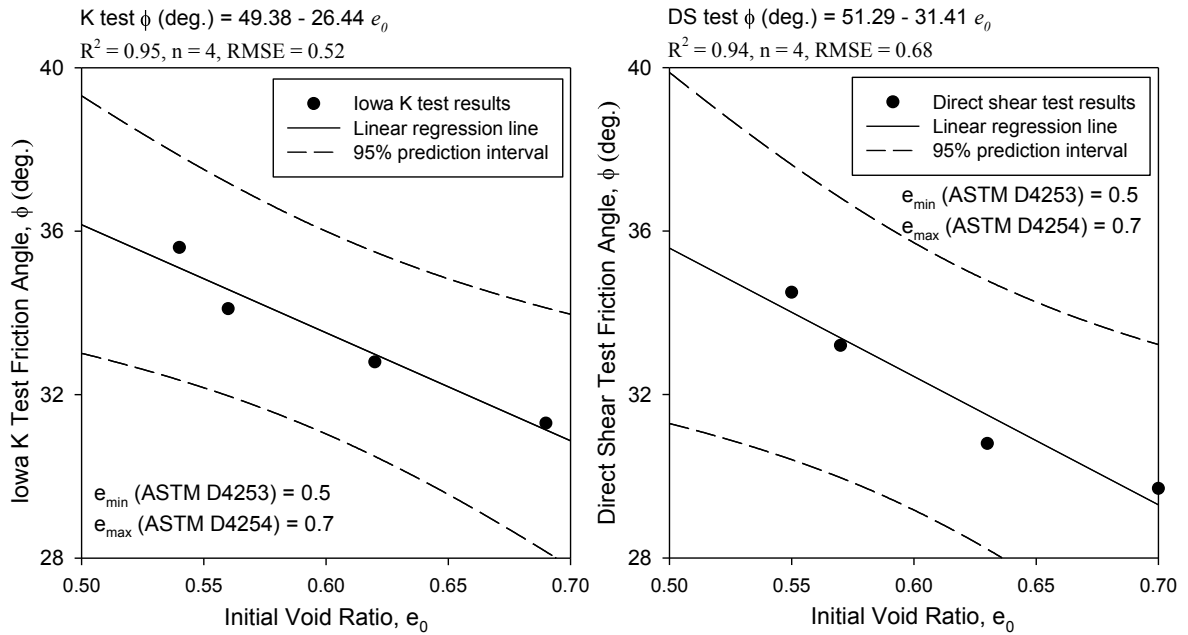


Figure 130. The statistical relationships between the dry unit weight and undrained friction angle of Ottawa sand samples

Vertical elastic modulus

The vertical elastic modulus (E_v) of the 4 samples under 50 to 100 psi vertical pressure of the two loadings of the Iowa K tests were determined. The vertical elastic modulus ranges between 12.4 to 17.0 ksi under the first loading and 23.0 to 29.1 ksi under the second loading. The elastic modulus tends to increase as the initial void ratio decreases, and the second loading modulus of the samples are higher than the first loading.

Table 60. Iowa K test vertical elastic modulus of Ottawa sand samples for loading 1 and

2

Loading 1 Data			Loading 2 Data		
γ_d (pcf)	e_0	E_v (ksi) $\sigma_v = 50-100$ psi	γ_d (pcf)	e_0	E_v (ksi) $\sigma_v = 50-100$ psi
97.6	0.69	12.4	100.0	0.65	23.0
101.8	0.62	13.6	104.0	0.59	19.8
105.9	0.56	19.6	107.6	0.54	30.4
107.7	0.54	17.0	109.5	0.51	29.1

Poisson's ratio and lateral stress ratio

The Poisson's ratio and lateral stress ratio under 100 psi of the first loading and 30 psi of the second loading were selected (Table 61). Under the first loading, the Poisson's ratio and lateral stress ratio decreases as the initial void ratio decreases. However, under the second loading, the data shows nearly same values for each of the parameters of the four samples.

Table 61. Iowa K test Poisson's ratio and lateral stress ratio of the Ottawa sand samples for loadings 1 and 2

Loading 1 Data				Loading 2 Data			
γ_d (pcf)	e_0	v $\sigma_v = 100$ psi	K $\sigma_v = 100$ psi	γ_d (pcf)	e_0	v $\sigma_v = 30$ psi	K $\sigma_v = 30$ psi
97.6	0.69	0.21	0.39	100.0	0.65	0.36	0.64
101.8	0.62	0.20	0.38	104.0	0.59	0.35	0.60
105.9	0.56	0.15	0.37	107.6	0.54	0.37	0.65
107.7	0.54	0.15	0.37	109.5	0.51	0.38	0.67

Soil to steel friction

Table 62 summarizes the soil to soil and soil to steel shear strength parameters. The ϕ_s/ϕ is about 0.9 for the four samples with different void ratios. The soil to steel adhesions of the four samples also show negative values.

Table 62. Soil to soil and soil to steel shear strength parameters of the Ottawa sand samples

γ_d (pcf)	e_0	ϕ (deg.)	ϕ_s (deg.)	ϕ_s/ϕ	c (psi)	c_s (psi)
97.6	0.69	31.3	30.8	1.0	-5.4	-3.8
101.8	0.62	32.8	25.8	0.8	-6.0	-2.8
105.9	0.56	34.1	29.7	0.9	-6.0	-5.3
107.7	0.54	35.6	33.7	0.9	-7.6	-9.2

Summary of the Iowa K test results of Ottawa sand

Table 63 summarizes the Iowa K test results of the four Ottawa sand samples. The initial dry unit weights of the samples were between 97.6 to 107.7 pcf and void ratio ranged between 0.54 to 0.69 ($e_{min} = 0.50$ and $e_{max} = 0.70$).

The undrained soil to soil friction angles of the samples ranged between 31.3° to 35.6° and increased as initial void ratio decreased. The ϕ_s/ϕ of the four samples was between 0.8 and 1.0. The vertical elastic modulus of the samples under the first loading ranged from

12.4 to 19.6 ksi, and the second loading vertical elastic modulus ranged between 19.8 to 30.4 ksi. The elastic modulus tended to increase as the initial void ratio decreased under both of the two loadings. The Poisson's ratio of the samples under first loading ranged between 0.15 to 0.21, and 0.35 to 0.38 under the second loading. The lateral stress ratio of the samples ranged between 0.37 to 0.39 under the first loading, and 0.60 to 0.67 under the second loading.

Table 63. Summary of the Iowa K test results for the Ottawa sand

Loading 1 Data	γ_d (pcf)	97.6	101.8	105.9	107.7
	e_0	0.69	0.62	0.56	0.54
	ϕ (deg.)	31.3	32.8	34.1	35.6
	ϕ_s (deg.)	30.8	25.8	29.7	33.7
	ϕ_s/ϕ	1.0	0.8	0.9	0.9
	c (psi)	-5.4	-6.0	-6.0	-7.6
	c_s (psi)	-3.8	-2.8	-5.3	-9.2
	E_v (ksi) ($\sigma_v = 50-100$ psi)	12.4	13.6	19.6	17.0
	ν ($\sigma_v = 100$ psi)	0.21	0.2	0.15	0.15
	K ($\sigma_v = 100$ psi)	0.39	0.38	0.37	0.37
Loading 2 Data	γ_d (pcf)	100.0	104.0	107.6	109.5
	e_0	0.65	0.59	0.54	0.51
	E_v (ksi) ($\sigma_v = 50-100$ psi)	23.0	19.8	30.4	29.1
	ν ($\sigma_v = 30$ psi)	0.36	0.35	0.37	0.38
	K ($\sigma_v = 30$ psi)	0.64	0.60	0.65	0.67

Improving CFED Using Gyratory Compaction Test to Determine Compaction Behavior and Shear Resistance

Gyratory compaction tests were conducted on six types of geomaterials to evaluate the feasibility for determining the compaction behaviors, shear strength and stiffness properties of geomaterials. Table 64 shows the CFED soil IDs, material descriptions, and USCS classifications of the materials. The test and statistical analysis results are presented in two sections: the repeatability and reproducibility of the test devices and the feasibility of linking shear resistance with moisture-density-compaction energy relationships of compacted geomaterials.

Table 64. The geomaterials used for gyratory compaction tests

CFED Soil ID	Description	USCS Classification
2053	WCF fly ash	ML
2054	WCF gypsum	ML
2061	2012 Manatt's RAP	GW
2062	RPCC and RAP mixture	GW
2063	Crushed limestone	GP-GM
N/A	Ottawa sand	SP

Repeatability and reproducibility (R&R) analysis for the gyratory compaction test devices

A gyratory compactor (Brovold Inc. SN: AFGB1A) and two PDAs (Test Quip LLC. SN 110 and 120) were used to measure variations in dry unit weight and shear resistance of the six geomaterials. A total of 20 tests with 200 gyrations for each test were conducted on constant mass Ottawa sand samples to assess the repeatability and reproducibility of the testing device. Results from four sets of five tests with two vertical pressures (6266 and 12531 psf) and PDA (PDA 1 and PDA 2) combinations were statistically evaluated. Table 65 shows the repeatability and reproducibility of using the gyratory compactor and the two PDAs to measure the dry unit weight (γ_d), total load (P), eccentricity (e), and shear resistance (τ_G) on Ottawa sand for 6266 and 12531 psf vertical pressure tests.

A pooled estimator of the standard deviations (S_p) that combined the standard deviations of the 200 gyrations of the 5 repeated tests was calculated to evaluate the repeatability

($\sigma_{\text{repeatability}}$) of the devices for measuring each the parameters. For dry unit weight, the within-laboratory repeatability of the vibratory compaction test (ASTM D4253) for a USCS: SP material was reported as 0.6 pcf. Compared to the ASTM D4253, the gyratory compaction test shows better repeatability which ranges from 0.11 to 0.37 pcf for the 6266 and 12531 psf (300 and 600 kPa) vertical pressure tests on Ottawa sand (USCS: SP).

R&R analyses were performed for the three parameters (total load, eccentricity, and shear resistance) that were measured using the two PDAs. A statistical analysis software, JMP 10, was used to generate the Two-Way ANOVA tables for calculating the $\sigma_{\text{repeatability}}$ and $\sigma_{\text{reproducibility}}$ of each parameter. All of the JMP outputs and an Excel spreadsheet for the R&R analyses are included in Appendix F. Table 65 summarizes the $\sigma_{\text{reproducibility}}$ and $\sigma_{\text{R\&R}}$ for each of the parameters. In this study, the dry unit weight is determined using only one gyratory compactor, so the reproducibility for determining dry unit weight was not evaluated. The contribution of $\sigma_{\text{reproducibility}}$ to the $\sigma_{\text{R\&R}}$ for each of the parameters are also calculated to evaluate the impact of changing the PDAs to the overall variability of the test results. The analysis results showed that the impact of changing the PDAs is considered statistically significant. The Satterthwaite approximate confidence limits for each parameter were calculated and shown in Table 65 as well. However, these intervals show that none of these standard deviations are terribly well-determined, because the degrees of freedom are small and intervals are wide, so more data is needed for better information.

The statistical analysis methods and computational equations for the R&R analysis are presented in Chapter 3 of this thesis. The dry unit weights, total load, eccentricity, and shear resistances versus number of gyrations for the four sets tests are shown in Figure 131 through Figure 138.

Table 65. Results of R&R analysis for the gyratory compactor and two PDAs

Vertical pressure (psf)	Parameter	PDA	S_p	95% confidence interval	$\sigma_{\text{reproducibility}}$	95% confidence interval	$\sigma_{\text{R\&R}}$	95% confidence interval	Contribution of $\sigma_{\text{reproducibility}}$ to $\sigma_{\text{R\&R}}$ (%)
6266	γ_d (pcf)	1	0.11	± 0.10	N/A	N/A	N/A	N/A	N/A
		2	0.14	± 0.12					
	P (lb)	1	28.73	± 25.21	37.98	19.11–230.70	46.94	29.34–140.73	80.9
		2	26.36	± 23.13					
	e (in)	1	0.12	± 0.11	0.13	0.06–0.73	0.17	0.11–0.51	77.0
		2	0.09	± 0.08					
	τ_G (psi)	1	0.71	± 0.63	0.57	0.33–3.97	0.80	0.55–1.39	71.0
		2	0.36	± 0.32					
12531	γ_d (pcf)	1	0.37	± 0.32	N/A	N/A	N/A	N/A	N/A
		2	0.15	± 0.13					
	P (lb)	1	79.85	± 70.06	16.98	11.98–31.80	69.77	79.94–87.27	24.3
		2	52.74	± 46.28					
	e (in)	1	0.06	± 0.05	0.08	0.05–0.14	0.10	0.07–0.14	79.3
		2	0.06	± 0.05					
	τ_G (psi)	1	0.46	± 0.41	0.81	0.52–2.05	0.94	0.66–1.65	85.7
		2	0.51	± 0.45					

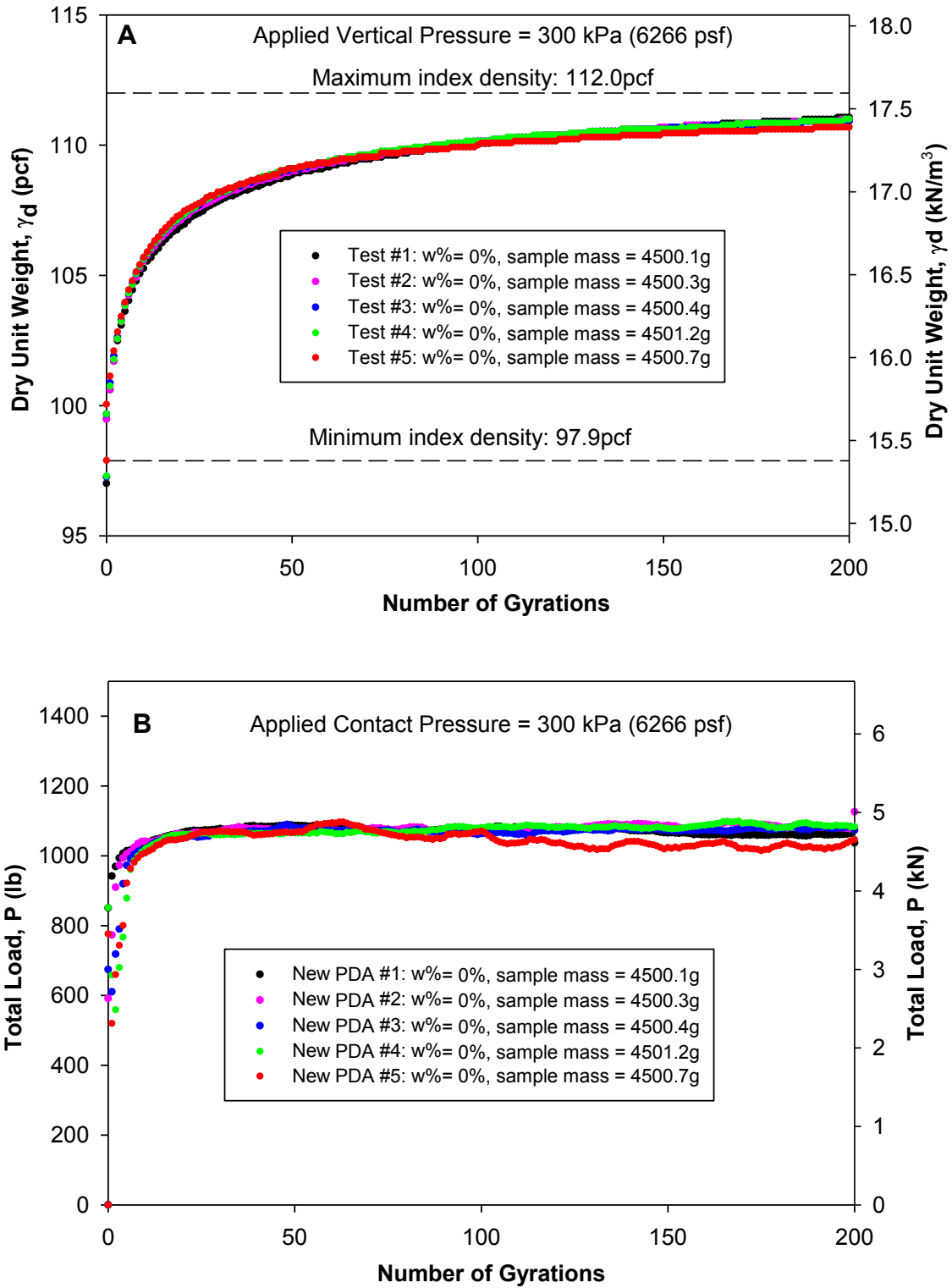


Figure 131. The (A) dry unit weight and (B) total load versus number of gyrations of Ottawa sand under 300 kPa vertical pressure with PDA 1

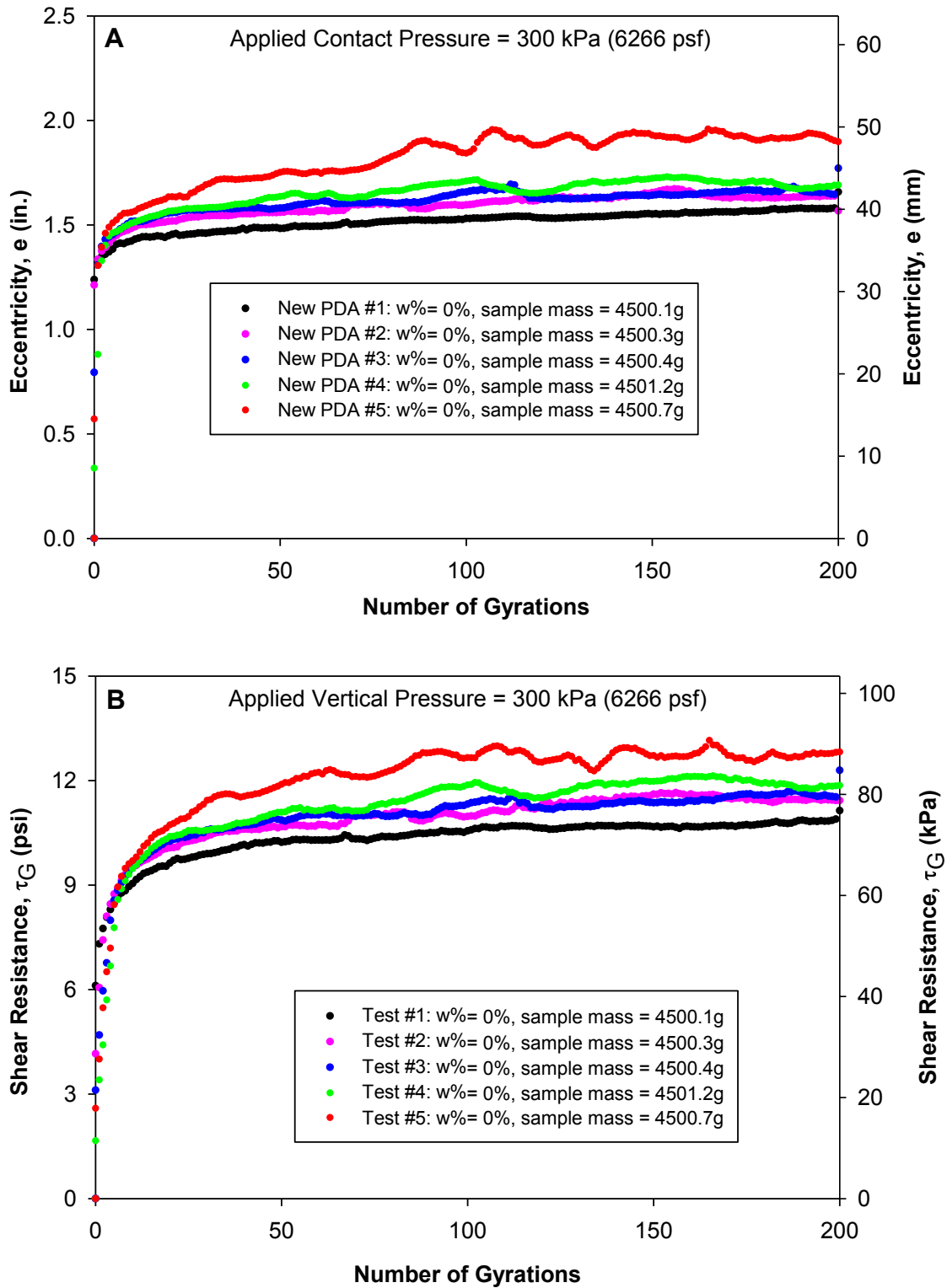


Figure 132. The (A) eccentricity and (B) shear resistance versus number of gyrations of Ottawa sand under 300 kPa vertical pressure with PDA 1

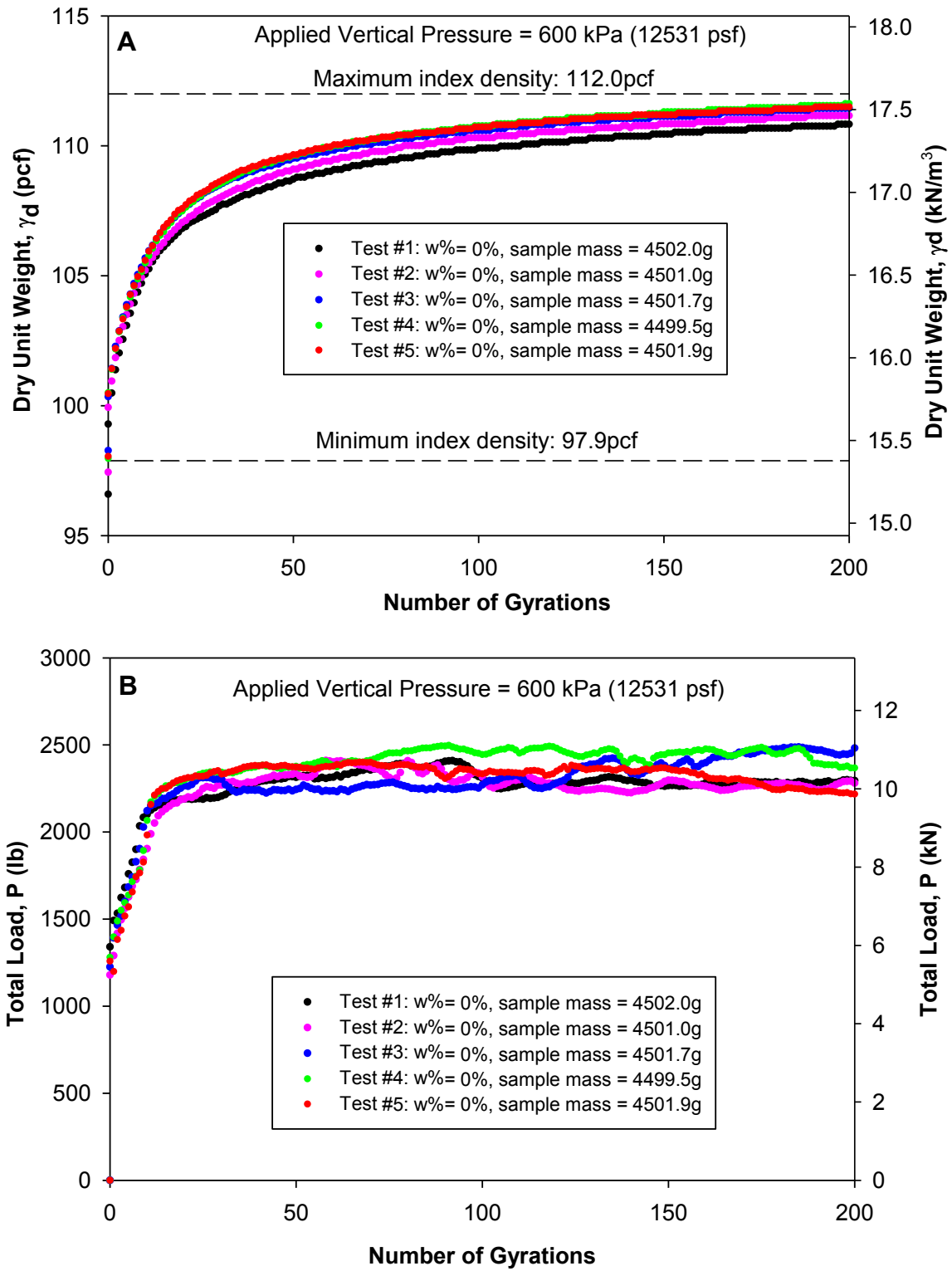


Figure 133. The (A) dry unit weight and (B) total load versus number of gyrations of Ottawa sand under 600 kPa vertical pressure with PDA 1

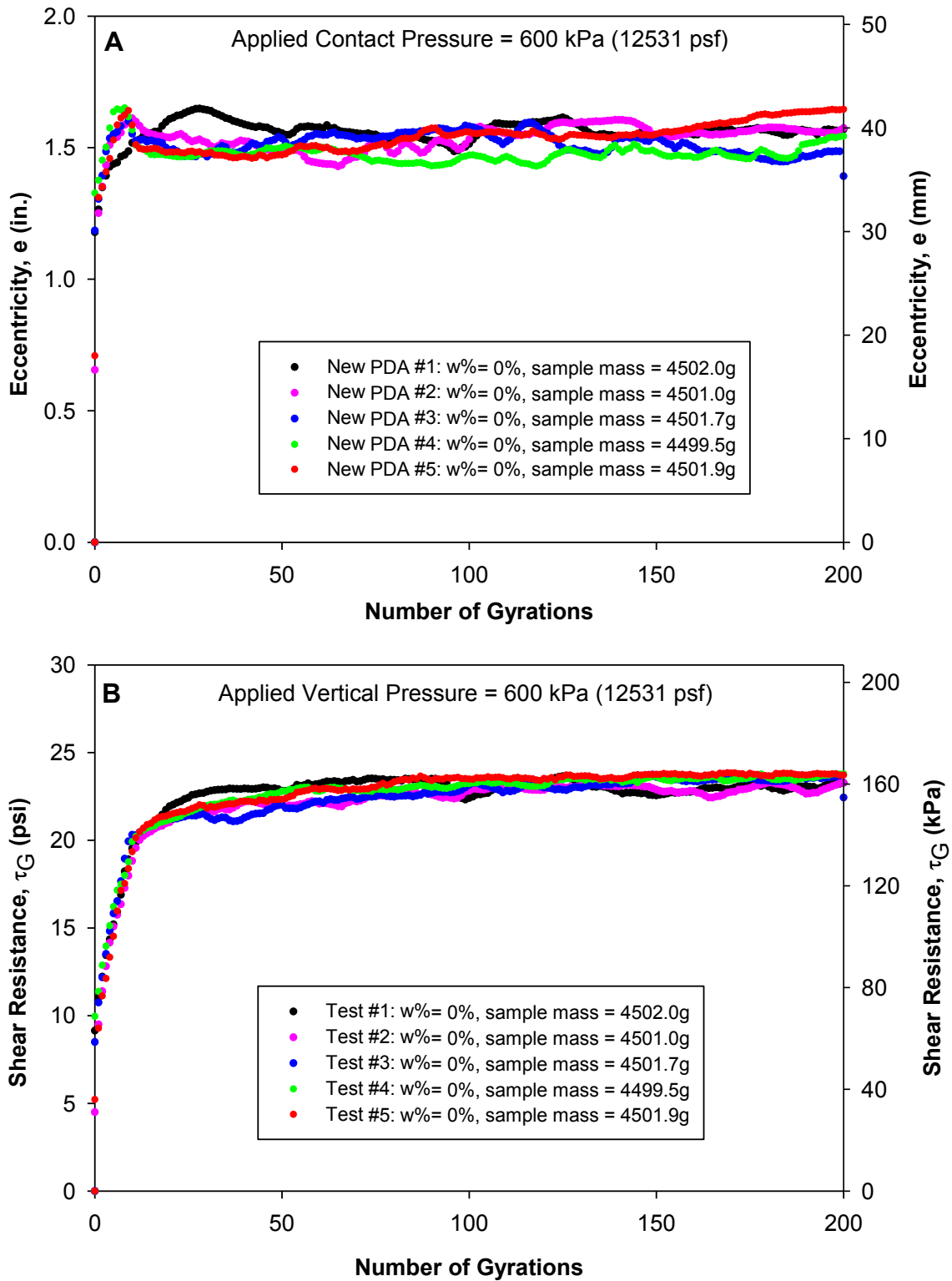


Figure 134. The (A) eccentricity and (B) shear resistance versus number of gyrations of Ottawa sand under 600 kPa vertical pressure with PDA 1

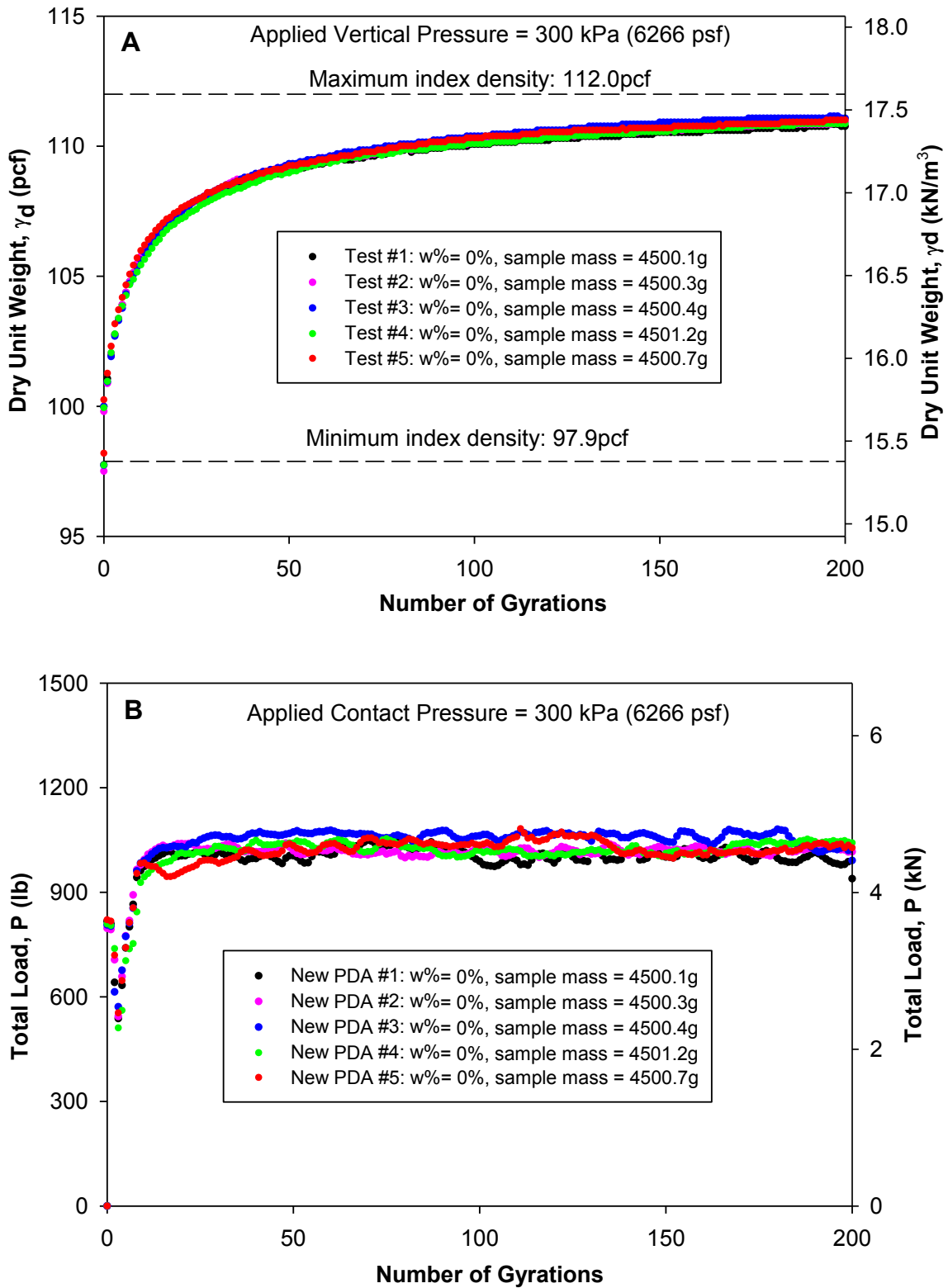


Figure 135. The (A) dry unit weight and (B) total load versus number of gyrations of Ottawa sand under 300 kPa vertical pressure with PDA 2

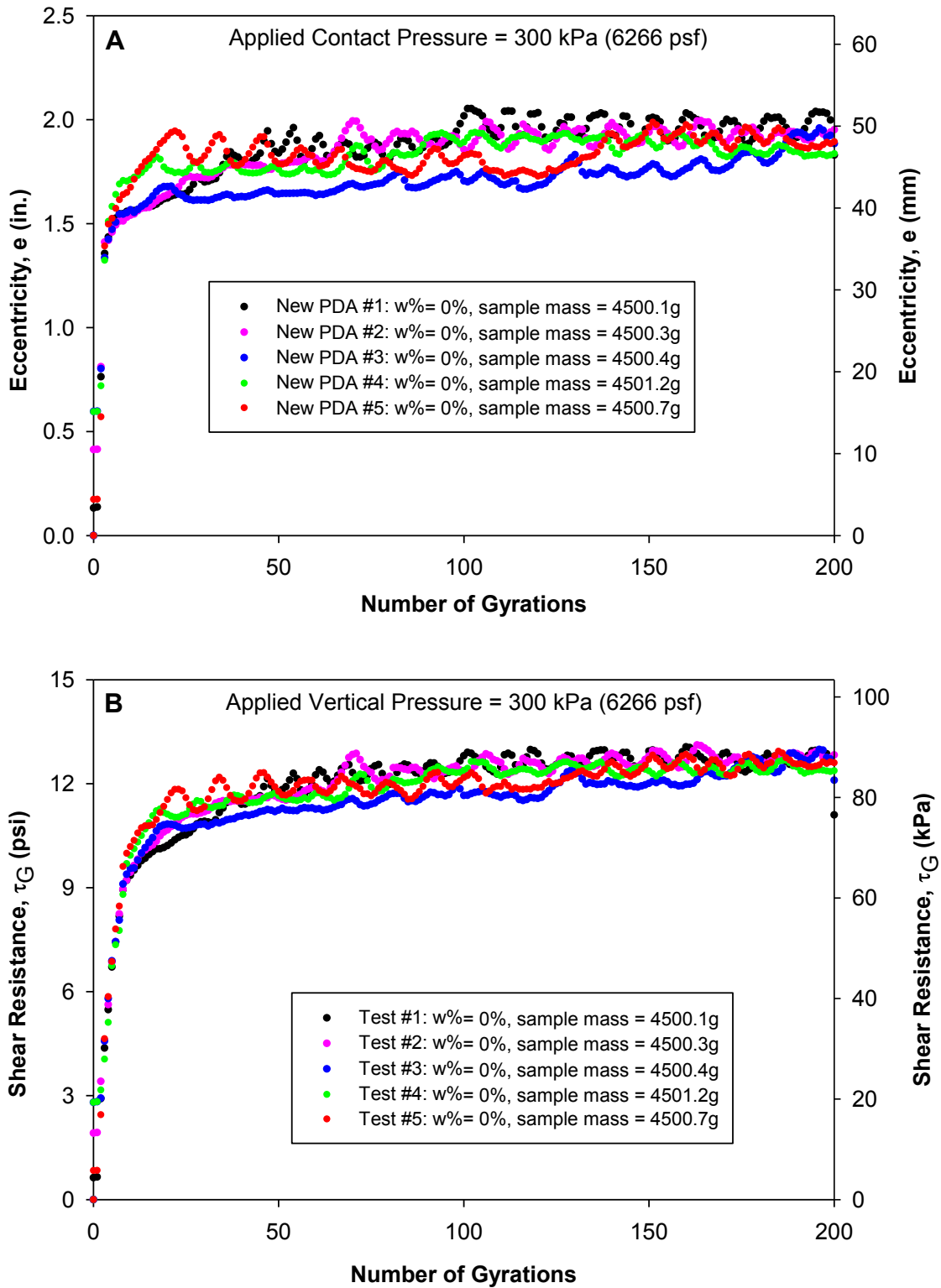


Figure 136. The (A) eccentricity and (B) shear resistance versus number of gyrations of Ottawa sand under 300 kPa vertical pressure with PDA 2

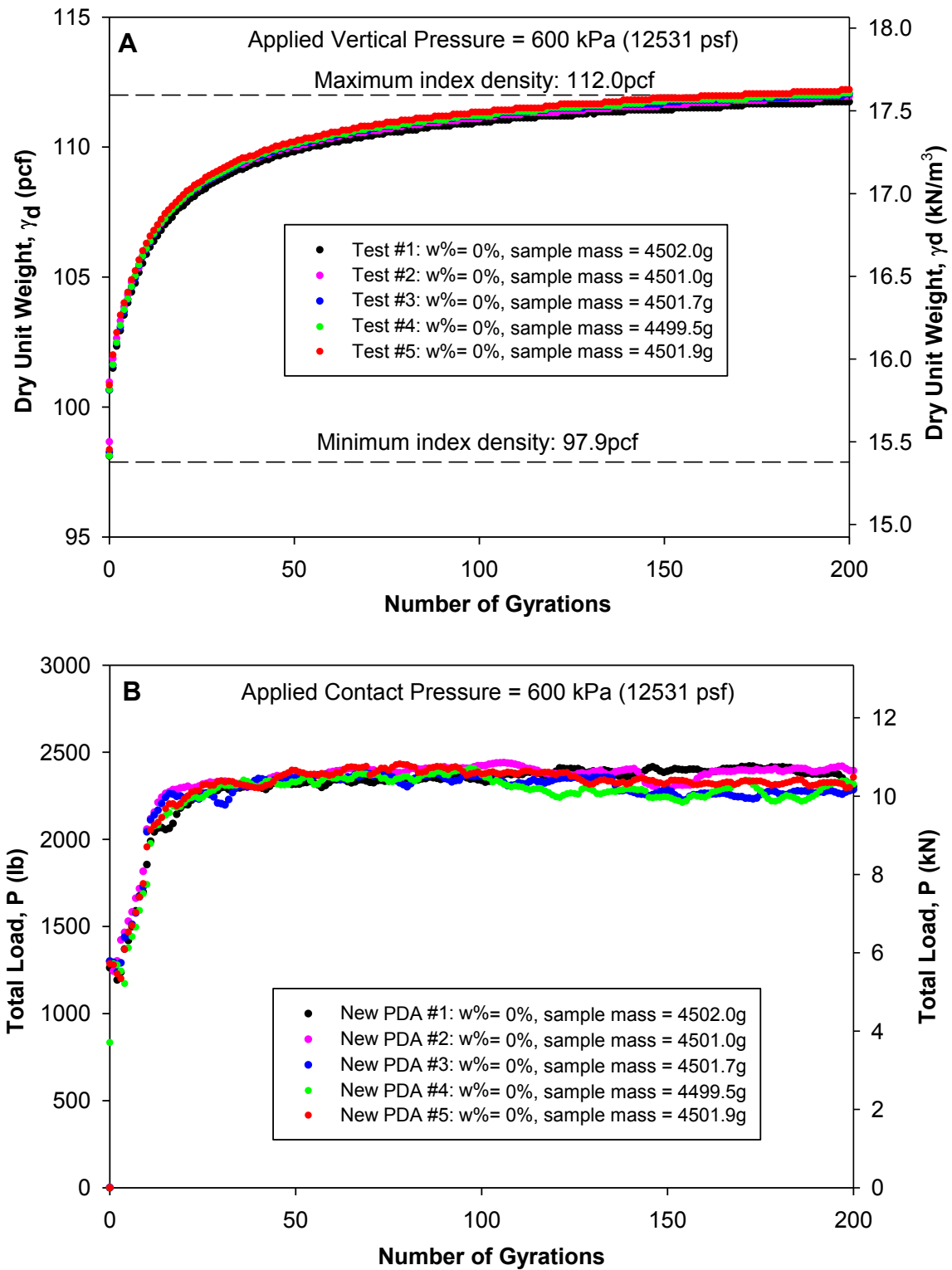


Figure 137. The (A) dry unit weight and (B) total load versus number of gyrations of Ottawa sand under 600 kPa vertical pressure with PDA 2

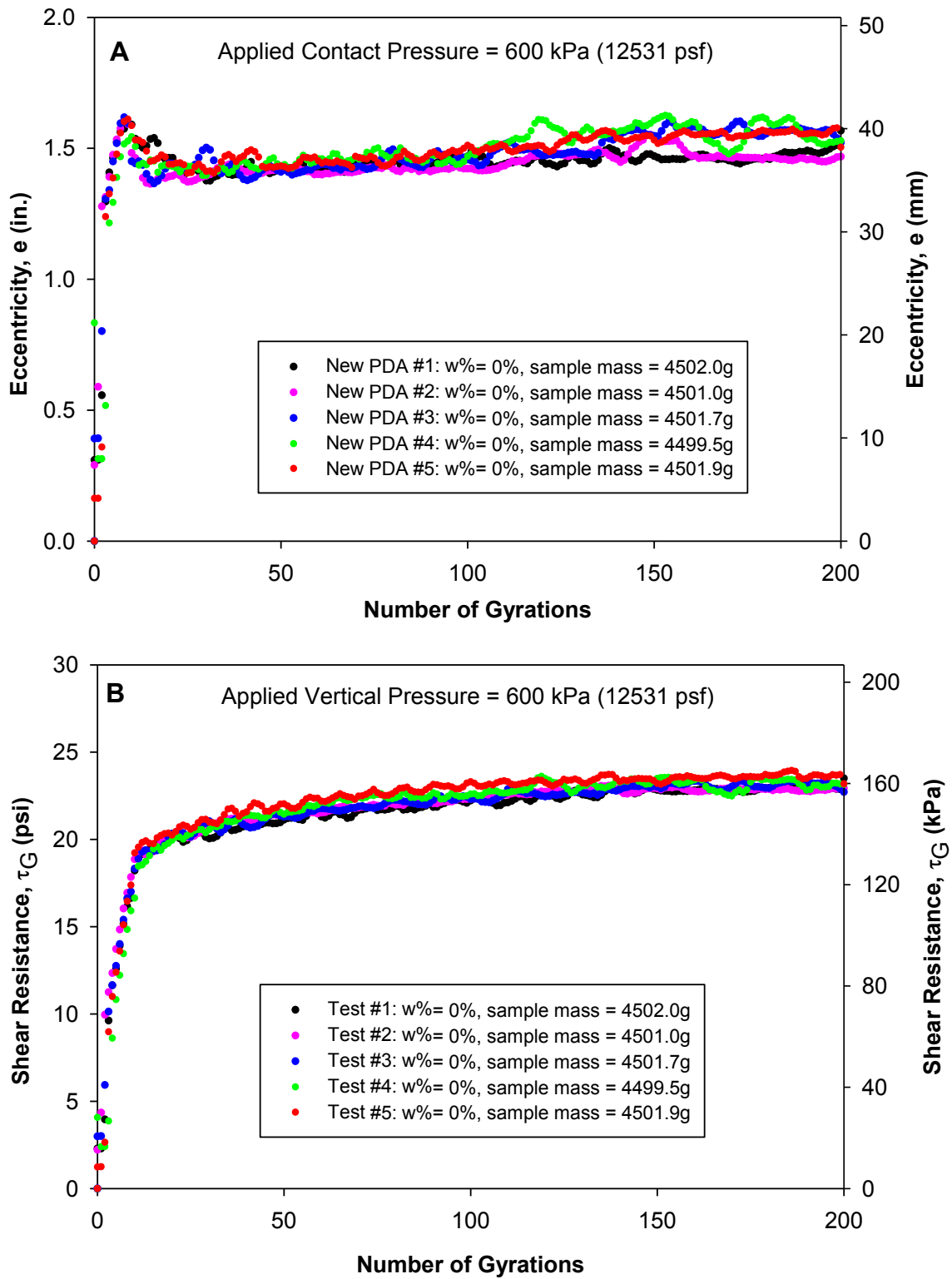


Figure 138. The (A) eccentricity and (B) shear resistance versus number of gyrations of Ottawa sand under 600 kPa vertical pressure with PDA 2

Feasibility of linking the shear resistance with moisture-density-compaction energy relationships

In this study, gyratory compaction tests were conducted on two fine grained free-draining ML geomaterials (WCF fly ash and gypsum) and three coarse grained GW and GP-GM geomaterials (2012 Manatt's RAP, RPCC and RAP mixture, and crushed limestone) to evaluate the feasibility of linking the shear resistance with moisture-density-compaction energy relationships for compacted geomaterials. Gyratory compaction test results were compared with conventional laboratory test results.

WCF fly ash and gypsum (CFED 2053 and 2054)

Gyratory compaction tests were conducted on WCF fly ash and gypsum (CFED 2053 and 2054) to determine the moisture-density-compaction energy relationships and compare with Proctor and unconfined compression (UC) test results. Six WCF fly ash samples and five gypsum samples with different moisture contents were prepared for the gyratory compaction tests. The tests ran 100 gyrations with 300 kPa (6265 psf) vertical pressure for all the samples and the γ_{dmax} values were determined at the 100 gyration. The shear resistance was calculated based on the PDA data for each gyration during the tests. The moisture contents of the samples were determined before and after each test because both of the geomaterials are free-draining, and for high moisture content samples, some water was squeezed out of the samples during compaction. A linear change in moisture content from 0 to 100 gyrations is assumed in determining the dry unit weights. For WCF gypsum, 60°C oven-drying temperatures was used to reduce the degree of dehydration of gypsum in accordance with ASTM D2216.

The dry unit weight and shear resistance (τ_G) versus number of gyrations for the WCF fly ash and gypsum samples are shown in Figure 139 and Figure 141. The comparisons between Proctor and gyratory compaction test results for the two geomaterials are shown in Figure 140 and Figure 142, respectively.

As shown in Figure 139 and Figure 141, for both of the two geomaterials, the dry unit weight increased as the number of gyrations increased and the dry unit weights achieved at the end of the tests are between the standard (i.e., γ_{dmax} at $w_{\text{opt}} = 25.8\%$) and modified Proctor tests (i.e., γ_{dmax} at $w_{\text{opt}} = 20.8\%$). The shear resistance at 100 gyration of the samples decreased with the increases of moisture contents. The biggest difference between the

samples are about 500 psf for both of the two geomaterials. The majority of the dry unit weight and shear resistance increases were obtained in the first 20 gyrations during the tests.

The relationship between dry unit weight, moisture content, and compaction energy of gyratory compaction and Proctor tests are shown in Figure 140 and Figure 142. For both of the two geomaterials, the dry unit weights achieved at the end of 100 gyrations with 300 kPa applied vertical pressure were close to the dry unit weights achieved with modified Proctor compaction energy. However, the compaction energy produced by the gyratory compactor with 300 kPa vertical pressure at 100 gyrations was about the same as standard Proctor compaction energy. The dry unit weights of the gyratory compaction test samples achieved by the same amount of energy as the standard Proctor test (12375 lb-ft/ft^3) were selected for comparison with the relationships between dry unit weight and moisture content that were determined by Proctor tests. As shown in Figure 139B and Figure 141B, the dry unit weight and moisture content relationship of the gyratory compaction test samples with low moisture contents shows a similar trend with the Proctor curves, but the samples with high moisture contents resulted in higher dry unit weights and did not follow the expected trend as the Proctor curves. For these high moisture content samples, some water was squeezed out during the tests due to the free-draining characteristics of the two geomaterials. The moisture content and dry unit weight shown in the figures were calculated based on the assumption that the moisture contents linearly changed during the tests.

The advantage of gyratory compaction is that a full compaction curve (i.e., changes in density with increasing compaction energy) at a given moisture content can be generated for each sample, while generating one compaction curve using the Proctor compaction method requires that multiple samples must be compacted with different compaction energies. However, the dry unit weight and moisture content curves determined by gyratory compaction did not allow the optimum moisture content and maximum dry unit weight to be readily estimated for the two free-draining geomaterials. An advantage of using a PDA is that the τ_G values can be calculated for each gyration during the test and correlated to soil undrained shear strength and stiffness properties. Statistical analysis results of the gyratory compaction and unconfined compression (UC) test will be shown below.

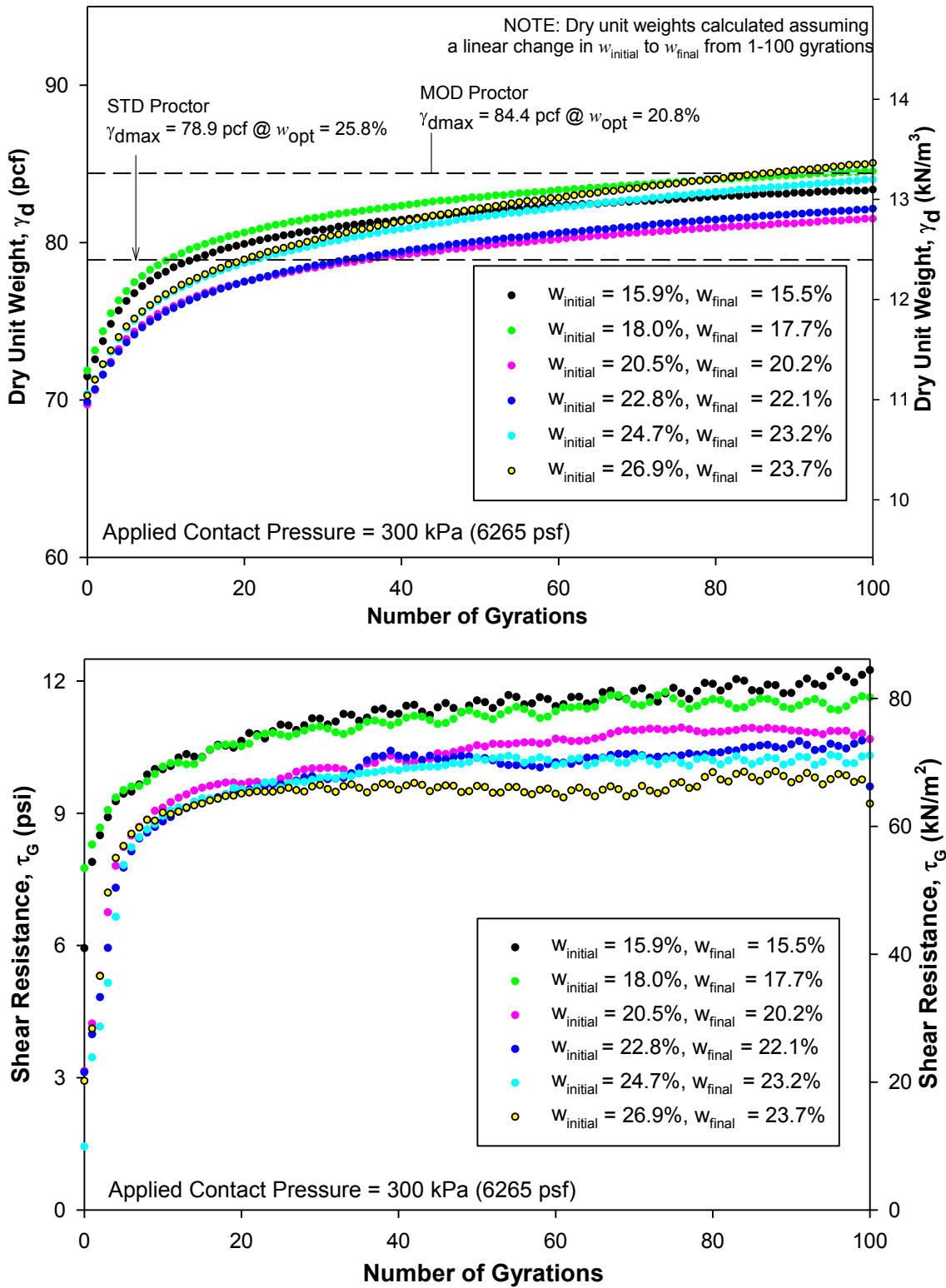
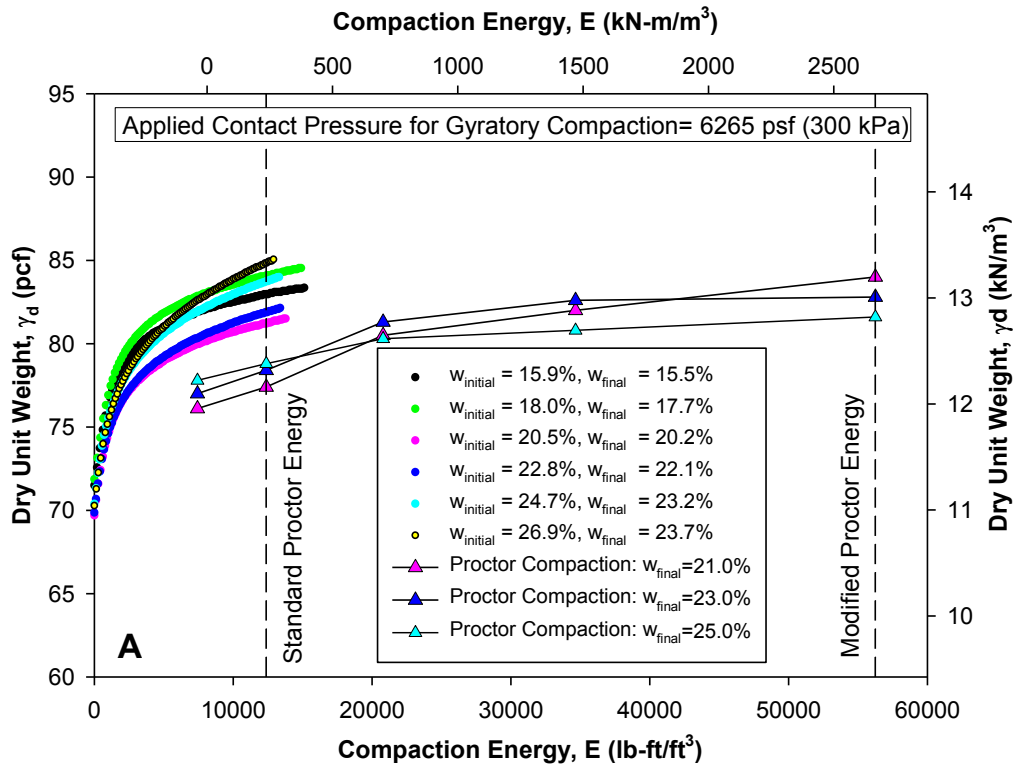


Figure 139. The (A) dry unit weight and (B) shear resistance versus number of gyrations for WCF fly ash



Note: Dry unit weights calculated assuming a linear change in $w_{initial}$ to w_{final} from 1-100 gyrations

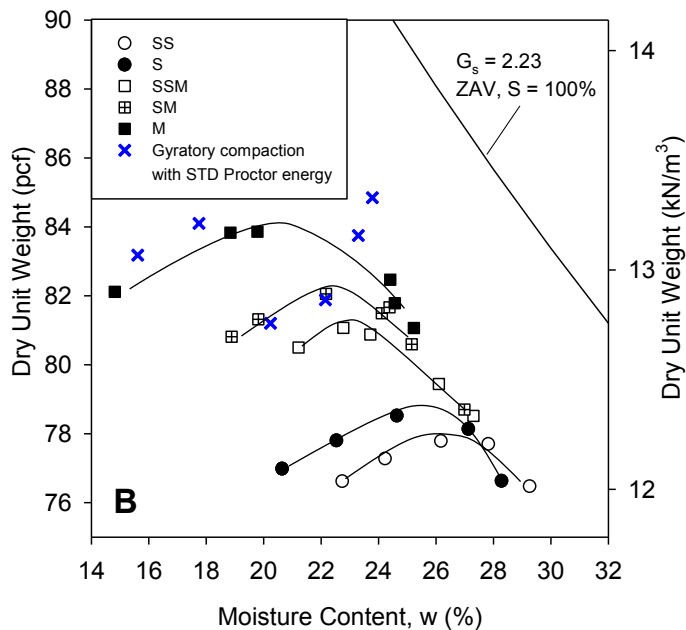


Figure 140. (A) The dry unit weight-compaction energy and (B) dry unit weight-moisture content relationships of Proctor and gyratory compaction tests for WCF fly ash

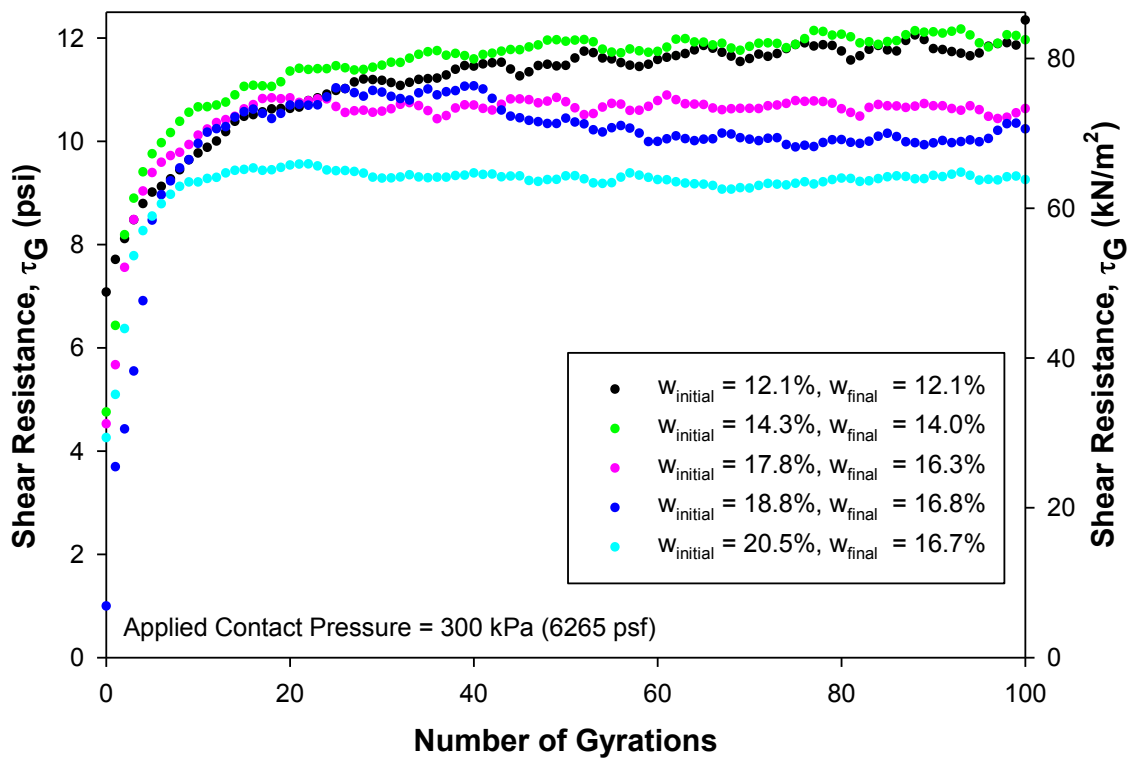
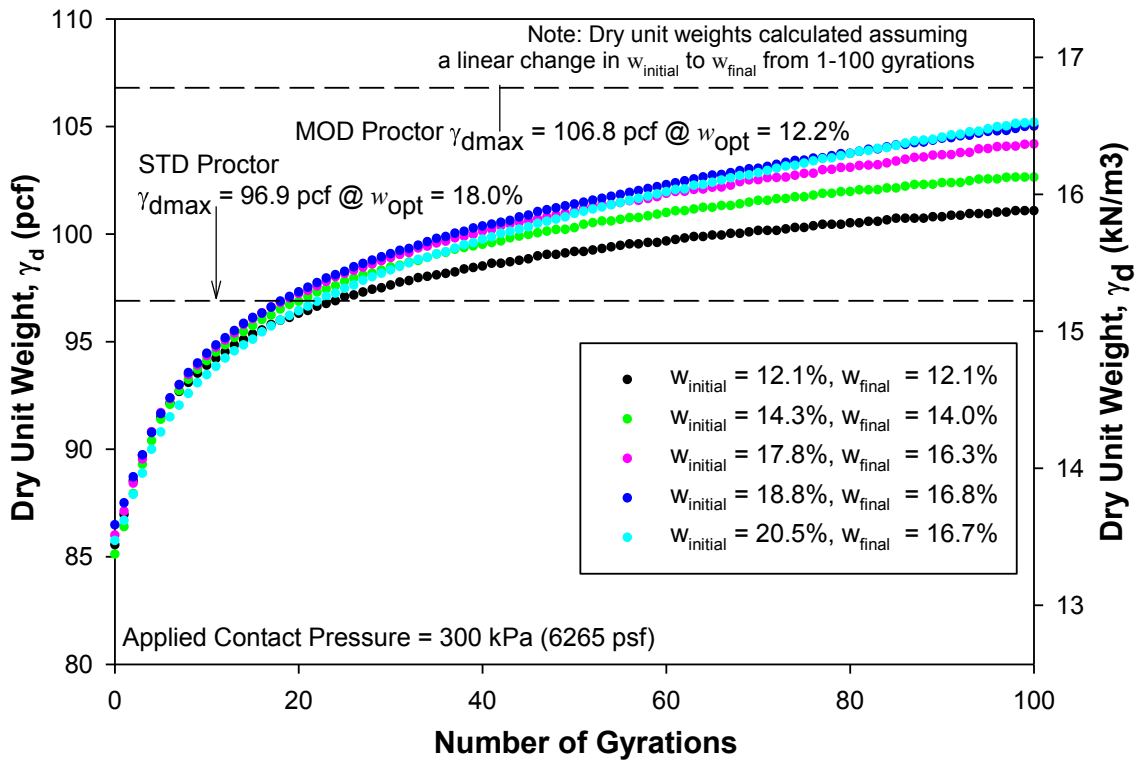
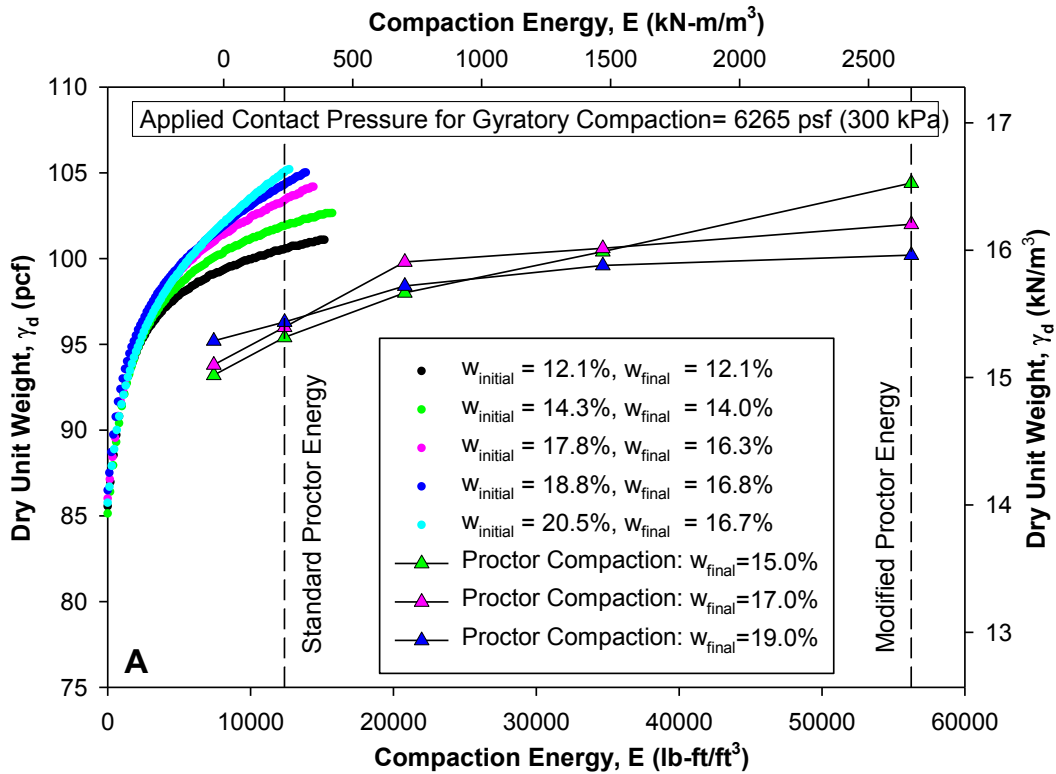


Figure 141. The (A) dry unit weight and (B) shear resistance versus number of gyrations for WCF gypsum



Note: Dry unit weights calculated assuming a linear change in $w_{initial}$ to w_{final} from 1-100 gyrations

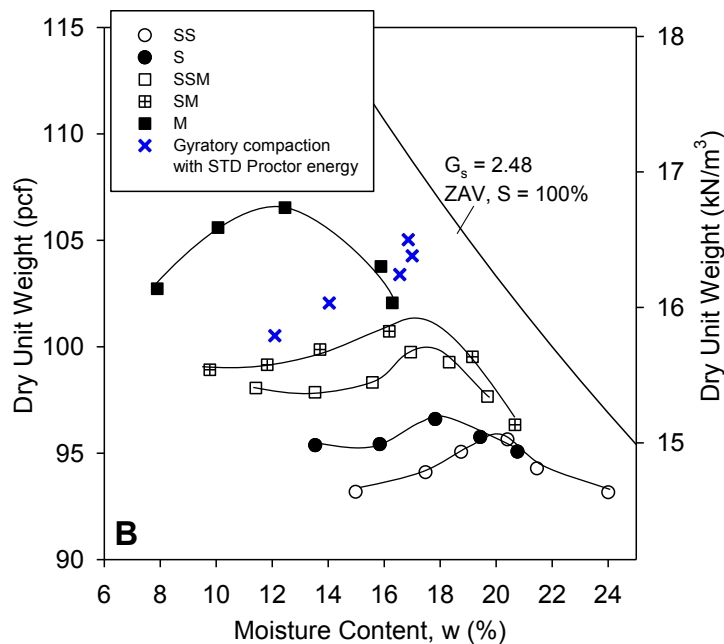


Figure 142. (A) The dry unit weight-compaction energy and (B) dry unit weight-moisture content relationships of Proctor and gyratory compaction tests for WCF gypsum

UC tests were conducted on 1 hour and 48 hours curing WCF fly ash and gypsum samples with 16 different moisture and dry density combinations to compare with the shear resistance determined using gyration compaction tests. The UC test samples were 2.8 in. in diameter and 5.6 in. high ($H/D = 2$). The undrained shear strength and secant modulus of the samples at 0.5%, 1.0%, 1.5%, and 50% of the peak strain were determined; all results are included in Appendix G. An example of determining undrained shear strength and secant modulus from the applied stress versus axial strain curve is shown in Figure 143.

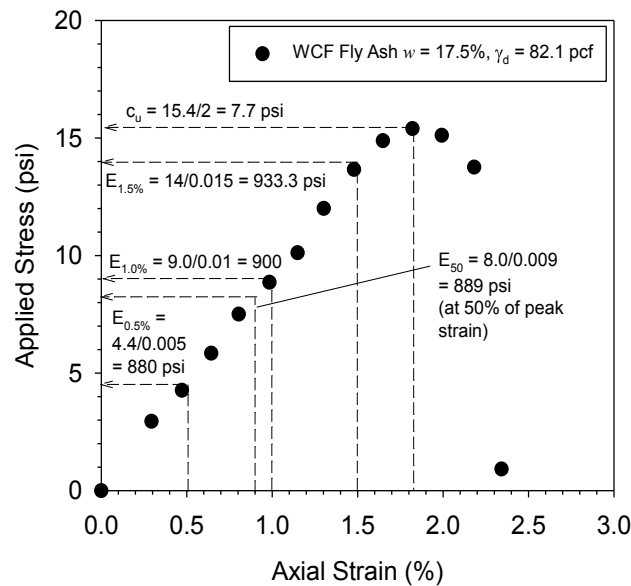


Figure 143. An example of determining undrained shear strength and secant modulus from the applied stress versus axial strain curve

Statistical analyses were performed on the shear resistance and UC test data. The statistical models and contour lines for the 1-hr and 48-hr samples of the two geomaterials are shown in Figure 144 through Figure 147. The contour lines show similar trends of the shear resistance and undrained shear strength and stiffness parameters, but the shear resistance values are higher than the undrained shear strength determined by UC tests. The different boundary conditions of the two tests may cause this difference. However, based on the test data and comparisons with the conventional test results, the gyratory compaction test can be a quick and economical laboratory test method to link the shear strength and stiffness properties with moisture-density-compaction energy relationships of compacted geomaterials.

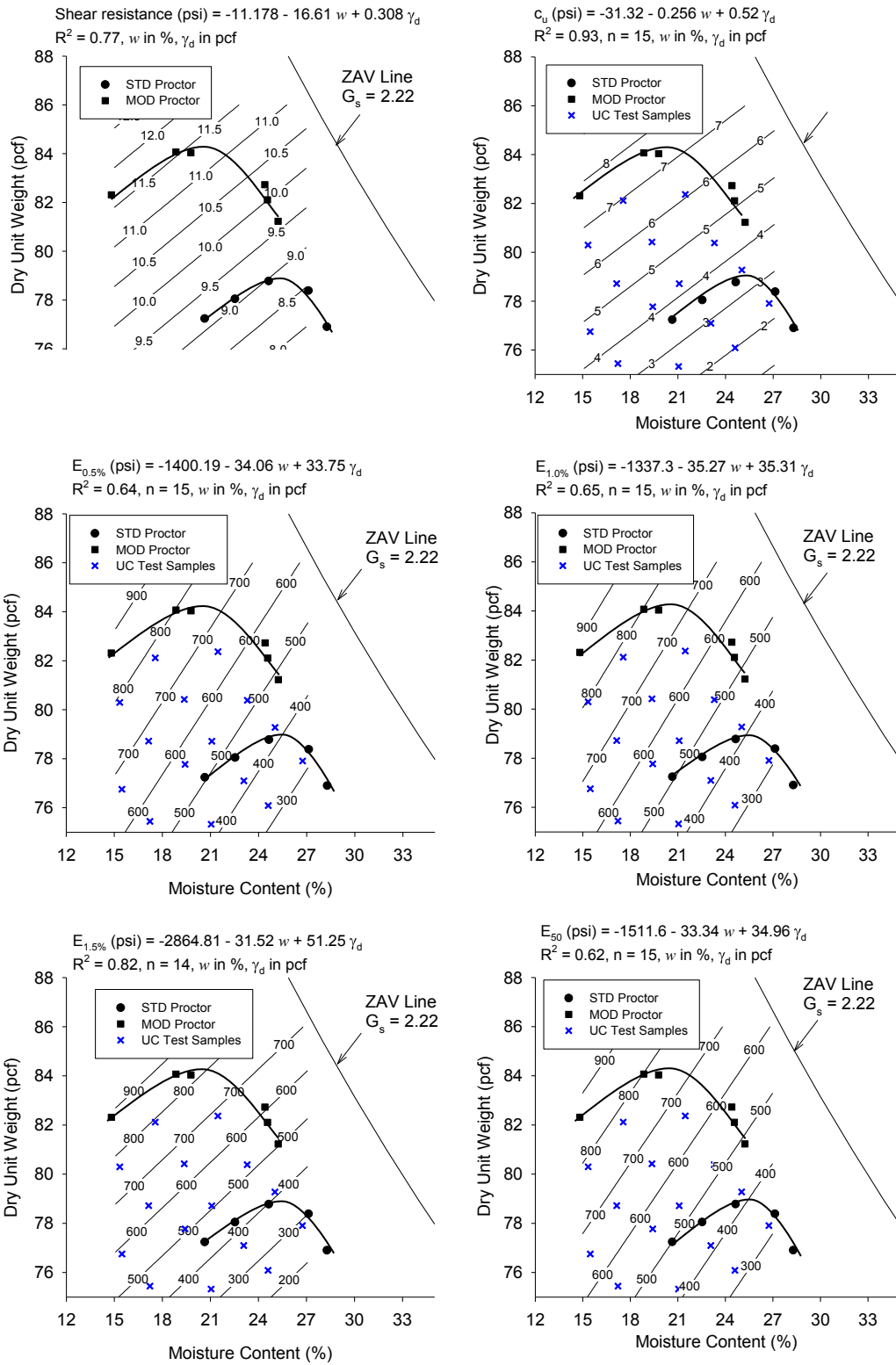


Figure 144. Statistical analysis results of gyratory compaction and 1-hr curing UC test of WCF fly ash

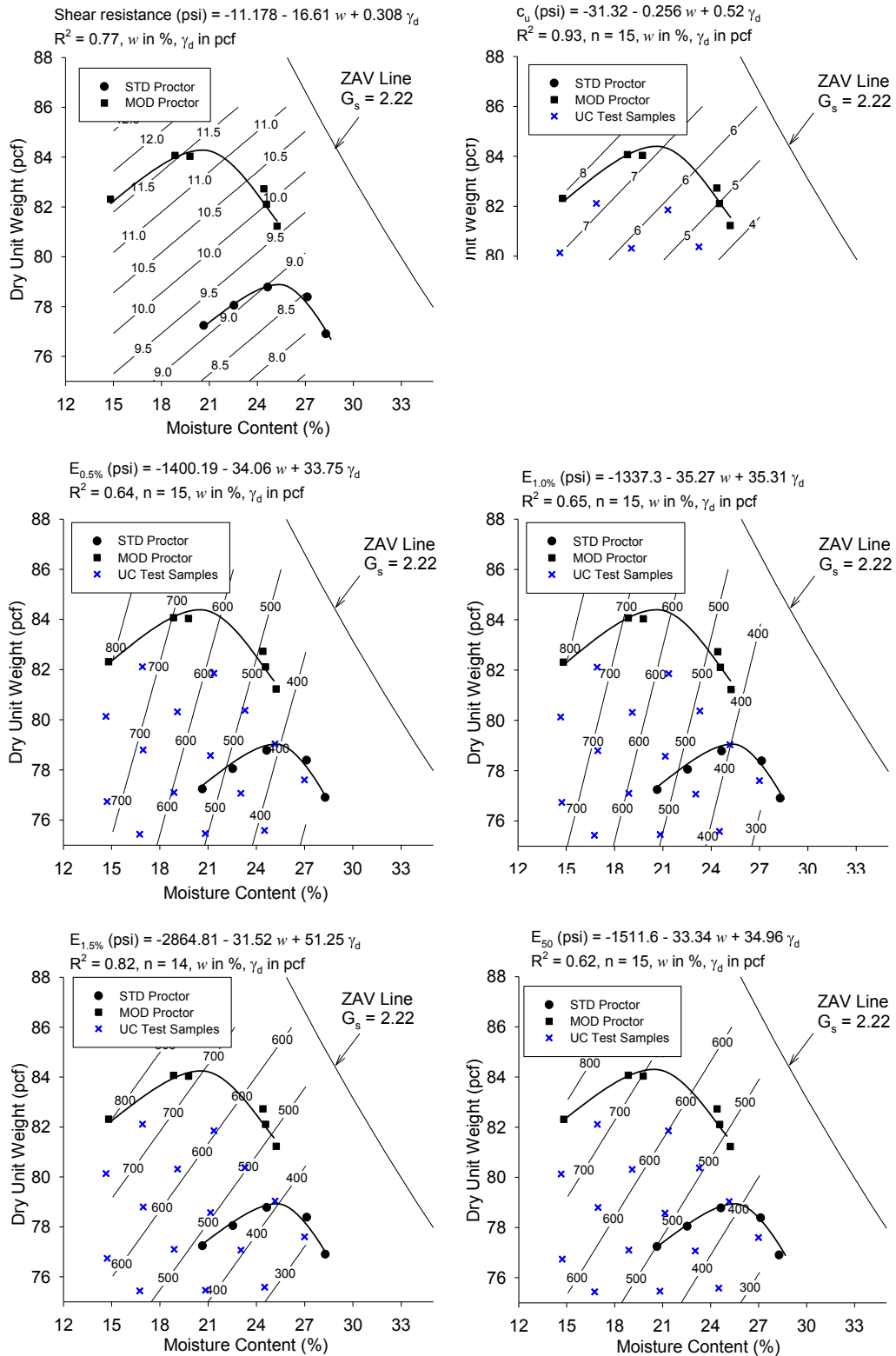


Figure 145. Statistical analysis results of gyratory compaction and 48-hr curing UC test of WCF fly ash

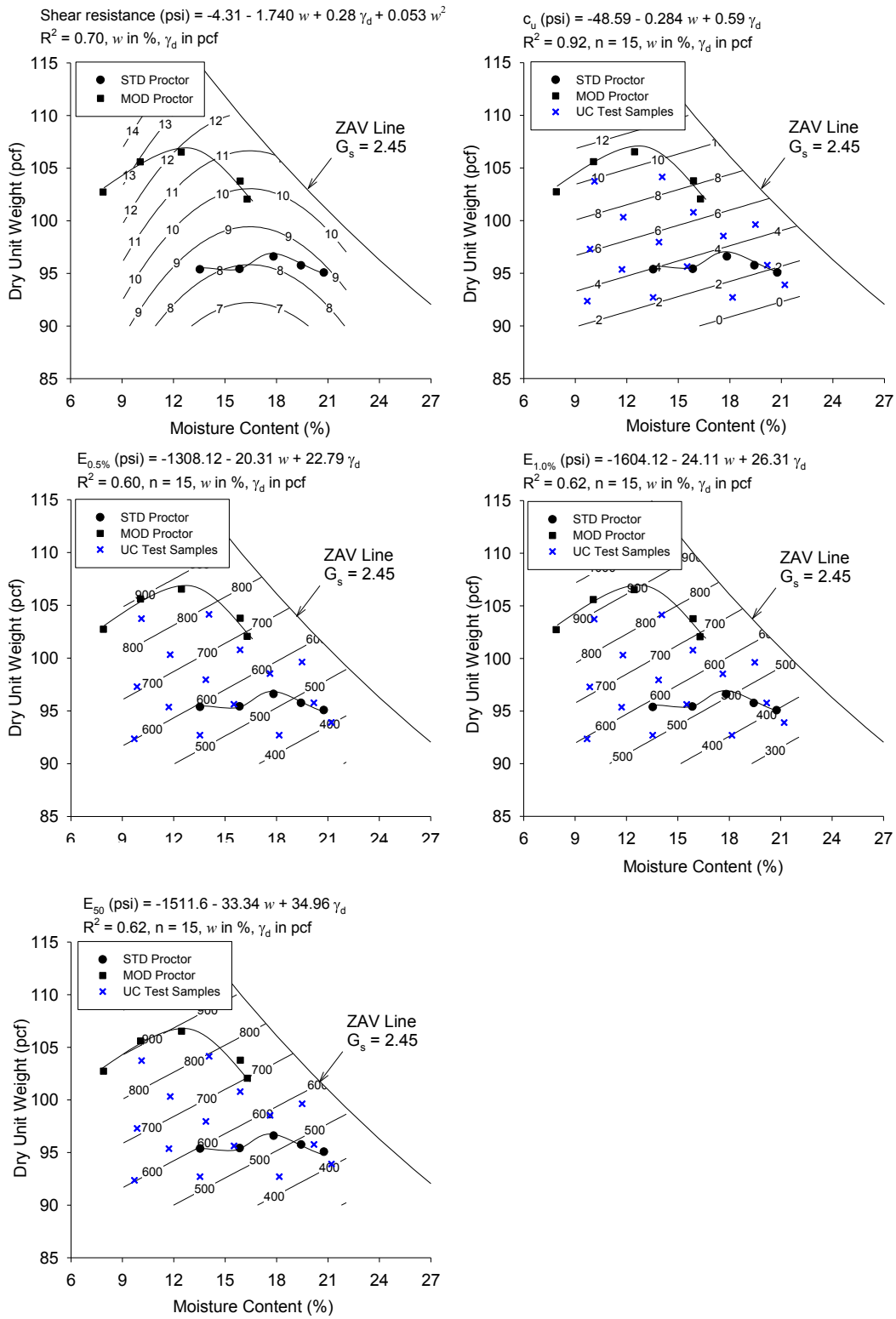


Figure 146. Statistical analysis results of gyratory compaction and UC test of 1-hr curing WCF fly ash

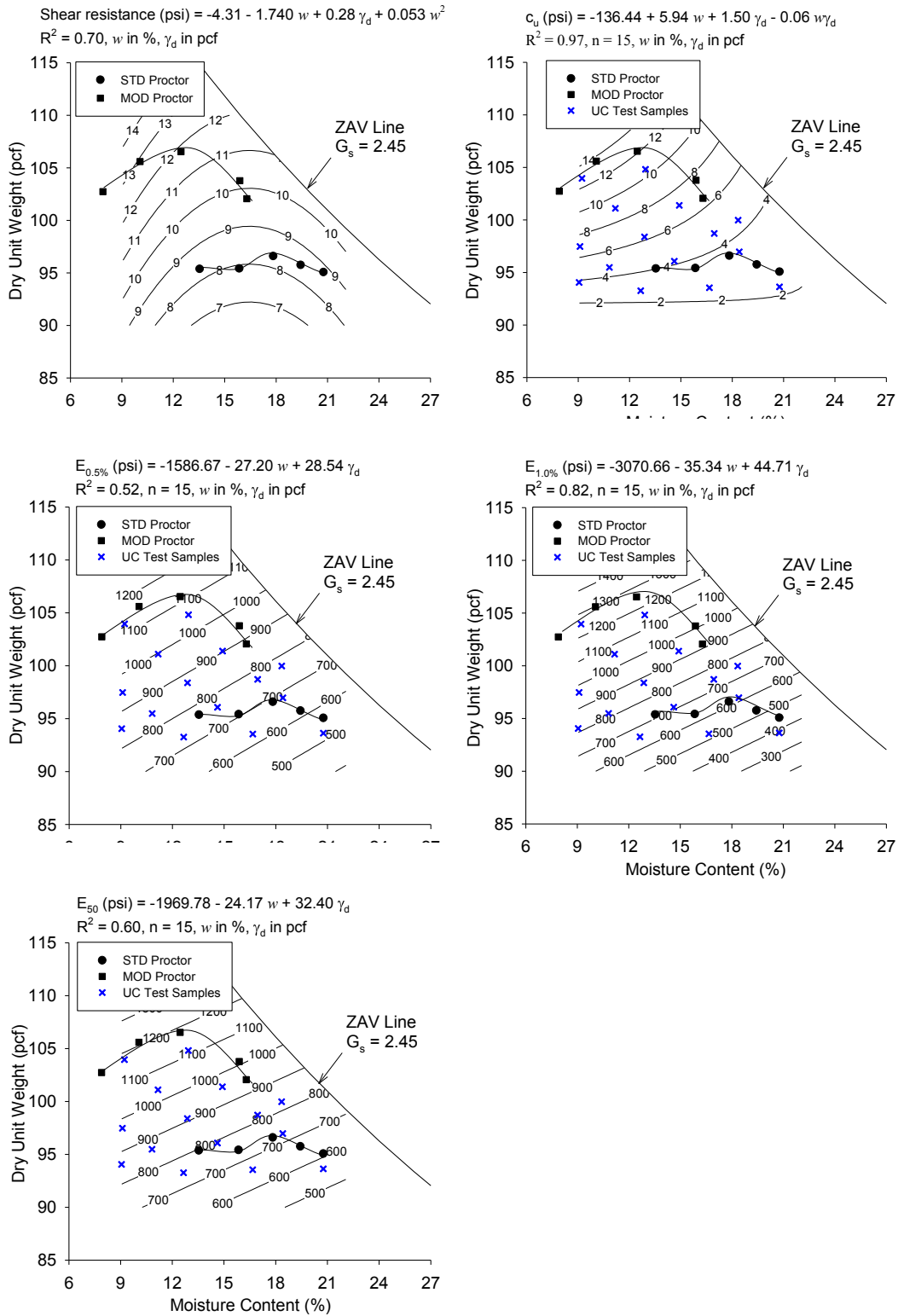


Figure 147. Statistical analysis results of gyratory compaction and UC test of 48-hr curing WCF fly ash

2012 Manatt's RAP, RPCC and RAP mixture, and crushed limestone (CFED 2061, 2062 and 2063)

Gyratory compaction tests with two vertical pressures (300 and 600 kPa) were conducted on 2012 Manatt's RAP (CFED 2061), RPCC and RAP mixture (CFED 2062), and crushed limestone (CFED 2063) to evaluate how changes in maximum grain size (MGS) and applied compaction stresses influenced the compaction behavior of the coarse grained geomaterials. The test results were compared with Proctor and vibratory compaction test results. The samples were prepared using a splitter. Sieve analysis were conducted before and after the tests at each vertical pressure. Results for all of the samples are shown in Appendix H. All of the samples were oven dried and the particles retained on $\frac{3}{4}$ in. sieve were scalped off, so the maximum grain size (MGS) of the samples was 0.75 inch. The Proctor, vibratory, and gyratory compaction test results for the three geomaterials are shown in Figure 148 through Figure 150. For the three geomaterials, both the Proctor and gyratory compaction test yielded higher dry unit weights compared with the maximum dry unit weights determined by the vibratory compaction test. The gyratory compaction test curves show that the applied vertical pressure was the dominant factor for the increases of dry unit weight for the 2012 Manatt's RAP and the RPCC + RAP. For the crushed limestone, the difference of the dry unit weights between 300 and 600 kPa vertical pressure was only about 1 pcf. Similar behavior was observed for the tests on Ottawa sand (See Figure 135 and Figure 137).

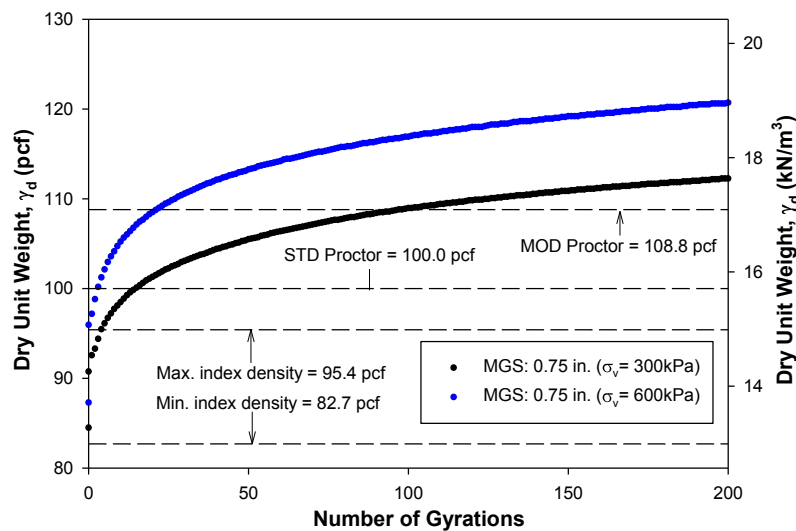


Figure 148. Gyratory, Proctor, and vibratory compaction test results for 2012 Manatt's RAP

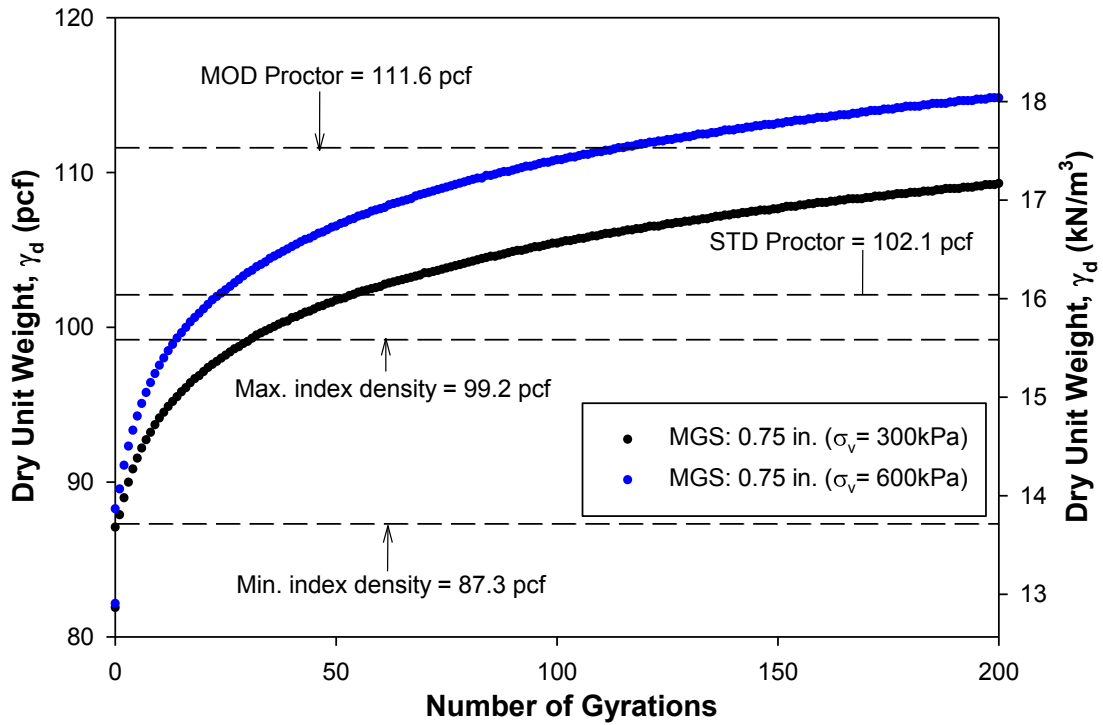


Figure 149. Gyratory, Proctor, and vibratory compaction test results for RPCC+RAP

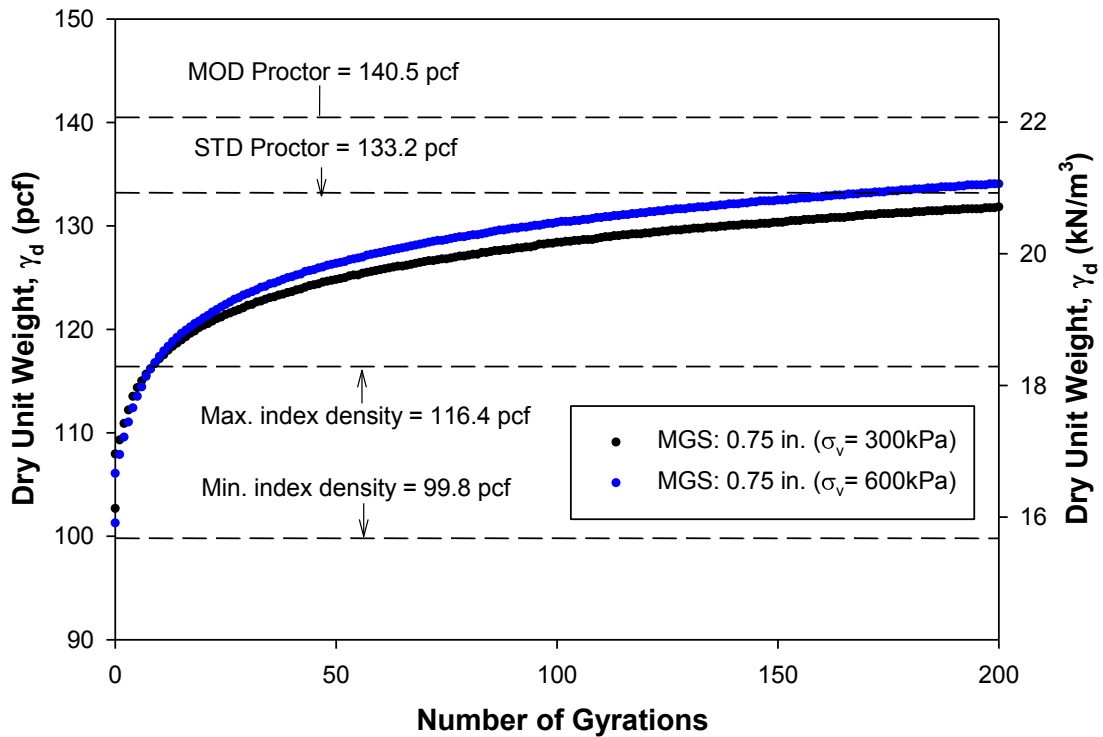


Figure 150. Gyratory, Proctor, and vibratory compaction test results for the crushed limestone

The gyratory compaction test was used to evaluate the effects of changes in MGS on compaction behaviors and shear resistance of the three coarse grained geomaterials. Two samples of each material passing $\frac{3}{4}$ in. sieve with the same mass were prepared for the 300 and 600 kPa vertical pressure tests. The samples were sieved between the tests at each vertical pressure to reduce the MGS (from 0.75 to 0.5 and 0.375 in.). Sieve analysis tests were conducted before and after the gyratory compaction tests at each vertical pressure to compare the difference of gradations.

The dry unit weight and shear resistance versus the number of gyrations for the samples with different MGS are shown in Figure 151 to Figure 153. The compaction curves for each material at different MGS under the same vertical pressures are nearly parallel. Most of the maximum dry unit weight and shear resistance was achieved in the first 30 gyrations for all three geomaterials. For 2012 Manatt's RAP, the different MGS size samples yielded different dry unit weights as the number of gyrations increased but the resulting shear resistances of the samples under the two different vertical pressures were almost same. Similar behaviors were observed for RPCC and RAP mixture under 300 kPa vertical pressure tests. For the 600 kPa tests, the smaller MGS sample yielded higher shear resistance. The crushed limestone test results showed that higher applied vertical pressure yielded higher dry unit weight and shear resistance of the same MGS samples, and the smaller MGS samples resulted in higher dry unit weight and shear resistance during the tests.

In a word, the results showed that higher applied vertical pressure can yield higher dry unit weight for samples with the same MGS, and the smaller the grain size is, the greater densities are reached. However, the trends of the shear resistance variation between the different MGS samples under different vertical pressure cannot be predicted based only on the dry unit weight changes.

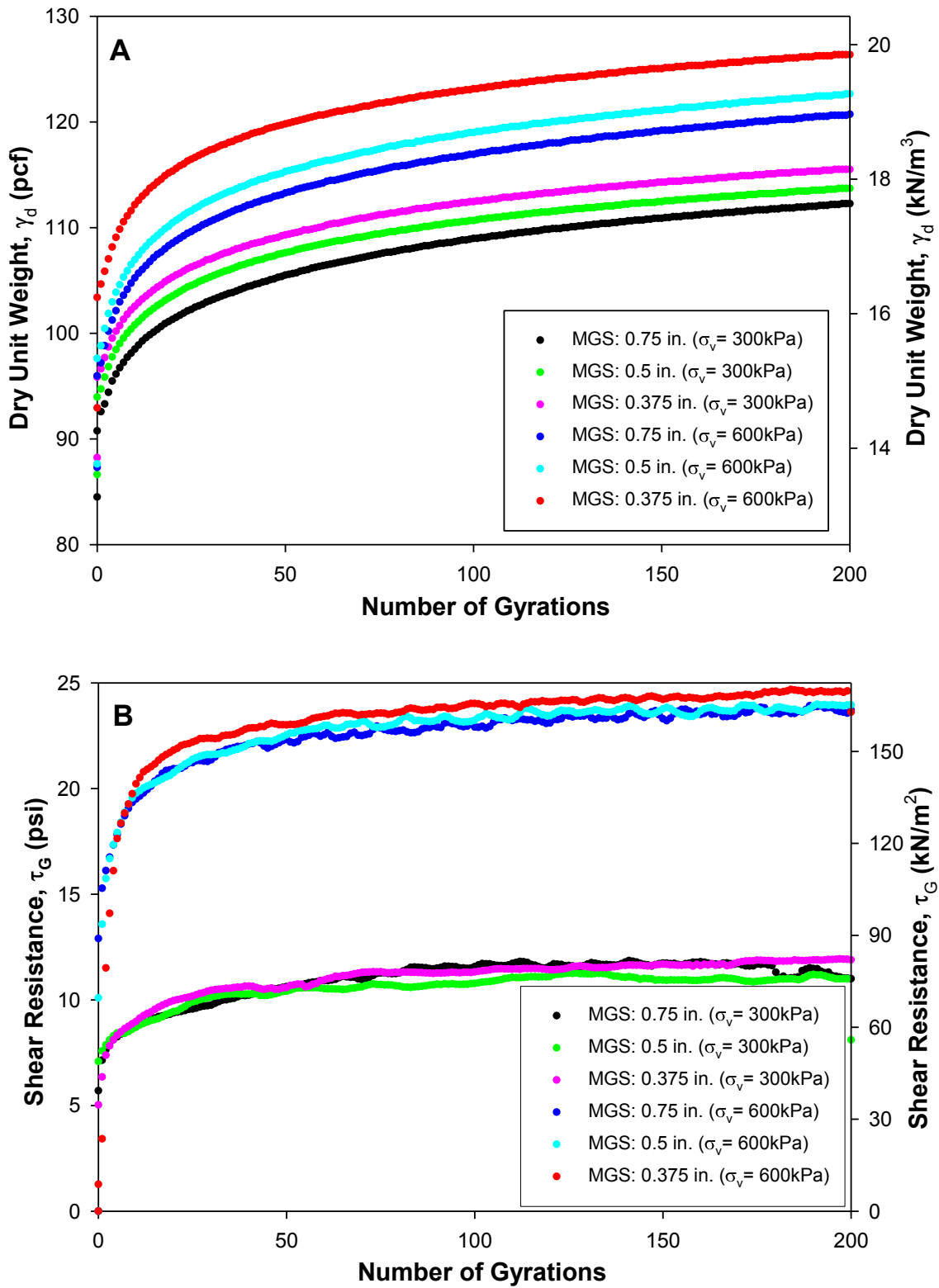


Figure 151. Effect of the maximum grain size on the (A) dry unit weight and (B) shear resistance of 2012 Manatt's RAP

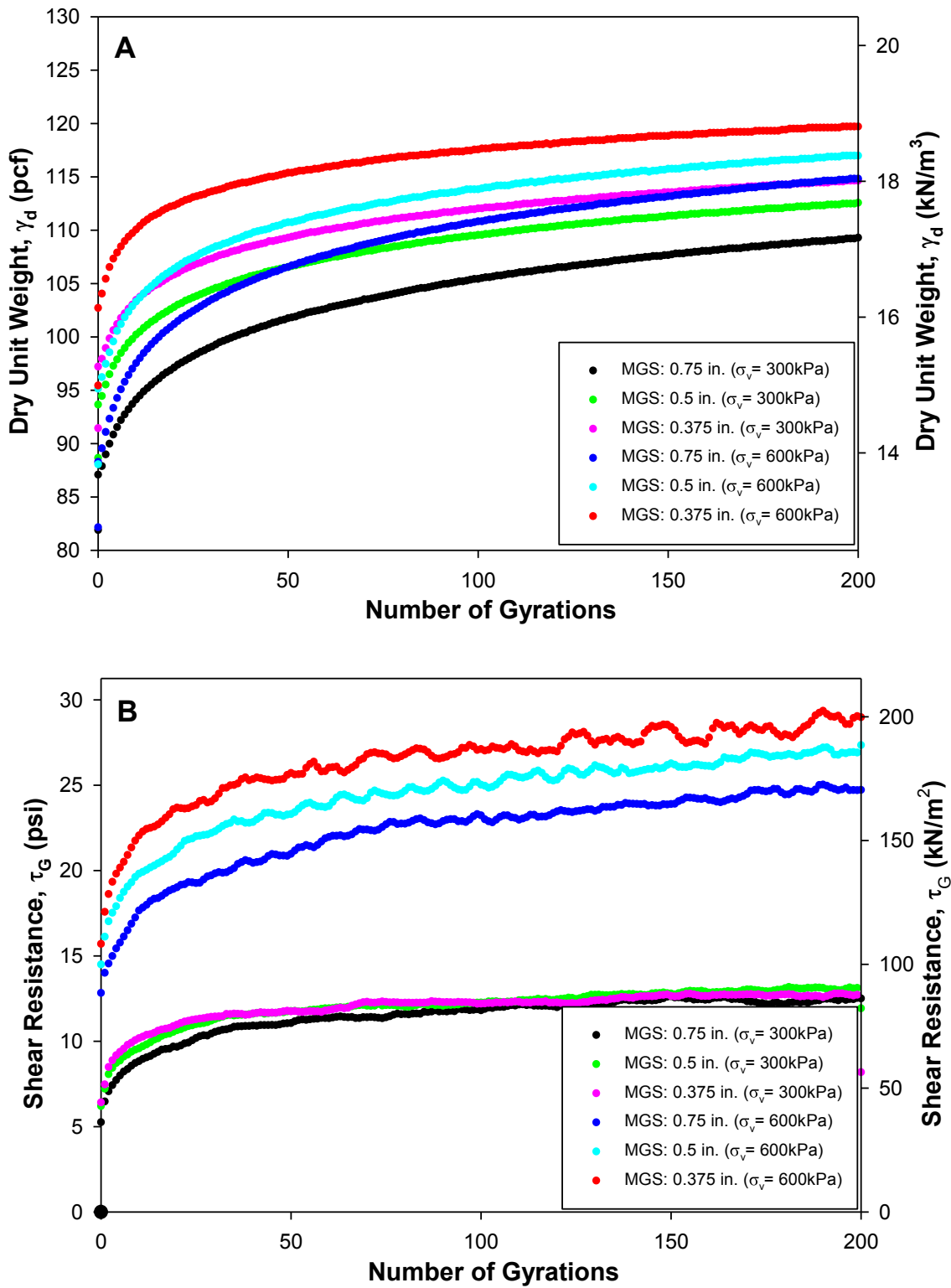


Figure 152. Effect of the maximum grain size on the (A) dry unit weight and (B) shear resistance of RPCC+RAP

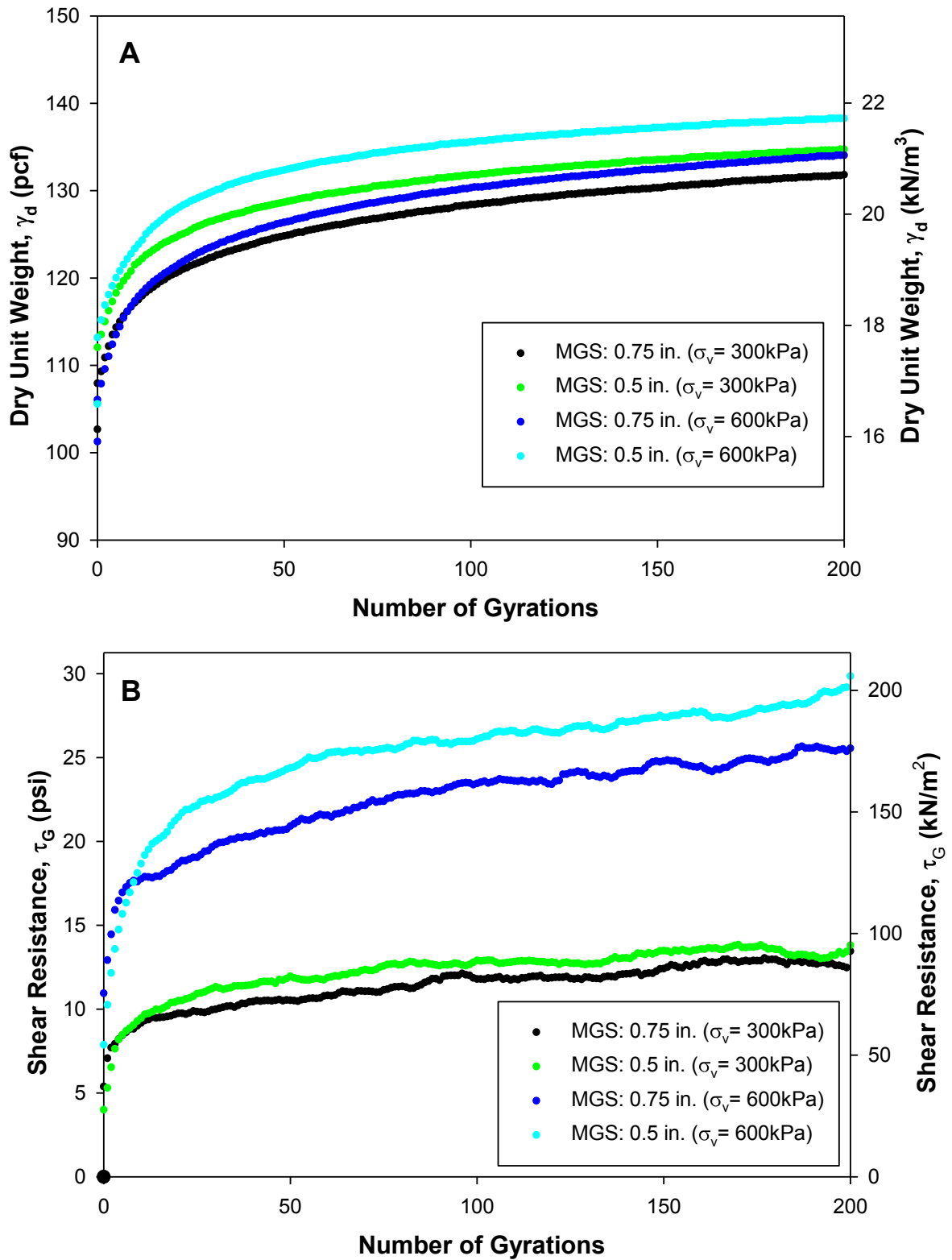


Figure 153. Effect of the maximum grain size on the (A) dry unit weight and (B) shear resistance of the crushed limestone

The dry unit weight versus compaction energy of the Proctor, gyratory, and vibratory compaction tests for the three geomaterials are shown in Figure 154 through Figure 156. The gyratory compaction test with 600 kPa vertical pressure produced the most compaction energy and yielded the highest dry unit weights. The maximum dry unit weights determined by the vibratory compaction tests were lower than the gyratory compaction and Proctor test results for the 0.75 in. MGS samples.

As shown in Figure 154, with producing same amount of compaction energy, gyratory compaction with 600 kPa vertical pressure resulted in higher dry unit weights than other compaction methods for 2012 Manatt's RAP. From the results, increasing the applied vertical pressure can be considered as the most effective way to compact this geomaterial. Figure 155 shows that when the compaction energies are below standard Proctor compaction energy, the compaction curves of the RPCC and RAP mixture between 300 and 600 kPa vertical pressure are very similar but after the compaction energy passed the standard Proctor, the higher vertical pressure yielded higher dry unit weights. For the crushed limestone, Figure 156 shows that at same compaction energy level, the gyratory compaction tests with 300 kPa vertical pressure yielded higher dry unit weight than the 600 kPa tests. This phenomenon may be due to either over-compaction caused by the high vertical pressure or the difference between the gradations of the two samples. Compared the gradation curves of the two crushed limestone samples, the gradation differences between the two samples can be negligible.

In gyratory compaction test, the applied vertical pressure is an important influence factor to the compaction behaviors of the geomaterials. Gyratory compaction tests with different vertical pressures can determine the relationships of the applied vertical pressure, compaction energy, and as compacted dry unit weight of the geomaterials and then select the most suitable compactor.

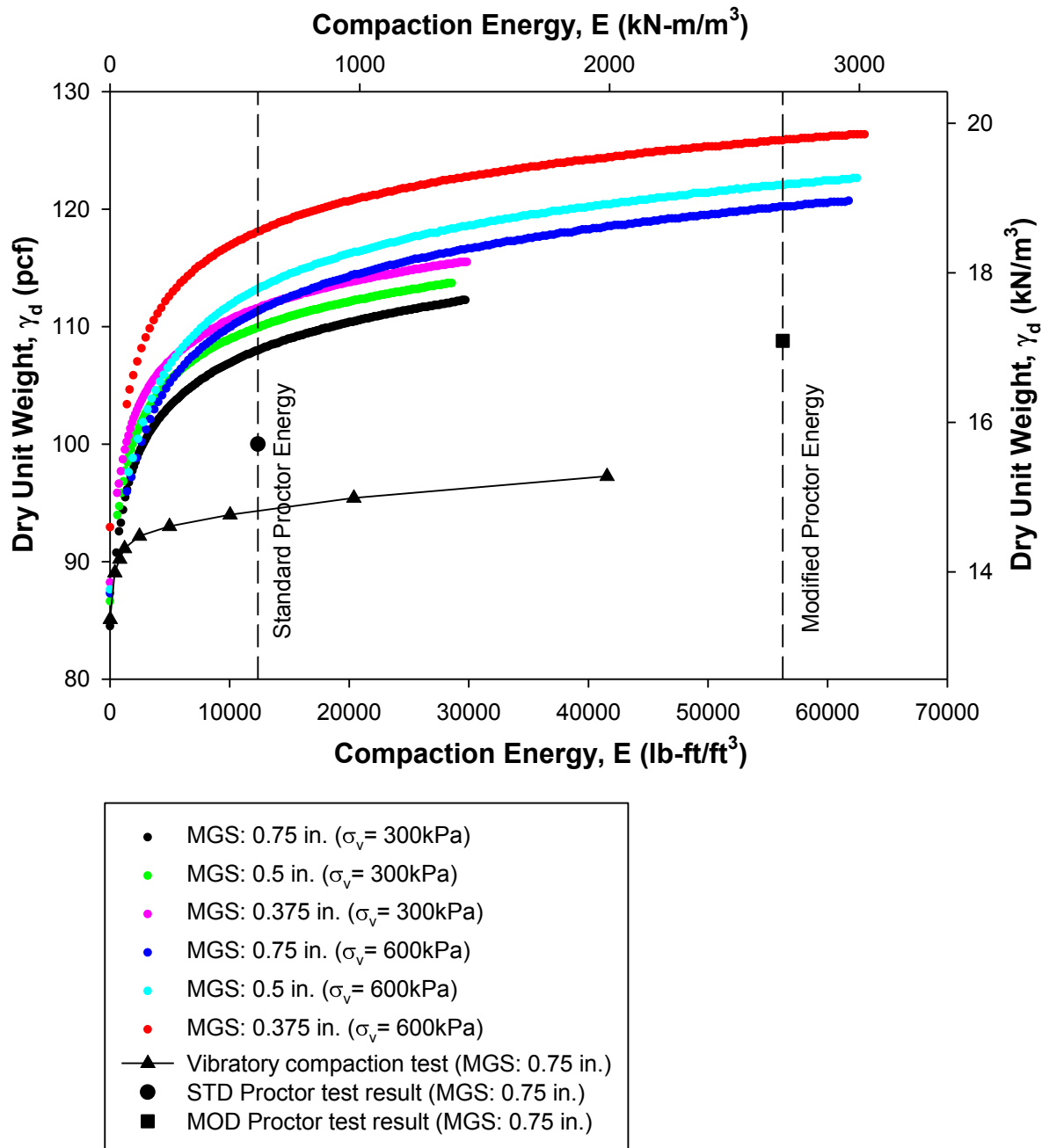


Figure 154. Dry unit weight versus compaction energy of gyratory, Proctor, and vibratory compaction test for 2012 Manatt's RAP

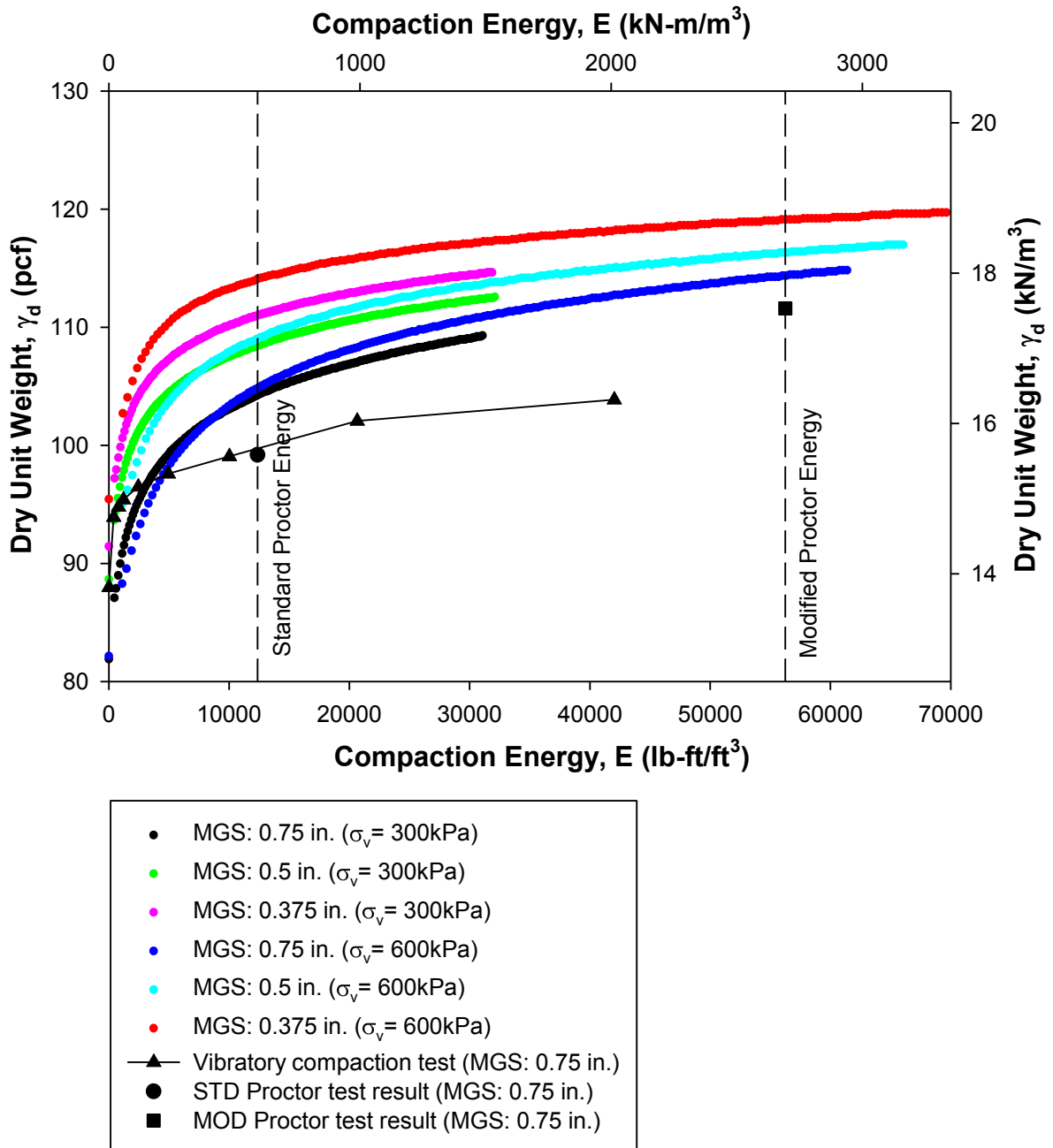


Figure 155. Dry unit weight versus compaction energy of gyratory, Proctor, and vibratory compaction test for RPCC and RAP mixture

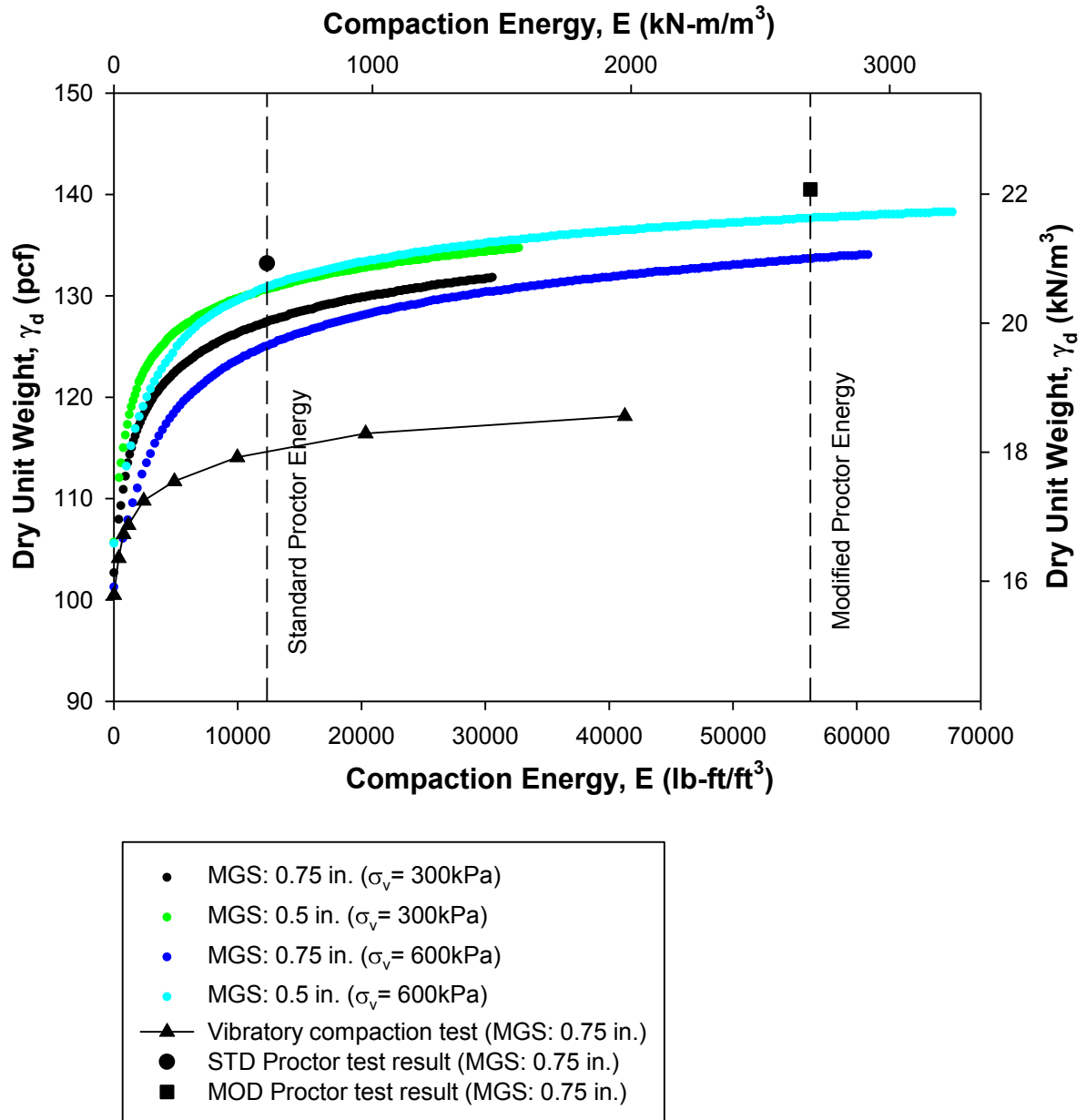


Figure 156. Dry unit weight versus compaction energy of gyratory, Proctor, and vibratory compaction test for the crushed limestone

Table 66 summarizes the laboratory compaction test results of the three geomaterials and Ottawa sand for repeatability and reproducibility analysis. The compactibility were calculated based on the maximum void ratios that were determined by the vibratory compaction tests and the minimum void ratios from each compaction method. Hilf (1991) pointed out that well-graded cohesionless soils has large compactibility (F) and the F of uniform soils is small. Hence, the F is large, the soils are easily compacted. Table 66 shows, for Ottawa sand, the F from the vibratory and gyratory compaction tests are very close, but for other three geomaterials, the different compaction methods resulted in very different F. Based on the comparison, the most effective compaction method can be selected for the three geomaterials.

Table 66. Proctor, vibratory, and gyratory compaction test results of the geomaterials

	Parameters	2012 Manatt's RAP	RPCC + RAP	Crushed limestone	Ottawa sand
Density	Minimum index density, ρ_{dmin} , (pcf)	82.7	87.3	99.8	97.5
	Maximum index density, ρ_{dmax} , (pcf)	95.4	102.1	116.4	110.3
	Standard Proctor density, STD γ_d , (pcf)	100.0	99.2	133.2	—
	Modified Proctor density, MOD γ_d , (pcf)	108.8	111.6	140.5	—
	300 kPa Gyratory compaction density at 200 gyration, γ_d , (pcf)	112.4	109.3	123.0	110.8
	600 kPa Gyratory compaction density at 200 gyration, γ_d , (pcf)	120.7	114.8	124.4	110.8
Void ratio	Vibratory compaction maximum index void ratio, e_{max}	0.86	0.50	0.69	0.70
	Vibratory compaction minimum index void ratio, e_{min}	0.62	0.28	0.45	0.53
	STD Proctor void ratio, e	0.54	0.32	0.27	—
	MOD Proctor void ratio, e	0.42	0.17	0.20	—
	300 kPa gyratory compaction void ratio at 200 gyration, e	0.37	0.20	0.37	0.49
	600 kPa gyratory compaction void ratio at 200 gyration, e	0.28	0.14	0.36	0.48
Compactibility	Vibratory compaction compactibility, F	0.403	0.768	0.534	0.394
	STD Proctor compactibility, F	0.596	0.561	1.576	—
	MOD Proctor compactibility, F	1.073	1.876	2.411	—
	300 kPa gyratory compaction compactibility, F	1.326	1.519	0.853	0.418
	600 kPa gyratory compaction compactibility, F	2.119	2.542	0.932	0.461

Note: — test not performed

CHAPTER 6. CONCLUSIONS

This chapter summarizes the laboratory test results and key findings from statistical analysis of the factors that influence shear strength and stiffness of compacted geomaterials. This summary is presented in three sections: laboratory compaction test results, Iowa K test results, and gyratory compaction test results.

Laboratory Compaction Test Results

Proctor compaction and vibratory compaction tests were conducted on 13 geomaterials to determine the compaction behaviors.

Proctor compaction test

Proctor compaction test results of 9 geomaterials including waste by-product materials, recycled aggregates, chemically stabilized soils, and virgin aggregate materials obtained from Alabama, Florida, Illinois, Iowa, and Tennessee were incorporated into the existing Compaction Forecasting Expert Database (CFED).

Proctor test results of the geomaterials generally indicated that with higher Proctor compaction energy, the materials achieved higher maximum dry unit weight and lower optimum moisture content. However, for a poorly graded sand material (CFED 2059 Florida 9B fill), there was a reduction in the maximum dry unit weight as Proctor compaction energy increased from SM to M energy level that may be caused by sample disturbance (or de-compaction) in the Proctor mold due to over-compaction. The curves on the wet side of optimum generally tend to parallel the 100% saturation line, and the points of optimum moisture content at each energy level also tend to parallel the ZAV line. For two granular materials CFED 2052 and 2059 (SW-SM and SP), the Proctor curves showed the lowest dry unit weight at the “bulking” moisture content.

Unconfined compression (UC) tests to determine compressive strength were conducted on the Proctor samples of the western Iowa loess stabilized with 15% fly ash and 9% type I cement (CFED 2057 and 2058). The results showed that increasing compaction energy levels increases the compressive strength on the dry side of optimum moisture content, while there is little change in compressive strength as compaction energy increases on the wet of optimum. Also, the unconfined compressive strength of the samples wet of optimum

moisture content were significantly lower than the samples dry of optimum. Both the compaction energy and moisture content were considered as the statistical significant factors to the compressive strength of chemically stabilized loess.

Vibratory compaction test

Vibratory compaction tests were conducted on 2012 Manatt's RAP (CFED 2061), RPCC and RAP mixture (CFED 2062), crushed limestone (CFED 2063), and Ottawa sand (ASTM 20-30 sand) to determine the compaction behaviors. Only oven dried samples were used in this study. The tests results showed that, for the four materials, most of the compaction was achieved in the first 60 sec of the test and no over-compaction was observed during the tests. Standard and modified Proctor tests were also conducted on the 2012 Manatt's RAP, RPCC + RAP, and crushed limestone to compare with the vibratory compaction test results. The vibratory compaction test yielded the lowest dry unit weights of the three compaction methods.

Iowa K Test Results

The Iowa K test was conducted on five geomaterials to evaluate its performance for measuring undrained shear strength and stiffness properties of compacted geomaterials. Samples with varied moisture content and dry unit weight combinations were prepared to evaluate how changes in the moisture content and dry unit weight influenced the shear strength and stiffness of the compacted samples. Statistical analyses were conducted based on the Iowa K test data to determine influence factors for each parameter.

Western Iowa loess (CFED 1634)

The initial moisture contents and dry unit weights of the western Iowa loess samples ranged from 12.2% to 21.9% and 95.6 to 115.2 pcf (STD $w_{opt} = 18.6\%$ and STD $\gamma_{dmax} = 101.1$ pcf). The Iowa K test results of the samples showed the undrained friction angle ranged between 8.6° to 48.0° and decreased as the moisture content increased and dry unit weight decreased. The ϕ_s/ϕ ratios ranged from 0.5 to 1.2, but no specified ratio can be determined as often assumed for pile design. The undrained cohesion of the samples ranged between 0.2 to 16.9 psi and increased as the dry unit weight increased and moisture content decreased.

The vertical elastic modulus of the samples under 100 psi vertical stress of the first loading ranged from 2.0 to 9.1 ksi and decreased as moisture content increased and dry unit weight increased. The samples under the same stress of the second loading showed higher vertical elastic modulus that ranged between 5.7 to 62.0 ksi. The Poisson's ratio of samples under 100 psi of the first loading ranged between 0.10 and 0.39 and lateral stress ratios were between 0.01 and 0.67. Under 25 psi of the second loading, the Poisson's ratio ranged between 0.19 and 0.56, and lateral stress ratio were between 0.23 and 1.27. Also, both of the parameters tended to increase as the moisture content increased and dry unit weight decreased.

Texas fat clay (CFED 2043)

The initial moisture contents and dry unit weights of the Texas fat clay samples ranged from 15.7% to 28.2% and 80.5 to 104.9 pcf (STD $w_{opt} = 23.8\%$ and STD $\gamma_{dmax} = 93.4$ pcf). The Iowa K test results of the samples showed the undrained friction angle ranged between 4.7° to 34.1° and decreased as the moisture content increased. The ϕ_s/ϕ ratios ranged from 0.2 to 1.5. The undrained cohesion of the samples ranged between 6.9 to 47.9 psi and increased as the dry unit weight increased.

The vertical elastic modulus of the samples under 100 psi vertical stress of the first loading ranged from 0.6 to 16.5 ksi. The samples under the same stress of the second loading showed higher vertical elastic modulus that ranged between 3.5 to 66.5 ksi. For both of the loadings, vertical elastic modulus of the samples increased as the dry unit weight increased and moisture content decreased. The Poisson's ratio of the samples under 100 psi of the first loading ranged between 0.04 and 0.29 and lateral stress ratios were between 0.05 and 0.61. Under 30 psi of the second loading, the Poisson's ratio ranged between 0.32 and 0.54, and lateral stress ratio were between 0.49 and 1.68. Both of the parameters increased as the moisture content increased and dry unit weight decreased.

WCF fly ash (CFED 2053)

The initial moisture contents and dry unit weights of the WCF fly ash samples ranged from 15.6% to 27.9% and 78.7 to 86.6 pcf (STD $w_{opt} = 25.8\%$ and STD $\gamma_{dmax} = 78.9$ pcf). The Iowa K test results showed the undrained friction angle ranged between 32.6° to 43.4° and

increased as the dry unit weight increased. The ϕ_s/ϕ ratios maintained at approximately 0.7. The undrained cohesion of the samples showed negative values for all the samples.

The vertical elastic modulus of the samples under 100 psi vertical stress of the first loading ranged from 5.5 to 12.4 ksi. The samples under the same stress of the second loading showed higher vertical elastic modulus that ranged between 18.3 to 45.2 ksi. The Poisson's ratio of the samples under 100 psi of the first loading ranged between 0.13 and 0.25 and lateral stress ratios were between 0.20 and 0.38. Under 30 psi of the second loading, the Poisson's ratio ranged between 0.32 and 0.48, and lateral stress ratio were between 0.51 and 0.74. Both of the parameters increased as the moisture content increased and dry unit weight decreased.

WCF gypsum (CFED 2054)

The initial moisture contents and dry unit weights of the WCF gypsum samples ranged from 9.5% to 20.8% and 95.9 to 106.9 pcf (STD $w_{opt} = 18.0\%$ and STD $\gamma_{dmax} = 96.9$ pcf). The Iowa K test results of the samples showed the undrained friction angle ranged between 30.2° to 44.8° and increased as the dry unit weight increased. The ϕ_s/ϕ ratios maintained at approximately 0.8. The undrained cohesion of the samples also showed negative values for all the samples.

The vertical elastic modulus of the samples under 100 psi vertical stress of the first loading ranged from 4.6 to 11.2 ksi, and decreased as moisture content increased. The samples under the same stress of the second loading showed higher vertical elastic modulus that ranged between 8.8 to 61.6 ksi. The Poisson's ratio of the samples under 100 psi of the first loading ranged between 0.13 and 0.25, and lateral stress ratios were between 0.17 and 0.35. Under 30 psi of the second loading, the Poisson's ratio ranged between 0.26 and 0.34, and lateral stress ratio were between 0.41 and 0.58. Both of the parameters increased as the moisture content increased.

Ottawa sand (ASTM 20-30)

The initial dry unit weights of the Ottawa sand samples were between 97.6 to 107.7 pcf and void ratio ranged between 0.54 to 0.69 ($e_{min} = 0.50$ and $e_{max} = 0.70$). The Iowa K test results of the samples showed the friction angle ranged between 31.3° to 35.6° , and increased as the dry unit weight increased and void ratio decreased. The ϕ_s/ϕ ratios maintained at

approximate 0.9. The vertical elastic modulus of the samples under 100 psi vertical stress of the first loading ranged from 12.4 to 19.6 ksi, and increased as dry unit weight increased. The samples under the same stress of the second loading showed higher vertical elastic modulus that ranged between 19.8 to 30.4 ksi. The Poisson's ratio of the samples under 100 psi of the first loading were between 0.15 and 0.21 and lateral stress ratio was approximately 0.38 for all the four samples. Under 30 psi of the second loading, the Poisson's ratio was between 0.35 and 0.38, and lateral stress ratio were between 0.60 and 0.67.

Gyratory Compaction Test Results

Gyratory compaction tests were conducted on constant mass Ottawa sand samples to assess the repeatability and reproducibility of the testing devices. The R&R analysis results showed that the gyratory compaction test can provided better repeatability for than using the vibratory compaction test (ASTM D4253). The reproducibility of using the PDAs to measure the total load, eccentricity, and shear resistance for compacting geomaterials were also statistically evaluated. However, the results showed that none of these standard deviations are terribly well-determined, because the degrees of freedom were small and intervals were wide, so more data will be needed for better information.

Gyratory compaction tests were conducted on WCF fly ash and gypsum (CFED 2053 and 2054) to evaluate the feasibility of linking the shear resistance with moisture-density-compaction energy relationships for compaction of geomaterials. For both of the two geomaterials, the dry unit weight and moisture content relationship of the gyratory compaction test samples with low moisture contents shows similar trends with the Proctor curves, but the samples with high moisture contents yielded higher dry unit weights and did not follow the expected trend as the Proctor curves that may be due to the water was squeezed out from the samples during the tests. Unconfined compression (UC) test were also conducted on the two samples of these two geomaterials to compare with the shear resistances determined using the PDA. The statistical analysis results showed similar trends of the shear resistance and undrained shear strength and stiffness parameters, but the shear resistance values are higher than the undrained shear strength determined by UC tests. The difference may be caused by the different boundary conditions of the two tests.

Gyratory compaction tests were also conducted on 2012 Manatt's RAP (CFED 2061), RPCC and RAP mixture (CFED 2062), and crushed limestone (CFED 2063) to evaluate how changes in maximum grain size (MGS) and applied compaction stress influenced the compaction behavior of the coarse grained geomaterials. For 2012 Manatt's RAP, the different MGS size samples yielded different dry unit weights as the number of gyrations increased but the resulting shear resistances of the samples under the two different vertical pressures were almost same. Similar behaviors were observed for RPCC and RAP mixture under 300 kPa vertical pressure tests. However, under 600 kPa vertical pressure tests, the smaller MGS sample yielded higher shear resistance. The crushed limestone test results showed that higher applied vertical pressure yielded higher dry unit weight and shear resistance for the same MGS samples, and the smaller MGS samples resulted in higher dry unit weight and shear resistance during the tests.

The gyratory compaction test results also showed that the applied vertical pressure was the dominant factor for increasing the dry unit weight of the 2012 RAP and RPCC + RAP. For the crushed limestone, the higher vertical pressures was not significantly increased the maximum dry unit weight of the samples. Similar behavior was observed for the tests on Ottawa sand. The results also showed most of the maximum dry unit weight and shear resistance of each of the geomaterials was achieved in the first 30 gyrations of the tests.

Standard and modified Proctor, and vibratory compaction test were also conducted on the three materials to compare with the gyratory compaction test. Both the Proctor and gyratory compaction test yielded higher dry unit weights compared to the maximum dry unit weights determined by the vibratory compaction test.

Summary of Conclusions

The goal of this research was to improve the CFED by linking the moisture-density-compaction energy relationships with shear strength and stiffness properties to predict and monitor the compaction performance of geomaterials. This research demonstrated that both the Iowa K and gyratory compaction tests can simply, quickly, and inexpensively simulate field conditions, determine compaction behaviors, and measure the shear strength and stiffness of compacted geomaterials.

The test results also indicated that moisture content and dry unit weight can significantly influence shear strength and stiffness properties of fine-grained compacted geomaterials. For coarse-grained materials, the maximum aggregate size and applied compaction pressure are significant factors that can influence compaction behavior and shear resistance.

CHAPTER 7. RECOMMENDATIONS

This chapter presents recommendations in two parts: recommendations for future research and recommendations for future practice.

Recommendations for Future Research

As I conducted this research, I recognized some directions for future research. These are some research activities related to the Iowa K test.

- Study the causes of the negative cohesions and Poisson's ratios that were measured using the Iowa K test.
- Study the boundary conditions of the Iowa K test and determine a correction method to better estimate the major and minor principal stresses on samples during the tests.
- Study the relationships between the shear strength and stiffness of compacted geomaterial and vertical and confining stress conditions using the Iowa K test.
- Perform the Iowa K test on additional materials and compare the results with standardized laboratory test results to further confirm that the Iowa K test can simulate field conditions.
- Conduct a field study using the nuclear gauge, borehole shear test (BST), dynamic cone penetration test (DCP), and light weight deflectometer (LWD) test to compare and validate the Iowa K test results.
- Design and build a new Iowa K test mold that can adjust confining stresses for different types of geomaterials, measure shear strength and stiffness parameters of samples at small stresses or strains, and also can be used as a standardized Proctor mold. Figure 157 shows a drawing of the proposed Iowa K test mold. It consists of four segments and flexible Teflon stripes that are restrained using springs. The four segments and Teflon strips also can maintain the mold in a nearly circular shape when the mold expands. The inside dimension of the mold is same with 4 in. Proctor mold (4 in. diameter and 4.584 in. height). The springs can be replaced, and different stiffness springs will be used for testing different materials. Two expandable clamps are attached on the top and bottom of the mold for mounting the LVDTs during the test. Also, if samples need to be directly compacted in the mold, an extension collar

will be assembled with the mold. The two clamps also can be locked to prevent expansion of the mold during compaction. The spring constant can be determined according to Hooke's law, so the applied confining stress can be calculated based on the expansion of the mold. The proposed mold also can be calibrated using the same method for calibrating the current Iowa K test mold which has been introduced in Chapter 3 of this thesis.

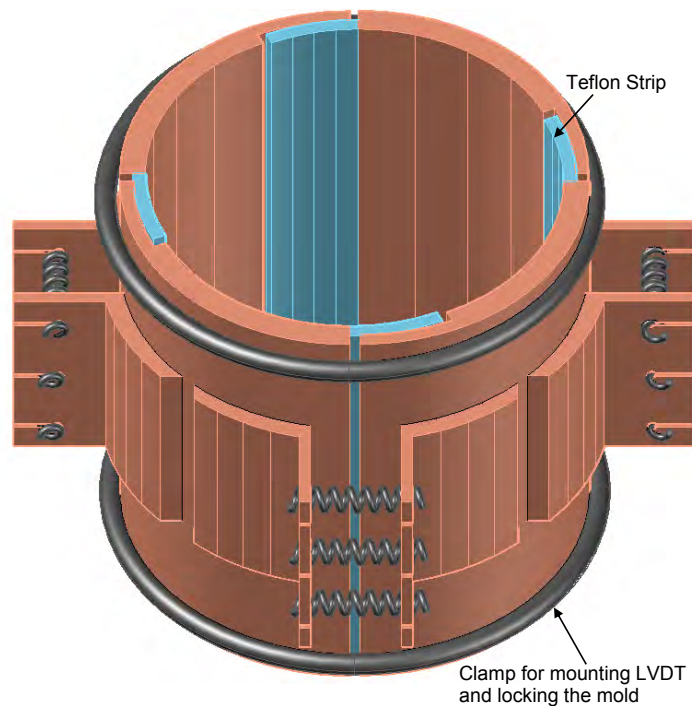


Figure 157. The proposed Iowa K test mold

These are some activities that would extend research into the gyratory compaction test.

- Improve the gyratory compaction device to prevent the moisture loss for testing free-draining geomaterials (e.g., O-rings may be attached on the top and bottom loading plates).
- Compare the gyratory compaction test results with Proctor test results to confirm whether the gyratory compaction test can determine the optimum moisture content and maximum dry unit weight of compacted geomaterials.
- Correlate the shear resistance determined using the PDA to some standardized laboratory test results.

- Build a mathematical model for the compaction curves determined using the gyratory compaction test and use the gyratory compaction test to expand CFED.
- Conduct a field study using some in situ tests such as BST, DCP, and LWD test to measure the shear strength and stiffness parameters after each pass of the compactor and compare the results with the compaction curves and shear resistances determined using the laboratory gyratory compaction test.

Recommendations for Future Practice

- Use the Iowa K test to measure undrained shear strength and stiffness parameters of compacted geomaterials to evaluate how changes in moisture content and dry unit weight can influence these properties.
- Use the gyratory compaction test to determine compaction behaviors and the changes in shear resistance of geomaterials during compaction process.
- Evaluate the relationships between moisture content, dry unit weight, shear strength and stiffness properties of compacted geomaterials and set specifications for field compaction to include requirements for shear strength and stiffness parameters.

WORKS CITED

- AASHTO. (2004). "Standard Method of Test for Preparing and Determining the Density of Hot-Mix Asphalt (HMA) Specimens by Means of the Superpave Gyrotory Compactor." T-307, American Association of State Highway and Transportation Officials, Washington, D.C.
- AASHTO. (1999). "Standard Method of Test for Resilient Modulus of Unbound Granular Base/Subbase Materials and Subgrade Soils." T-294, American Association of State Highway and Transportation Officials, Washington, D.C.
- ASTM. (2007). "Standard Test Method for Density, Relative Density (Specific Gravity), and Absorption of Coarse Aggregate." Annual book of ASTM standards, ASTM C127, West Conshohocken, PA.
- ASTM. (2007). "Standard Specification for Portland Cement." Annual book of ASTM standards, ASTM C150, West Conshohocken, PA.
- ASTM. (2007). "Standard Specification for Coal Fly Ash and Raw or Calcined Natural Pozzolan for Use in Concrete." Annual book of ASTM standards, ASTM C618, West Conshohocken, PA.
- ASTM. (2007). "Standard Practice for Reducing Samples of Aggregate to Testing Size." Annual book of ASTM standards, ASTM C702, West Conshohocken, PA.
- ASTM. (2007). "Standard Practice for Dry Preparation of Soil Samples for Particle-Size Analysis and Determination of Soil Constants." Annual book of ASTM standards, ASTM D421, West Conshohocken, PA.
- ASTM. (2007). "Standard Test Method for Particle-Size Analysis of Soils." Annual book of ASTM standards, ASTM D422, West Conshohocken, PA.
- ASTM. (2007). "Standard Test Methods for Laboratory Compaction Characteristics of Soil Using Standard Effort (12 400 ft-lb/ft³ (600 kN-m/m³))." Annual book of ASTM standards, ASTM D698, West Conshohocken, PA.
- ASTM. (2007). "Standard Test Methods for Specific Gravity of Soil Solids by Water Pycnometer." Annual book of ASTM standards, ASTM D854, West Conshohocken, PA.
- ASTM. (2007). "Standard Test Methods for Laboratory Compaction Characteristics of Soil Using Modified Effort (56,000 ft-lb/ft³ (2,700 kN-m/m³))." Annual book of ASTM standards, ASTM D1557, West Conshohocken, PA.
- ASTM. (2007). "Standard Test Methods for Compressive Strength of Molded Soil-Cement Cylinders." Annual book of ASTM standards, ASTM D1633, West Conshohocken, PA.
- ASTM. (2007). "Standard Test Methods for Unconfined Compressive Strength of Cohesive Soil." Annual book of ASTM standards, ASTM D2166, West Conshohocken, PA.
- ASTM. (2007). "Standard Test Methods for Laboratory Determination of Water (Moisture) Content of Soil and Rock by Mass." Annual book of ASTM standards, ASTM D2216, West Conshohocken, PA.

- ASTM. (2007). "Standard Test Methods for One-Dimensional Consolidation Properties of Soils Using Incremental Loading." Annual book of ASTM standards, ASTM D2435, West Conshohocken, PA.
- ASTM. (2007). "Standard Practice for Classification of Soils for Engineering Purposes (Unified Soil Classification System (USCS))." Annual book of ASTM standards, ASTM D2487, West Conshohocken, PA.
- ASTM. (2007). "Standard Test Method for Resistance R-Value and Expansion Pressure of Compacted Soil." Annual book of ASTM standards, ASTM D2844, West Conshohocken, PA.
- ASTM. (2007). "Standard Test Method for Unconsolidated-Undrained Triaxial Compression Test on Cohesive Soils." Annual book of ASTM standards, ASTM D2850, West Conshohocken, PA.
- ASTM. (2007). "Standard Test Method for Direct Shear Test of Soils under Consolidated Drained Conditions." Annual book of ASTM standards, ASTM D3080, West Conshohocken, PA.
- ASTM. (2007). "Standard Practice for Classification of Soils and Soil-Aggregate Mixtures for Highway Construction Purposes." Annual book of ASTM standards, ASTM D3282, West Conshohocken, PA.
- ASTM. (2007). "Standard Test Method for Compaction and Shear Properties of Bituminous Mixtures by Means of the U.S. Corps of Engineers Gyratory Testing Machine (GTM)." Annual book of ASTM standards, ASTM D3387, West Conshohocken, PA.
- ASTM. (2007). "Standard Test Methods for Maximum Index Density and Unit Weight of Soils Using a Vibratory Table." Annual book of ASTM standards, ASTM D4253, West Conshohocken, PA.
- ASTM. (2007). "Standard Test Methods for Minimum Index Density and Unit Weight of Soils and Calculation of Relative Density." Annual book of ASTM standards, ASTM D4254, West Conshohocken, PA.
- ASTM. (2007). "Standard Test Methods for Liquid Limit, Plastic Limit, and Plasticity Index of Soils." Annual book of ASTM standards, ASTM D4318, West Conshohocken, PA.
- ASTM. (2007). "Standard Practice for Correction of Unit Weight and Water Content for Soils Containing Oversize Particles." Annual book of ASTM standards, ASTM D4718, West Conshohocken, PA.
- ASTM. (2007). "Standard Test Method for Consolidated Undrained Triaxial Compression Test for Cohesive Soils." Annual book of ASTM standards, ASTM D4767, West Conshohocken, PA.
- ASTM. (2007). "Standard Test Method for Consolidated Drained Triaxial Compression Test for Soils." Annual book of ASTM standards, ASTM D7181, West Conshohocken, PA.
- Atkinson, J. H. (2007). *The mechanics of soils and foundations*. 2nd Ed., Taylor & Francis, New York, NY, USA.

- Bahia, H. U. (2002). *Minimum pavement lift thickness for superpave mixes*. Final report submitted to Wisconsin Highway Research Program Flexible Pavements Technical Oversight Committee and Wisconsin Department of Transportation, Madison, WI.
- Bowers, C. R., (1978). "Measurement of Poisson' ratio and tangent modulus of a loess." M.S. Thesis, University of Missouri-Rolla, Rolla, MO.
- Brooker, E. W., and Ireland, H. O. (1965). "Earth pressures at rest related to stress history." *Canadian Geotechnical Journal*, NRC Research Press, 2(1), 1–15.
- Brown, S., and Hyde, A. (1975). "Significance of cyclic confining stress in repeated-load triaxial testing of granular material." *Transportation Research Record*, (537).
- Browne, M. J. (2006). "Feasibility of using a gyratory compactor to determine compaction characteristics of soil." M.S. Thesis, Montana State University, Bozeman, MT.
- Chua, K. M., and Tenison, J. (2003). "Explaining the Hveem stabilometer test: relating R-value, S-value, and the elastic modulus." *Journal of testing and evaluation*, 31(4), 269–276.
- Coyle, H. M., and West, E. C. (1956). "Laboratory compaction of a silty clay to simulate field density curves", MS Thesis, Massachusetts Institute of Technology, MA.
- Das, B. M. (2009). *Principles of geotechnical engineering*. 7th Ed., Cengage Learning, Stamford, CT, USA.
- DelRio-Prat, M., Vega-Zamanillo, A., Castro-Fresno, D., and Calzada-Pérez, M. Á. (2011). "Energy consumption during compaction with a Gyratory Intensive Compactor Tester." *Construction and Building Materials*, Elsevier, 25(2), 979–986.
- Duncan, J. M., and Chang, C. Y. (1970). "Nonlinear analysis of stress and strain in soils." *Journal of the Soil Mechanics and Foundations Division*, ASCE, 96(5), 1629–1653.
- Duncan, J. M., and Seed, R. B. (1986). "Compaction-induced earth pressures under K_0 -conditions." *Journal of Geotechnical Engineering*, ASCE, 112(1), 1–22.
- Faheem, A., and Bahia, H. U. (2012). "*Using gyratory compactor to measure mechanical stability of asphalt mixtures*. Final report submitted to Wisconsin Department of Transportation, Madison, WI.
- Garber, N. J., and Hoel, L. A. (2009). *Traffic and highway engineering*. Thomson Engineering.
- Guler, M., Bahia, H. U., Bosscher, P. J., and Plesha, M. E. (2000). "Device for measuring shear resistance of Hot-Mix asphalt in gyratory compactor." *Transportation Research Record*, 1723(1), 116-124.
- Handy, R. L. (1995). "A stress path model for collapsible loess. *Genesis and properties of collapsible soils*, Springer, 33–47.
- Handy, R. L., Lutenecker, A. J., and Hoover, J. M. (1978). "The Iowa K-test." *Transportation Research Record*, 678. Washington, D.C. 59–66.

- Hilf, J. W. (1991). "Compacted fill." *Foundation Engineering Handbook*. Ed. Fang, H. Y. Chapman & Hall Ltd., London, U.K. 249–316.
- Hoover, J. M., Moeller, D. T., Pitt, J. M., Smith, S. G., and Wainaina, N.W. (1982). *Performance of randomly oriented fiber-reinforced roadway Soils*. Final report submitted to Iowa Department of Transportation, Iowa State University, Ames, IA.
- Huber, G. A. (1996). "Development of the Superpave gyratory compactor." The Superpave Asphalt Research Program, University of Texas at Austin.
- Kevern, J. T., Schaefer, V. R., Wang, K. (2009). "Evaluation of pervious concrete workability using gyratory compaction." *Journal of Materials in Civil Engineering*, 21, 764.
- Lambe, T. W. (1958). "The structure of compacted clay." *Journal of the Soil Mechanics and Foundations Division*, ASCE, 84(SM2), 1–35.
- Lambe, T. W. (1967). "Stress path method." *Journal of Soil Mechanics & Foundations Division*, ASCE, 93(6), 309–331.
- Lambe, T. W., and Marr, W. A. (1979). "Stress path method: second edition." *Journal of Geotechnical and Geoenvironmental Engineering*, 105(ASCE 14655 Proceeding).
- Lohnes, R. A., and Handy, R. L. (1968). "Slope angles in friable loess." *Journal of Geology*, 76, 247–258.
- Lutenegger, A. J. (1977). "The Iowa continuous K-test: a laboratory test for measuring lateral stresses in soils induced by vertical applied loads." M.S. Thesis, Iowa State University, Ames, IA.
- Lutenegger, A. J., Handy, R. L., and Hoover, J. M. "Portable variable expansion testing device for measuring lateral pressure induced on a material by a vertical applied pressure." U.S. Patent 4,122,704, issued October 31, 1978.
- Olson, R. E., (1989). "Direct shear testing." Lecture Notes, University of Texas at Austin, Austin, TX.
- Pitt, J. M. (1981). "Deformation restraint and the mechanics of soil behavior." Ph.D. dissertation, Iowa State University, Ames, IA.
- Ping, W., Xing, G., Leonard, M., and Yang, Z. (2003). *Evaluation of laboratory compaction techniques for simulating field soil compaction (Phase II)*. Final report submitted to Florida Department of Transportation, Tallahassee, Florida.
- Puls, J. M. (2008). "Compaction models for predicting moisture-density-energy relationship for earth materials." M.S. Thesis, Iowa State University, Ames, IA.
- Seed, H., Mitchell, J., and Chan, C. (1960). "The Strength of Compacted Cohesive Soils." *Research Conference on Shear Strength of Cohesive Soils*, 877–964.
- Semmelink, C. J., and de Beer, M. (1995). "Rapid determination of elastic and shear properties of road-building materials with the K-mould." Unbound Aggregates in Roads. *Proceedings of the Fourth International Symposium on Unbound Aggregates in Roads*, July 1995, University of Nottingham.

- Seyhan, U., and Tutumluer, E. (2002). "Anisotropic modular ratios as unbound aggregate performance indicators." *Journal of materials in civil engineering*, American Society of Civil Engineers, 14(5), 409-416.
- Taylor, D.W., and Leps, T. M. (1938). "Shearing strength of Ottawa standard sand as determined by the M.I.T. strain-controlled direct shearing machine." *Proceedings, Soils and Foundation Conference*, U.S. Engineering Department. Boston.
- Terzaghi, K. (1943). *Theoretical soil mechanics*. J. Wiley & Sons, Inc, New York.
- Tutumluer, E., and Seyhan, U. (1999). "Laboratory determination of anisotropic aggregate resilient moduli using an innovative test device." *Transportation Research Record: Journal of the Transportation Research Board*, Trans Res Board, 1687(1), 13–21.
- Vardeman, S. B., and Jobe, J. M. (1999). *Statistical quality assurance methods for engineers*. John Wiley.
- White, D. J. (2010). "*Intelligent compaction field validation – DFW connector project.*" Preliminary data report submitted to Kiewit Infrastructure Group.
- White, D. J., Vennapusa, P., Li, C. (2012). *Laboratory characterization of additional CFED soils: CFED Phase V*. Final report submitted to Tennessee Valley Authority, Widows Creek, Alabama
- White, D. J., Thompson, M., Vennapusa, P. (2007). *Field Validation of Intelligent Compaction Monitoring Technology for Unbound Materials*. Final Report submitted to Minnesota Department of Transportation, Earthworks Engineering Research Center, Iowa State University, Ames, IA.
- White, D. J., Vennapusa, P., Zhang, J. (2010). *Earthwork volumetric calculations and characterization of additional CFED soils – CFED Phase IV*. No. ER10-11, Final report submitted to Caterpillar, Inc., Iowa State University, Ames, IA.
- White, D. J., Vennapusa, P., Zhang, J. Gieselman, H. and Morris, M. (2009). *Implementation of intelligent compaction performance based specifications in Minnesota*. Final Report, EERC 09-02, Earthworks Engineering Research Center, Iowa State University, Ames, IA.
- Winterkorn, H., and Pamukcu, S. (1991). "Soil stabilization and grouting." *Foundation Engineering Handbook*, Van Nostrand Reinhold, New York, 317-378.
- Wolfe, A. J. (2011). "Behavior of composite pavement foundation materials subjected to cyclic loading." M.S. Thesis, Iowa State University, Ames, IA.
- Zhang, J. (2010). "Evaluation of mechanistic-based compaction measurements for earthwork QC/QA." M.S. Thesis, Iowa State University, Ames, IA.

APPENDIX A. PROCTOR AND VIBRATORY COMPACTION TEST RAW DATA

Table 67. Proctor test raw data of the 11 geomaterials

Soil ID	CFED 1634		CFED 2043		CFED 2051		CFED 2052	
Description	Western Iowa Loess		Texas Fat Clay		2011 RAP		Edwards CA6- G	
Energy Level	w (%)	γ_d (lb/ft ³)	w (%)	γ_d (lb/ft ³)	w (%)	γ_d (lb/ft ³)	w (%)	γ_d (lb/ft ³)
SS	12.3	94.1	20.3	82.3	0.1	102.5	0.1	125.5
	14.8	95.6	22.1	80.5	2.3	109.9	3.2	122.4
	16.4	96.9	24.3	82.6	4.2	111.7	5.2	126.2
	20.2	97.6	25.1	83.5	5.5	112.5	8.0	136.4
	21.6	96.6	29.4	83.7	8.2	116.4	9.0	138.2
	—		26.5	86.1	9.9	115.9	11.1	132.8
S	14.5	98.9	16.9	85.4	0.2	103.0	0.2	127.4
	16.4	100.4	20.7	89.6	1.8	110.2	1.9	130.1
	18.6	101.1	23.4	93.3	3.8	113.7	3.9	128.1
	20.0	100.3	24.6	92.4	6.7	117.2	6.1	131.9
	22.1	96.4	28.2	89.8	8.2	118.3	8.4	140.3
	—		—		10.0	119.2	9.0	138.8
SSM	12.1	102.3	16.6	91.4	0.2	106.8	0.3	130.5
	14.3	104.3	18.4	91.7	2.3	115.5	3.2	130.3
	16.1	104.1	24.6	96.2	4.1	116.9	5.1	135.6
	18.3	104.3	20.6	95.4	5.7	117.1	6.4	140.5
	19.9	101.6	22.8	97.0	8.3	120.8	8.4	139.4
	—		26.9	93.8	9.3	122.4	11.0	133.3
SM	12.2	103.6	16.9	96.4	0.2	107.8	0.2	133.6
	14.8	105.1	17.9	96.7	2.3	116.6	3.2	131.9
	15.8	105.7	20.4	100.3	4.5	117.8	5.3	138.7
	18.0	105.7	22.3	100.8	5.5	118.2	6.7	141.0
	19.9	101.4	26.9	96.0	7.3	121.4	8.5	138.8
	—		—		8.7	122.6	10.0	135.5
M	12.4	108.7	11.1	104.2	0.2	110.3	0.1	135.5
	14.0	110.2	14.8	106.5	2.4	118.5	3.1	134.9
	16.0	110.3	16.3	107.7	4.4	120.8	5.6	141.4
	18.0	106.6	17.6	108.5	5.8	121.5	6.5	143.0
	19.8	103.0	20.5	106.6	7.2	124.0	8.8	138.7
	20.9	99.9	—		8.6	124.9	—	
—		—		9.9	124.3	—		

Table 67 (continued). Proctor test raw data of the 11 geomaterials

Soil ID	CFED 2053		CFED 2054		CFED 2055		CFED 2056	
Description	WCF Fly Ash		WCF Gypsum		Temple Gypsum		Reject Gypsum	
Energy Level	w (%)	γ_d (lb/ft ³)	w (%)	γ_d (lb/ft ³)	w (%)	γ_d (lb/ft ³)	w (%)	γ_d (lb/ft ³)
SS	22.7	76.9	15.0	93.2	—	—	—	—
	24.2	77.6	17.5	94.1				
	26.2	78.1	18.7	95.1				
	27.8	78.0	20.4	95.6				
	29.3	76.5	21.5	94.3				
	—	—	24.0	93.2				
S	20.6	77.2	13.5	95.4	11.2	89.7	11.7	94.5
	22.5	78.0	15.8	95.4	12.9	90.2	13.5	94.9
	24.6	78.8	17.8	96.6	15.2	90.6	16.2	95.7
	27.1	78.4	19.4	95.8	17.9	91.1	17.9	94.0
	28.3	76.9	20.8	95.1	19.5	90.1	19.9	92.0
	—	—	—	—	21.3	88.8	11.7	94.5
SSM	21.2	80.6	9.4	97.8	—	—	—	—
	22.8	81.3	11.4	98.1				
	23.7	81.1	13.5	97.9				
	27.3	78.8	15.6	98.3				
	26.1	79.7	16.9	99.7				
	—	—	18.3	99.3				
—	—	19.7	97.7					
SM	18.9	81.1	13.7	99.9	—	—	—	—
	19.8	81.5	15.9	100.1				
	22.2	82.3	18.8	99.6				
	24.1	81.8	19.2	99.5				
	24.4	82.0	20.7	96.3				
	25.2	80.8	9.8	98.9				
	27.0	79.0	11.8	99.2				
	—	—	13.6	100.2				
—	—	16.2	100.7					
M	14.8	82.3	7.9	102.7	9.4	94.1	7.5	98.9
	18.8	84.1	10.1	105.6	11.5	94.5	9.4	99.6
	19.8	84.0	12.5	106.5	13.7	95.1	12.3	101.3
	24.4	82.7	15.9	103.8	17.6	93.9	15.3	98.7
	24.6	82.1	16.3	102.1	19.2	91.8	16.3	96.1
	25.2	81.2	—	—	—	—	—	—
	14.8	82.3						

Table 67 (continued). Proctor test raw data of the 11 geomaterials

Soil ID	CFED 2057		CFED 2058		CFED 2059	
Description	Loess + 15% FA		Loess + 9% Cement		Florida 9B Fill	
Energy Level	w (%)	γ_d (lb/ft ³)	w (%)	γ_d (lb/ft ³)	w (%)	γ_d (lb/ft ³)
SS	13.2	97.2	15.3	102.0	0.1	96.6
	14.4	99.6	17.0	102.2	2.6	94.2
	16.3	103.3	18.9	102.9	5.6	94.8
	18.1	105.1	21.3	102.0	8.5	95.1
	19.6	104.3	22.3	101.0	11.0	95.6
	20.0	104.7			13.5	96.5
	21.7	101.4			19.1	95.8
	—		—			
S	12.9	101.7	15.1	103.7	0.2	97.9
	14.5	104.7	16.8	104.0	2.0	95.0
	16.1	107.3	18.8	105.7	4.8	95.2
	18.3	106.5	20.9	103.4	7.9	95.7
	19.8	104.7	22.3	101.8	10.8	96.2
	19.8	105.2			13.1	97.4
	21.7	101.9			15.1	98.5
	—		—		21.0	93.9
SSM	11.3	103.6	13.1	105.4	0.0	98.9
	13.0	106.7	15.3	107.1	2.3	95.6
	14.8	109.0	16.8	109.0	5.3	97.0
	16.7	111.3	18.5	108.2	8.0	98.0
	18.2	107.6	20.9	103.3	10.1	98.6
	19.9	104.1			12.8	98.7
	—		—		19.4	96.2
SM	11.3	107.0	13.2	109.2	0.1	99.8
	13.2	110.0	15.0	109.6	2.3	96.5
	14.9	112.1	17.3	111.2	5.3	97.2
	16.8	112.0	18.9	107.5	8.3	97.4
	18.3	107.9	20.7	104.2	10.8	98.2
					12.6	99.9
	—		—		19.7	96.4
M	11.7	113.6	12.1	110.7	0.1	99.6
	12.6	114.3	13.5	111.5	2.1	95.4
	14.5	115.9	15.2	113.0	5.2	96.5
	16.6	112.9	17.7	111.5	8.1	96.8
	19.9	106.8	18.9	107.9	11.4	97.3
					13.2	98.4
	—		—		19.0	96.5

Table 68. Vibratory compaction test raw data of the four oven-dried geomaterials

Soil ID	CFED 2061		CFED 2062		CFED 2063		—	
Description	2012 Manatt's RAP		RPCC+RAP		Crushed Limestone		Ottawa Sand	
Compaction Time (sec)	Dry Unit Weight (pcf)	Compaction Energy (lb-ft/ft ³)	Dry Unit Weight (pcf)	Compaction Energy (lb-ft/ft ³)	Dry Unit Weight (pcf)	Compaction Energy (lb-ft/ft ³)	Dry Unit Weight (pcf)	Compaction Energy (lb-ft/ft ³)
0	85.1	0.0	88.0	0.0	100.5	0.0	99.8	0.0
10	89.1	396.2	93.9	395.8	104.1	378.7	104.3	393.5
20	90.2	802.9	94.8	799.0	106.5	774.6	105.6	796.8
30	91.1	1216.3	95.4	1206.2	107.4	1171.8	106.2	1202.0
60	92.2	2460.6	96.5	2439.8	109.8	2395.9	107.6	2435.6
120	93.0	4965.6	97.6	4935.3	111.7	4875.9	108.7	4921.2
240	94.0	10036.5	99.1	10019.7	114.1	9956.8	109.4	9908.1
480	95.4	20377.4	102.1	20645.1	116.4	20325.0	110.3	19975.1
960	97.3	41544.6	103.9	42021.8	118.1	41250.8	111.0	40210.7

**APPENDIX B. PROCTOR AND UNCONFINED COMPRESSION TEST
RESULTS OF STABILIZED WESTERN IOWA LOESS**

**Table 69. Proctor and unconfined compression test results for western Iowa loess with 15%
fly ash**

Compaction Energy (lb-ft/ft³)	Moisture Content Before Compaction (%)	Dry Unit Weight (pcf)	Moisture Content After UC Test (%)	Compressive Stress (psi)
7425	13.2	97.2	12.3	101.4
7425	14.4	99.6	13.7	133.3
7425	16.3	103.3	15.7	126.2
7425	18.1	105.1	17.6	111.4
7425	19.6	104.3	19.3	80.1
7425	20.0	104.7	19.3	76.6
7425	21.7	101.4	21.2	58.8
12375	12.9	101.7	12.5	139.2
12375	14.5	104.7	14.0	168.8
12375	16.1	107.3	15.8	164.6
12375	18.3	106.5	17.5	117.3
12375	19.8	104.7	19.2	78.9
12375	19.8	105.2	19.3	83.1
12375	21.7	101.9	21.0	55.3
20790	11.3	103.6	10.5	210.7
20790	13.0	106.7	12.3	252.1
20790	14.8	109.0	14.0	217.2
20790	16.7	111.3	15.8	219.0
20790	18.2	107.6	17.6	123.3
20790	19.9	104.1	19.2	74.2
34650	11.3	107.0	10.8	250.9
34650	13.2	110.0	12.6	263.9
34650	14.9	112.1	14.3	279.3
34650	16.8	112.0	16.0	171.7
34650	18.3	107.9	17.7	122.1
56250	11.7	113.6	10.7	365.3
56250	12.6	114.3	11.8	351.5
56250	14.5	115.9	13.6	325.3
56250	16.6	112.9	15.6	158.5
56250	19.9	106.8	17.0	122.2

Table 70. Proctor and unconfined compression test results for western Iowa loess with 9% type I cement

Compaction Energy (lb-ft/ft³)	Moisture Content Before Compaction (%)	Dry Unit Weight (pcf)	Moisture Content After UC Test (%)	Compressive Stress (psi)
7425	15.3	102.0	14.6	585.2
7425	17.0	102.2	16.6	616.2
7425	18.9	102.9	18.3	561.3
7425	21.3	102.0	21.0	352.0
7425	22.3	101.0	22.2	291.6
12375	15.1	103.7	14.2	661.6
12375	16.8	104.0	15.9	688.6
12375	18.8	105.7	18.2	597.1
12375	20.9	103.4	20.3	354.4
12375	22.3	101.8	21.7	299.5
20790	13.1	105.4	12.2	763.4
20790	15.3	107.1	14.6	847.0
20790	16.8	109.0	16.2	866.1
20790	18.5	108.2	18.1	511.2
20790	20.9	103.3	20.5	326.6
34650	13.2	109.2	12.0	818.4
34650	15.0	109.6	14.9	925.5
34650	17.3	111.2	16.6	974.0
34650	18.9	107.5	18.7	456.0
34650	20.7	104.2	20.1	331.0
56250	12.1	110.7	11.2	1046.4
56250	13.5	111.5	12.6	1049.9
56250	15.2	113.0	14.2	1036.2
56250	17.7	111.5	16.8	597.1
56250	18.9	107.9	18.3	469.8

APPENDIX C. IOWA K TEST RESULTS OF THE FIVE COMPACTED GEOMATERIALS

Western Iowa loess (CFED 1634)

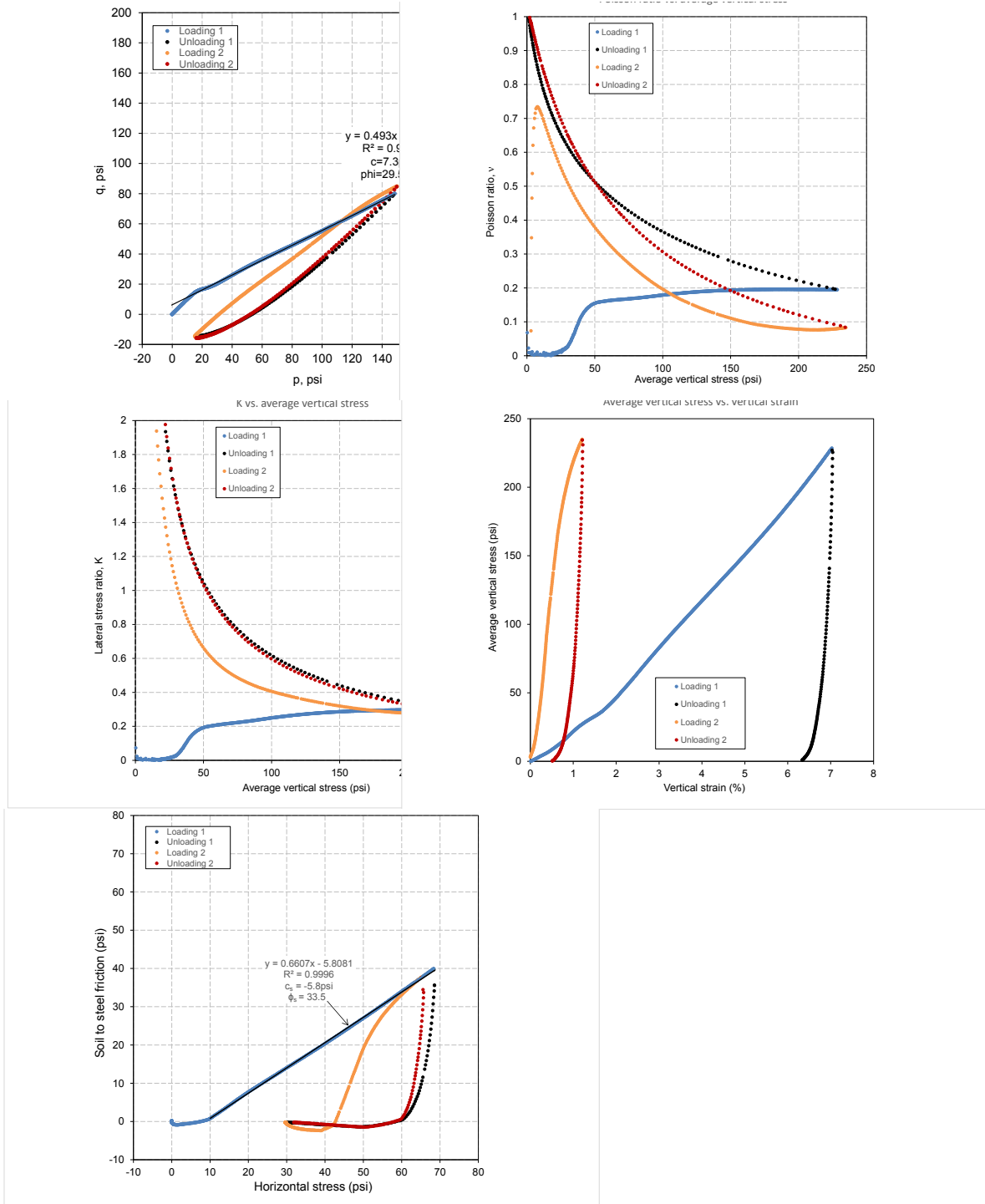


Figure 158. Iowa K test results for western Iowa loess ($w\% = 12.2\%$ and $\gamma_d = 96.9 \text{ pcf}$)

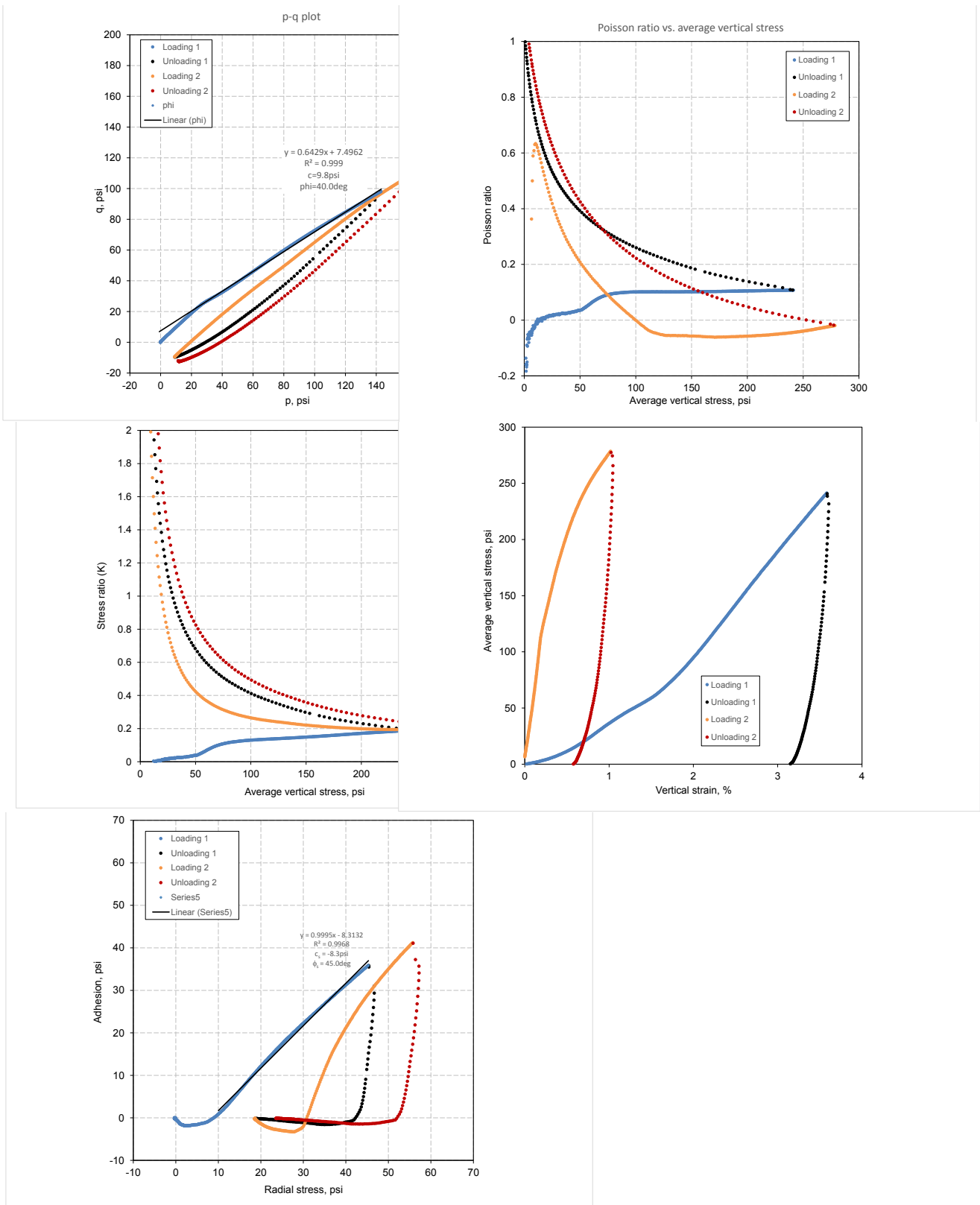


Figure 159. Iowa K test results for western Iowa loess ($w\% = 12.3\%$ and $\gamma_d = 103.5 \text{ pcf}$)

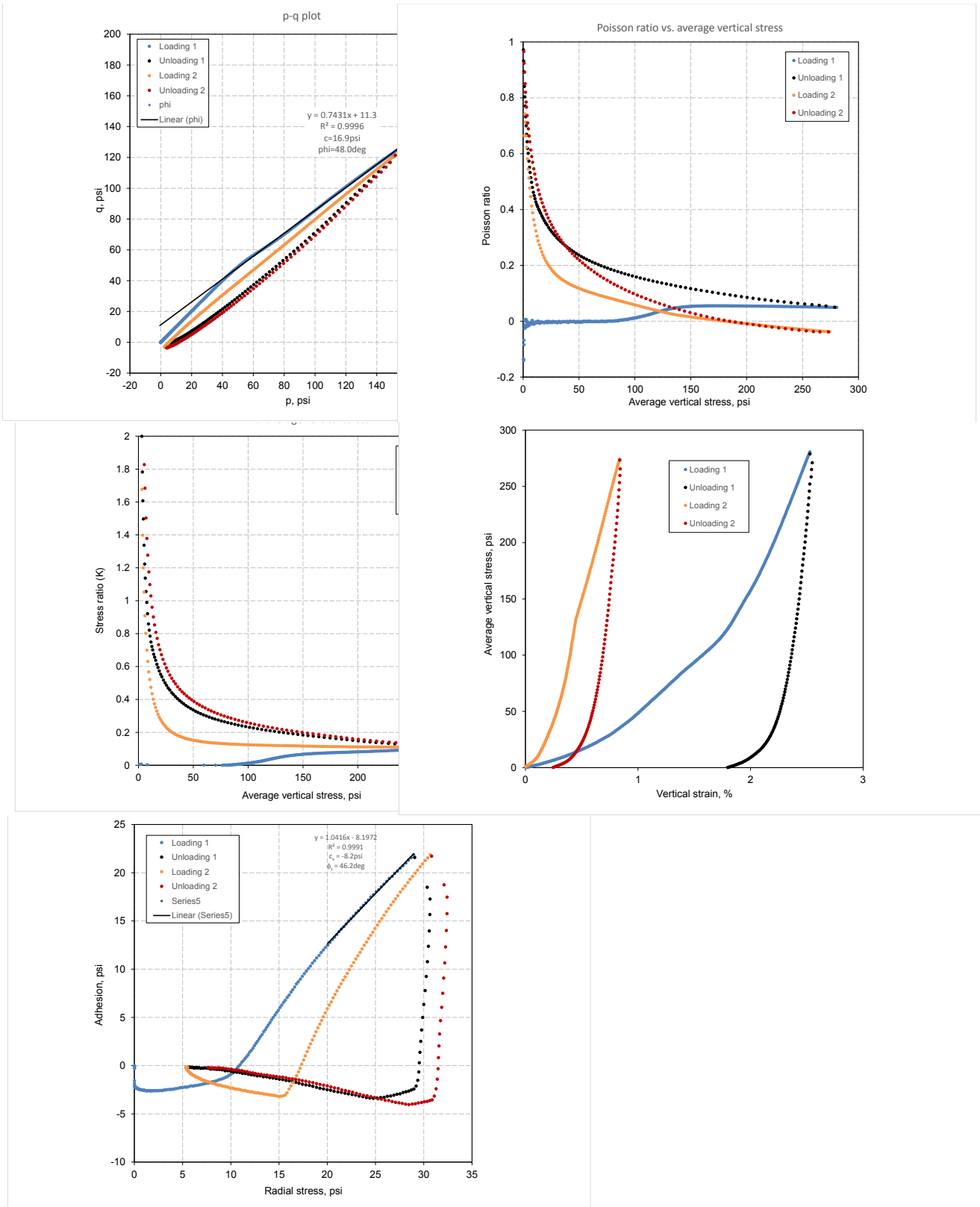


Figure 160. Iowa K test results for western Iowa loess ($w\% = 12.3\%$ and $\gamma_d = 112.7$ pcf)

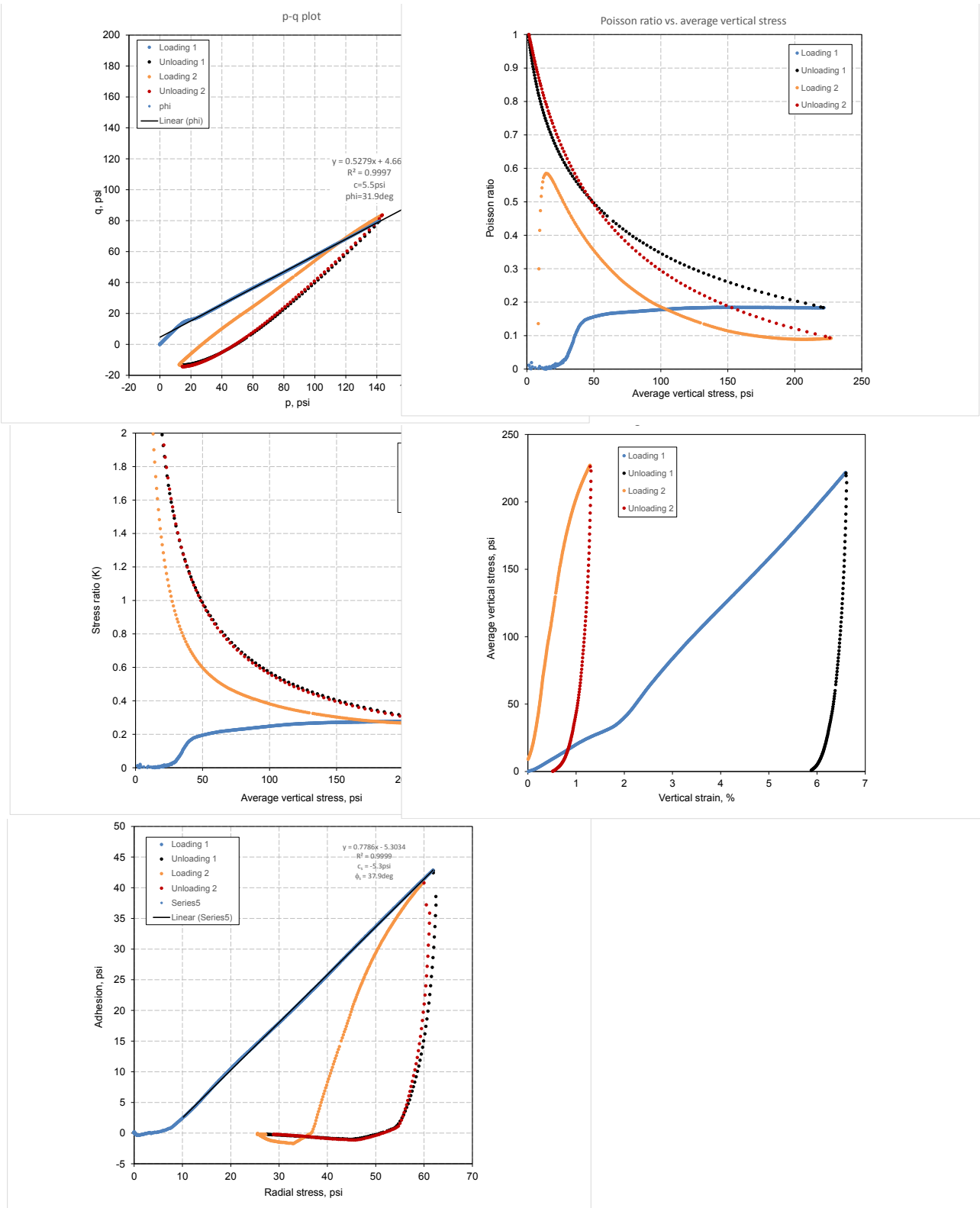


Figure 161. Iowa K test results for western Iowa loess ($w\% = 14.1\%$ and $\gamma_d = 98.5 \text{ pcf}$)

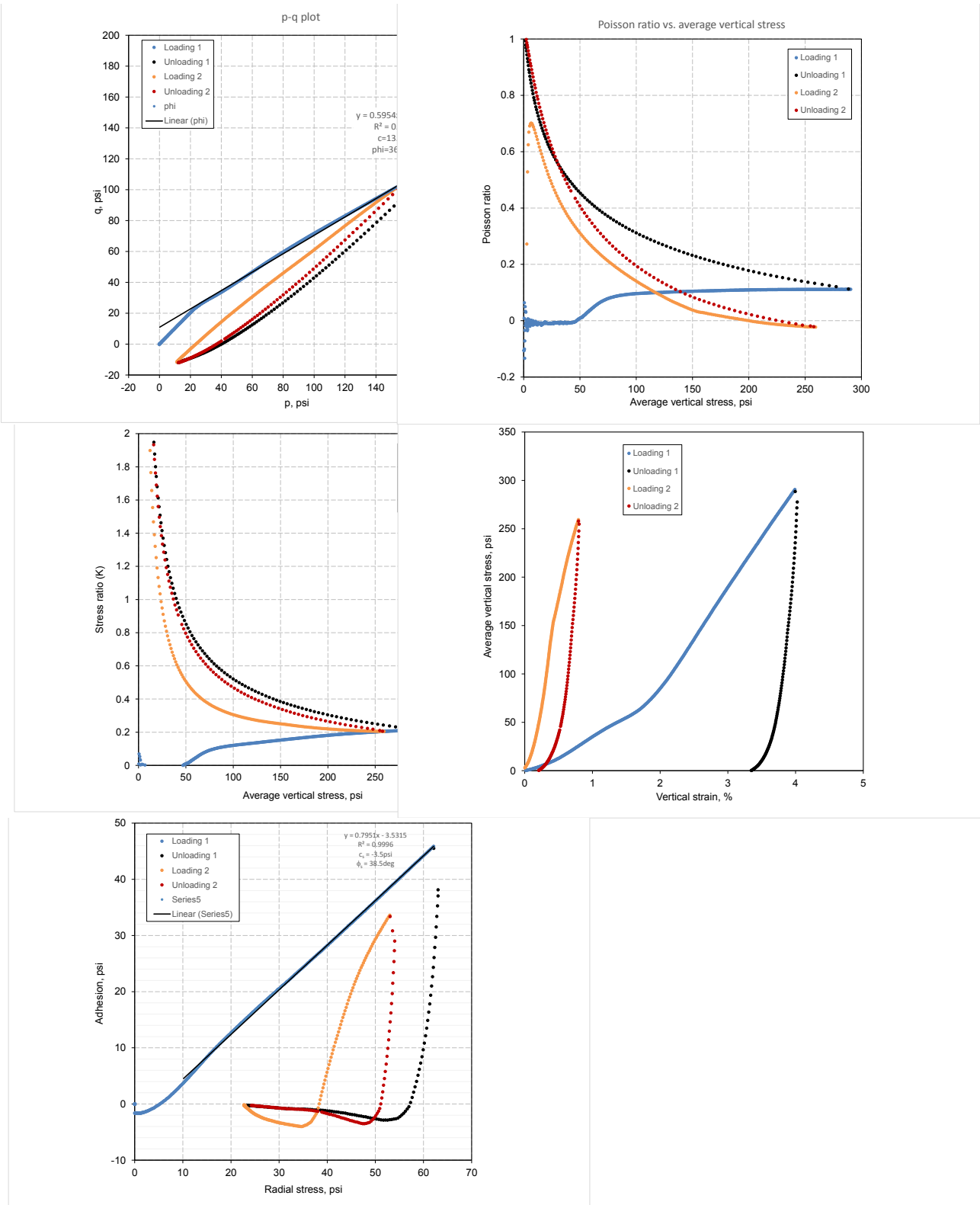


Figure 162. Iowa K test results for western Iowa loess ($w\% = 14.1\%$ and $\gamma_d = 105.8\text{pcf}$)

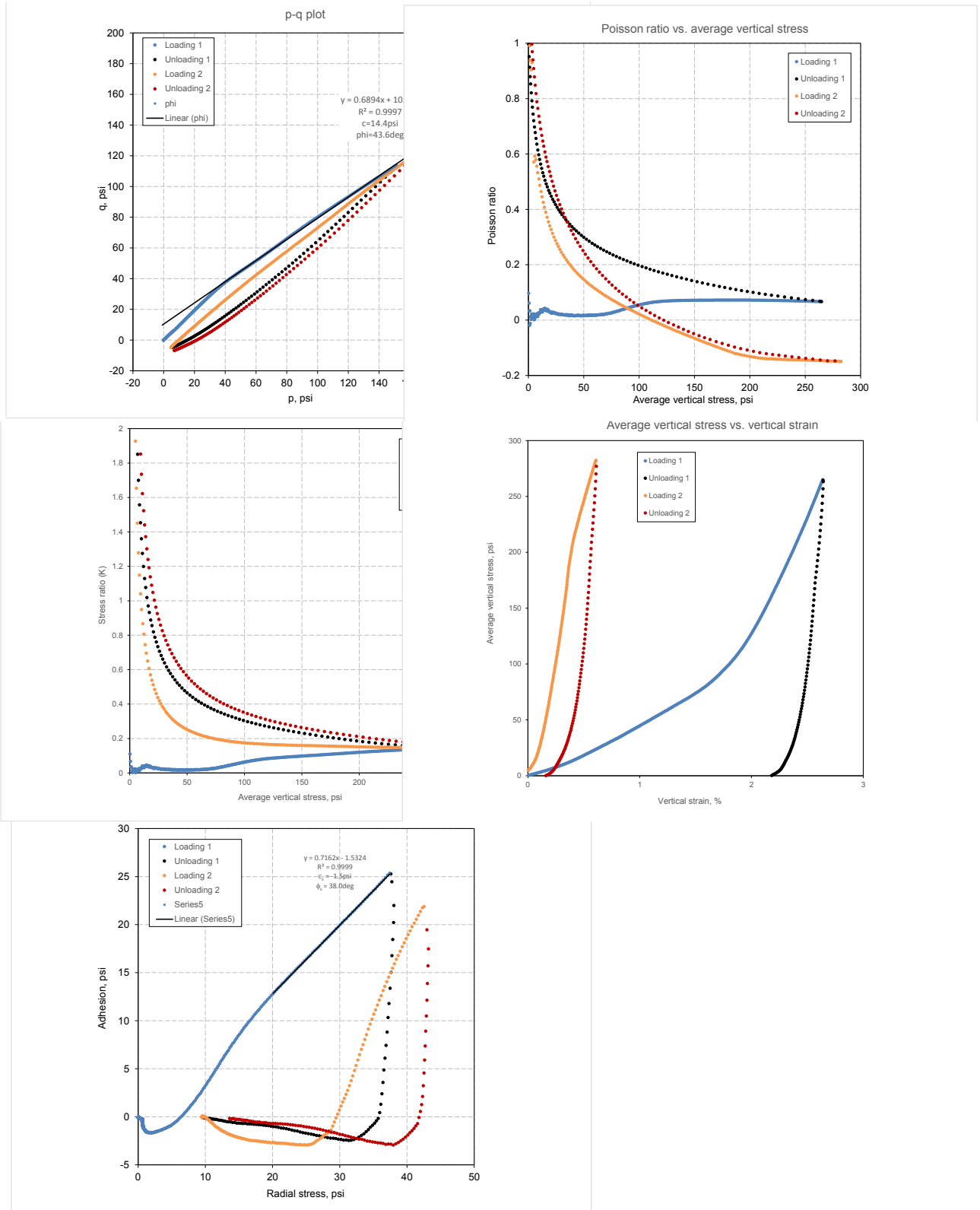


Figure 163. Iowa K test results for western Iowa loess ($w\% = 14.2\%$ and $\gamma_d = 115.2 \text{pcf}$)

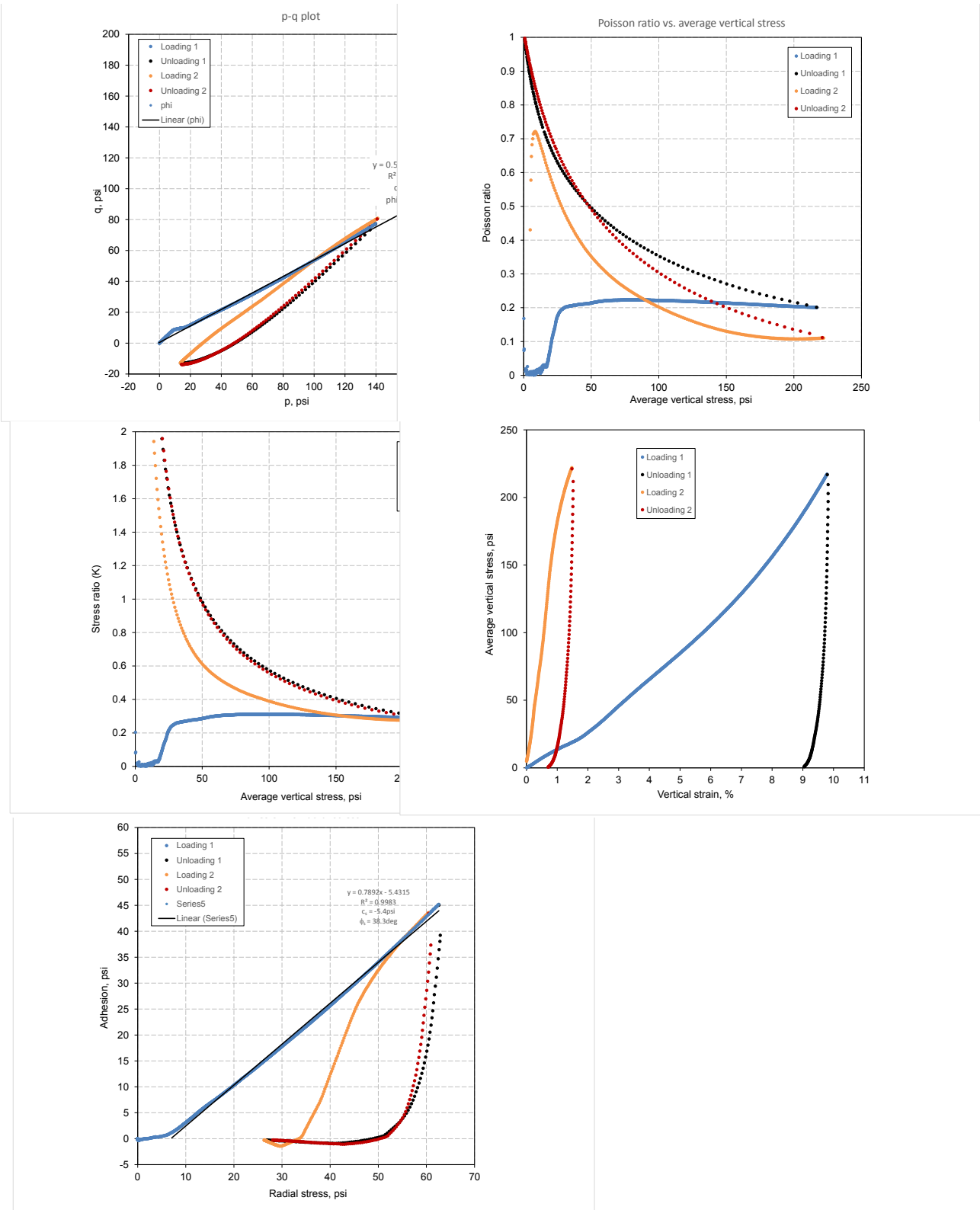


Figure 164. Iowa K test results for western Iowa loess ($w\% = 15.9\%$ and $\gamma_d = 95.6$ pcf)

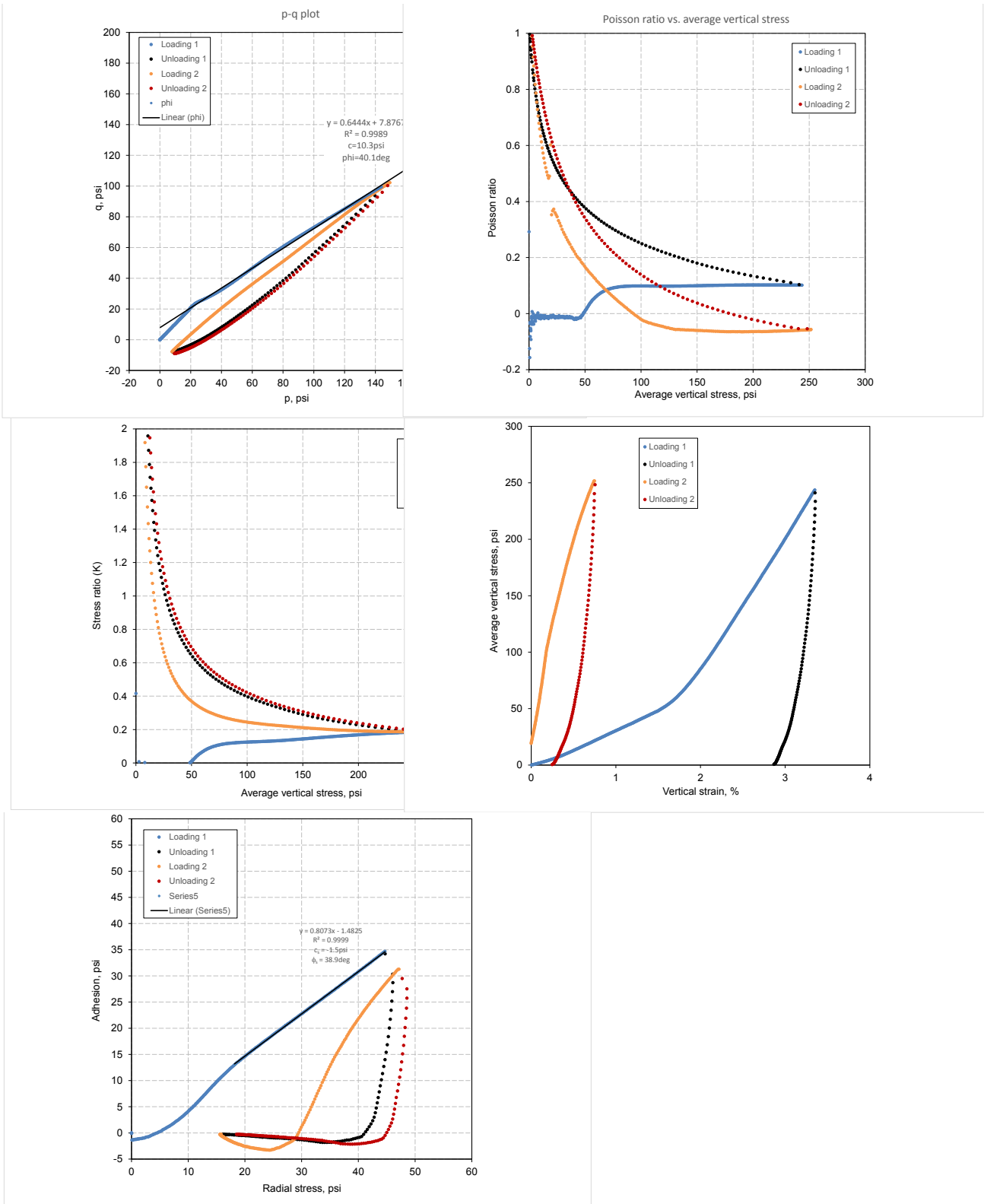


Figure 165. Iowa K test results for western Iowa loess ($w\% = 15.9\%$ and $\gamma_d = 108.2\text{pcf}$)

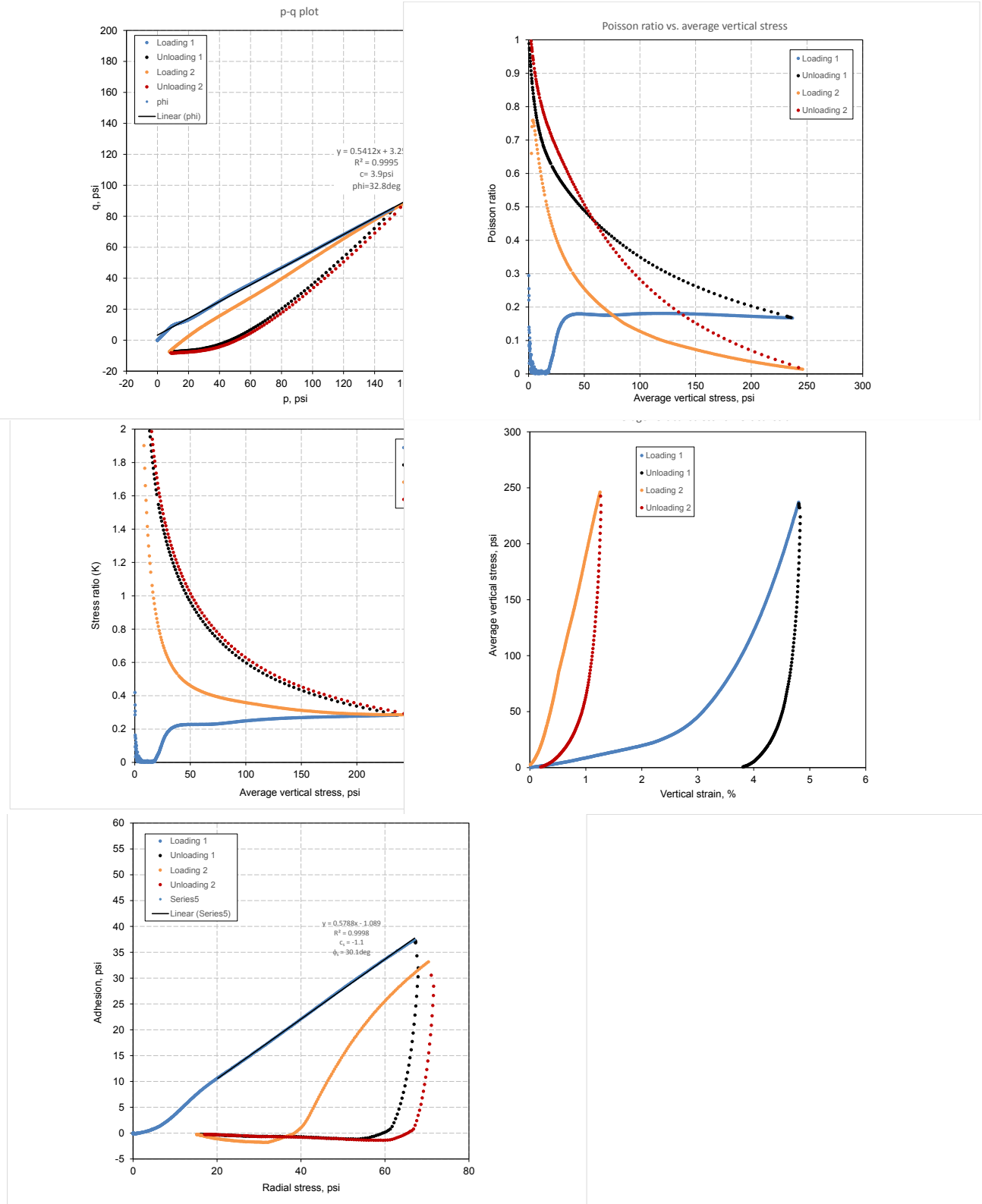


Figure 166. Iowa K test results for western Iowa loess ($w\% = 15.9\%$ and $\gamma_d = 114.9\text{pcf}$)

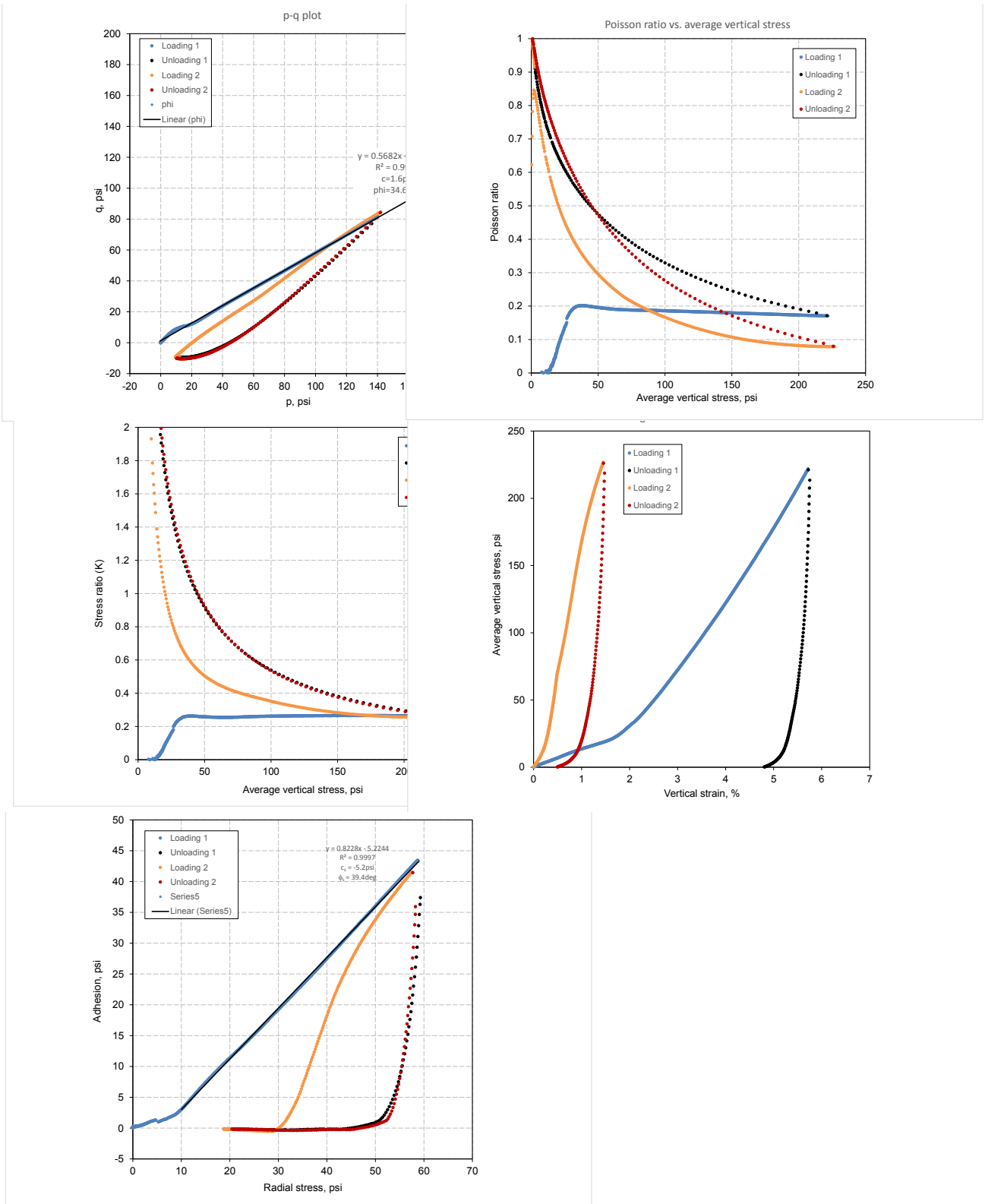


Figure 167. Iowa K test results for western Iowa loess ($w\% = 18.3\%$ and $\gamma_d = 103.5$ pcf)

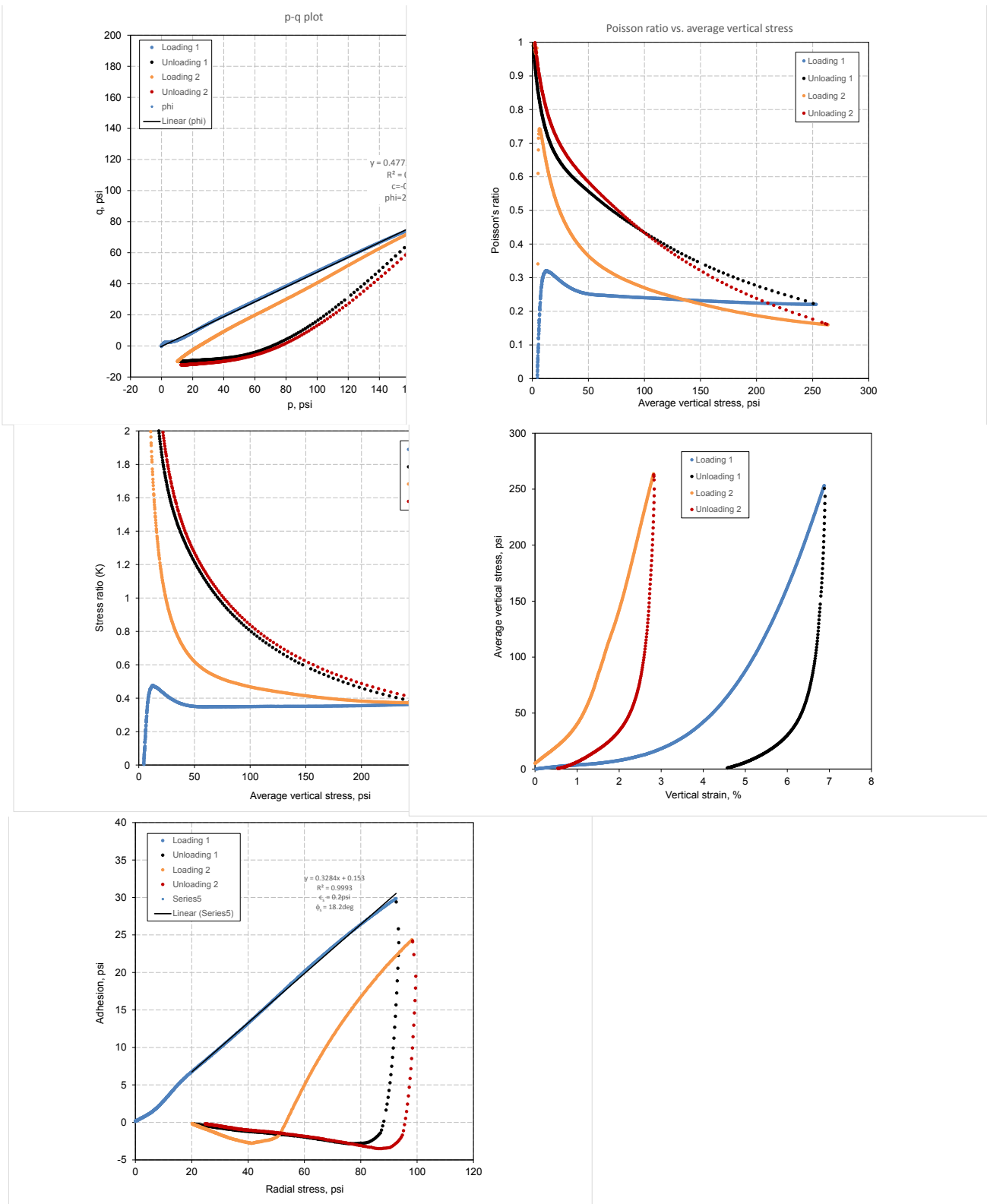


Figure 168. Iowa K test results for western Iowa loess ($w\% = 18.5\%$ and $\gamma_d = 108.3$ pcf)

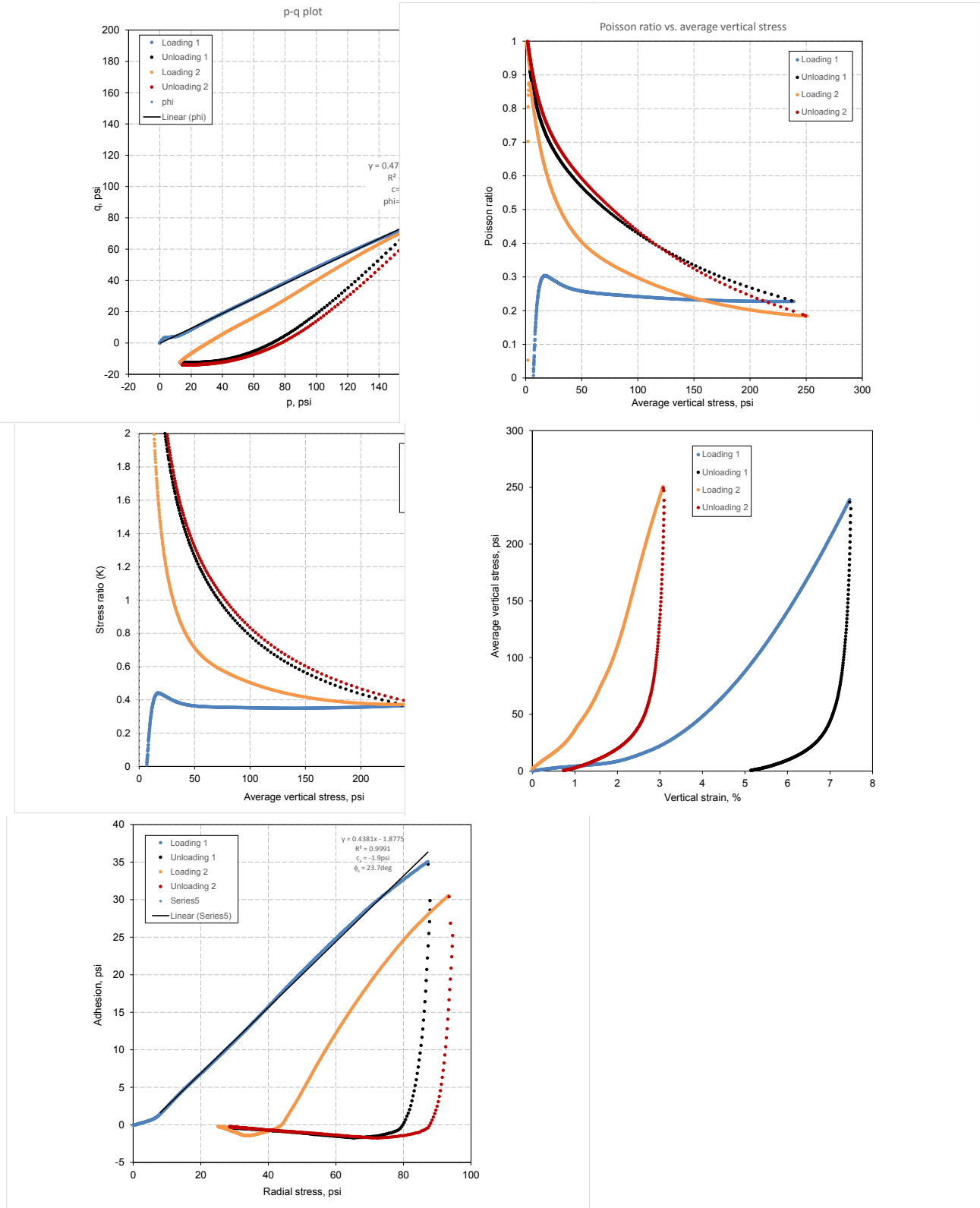


Figure 169. Iowa K test results for western Iowa loess ($w\% = 20.6\%$ and $\gamma_d = 103.2$ pcf)

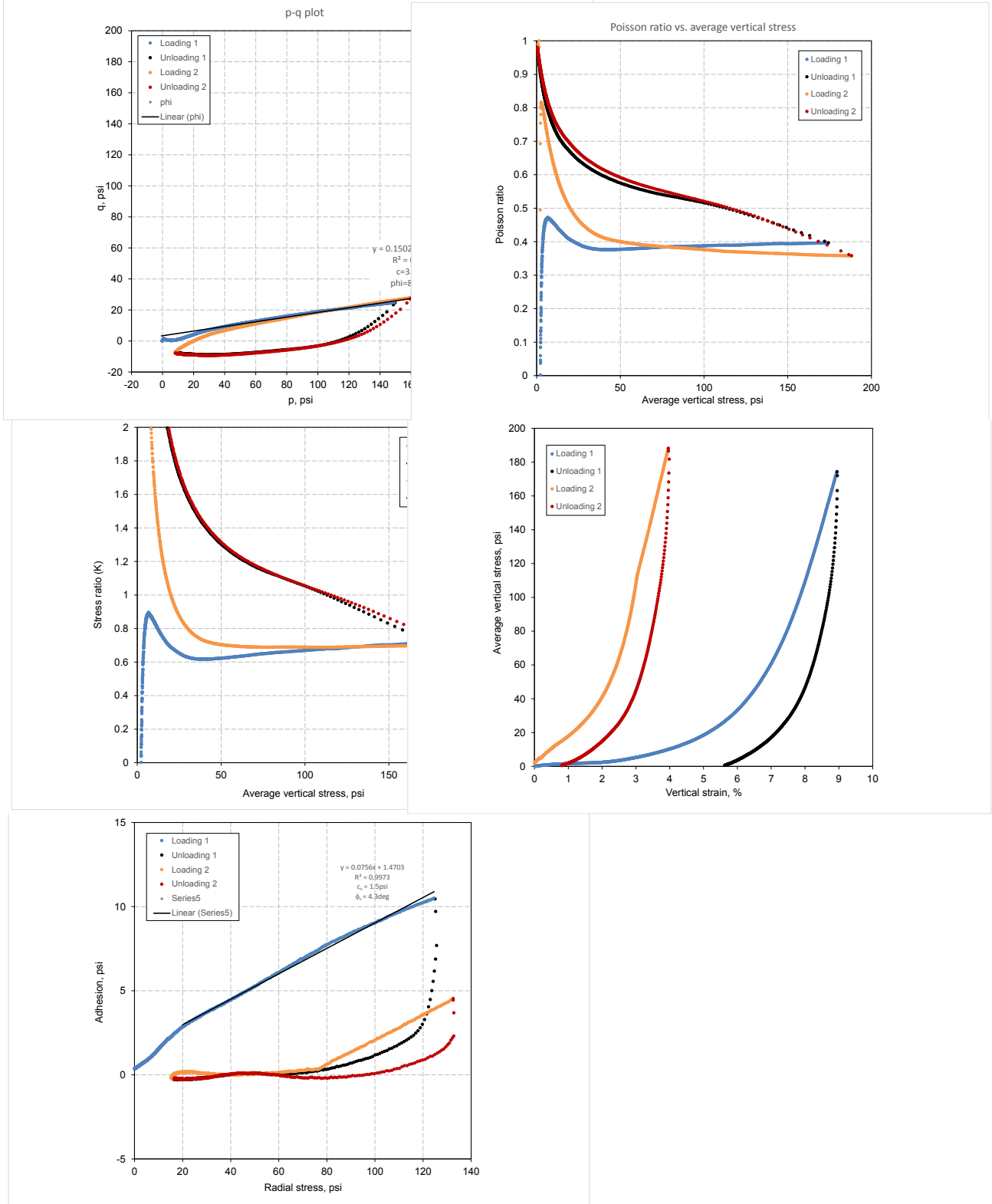


Figure 170. Iowa K test results for western Iowa loess ($w\% = 21.6\%$ and $\gamma_d = 102.4\text{pcf}$)

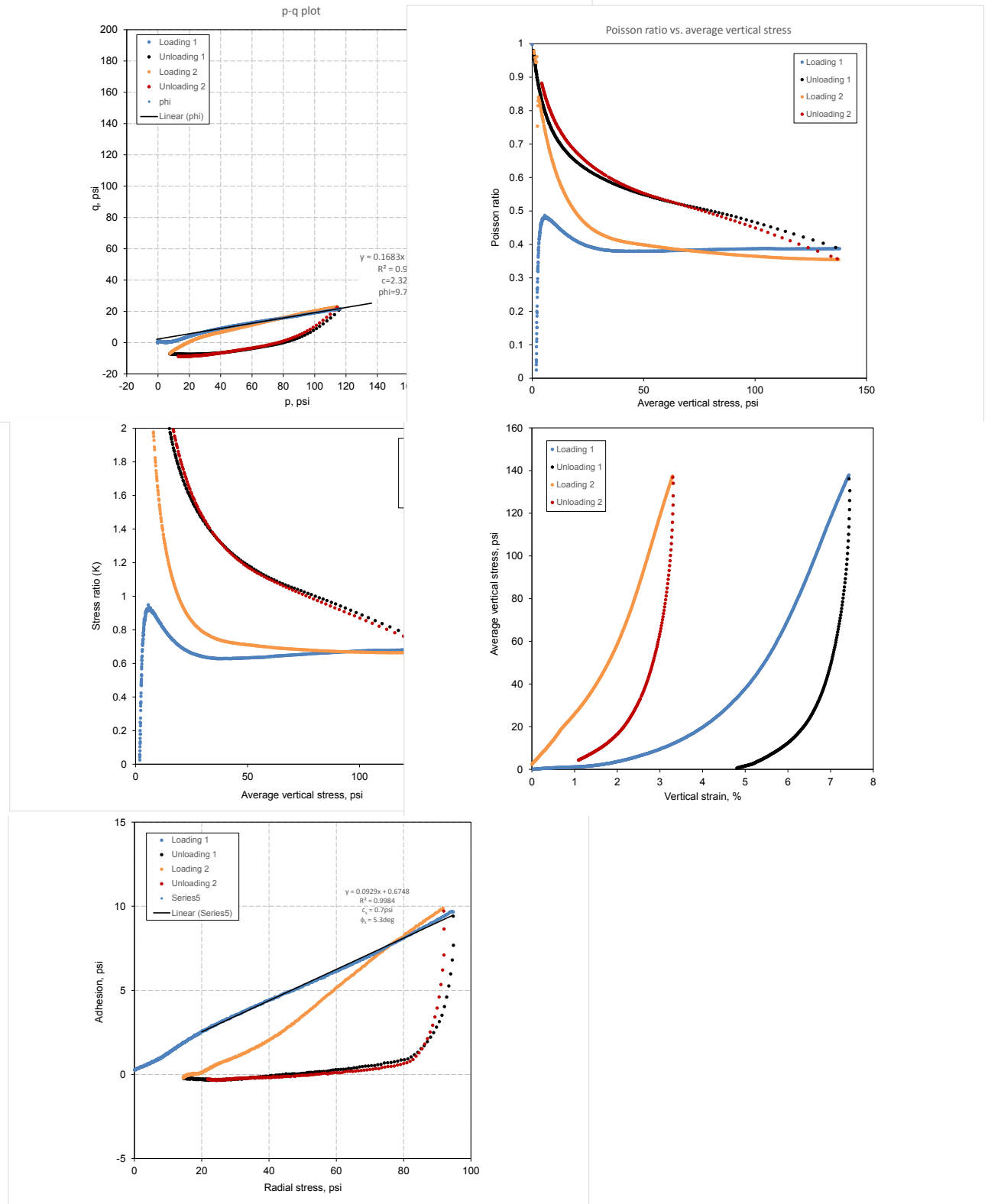


Figure 171. Iowa K test results for western Iowa loess ($w\% = 21.9\%$ and $\gamma_d = 101.6\text{pcf}$)

Texas fat clay (CFED 2043)

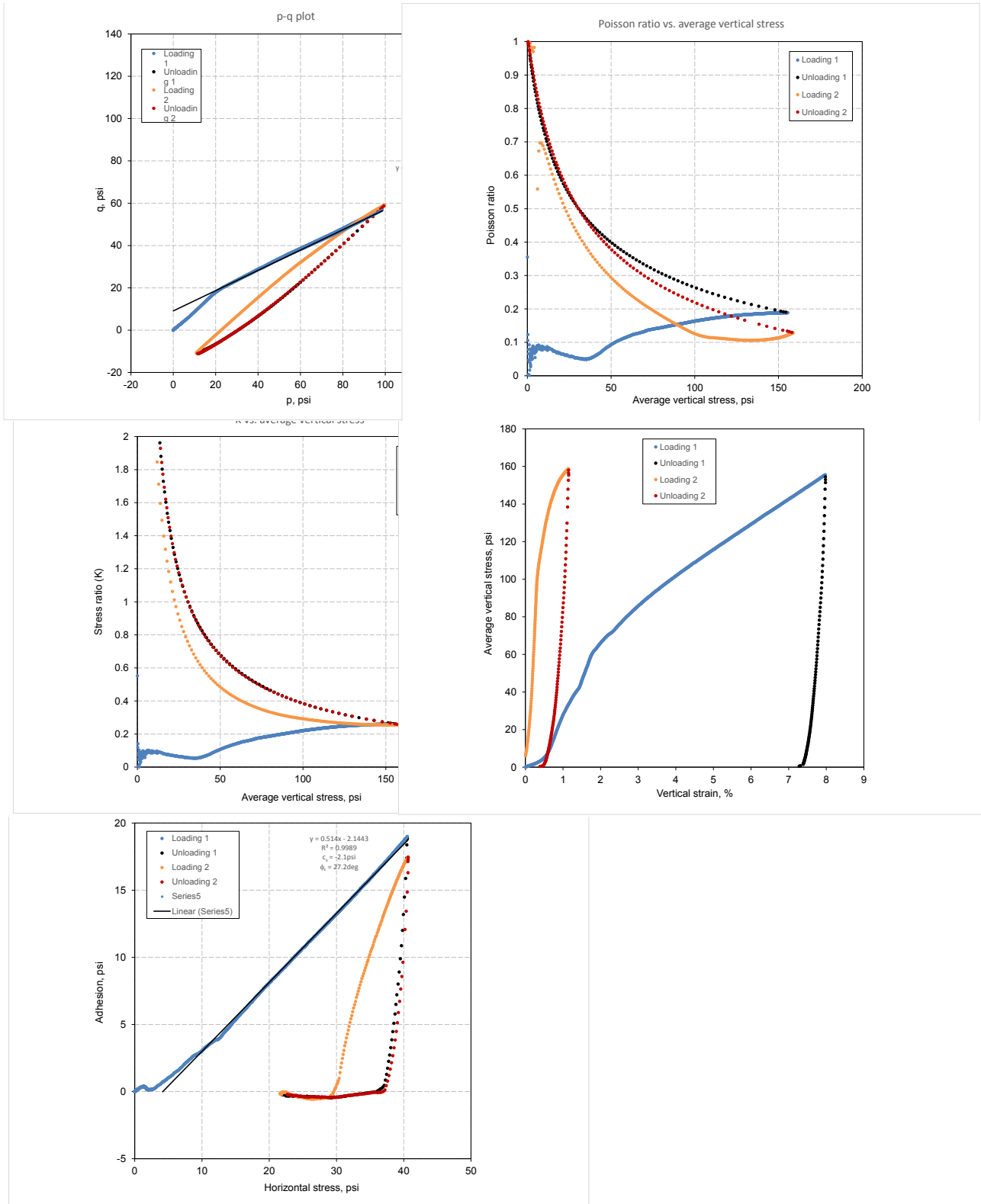


Figure 172. Iowa K test results for Texas fat clay ($w\% = 15.7\%$ and $\gamma_a = 83.0 \text{ pcf}$)

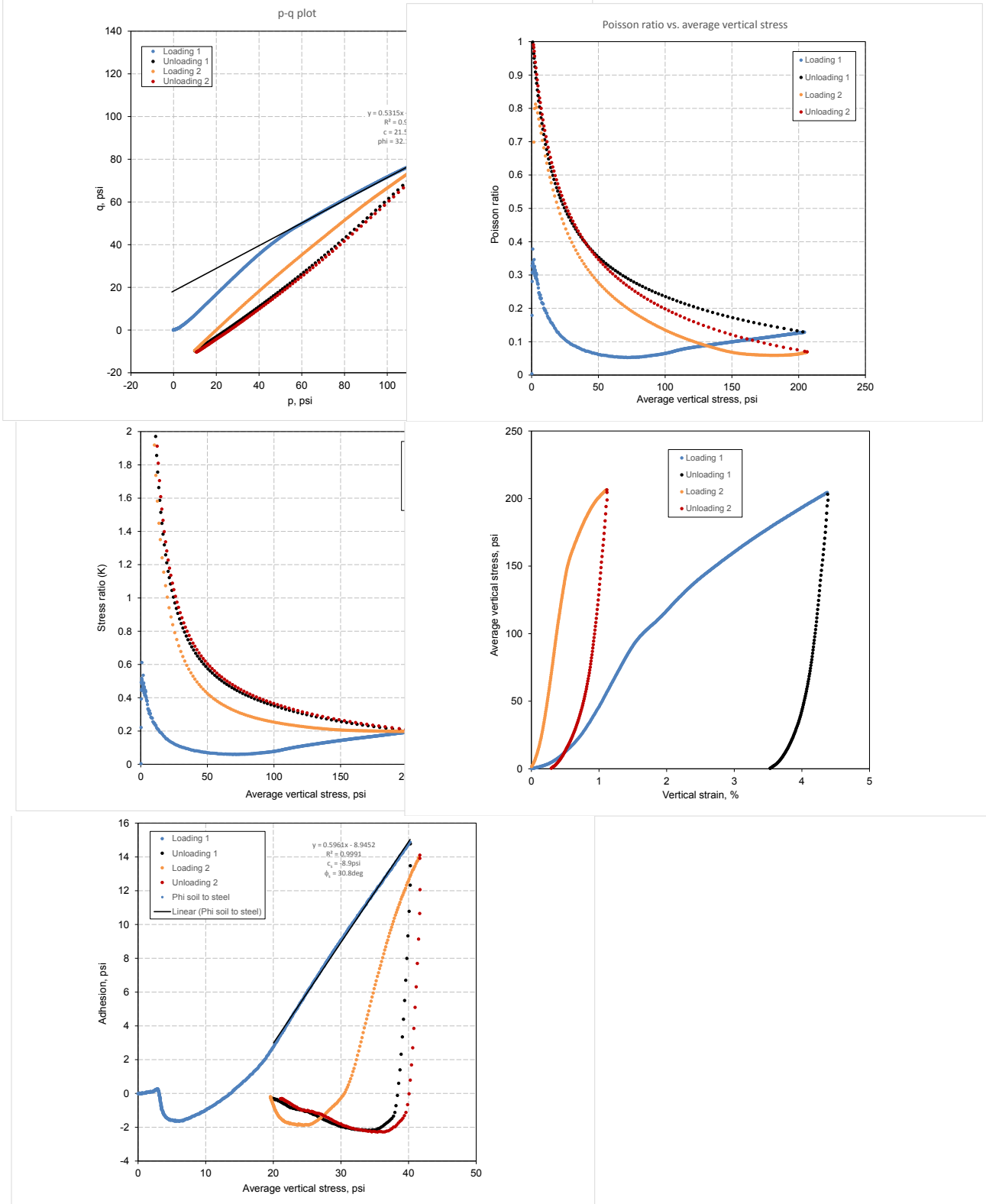


Figure 173. Iowa K test results for Texas fat clay ($w\% = 15.7\%$ and $\gamma_d = 92.7\text{pcf}$)

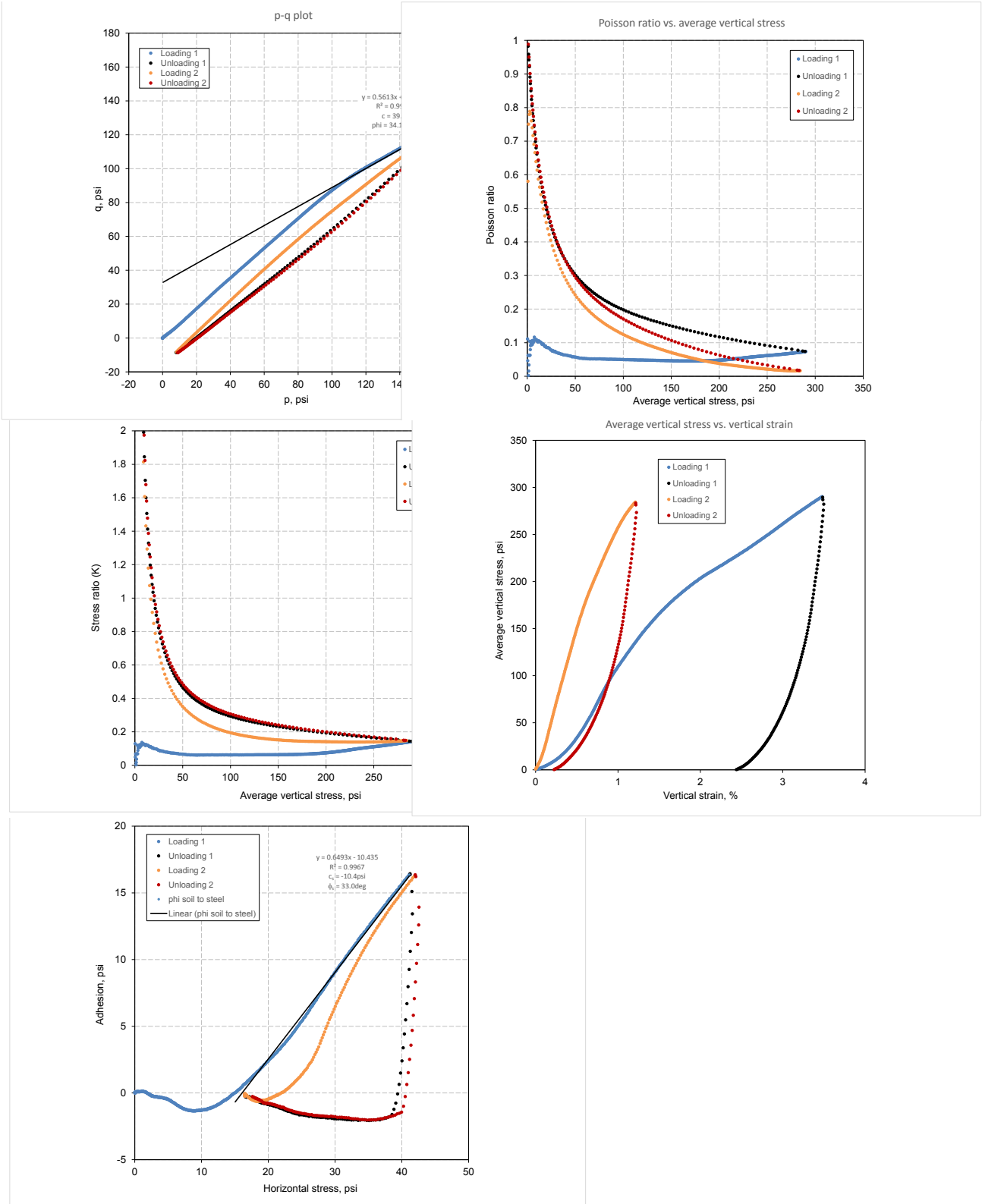


Figure 174. Iowa K test results for Texas fat clay ($w\% = 16.6\%$ and $\gamma_d = 100.4 \text{pcf}$)

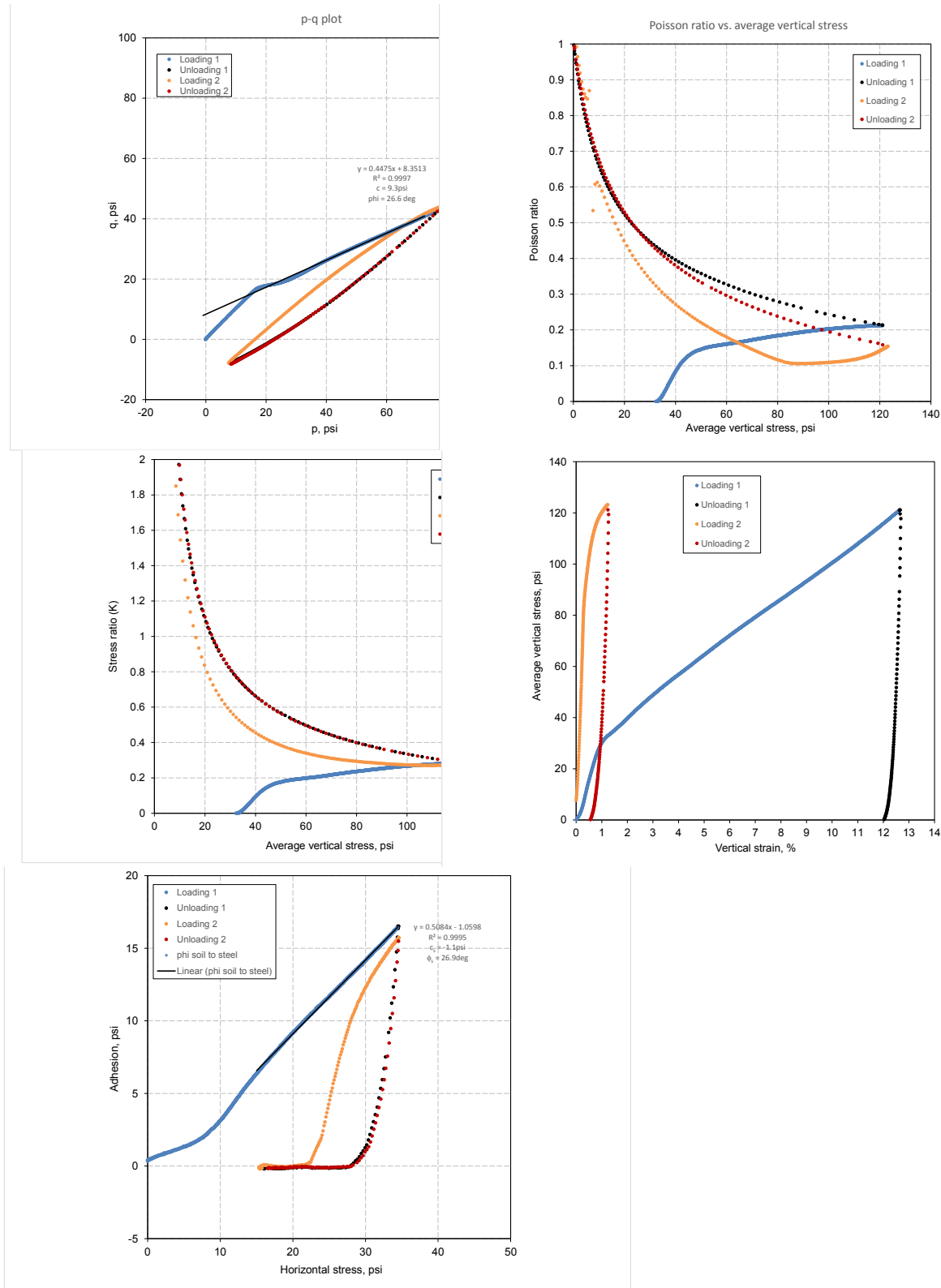


Figure 175. Iowa K test results for Texas fat clay (w% = 18.2% and $\gamma_d = 80.5$ pcf)

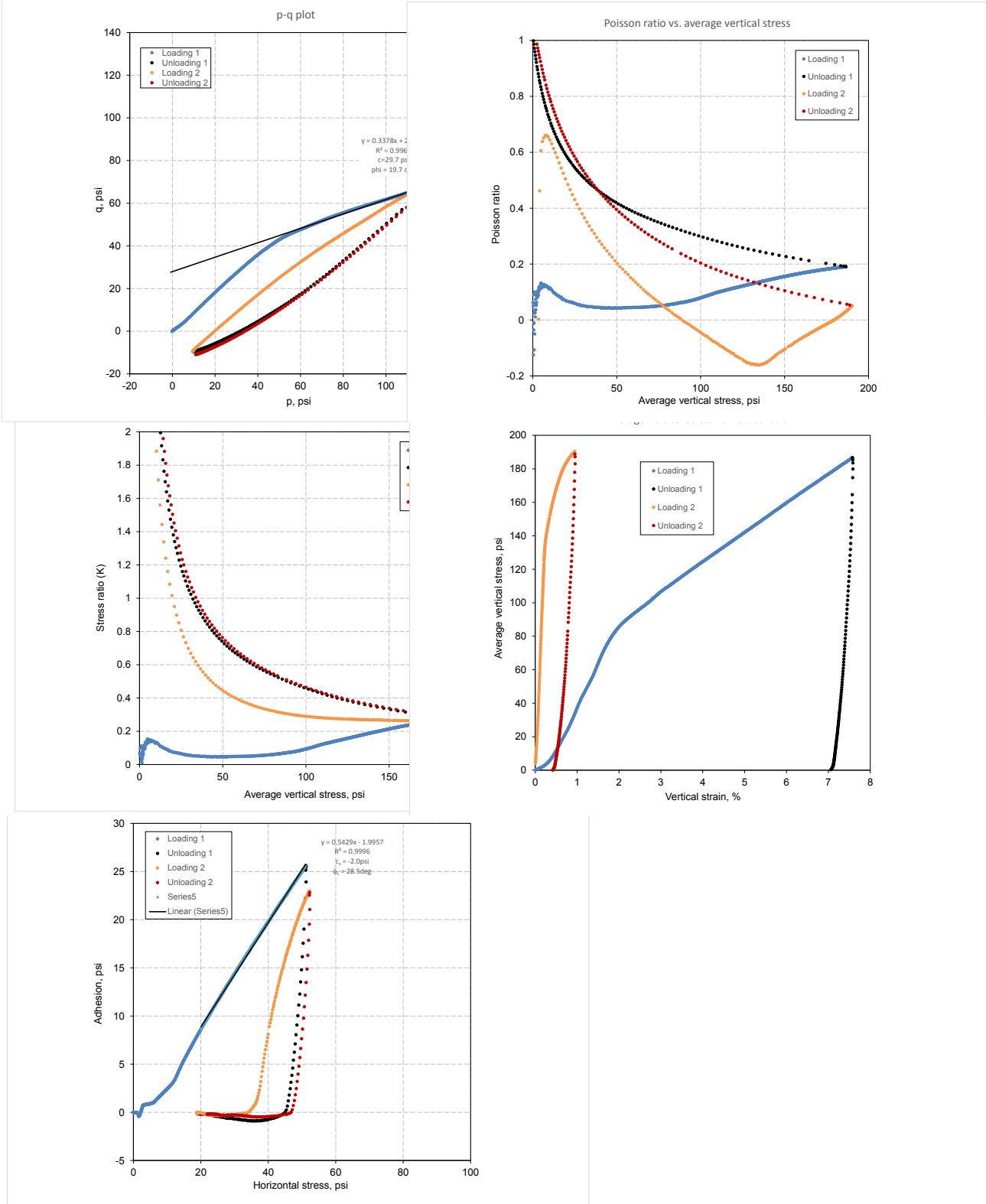


Figure 176. Iowa K test results for Texas fat clay (w% = 18.6% and $\gamma_d = 91.9$ pcf)

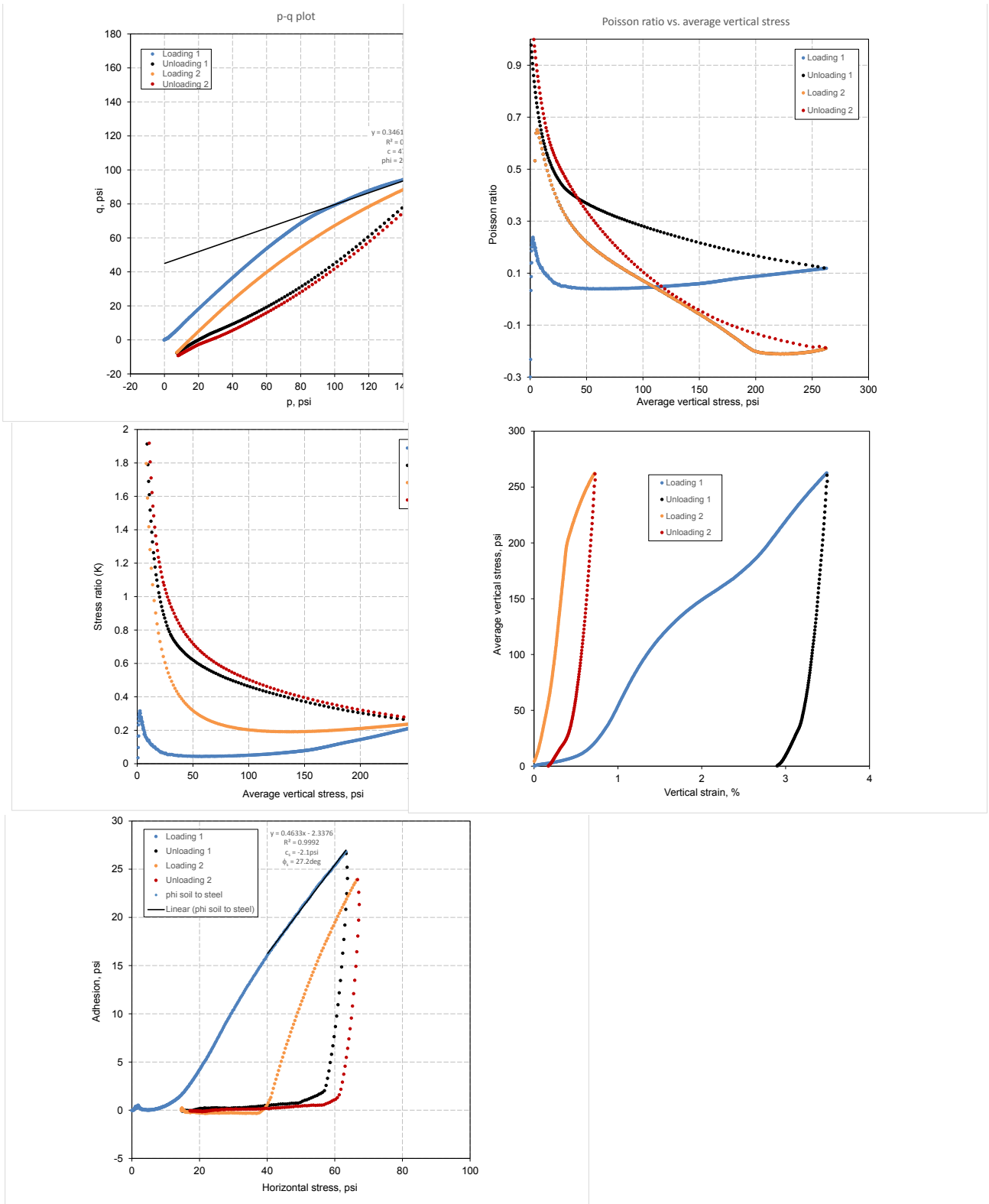


Figure 177. Iowa K test results for Texas fat clay (w% = 19.8% and $\gamma_d = 104.9$ pcf)

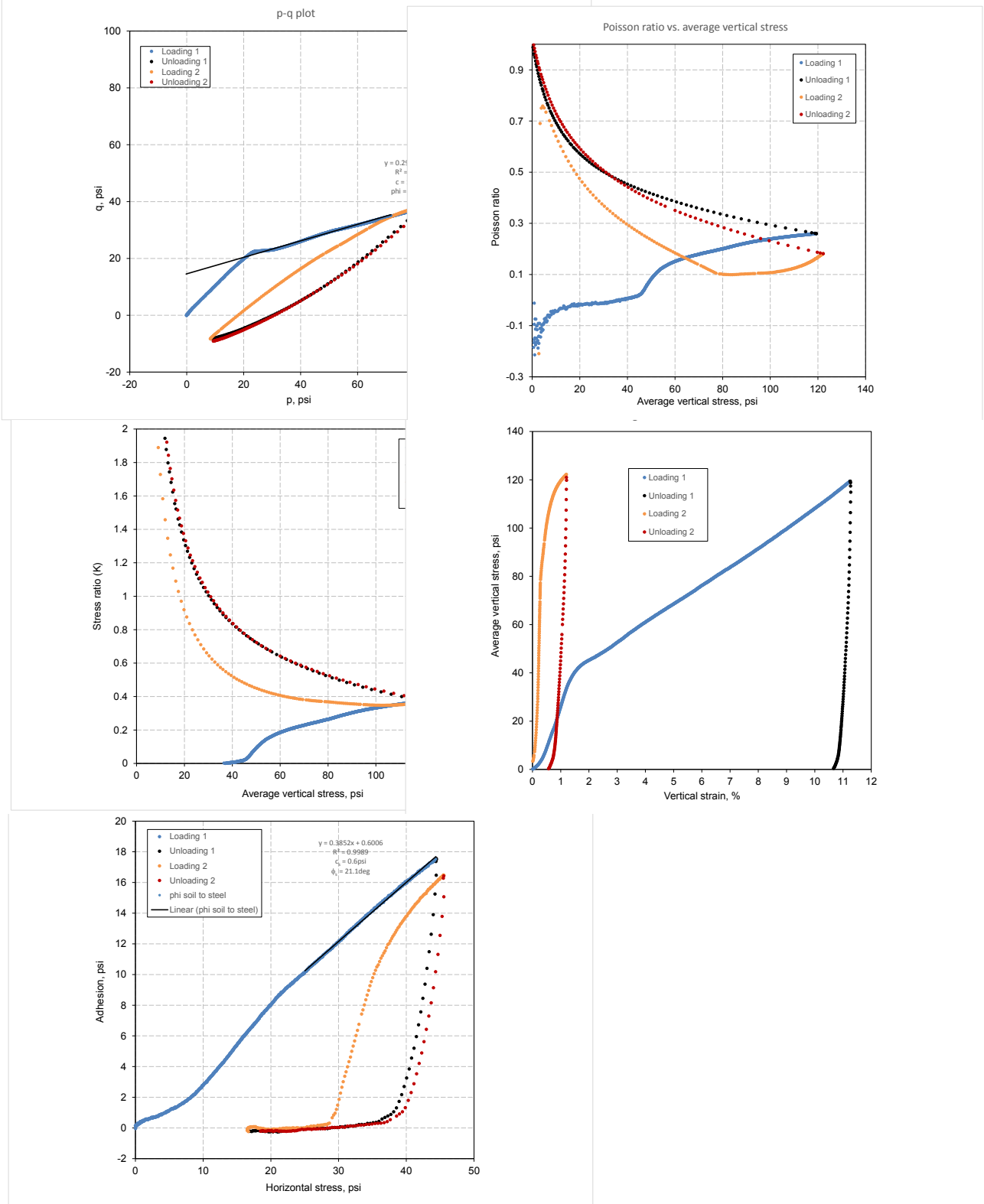


Figure 178. Iowa K test results for Texas fat clay ($w\% = 22.5\%$ and $\gamma_d = 85.1 \text{ pcf}$)

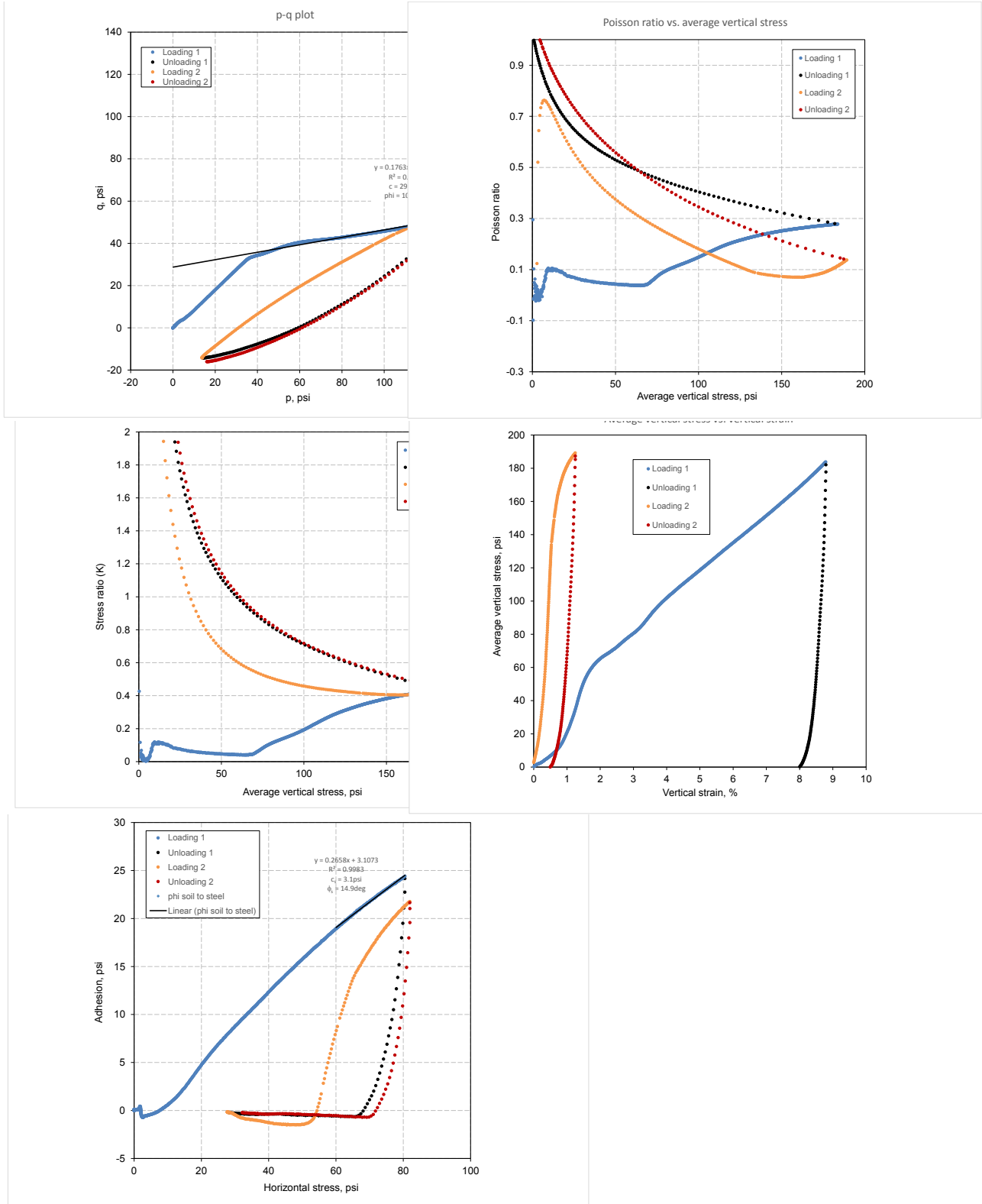


Figure 179. Iowa K test results for Texas fat clay (w% = 21.6% and $\gamma_d = 92.7$ pcf)

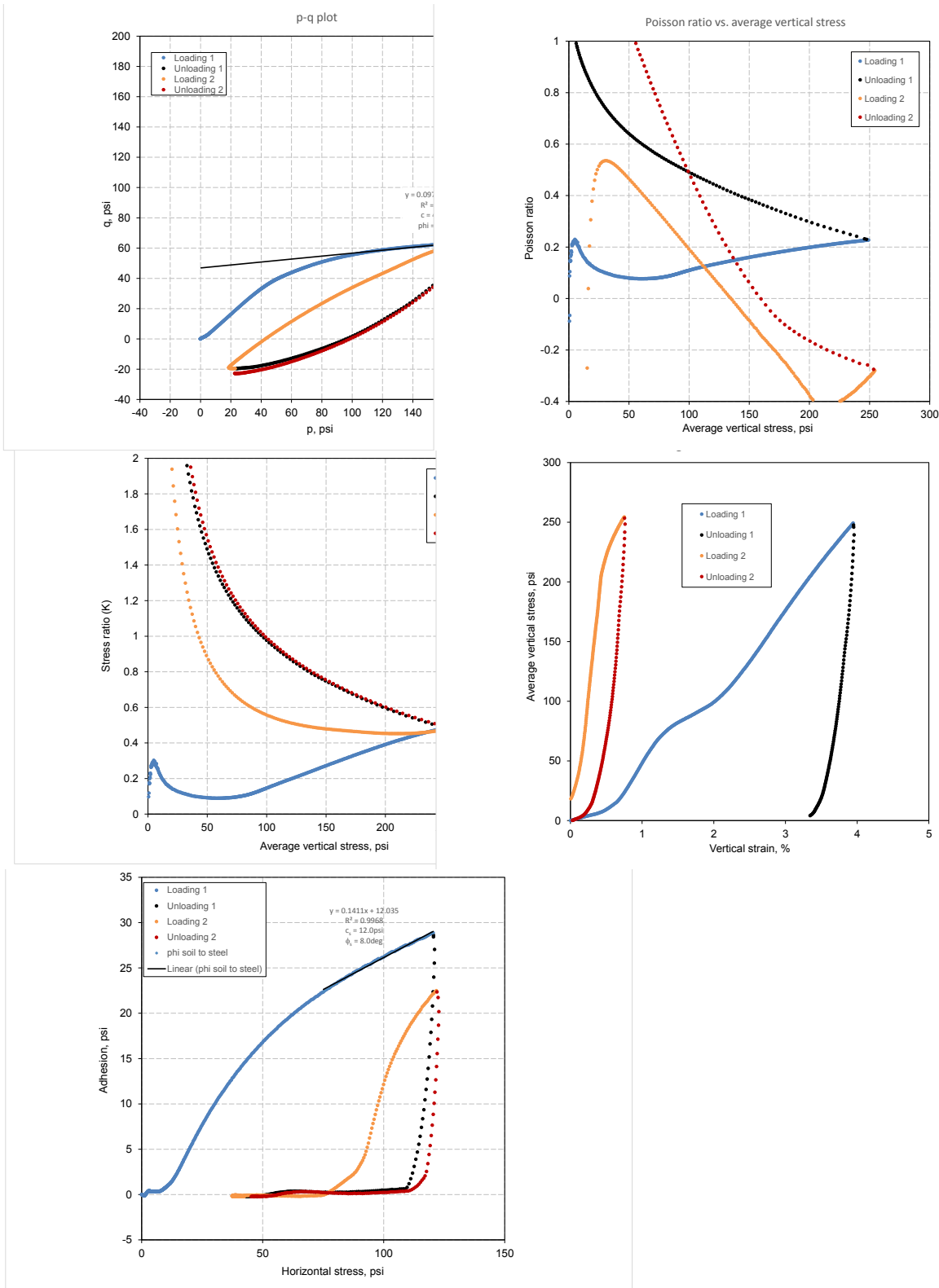


Figure 180. Iowa K test results for Texas fat clay ($w\% = 22.9\%$ and $\gamma_d = 103.6\text{pcf}$)

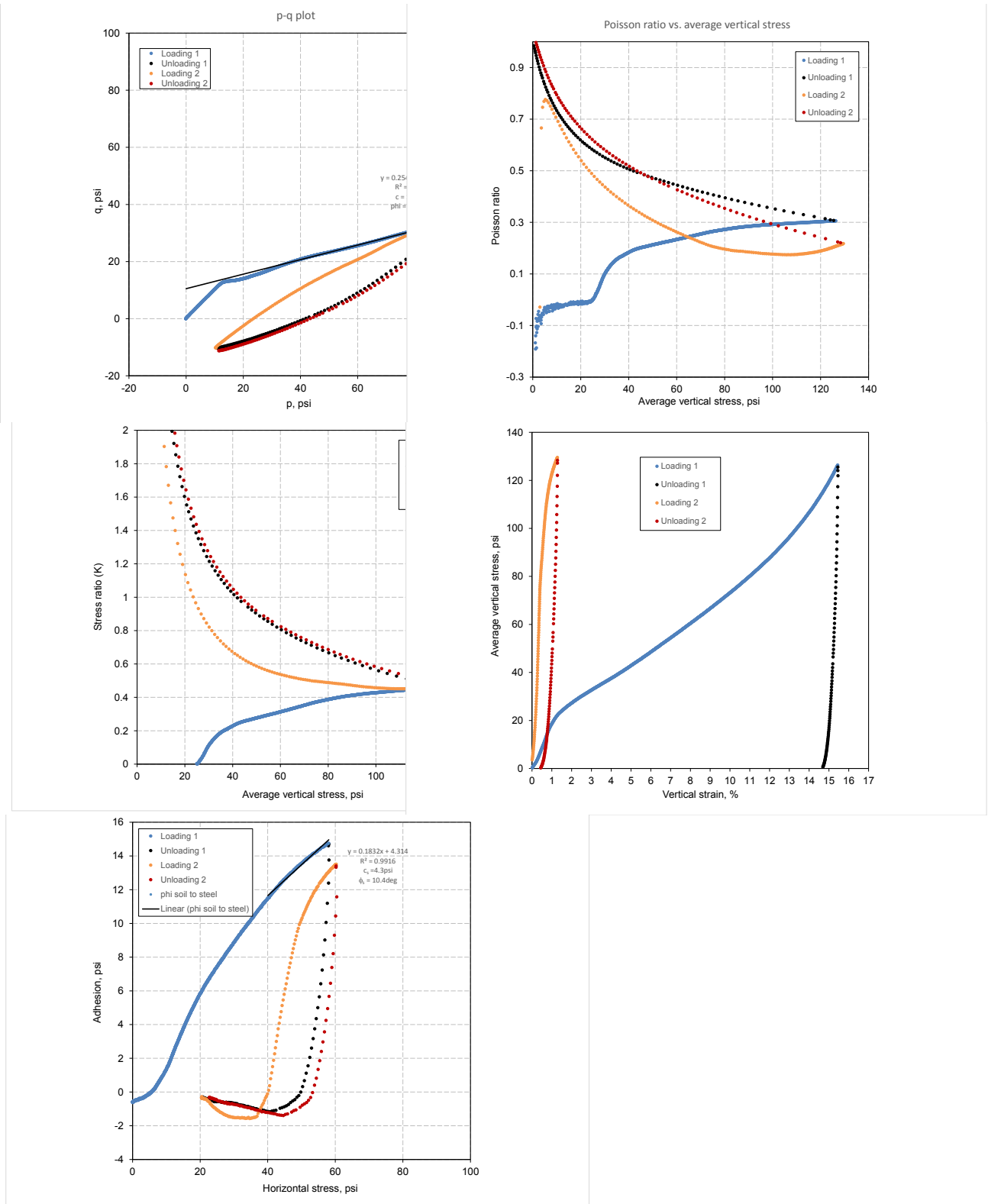


Figure 181. Iowa K test results for Texas fat clay (w% = 24.5% and $\gamma_d = 81.6$ pcf)

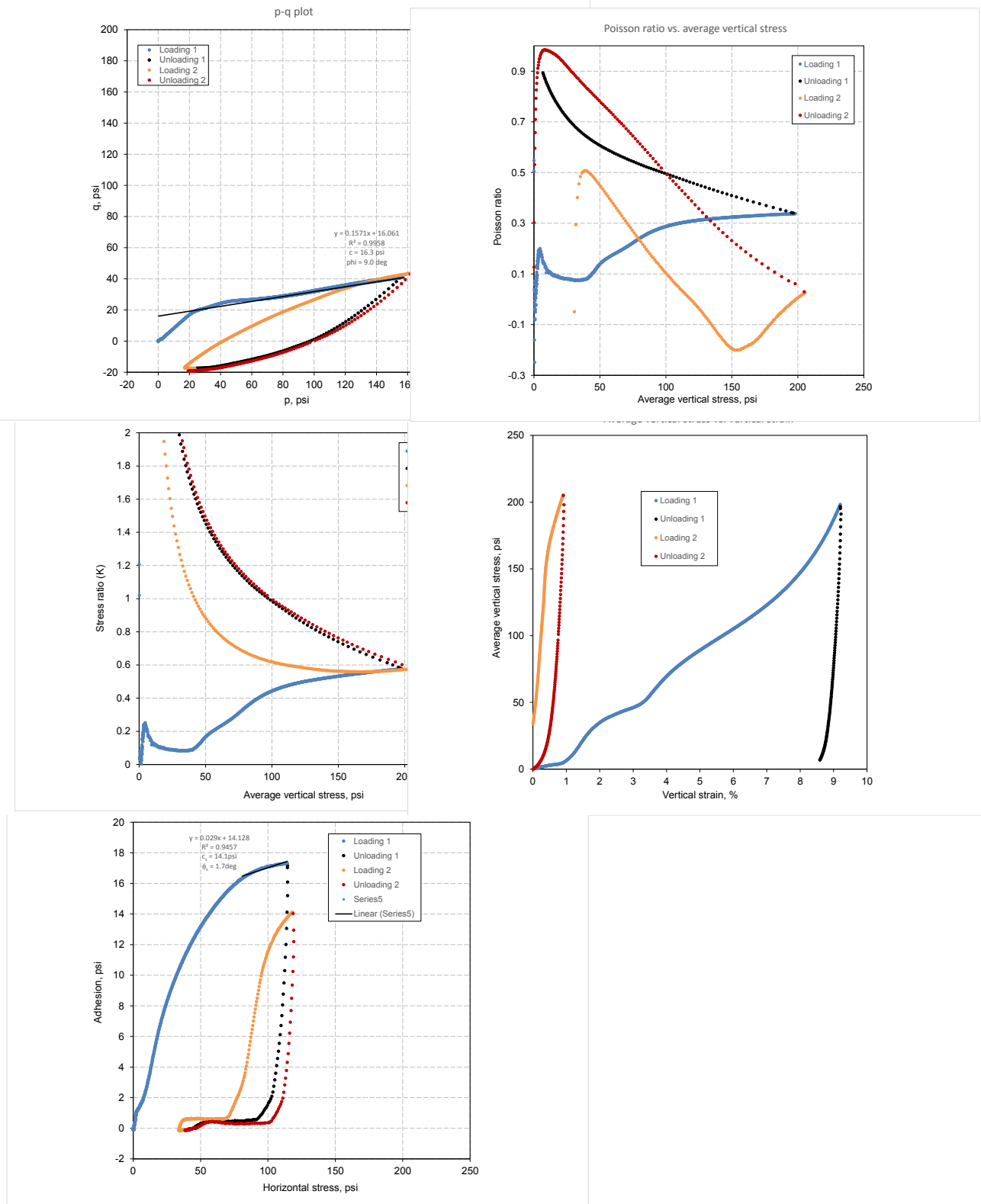


Figure 182. Iowa K test results for Texas fat clay ($w\% = 25.6\%$ and $\gamma_a = 91.6\text{pcf}$)

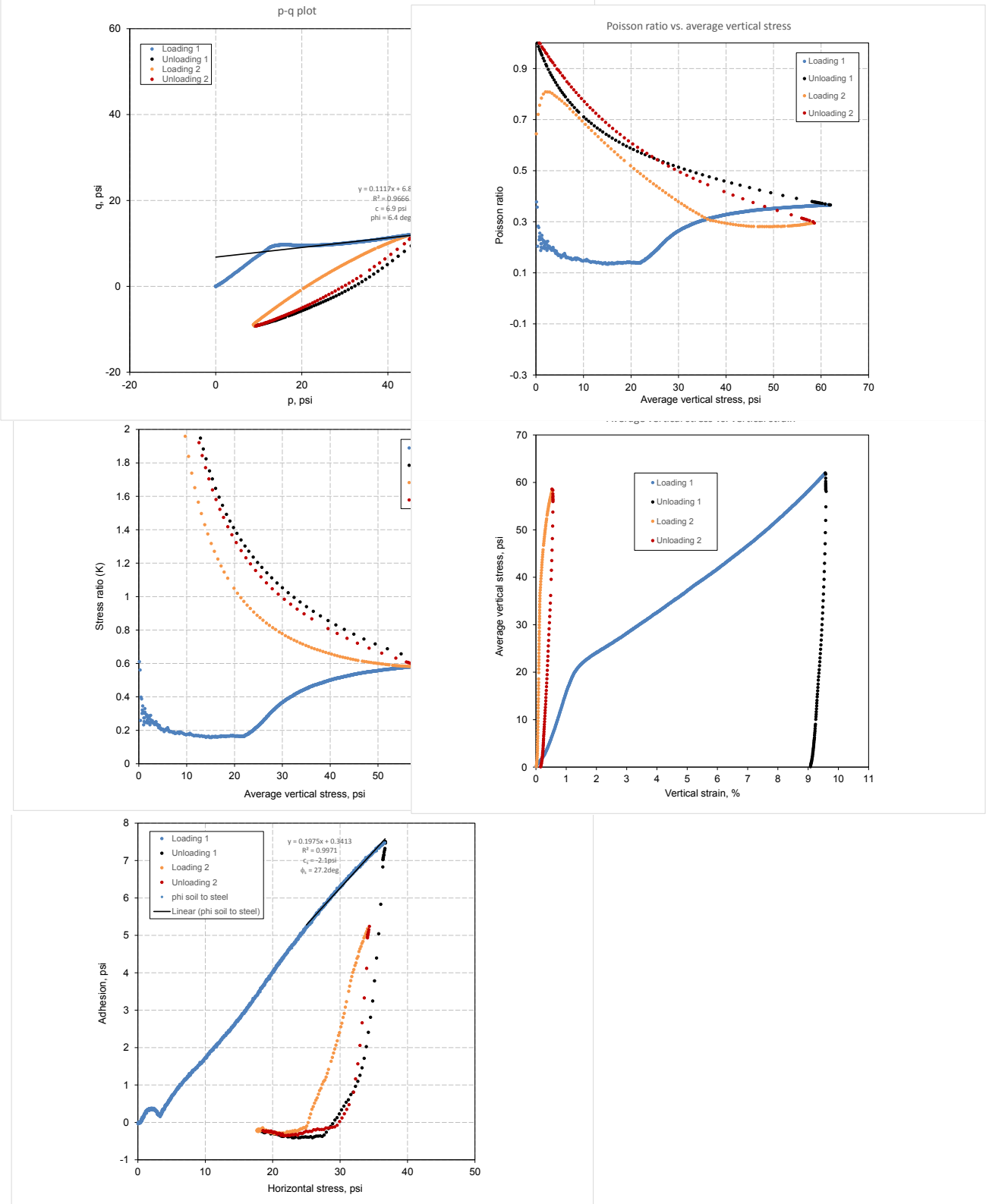


Figure 183. Iowa K test results for Texas fat clay ($w\% = 28.2\%$ and $\gamma_d = 83.6$ pcf)

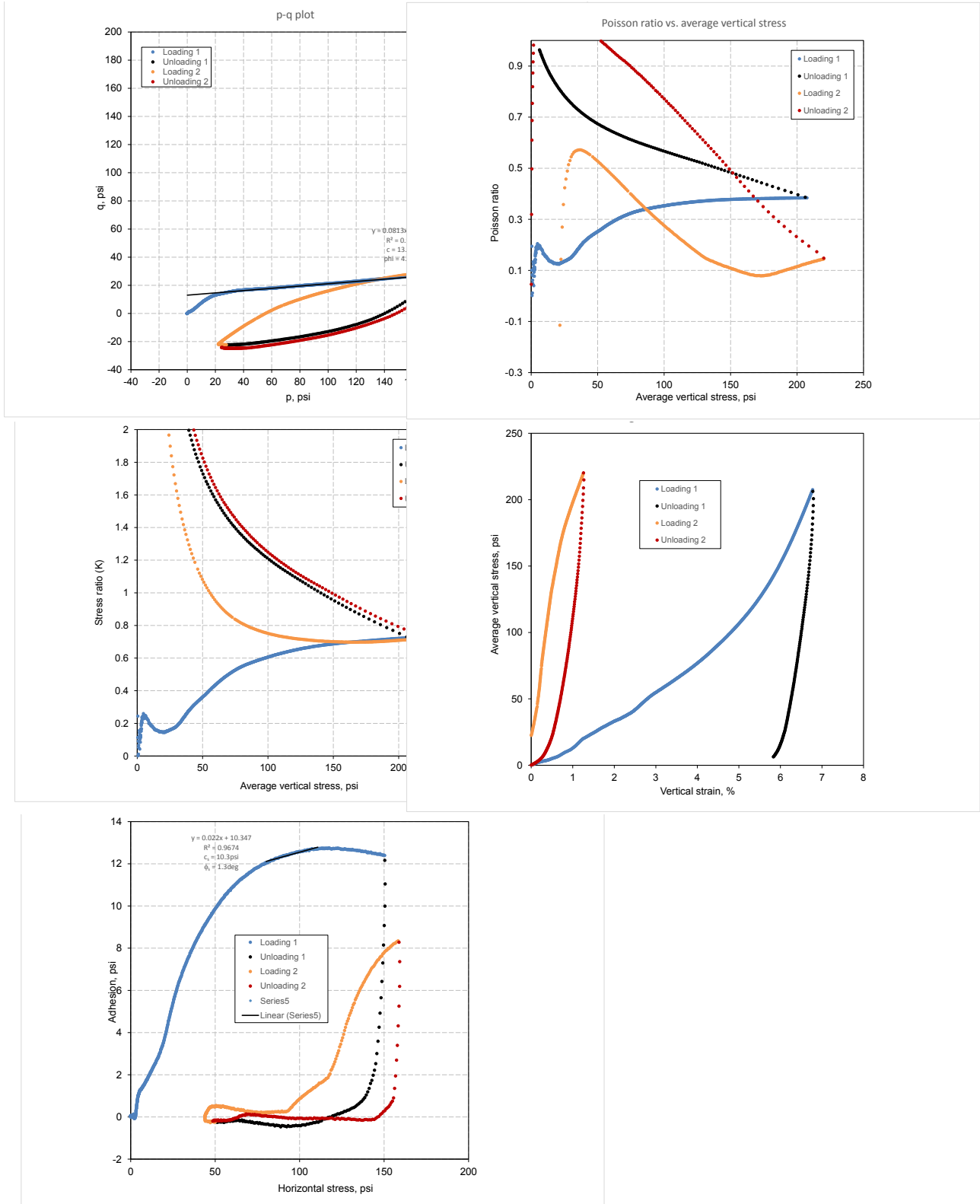


Figure 184. Iowa K test results for Texas fat clay ($w\% = 27.8\%$ and $\gamma_d = 93.7\text{pcf}$)

WCF fly ash (CFED 2053)

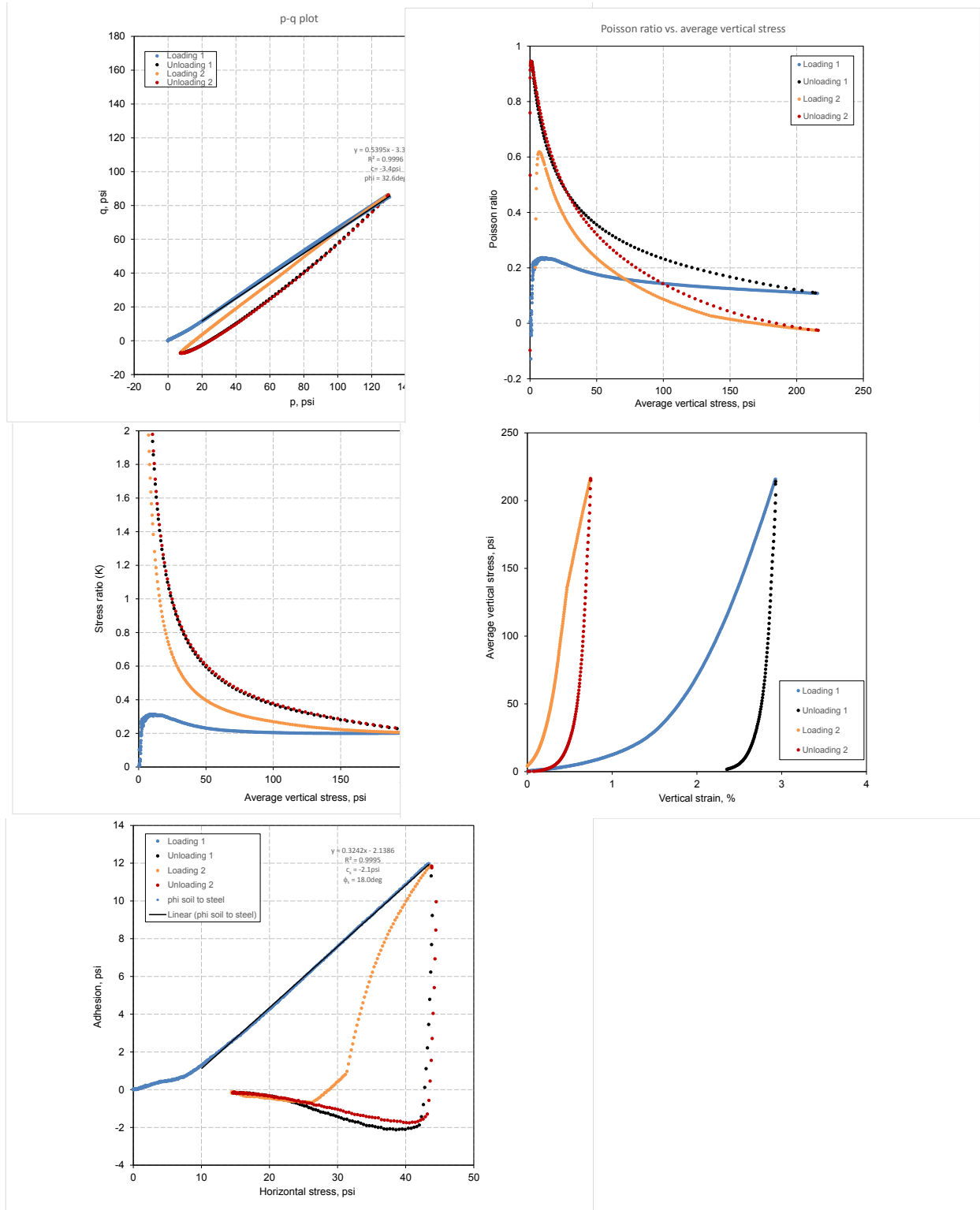


Figure 185. Iowa K test results for WCF fly ash (w% = 15.9% and $\gamma_d = 84.4$ pcf)

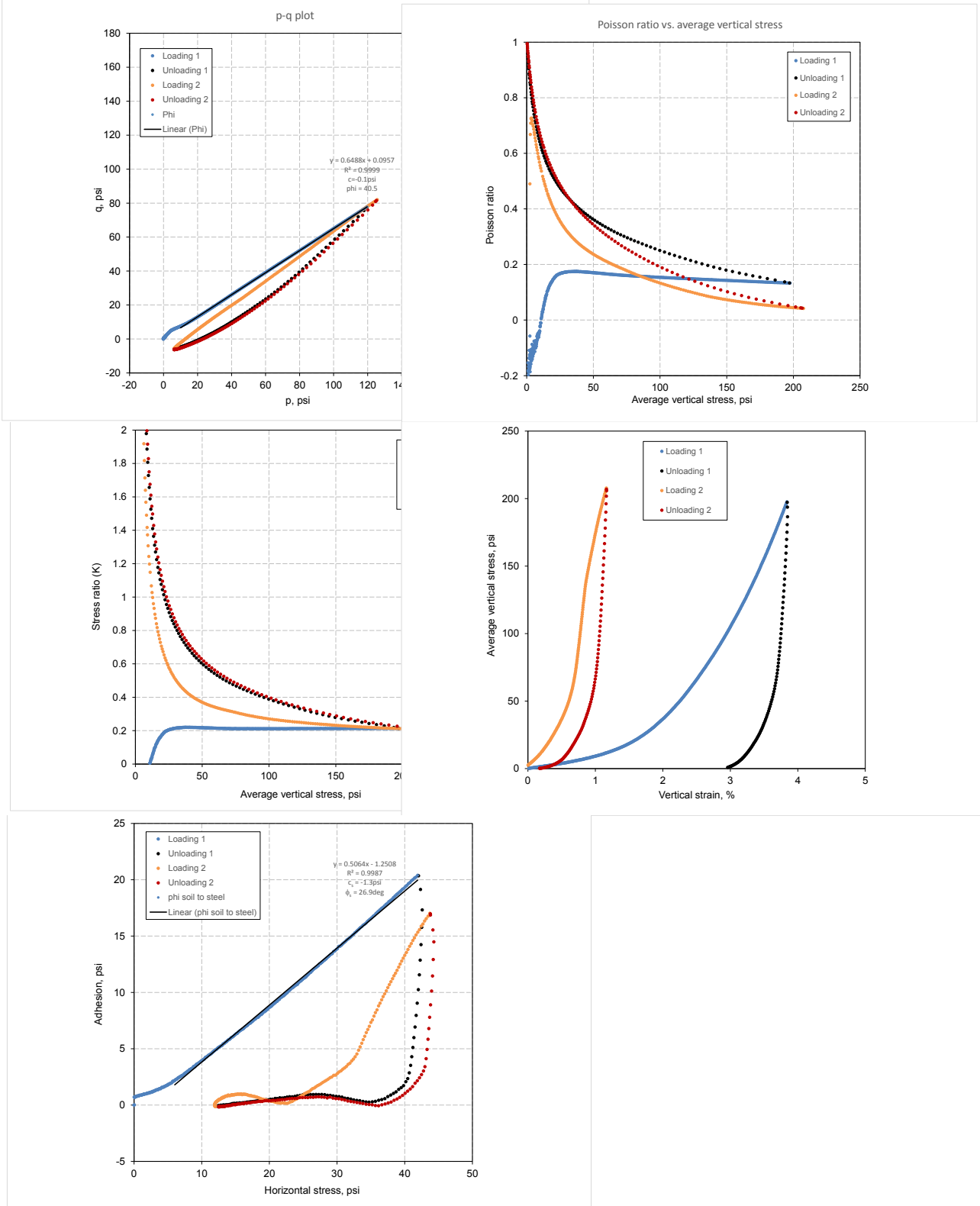


Figure 186. Iowa K test results for WCF fly ash ($w\% = 15.6\%$ and $\gamma_d = 85.8\text{pcf}$)

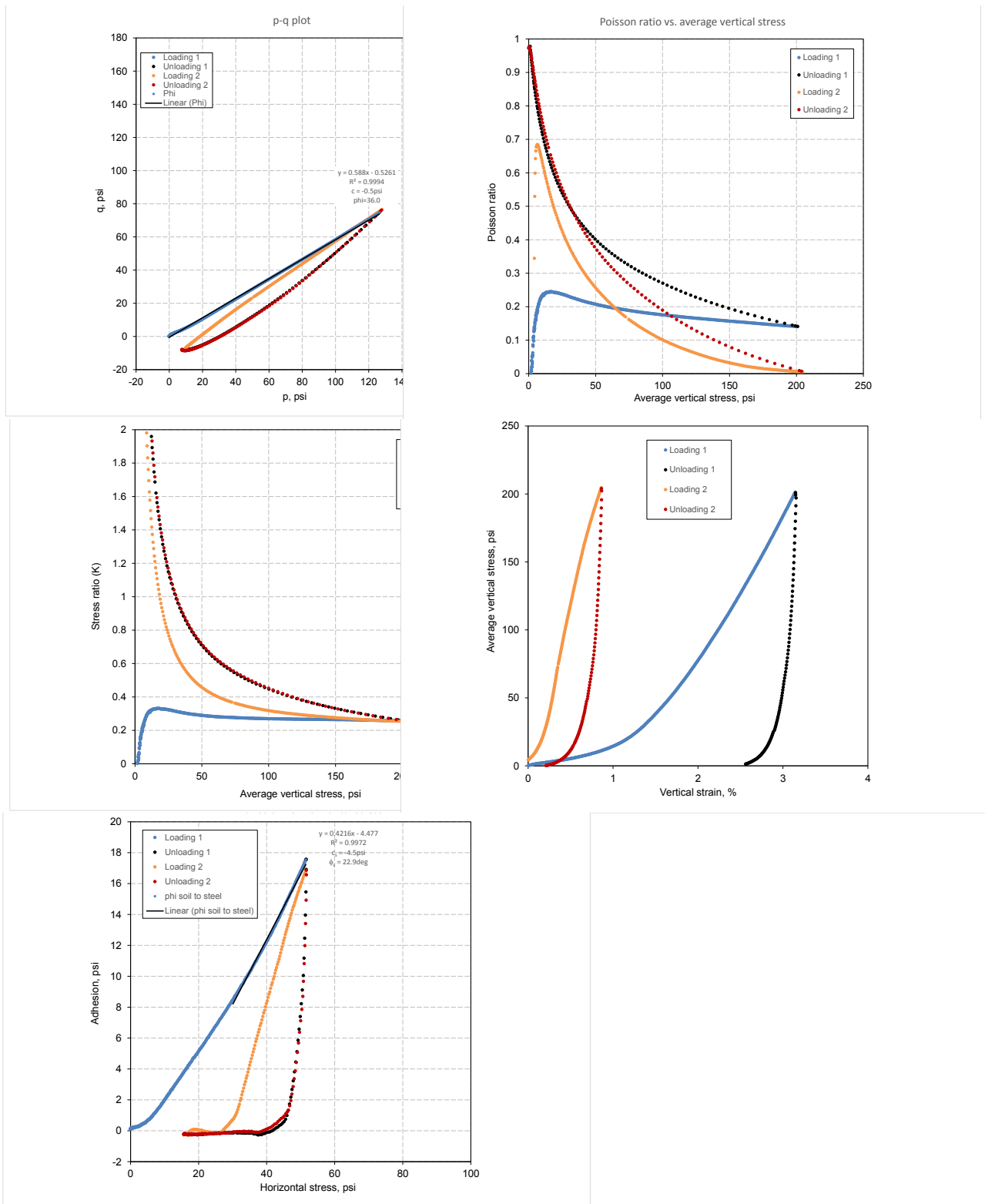


Figure 187. Iowa K test results for WCF fly ash (w% = 17.4% and $\gamma_d = 81.2$ pcf)

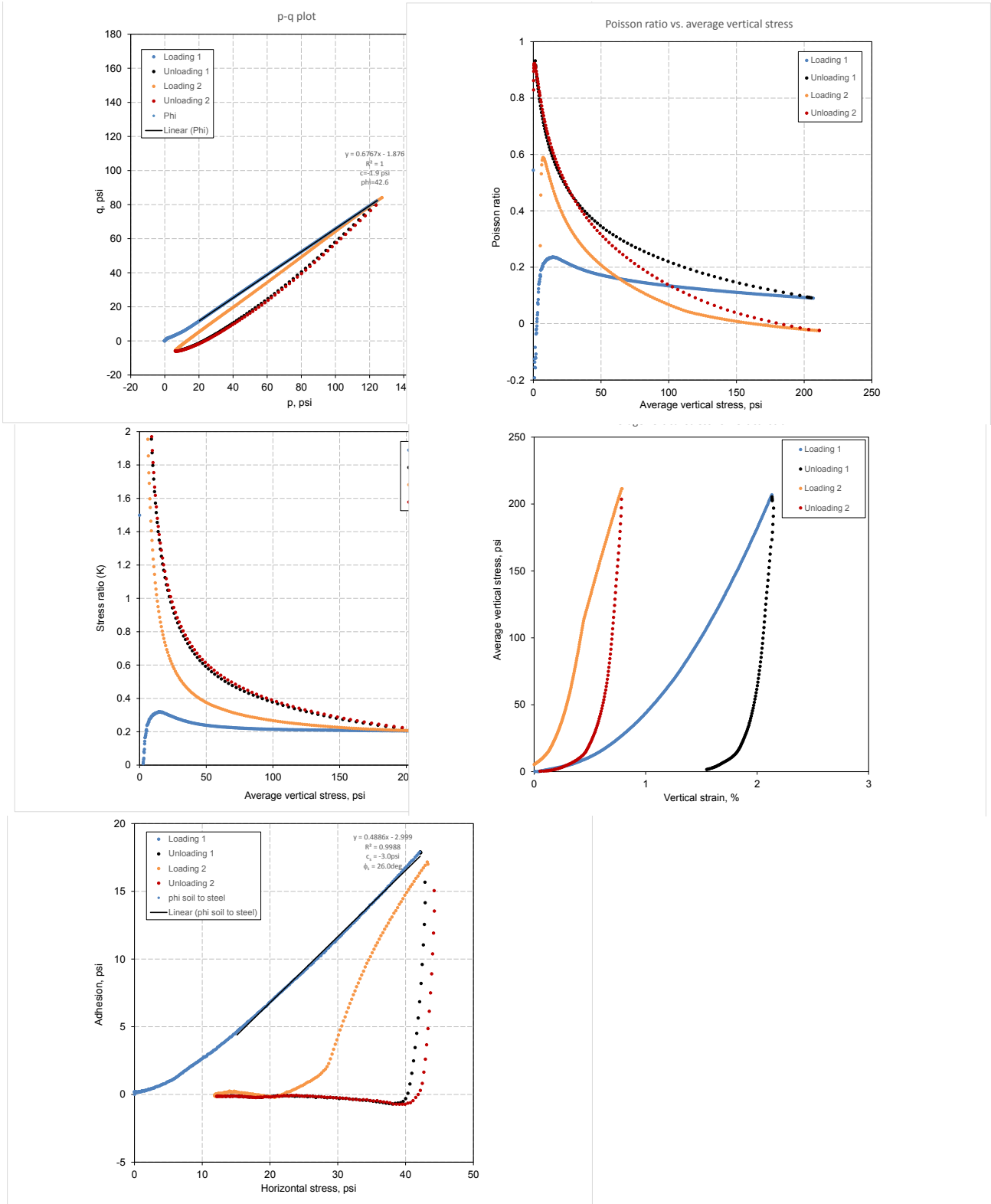


Figure 188. Iowa K test results for WCF fly ash ($w\% = 17.7\%$ and $\gamma_d = 84.2 \text{ pcf}$)

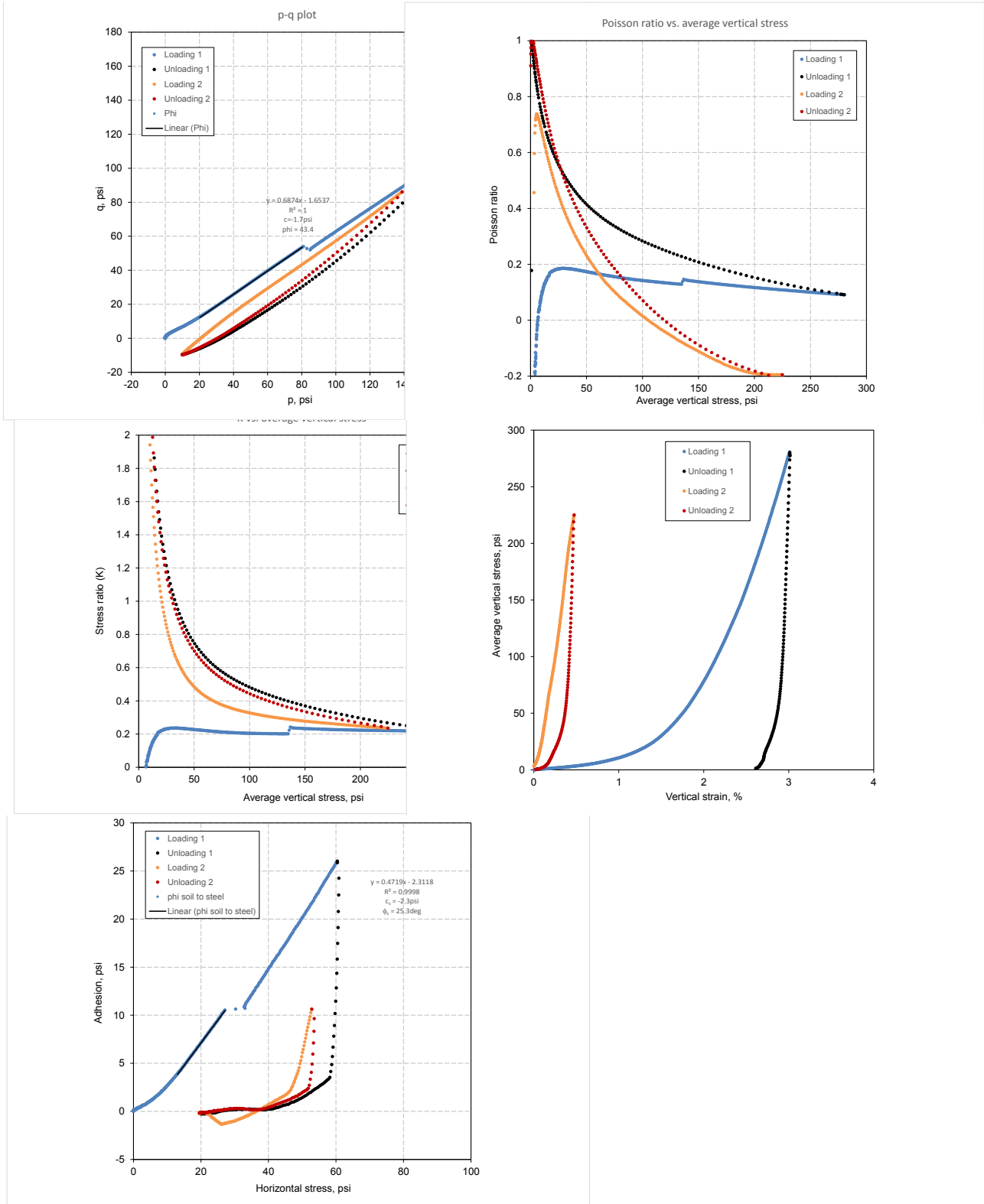


Figure 189. Iowa K test results for WCF fly ash (w% = 18.0% and $\gamma_d = 86.6$ pcf)

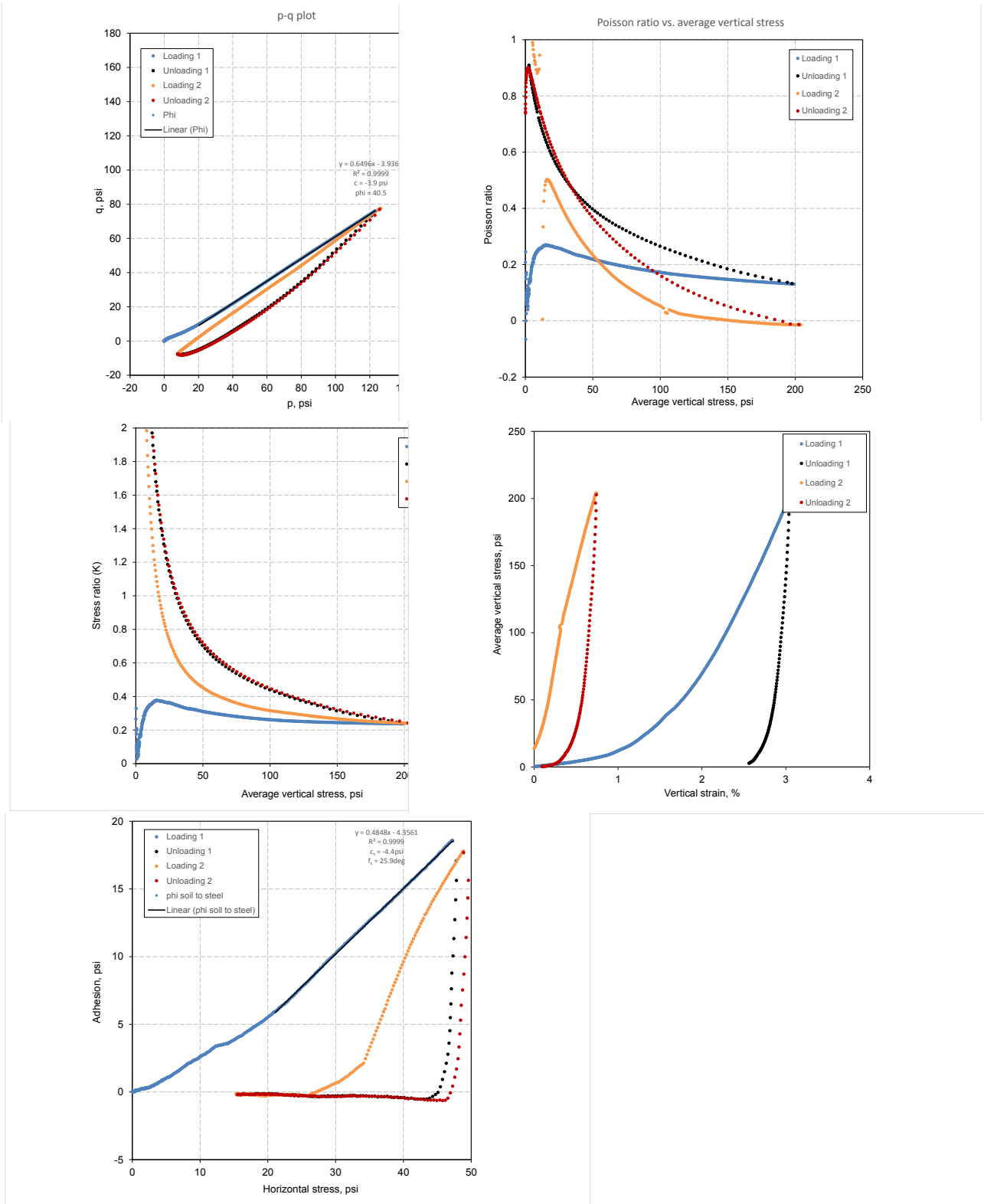


Figure 190. Iowa K test results for WCF fly ash ($w\% = 18.9\%$ and $\gamma_d = 82.7 \text{ pcf}$)

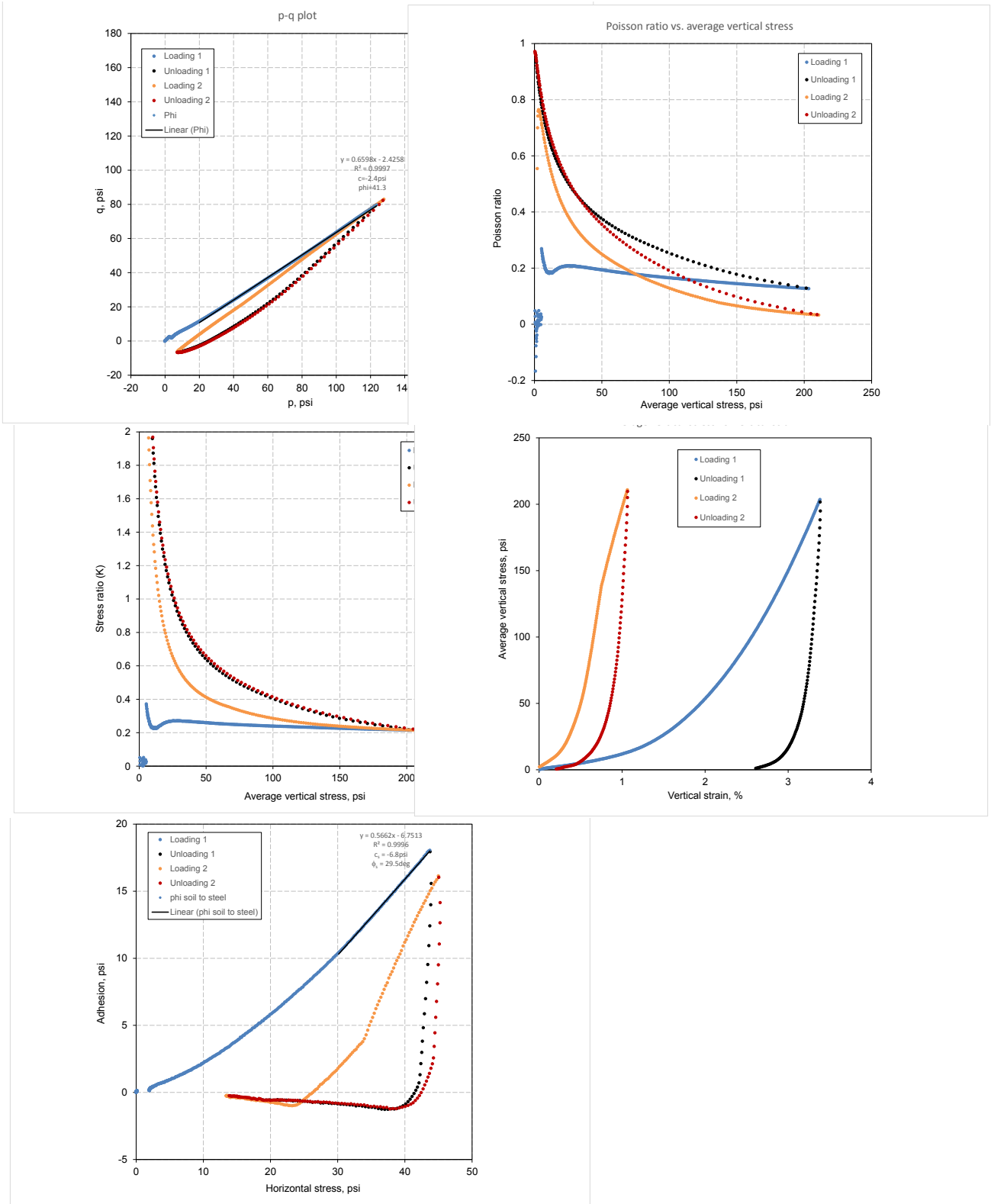


Figure 191. Iowa K test results for WCF fly ash ($w\% = 18.9\%$ and $\gamma_d = 85.2\text{pcf}$)

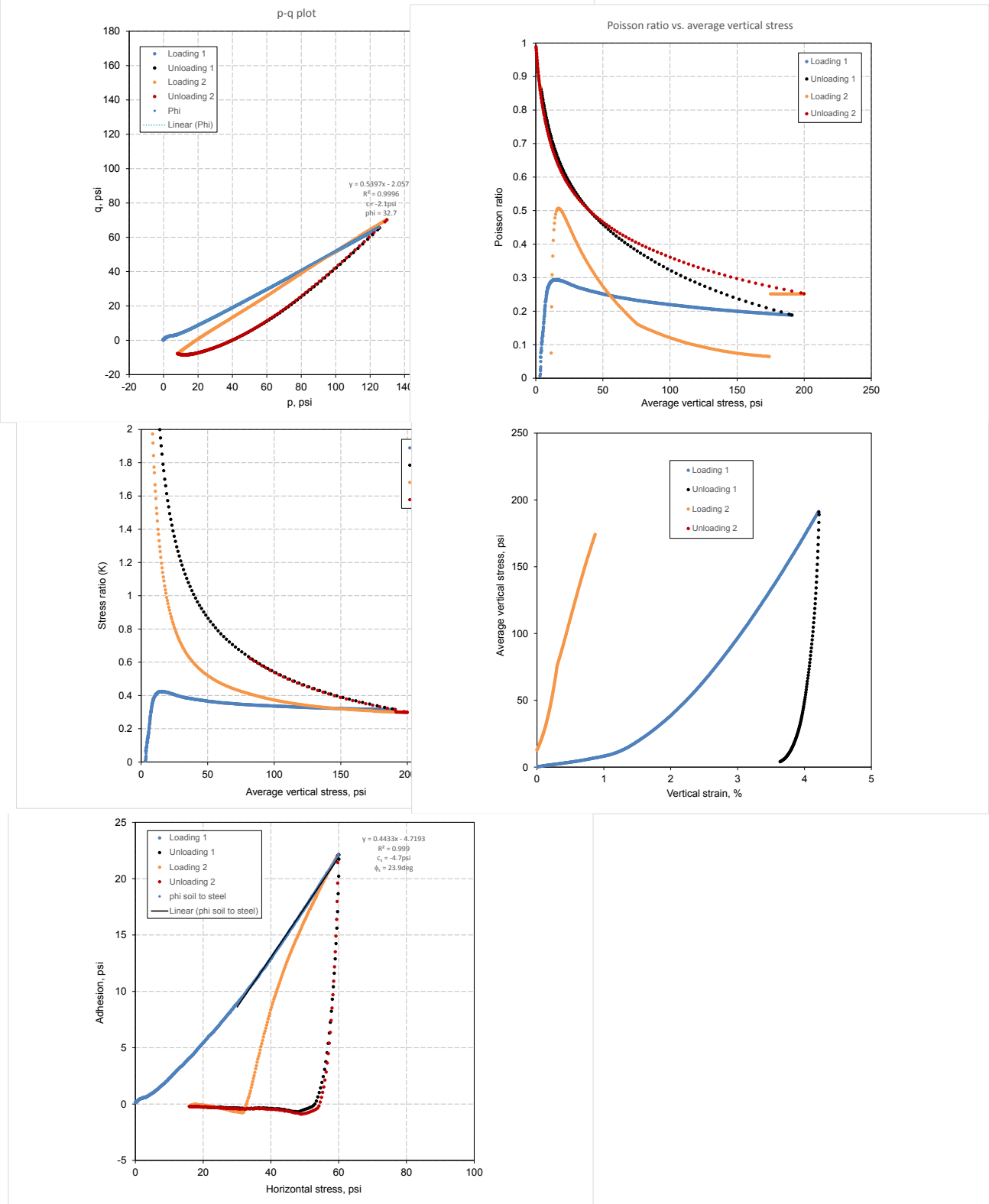


Figure 192. Iowa K test results for WCF fly ash ($w\% = 21.2\%$ and $\gamma_d = 79.6\text{pcf}$)

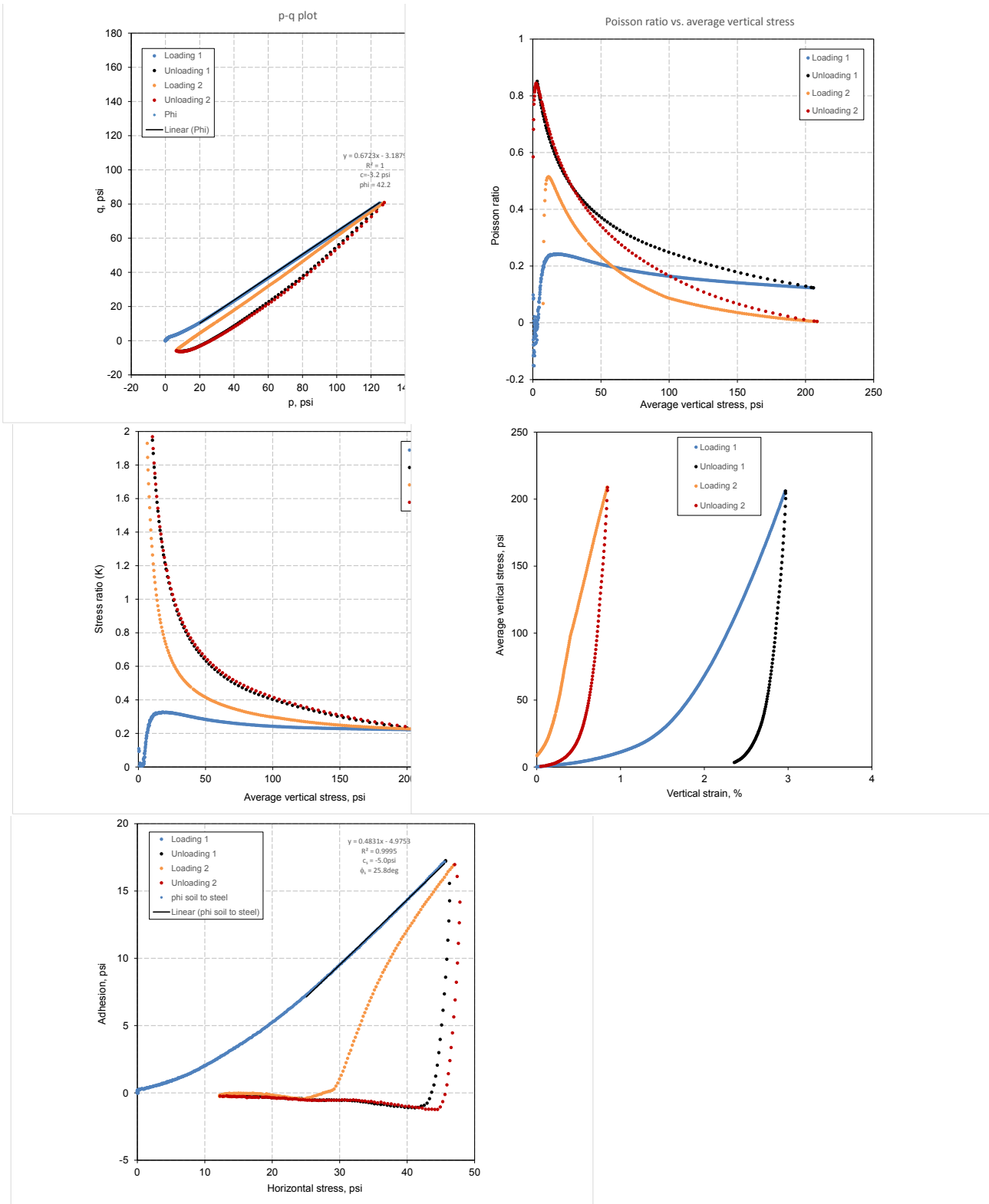


Figure 193. Iowa K test results for WCF fly ash ($w\% = 22.4\%$ and $\gamma_d = 84.4 \text{ pcf}$)

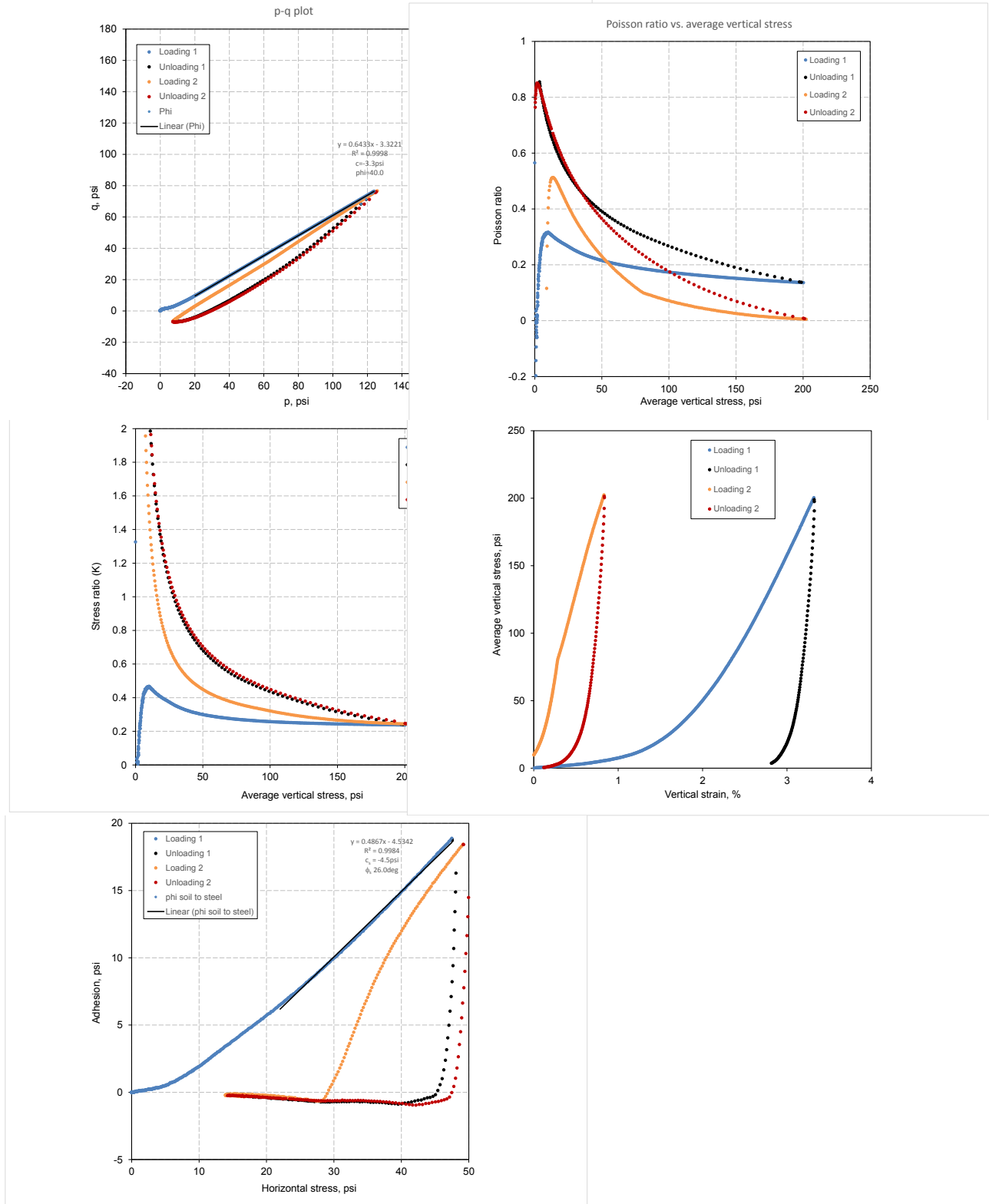


Figure 194. Iowa K test results for WCF fly ash ($w\% = 24.3\%$ and $\gamma_d = 82.3\text{pcf}$)

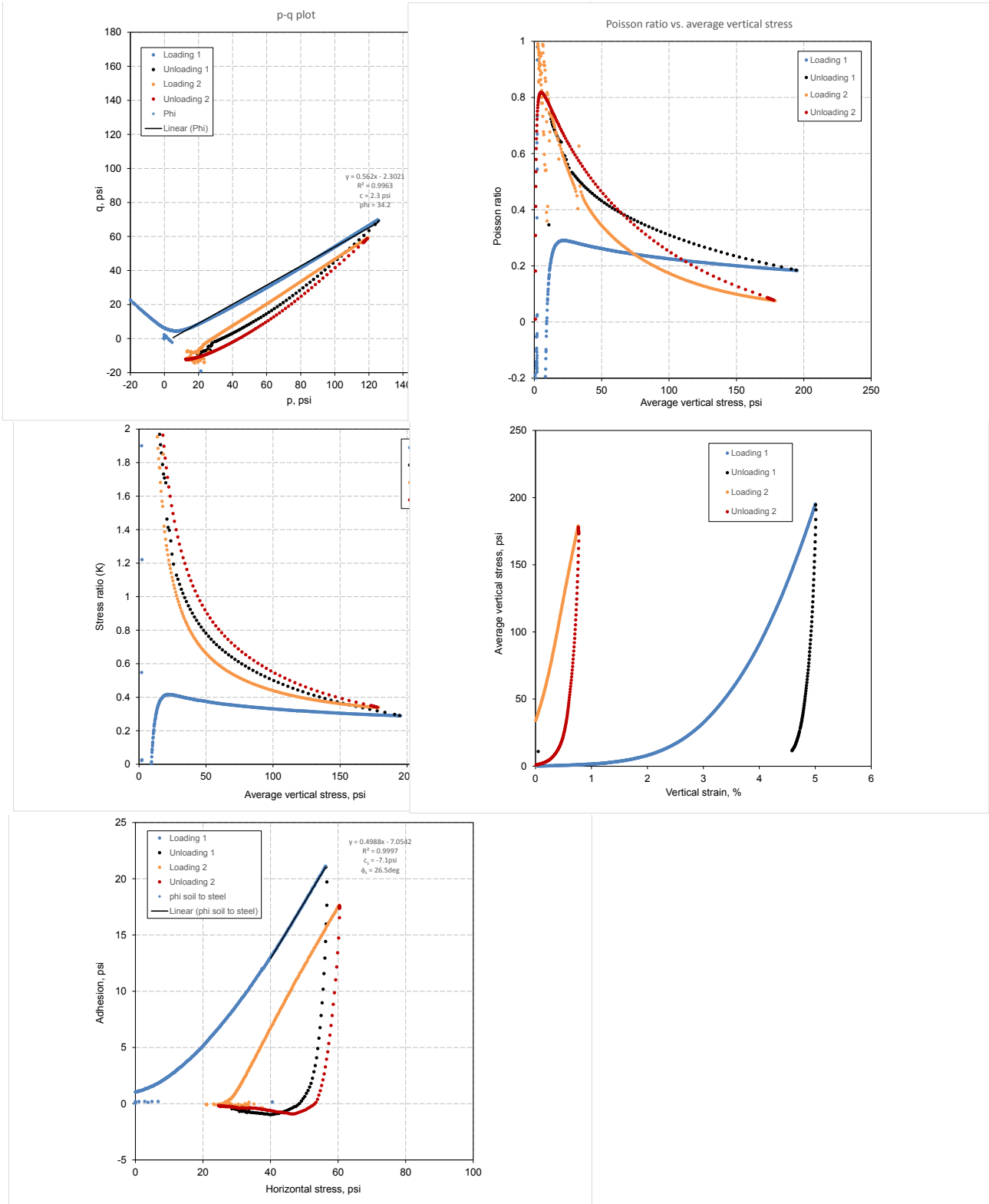


Figure 195. Iowa K test results for WCF fly ash ($w\% = 24.4\%$ and $\gamma_d = 81.5 \text{ pcf}$)

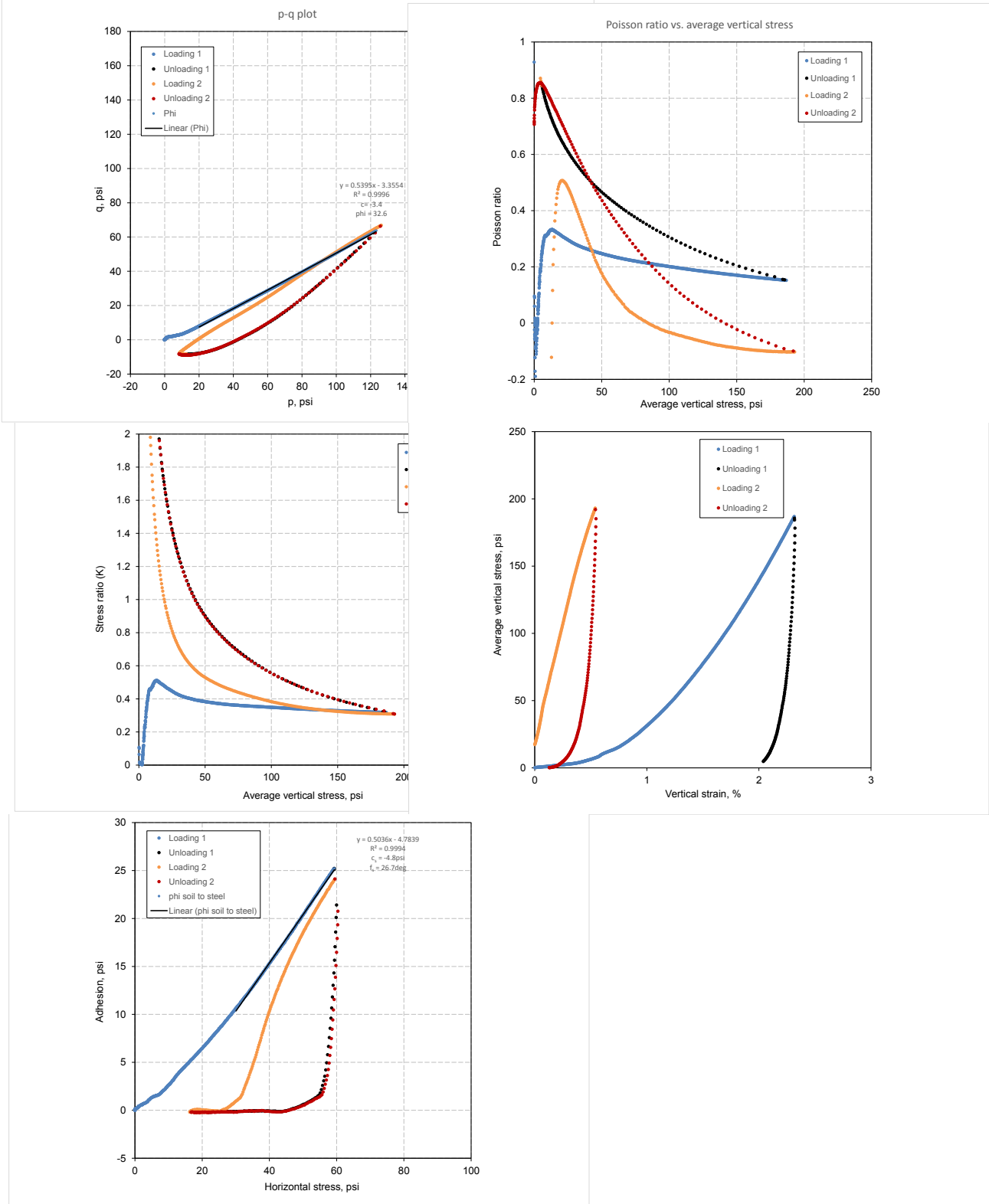


Figure 196. Iowa K test results for WCF fly ash ($w\% = 25.6\%$ and $\gamma_d = 78.7\text{pcf}$)

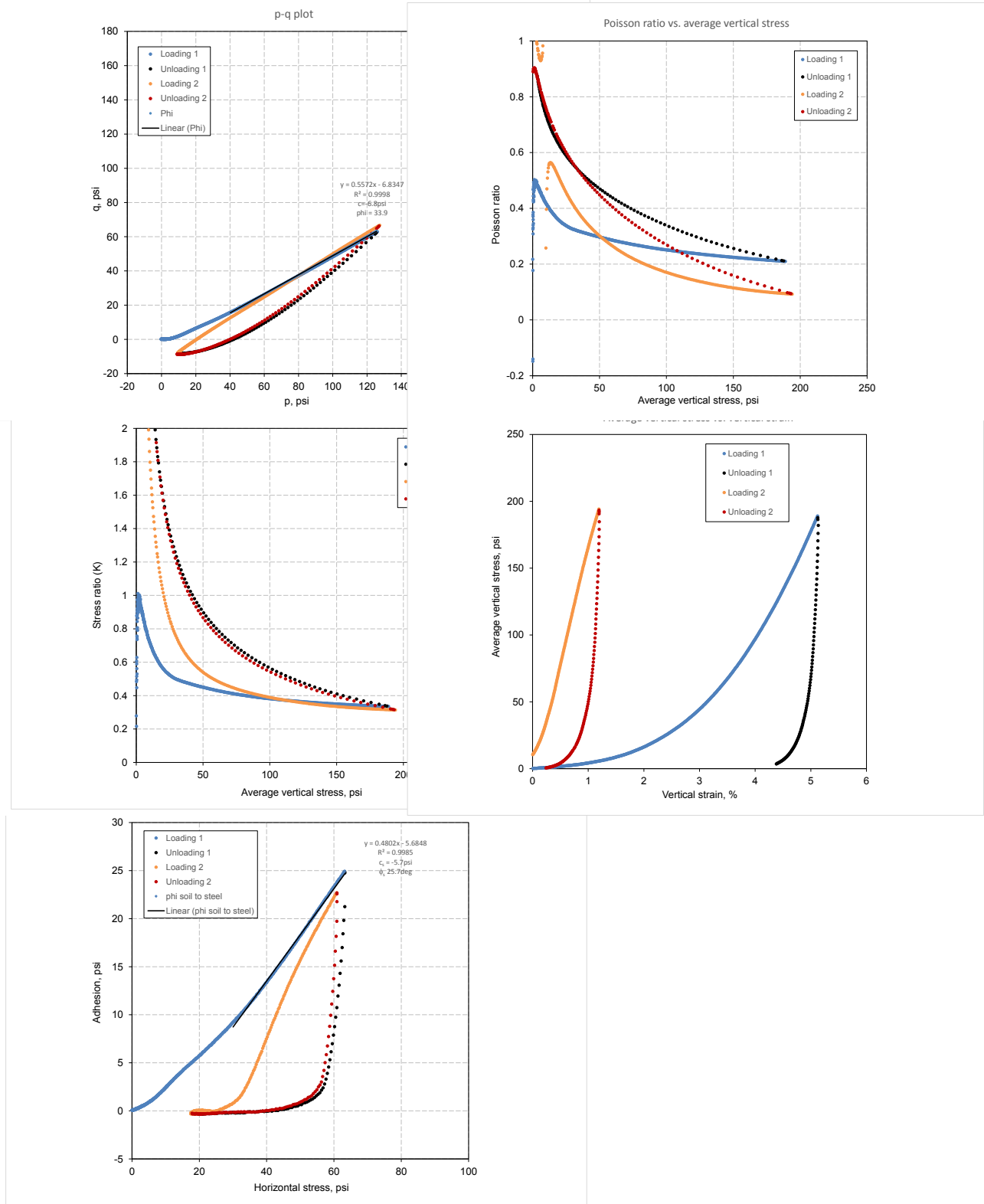


Figure 197. Iowa K test results for WCF fly ash (w% = 27.5% and $\gamma_d = 79.5$ pcf)

WCF gypsum (CFED 2054)

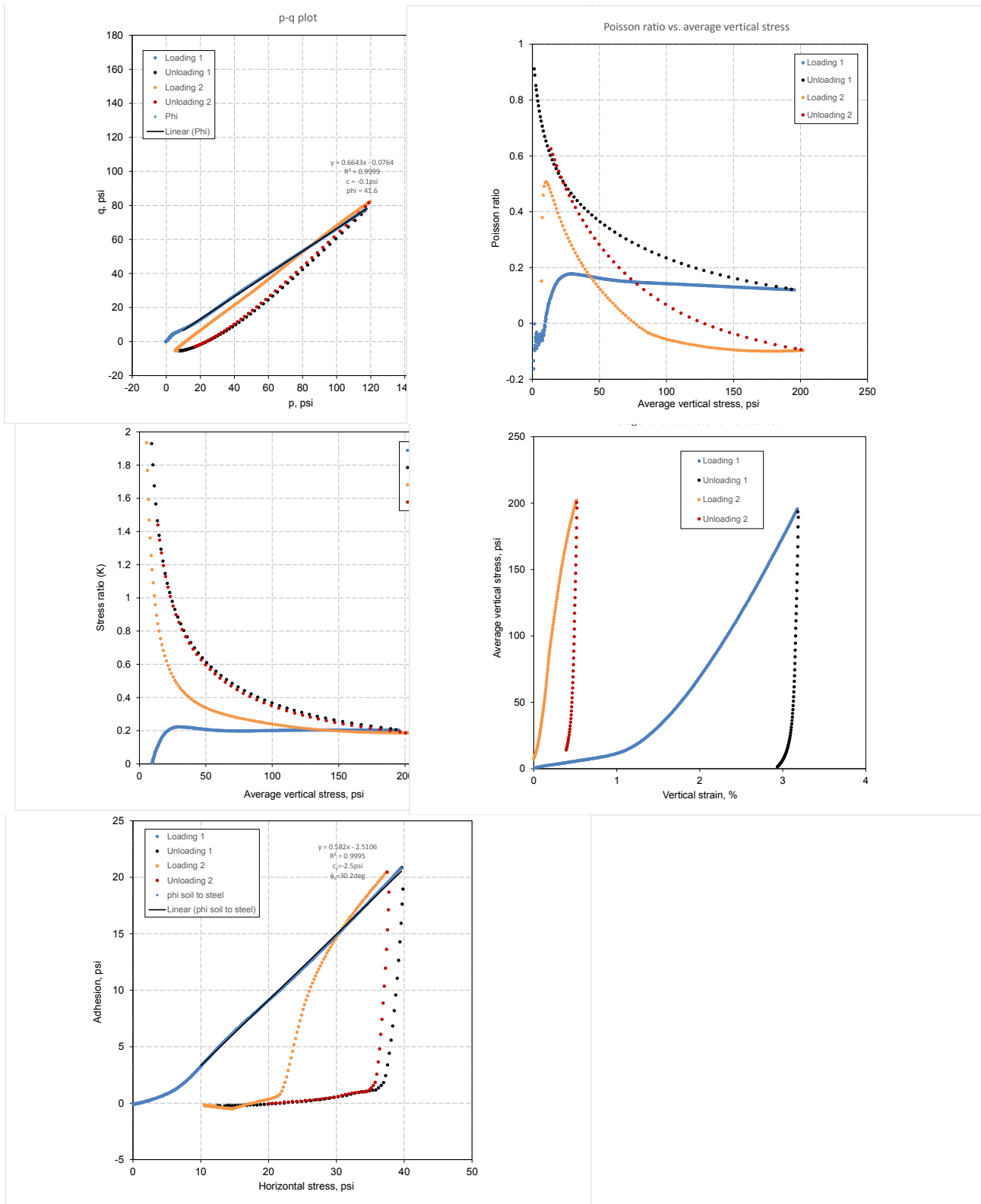


Figure 198. Iowa K test results for WCF gypsum (w% = 9.5% and $\gamma_d = 97.7\text{pcf}$)

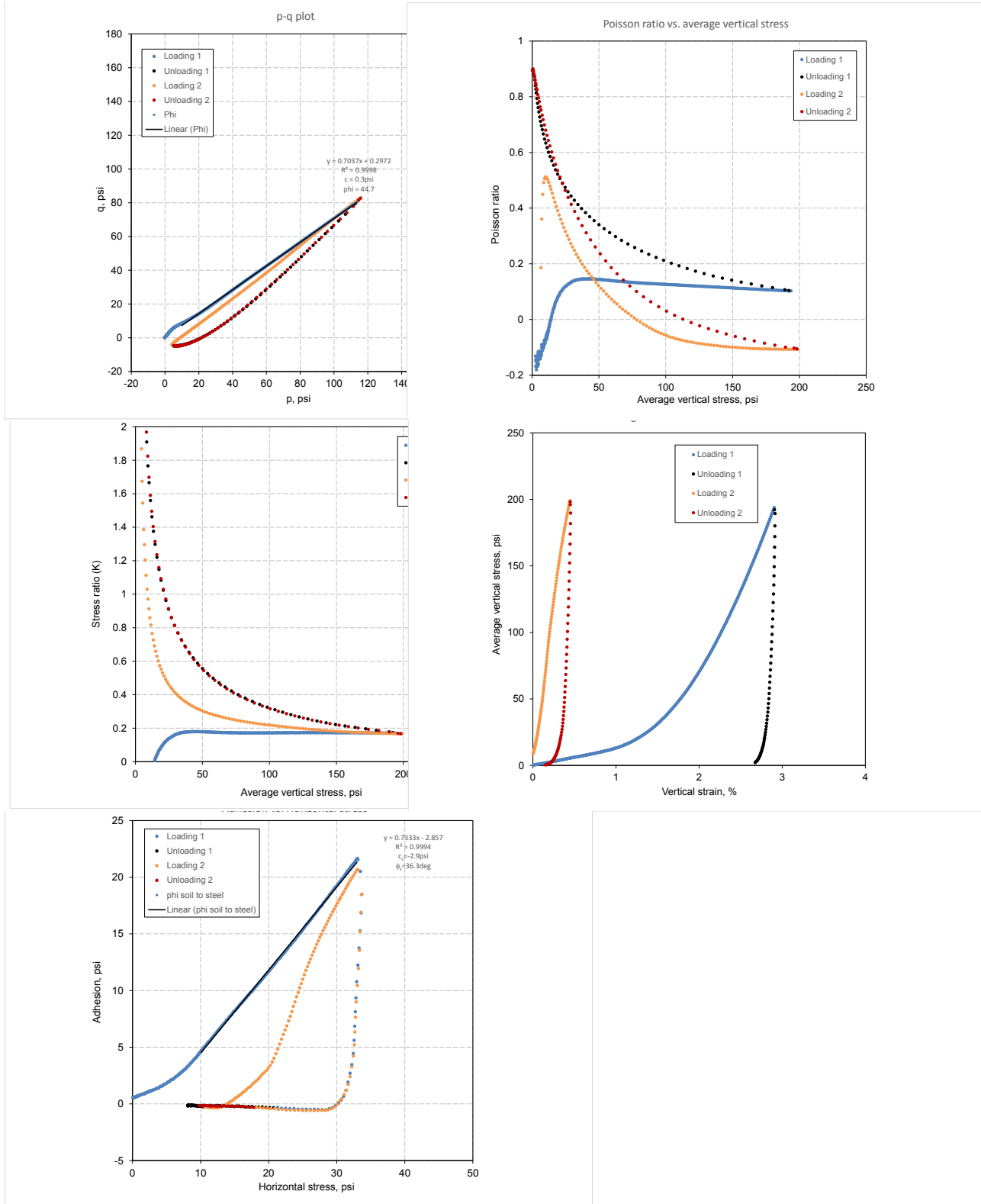


Figure 199. Iowa K test results for WCF gypsum ($w\% = 9.7\%$ and $\gamma_d = 101.3\text{pcf}$)

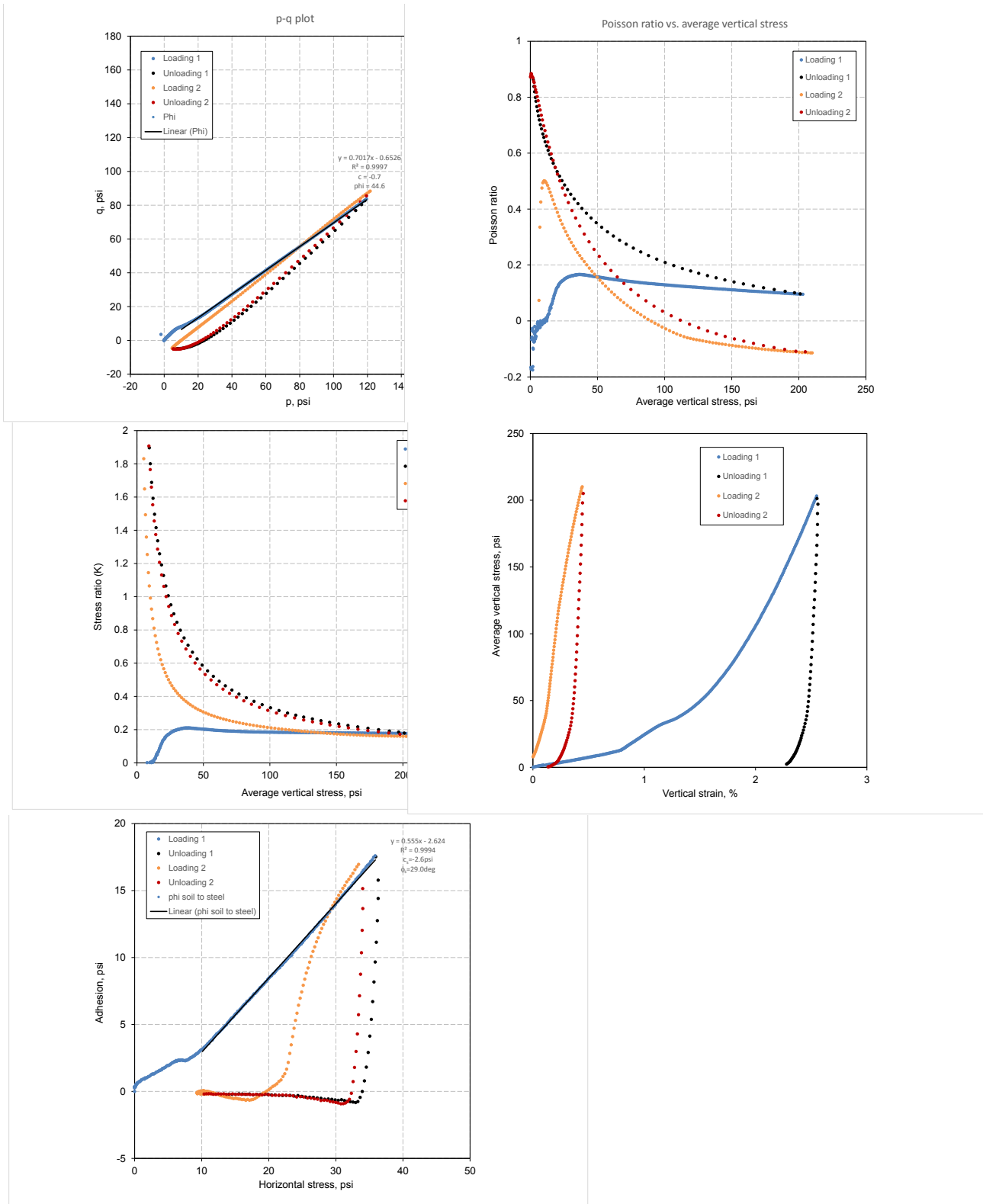


Figure 200. Iowa K test results for WCF gypsum (w% = 9.9% and $\gamma_d = 106.1$ pcf)

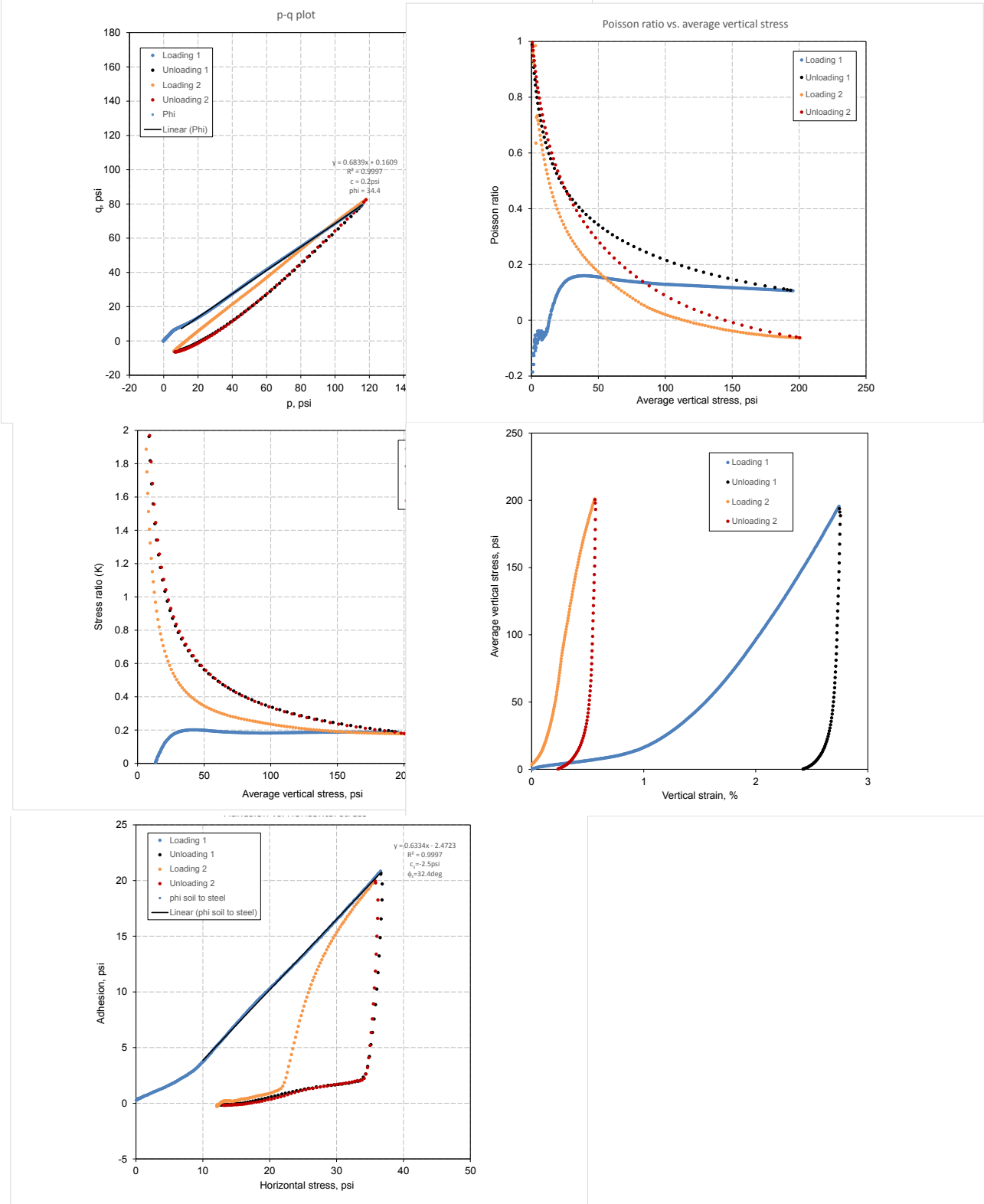


Figure 201. Iowa K test results for WCF gypsum ($w\% = 10.9\%$ and $\gamma_d = 100.9\text{pcf}$)

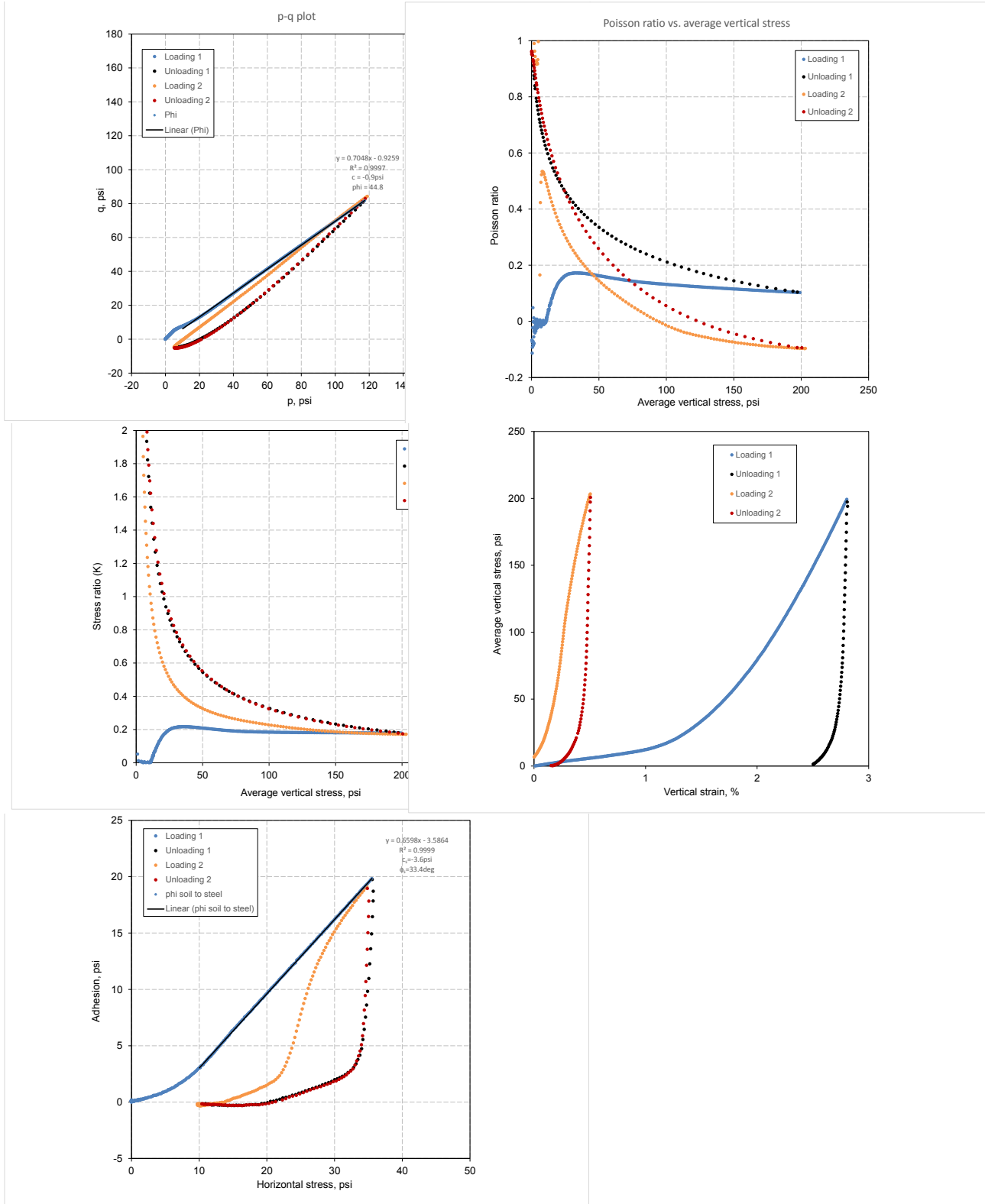


Figure 202. Iowa K test results for WCF gypsum ($w\% = 11.6\%$ and $\gamma_d = 103.5 \text{ pcf}$)

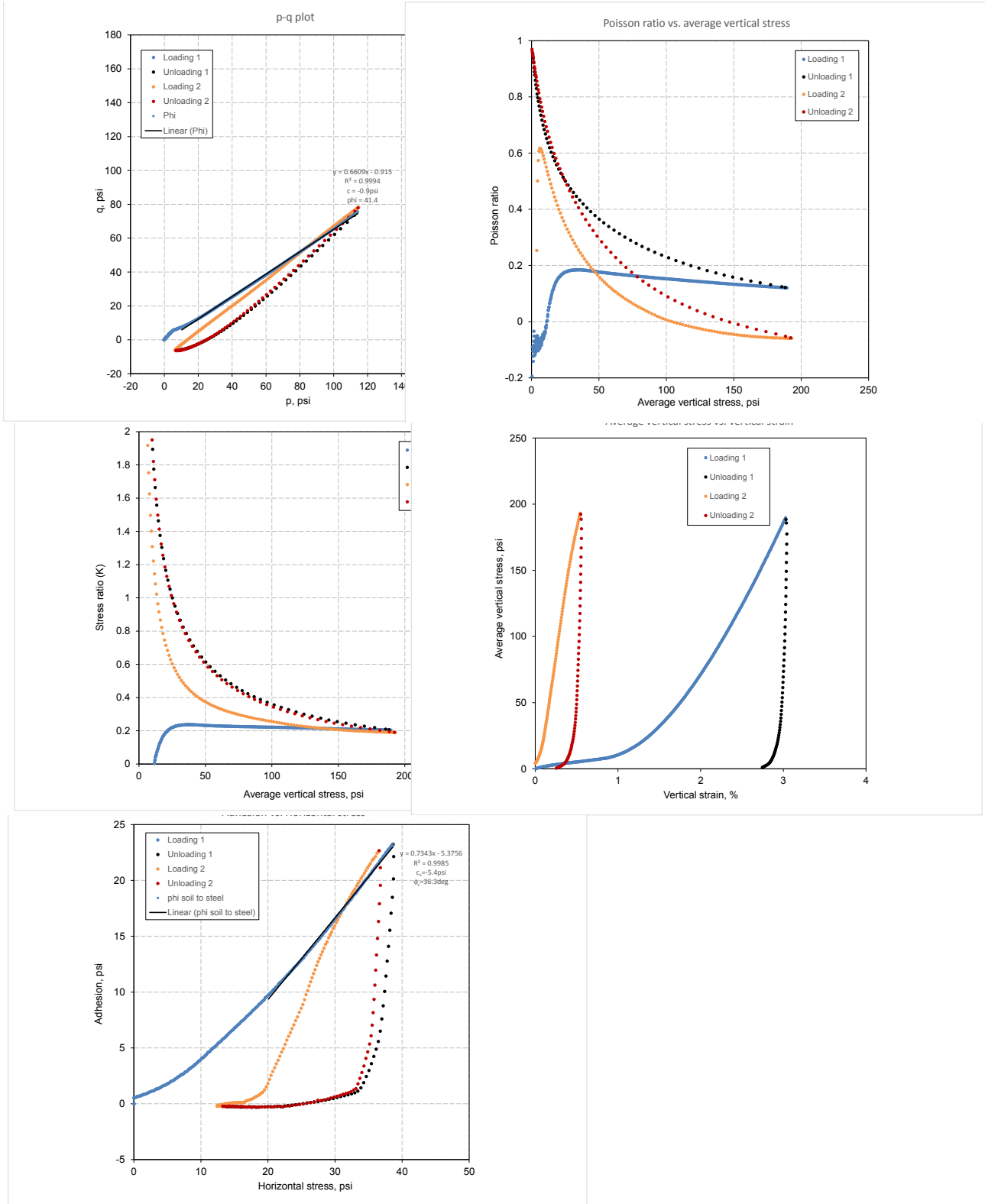


Figure 203. Iowa K test results for WCF gypsum ($w\% = 15.5\%$ and $\gamma_d = 100.4 \text{ pcf}$)

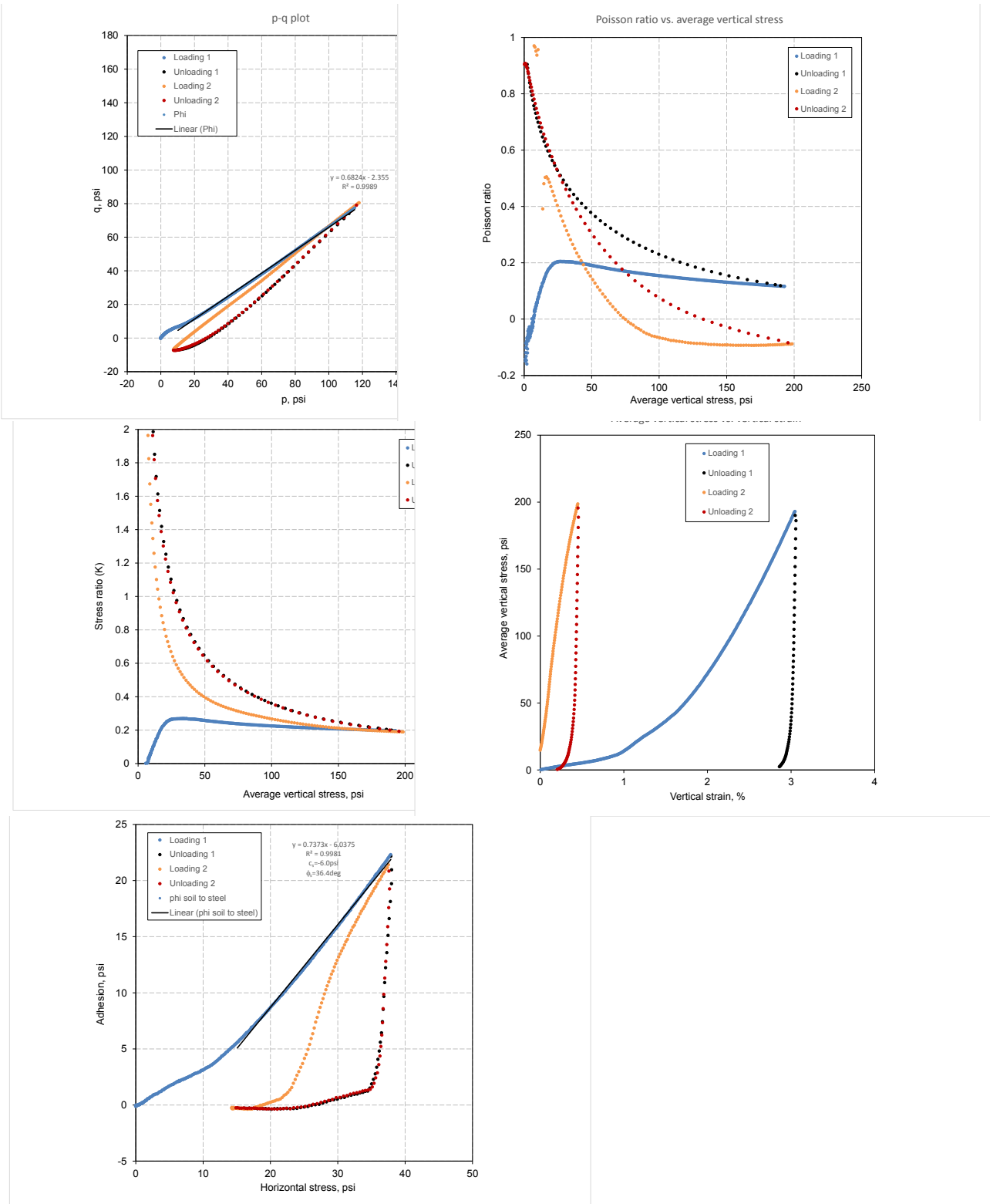


Figure 204. Iowa K test results for WCF gypsum (w% = 15.4% and $\gamma_d = 100.5$ pcf)

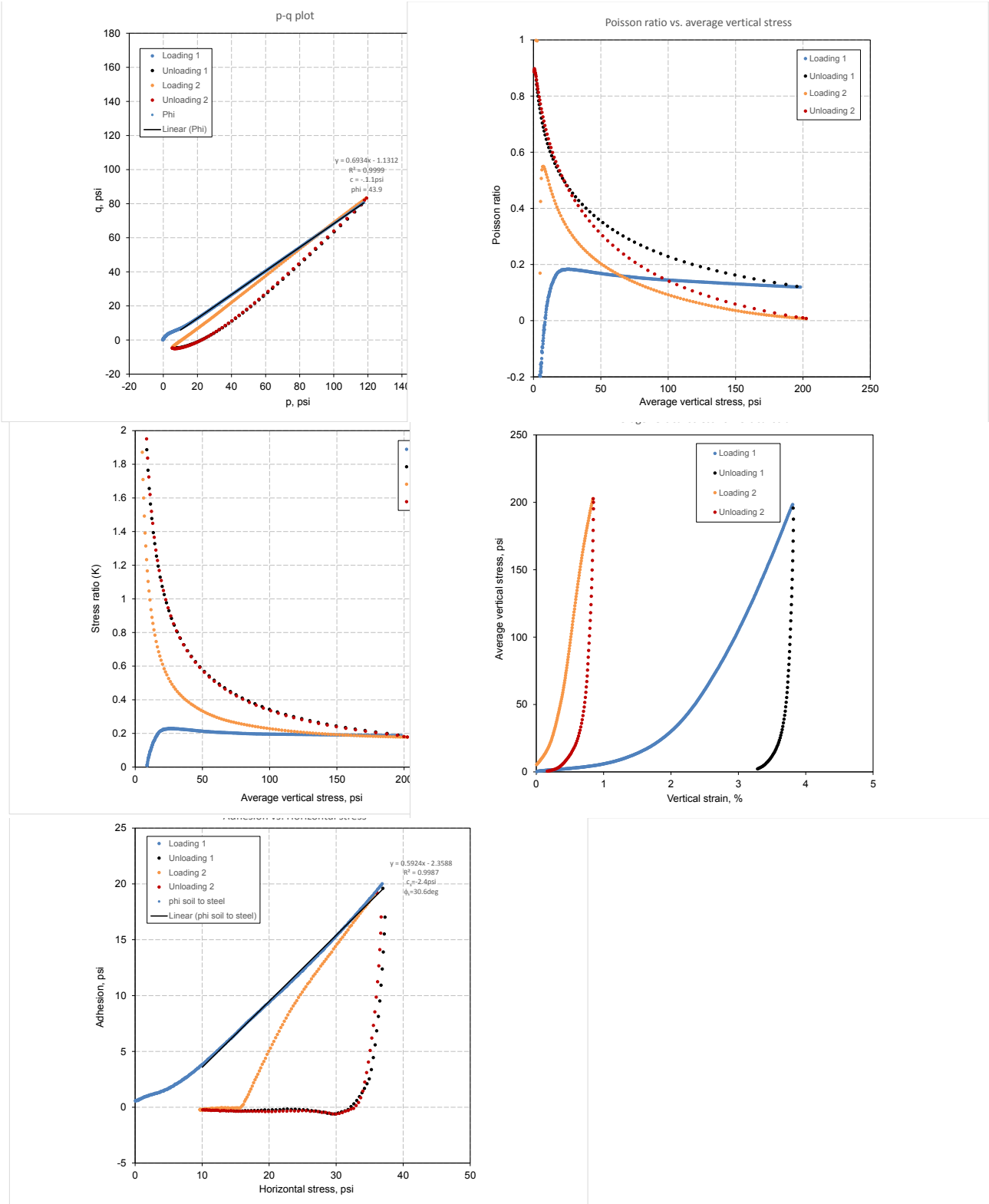


Figure 205. Iowa K test results for WCF gypsum ($w\% = 17.8\%$ and $\gamma_d = 101.9\text{pcf}$)

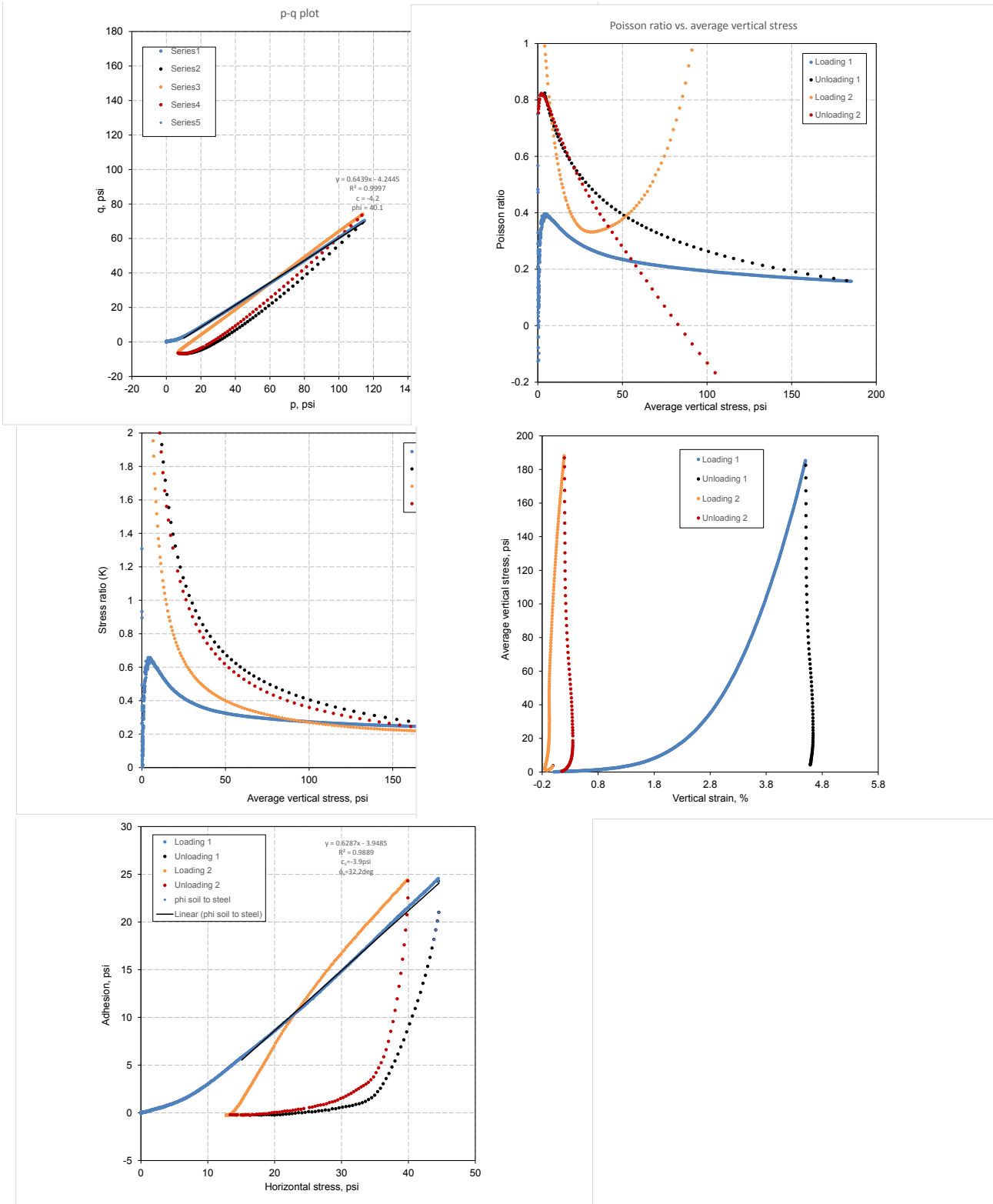


Figure 206. Iowa K test results for WCF gypsum (w% = 17.9% and $\gamma_d = 101.0$ pcf)

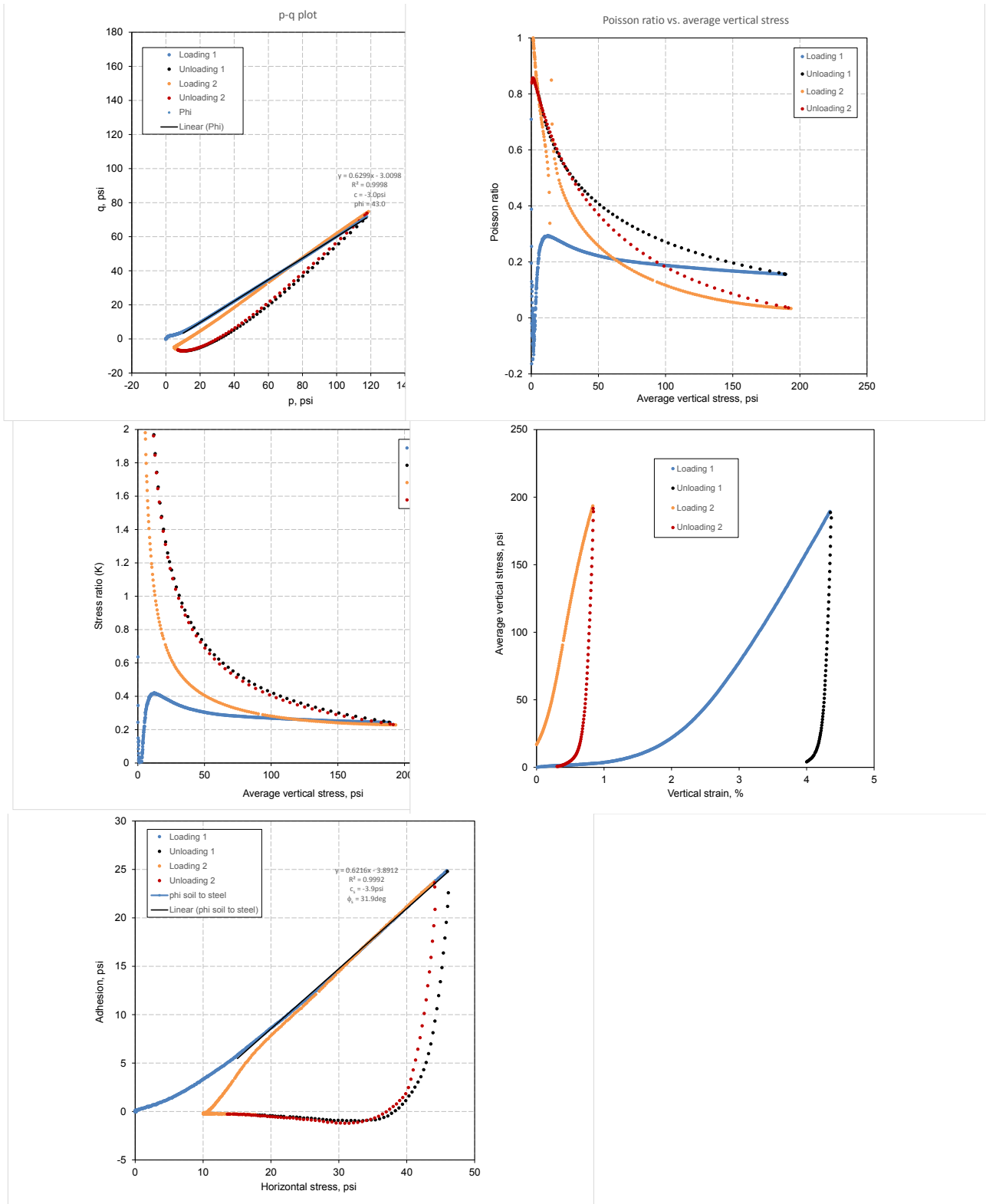


Figure 207. Iowa K test results for WCF gypsum ($w\% = 18.0\%$ and $\gamma_d = 100.5 \text{ pcf}$)

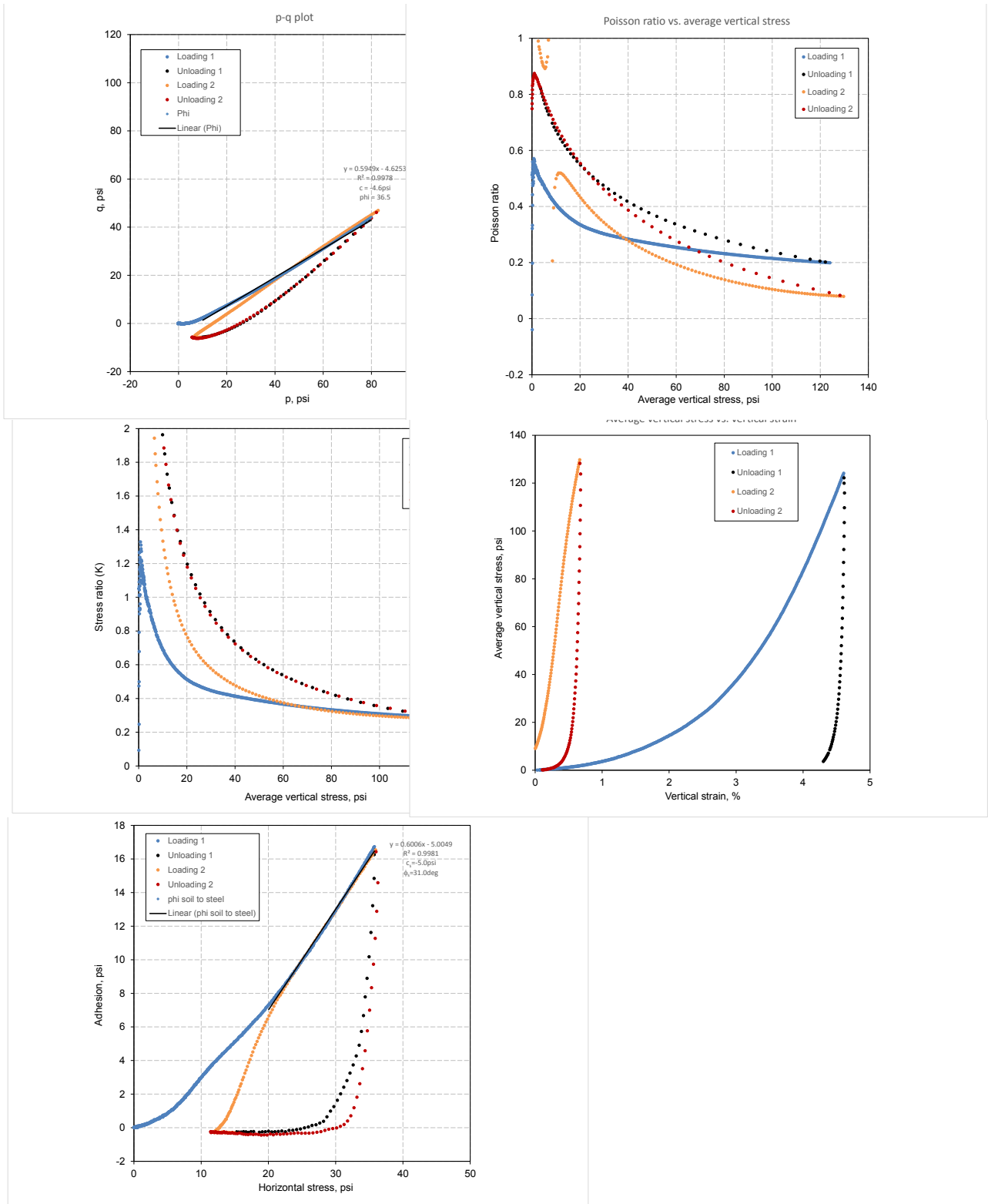


Figure 208. Iowa K test results for WCF gypsum ($w\% = 17.1\%$ and $\gamma_d = 100.0\text{pcf}$)

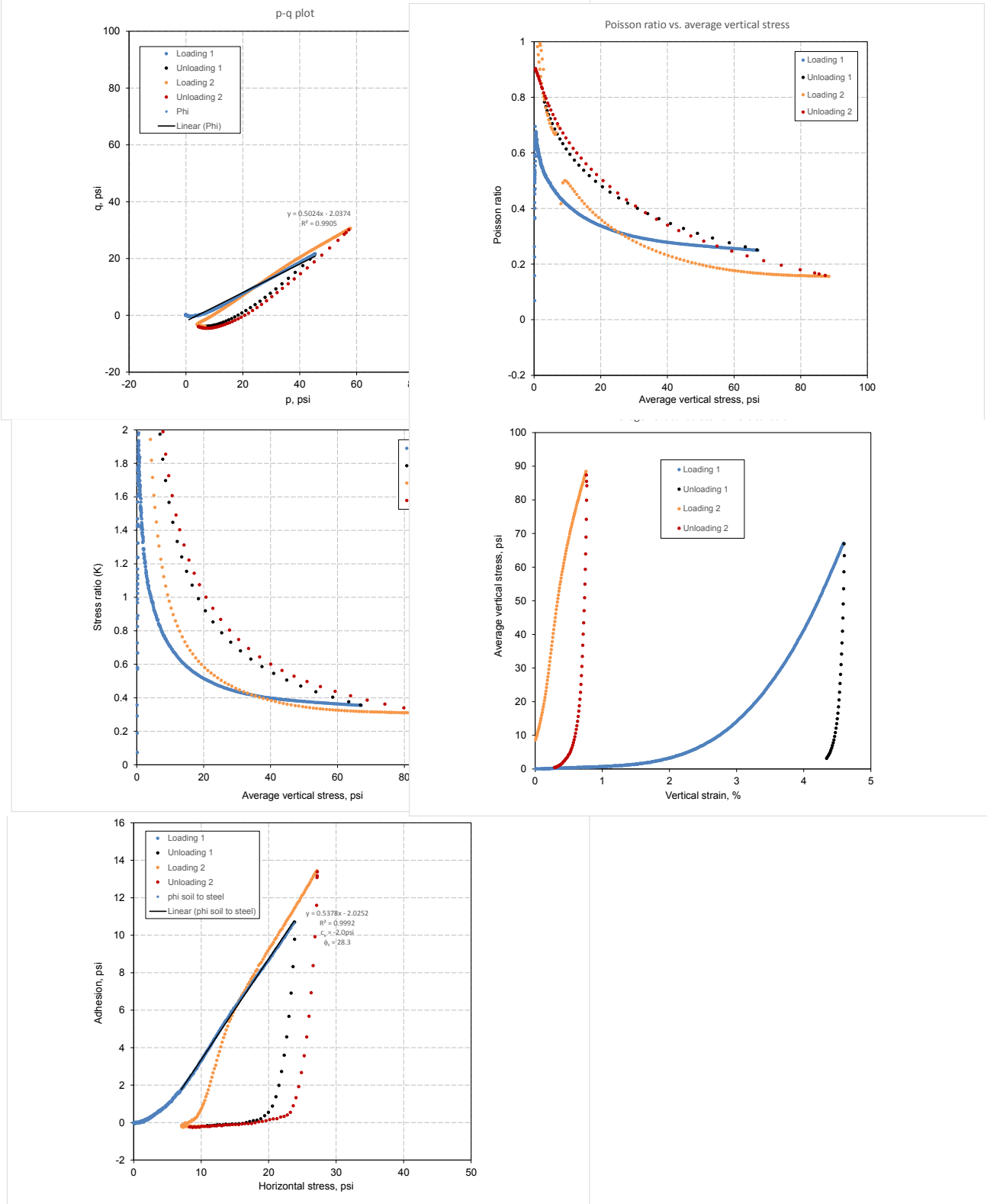


Figure 209. Iowa K test results for WCF gypsum (w% = 20.8% and $\gamma_d = 95.9$ pcf)

Ottawa sand (ASTM 20-30)

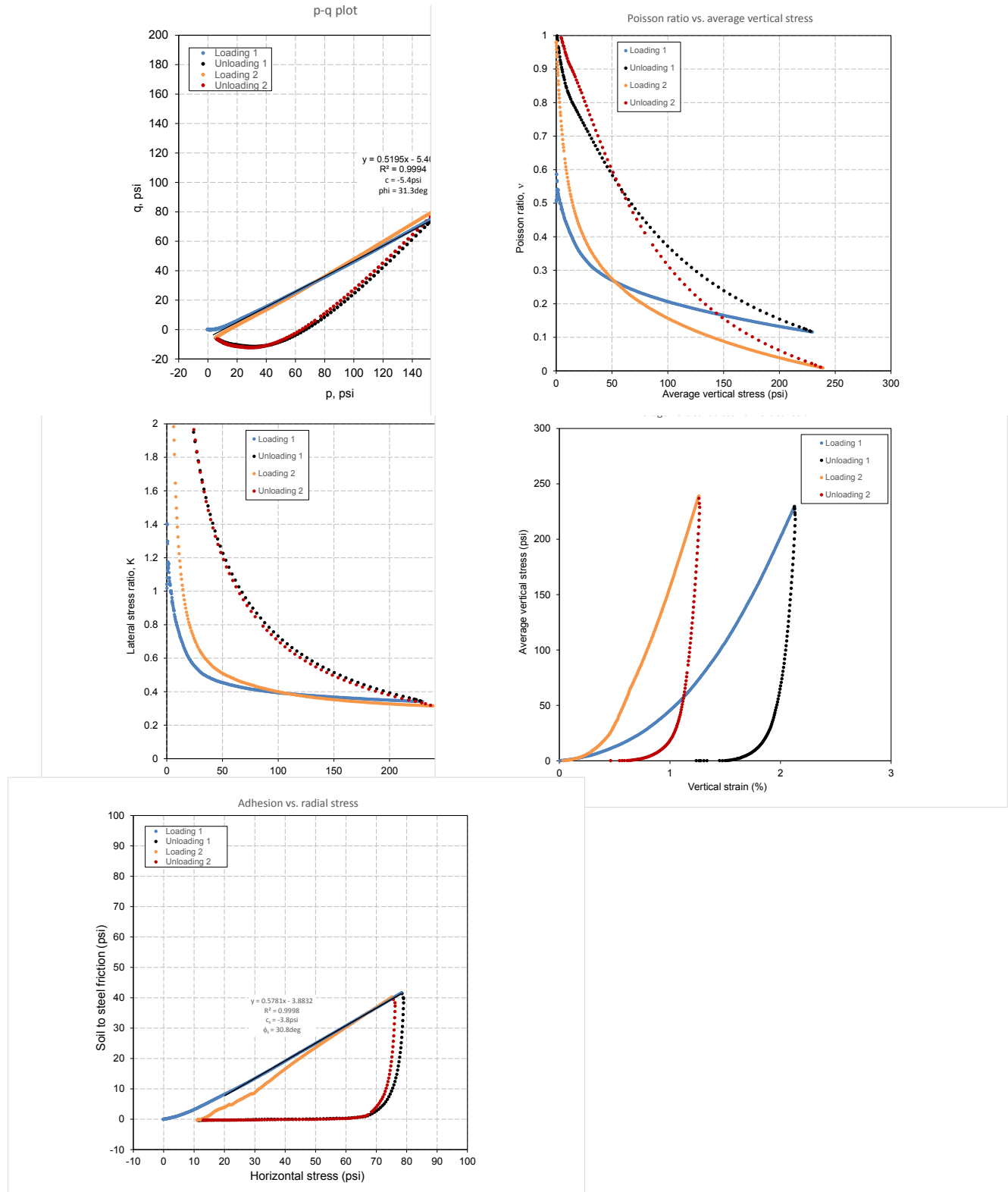


Figure 210. Iowa K test results for Ottawa sand ($\gamma_d = 97.6 \text{ pcf}$ and $e_0 = 0.69$)

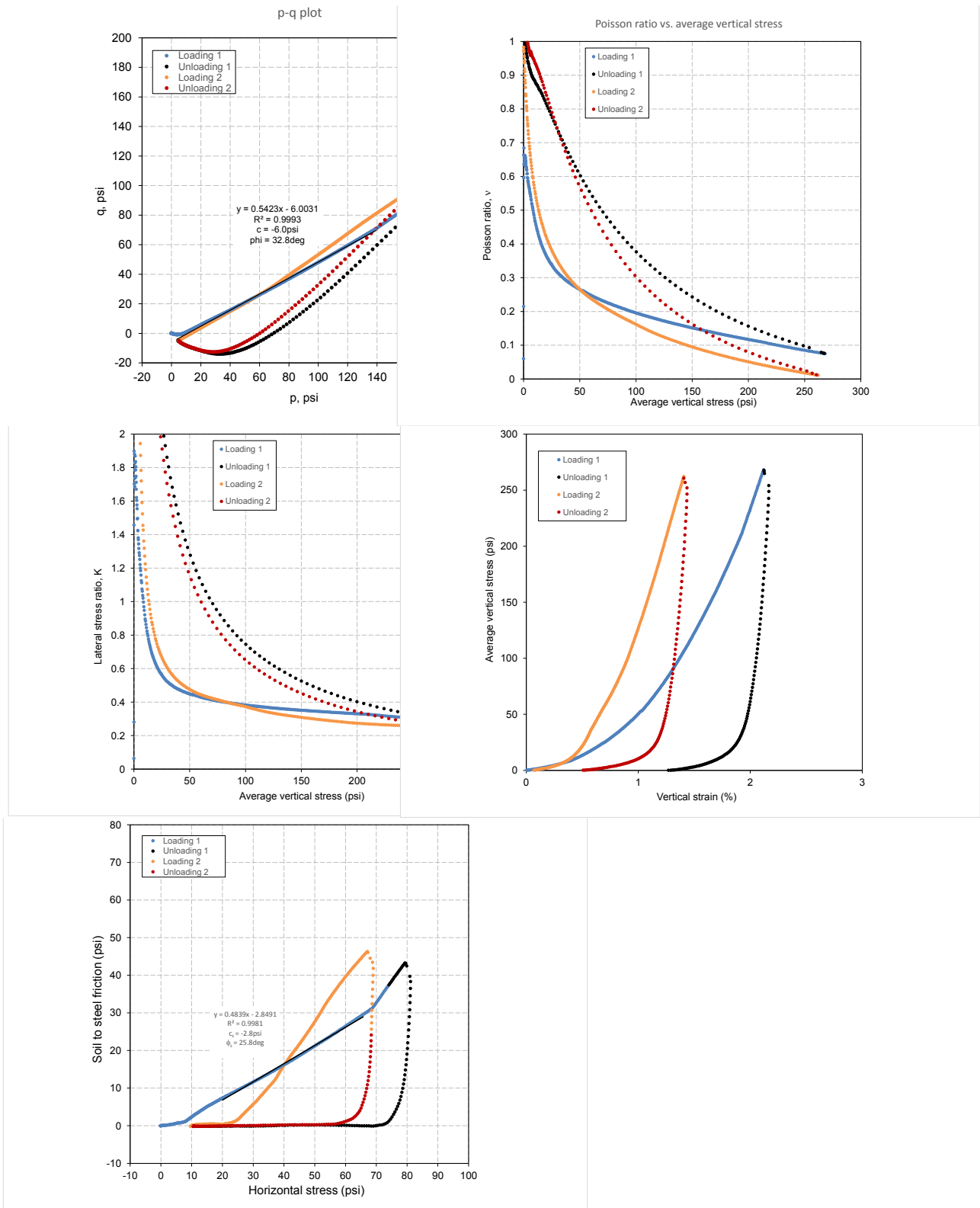


Figure 211. Iowa K test results for Ottawa sand ($\gamma_d = 101.8\text{pcf}$ and $e_0 = 0.62$)

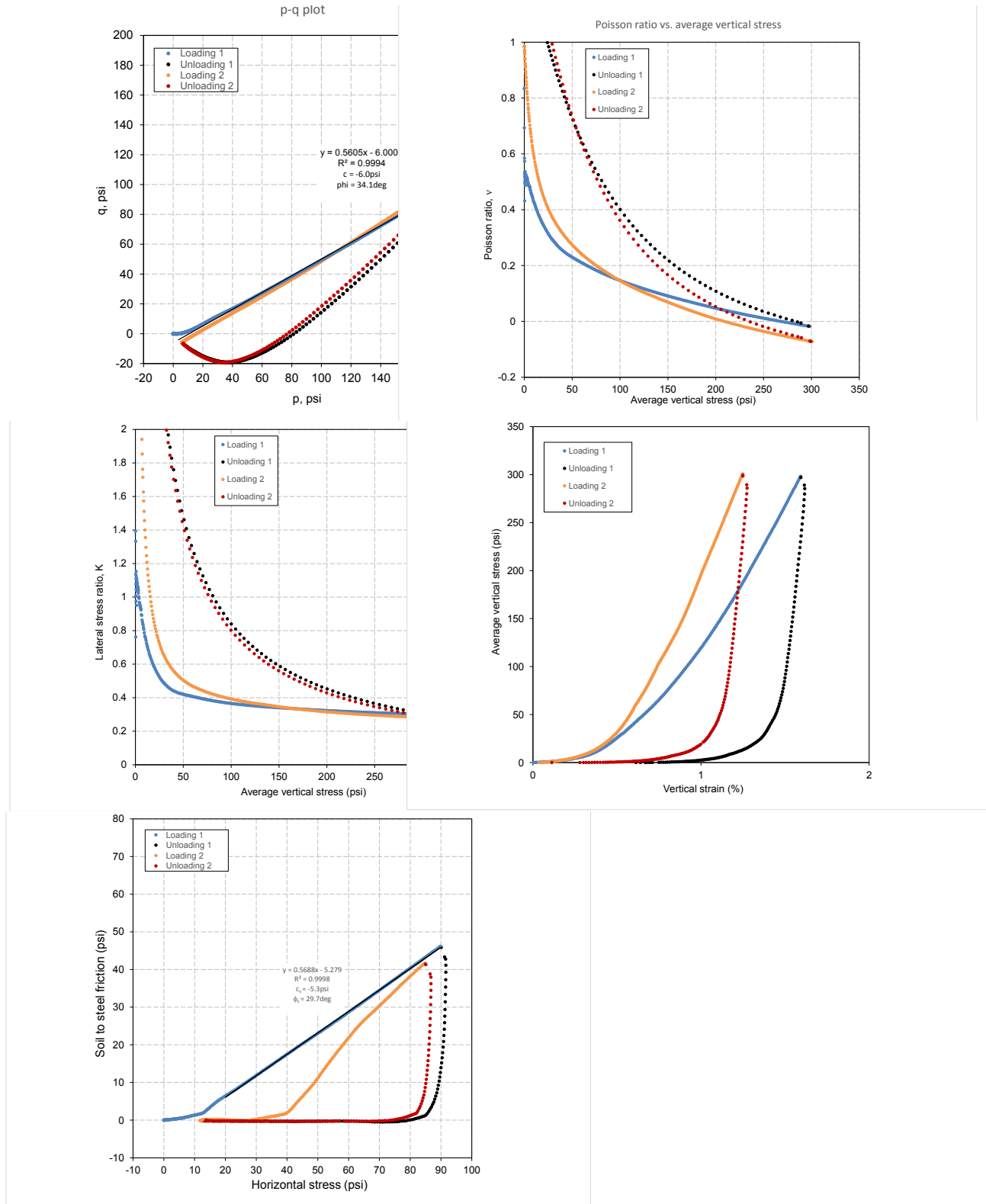


Figure 212. Iowa K test results for Ottawa sand ($\gamma_d = 105.9\text{pcf}$ and $e_0 = 0.56$)

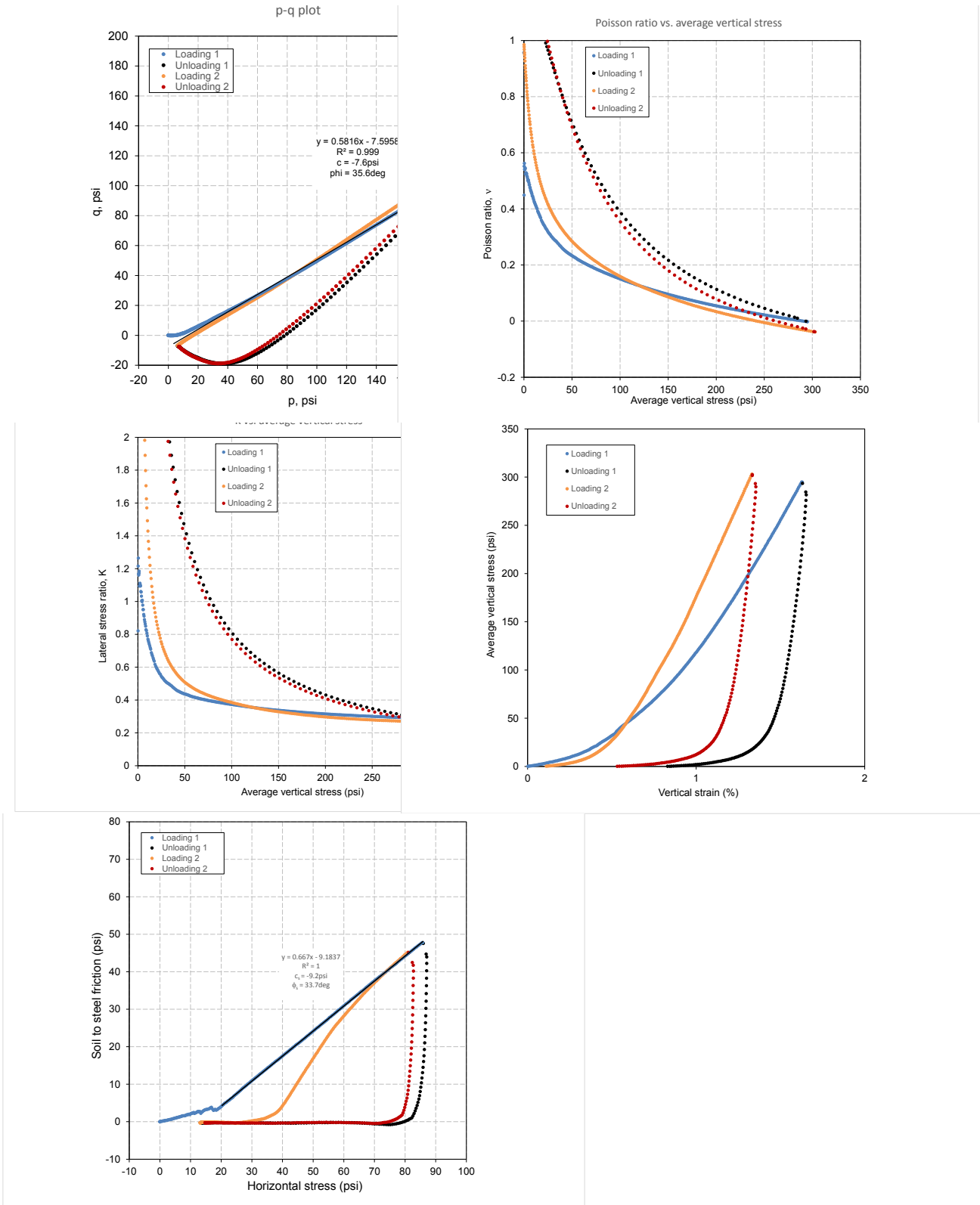


Figure 213. Iowa K test results for Ottawa sand ($\gamma_d = 107.7 \text{ pcf}$ and $e_0 = 0.54$)

APPENDIX D. DIRECT SHEAR TEST RESULTS OF THE FIVE COMPACTED GEOMATERIALS

Western Iowa loess (CFED 1634)

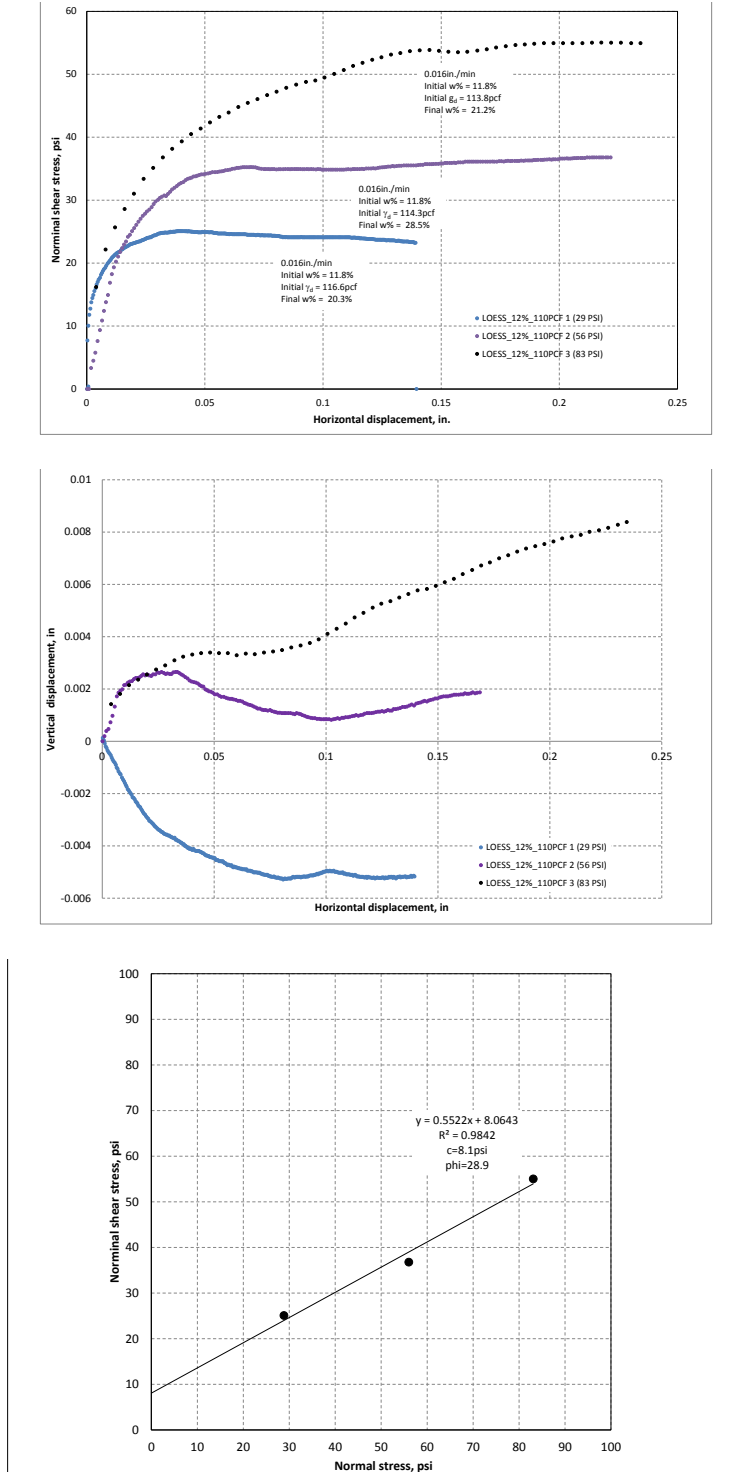


Figure 214. Direct shear test results of western Iowa loess ($w\% = 11.8\%$ and $\gamma_d = 114.9\text{pcf}$)

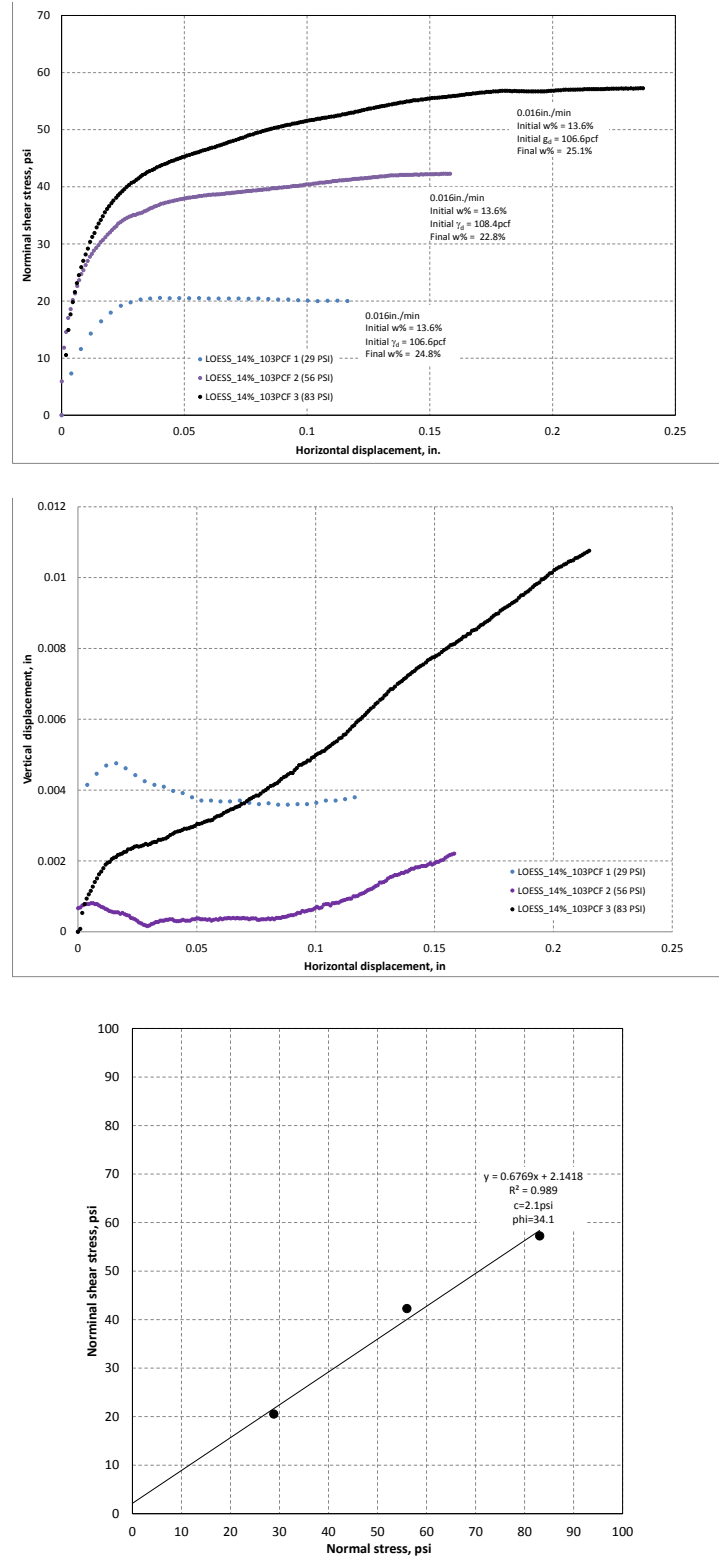


Figure 215. Direct shear test results of western Iowa loess (w% = 13.6% and $\gamma_d = 107.2$ pcf)

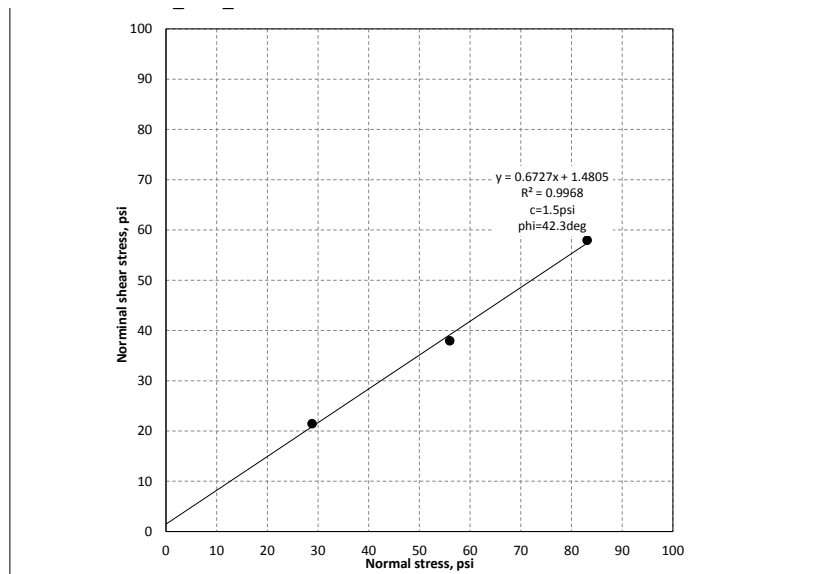
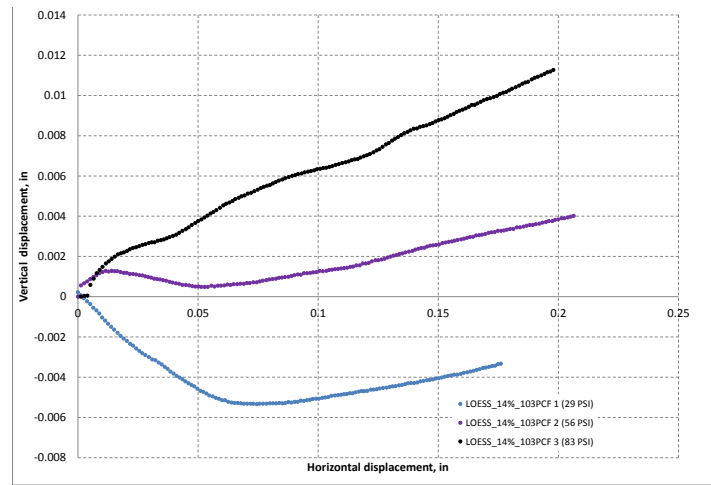
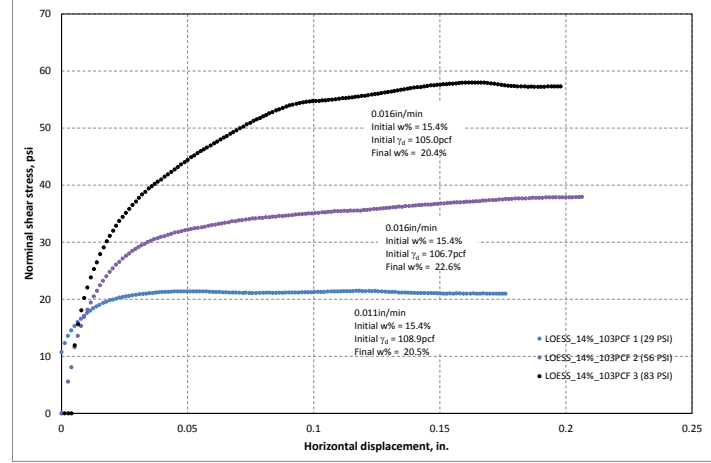


Figure 216. Direct shear test results of western Iowa loess (w% = 15.4% and $\gamma_d = 106.9$ pcf)

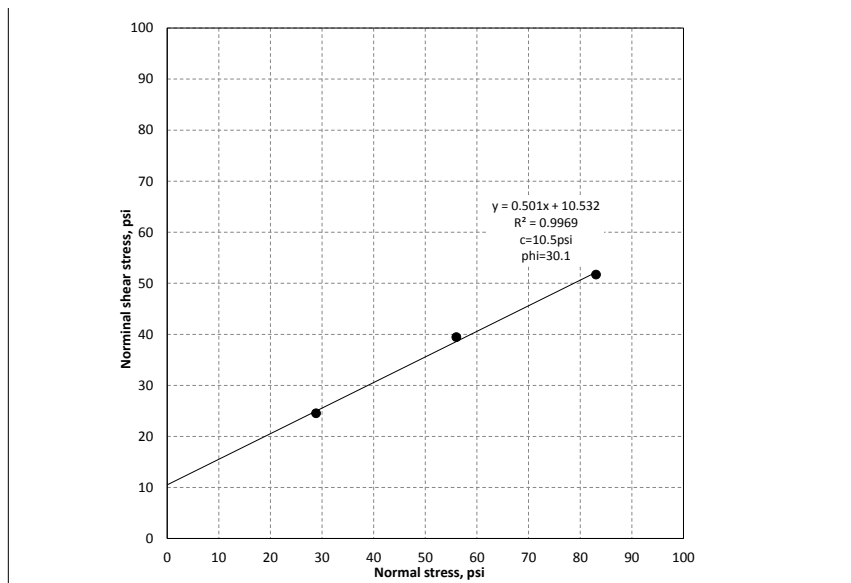
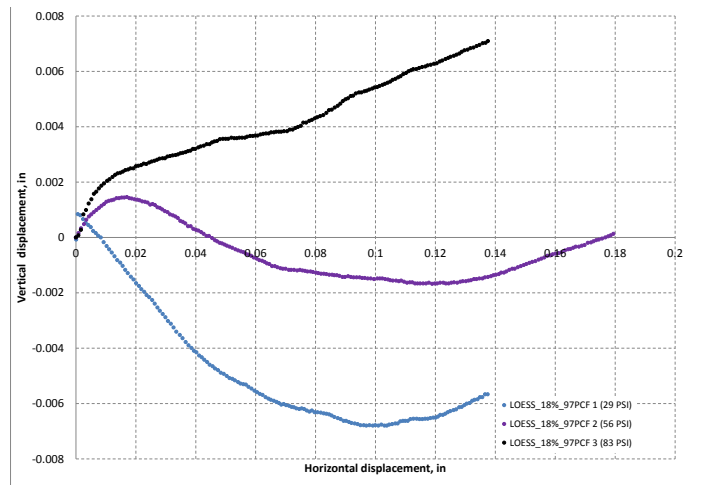
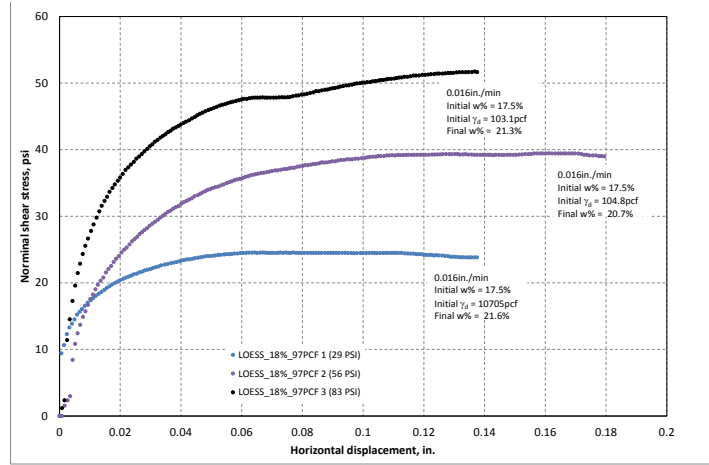


Figure 217. Direct shear test results of western Iowa loess (w% = 17.5% and $\gamma_d = 105.0\text{pcf}$)

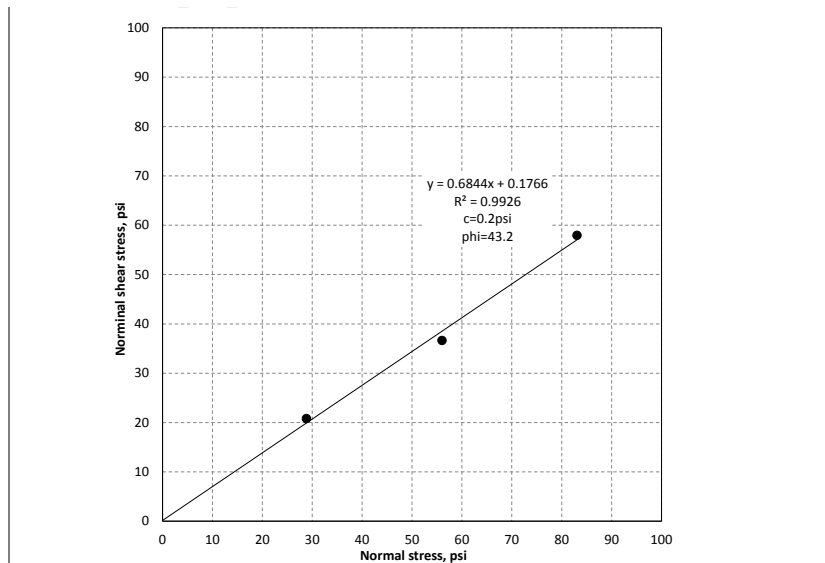
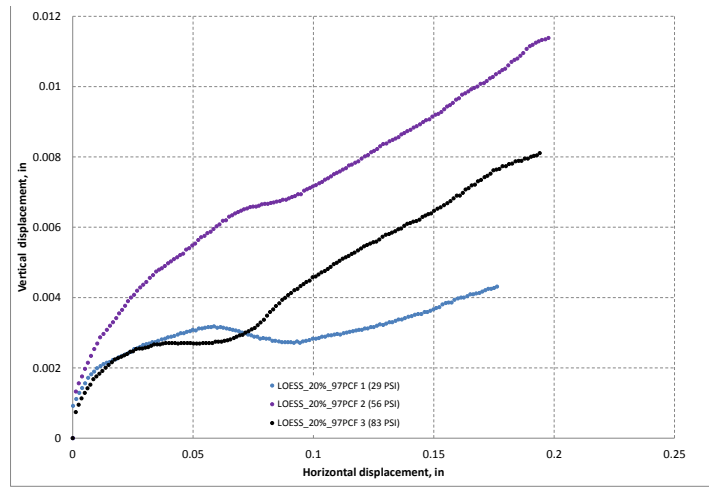
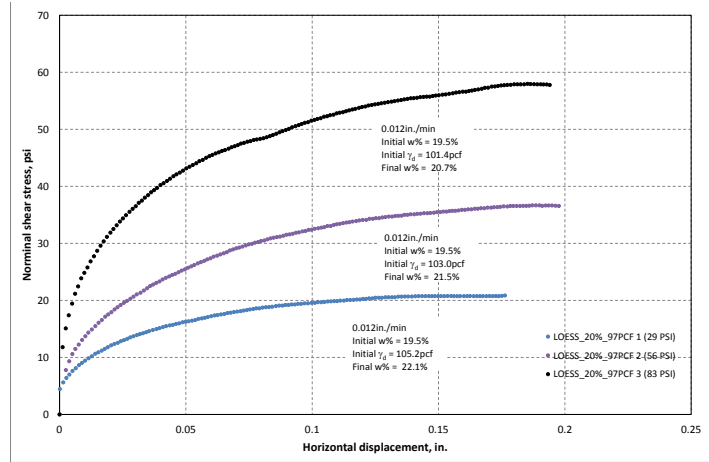


Figure 218. Direct shear test results of western Iowa loess (w% = 19.5% and $\gamma_d = 103.2\text{pcf}$)

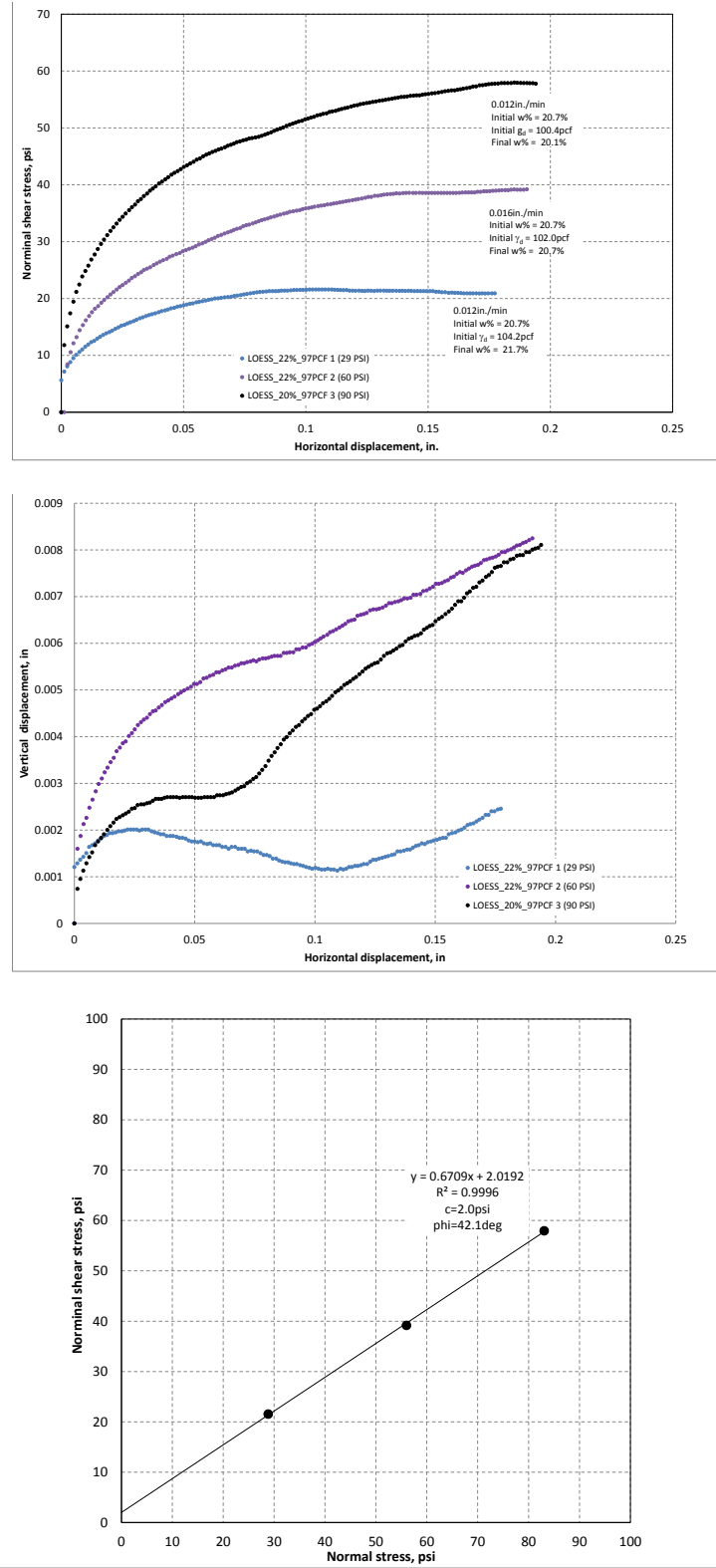


Figure 219. Direct shear test results of western Iowa loess (w% = 20.7% and $\gamma_d = 102.2$ pcf)

Texas fat clay (CFED 2043)

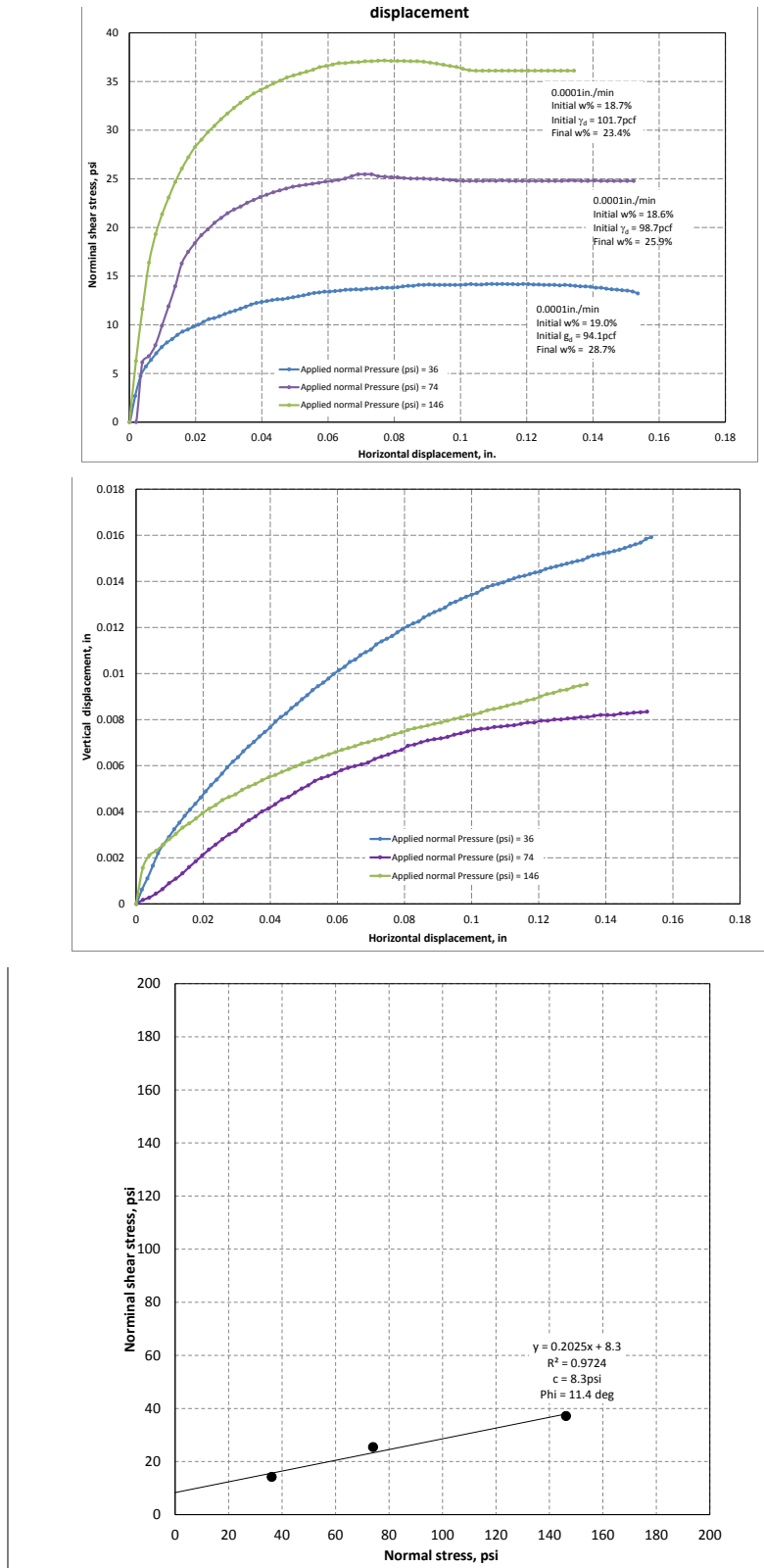


Figure 220. Direct shear test results of Texas fat clay ($w\% = 18.6\%$ and $\gamma_d = 98.2$ pcf)

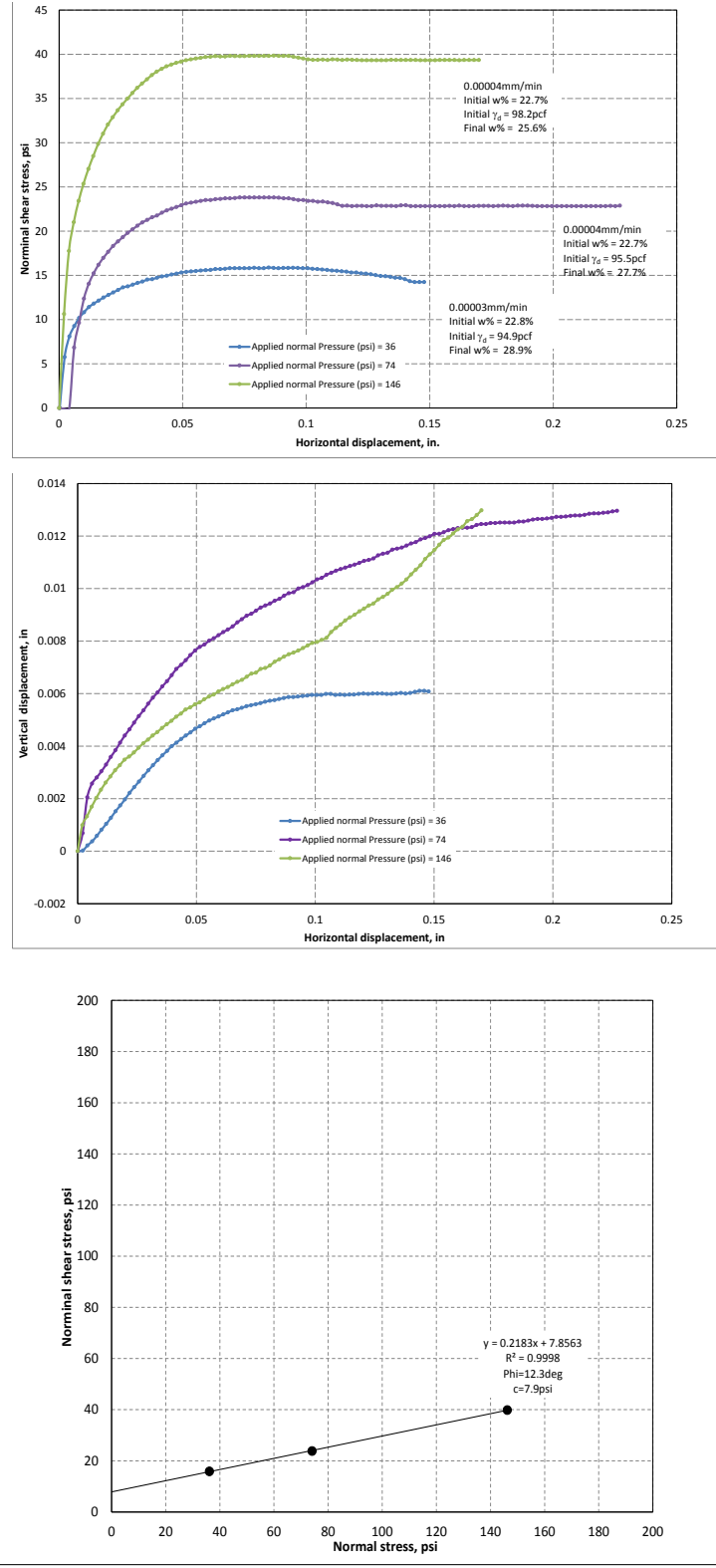


Figure 221. Direct shear test results of Texas fat clay ($w\% = 22.8\%$ and $\gamma_d = 96.2 \text{pcf}$)

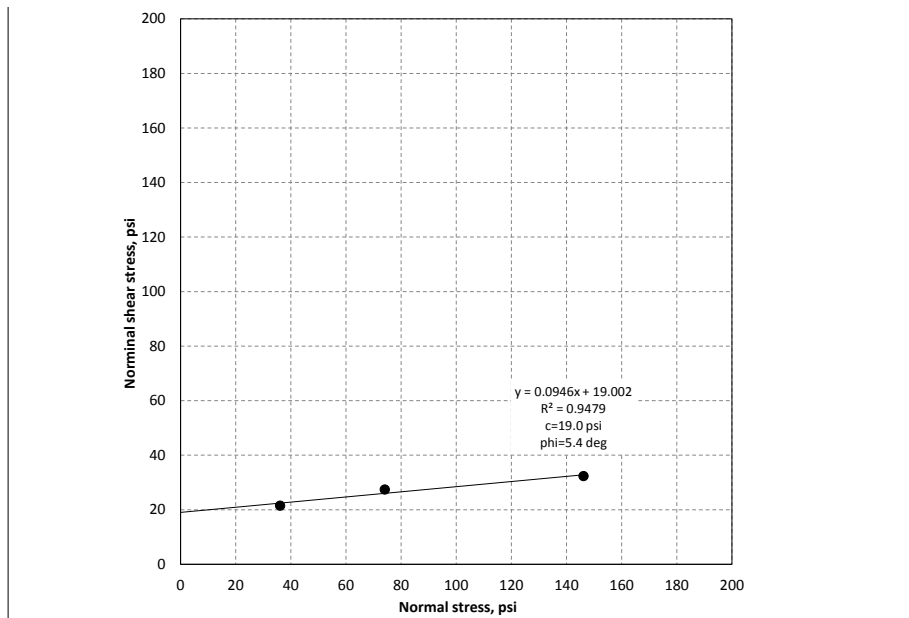
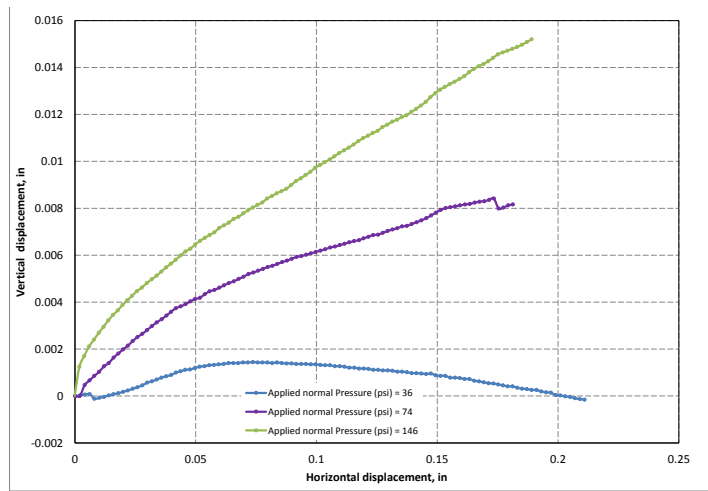
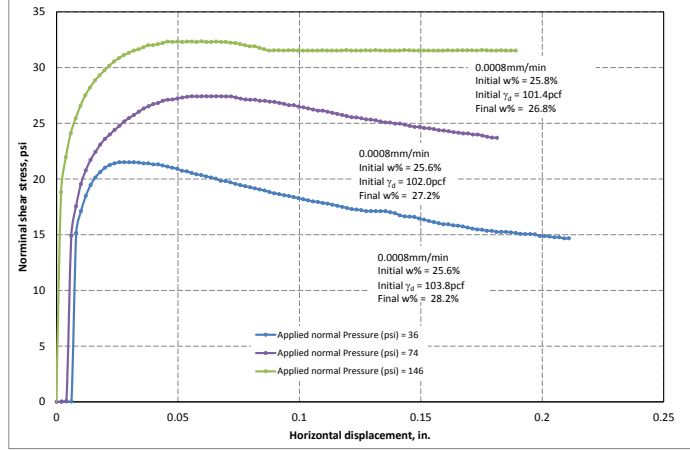


Figure 222. Direct shear test results of Texas fat clay (w% = 25.7% and $\gamma_d = 102.4\text{pcf}$)

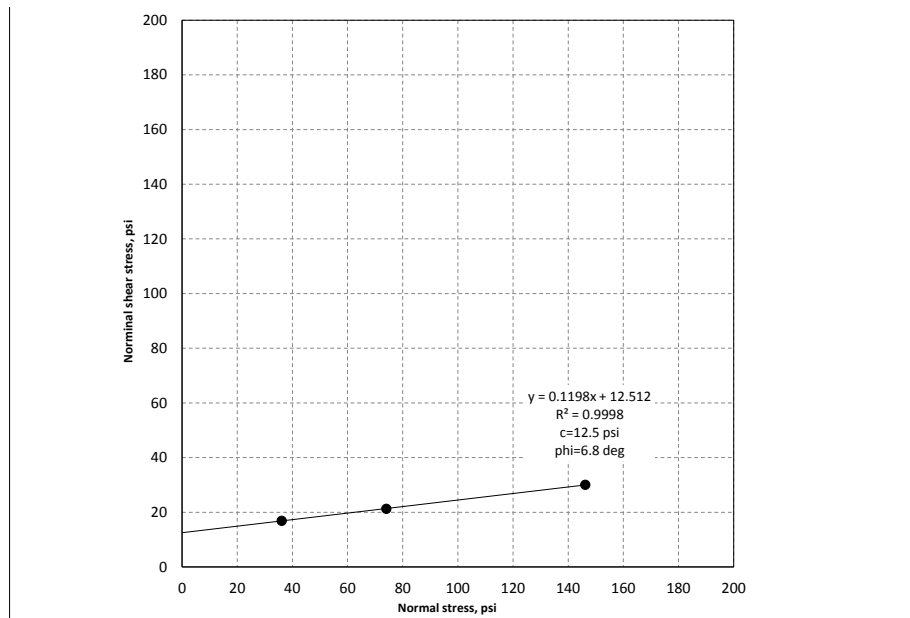
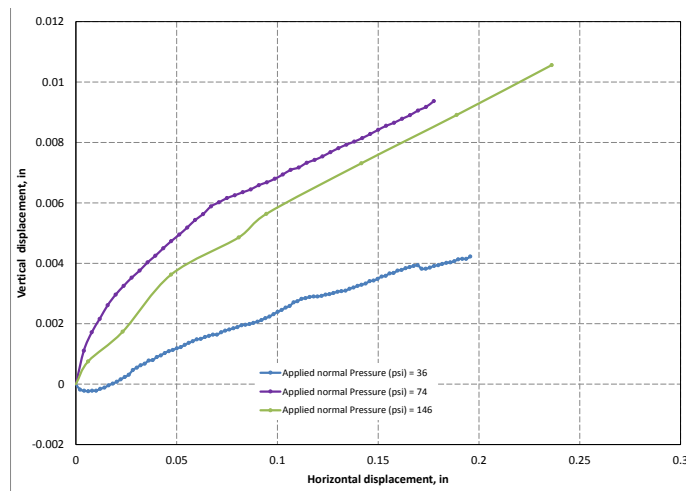
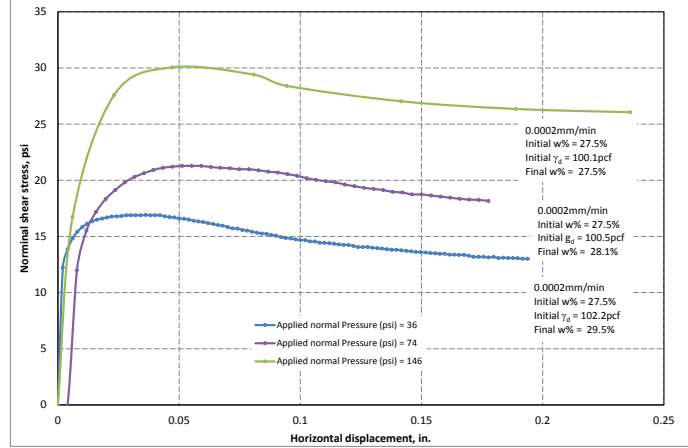


Figure 223. Direct shear test results of Texas fat clay (w% = 27.5% and $\gamma_d = 100.9pcf$)

WCF fly ash (CFED 2053)

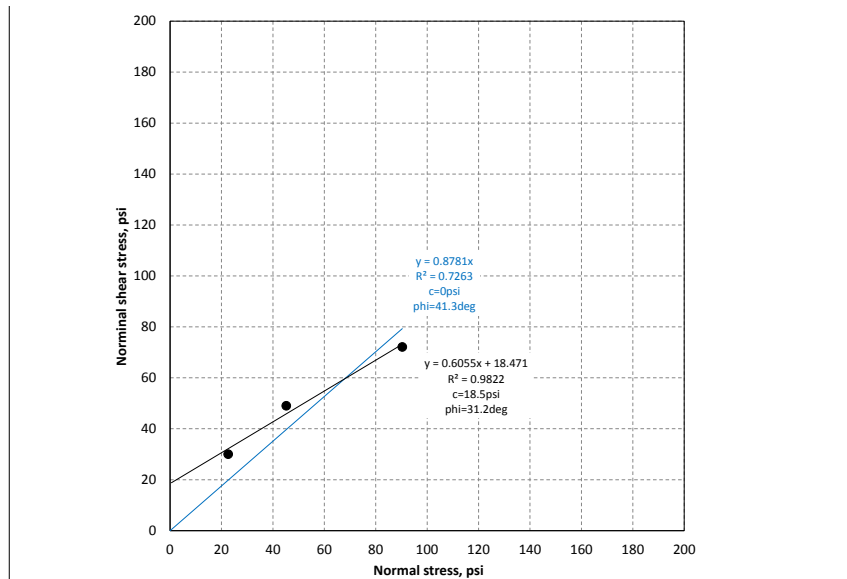
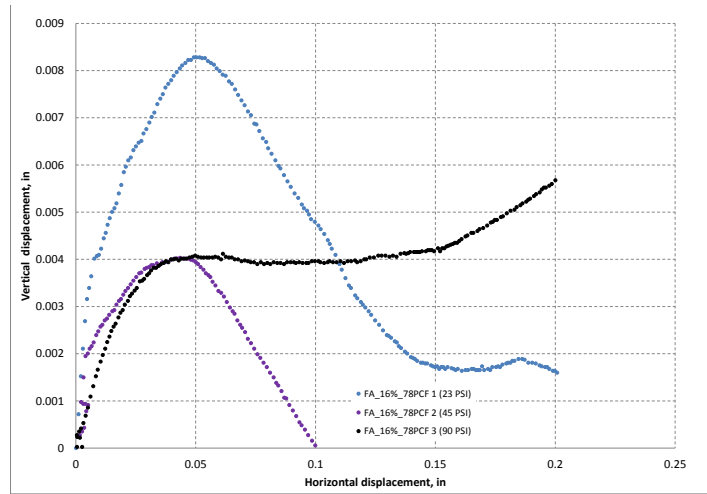
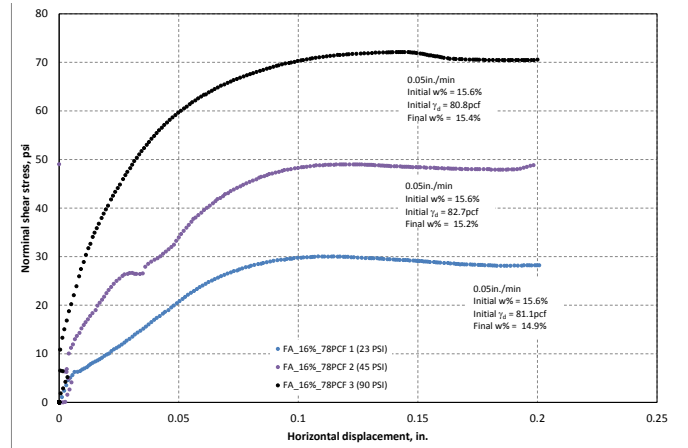


Figure 224. Direct shear test results of WCF fly ash ($w\% = 15.6\%$ and $\gamma_d = 81.5\text{pcf}$)

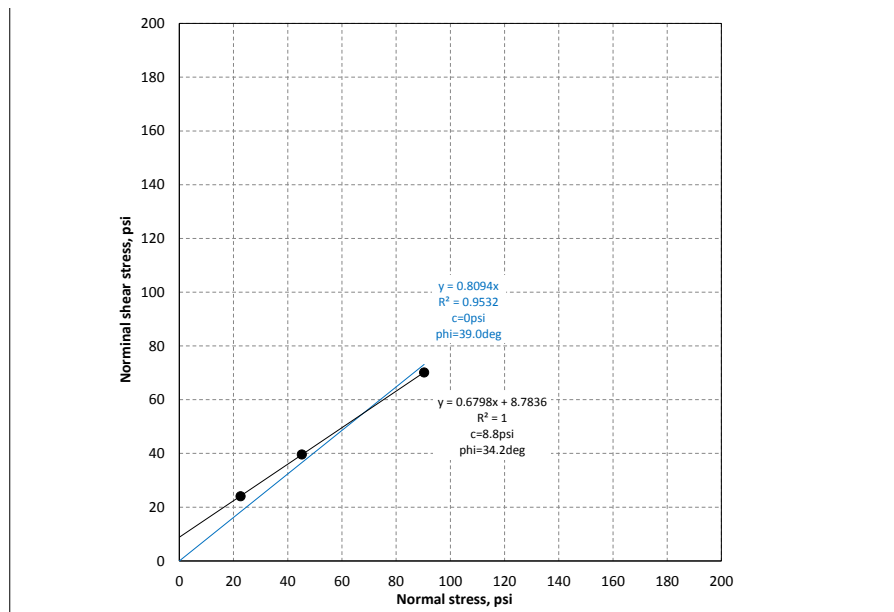
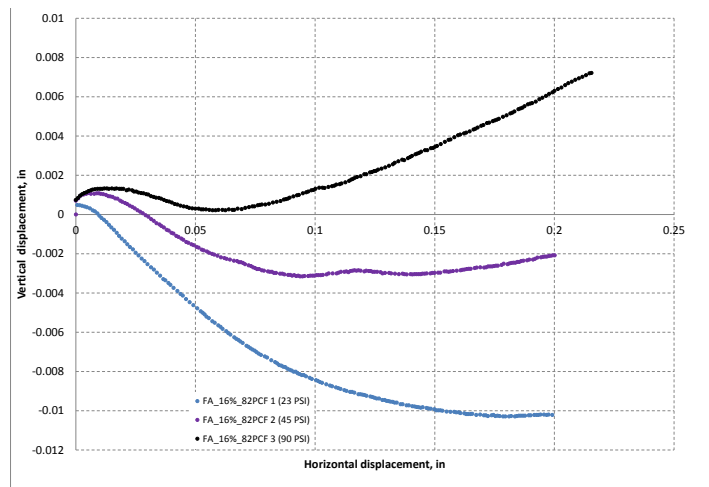
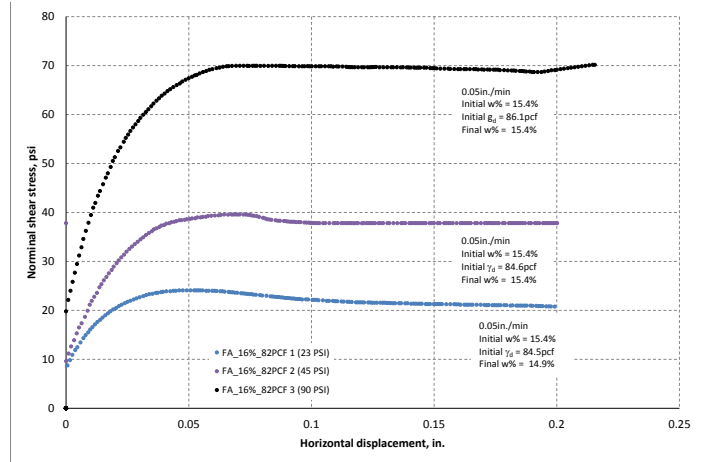


Figure 225. Direct shear test results of WCF fly ash (w% = 15.4% and $\gamma_d = 85.1pcf$)

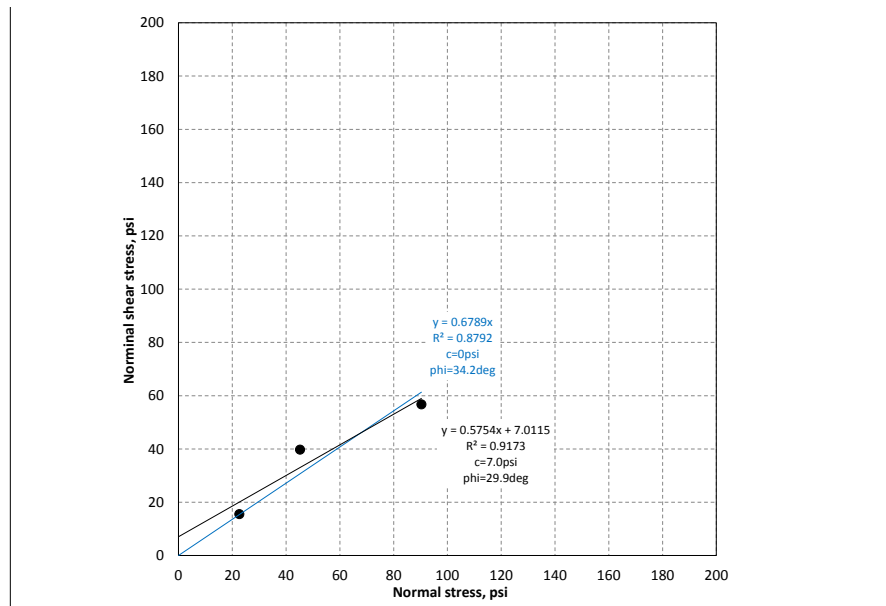
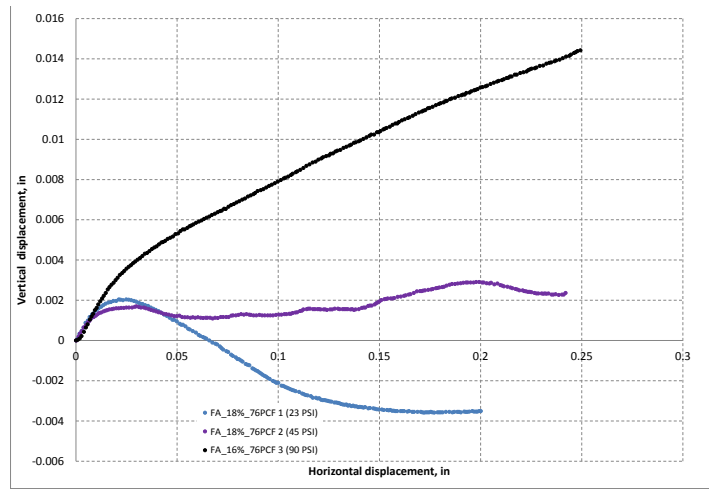
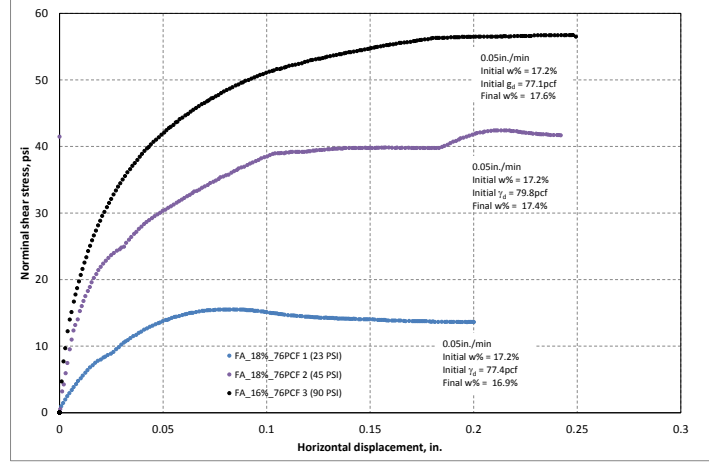


Figure 226. Direct shear test results of WCF fly ash ($w\% = 17.2\%$ and $\gamma_d = 78.1pcf$)

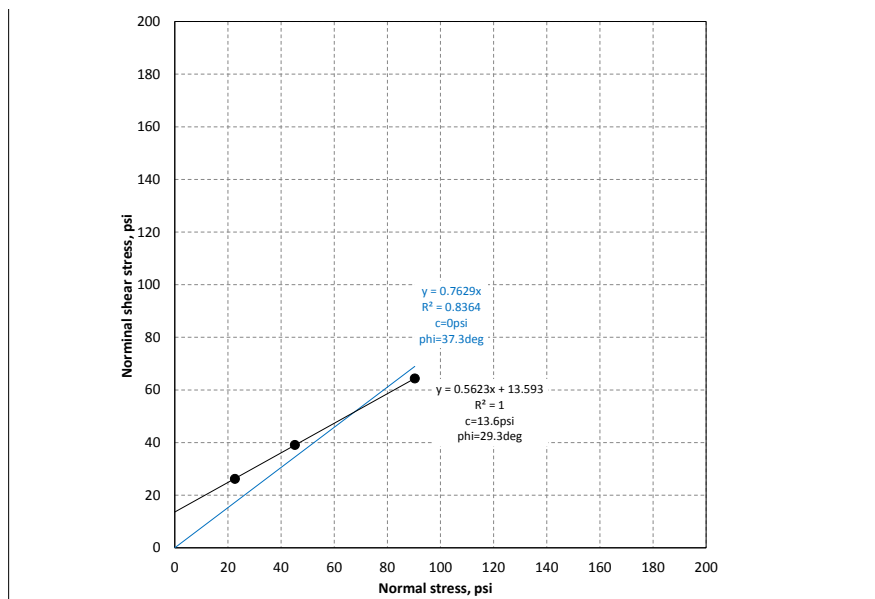
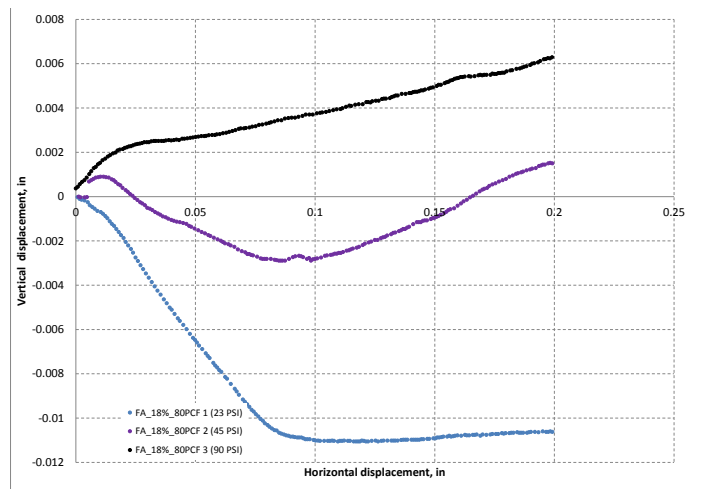
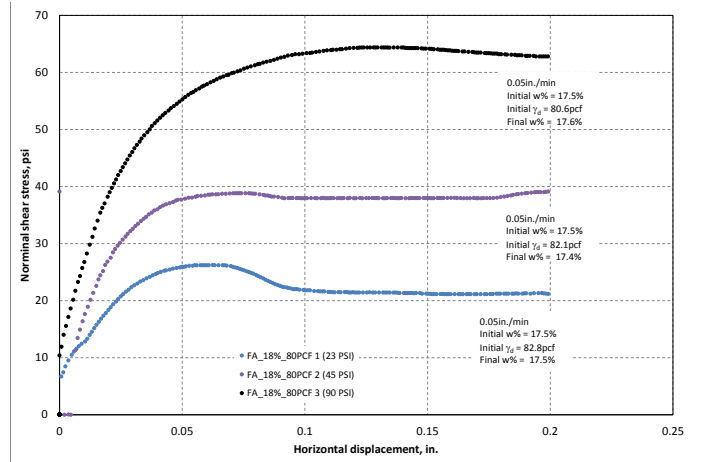


Figure 227. Direct shear test results of WCF fly ash (w% = 17.5% and $\gamma_d = 81.8\text{pcf}$)

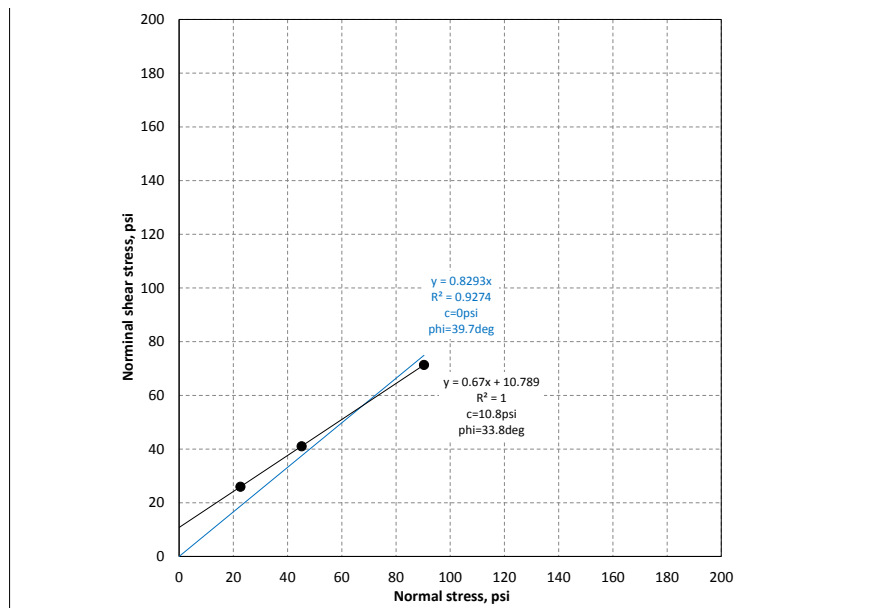
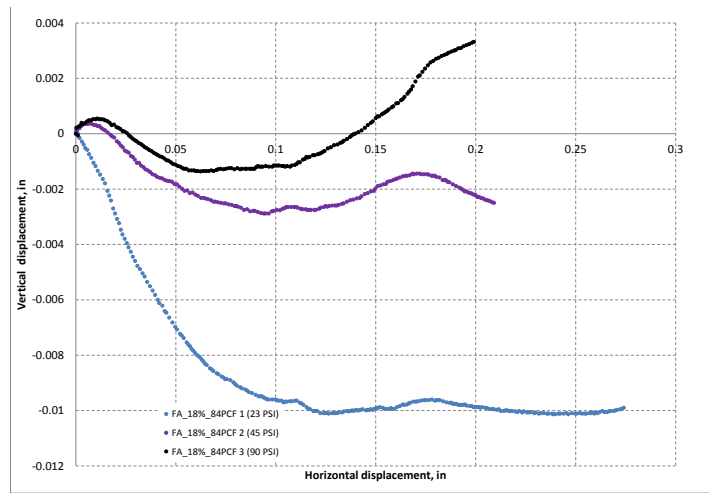
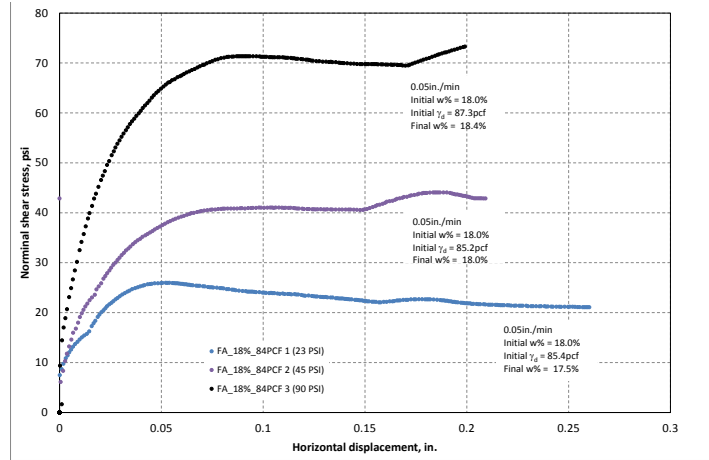


Figure 228. Direct shear test results of WCF fly ash (w% = 18.0% and $\gamma_d = 86.0\text{pcf}$)

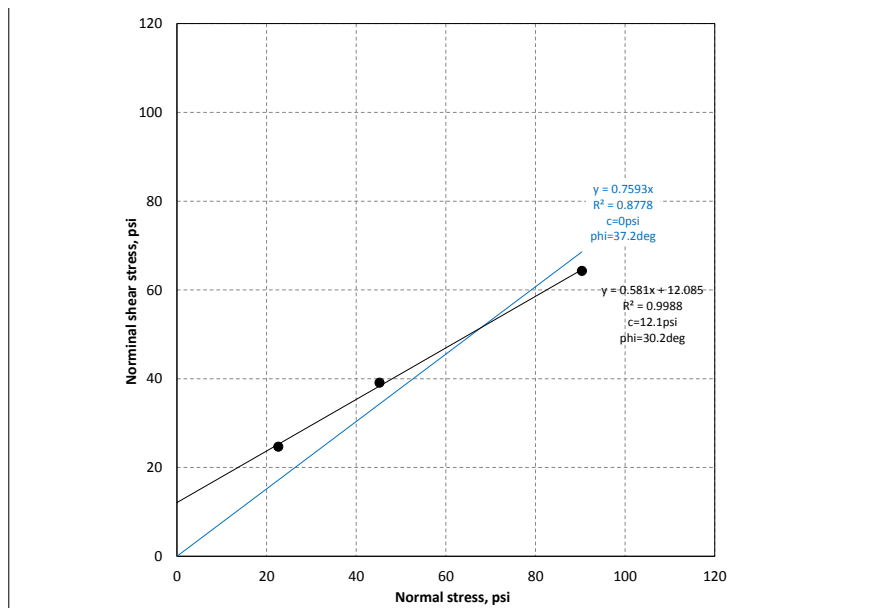
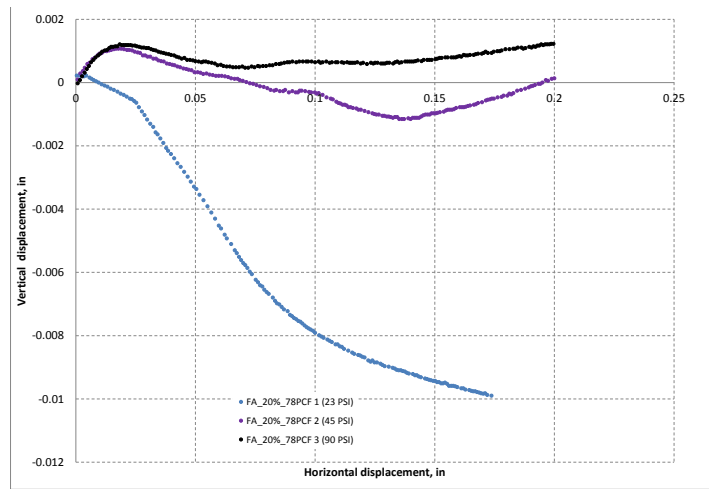
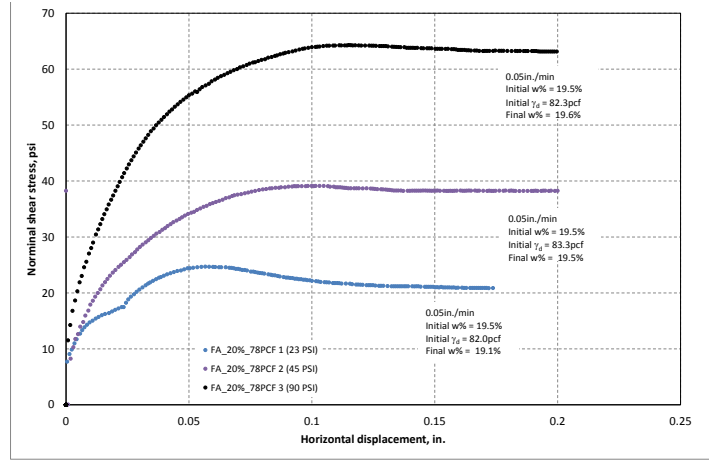


Figure 229. Direct shear test results of WCF fly ash (w% = 19.5% and $\gamma_d = 82.6pcf$)

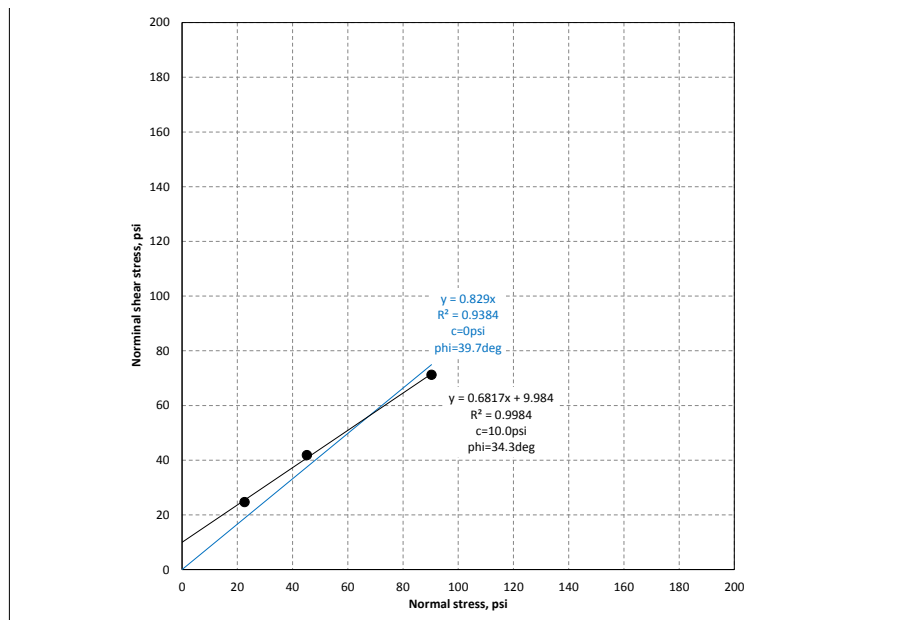
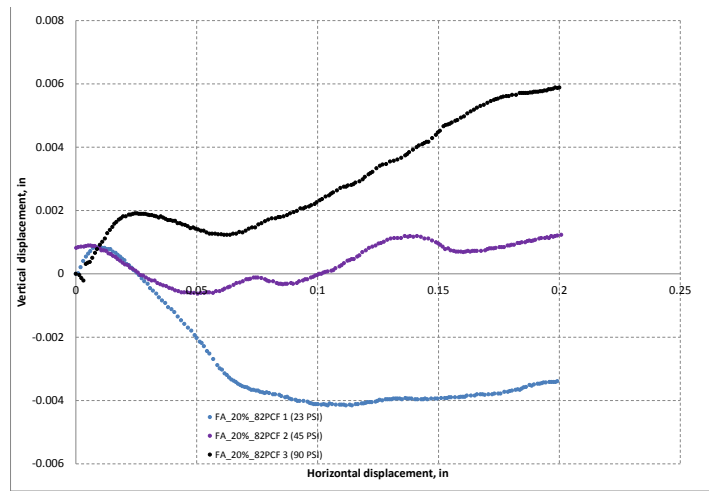
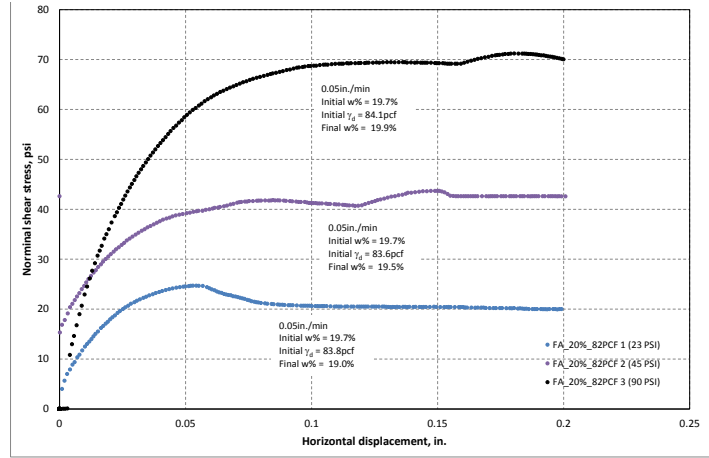


Figure 230. Direct shear test results of WCF fly ash (w% = 19.7% and $\gamma_d = 83.8$ pcf)

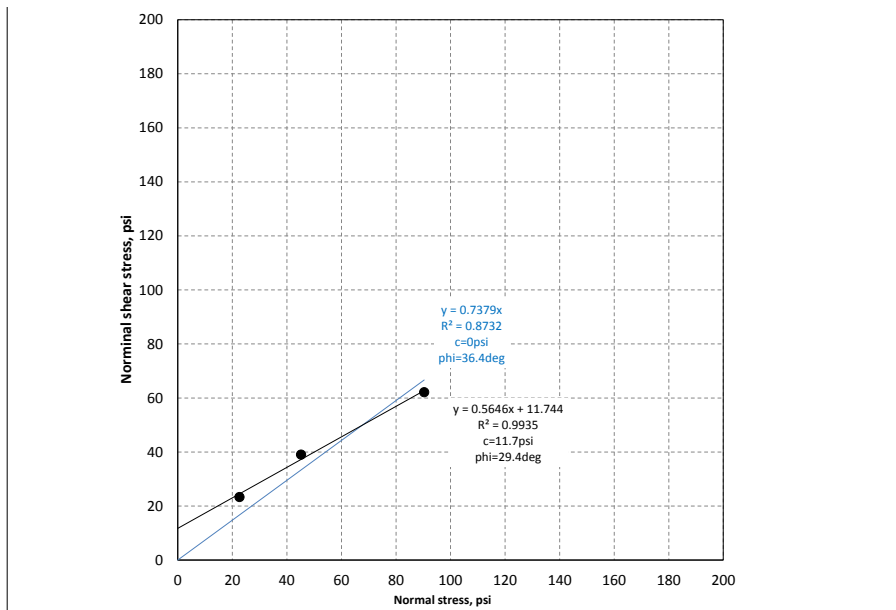
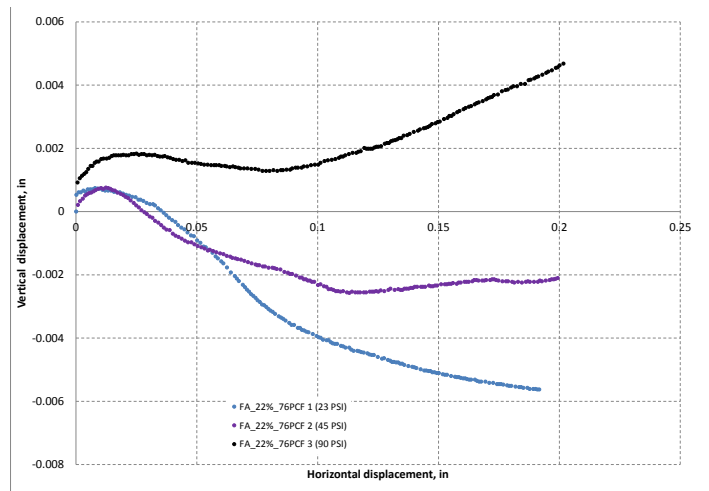
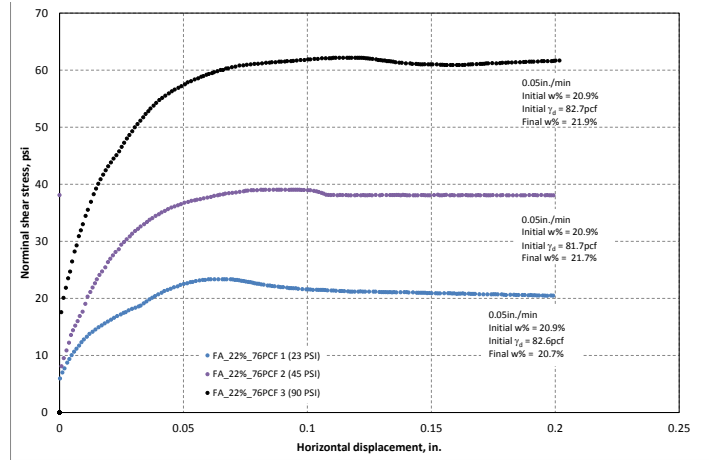


Figure 231. Direct shear test results of WCF fly ash ($w\% = 21.7\%$ and $\gamma_d = 82.3pcf$)

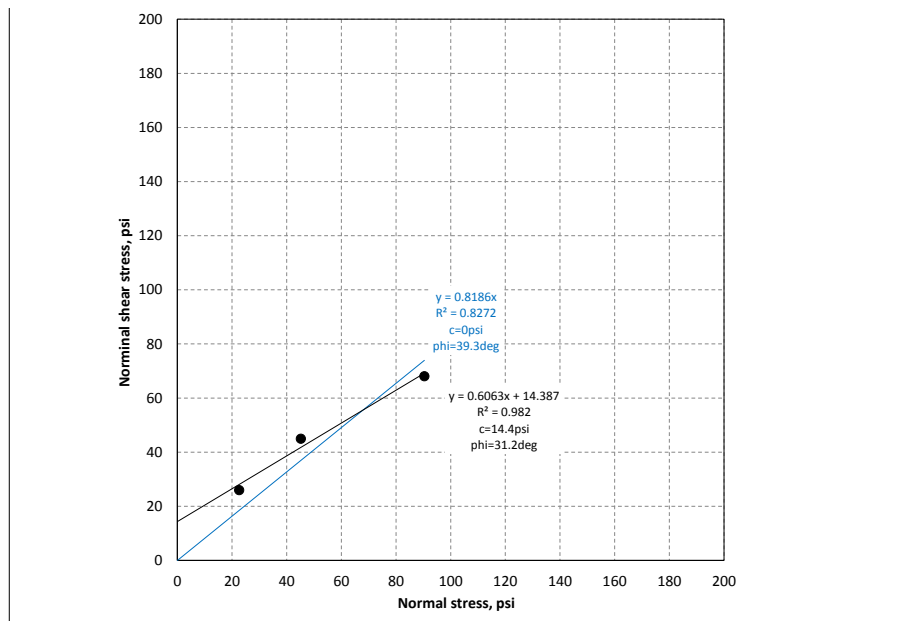
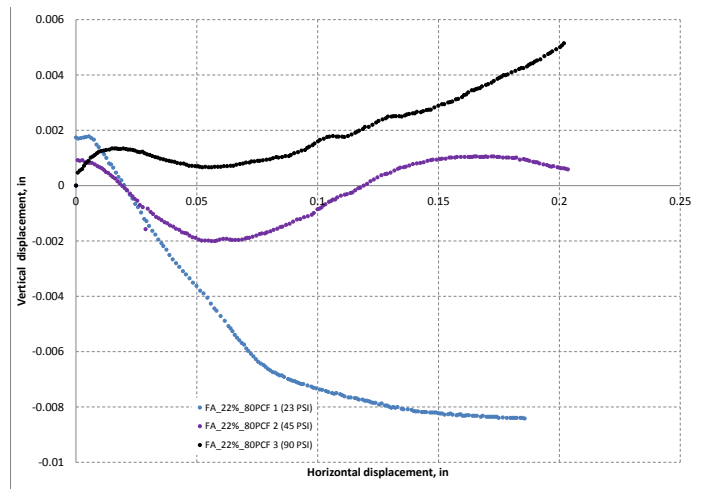
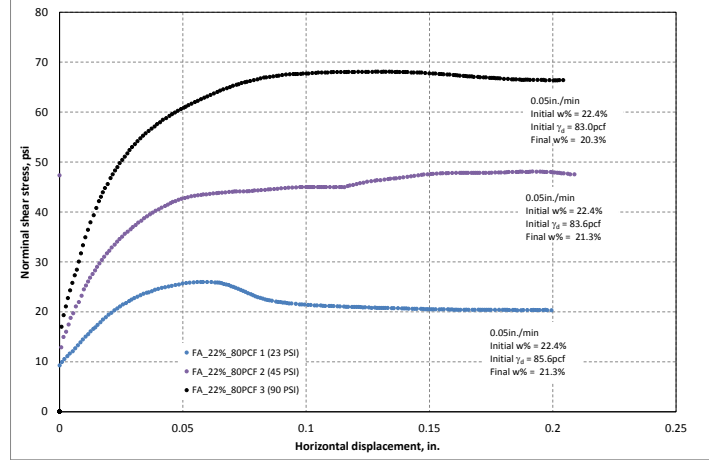


Figure 232. Direct shear test results of WCF fly ash ($w\% = 22.4\%$ and $\gamma_d = 84.1\text{pcf}$)

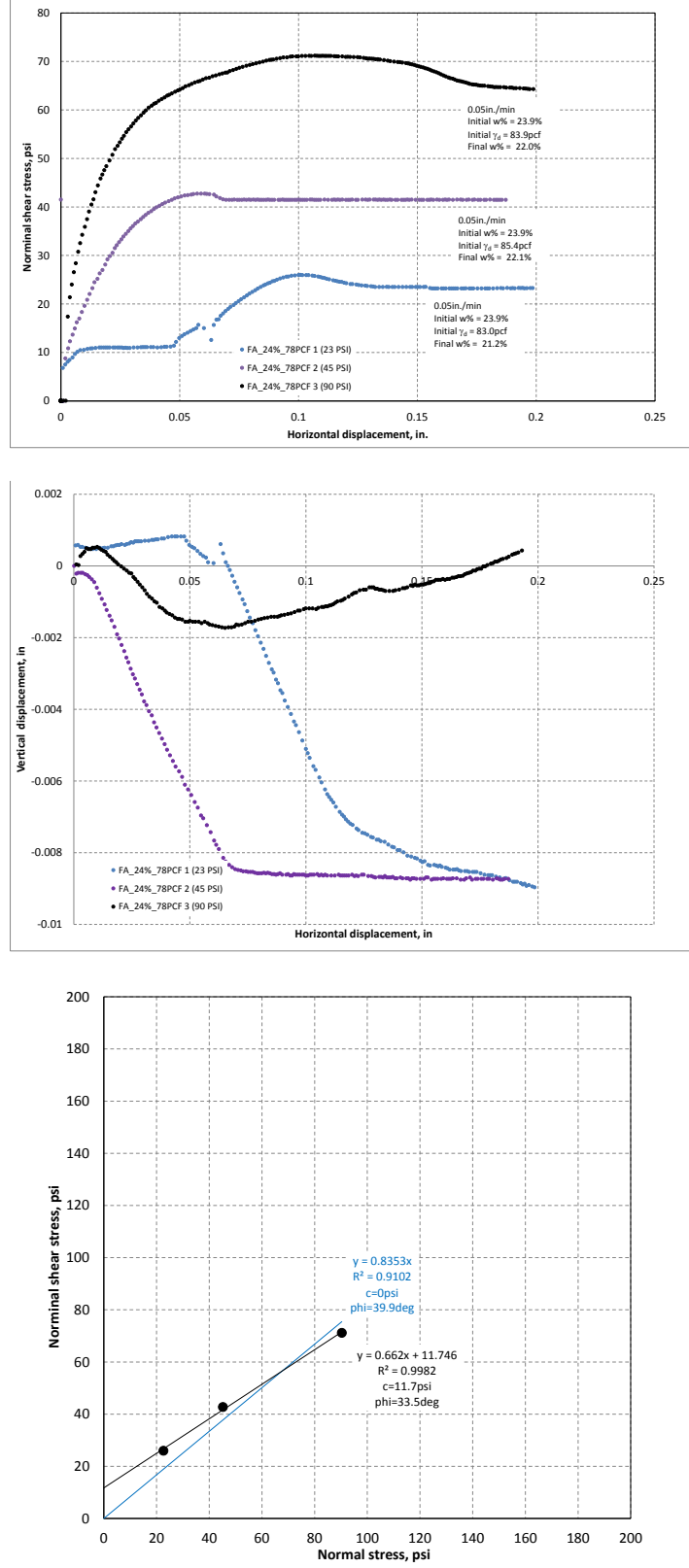


Figure 233. Direct shear test results of WCF fly ash (w% = 23.9% and $\gamma_d = 84.1$ pcf)

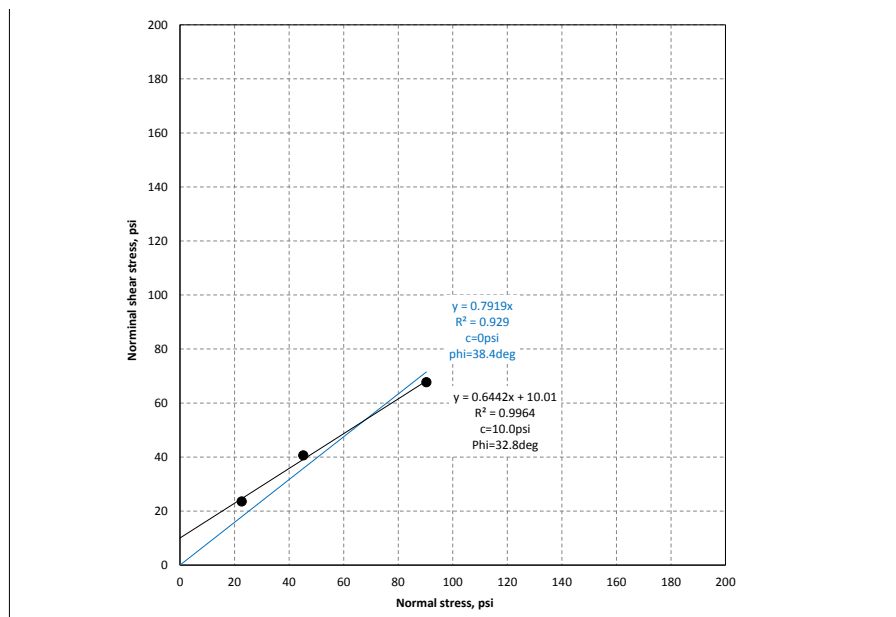
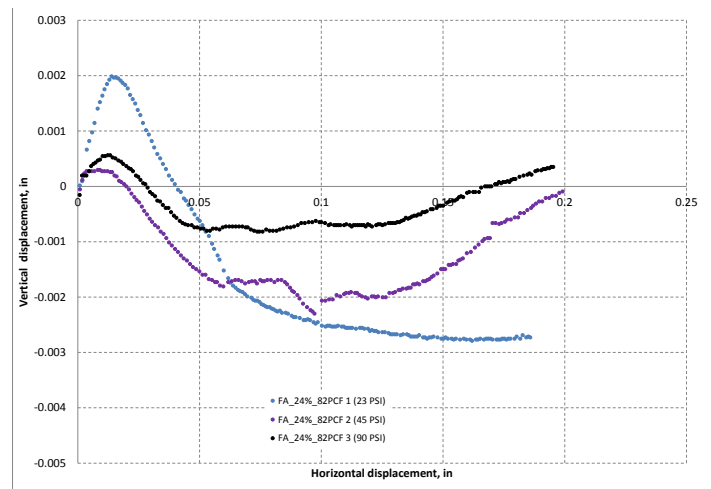
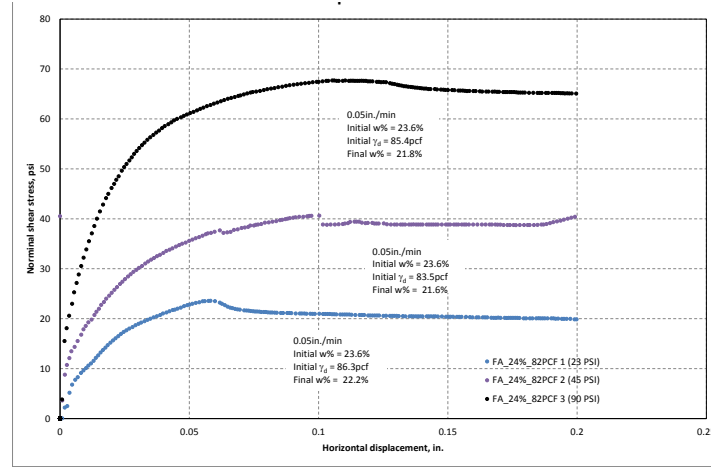


Figure 234. Direct shear test results of WCF fly ash (w% = 23.6% and $\gamma_d = 85.1\text{pcf}$)

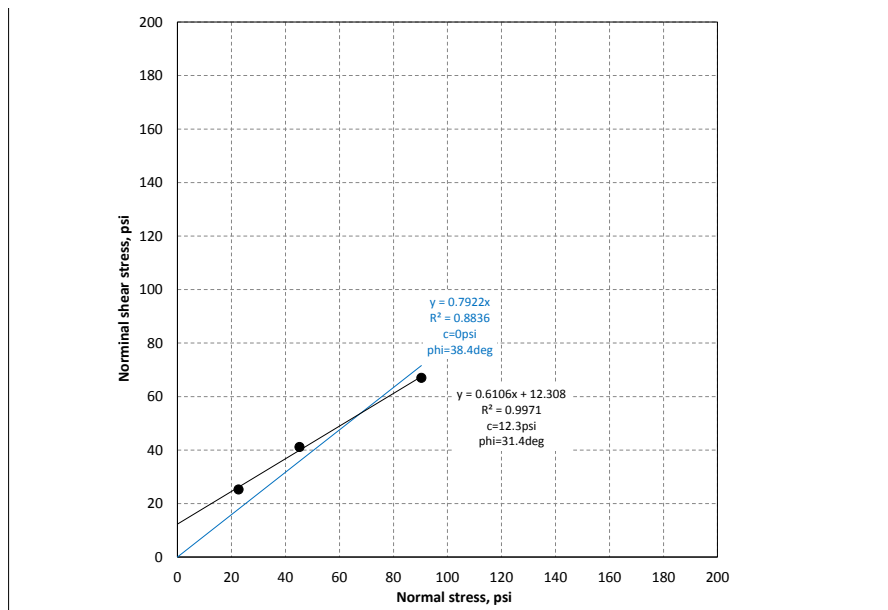
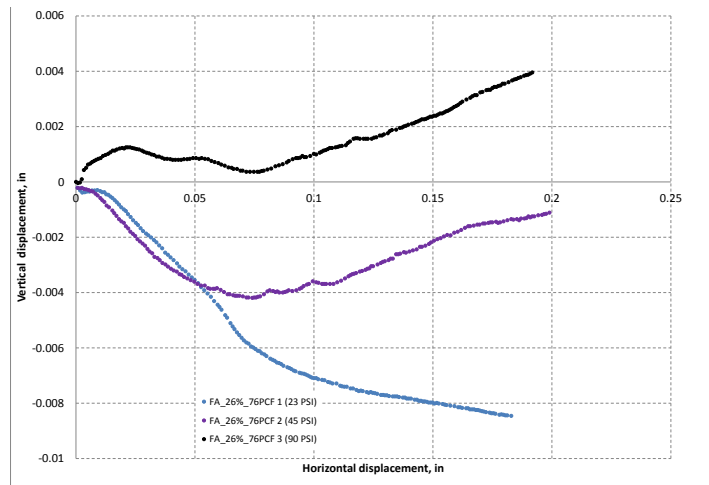
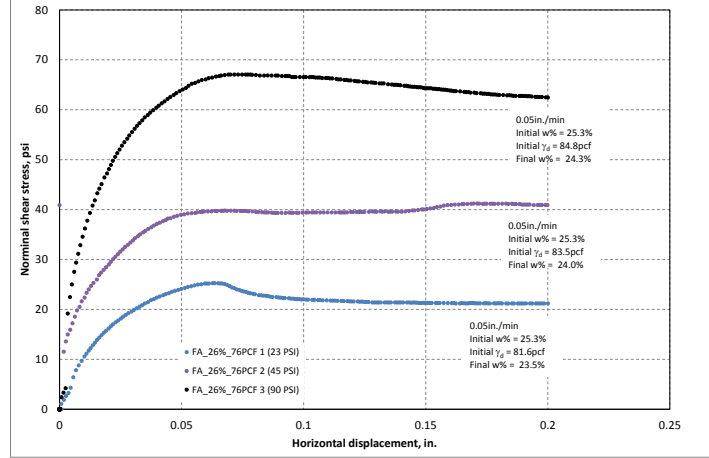


Figure 235. Direct shear test results of WCF fly ash (w% = 25.3% and $\gamma_d = 83.3\text{pcf}$)

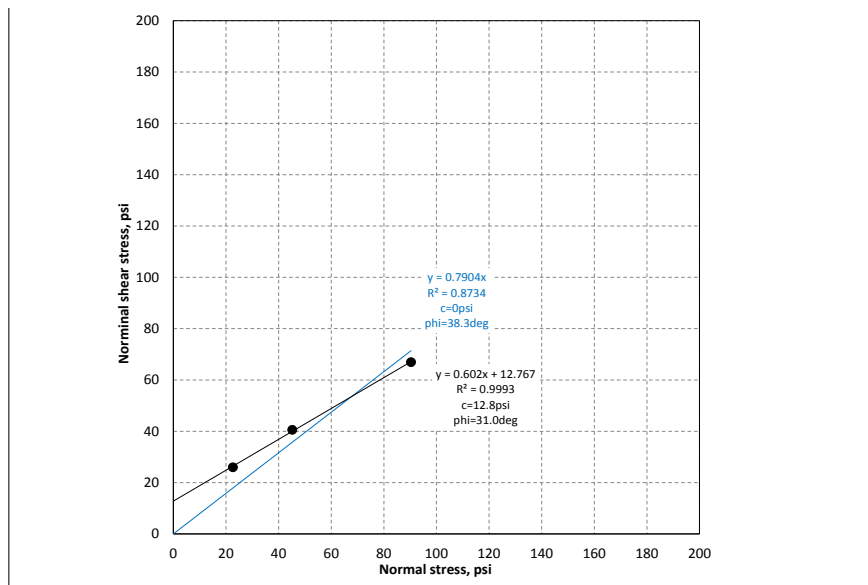
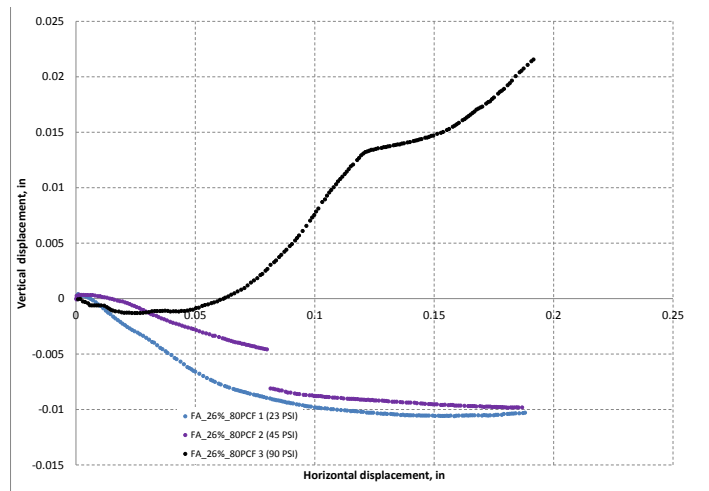
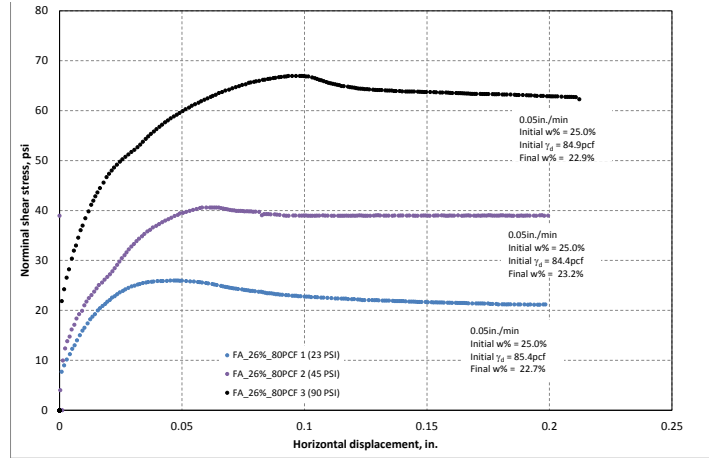


Figure 236. Direct shear test results of WCF fly ash ($w\% = 25.0\%$, $\gamma_d = 84.9\text{pcf}$)

WCF gypsum (CFED 2054)

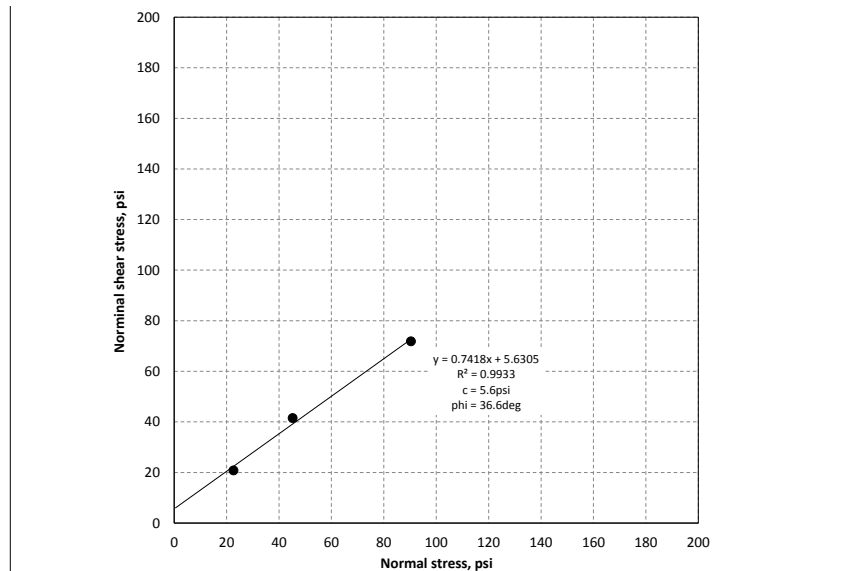
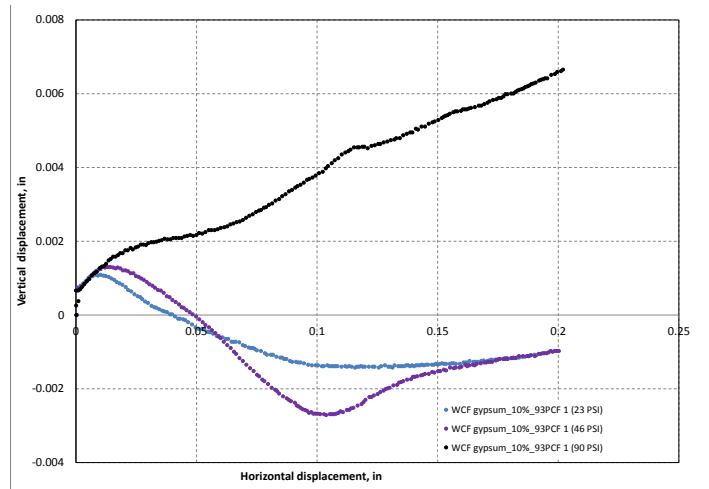
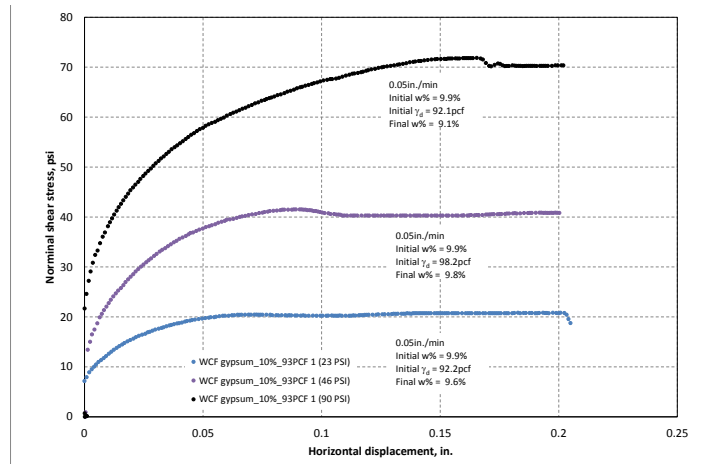


Figure 237. Direct shear test results of WCF gypsum (w% = 9.9% and $\gamma_d = 94.2\text{pcf}$)

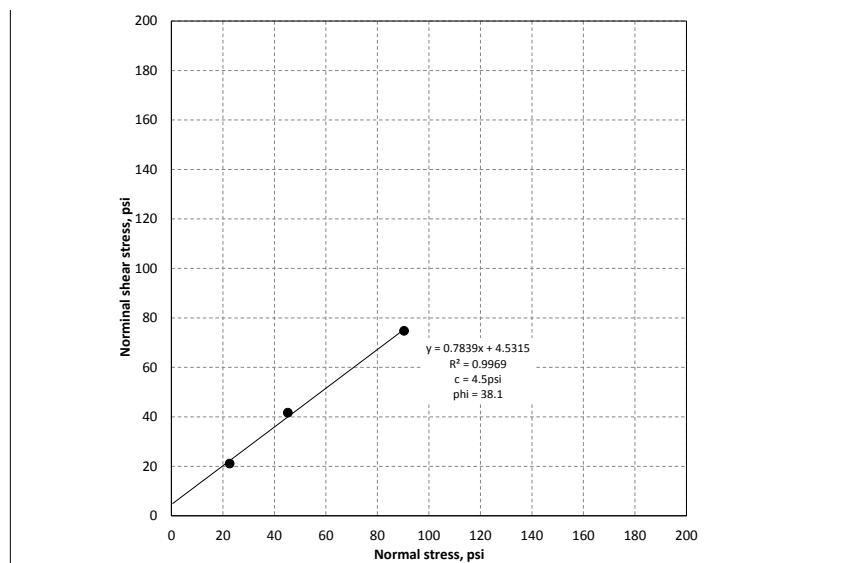
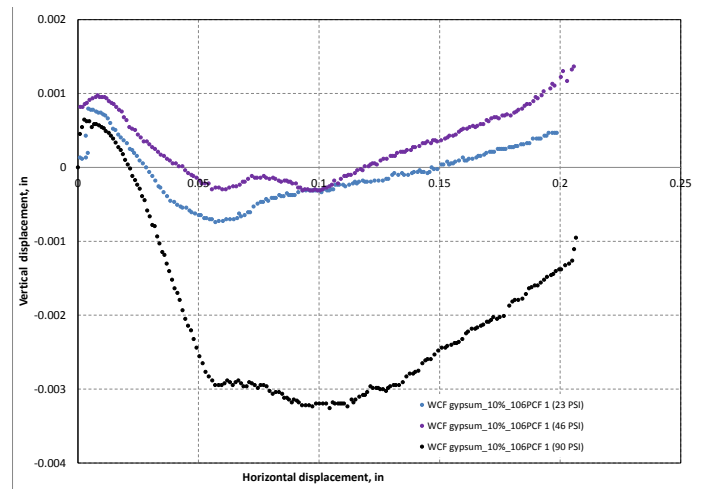
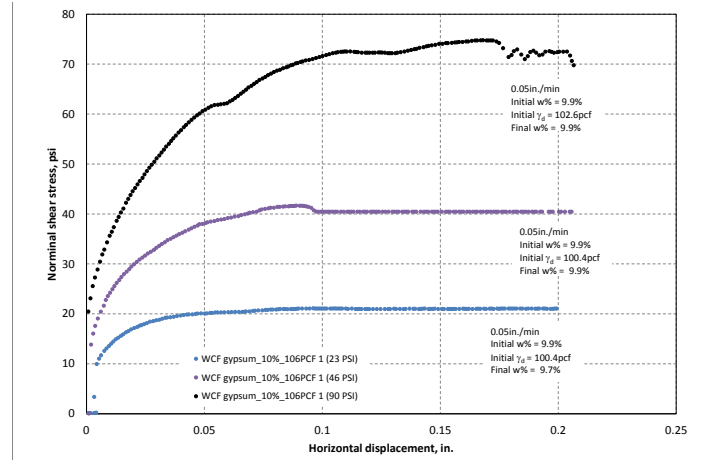


Figure 238. Direct shear test results of WCF gypsum ($w\% = 9.9\%$ and $\gamma_d = 102.3$ pcf)

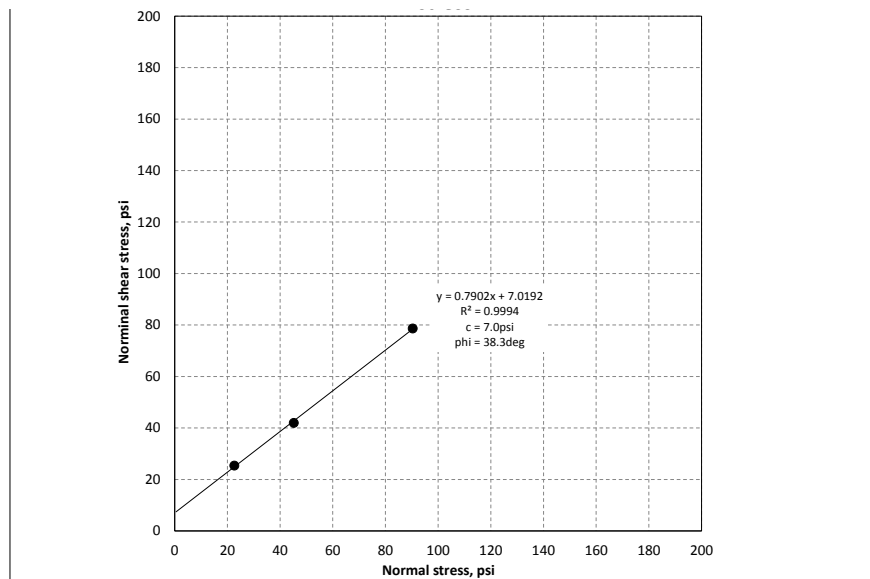
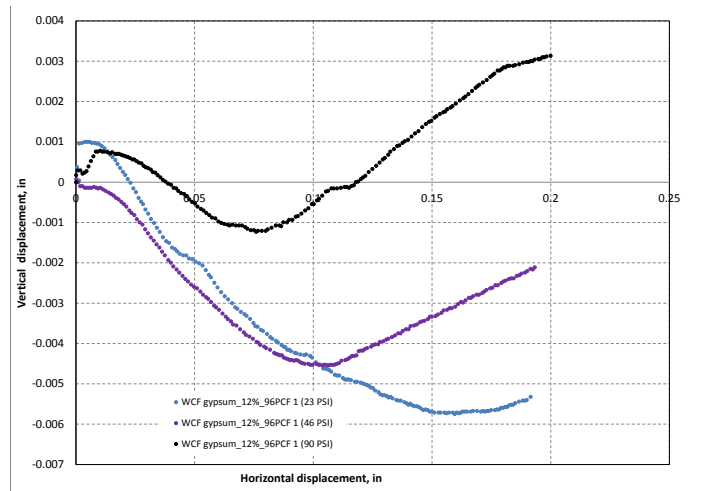
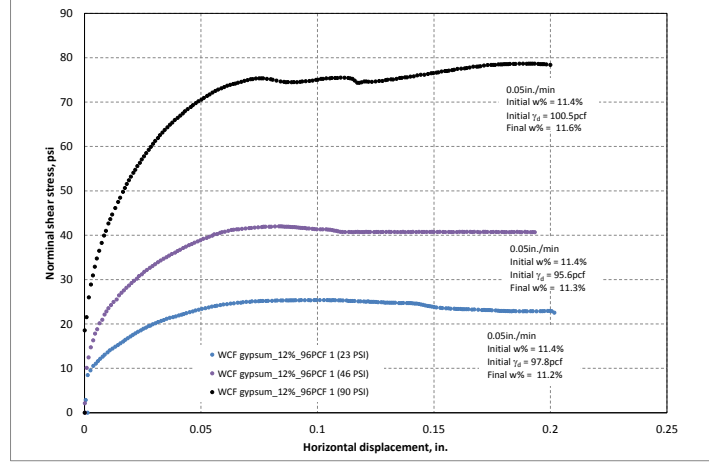


Figure 239. Direct shear test results of WCF gypsum ($w\% = 11.6\%$ and $\gamma_d = 97.9\text{pcf}$)

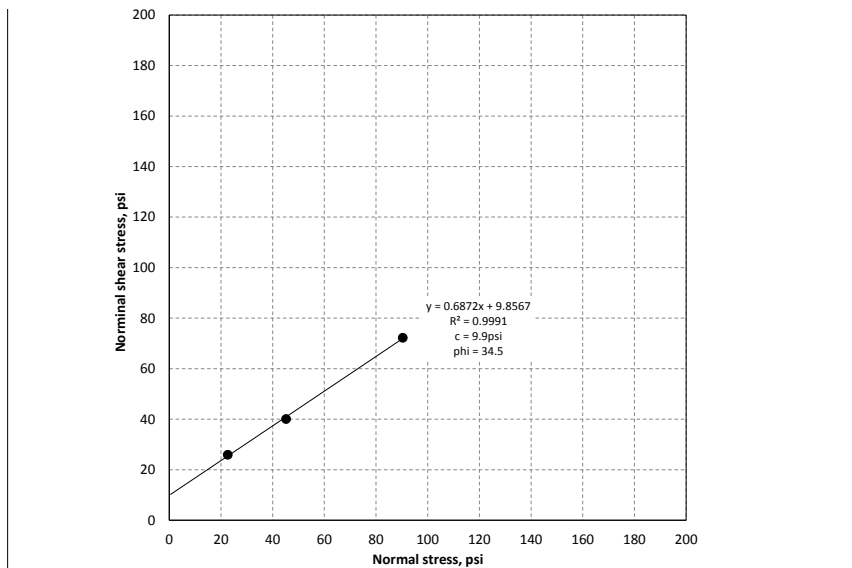
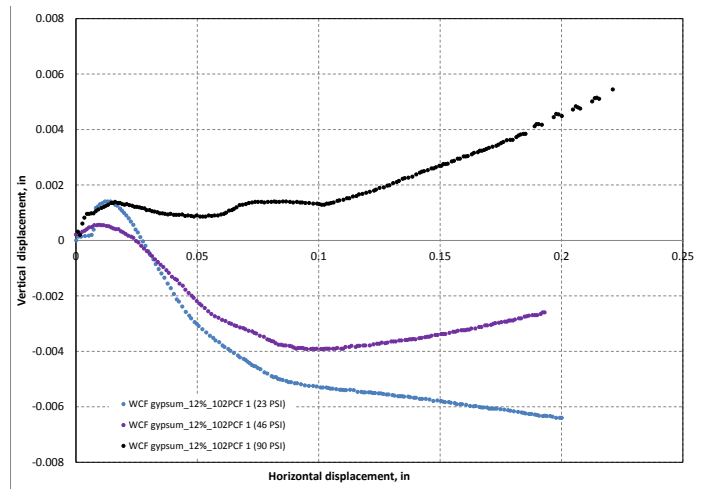
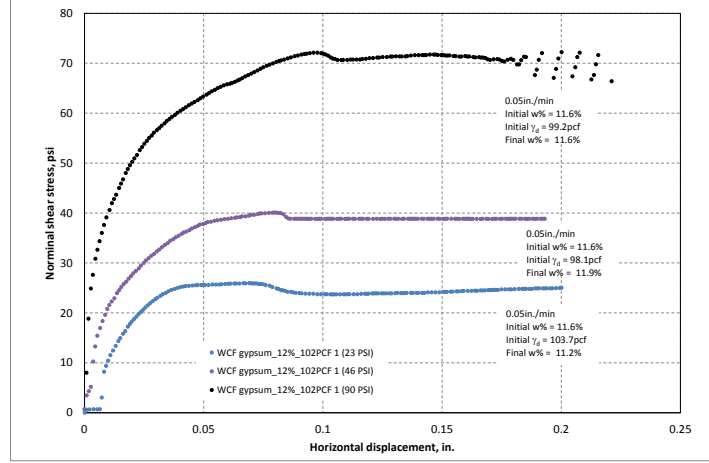


Figure 240. Direct shear test results of WCF gypsum ($w\% = 11.6\%$ and $\gamma_d = 100.3\text{pcf}$)

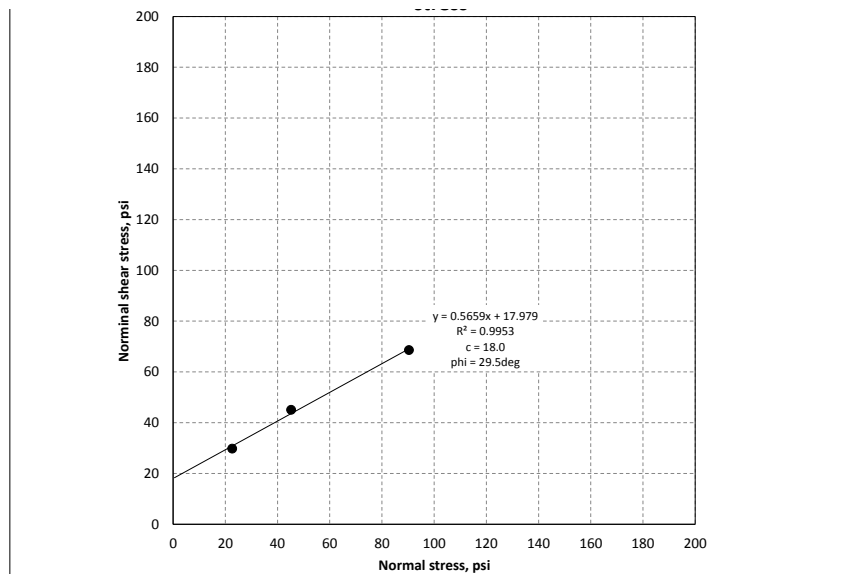
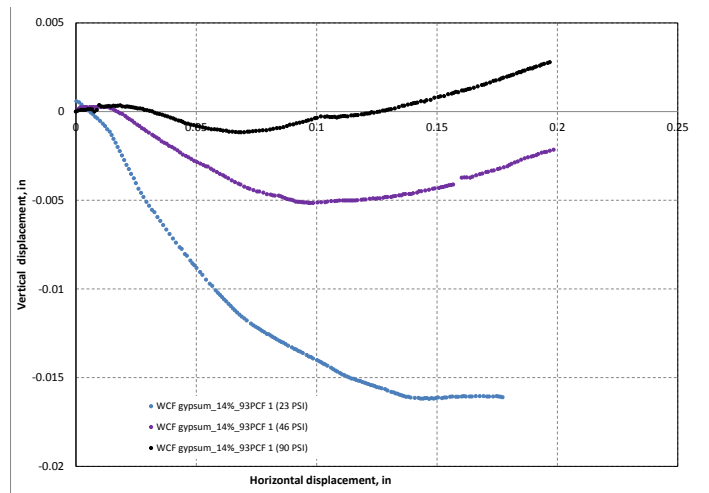
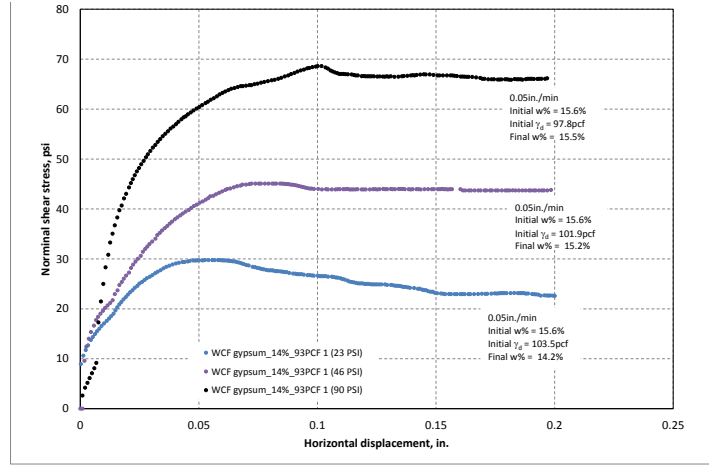


Figure 241. Direct shear test results of WCF gypsum ($w\% = 15.6\%$ and $\gamma_d = 101.1\text{pcf}$)

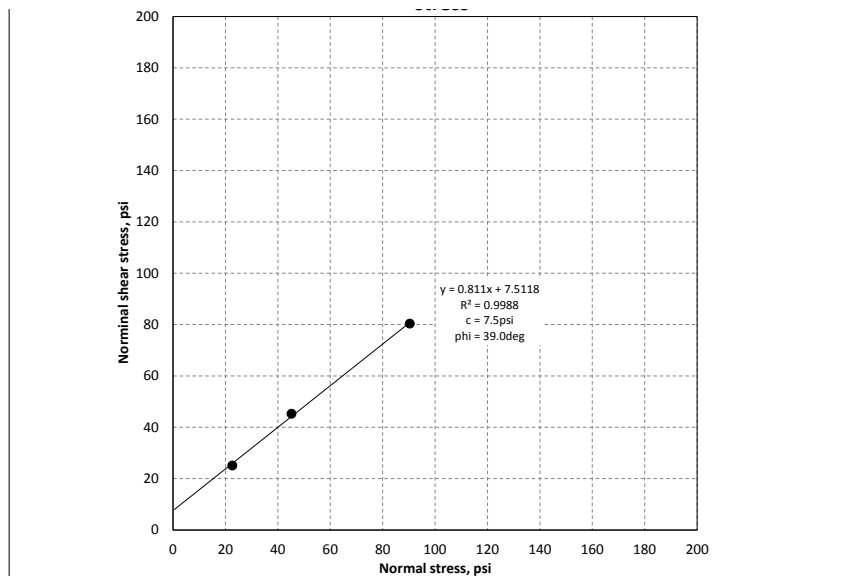
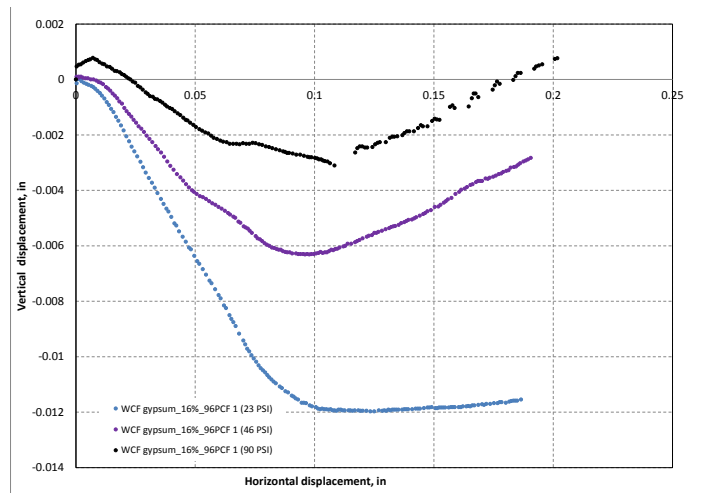
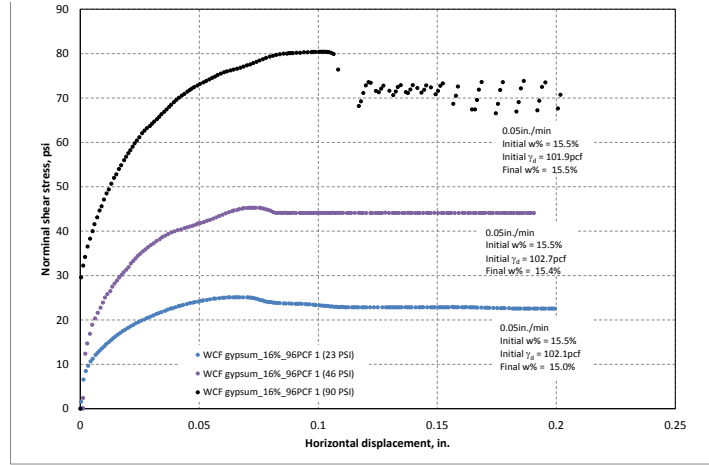


Figure 242. Direct shear test results of WCF gypsum (w% = 15.5% and $\gamma_d = 102.2\text{pcf}$)

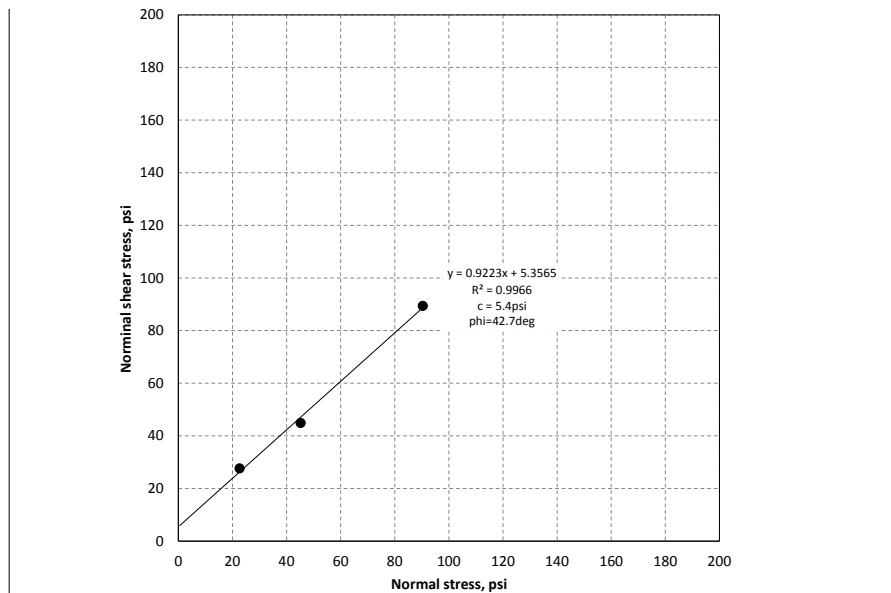
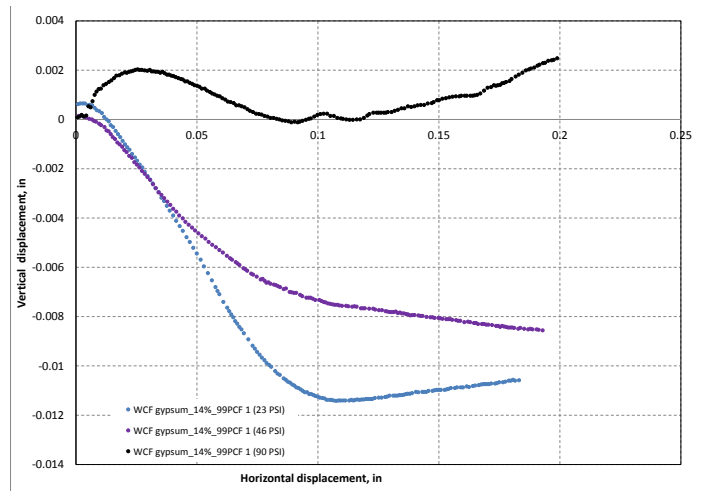
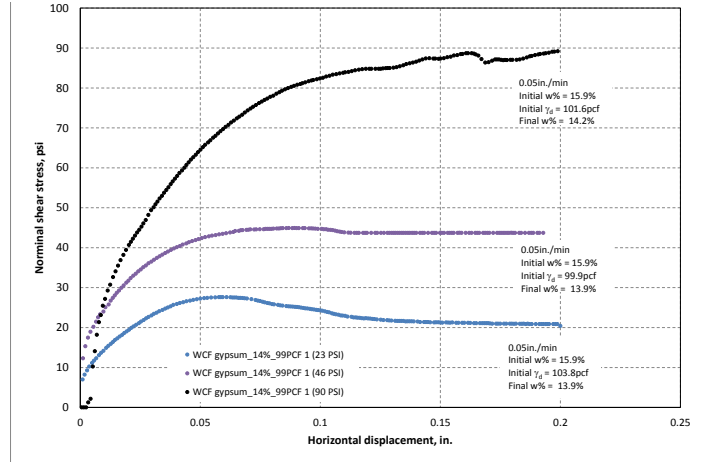


Figure 243. Direct shear test results of WCF gypsum (w% = 15.9% and $\gamma_d = 101.8pcf$)

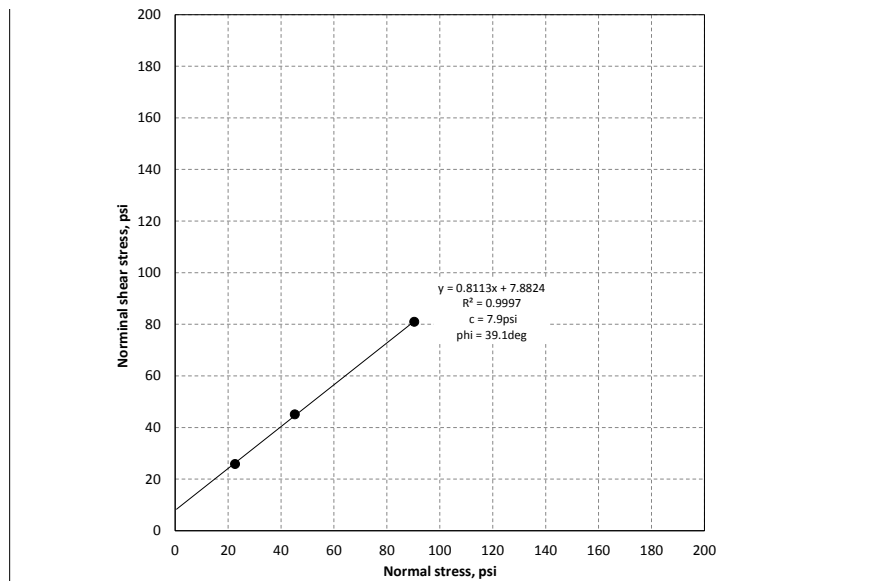
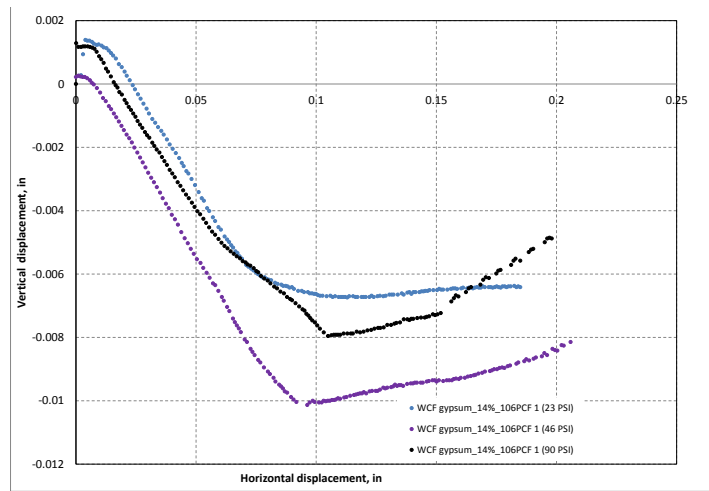
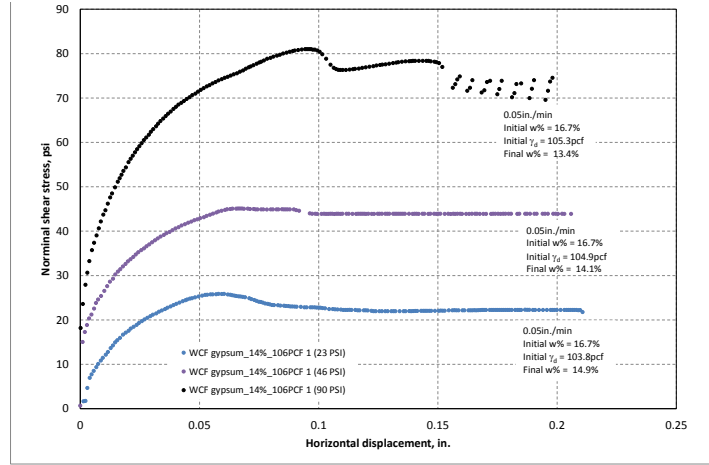


Figure 244. Direct shear test results of WCF gypsum (w% = 16.7% and $\gamma_d = 104.7pcf$)

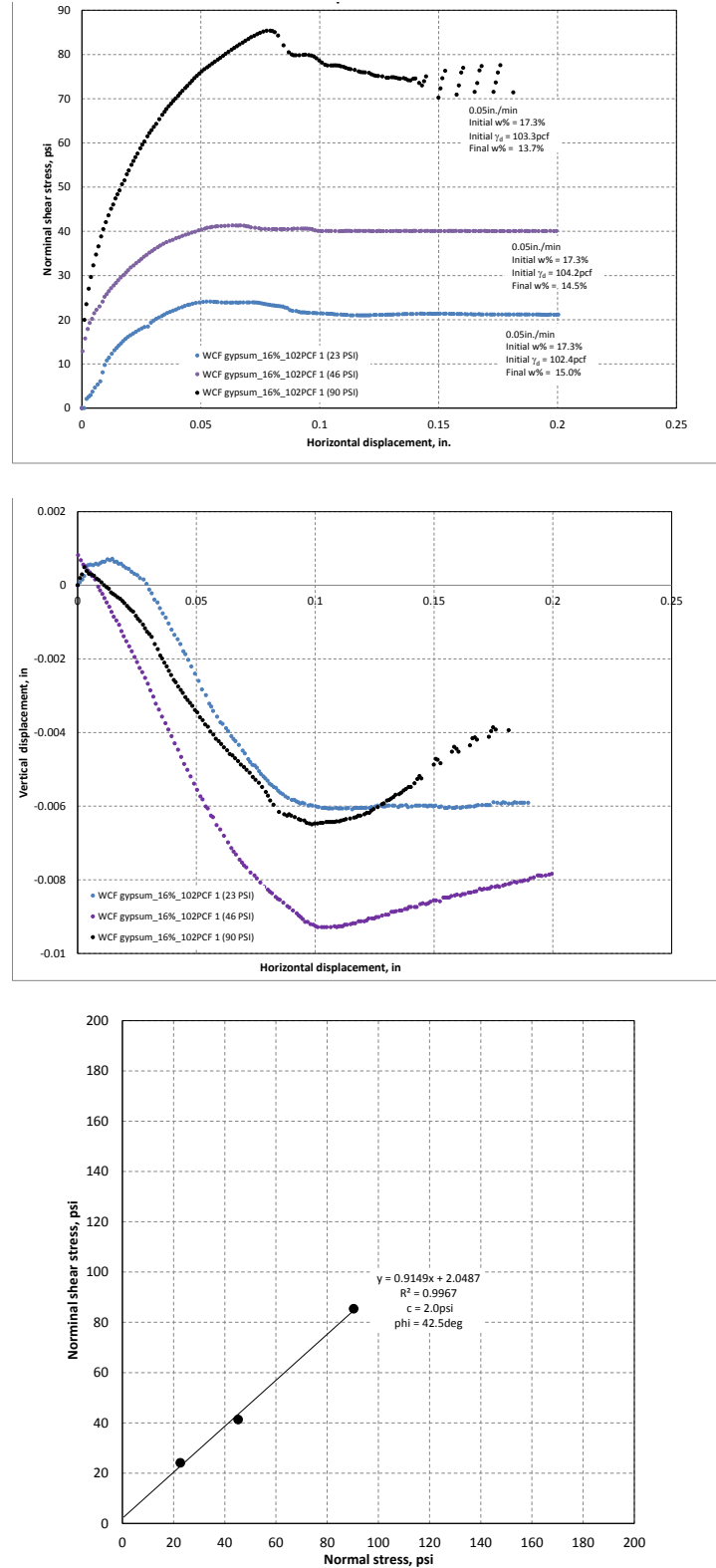


Figure 245. Direct shear test results of WCF gypsum (w% = 17.3% and $\gamma_d = 103.3\text{pcf}$)

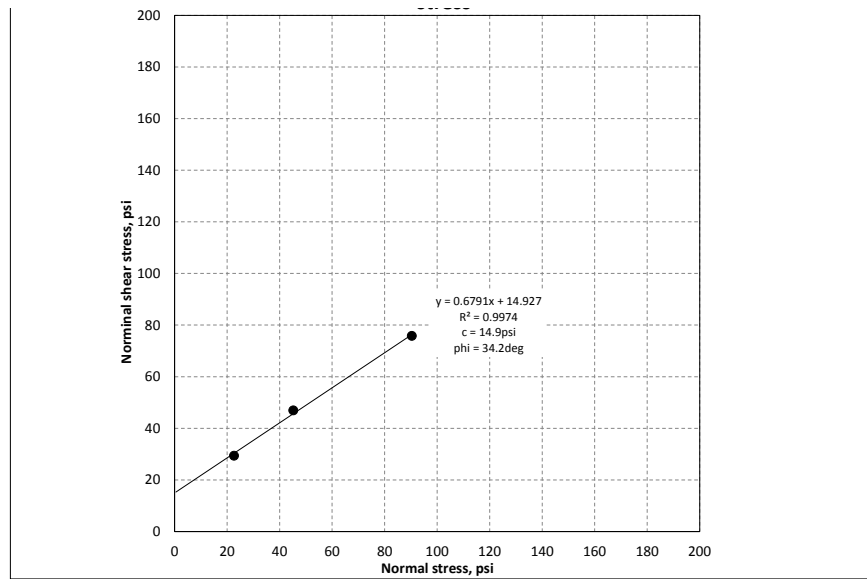
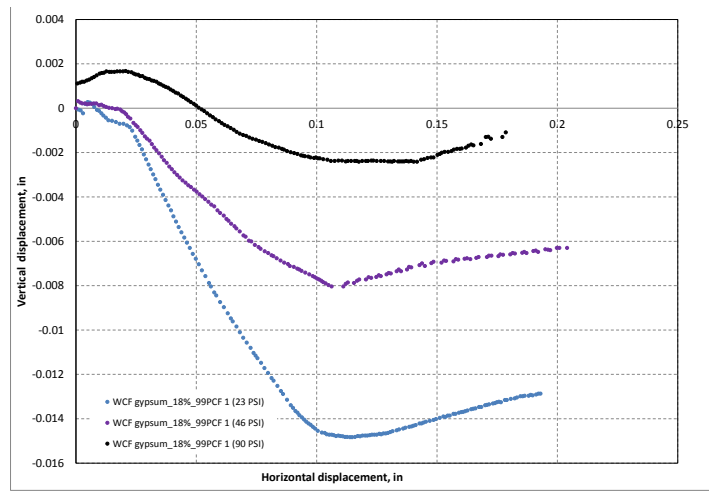
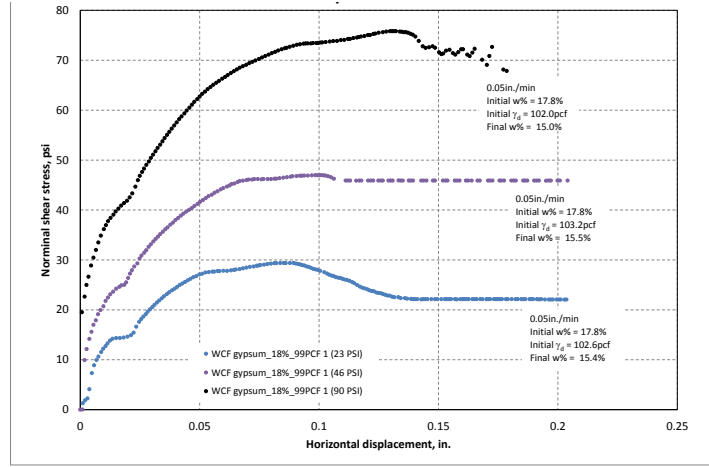


Figure 246. Direct shear test results of WCF gypsum ($w\% = 17.8\%$ and $\gamma_d = 102.6\text{pcf}$)

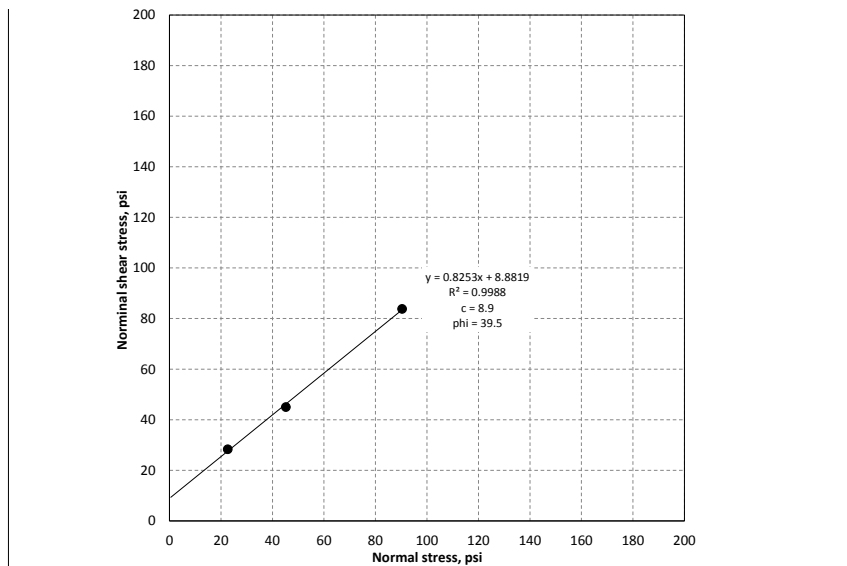
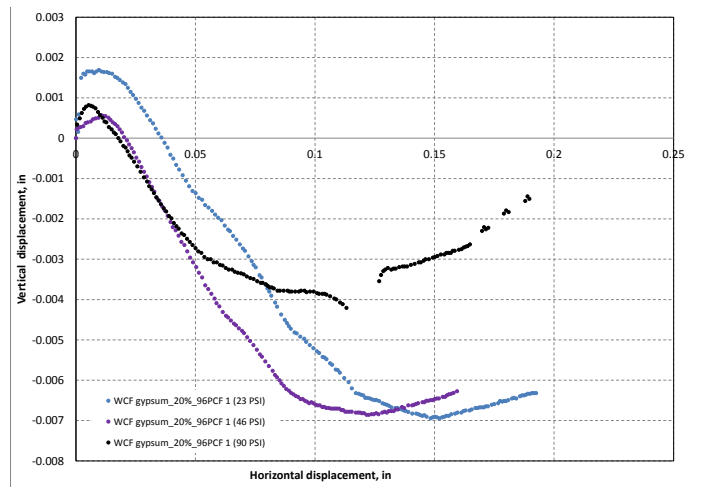
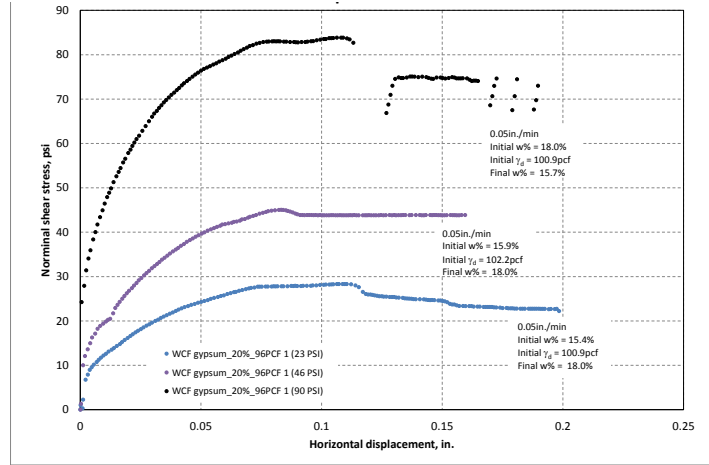


Figure 247. Direct shear test results of WCF gypsum ($w\% = 18.0\%$ and $\gamma_d = 101.3pcf$)

Ottawa Sand (ASTM 20-30)

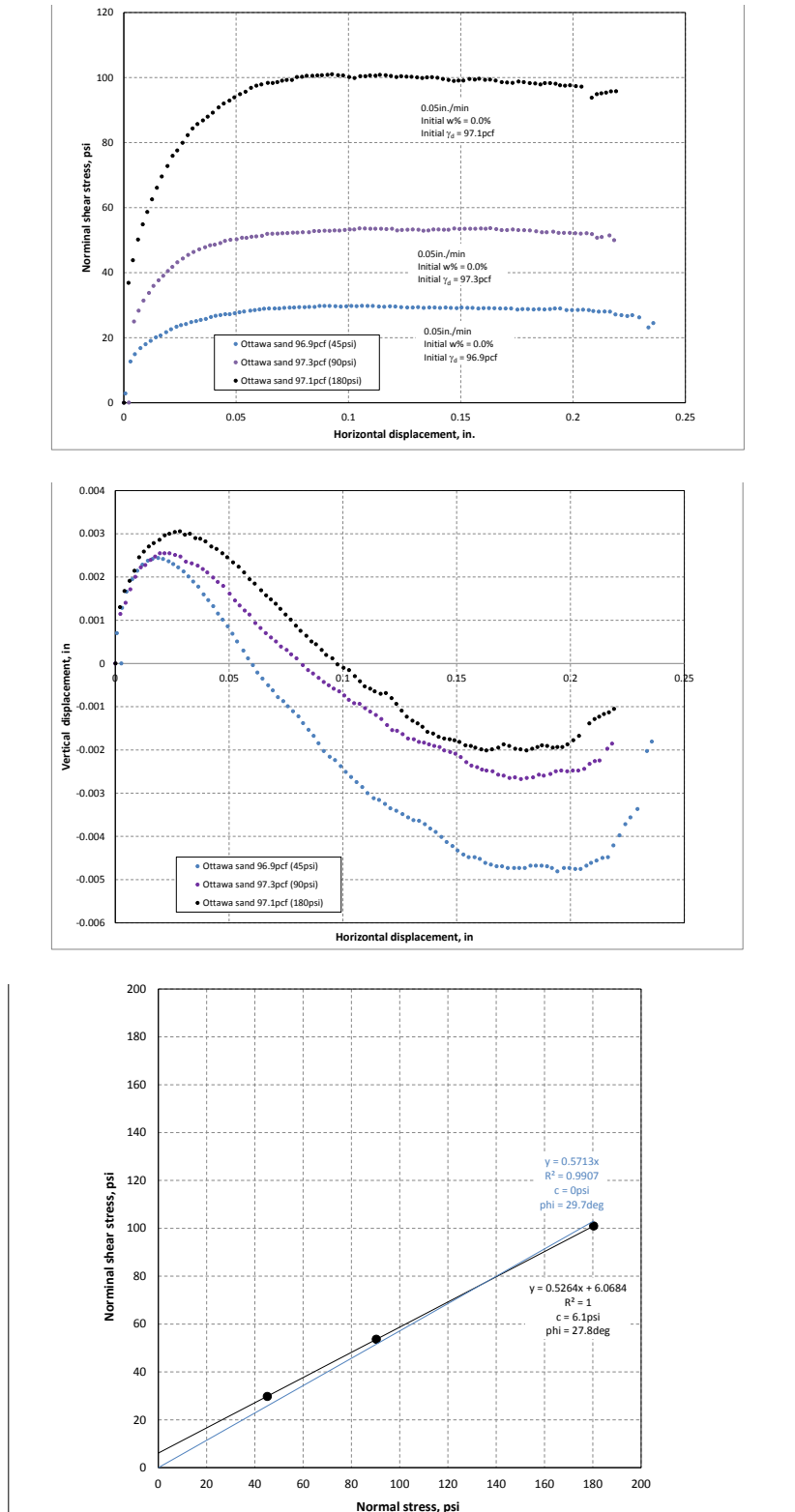


Figure 248. Direct shear test results of Ottawa sand ($\gamma_d = 97.1$ pcf and $e_0 = 0.70$)

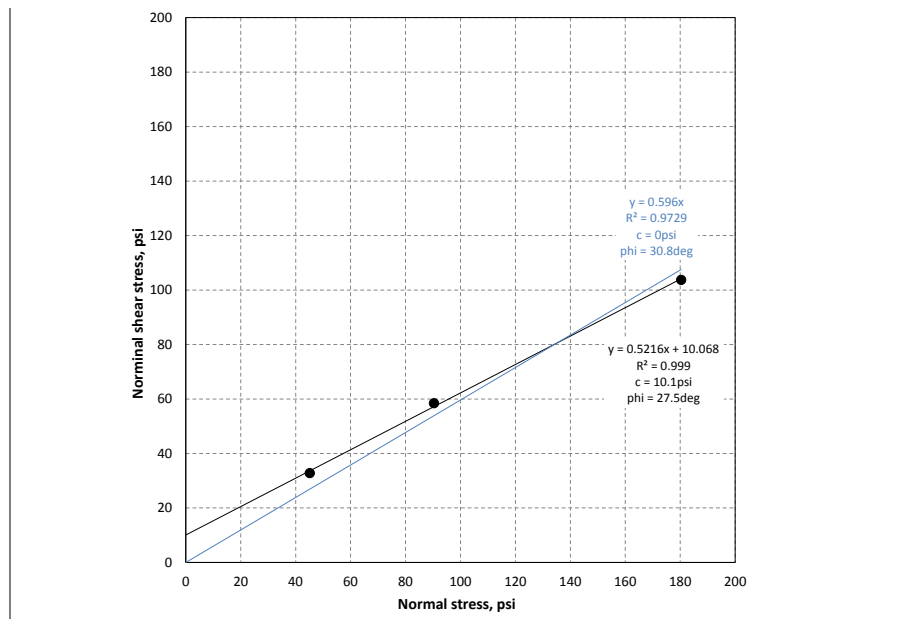
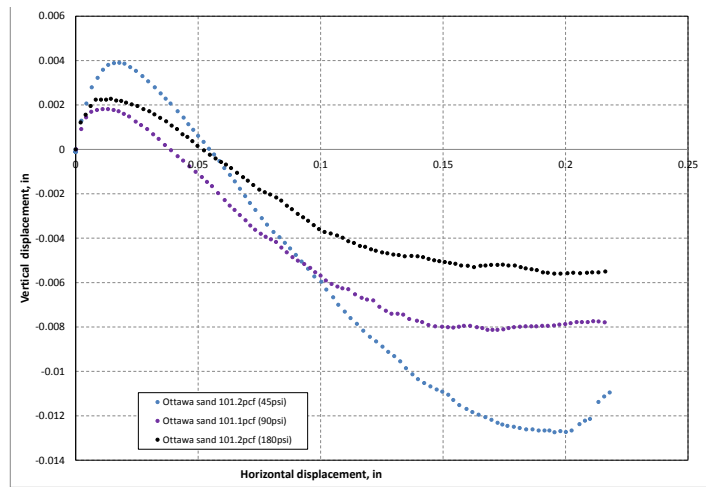
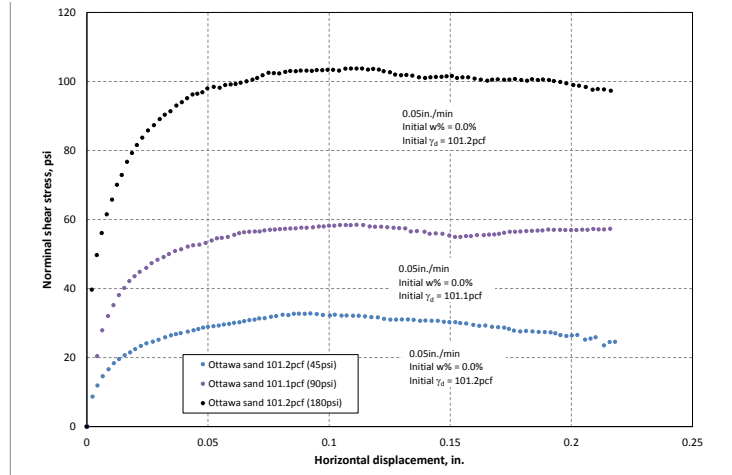


Figure 249. Direct shear test results of Ottawa sand ($\gamma_d = 101.2\text{pcf}$ and $e_0 = 0.63$)

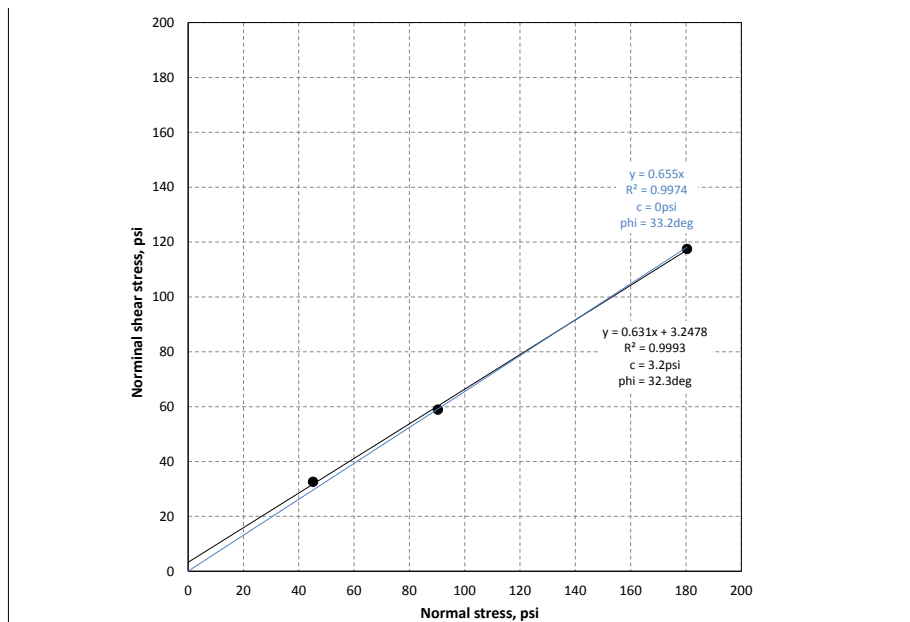
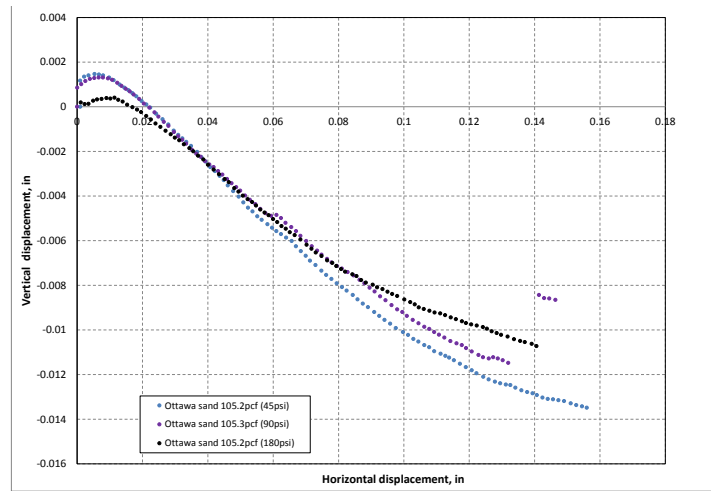
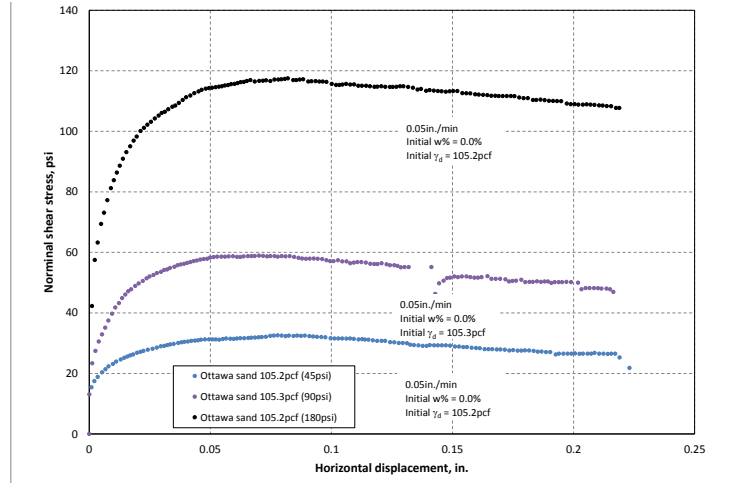


Figure 250. Direct shear test results of Ottawa sand ($\gamma_d = 105.2$ pcf and $e_0 = 0.57$)

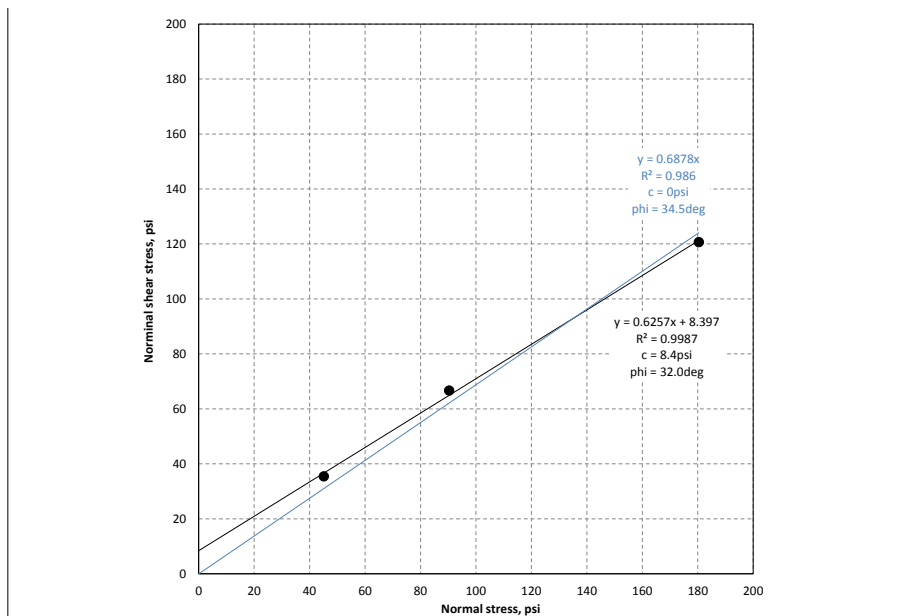
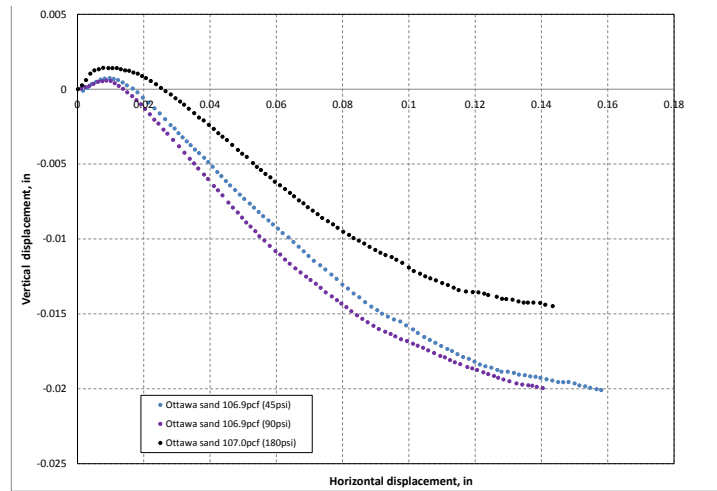
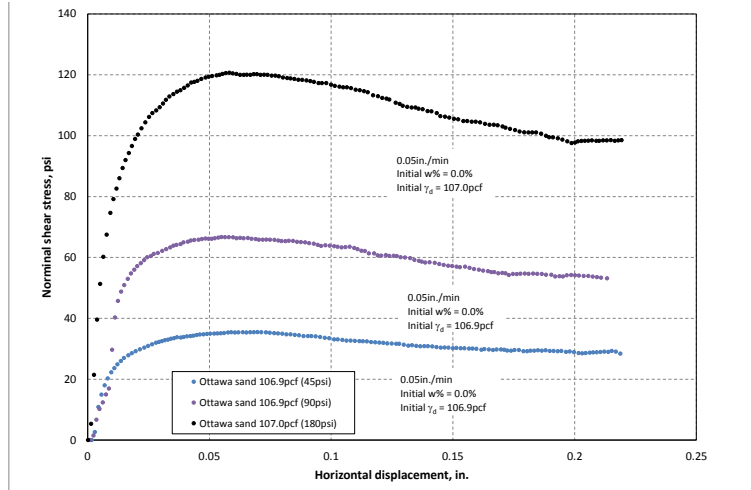


Figure 251. Direct shear test results of Ottawa sand ($\gamma_d = 106.9\text{pcf}$ and $e_0 = 0.55$)

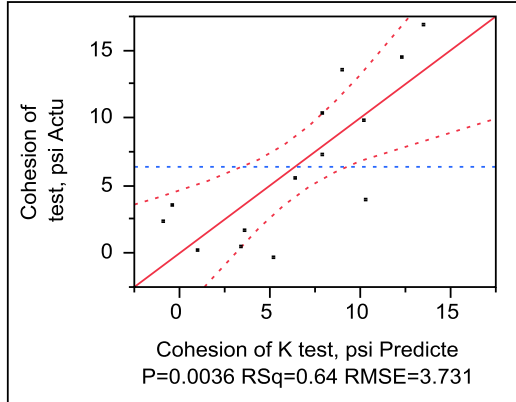
APPENDIX E. STATISTICAL MODELS FOR THE IOWA K TEST RESULTS

Western Iowa loess (CFED 1634)

Iowa K test cohesion of western Iowa loess, psi

Whole Model

Actual by Predicted Plot



Summary of Fit

RSquare	0.640178
RSquare Adj	0.574756
Root Mean Square Error	3.731622
Mean of Response	6.385714
Observations (or Sum Wgts)	14

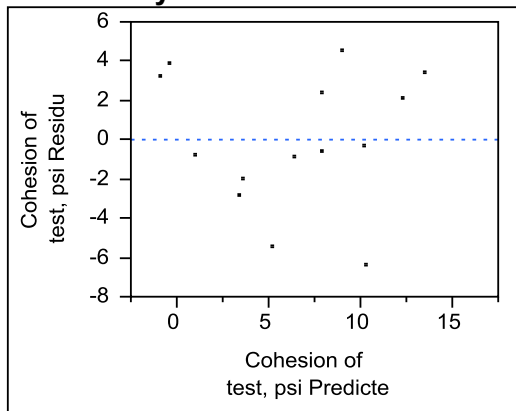
Analysis of Variance

Source	DF	Sum of Squares	Mean Square	F Ratio
Model	2	272.52211	136.261	9.7854
Error	11	153.17503	13.925	Prob > F
C. Total	13	425.69714		0.0036*

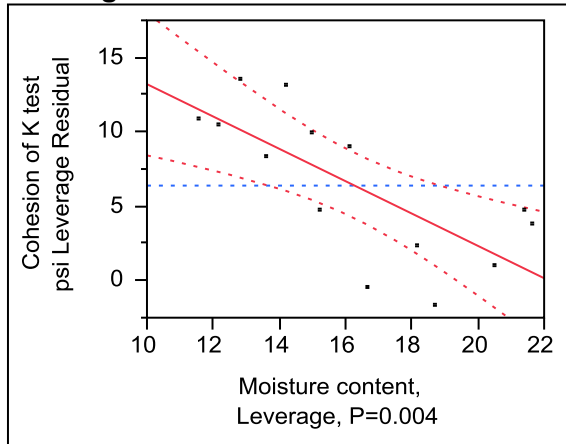
Parameter Estimates

Term	Estimate	Std Error	t Ratio	Prob> t
Intercept	-13.6533	19.00876	-0.72	0.4876
Moisture content, %	-1.087671	0.30726	-3.54	0.0046*
Loading 1 Dry unit weight, pcf	0.3593188	0.167923	2.14	0.0556

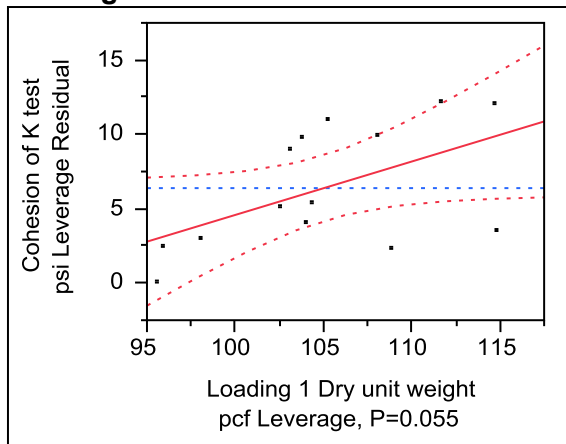
Residual by Predicted Plot



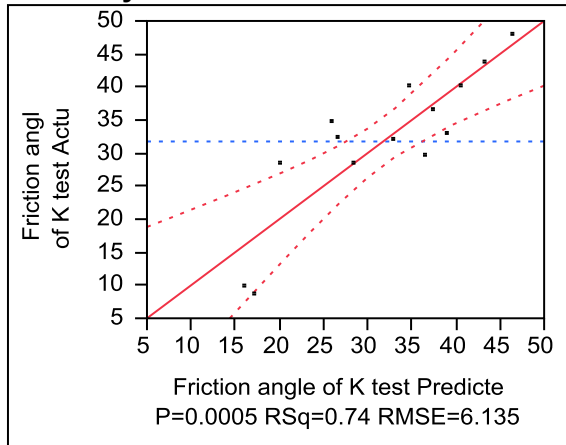
**Moisture content, %
Leverage Plot**



**Loading 1 Dry unit weight, pcf
Leverage Plot**



**Iowa K test friction angle of western Iowa loess
Whole Model
Actual by Predicted Plot**



Summary of Fit

RSquare	0.744783
RSquare Adj	0.698379
Root Mean Square Error	6.135884
Mean of Response	31.75714
Observations (or Sum Wgts)	14

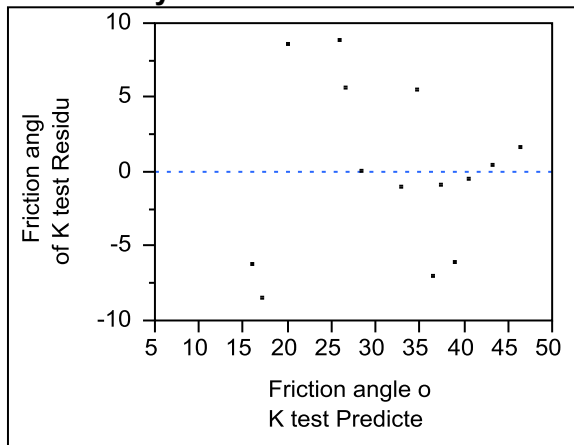
Analysis of Variance

Source	DF	Sum of Squares	Mean Square	F Ratio
Model	2	1208.5544	604.277	16.0503
Error	11	414.1398	37.649	Prob > F
C. Total	13	1622.6943		0.0005*

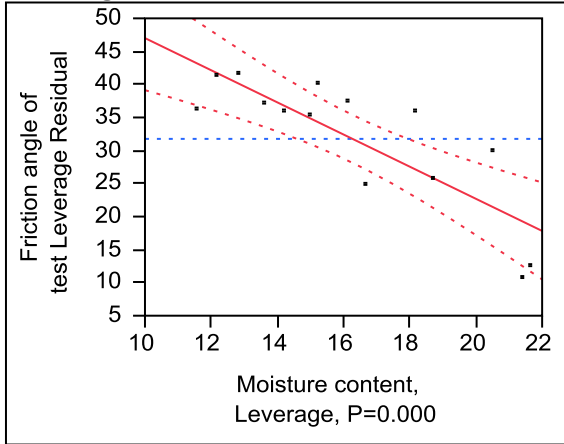
Parameter Estimates

Term	Estimate	Std Error	t Ratio	Prob> t
Intercept	4.7828614	31.256	0.15	0.8812
Moisture content, %	-2.432247	0.505226	-4.81	0.0005*
Dry unit weight, pcf	0.6336715	0.276114	2.29	0.0424*

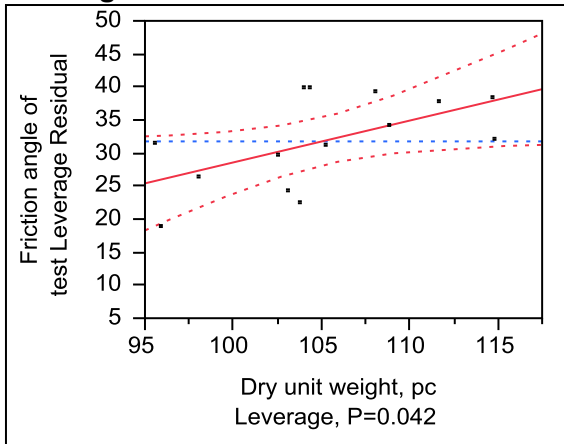
Residual by Predicted Plot



**Moisture content, %
Leverage Plot**



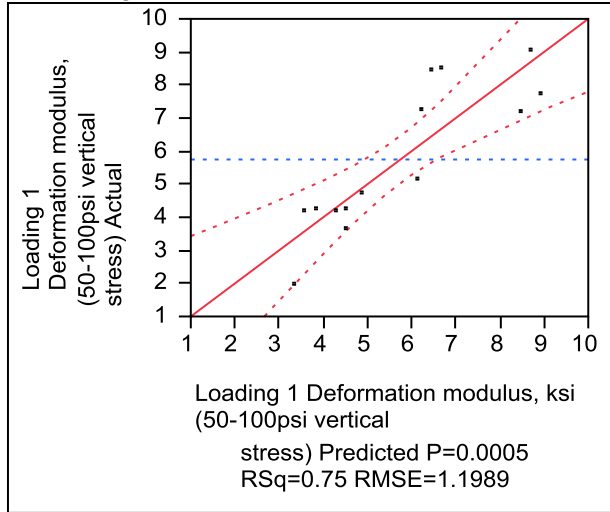
**Dry unit weight, pcf
Leverage Plot**



Iowa K test Loading 1 Deformation modulus of western Iowa loess, ksi (50-100psi vertical stress)

Whole Model

Actual by Predicted Plot



Summary of Fit

RSquare	0.751901
RSquare Adj	0.706792
Root Mean Square Error	1.198943
Mean of Response	5.746786
Observations (or Sum Wgts)	14

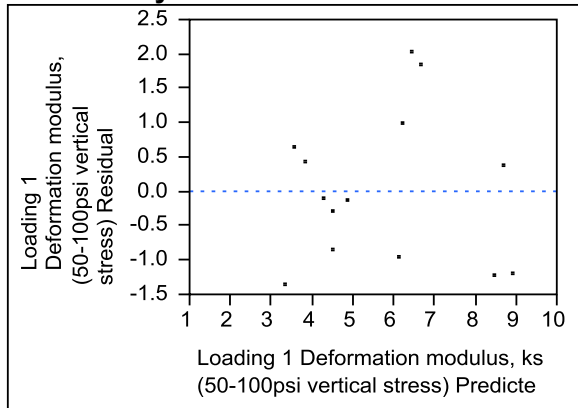
Analysis of Variance

Source	DF	Sum of Squares	Mean Square	F Ratio	Prob > F
Model	2	47.920888	23.9604	16.6685	
Error	11	15.812106	1.4375		
C. Total	13	63.732994			0.0005*

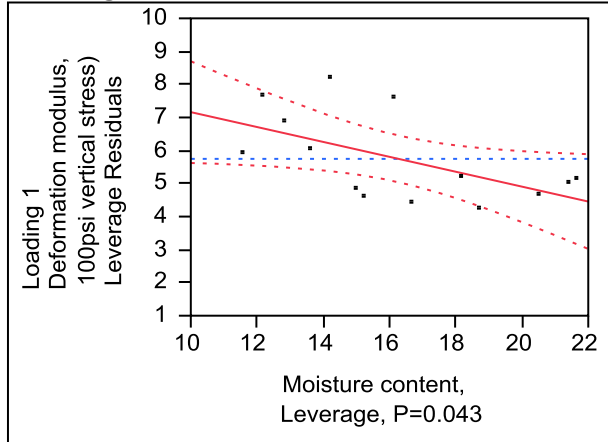
Parameter Estimates

Term	Estimate	Std Error	t Ratio	Prob> t
Intercept	-18.55772	6.107377	-3.04	0.0113*
Moisture content, %	-0.225531	0.09872	-2.28	0.0432*
Loading 1 Dry unit weight, pcf	0.2663606	0.053952	4.94	0.0004*

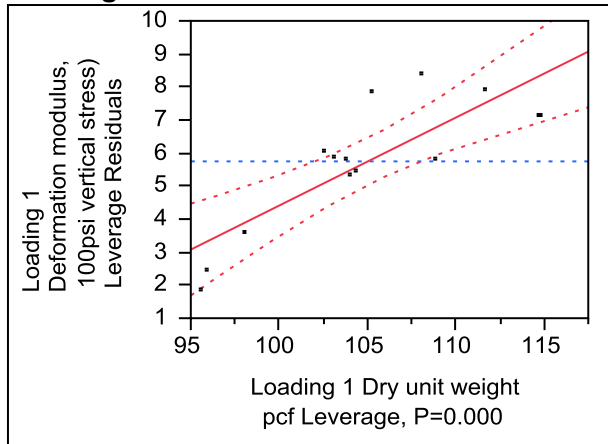
Residual by Predicted Plot



**Moisture content, %
Leverage Plot**

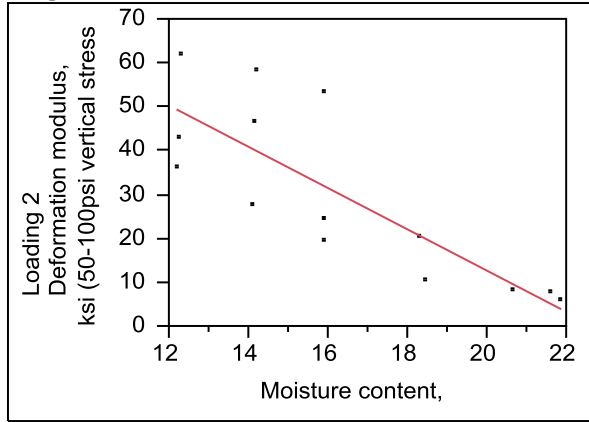


**Loading 1 Dry unit weight, pcf
Leverage Plot**

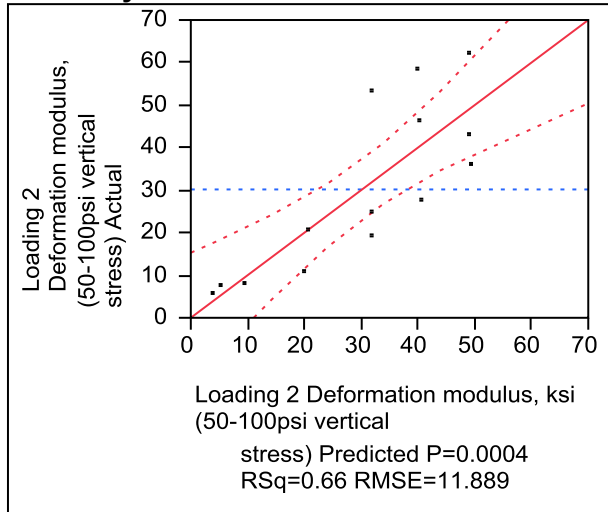


Iowa K test Loading 2 Deformation modulus of western Iowa loess, ksi (50-100psi vertical stress)

**Whole Model
Regression Plot**



Actual by Predicted Plot



Summary of Fit

RSquare	0.662386
RSquare Adj	0.634251
Root Mean Square Error	11.88931
Mean of Response	30.17436
Observations (or Sum Wgts)	14

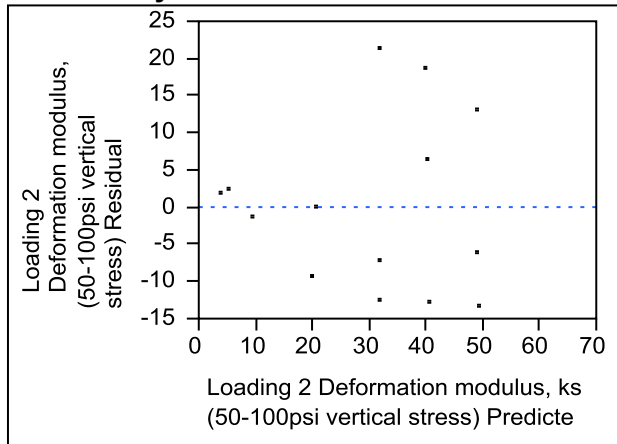
Analysis of Variance

Source	DF	Sum of Squares	Mean Square	F Ratio
Model	1	3328.0107	3328.01	23.5435
Error	12	1696.2697	141.36	Prob > F
C. Total	13	5024.2804		0.0004*

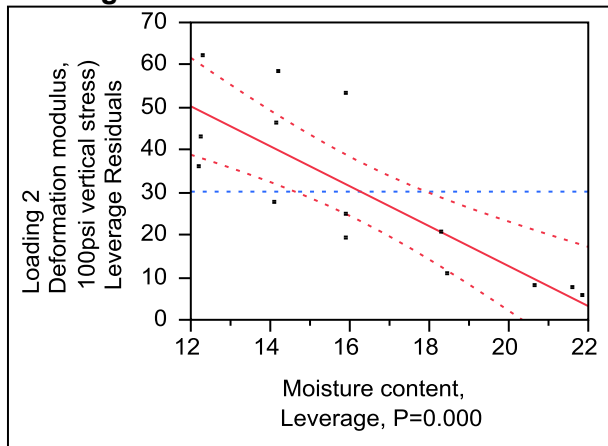
Parameter Estimates

Term	Estimate	Std Error	t Ratio	Prob> t
Intercept	106.72711	16.09384	6.63	<.0001*
Moisture content, %	-4.7047	0.969608	-4.85	0.0004*

Residual by Predicted Plot



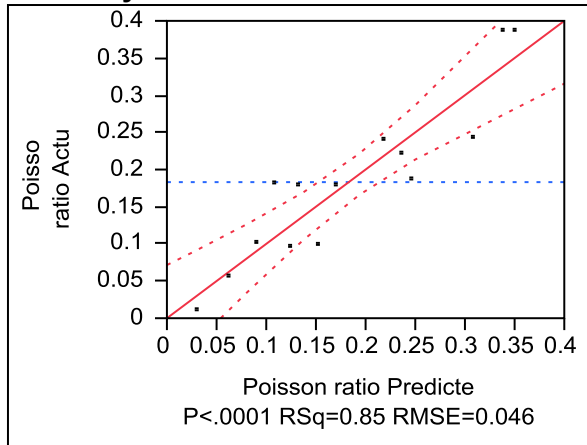
**Moisture content, %
Leverage Plot**



Iowa K test Loading 1 Poisson ratio of western Iowa loess (100psi vertical stress)

Whole Model

Actual by Predicted Plot



Summary of Fit

RSquare	0.848652
RSquare Adj	0.821134
Root Mean Square Error	0.046734
Mean of Response	0.183063
Observations (or Sum Wgts)	14

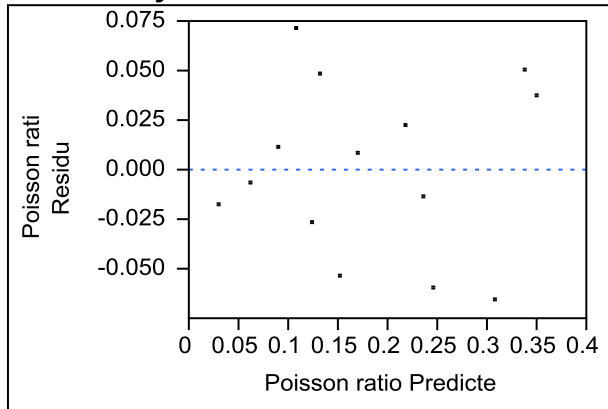
Analysis of Variance

Source	DF	Sum of Squares	Mean Square	F Ratio
Model	2	0.13471086	0.067355	30.8400
Error	11	0.02402430	0.002184	Prob > F
C. Total	13	0.15873516		<.0001*

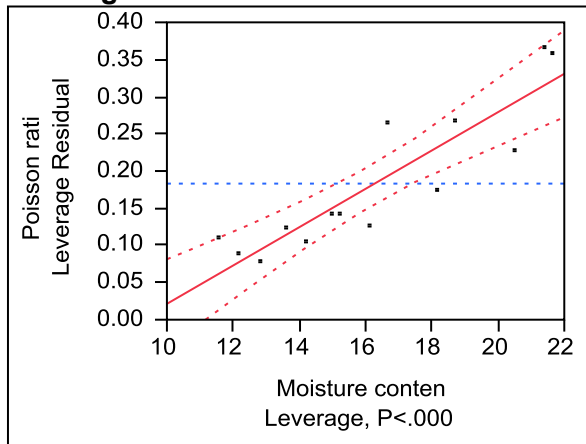
Parameter Estimates

Term	Estimate	Std Error	t Ratio	Prob> t
Intercept	0.4548325	0.238059	1.91	0.0825
Moisture content	0.0257906	0.003848	6.70	<.0001*
Dry unit weight	-0.006583	0.002103	-3.13	0.0096*

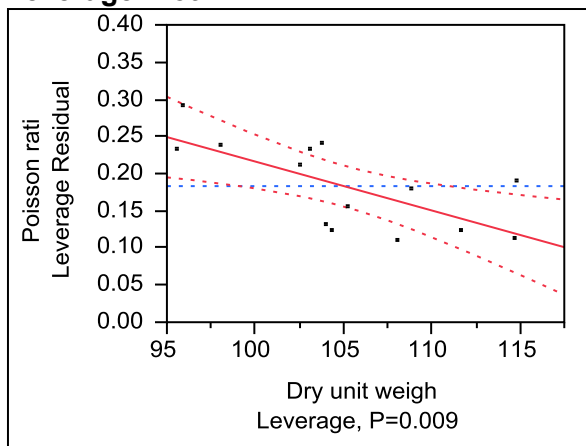
Residual by Predicted Plot



Moisture content Leverage Plot



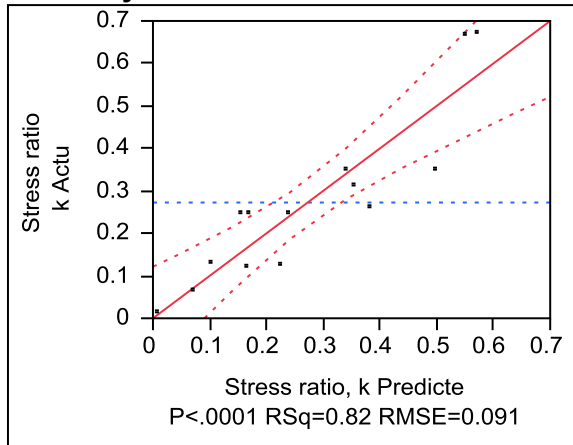
Dry unit weight Leverage Plot



Iowa K test Loading 1 lateral stress ratio, k of western Iowa loess (100psi vertical stress)

Whole Model

Actual by Predicted Plot



Summary of Fit

RSquare	0.821159
RSquare Adj	0.788643
Root Mean Square Error	0.09108
Mean of Response	0.272502
Observations (or Sum Wgts)	14

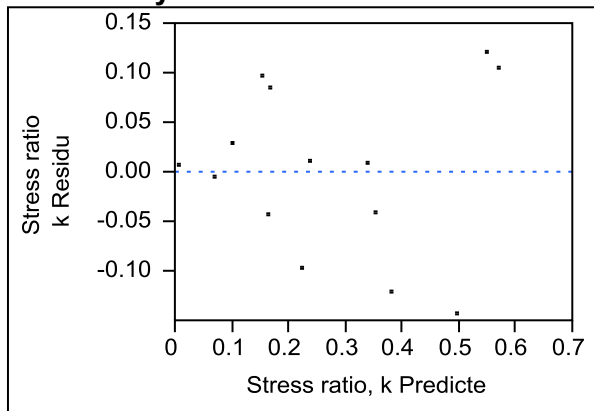
Analysis of Variance

Source	DF	Sum of Squares	Mean Square	F Ratio
Model	2	0.41898811	0.209494	25.2536
Error	11	0.09125178	0.008296	Prob > F
C. Total	13	0.51023989		<.0001*

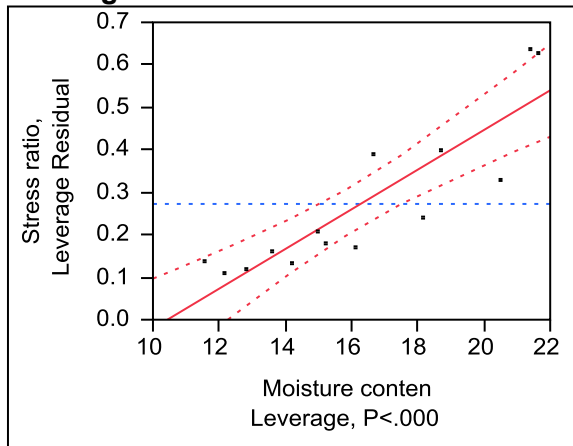
Parameter Estimates

Term	Estimate	Std Error	t Ratio	Prob> t
Intercept	0.6037332	0.46396	1.30	0.2198
Moisture content	0.046696	0.0075	6.23	<.0001*
Dry unit weight	-0.010389	0.004099	-2.53	0.0277*

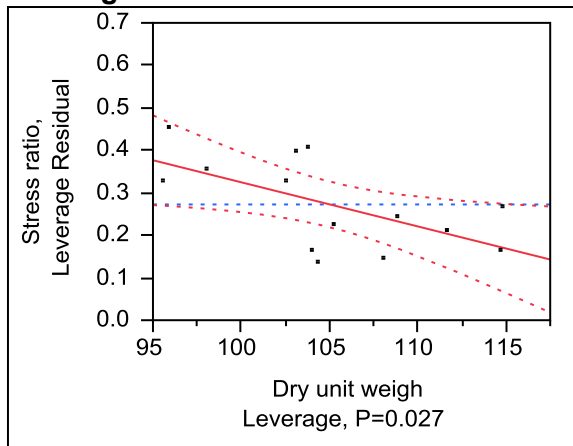
Residual by Predicted Plot



**Moisture content
Leverage Plot**

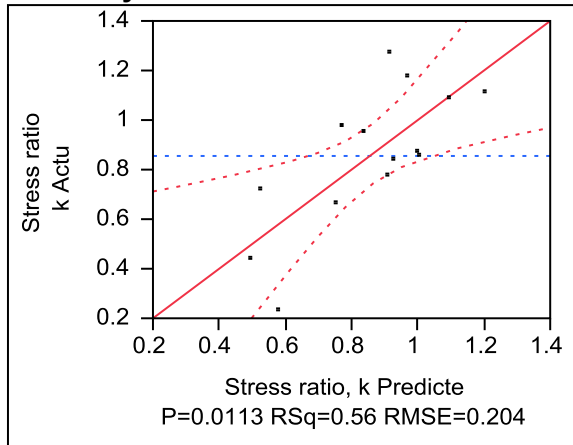


**Dry unit weight
Leverage Plot**



**Iowa K test Loading 2 lateral stress ratio, k of western Iowa loess (25psi vertical stress)
Whole Model**

Actual by Predicted Plot



Summary of Fit

RSquare	0.557321
RSquare Adj	0.476834
Root Mean Square Error	0.204662
Mean of Response	0.855128
Observations (or Sum Wgts)	14

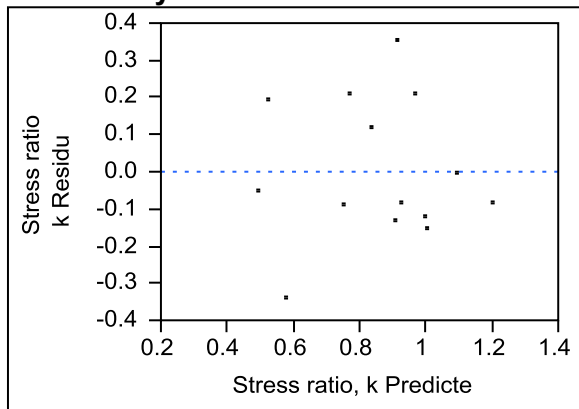
Analysis of Variance

Source	DF	Sum of Squares	Mean Square	F Ratio
Model	2	0.5800760	0.290038	6.9244
Error	11	0.4607526	0.041887	Prob > F
C. Total	13	1.0408286		0.0113*

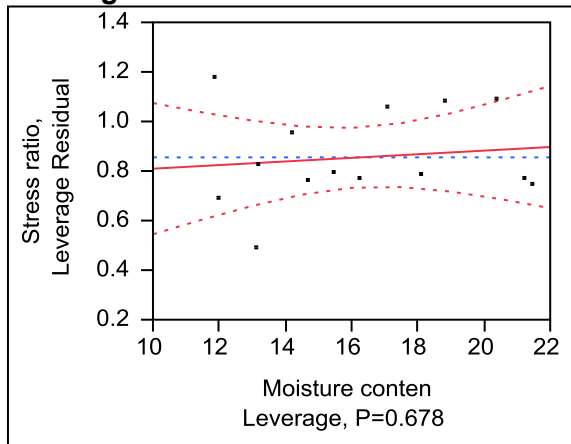
Parameter Estimates

Term	Estimate	Std Error	t Ratio	Prob> t
Intercept	4.625112	1.195245	3.87	0.0026*
Moisture content	0.0072771	0.017079	0.43	0.6783
Loading 2 Dry unit weight	-0.036094	0.010246	-3.52	0.0048*

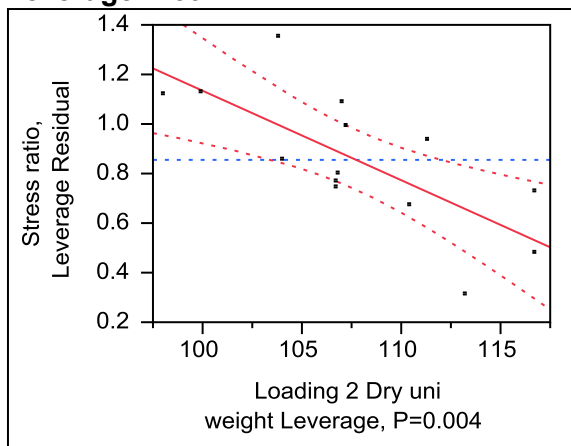
Residual by Predicted Plot



Moisture content Leverage Plot



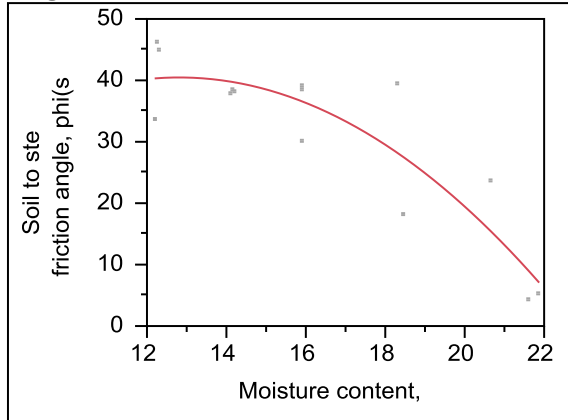
Loading 2 Dry unit weight Leverage Plot



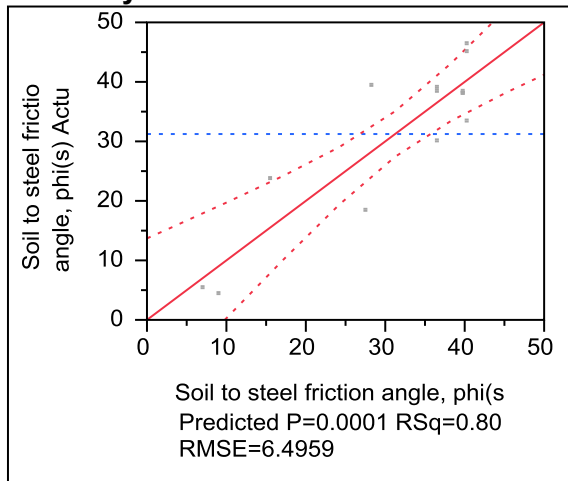
Iowa K test soil to steel friction angle, phi(s) of western Iowa loess

Whole Model

Regression Plot



Actual by Predicted Plot



Summary of Fit

RSquare	0.803569
RSquare Adj	0.767854
Root Mean Square Error	6.495857
Mean of Response	31.23571
Observations (or Sum Wgts)	14

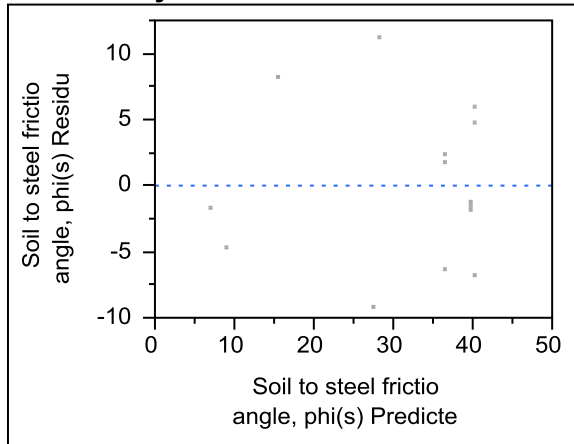
Analysis of Variance

Source	DF	Sum of Squares	Mean Square	F Ratio
Model	2	1898.7945	949.397	22.4996
Error	11	464.1577	42.196	Prob > F
C. Total	13	2362.9521		0.0001*

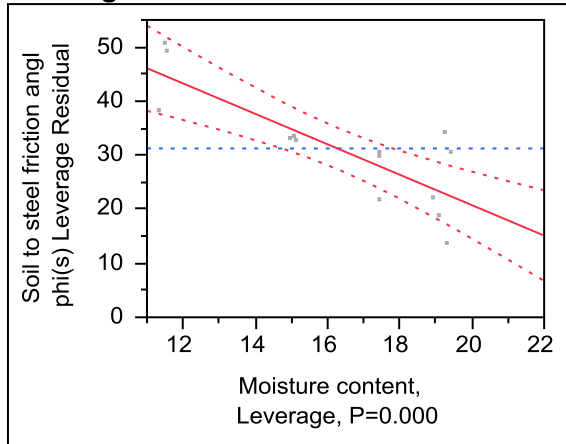
Parameter Estimates

Term	Estimate	Std Error	t Ratio	Prob> t
Intercept	81.396483	9.06611	8.98	<.0001*
Moisture content, %	-2.814328	0.591054	-4.76	0.0006*
(Moisture content, %-16.2715)*(Moisture content, %-16.2715)	-0.406649	0.191498	-2.12	0.0572

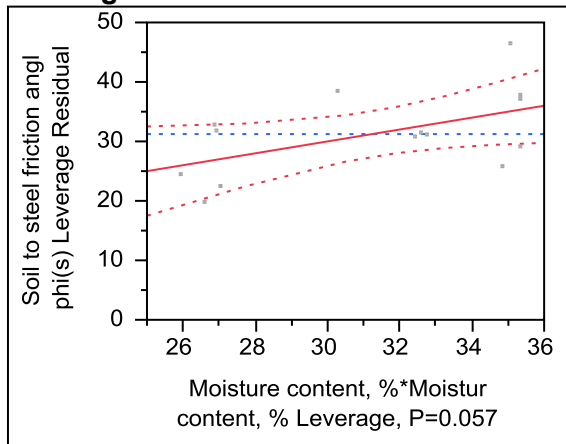
Residual by Predicted Plot



**Moisture content, %
Leverage Plot**



**Moisture content, %*Moisture content, %
Leverage Plot**

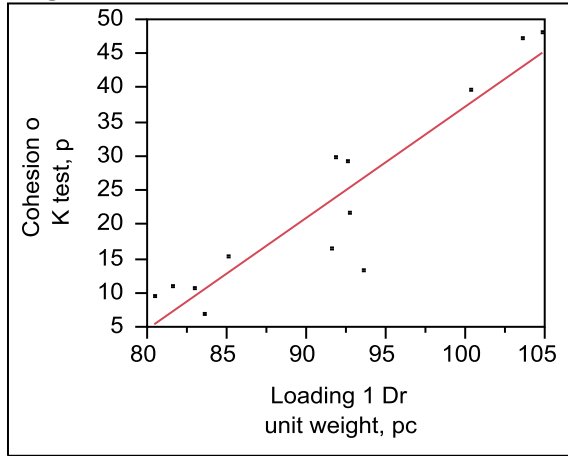


Texas fat clay (CFED 2043)

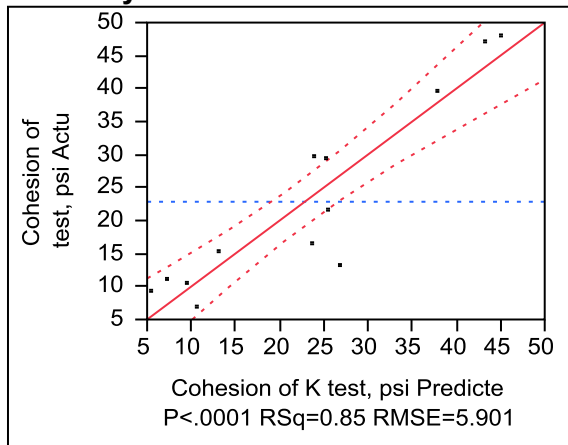
Iowa K test cohesion (psi) of Texas fat clay

Whole Model

Regression Plot



Actual by Predicted Plot



Summary of Fit

RSquare	0.848101
RSquare Adj	0.834292
Root Mean Square Error	5.901685
Mean of Response	22.84489
Observations (or Sum Wgts)	13

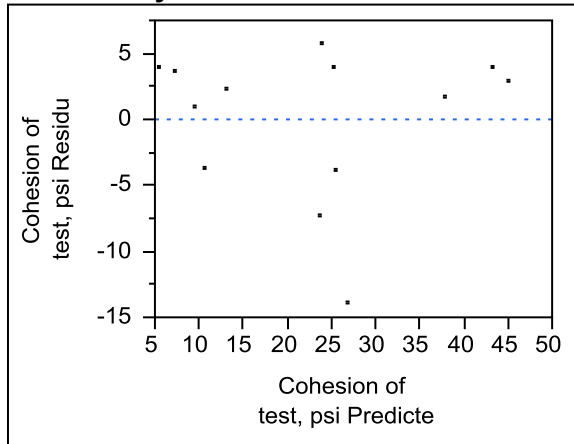
Analysis of Variance

Source	DF	Sum of Squares	Mean Square	F Ratio
Model	1	2139.1354	2139.14	61.4167
Error	11	383.1287	34.83	Prob > F
C. Total	12	2522.2641		<.0001*

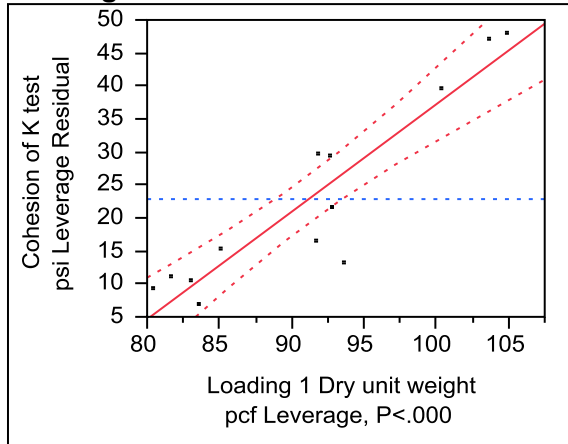
Parameter Estimates

Term	Estimate	Std Error	t Ratio	Prob> t
Intercept	-125.6721	19.0216	-6.61	<.0001*
Loading 1 Dry unit weight, pcf	1.6289298	0.207854	7.84	<.0001*

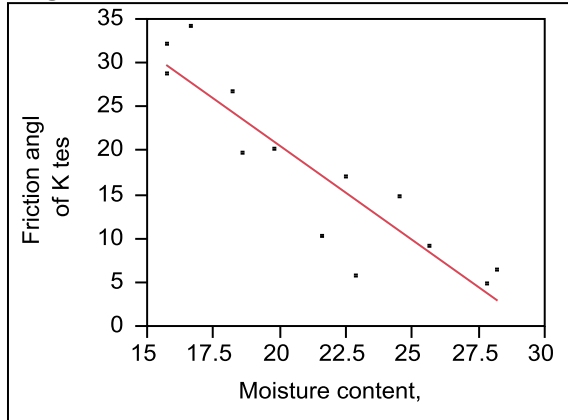
Residual by Predicted Plot



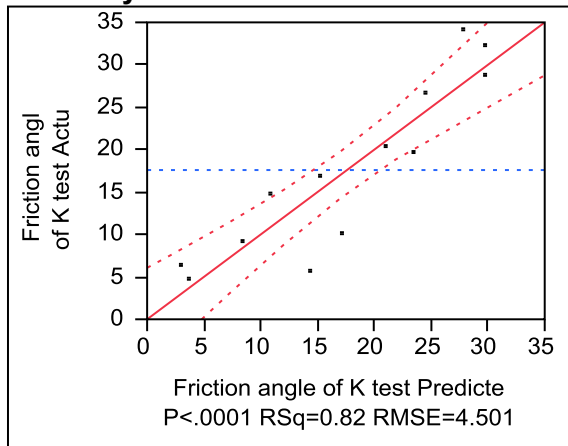
**Loading 1 Dry unit weight, pcf
Leverage Plot**



**Iowa K test Friction angle of Texas fat clay
Whole Model
Regression Plot**



Actual by Predicted Plot



Summary of Fit

RSquare	0.824578
RSquare Adj	0.808631
Root Mean Square Error	4.501478
Mean of Response	17.59231
Observations (or Sum Wgts)	13

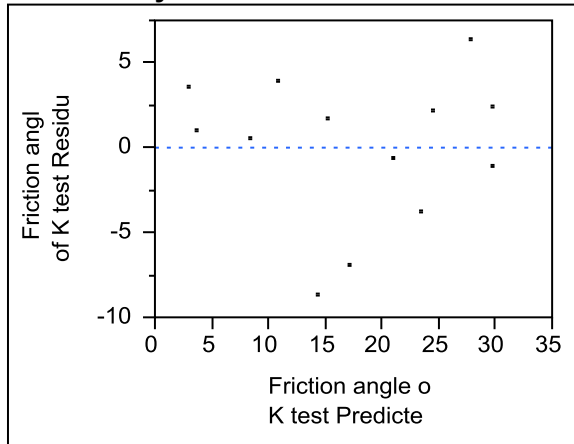
Analysis of Variance

Source	DF	Sum of Squares	Mean Square	F Ratio
Model	1	1047.7329	1047.73	51.7059
Error	11	222.8964	20.26	Prob > F
C. Total	12	1270.6292		<.0001*

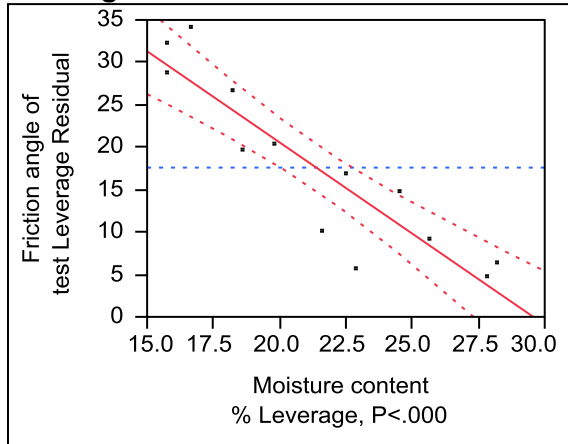
Parameter Estimates

Term	Estimate	Std Error	t Ratio	Prob> t
Intercept	63.543028	6.511131	9.76	<.0001*
Moisture content, %	-2.148983	0.298857	-7.19	<.0001*

Residual by Predicted Plot



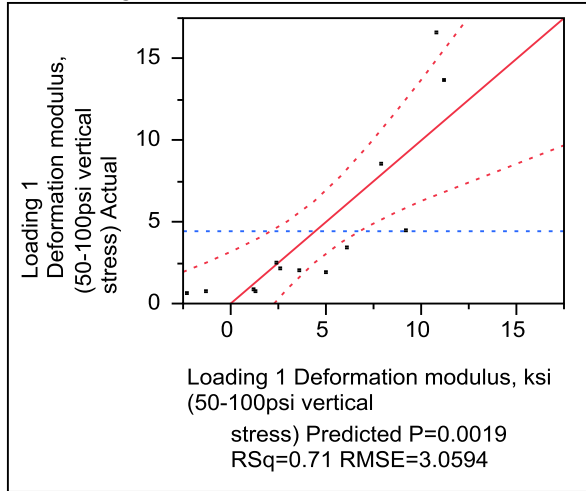
**Moisture content, %
Leverage Plot**



Iowa K test Loading 1 Deformation modulus, ksi of Texas fat clay (50-100psi vertical stress)

Whole Model

Actual by Predicted Plot



Summary of Fit

RSquare	0.713162
RSquare Adj	0.655795
Root Mean Square Error	3.059351
Mean of Response	4.435538
Observations (or Sum Wgts)	13

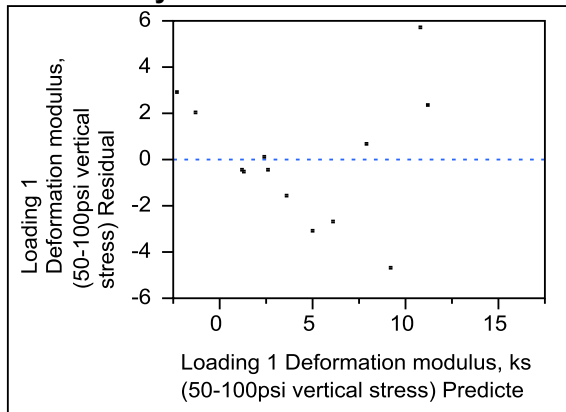
Analysis of Variance

Source	DF	Sum of Squares	Mean Square	F Ratio
Model	2	232.70774	116.354	12.4315
Error	10	93.59631	9.360	Prob > F
C. Total	12	326.30405		0.0019*

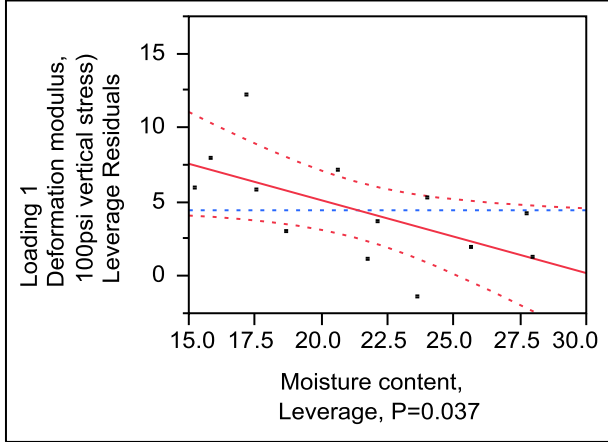
Parameter Estimates

Term	Estimate	Std Error	t Ratio	Prob> t
Intercept	-25.41412	11.26374	-2.26	0.0477*
Moisture content, %	-0.490782	0.204326	-2.40	0.0372*
Loading 1 Dry unit weight, pcf	0.4424898	0.108393	4.08	0.0022*

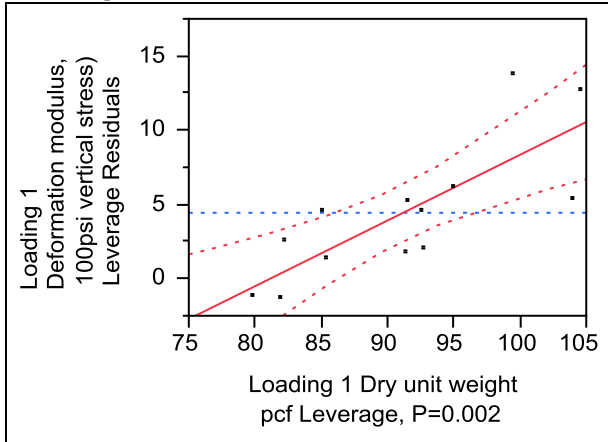
Residual by Predicted Plot



**Moisture content, %
Leverage Plot**



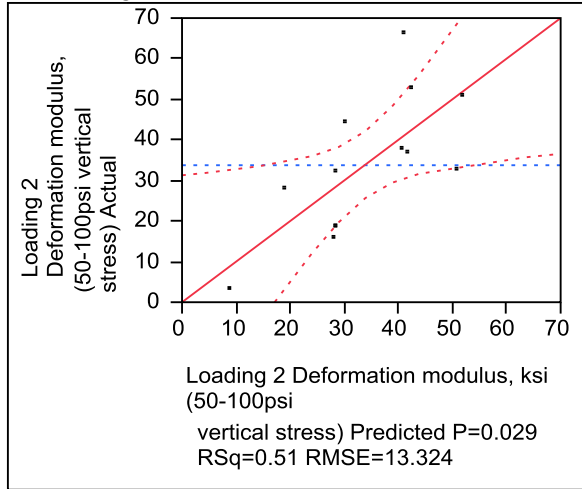
**Loading 1 Dry unit weight, pcf
Leverage Plot**



Iowa K test Loading 2 Deformation modulus, ksi of Texas fat clay (50-100psi vertical stress)

Whole Model

Actual by Predicted Plot



Summary of Fit

RSquare	0.507434
RSquare Adj	0.408921
Root Mean Square Error	13.32422
Mean of Response	33.75031
Observations (or Sum Wgts)	13

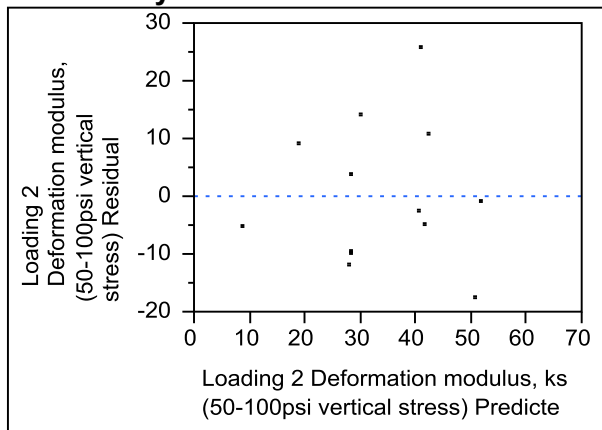
Analysis of Variance

Source	DF	Sum of Squares	Mean Square	F Ratio
Model	2	1828.9358	914.468	5.1509
Error	10	1775.3472	177.535	Prob > F
C. Total	12	3604.2830		0.0290*

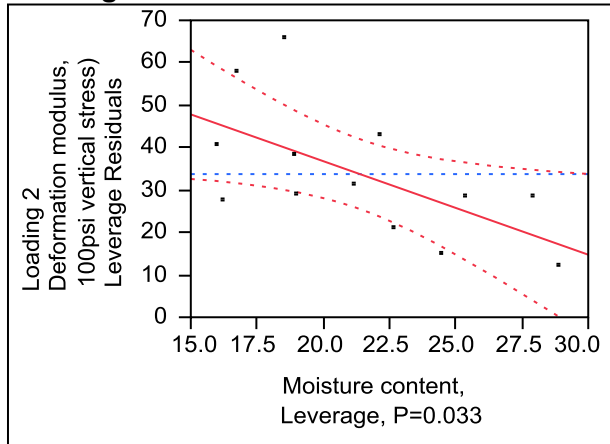
Parameter Estimates

Term	Estimate	Std Error	t Ratio	Prob> t
Intercept	-79.41964	68.20628	-1.16	0.2713
Moisture content, %	-2.204977	0.892512	-2.47	0.0331*
Loading 2 Dry unit weight, pcf	1.6267162	0.689592	2.36	0.0400*

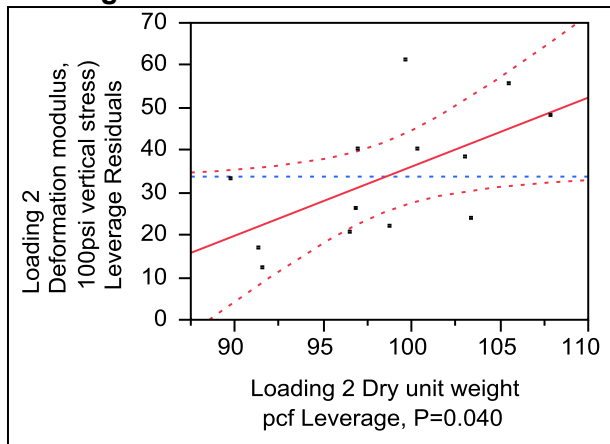
Residual by Predicted Plot



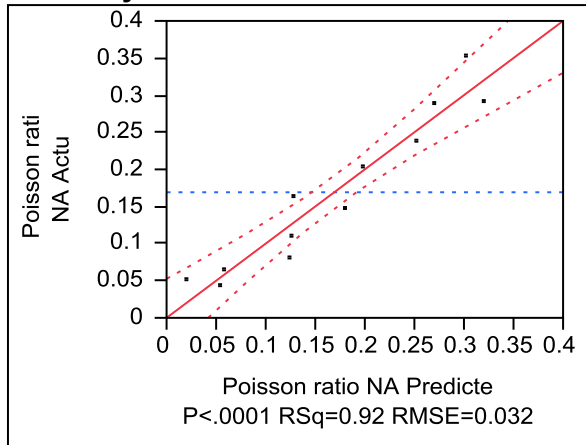
**Moisture content, %
Leverage Plot**



**Loading 2 Dry unit weight, pcf
Leverage Plot**



**Iowa K test Loading 1 Poisson ratio of Texas fat clay (100psi vertical stress)
Whole Model
Actual by Predicted Plot**



Summary of Fit

RSquare	0.921905
RSquare Adj	0.90455
Root Mean Square Error	0.032486
Mean of Response	0.169164
Observations (or Sum Wgts)	12

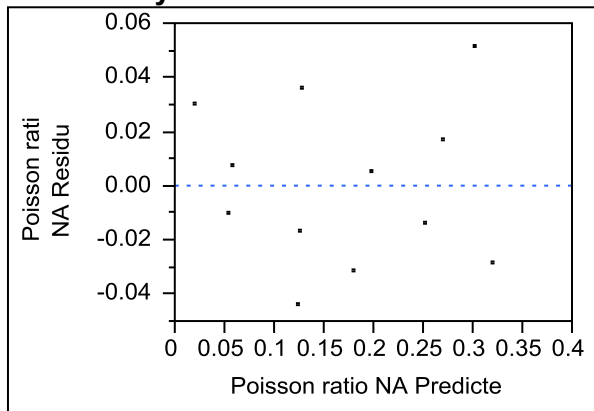
Analysis of Variance

Source	DF	Sum of Squares	Mean Square	F Ratio
Model	2	0.11212238	0.056061	53.1218
Error	9	0.00949800	0.001055	Prob > F
C. Total	11	0.12162037		<.0001*

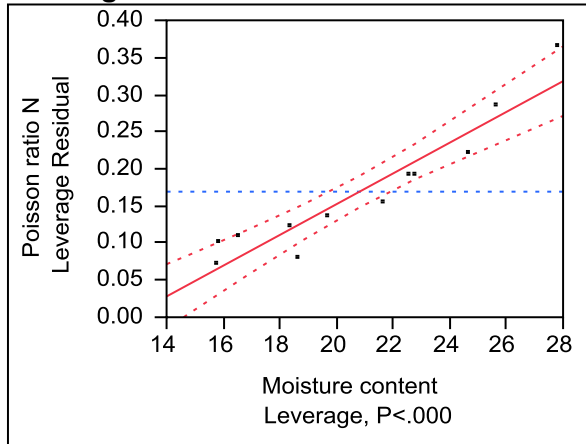
Parameter Estimates

Term	Estimate	Std Error	t Ratio	Prob> t
Intercept	0.4050633	0.119798	3.38	0.0081*
Moisture content %	0.0207192	0.002448	8.46	<.0001*
Dry unit weight pcf	-0.007267	0.001191	-6.10	0.0002*

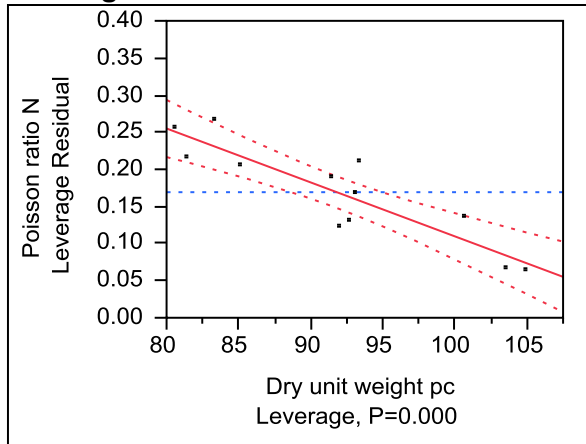
Residual by Predicted Plot



**Moisture content %
Leverage Plot**

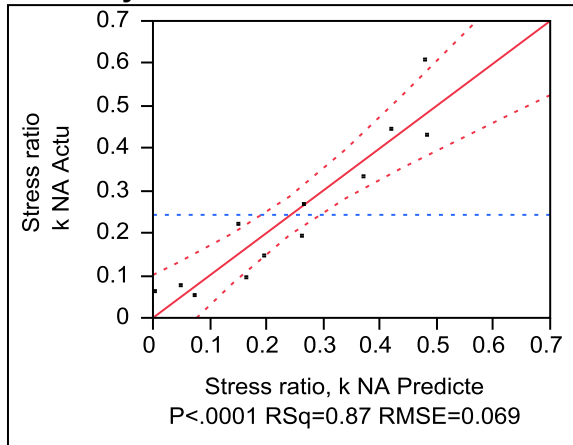


**Dry unit weight pcf
Leverage Plot**



Iowa K test loading 1 lateral stress ratio, of Texas fat clay (100psi vertical stress)
Whole Model

Actual by Predicted Plot



Summary of Fit

RSquare	0.874357
RSquare Adj	0.846437
Root Mean Square Error	0.069542
Mean of Response	0.242835
Observations (or Sum Wgts)	12

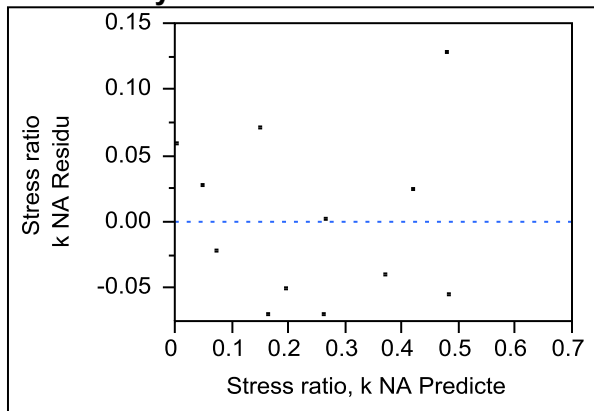
Analysis of Variance

Source	DF	Sum of Squares	Mean Square	F Ratio
Model	2	0.30289319	0.151447	31.3158
Error	9	0.04352494	0.004836	Prob > F
C. Total	11	0.34641813		<.0001*

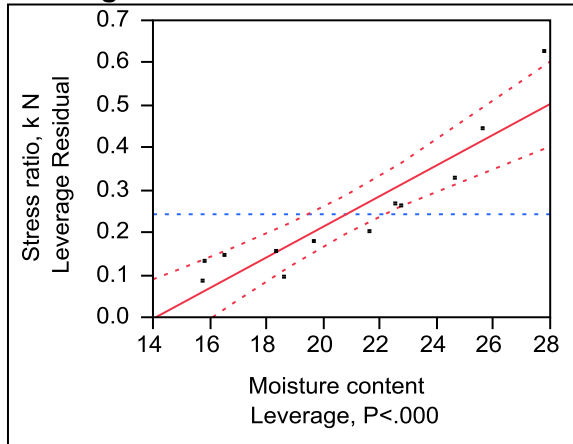
Parameter Estimates

Term	Estimate	Std Error	t Ratio	Prob> t
Intercept	0.4369654	0.25645	1.70	0.1226
Moisture content %	0.0361811	0.00524	6.90	<.0001*
Dry unit weight pcf	-0.010317	0.00255	-4.05	0.0029*

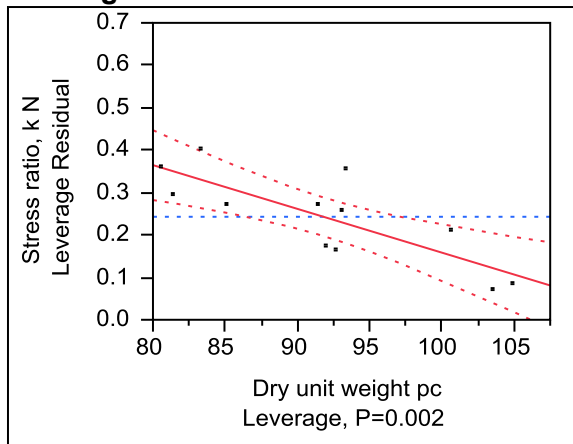
Residual by Predicted Plot



**Moisture content %
Leverage Plot**



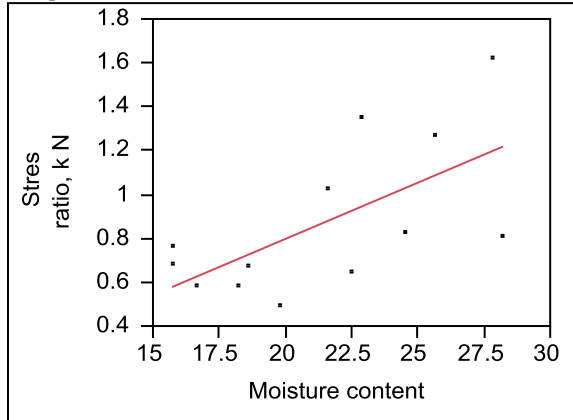
**Dry unit weight pcf
Leverage Plot**



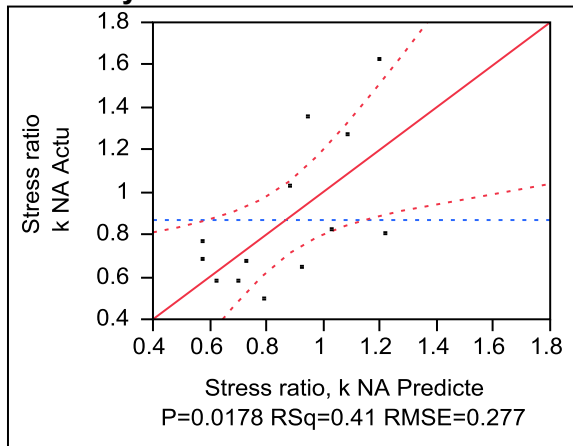
Iowa K test loading 2 lateral stress ratio, of Texas fat clay (30psi vertical stress)

Whole Model

Regression Plot



Actual by Predicted Plot



Summary of Fit

RSquare	0.412951
RSquare Adj	0.359583
Root Mean Square Error	0.277516
Mean of Response	0.867977
Observations (or Sum Wgts)	13

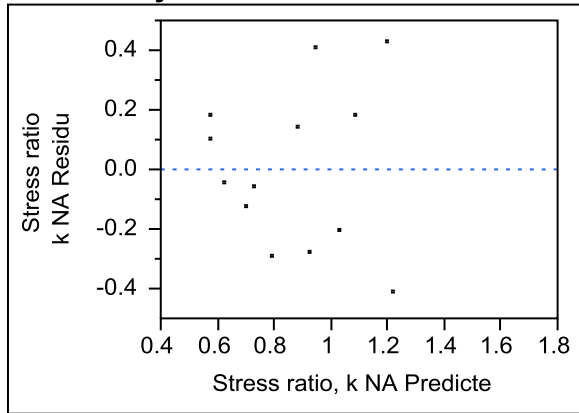
Analysis of Variance

Source	DF	Sum of Squares	Mean Square	F Ratio
Model	1	0.5959261	0.595926	7.7378
Error	11	0.8471643	0.077015	Prob > F
C. Total	12	1.4430904		0.0178*

Parameter Estimates

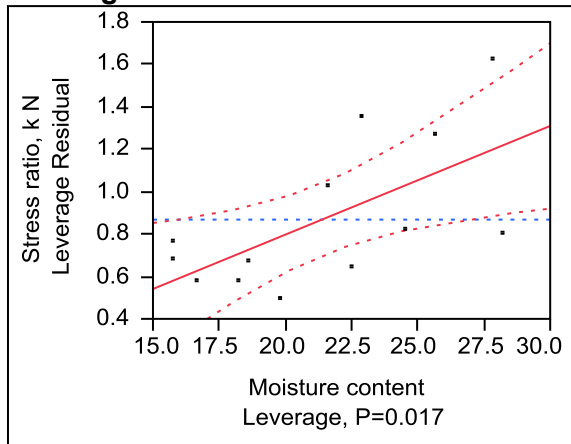
Term	Estimate	Std Error	t Ratio	Prob> t
Intercept	-0.227903	0.401411	-0.57	0.5816
Moisture content %	0.0512512	0.018424	2.78	0.0178*

Residual by Predicted Plot



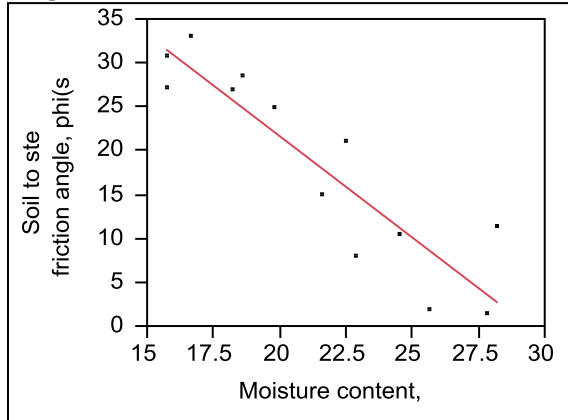
Moisture content %

Leverage Plot

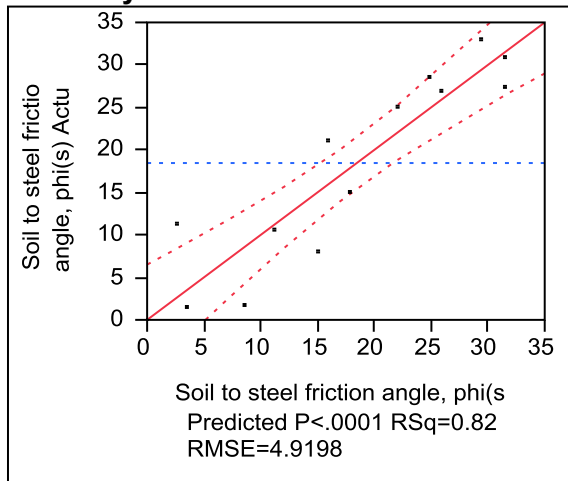


**Iowa K test soil to steel friction angle, phi(s) of Texas fat clay
Whole Model**

Regression Plot



Actual by Predicted Plot



Summary of Fit

RSquare	0.819575
RSquare Adj	0.803173
Root Mean Square Error	4.919788
Mean of Response	18.45385
Observations (or Sum Wgts)	13

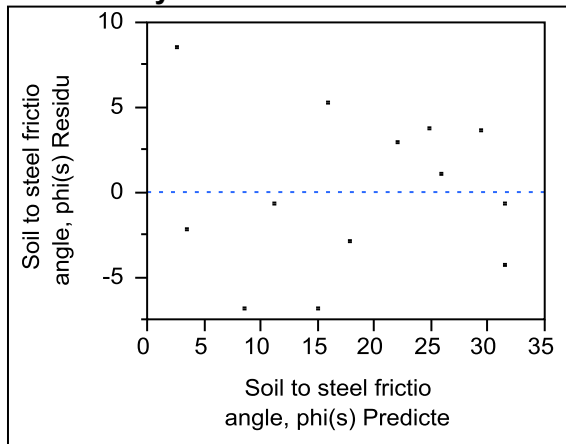
Analysis of Variance

Source	DF	Sum of Squares	Mean Square	F Ratio
Model	1	1209.4248	1209.42	49.9673
Error	11	266.2475	24.20	Prob > F
C. Total	12	1475.6723		<.0001*

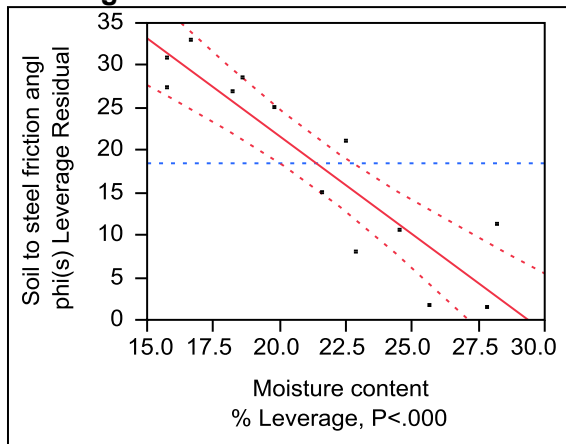
Parameter Estimates

Term	Estimate	Std Error	t Ratio	Prob> t
Intercept	67.82309	7.116193	9.53	<.0001*
Moisture content, %	-2.308858	0.326629	-7.07	<.0001*

Residual by Predicted Plot



Moisture content, % Leverage Plot

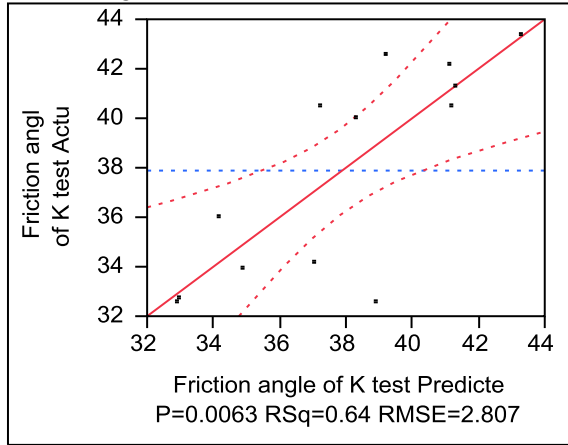


WCF fly ash (CFED 2053)

Iowa K test Friction angle of WCF fly ash

Whole Model

Actual by Predicted Plot



Summary of Fit

RSquare	0.636575
RSquare Adj	0.56389
Root Mean Square Error	2.807203
Mean of Response	37.88462
Observations (or Sum Wgts)	13

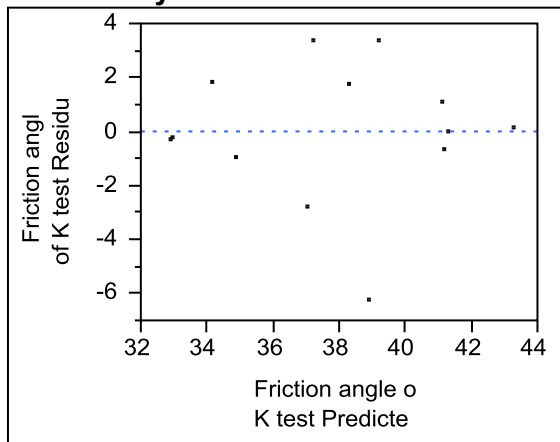
Analysis of Variance

Source	DF	Sum of Squares	Mean Square	F Ratio
Model	2	138.03305	69.0165	8.7580
Error	10	78.80387	7.8804	Prob > F
C. Total	12	216.83692		0.0063*

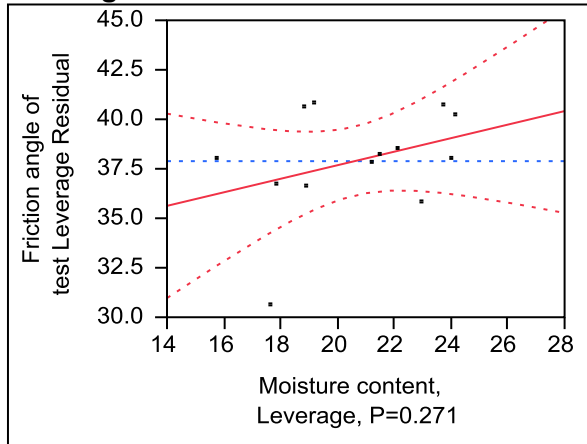
Parameter Estimates

Term	Estimate	Std Error	t Ratio	Prob> t
Intercept	-104.1125	41.22147	-2.53	0.0301*
Moisture content, %	0.3420086	0.293936	1.16	0.2716
Loading 1 Dry unit weight, pcf	1.6303831	0.443702	3.67	0.0043*

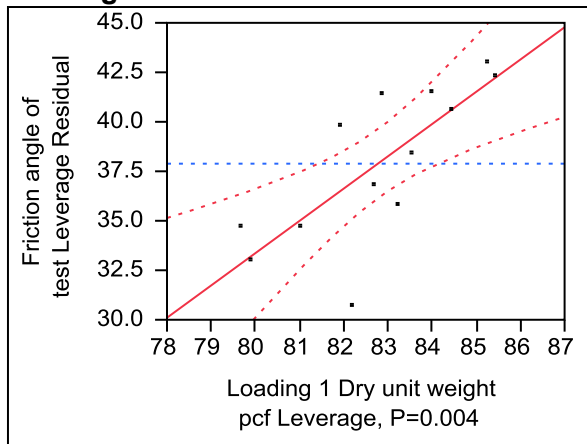
Residual by Predicted Plot



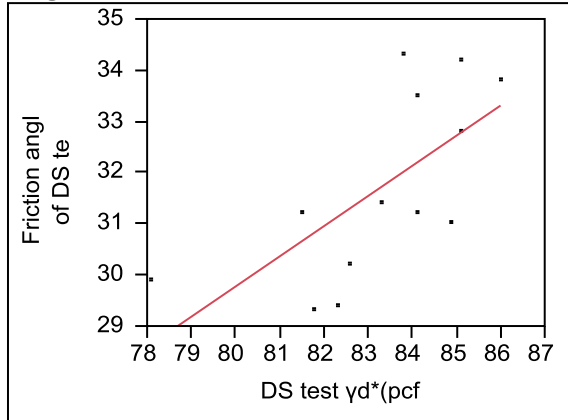
**Moisture content, %
Leverage Plot**



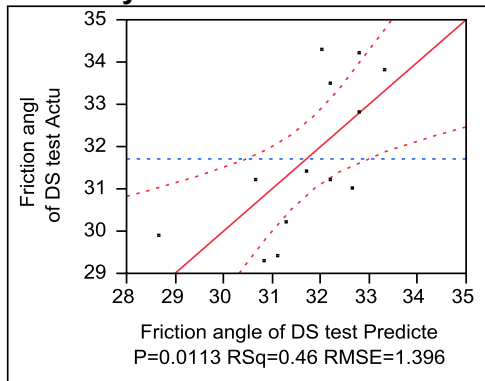
**Loading 1 Dry unit weight, pcf
Leverage Plot**



**Direct shear test friction angle of WCF fly ash
Whole Model
Regression Plot**



Actual by Predicted Plot



Summary of Fit

RSquare	0.456526
RSquare Adj	0.40712
Root Mean Square Error	1.396794
Mean of Response	31.70769
Observations (or Sum Wgts)	13

Analysis of Variance

Source	DF	Sum of Squares	Mean Square	F Ratio
Model	1	18.027871	18.0279	9.2402
Error	11	21.461359	1.9510	Prob > F
C. Total	12	39.489231		0.0113*

Lack of Fit

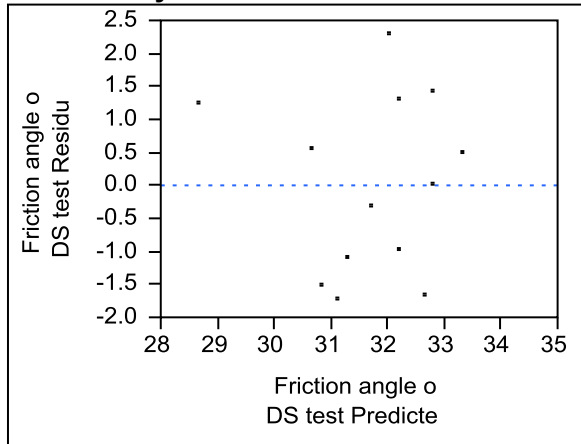
Source	DF	Sum of Squares	Mean Square	F Ratio
Lack Of Fit	9	17.836359	1.98182	1.0934
Pure Error	2	3.625000	1.81250	Prob > F
Total Error	11	21.461359		0.5651

Max RSq

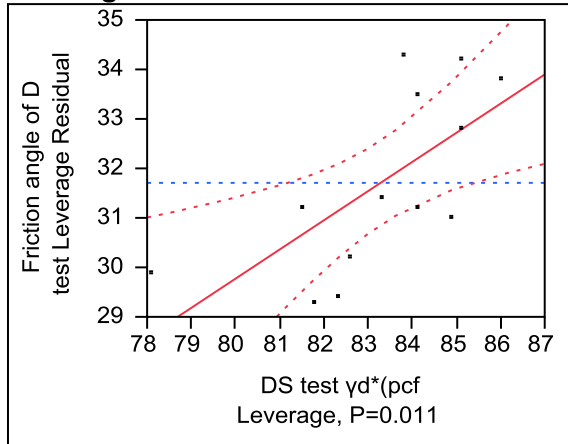
Parameter Estimates

Term	Estimate	Std Error	t Ratio	Prob> t
Intercept	-17.38874	16.15604	-1.08	0.3048
DS test γ_d *(pcf)	0.5895018	0.19393	3.04	0.0113*

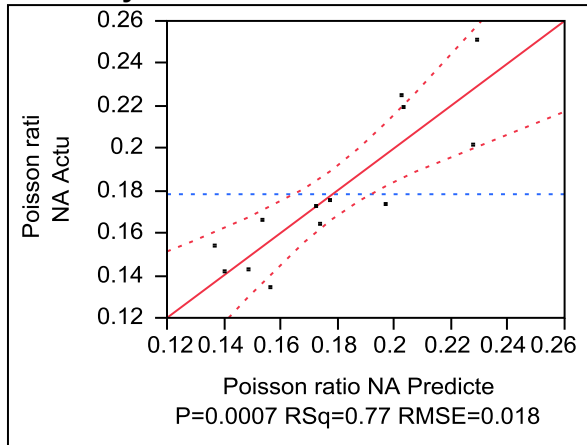
Residual by Predicted Plot



**DS test $\gamma_d^*(pcf)$
Leverage Plot**



**Iowa K test Loading 1 Poisson ratio of WCF fly ash (100psi vertical stress)
Whole Model
Actual by Predicted Plot**



Summary of Fit

RSquare	0.768862
RSquare Adj	0.722634
Root Mean Square Error	0.01878
Mean of Response	0.178286
Observations (or Sum Wgts)	13

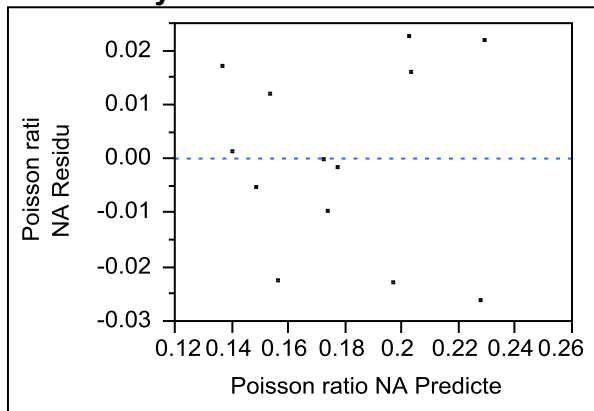
Analysis of Variance

Source	DF	Sum of Squares	Mean Square	F Ratio
Model	2	0.01173176	0.005866	16.6321
Error	10	0.00352684	0.000353	Prob > F
C. Total	12	0.01525860		0.0007*

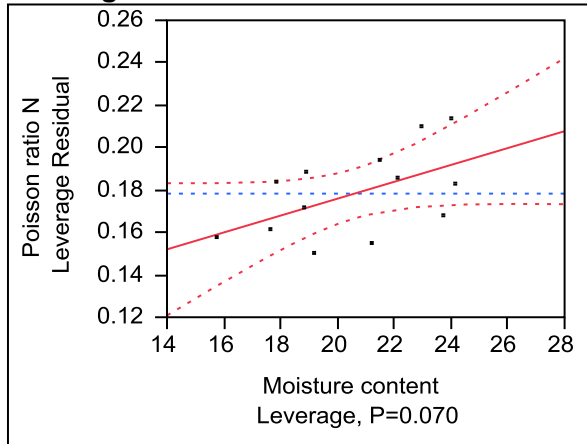
Parameter Estimates

Term	Estimate	Std Error	t Ratio	Prob> t
Intercept	0.6887366	0.275767	2.50	0.0316*
Moisture content %	0.0039798	0.001966	2.02	0.0705
Dry unit weight pcf	-0.007157	0.002968	-2.41	0.0366*

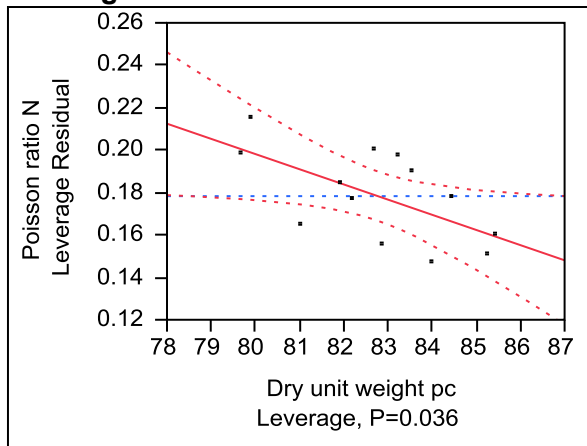
Residual by Predicted Plot



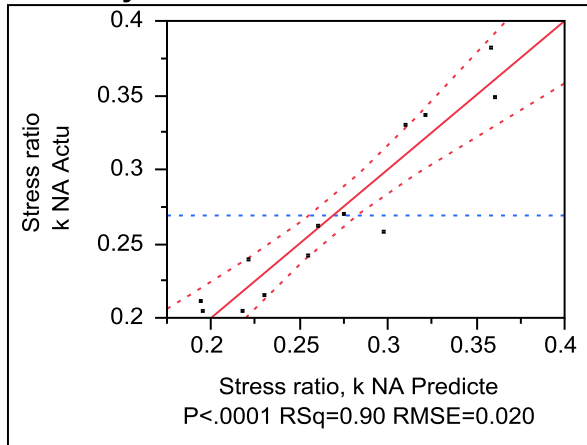
**Moisture content %
Leverage Plot**



**Dry unit weight pcf
Leverage Plot**



**Iowa K test Loading 1 lateral stress ratio, k of WCF fly ash (100psi vertical stress)
Whole Model
Actual by Predicted Plot**



Summary of Fit

RSquare	0.901142
RSquare Adj	0.881371
Root Mean Square Error	0.020762
Mean of Response	0.268935
Observations (or Sum Wgts)	13

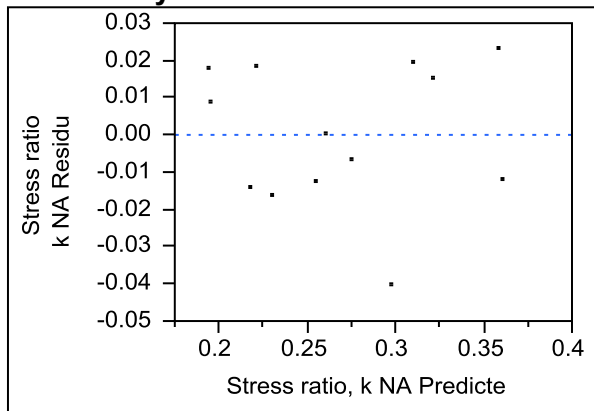
Analysis of Variance

Source	DF	Sum of Squares	Mean Square	F Ratio
Model	2	0.03929465	0.019647	45.5777
Error	10	0.00431074	0.000431	Prob > F
C. Total	12	0.04360538		<.0001*

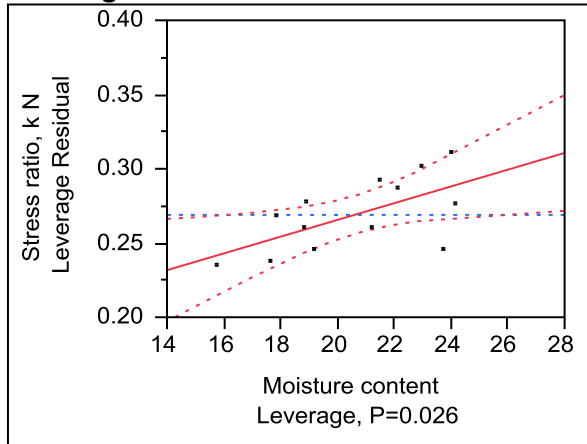
Parameter Estimates

Term	Estimate	Std Error	t Ratio	Prob> t
Intercept	1.4292674	0.304877	4.69	0.0009*
Moisture content %	0.005641	0.002174	2.59	0.0267*
Dry unit weight pcf	-0.015422	0.003282	-4.70	0.0008*

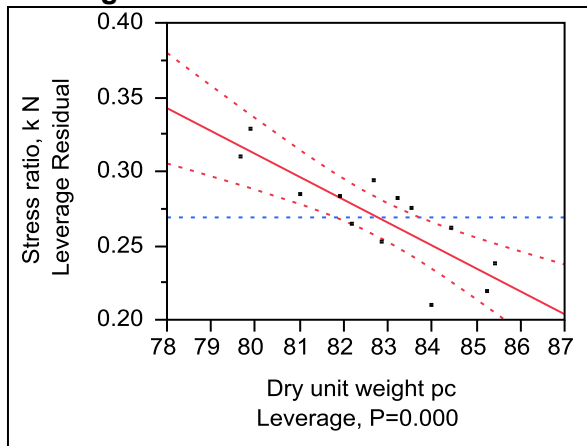
Residual by Predicted Plot



**Moisture content %
Leverage Plot**



**Dry unit weight pcf
Leverage Plot**

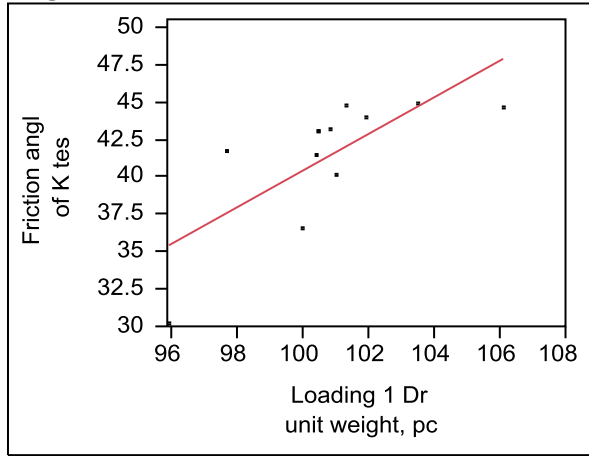


WCF gypsum (CFED 2054)

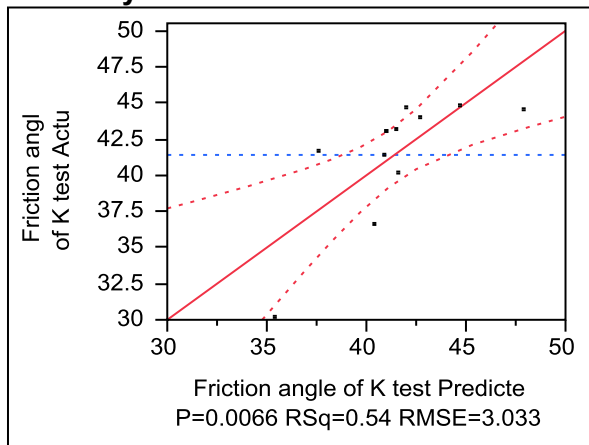
Iowa K test friction angle of WCF gypsum

Whole Model

Regression Plot



Actual by Predicted Plot



Summary of Fit

RSquare	0.538135
RSquare Adj	0.491948
Root Mean Square Error	3.033769
Mean of Response	41.40876
Observations (or Sum Wgts)	12

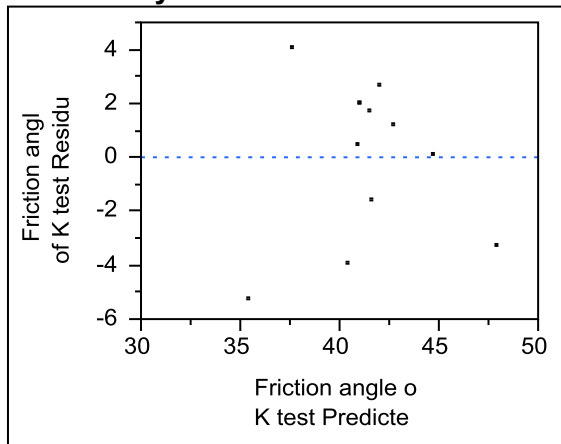
Analysis of Variance

Source	DF	Sum of Squares	Mean Square	F Ratio
Model	1	107.23607	107.236	11.6513
Error	10	92.03757	9.204	Prob > F
C. Total	11	199.27364		0.0066*

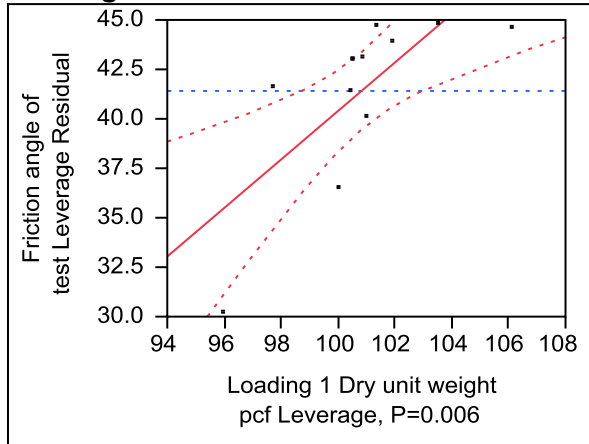
Parameter Estimates

Term	Estimate	Std Error	t Ratio	Prob> t
Intercept	-82.17389	36.21568	-2.27	0.0466*
Loading 1 Dry unit weight, pcf	1.2256679	0.359075	3.41	0.0066*

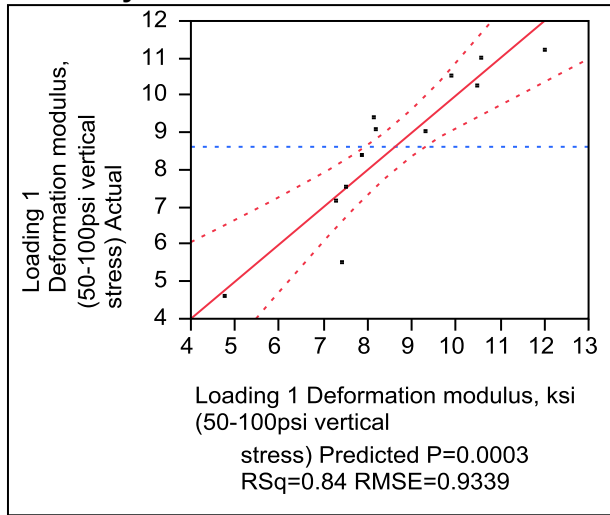
Residual by Predicted Plot



**Loading 1 Dry unit weight, pcf
Leverage Plot**



**Iowa K test loading 1 Deformation modulus, ksi (50-100psi vertical stress)
Whole Model
Actual by Predicted Plot**



Summary of Fit

RSquare	0.83964
RSquare Adj	0.804005
Root Mean Square Error	0.933942
Mean of Response	8.619142
Observations (or Sum Wgts)	12

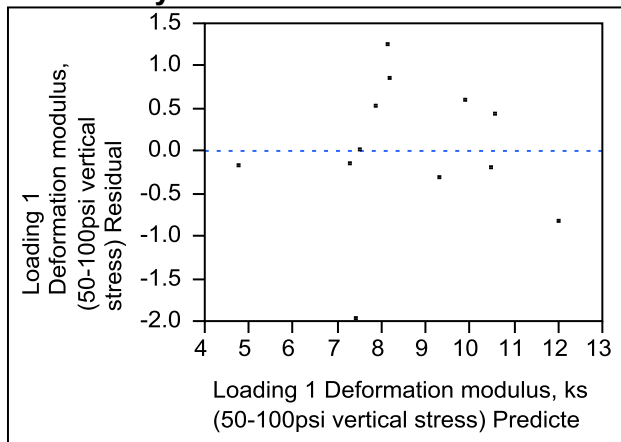
Analysis of Variance

Source	DF	Sum of Squares	Mean Square	F Ratio
Model	2	41.103663	20.5518	23.5619
Error	9	7.850235	0.8722	Prob > F
C. Total	11	48.953898		0.0003*

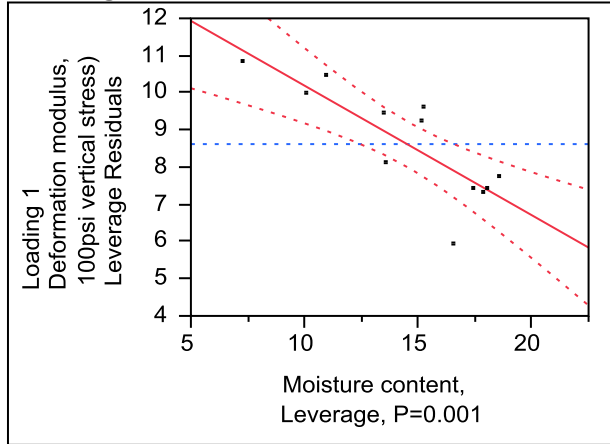
Parameter Estimates

Term	Estimate	Std Error	t Ratio	Prob> t
Intercept	-20.52828	13.00878	-1.58	0.1490
Moisture content, %	-0.34827	0.079054	-4.41	0.0017*
Loading 1 Dry unit weight, pcf	0.3392043	0.123512	2.75	0.0226*

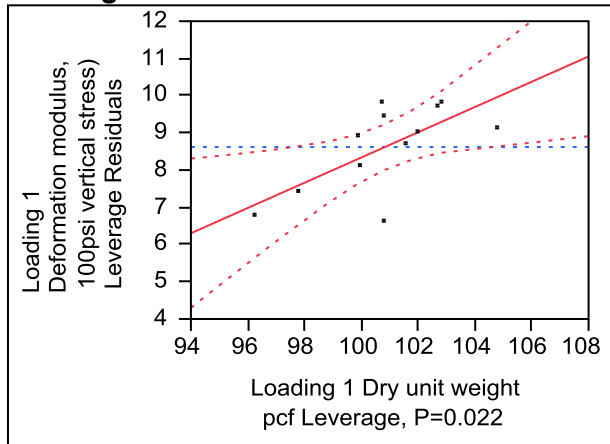
Residual by Predicted Plot



**Moisture content, %
Leverage Plot**



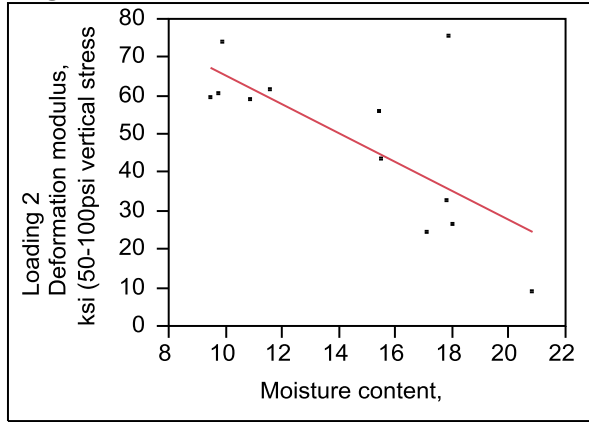
**Loading 1 Dry unit weight, pcf
Leverage Plot**



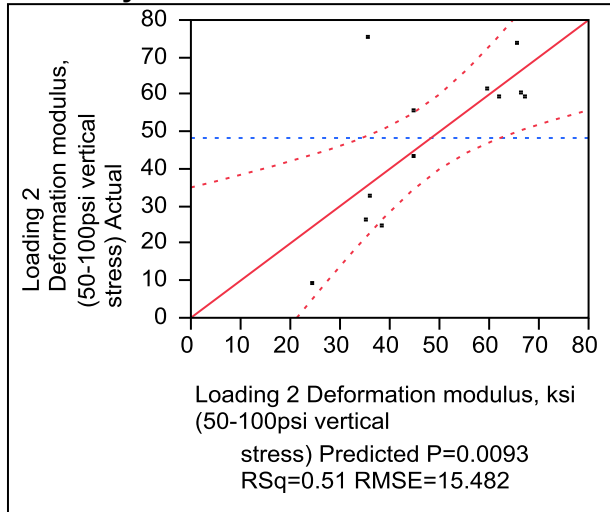
Iowa K test loading 2 Deformation modulus, ksi of WCF gypsum (50-100psi vertical stress)

Whole Model

Regression Plot



Actual by Predicted Plot



Summary of Fit

RSquare	0.507562
RSquare Adj	0.458319
Root Mean Square Error	15.48228
Mean of Response	48.30298
Observations (or Sum Wgts)	12

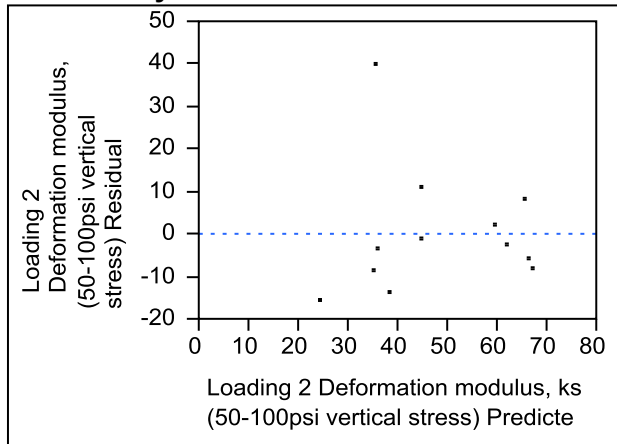
Analysis of Variance

Source	DF	Sum of Squares	Mean Square	F Ratio
Model	1	2470.6315	2470.63	10.3071
Error	10	2397.0086	239.70	Prob > F
C. Total	11	4867.6402		0.0093*

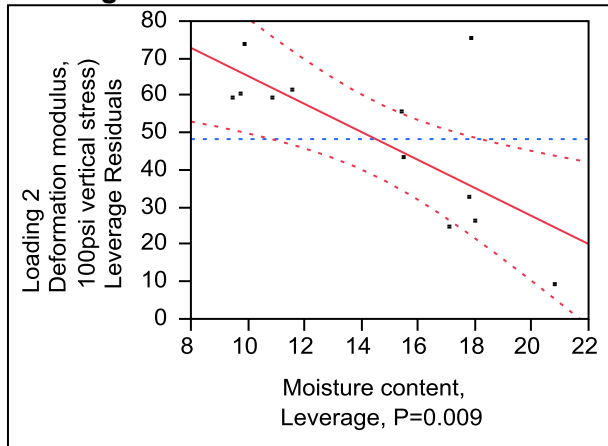
Parameter Estimates

Term	Estimate	Std Error	t Ratio	Prob> t
Intercept	102.94794	17.59784	5.85	0.0002*
Moisture content, %	-3.76546	1.172867	-3.21	0.0093*

Residual by Predicted Plot

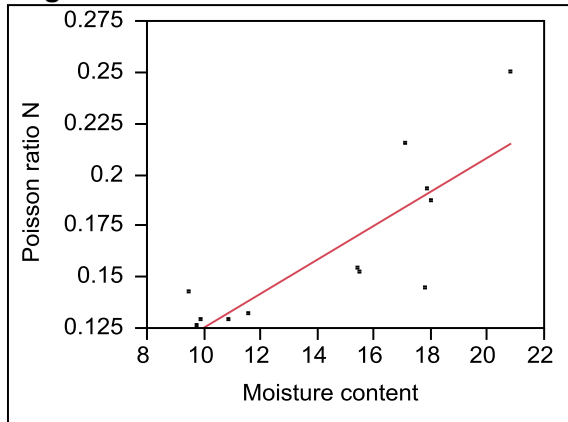


**Moisture content, %
Leverage Plot**

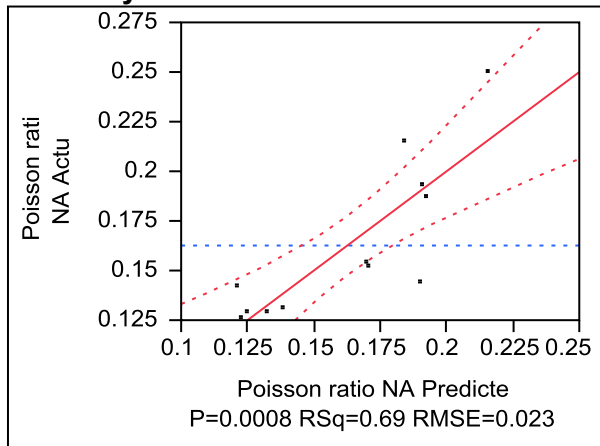


Iowa K test loading 1 Poisson ratio of WCF gypsum (100psi vertical stress)

**Whole Model
Regression Plot**



Actual by Predicted Plot



Summary of Fit

RSquare	0.692531
RSquare Adj	0.661785
Root Mean Square Error	0.023106
Mean of Response	0.162605
Observations (or Sum Wgts)	12

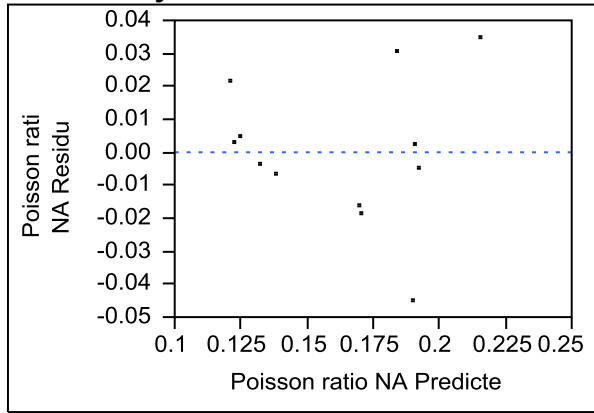
Analysis of Variance

Source	DF	Sum of Squares	Mean Square	F Ratio
Model	1	0.01202505	0.012025	22.5236
Error	10	0.00533886	0.000534	Prob > F
C. Total	11	0.01736391		0.0008*

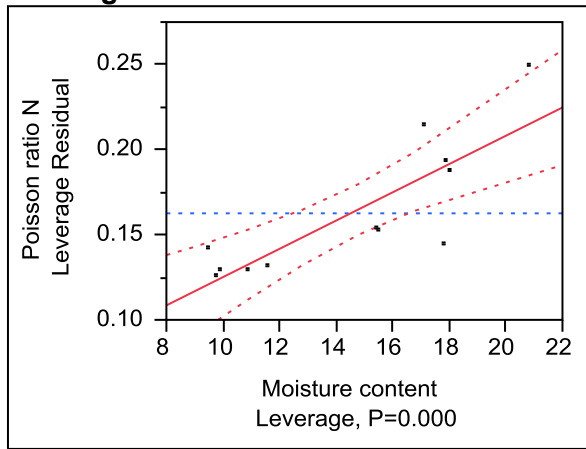
Parameter Estimates

Term	Estimate	Std Error	t Ratio	Prob> t
Intercept	0.0420492	0.026263	1.60	0.1404
Moisture content %	0.0083073	0.00175	4.75	0.0008*

Residual by Predicted Plot

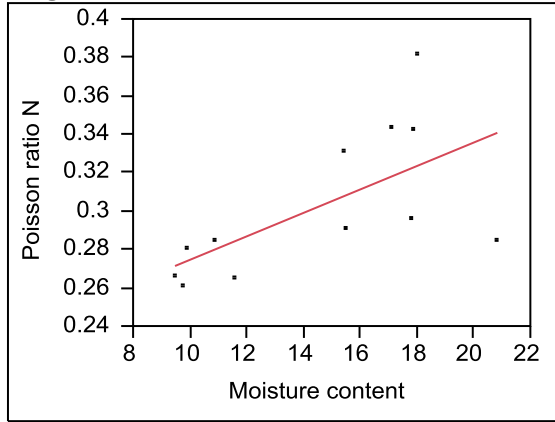


**Moisture content %
Leverage Plot**

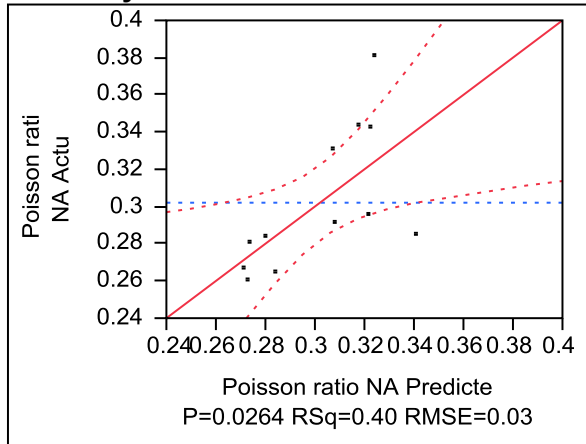


Iowa K test loading 2 Poisson ratio of WCF gypsum (30psi vertical stress)

Whole Model
Regression Plot



Actual by Predicted Plot



Summary of Fit

RSquare	0.403624
RSquare Adj	0.343987
Root Mean Square Error	0.030999
Mean of Response	0.302047
Observations (or Sum Wgts)	12

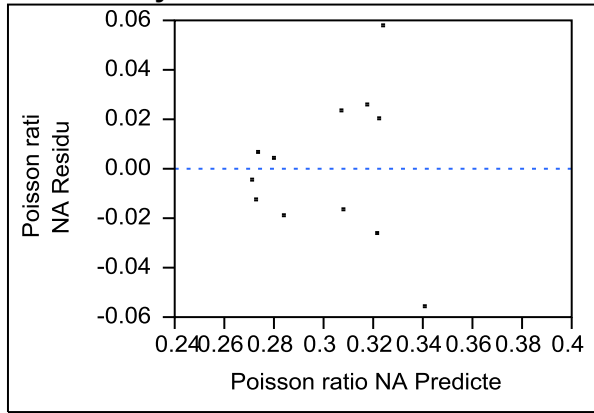
Analysis of Variance

Source	DF	Sum of Squares	Mean Square	F Ratio
Model	1	0.00650375	0.006504	6.7680
Error	10	0.00960963	0.000961	Prob > F
C. Total	11	0.01611339		0.0264*

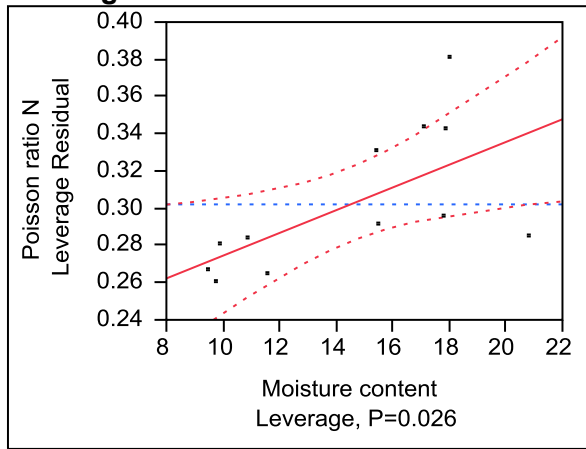
Parameter Estimates

Term	Estimate	Std Error	t Ratio	Prob> t
Intercept	0.2133869	0.035235	6.06	0.0001*
Moisture content %	0.0061094	0.002348	2.60	0.0264*

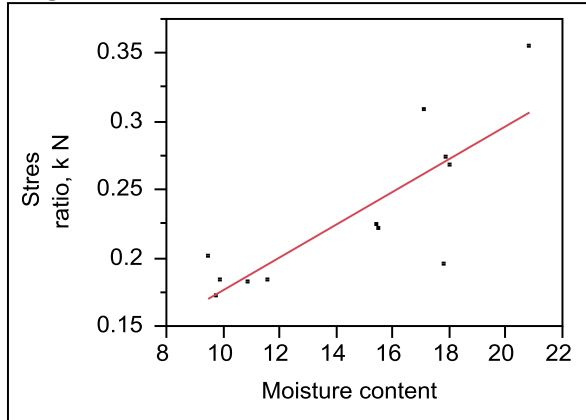
Residual by Predicted Plot



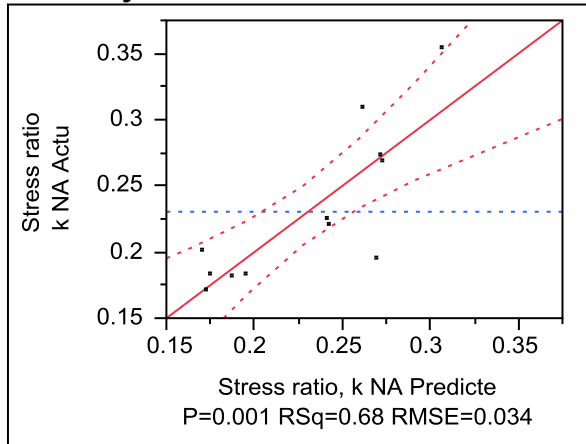
**Moisture content %
Leverage Plot**



**Iowa K test loading 1 lateral stress ratio, k of WCF gypsum (100psi vertical stress)
Response Whole Model
Regression Plot**



Actual by Predicted Plot



Summary of Fit

RSquare	0.678617
RSquare Adj	0.646479
Root Mean Square Error	0.034556
Mean of Response	0.230422
Observations (or Sum Wgts)	12

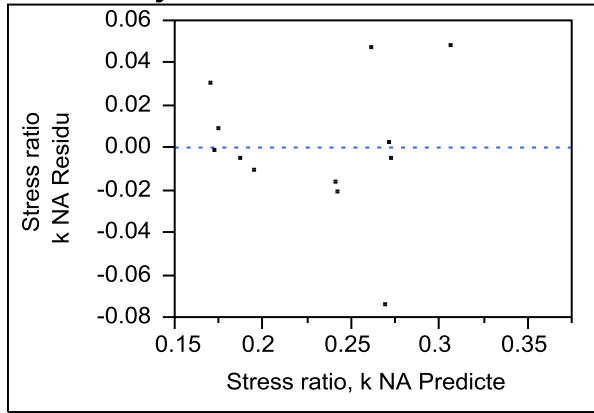
Analysis of Variance

Source	DF	Sum of Squares	Mean Square	F Ratio
Model	1	0.02521511	0.025215	21.1155
Error	10	0.01194151	0.001194	Prob > F
C. Total	11	0.03715662		0.0010*

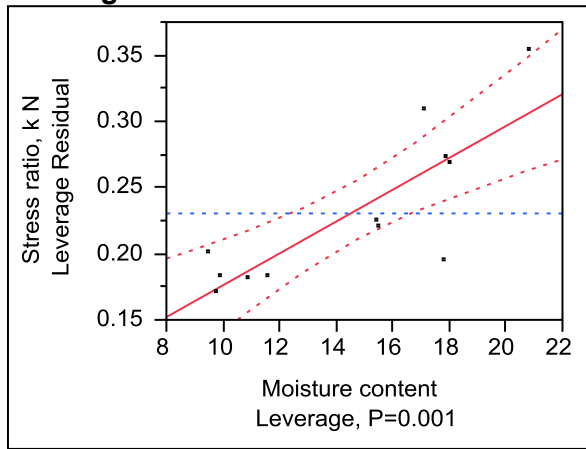
Parameter Estimates

Term	Estimate	Std Error	t Ratio	Prob> t
Intercept	0.0558496	0.039278	1.42	0.1855
Moisture content %	0.0120294	0.002618	4.60	0.0010*

Residual by Predicted Plot

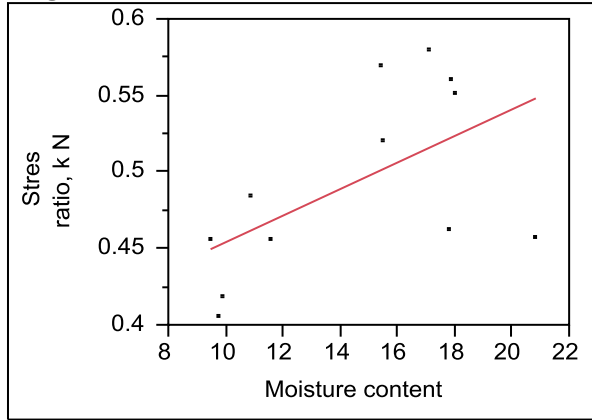


**Moisture content %
Leverage Plot**

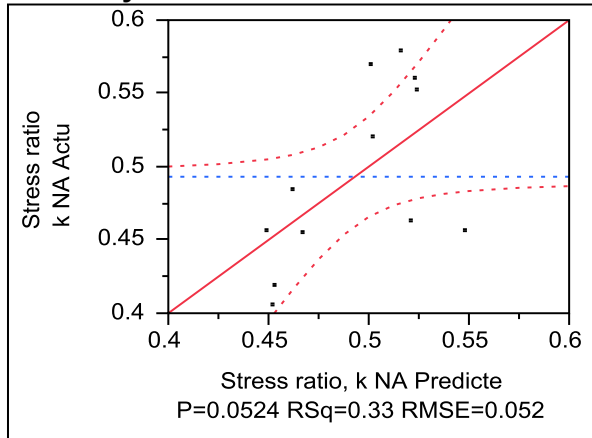


Iowa K test loading 2 lateral stress ratio, k of WCF gypsum (30psi vertical stress)

Whole Model
Regression Plot



Actual by Predicted Plot



Summary of Fit

RSquare	0.326201
RSquare Adj	0.258821
Root Mean Square Error	0.052093
Mean of Response	0.493134
Observations (or Sum Wgts)	12

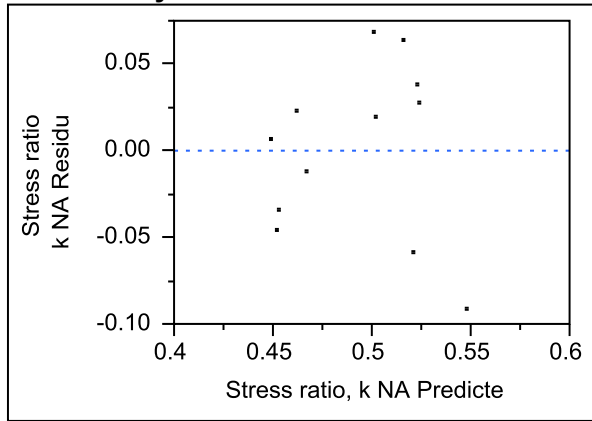
Analysis of Variance

Source	DF	Sum of Squares	Mean Square	F Ratio
Model	1	0.01313771	0.013138	4.8412
Error	10	0.02713718	0.002714	Prob > F
C. Total	11	0.04027489		0.0524

Parameter Estimates

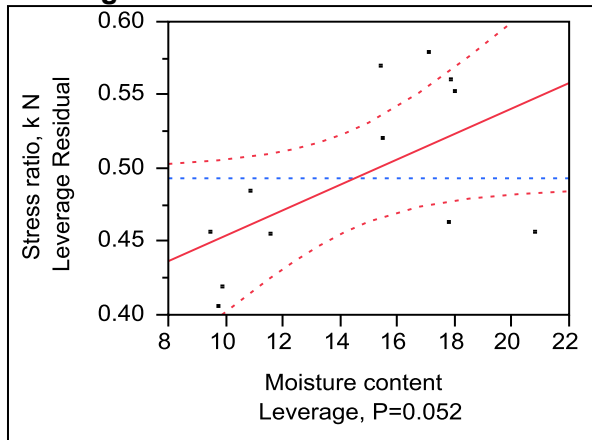
Term	Estimate	Std Error	t Ratio	Prob> t
Intercept	0.3671235	0.059212	6.20	0.0001*
Moisture content %	0.0086831	0.003946	2.20	0.0524

Residual by Predicted Plot



Moisture content %

Leverage Plot

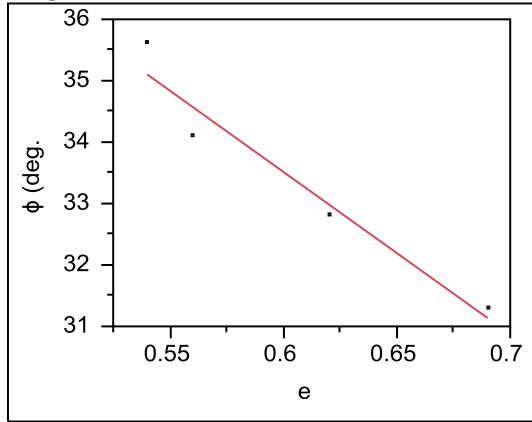


Ottawa sand (ASTM 20-30)

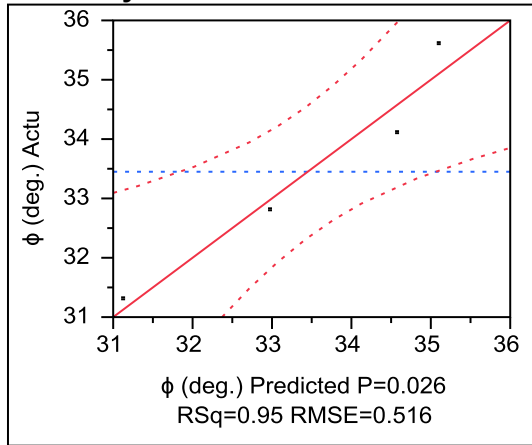
Iowa K test friction angle of Ottawa sand

Whole Model

Regression Plot



Actual by Predicted Plot



Summary of Fit

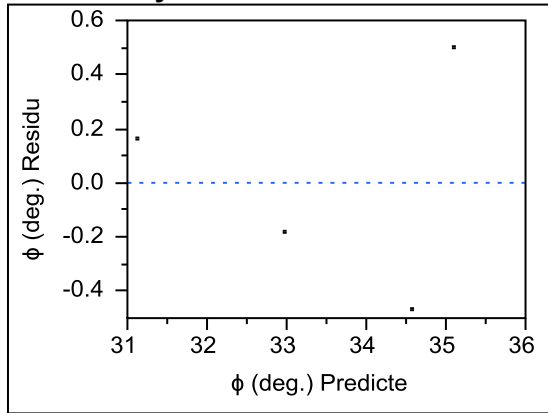
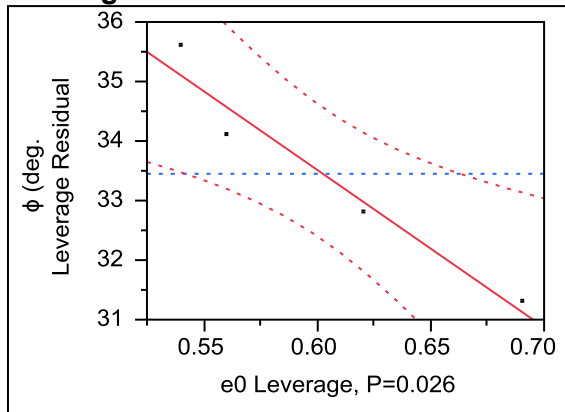
RSquare	0.947105
RSquare Adj	0.920657
Root Mean Square Error	0.516581
Mean of Response	33.45
Observations (or Sum Wgts)	4

Analysis of Variance

Source	DF	Sum of Squares	Mean Square	F Ratio
Model	1	9.556289	9.55629	35.8107
Error	2	0.533711	0.26686	Prob > F
C. Total	3	10.090000		0.0268*

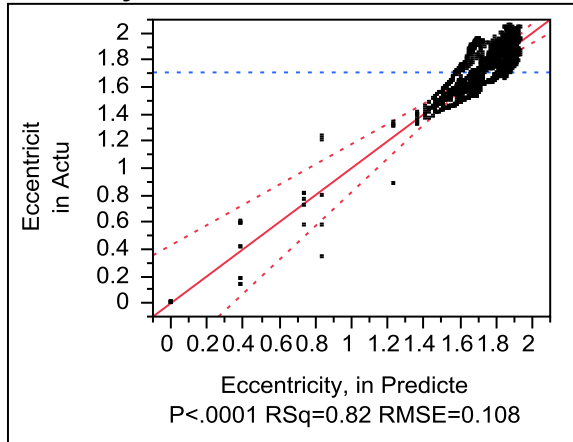
Parameter Estimates

Term	Estimate	Std Error	t Ratio	Prob> t
Intercept	49.377148	2.674035	18.47	0.0029*
e0	-26.4351	4.417479	-5.98	0.0268*

Residual by Predicted Plot**e0****Leverage Plot**

APPENDIX F. JMP OUTPUTS AND SPREADSHEETS FOR R&R ANALYSIS

300kPa Eccentricity, in Whole Model Actual by Predicted Plot



Summary of Fit

RSquare	0.817926
RSquare Adj	0.77252
Root Mean Square Error	0.108912
Mean of Response	1.70915
Observations (or Sum Wgts)	2020

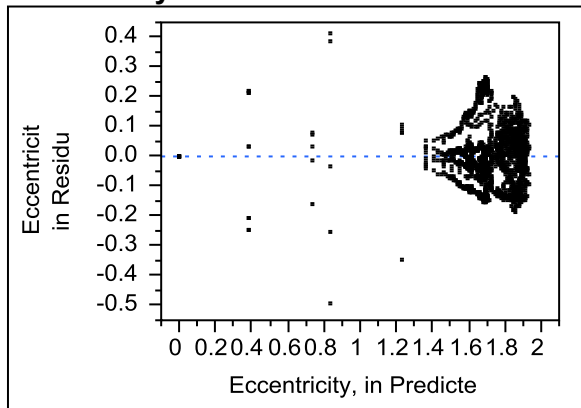
Analysis of Variance

Source	DF	Sum of Squares	Mean Square	F Ratio	Prob > F
Model	403	86.11136	0.213676	18.0136	
Error	1616	19.16881	0.011862		
C. Total	2019	105.28017			<.0001*

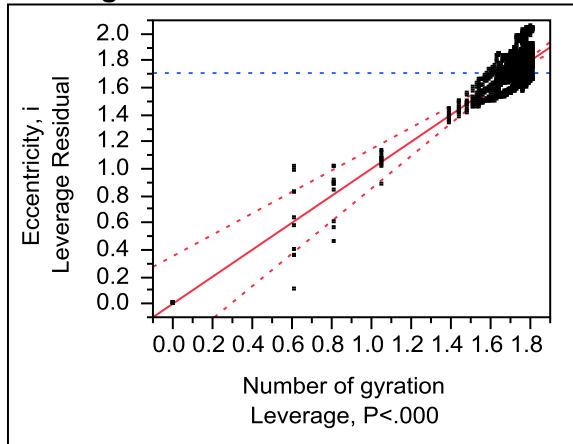
Effect Tests

Source	Nparm	DF	Sum of Squares	F Ratio	Prob > F
Number of gyrations	201	201	66.311995	27.8126	<.0001*
PDA number	1	1	13.995118	1179.839	<.0001*
Number of gyrations*PDA number	201	201	5.804249	2.4344	<.0001*

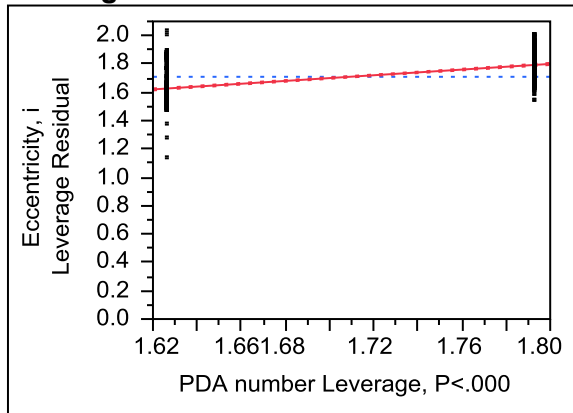
Residual by Predicted Plot



**Number of gyrations
Leverage Plot**



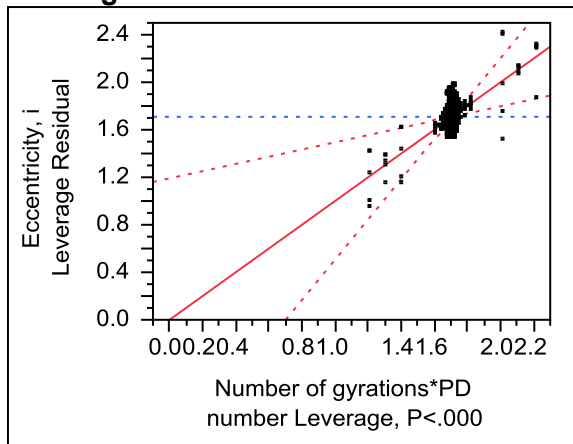
**PDA number
Leverage Plot**



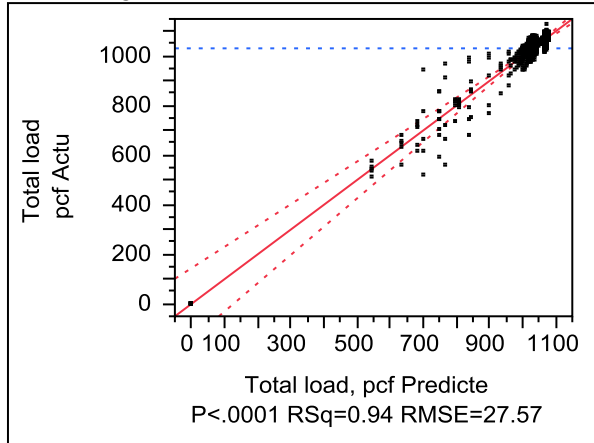
Least Squares Means Table

Level	Least Sq Mean	Std Error	Mean
1	1.6259142	0.00342702	1.62591
2	1.7923867	0.00342702	1.79239

**Number of gyrations*PDA number
Leverage Plot**



**300kPa total load, pcf
Whole Model
Actual by Predicted Plot**



Summary of Fit

RSquare	0.935275
RSquare Adj	0.919134
Root Mean Square Error	27.57221
Mean of Response	1031.37
Observations (or Sum Wgts)	2020

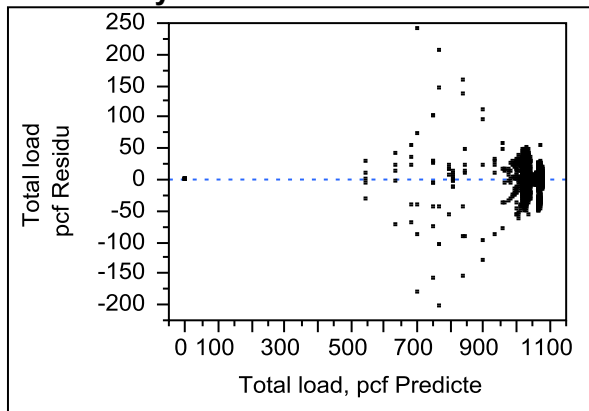
Analysis of Variance

Source	DF	Sum of Squares	Mean Square	F Ratio
Model	403	17752287	44050.3	57.9437
Error	1616	1228527	760.2	Prob > F
C. Total	2019	18980814		<.0001*

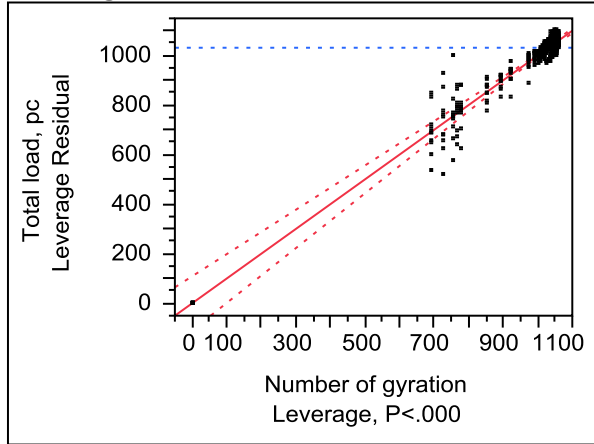
Effect Tests

Source	Nparm	DF	Sum of Squares	F Ratio	Prob > F
Number of gyrations	201	201	16141461	105.6340	<.0001*
PDA number	1	1	1065514	1401.574	<.0001*
Number of gyrations*PDA number	201	201	545313	3.5687	<.0001*

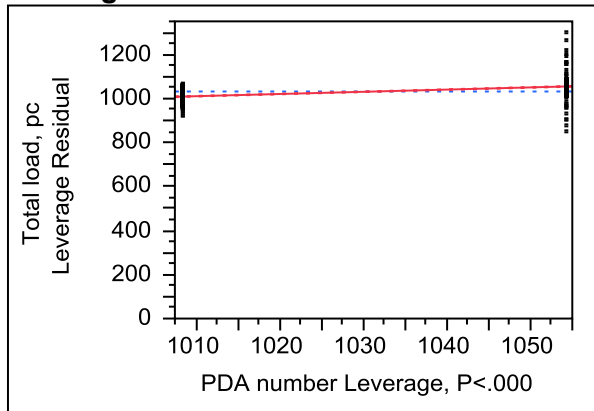
Residual by Predicted Plot



**Number of gyrations
Leverage Plot**



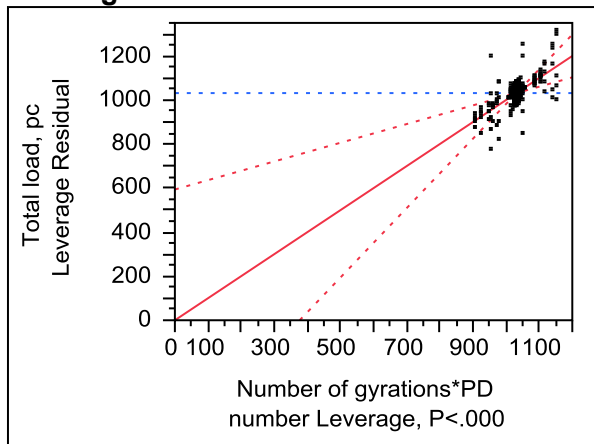
**PDA number
Leverage Plot**



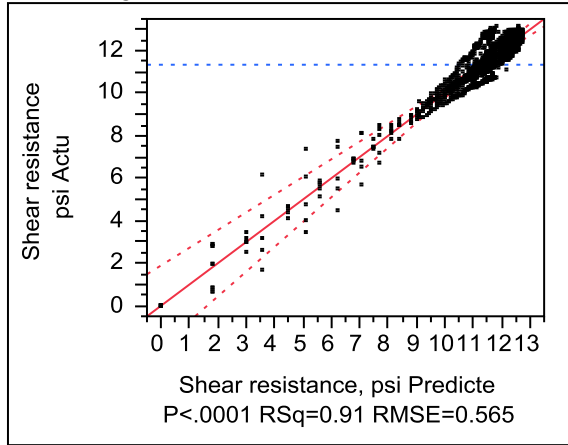
Least Squares Means Table

Level	Least Sq Mean	Std Error	Mean
1	1054.3368	0.86758279	1054.34
2	1008.4029	0.86758279	1008.40

**Number of gyrations*PDA number
Leverage Plot**



300kPa shear resistance, psi
Whole Model
Actual by Predicted Plot



Summary of Fit

RSquare	0.910171
RSquare Adj	0.88777
Root Mean Square Error	0.565153
Mean of Response	11.34385
Observations (or Sum Wgts)	2020

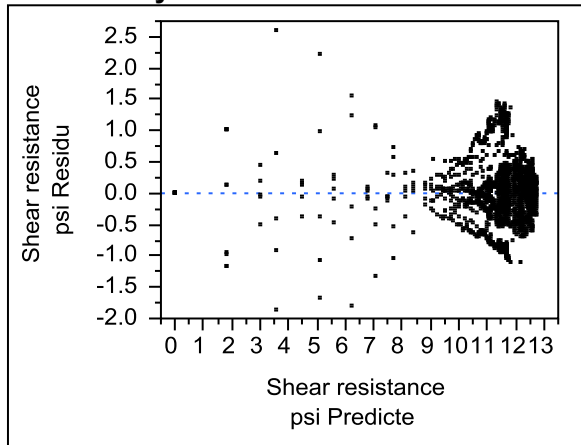
Analysis of Variance

Source	DF	Sum of Squares	Mean Square	F Ratio
Model	403	5229.7522	12.9771	40.6298
Error	1616	516.1466	0.3194	Prob > F
C. Total	2019	5745.8988		<.0001*

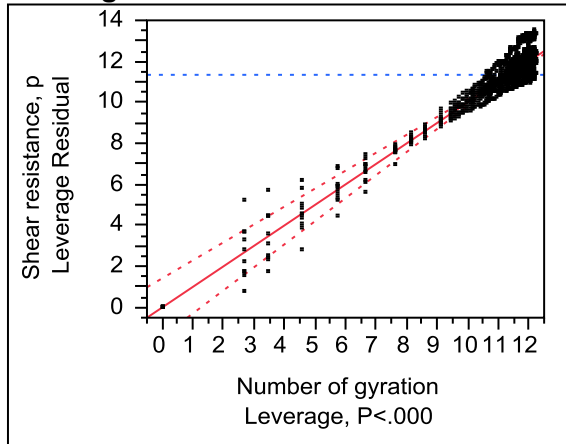
Effect Tests

Source	Nparm	DF	Sum of Squares	F Ratio	Prob > F
Number of gyrations	201	201	4837.3067	75.3487	<.0001*
PDA number	1	1	208.5551	652.9638	<.0001*
Number of gyrations*PDA number	201	201	183.8904	2.8644	<.0001*

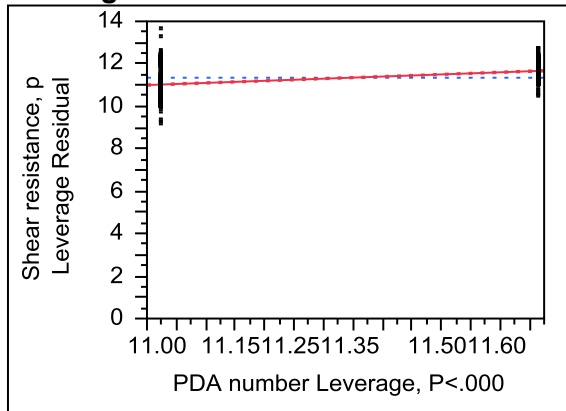
Residual by Predicted Plot



**Number of gyrations
Leverage Plot**



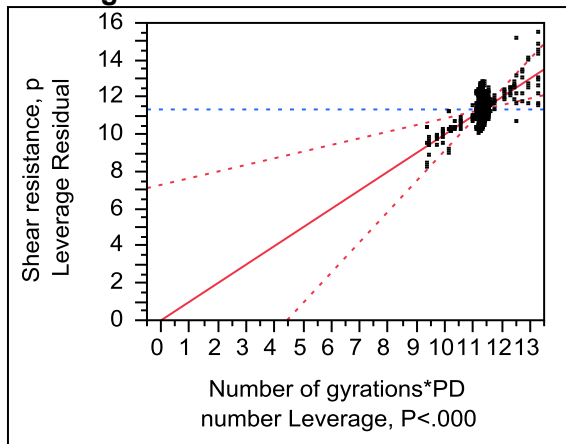
**PDA number
Leverage Plot**



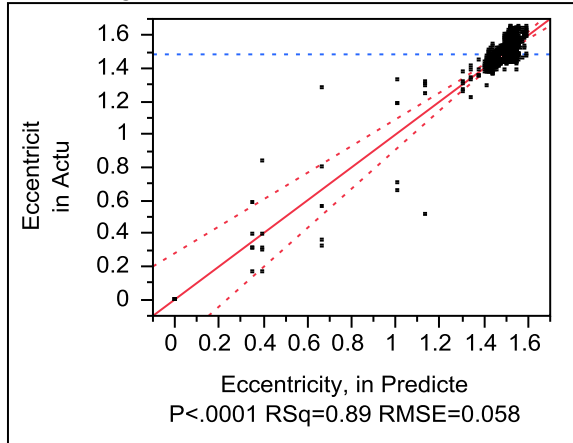
Least Squares Means Table

Level	Least Sq Mean	Std Error	Mean
1	11.022535	0.01778301	11.0225
2	11.665170	0.01778301	11.6652

**Number of gyrations*PDA number
Leverage Plot**



600kPa Eccentricity, in Whole Model Actual by Predicted Plot



Summary of Fit

RSquare	0.888035
RSquare Adj	0.860113
Root Mean Square Error	0.058522
Mean of Response	1.48503
Observations (or Sum Wgts)	2020

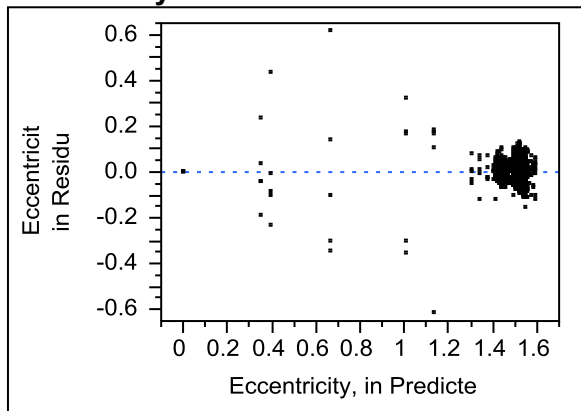
Analysis of Variance

Source	DF	Sum of Squares	Mean Square	F Ratio
Model	403	43.895480	0.108922	31.8041
Error	1616	5.534439	0.003425	Prob > F
C. Total	2019	49.429919		<.0001*

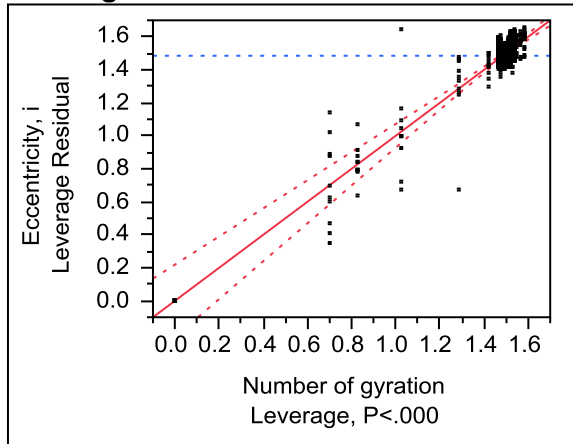
Effect Tests

Source	Nparm	DF	Sum of Squares	F Ratio	Prob > F
Number of gyrations	201	201	37.344942	54.2505	<.0001*
PDA number	1	1	1.952250	570.0371	<.0001*
Number of gyrations*PDA number	201	201	4.598288	6.6799	<.0001*

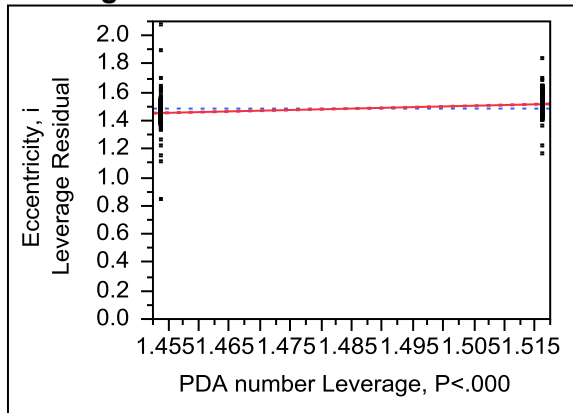
Residual by Predicted Plot



**Number of gyrations
Leverage Plot**



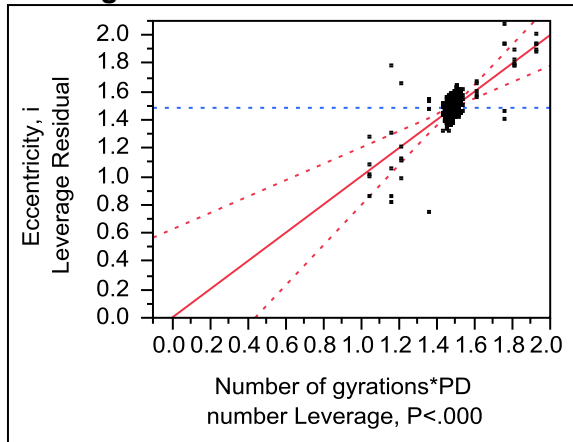
**PDA number
Leverage Plot**



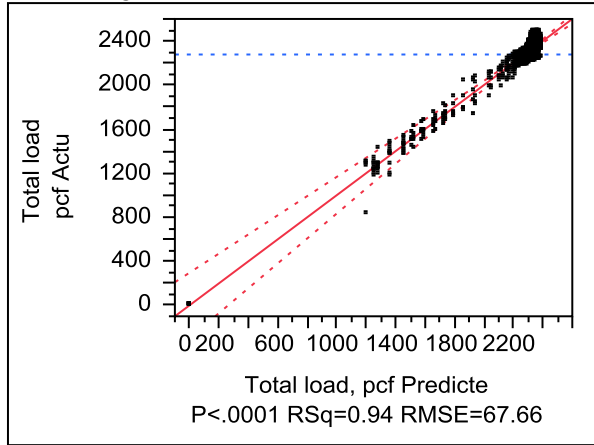
Least Squares Means Table

Level	Least Sq Mean	Std Error	Mean
1	1.5161181	0.00184143	1.51612
2	1.4539422	0.00184143	1.45394

**Number of gyrations*PDA number
Leverage Plot**



**600kPa total load, pcf
Whole Model
Actual by Predicted Plot**



Summary of Fit

RSquare	0.94353
RSquare Adj	0.929447
Root Mean Square Error	67.66802
Mean of Response	2277.129
Observations (or Sum Wgts)	2020

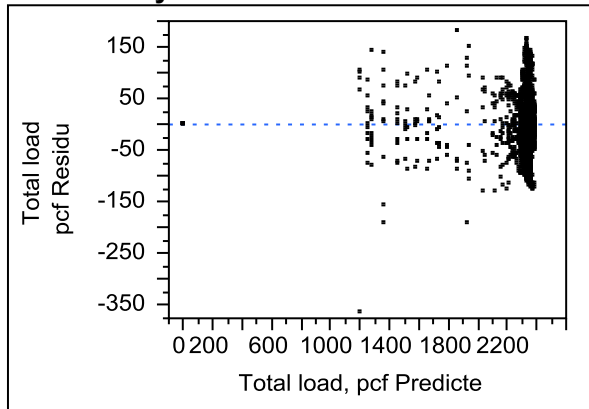
Analysis of Variance

Source	DF	Sum of Squares	Mean Square	F Ratio
Model	403	123636148	306789	66.9998
Error	1616	7399601	4579	Prob > F
C. Total	2019	131035750		<.0001*

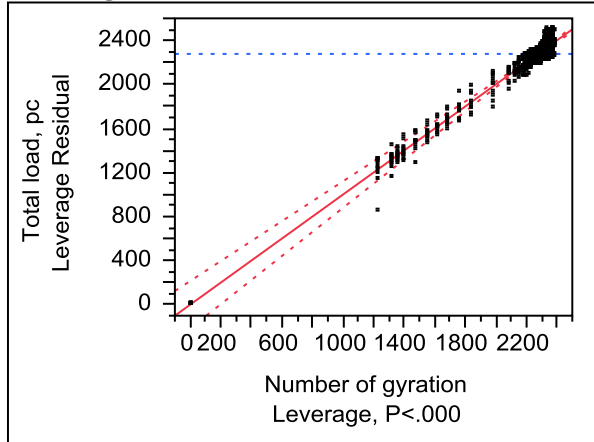
Effect Tests

Source	Nparm	DF	Sum of Squares	F Ratio	Prob > F
Number of gyrations	201	201	122420020	133.0116	<.0001*
PDA number	1	1	39124	8.5443	0.0035*
Number of gyrations*PDA number	201	201	1177005	1.2788	0.0076*

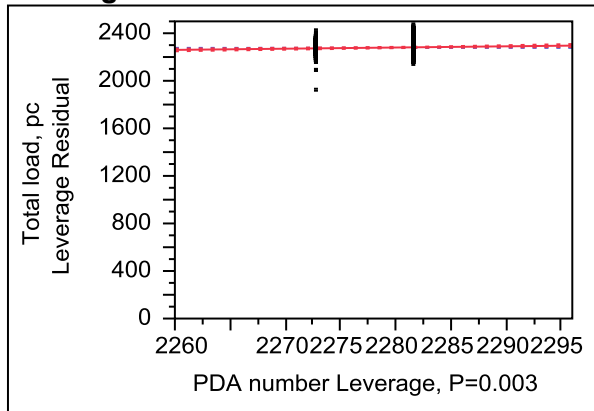
Residual by Predicted Plot



**Number of gyrations
Leverage Plot**



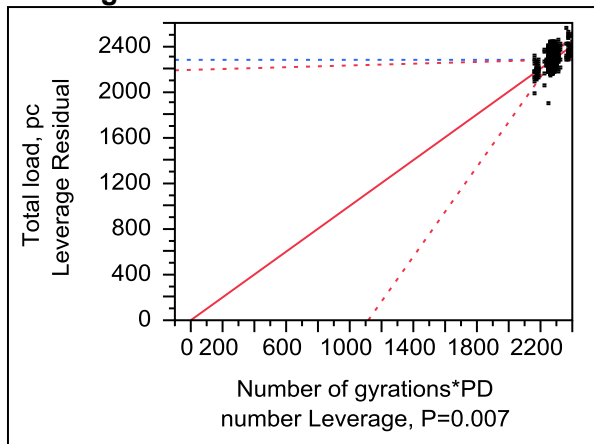
**PDA number
Leverage Plot**



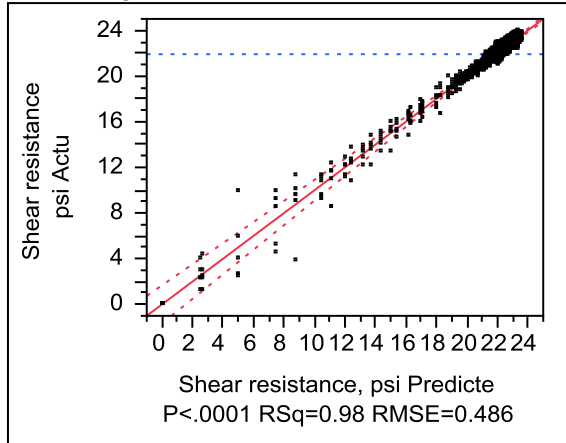
Least Squares Means Table

Level	Least Sq Mean	Std Error	Mean
1	2281.5298	2.1292311	2281.53
2	2272.7279	2.1292311	2272.73

**Number of gyrations*PDA number
Leverage Plot**



600kPa shear resistance, psi
Whole Model
Actual by Predicted Plot



Summary of Fit

RSquare	0.979893
RSquare Adj	0.974879
Root Mean Square Error	0.486342
Mean of Response	21.90853
Observations (or Sum Wgts)	2020

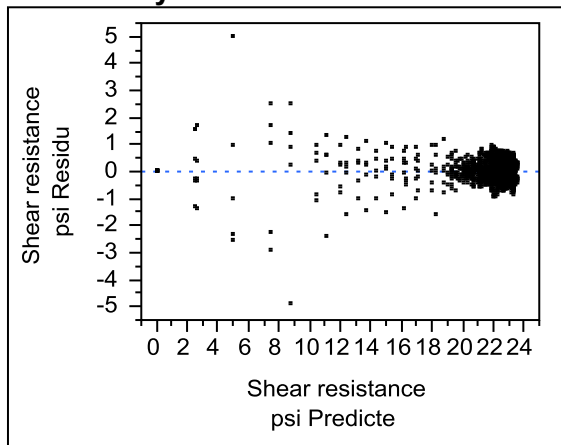
Analysis of Variance

Source	DF	Sum of Squares	Mean Square	F Ratio
Model	403	18627.741	46.2227	195.4210
Error	1616	382.230	0.2365	Prob > F
C. Total	2019	19009.972		<.0001*

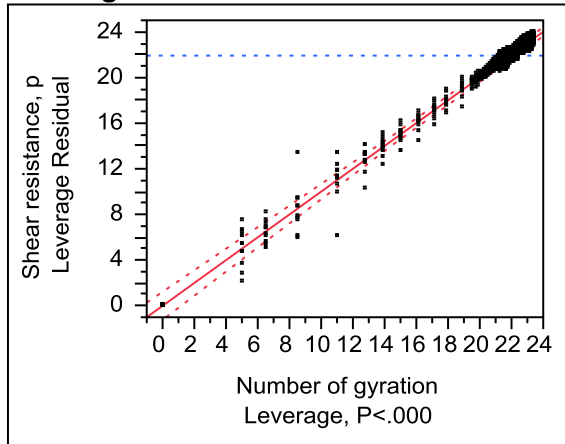
Effect Tests

Source	Nparm	DF	Sum of Squares	F Ratio	Prob > F
Number of gyrations	201	201	17917.930	376.8842	<.0001*
PDA number	1	1	284.892	1204.470	<.0001*
Number of gyrations*PDA number	201	201	424.920	8.9377	<.0001*

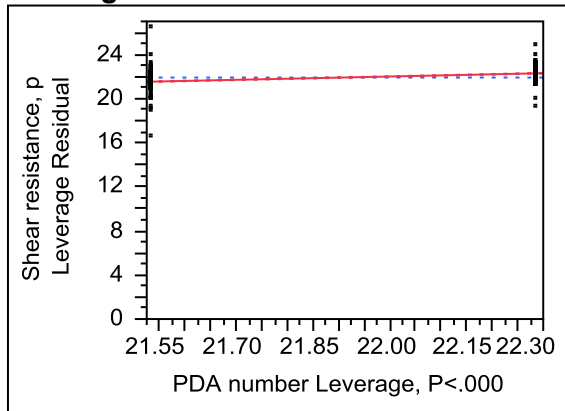
Residual by Predicted Plot



**Number of gyrations
Leverage Plot**



**PDA number
Leverage Plot**



Least Squares Means Table

Level	Least Sq Mean	Std Error	Mean
1	22.284075	0.01530316	22.2841
2	21.532981	0.01530316	21.5330

**Number of gyrations*PDA number
Leverage Plot**

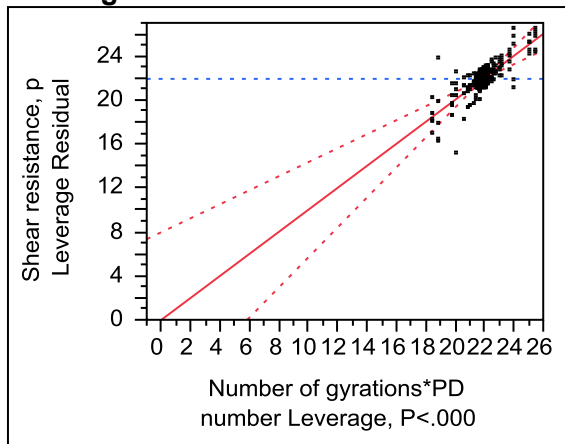


Table 71. R&R analysis spreadsheet for 300kPa total load, eccentricity, and shear resistance

300kPa total load		300kPa eccentricity		300kPa shear resistance	
M: number of measurements for total load		M: number of measurements for eccentricity		M: number of measurements for shear resistance	
I: number of gyrations		I: number of gyrations		I: number of gyrations	
J: PDA number		J: PDA number		J: PDA number	
M:	5	M:	5	M:	5
I:	202	I:	202	I:	202
J:	2	J:	2	J:	2
SSC	1065514.0	SSC	14.0	SSC	208.6
SSAC	545313.0	SSAC	5.8	SSAC	183.9
MSE	760.2	MSE	0.0	MSE	0.3
MSC	1065514.0	MSC	14.0	MSC	208.6
MSAC	2713.0	MSAC	0.0	MSAC	0.9
$\sigma_{\text{reproducibility}}$	38.0	$\sigma_{\text{reproducibility}}$	0.13	$\sigma_{\text{reproducibility}}$	0.6
$v_{\text{reproducibility}}$	2	$v_{\text{reproducibility}}$	2	$v_{\text{reproducibility}}$	2
α	0.975 or 0.025	α	0.975 or 0.025	α	0.975 or 0.025
df	2	df	2	df	2
X ² upper	7.378	X ² upper	7.378	X ² upper	7.378
X ² lower	0.05064	X ² lower	0.05064	X ² lower	0.05064
95% lower	19.113	95% lower	0.060	95% lower	0.329
95% upper	230.703	95% upper	0.725	95% upper	3.974
$\sigma_{\text{R\&R}}$	46.9	$\sigma_{\text{R\&R}}$	0.171	$\sigma_{\text{R\&R}}$	0.803
$v_{\text{R\&R}}$	4	$v_{\text{R\&R}}$	4	$v_{\text{R\&R}}$	10
α	0.975 or 0.025	α	0.975 or 0.025	α	0.975 or 0.025
df	4	df	4	df	10
X ² lower	0.4844	X ² lower	0.4844	X ² lower	3.247
X ² upper	11.14	X ² upper	11.14	X ² upper	20.48
95% lower	29.345	95% lower	0.107	95% lower	0.552
95% upper	140.725	95% upper	0.514	95% upper	1.386
Contribution of $\sigma_{\text{reproducibility}}$	80.9	Contribution of $\sigma_{\text{reproducibility}}$	77.0	Contribution of $\sigma_{\text{reproducibility}}$	71.0

Table 72. R&R analysis spreadsheet for 600kPa total load, eccentricity, and shear resistance

600kPa total load		600kPa eccentricity		600kPa shear resistance	
M: number of measurements for total load		M: number of measurements for eccentricity		M: number of measurements for shear resistance	
I: number of gyrations		I: number of gyrations		I: number of gyrations	
J: PDA number		J: PDA number		J: PDA number	
M:	5	M:	5	M:	5
I:	202	I:	202	I:	202
J:	2	J:	2	J:	2
SSC	39124.00	SSC	1.95	SSC	284.89
SSAC	1177005.00	SSAC	4.60	SSAC	424.92
MSE	4578.96	MSE	0.00	MSE	0.24
MSC	39124.00	MSC	1.95	MSC	284.89
MSAC	5855.75	MSAC	0.02	MSAC	2.11
$\sigma_{\text{reproducibility}}$	16.98	$\sigma_{\text{reproducibility}}$	0.0762	$\sigma_{\text{reproducibility}}$	0.8096
$V_{\text{reproducibility}}$	9	$V_{\text{reproducibility}}$	9	$V_{\text{reproducibility}}$	5
α	0.975 or 0.025	α	0.975 or 0.025	α	0.975 or 0.025
df	9	df	9	df	5
X^2 upper	19.02	X^2 upper	19.02	X^2 upper	12.83
X^2 lower	2.7	X^2 lower	2.7	X^2 lower	0.8312
95% lower	11.981	95% lower	0.052	95% lower	0.522
95% upper	31.800	95% upper	0.137	95% upper	2.052
$\sigma_{\text{R\&R}}$	69.766	$\sigma_{\text{R\&R}}$	0.096	$\sigma_{\text{R\&R}}$	0.944
$V_{\text{R\&R}}$	1431	$V_{\text{R\&R}}$	22	$V_{\text{R\&R}}$	10
α	0.975 or 0.025	α	0.975 or 0.025	α	0.975 or 0.025
df	1431	df	22	df	10
X^2 lower	914.257	X^2 lower	10.98	X^2 lower	3.247
X^2 upper	1089.531	X^2 upper	36.78	X^2 upper	20.48
95% lower	79.941	95% lower	0.075	95% lower	0.656
95% upper	87.268	95% upper	0.136	95% upper	1.648
Contribution of $\sigma_{\text{reproducibility}}$	24.3	Contribution of $\sigma_{\text{reproducibility}}$	79.3	Contribution of $\sigma_{\text{reproducibility}}$	85.7

APPENDIX G. UNCONFINED COMPRESSION TEST RESULTS FOR WCF FLY ASH AND GYPSUM

Table 73. Unconfined compression test results of 1 and 48-hr cured WCF fly ash samples

WCF FLY ASH 1 HR CURED SAMPLES								
w%	γ_d , pcf	E_{50}	C_u (psi)	E (0.1%)	E (0.5%)	E (1.0%)	E (1.5%)	E (50% of peak)
15.5%	76.8	639.7	4.3	600.0	640.0	661.0	586.7	628.6
15.3%	80.3	652.6	6.2	500.0	640.0	640.0	640.0	640.0
17.2%	75.4	593.8	3.8	500.0	630.0	640.0	—	600.0
17.1%	78.7	541.2	4.6	420.0	540.0	550.0	560.0	541.2
17.5%	82.1	916.7	7.7	900.0	880.0	900.0	933.3	888.9
19.4%	77.8	755.2	4.4	700.0	760.0	750.0	583.3	773.3
19.4%	80.4	633.3	5.7	650.0	640.0	631.0	616.0	631.0
21.0%	75.3	450.0	2.9	400.0	460.0	460.0	382.7	466.7
21.1%	78.7	490.5	4.1	400.0	480.0	490.0	493.3	488.9
21.5%	82.4	652.6	6.2	700.0	800.0	800.0	746.7	800.0
23.1%	77.1	418.9	3.1	380.0	420.0	430.0	400.0	422.2
23.3%	80.4	431.4	4.4	380.0	420.0	430.0	466.7	436.4
24.6%	76.1	318.2	2.1	320.0	320.0	320.0	270.0	311.1
25.0%	79.3	360.5	3.1	400.0	360.0	340.0	320.0	300.0
26.7%	77.9	301.4	2.2	270.0	300.0	305.0	273.3	338.9
WCF FLY ASH 48 HR CURED SAMPLES								
w%	γ_d , pcf	E_{50}	C_u (psi)	E (0.1%)	E (0.5%)	E (1.0%)	E (1.5%)	E (50% of peak)
14.7	76.7	720.0	5.40	750.0	720.0	710.0	604.0	720.0
14.7	80.1	533.3	6.40	500.0	560.0	580.0	580.0	533.3
16.7	75.4	358.3	4.30	600.0	660.0	660.0	—	358.3
17.0	78.8	906.7	6.80	800.0	884.0	920.0	773.3	906.7
16.9	82.1	730.0	7.30	700.0	760.0	730.0	773.3	730.0
18.9	77.1	621.2	4.10	600.0	620.0	621.0	540.0	621.2
19.1	80.3	615.4	5.60	600.0	680.0	690.0	680.0	615.4
20.8	75.5	484.4	3.10	500.0	480.0	460.0	406.7	484.4
21.1	78.6	543.2	4.40	550.0	540.0	540.0	540.0	543.2
21.4	81.9	578.4	5.90	580.0	580.0	580.0	573.3	578.4
23.0	77.1	415.6	3.20	450.0	430.0	428.0	412.0	415.6
23.3	80.4	493.5	4.54	450.0	480.0	440.0	493.3	493.5
24.5	75.6	336.4	2.22	370.0	346.0	348.0	307.3	336.4
25.2	79.0	390.0	3.12	400.0	388.0	382.0	380.0	390.0
27.0	77.6	325.0	2.34	300.0	330.0	330.0	290.0	325.0

Table 74. Unconfined compression test results of 1 and 48-hr cured WCF gypsum samples

GYPSUM 1 HR CURED SAMPLES								
w%	γ_d , pcf	E_{50}	C_u (psi)	E (0.1%)	E (0.5%)	E (1.0%)	E (1.5%)	E (50% of peak)
9.7%	92.3	538.6	3.07	500.0	530.0	540.0	—	538.6
9.9%	97.3	761.5	5.94	800.0	760.0	770.0	773.3	761.5
10.1%	103.7	771.6	9.95	750.0	780.0	780.0	1080.0	771.6
11.7%	95.4	566.6	3.91	550.0	560.0	560.0	—	566.6
11.8%	100.3	624.6	7.00	600.0	600.0	600.0	800.0	624.6
13.5%	92.7	494.5	2.87	550.0	510.0	510.0	—	494.5
13.9%	98.0	890.8	5.08	900.0	880.0	880.0	—	890.8
14.1%	104.1	870.8	10.62	850.0	840.0	870.0	—	870.8
15.5%	95.6	754.8	3.55	800.0	750.0	700.0	—	754.8
15.9%	100.8	684.4	6.16	700.0	680.0	680.0	813.3	684.4
18.2%	92.7	449.7	1.89	450.0	440.0	375.0	—	449.7
17.6%	98.5	538.4	3.55	500.0	540.0	570.0	—	538.4
20.2%	95.8	557.9	2.12	520.0	550.0	430.0	—	557.9
19.5%	99.6	460.1	3.77	400.0	460.0	480.0	500.0	460.1
21.2%	93.9	270.5	1.49	230.0	272.0	260.0	197.3	270.5
GYPSUM 48 HR CURED SAMPLES								
w%	γ_d , pcf	E_{50}	C_u (psi)	E (0.1%)	E (0.5%)	E (1.0%)	E (1.5%)	E (50% of peak)
9.1%	94.0	746.1	3.73	700.0	740.0	710.0	—	746.1
9.1%	97.5	829.8	6.06	800.0	820.0	840.0	813.3	829.8
9.2%	104.0	1269.2	13.07	1100.0	1040.0	1270.0	1500.0	1269.2
10.8%	95.5	821.5	5.26	800	840	840	—	821.4846
11.2%	101.1	1302.5	8.08	1250.0	1280.0	1280.0	—	1302.5
12.7%	93.3	820.3	3.45	800.0	860.0	680.0	—	820.3
12.9%	98.4	871.6	5.93	800.0	860.0	940.0	—	871.6
12.9%	104.8	1006.0	11.37	1000.0	1000.0	1050.0	1300.0	1006.0
14.6%	96.1	795.9	4.30	700.0	680.0	730.0	—	795.9
14.9%	101.4	959.4	6.91	1000.0	960.0	970.0	920.0	959.4
16.7%	93.5	780.3	2.65	750.0	780.0	530.0	—	780.3
16.9%	98.7	764.9	4.78	750.0	770.0	820.0	—	764.9
18.4%	97.0	865.7	3.29	800.0	860.0	640.0	—	865.7
18.3%	100.0	652.8	4.05	600.0	640.0	560.0	480.0	652.8
20.8%	93.6	523.6	1.99	550.0	320.0	394.0	—	523.6

APPENDIX H. SIEVE ANALYSIS RESULTS FOR 2012 RAP, RPCC+RAP, AND CRUSHED LIMESTONE BEFORE AND AFTER GYRATORY TESTS

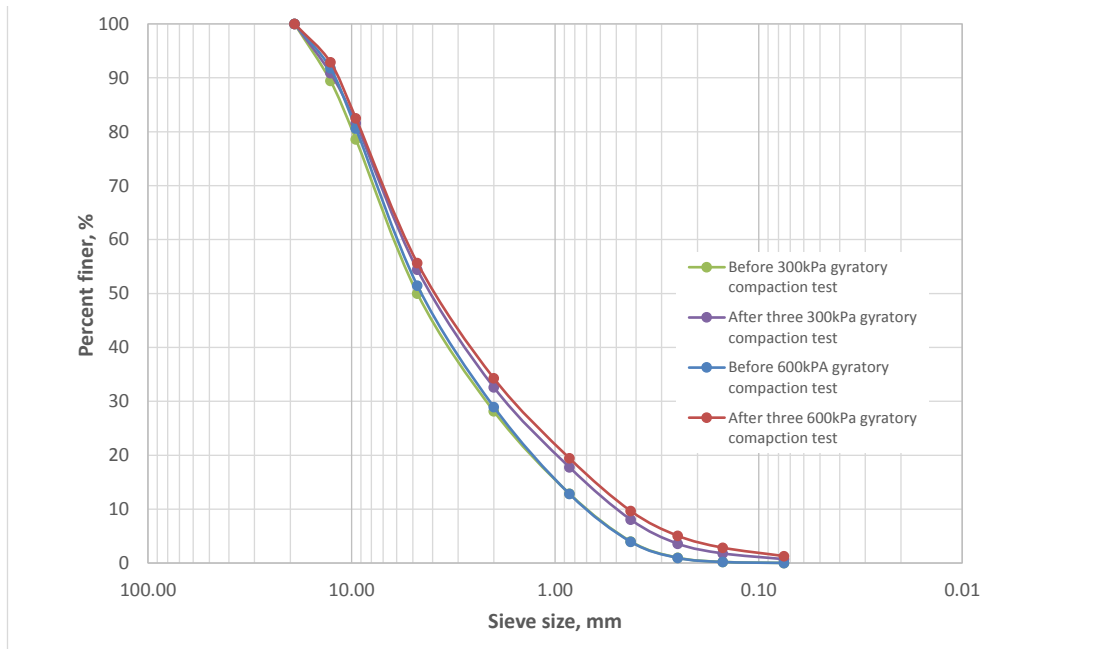


Figure 252. Sieve analysis results of 2012 Manatt's RAP (CFED 2061) before and after three gyratory compaction tests

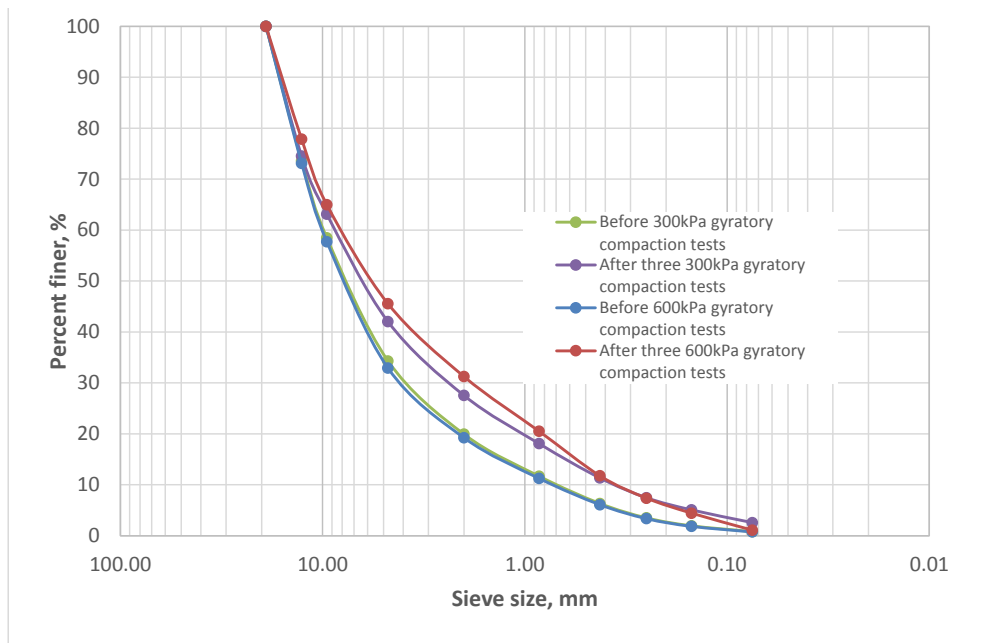


Figure 253. Sieve analysis results of RPCC + RAP (CFED 2062) before and after three gyratory compaction tests

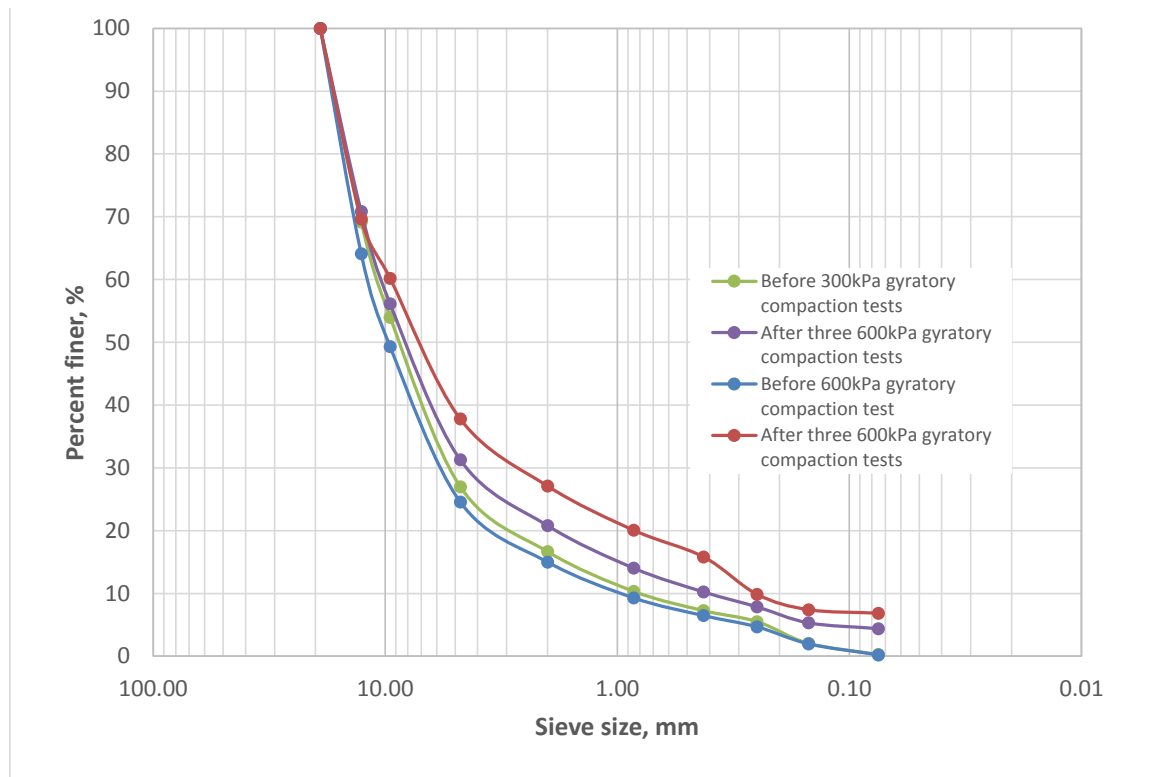


Figure 254. Sieve analysis results of crushed limestone (CFED 2063) before and after three gyratory compaction tests

APPENDIX I. IN SITU LWD TEST DATA FOR TEXAS FAT CLAY (CFED 2043)

Table 75. In situ LWD test data for Texas fat clay (CFED 2043)

Test Bed	Point ID	Distance (ft)	Pass Number	γ_a (pcf)	γ_a (kN/m ³)	w (%)	ELWD-Z2 ksi	ELWD-Z2 MPa
8	2-F1	81.5	0	68.5	10.75	17.5	0.7	4.6
8	4-F1	122.8	0	65.5	10.29	16.1	0.5	3.6
8	6-F1	162.3	0	67.2	10.56	16.7	0.5	3.3
8	8-F1	199.7	0	95.6	15.02	19.5	4.2	28.6
8	0-F1	0.0	2	86.0	13.51	20.9	3.2	22.2
8	0-F2	0.0	2	93.1	14.62	15.4	3.1	21.5
8	2-F1	81.5	2	76.2	11.97	19.1	2.0	14.0
8	2-F2	81.5	2	84.0	13.20	18.2	1.8	12.8
8	4-F1	122.8	2	82.1	12.90	21.1	2.8	19.0
8	4-F2	122.8	2	85.5	13.42	19.9	2.7	18.7
8	6-F1	162.3	2	77.3	12.14	23.5	1.7	12.0
8	6-F2	162.3	2	86.4	13.57	18.6	3.7	25.5
8	8-F1	199.7	2	85.4	13.41	21.5	2.8	19.5
8	8-F2	199.7	2	86.6	13.60	20.0	3.1	21.2
8	10-F1	257.7	2	76.4	12.00	23.6	1.8	12.2
8	10-F2	257.7	2	76.1	11.95	19.5	2.1	14.5
8	0-F1	0.0	4	97.7	15.34	19.6	7.1	48.7
8	0-F2	0.0	4	99.0	15.55	19.7	5.0	34.5
8	2-F1	81.5	4	87.8	13.79	18.9	3.5	24.2
8	2-F2	81.5	4	91.6	14.39	18.7	3.8	26.0
8	4-F1	122.8	4	89.5	14.06	22.9	4.1	28.4
8	4-F2	122.8	4	87.9	13.80	19.4	2.3	15.8
8	6-F1	162.3	4	85.9	13.49	21.1	2.9	19.9
8	6-F2	162.3	4	90.5	14.21	21.0	3.6	24.6
8	8-F1	199.7	4	89.8	14.10	21.8	4.2	29.2
8	8-F2	199.7	4	90.4	14.19	22.6	3.2	22.0
8	10-F1	257.7	4	80.2	12.59	23.9	2.6	18.0
8	10-F2	257.7	4	86.2	13.54	21.9	3.7	25.2
8	0-F1	0.0	8	94.6	14.86	21.5	4.6	31.4
8	0-F2	0.0	8	93.3	14.66	23.0	3.0	20.8
8	2-F1	81.5	8	83.9	13.17	22.8	2.4	16.3
8	2-F2	81.5	8	92.5	14.52	20.4	3.7	25.4
8	4-F1	122.8	8	97.0	15.24	22.1	6.2	42.9
8	4-F2	122.8	8	93.6	14.70	22.0	5.5	37.7
8	6-F1	162.3	8	90.0	14.13	23.0	4.2	28.9
8	6-F2	162.3	8	89.6	14.08	23.5	4.9	34.0
8	8-F1	199.7	8	92.8	14.57	21.2	4.8	33.0
8	8-F2	199.7	8	89.0	13.98	26.0	4.2	28.7
8	10-F1	257.7	8	88.5	13.90	23.4	4.5	31.3
8	10-F2	257.7	8	87.0	13.67	21.6	4.3	29.7
8	0-F1	0.0	16	98.1	15.41	17.5	5.3	36.4
8	0-F2	0.0	16	96.3	15.12	21.0	5.6	38.5
8	2-F1	81.5	16	93.6	14.70	19.0	2.4	16.2
8	2-F2	81.5	16	95.7	15.03	18.0	4.4	30.3
8	4-F1	122.8	16	97.8	15.36	21.8	6.3	43.1
8	4-F2	122.8	16	97.4	15.30	19.0	6.9	47.7
8	6-F1	162.3	16	92.5	14.53	24.2	2.7	18.5
8	6-F2	162.3	16	93.7	14.71	20.3	5.4	37.0
8	8-F1	199.7	16	93.0	14.61	23.0	6.6	45.3
8	8-F2	199.7	16	96.6	15.17	21.6	3.7	25.3

ACKNOWLEDGEMENTS

I would like to express my deeply grateful to my major professor Dr. David White for providing me with the opportunity that allowed me to pursue a Master of Science degree and learn from his expansive knowledge of geotechnical engineering. He constantly gave me creative ideas, supports, and guidance in the past two years. I would also like to thank Dr. David White and Caterpillar Inc. for providing the financial support and sponsoring the research project.

I would like to express my grateful to my committee member Dr. Shauna Hallmark for providing suggestions and improving my thesis. I would especially like to thank my committee member Dr. Pavana Vennapusa for providing me technical supports and trainings. I would also like to thank Dr. Christianna White for her patience and time she spent for improving my academic writing and communication skills.

Lastly, I would like to express my deepest love and grateful to my loving family, girlfriend, and dear friends for their supports and motivations throughout my study.